METALS. SUPERCONDUCTORS

EPR study of exchange interactions in the nonmagnetic Kondo system $La_{1-x}Ce_xCu_6$

T. S. Al'tshuler and S. G. L'vov

E. K. Zavoĭskiĭ Physicotechnical Institute, Russian Academy of Sciences, 420029 Kazan, Russia

M. S. Bresler

A. F. Ioffe Physicotechnical Institute, Russian Academy of Sciences, 194021 St. Petersburg, Russia

(Submitted October 22, 1997)
Fiz. Tverd. Tela (St. Petersburg) **40**, 593–599 (April 1998)

The EPR of paramagnetic impurities Gd^{3+} and Mn^{2+} was studied in nonmagnetic Kondo system $La_{1-x}Ce_xCu_6$ containing in the 1.6–200 K range. The exchange interaction parameters of gadolinium and manganese ions with conduction electrons, of cerium ions with conduction electrons and with one another, the Kondo temperature of cerium ions, and the temperature behavior of cerium-ion spin-fluctuation rate have been determined. A pseudogap in the density of states at the Fermi level has been detected in the $CeCu_6$ regular system, which is apparently due to s-f hybridization. This pseudogap can be destroyed by introducing an aluminum impurity, which induces strong conduction-electron scattering. It was also found that RKKY interaction among manganese ions in $CeCu_{6-y}Mn_y$ is considerably stronger than it is in $LaCu_{6-y}Mn_y$, which implies enhancement of nonlocal spin susceptibility due to an f band contribution to conduction-electron states. [S1063-7834(98)00104-X]

In the early stages of investigation of concentrated Kondo systems it was believed that the formation of a heavy-fermion band is a result of Kondo centers having translational symmetry, while RKKY-type exchange interactions between f electrons interfere with it by depressing Kondo fluctuations. Recent theoretical studies (c.f., Ref. 1) and the existence of heavy-fermion systems with a magnetic ground state show, however, that this concept is only a crude simplification, and that exchange interaction among Kondo ions apparently plays an active part in the formation of heavy-fermion liquid. In view of these ideas, the traditional condition $T_{\mathrm{RKKY}} \ll T_K$ for the existence of a nonmagnetic Kondo lattice appears too stringent. It would be useful, therefore, to know the scale of the RKKY exchange, in order to be able to compare it with Kondo energy.

EPR is a particularly convenient method to study exchange interaction parameters. Kondo fluctuations make direct observation of the EPR signal produced by spins of Kondo centers impossible because of the large resonance-line width. Therefore as a spin probe one conventionally uses a small amount of a dopant having a localized magnetic moment (gadolinium, manganese). The spin of the probe interacts with the surrounding electrons. The effect of this coupling on the EPR resonant-absorption line provides information on the density of states in the conduction band and cerium-ion spin fluctuation rate and permits one to estimate the parameters of various exchange interactions. This method was used, in particular, to study such compounds as $Y_{1-x-y}Ce_xGd_yAl_2$ (Ref. 2), $Ce_{1-y}Gd_yCu_2Si_2$, $Ce_{1-y}Gd_yAl_3$ (Ref. 3), and $La_{1-x-y}Ce_xGd_yInCu_2$ (Ref. 4).

This work makes use of EPR to study the Kondo system $La_{1-x}Ce_xCu_6$, containing a small amount (of the order of one per cent) of gadolinium and manganese as a spin probe.

1. EXPERIMENT

Polycrystalline samples of $La_{1-y}Gd_yCu_6$, $Ce_{1-y}Gd_yCu_6$ ($y=0.02$; 0.05); $La_{1-x}Ce_xCu_{6-y}Mn_y$ ($x=0$; 0.005; 0.02; 1; $y=0.02$; 0.05; 0.14); and $CeCu_{6-y-z}Mn_yAl_z$ ($y=0.02$; $z=0.02$; 0.1) were prepared in an induction furnace in a pure helium ambient. The purity of the starting components was 99.90 wt. %. The crucibles were made of molybdenum. X-ray diffraction showed all samples to be single phase and have orthorhombic structure[5] with lattice constants $a=8.11$ Å, $b=5.10$ Å, and $c=10.17$ Å. The volume per lattice site was $v_0=15.02$ Å^3. Small concentrations of gadolinium and manganese served as probes. EPR measurements were performed with a B-ER 418S radiospectrometer at a frequency of 9400 MHz within the 1.6–200 K temperature range. Samples doped both with gadolinium and manganese exhibited a single EPR line. The EPR line had an asymmetric shape typical of bulk metals and represented a sum of equally weighted dispersion and absorption Lorentzians ($\chi' + \chi''$). The signal/noise ratio was not less than 100.

Figure 1 presents the temperature dependence of the gadolinium EPR linewidth $\Delta H(T)$ for $La_{1-y}Gd_yCu_6$ and $Ce_{1-y}Gd_yCu_6$ with $y=0.02$. $La_{0.98}Gd_{0.02}Cu_6$ exhibits a linear relation typical of normal metals. When all La^{3+} ions are replaced by Ce^{3+}, the Gd^{3+} EPR linewidth increases, the $\Delta H(T)$ relation becomes nonlinear, and its initial slope $\delta(\Delta H)/\delta T$ increases.

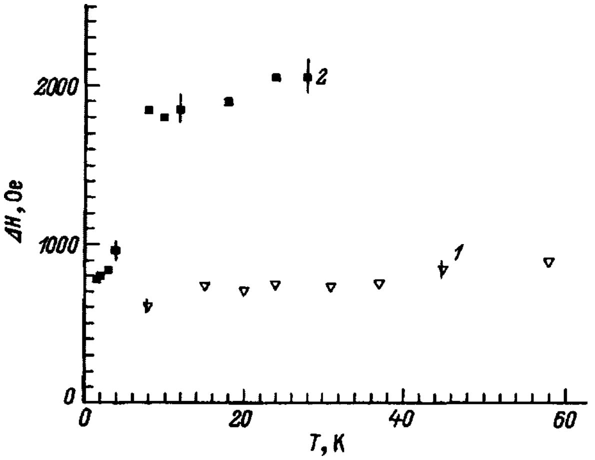

FIG. 1. Temperature dependence of Gd^{3+} EPR linewidth in (*1*) $La_{1-y}Gd_yCu_6$ and (*2*) $Ce_{1-y}Gd_yCu_6$ for $y=0.02$.

Shown in Fig. 2 is the temperature dependence of the Gd^{3+} EPR g factor for the above compounds. The error in measuring the position of the resonance line is determined by its width. In connection with this, the observed large widths of the resonance line, which grow as lanthanum ions are replaced by cerium ions, result in considerable errors in determining g. Nevertheless, the experimental data displayed in Fig. 2 permit a conclusion that the Gd^{3+} EPR g factor for $La_{1-y}Gd_yCu_6$ is constant within the temperature range studied and is 1.97 ± 0.02. With all La^{3+} ions substituted for by Ce^{3+} ions, the g factor depends in a complicated way on temperature; indeed, its initial increase is followed by subsequent (for $T<4$ K) decrease. This behavior (for $T<4$ K) is due to the low-temperature ordering of gadolinium ion spins. In our subsequent interpretation of the experimental results we are going to limit ourselves to the temperature region $T>4$ K, where the effect of ordering on Gd^{3+} EPR is insignificant compared to other mechanisms considered in this work.

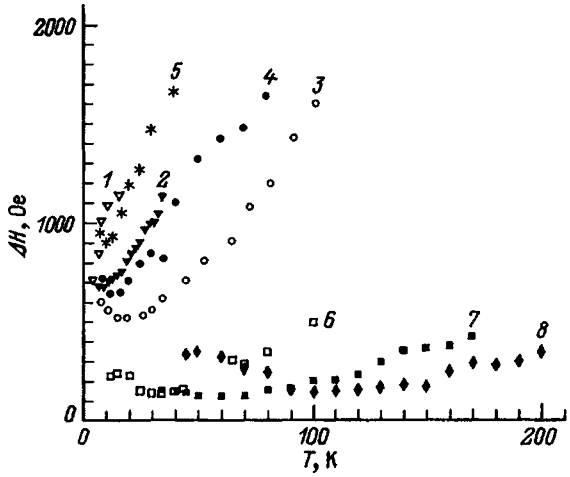

FIG. 3. Temperature dependence of Mn^{2+} EPR linewidth in $La_{1-x}Ce_xCu_{6-y}Mn_y$ for $x=0$ and (*1*) $y=0.02$, (*2*) $y=0.05$, (*3*) $y=0.14$; (*4*) $x=0.005, y=0.14$; (*5*) $x=0.02, y=0.14$; and for $x=1$ and (*6*) $y=0.02$, (*7*) $y=0.05$, (*8*) $y=0.14$.

Figure 3 presents the temperature behavior of manganese EPR linewidth for $La_{1-x}Ce_xCu_{6-y}Mn_y$. For $x=0$, as well as for low cerium contents ($x=0.02$), one observes a linear $\Delta H(T)$ relation, as for Gd^{3+} EPR in $La_{1-y}Gd_yCu_6$. The high-temperature slope of this relation decreases continually with increasing manganese content and increases when cerium is injected into the sample. At low temperatures, ΔH of the Mn^{2+} line passes through a minimum. For $x\geqslant0.1$, the EPR signal broadens considerably, to become unobservable in the temperature region chosen. At high ($0.8\leqslant x\leqslant1$) cerium contents, however, the Mn^{2+} EPR signal is narrow and strong. The position and width of the Mn^{2+} EPR line practically did not change with x in this cerium concentration range at any fixed temperature. For high x, the temperature dependence of linewidth coincided qualitatively with the behavior of $\Delta H(T)$ observed at low cerium contents, but its high-temperature slope, $\delta(\Delta H)/\delta T=6$ Oe/K for $y=0.02$, in $CeCu_6$ is substantially smaller than that for $LaCu_6$ (≈40 Oe/K). It decreases weakly with increasing Mn content.

Figure 4 presents the temperature dependence of the

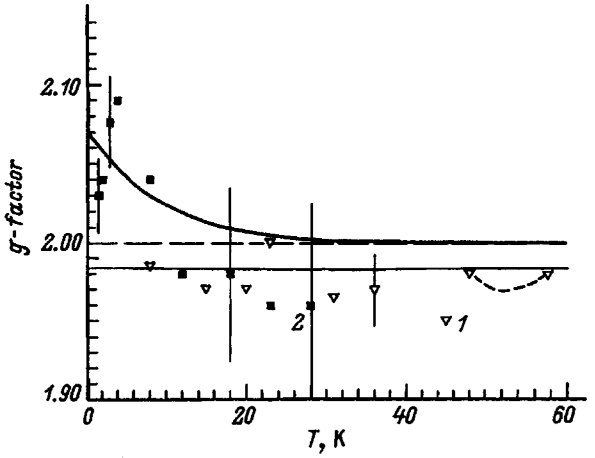

FIG. 2. Temperature dependence of Gd^{3+} EPR g factor in (*1*) $La_{1-y}Gd_yCu_6$ and (*2*) $Ce_{1-y}Gd_yCu_6$ for $y=0.02$.

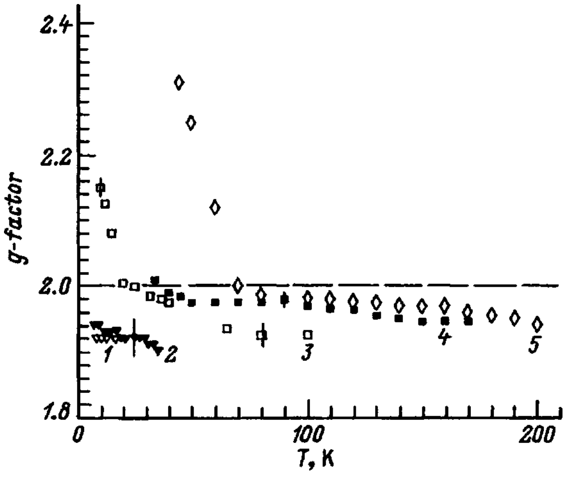

FIG. 4. Temperature dependence of Mn^{2+} EPR g factor in $La_{1-x}Ce_xCu_{6-y}Mn_y$ for $x=0$ and (*1*) $y=0.02$, (*2*) $y=0.05$; and for $x=1$ and (*3*) $y=0.02$, (*4*) $y=0.05$, (*5*) $y=0.14$.

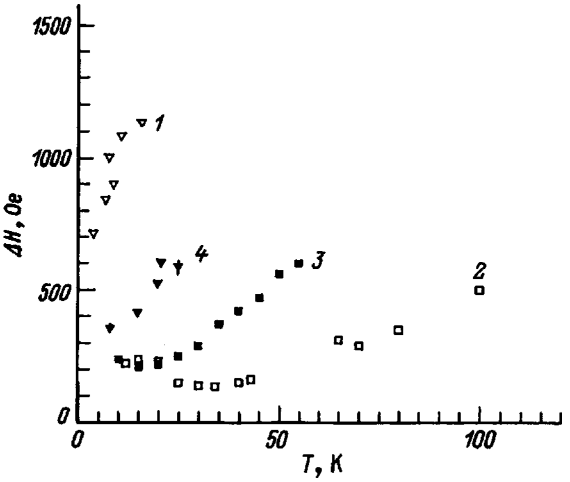

FIG. 5. Temperature dependence of Mn^{2+} EPR linewidth in $La_{1-x}Ce_xCu_{6-y}Mn_y$ for (*1*) $x=0, y=0.02$; (*2*) $x=1, y=0.02$, and in $CeCu_{6-y-z}Mn_yAl_z$ for $y=0.02$ and (*3*) $z=0.02$, (*4*) $z=0.1$.

Mn^{2+} EPR g factor in $La_{1-x}Ce_xCu_{6-y}Mn_y$. For low cerium contents ($x\leqslant 0.02$), g does not depend on temperature and concentrations x and y within experimental error, and is 1.92 ± 0.03. At $x=1$, in the low-temperature domain, the Mn^{2+} EPR line broadens considerably, and its g factor increases relative to its value for small x (see Fig. 4). The $\Delta H(T)$ relation for $CeCu_{6-y}Mn_y$ reaches here a minimum (Fig. 3), with the minimum in the Mn^{2+} EPR linewidth for $CeCu_6$ lying at substantially higher temperatures ($\theta_{Ce}\approx 60$ K for $y=0.05$) than that for $LaCu_{6-y}Mn_y$ ($\theta_{La}\approx 10$ K).

Figure 5 shows the temperature dependence of the Mn^{2+} EPR linewidth $\Delta H(T)$ for $CeCu_{6-y-z}Mn_yAl_z$ ($z\leqslant 0.1$). The high-temperature slope $\delta[\Delta H(T)]/\delta T$ grows continually with increasing substitution of aluminum ions z for copper [$\delta(\Delta H)/\delta T=6$ Oe/K for $z=0$ but 23 Oe/K for $z=0.1$].

The temperature dependence of the Mn^{2+} EPR g factor for this compound is shown in Fig. 6. Doping $CeCu_{6-y}Mn_y$ with a small amount of Al does not affect qualitatively the behavior of g, but the temperatures ($\theta\approx 20$ K for $z=0.1$, $y=0.02$) at which it is observed to shift relative to its value for $LaCu_{6-y}Mn_y$ are lower than those for $CeCu_{6-y}Mn_y$ ($\theta\approx 40$ K for $y=0.02$).

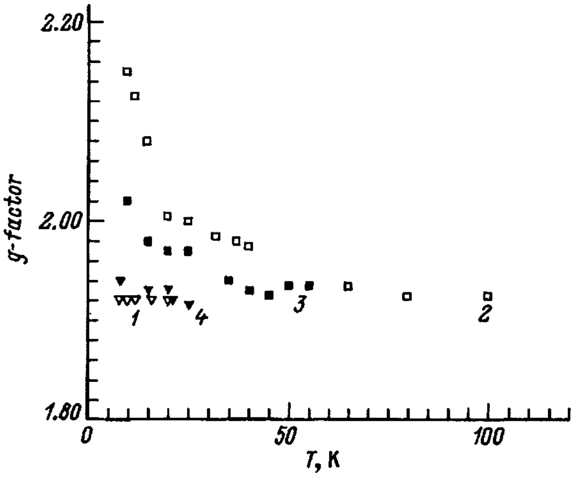

FIG. 6. Temperature dependence of Mn^{2+} EPR g factor in $La_{1-x}Ce_xCu_{6-y}Mn_y$ for (*1*) $x=0, y=0.02$; (*2*) $x=1, y=0.02$, and in $CeCu_{6-y-z}Mn_yAl_z$ for $y=0.02$ and (*3*) $z=0.02$ and (*4*) $z=0.1$.

2. DISCUSSION OF RESULTS

The Gd^{3+} EPR results for $La_{1-y}Gd_yCu_6$ and $Ce_{1-y}Gd_yCu_6$ are qualitatively similar to those obtained for Gd^{3+} in the systems $Y_{1-x-y}Ce_xGd_yAl_2$ (Ref. 2), $Ce_{1-y}Gd_yCu_2Si_2$ and $Ce_{1-y}Gd_yAl_3$ (Ref. 3), and $La_{1-x-y}Ce_xGd_yInCu_2$ (Ref. 4) and can be interpreted within the same concepts. In $La_{1-y}Gd_yCu_6$, where no Kondo impurities are present, the temperature dependence of the EPR linewidth (Fig. 1) is described by the relation typical of normal metals

$$\Delta H=a+bT. \tag{1}$$

The constant contribution $a\approx 600$ Oe is determined by fine-structure effects and dipole-dipole interactions between gadolinium ions. The part of the linewidth which depends linearly on temperature originates from exchange interaction of the gadolinium ion spin with thermal fluctuations in the conduction-electron spin density (Korringa relaxation). The expression for the temperature slope b depends on how close the system is to the electron bottleneck regime[6]. This regime comes into play when the rate of spin-lattice relaxation of conduction electrons δ_{eL} is small compared to that of Overhauser relaxation $\delta_{eGd}\sim y$ caused by their backscattering from gadolinium spins. In this case the Korringa relaxation does not fully manifest itself, and constant b starts to depend on the relative magnitude of the Overhauser and spin-lattice relaxation of conduction electrons.

We established that the high-temperature slope $\delta(\Delta H)/\delta T$ practically does not change with increasing gadolinium concentration (up to $y=0.05$) in $La_{1-y}Gd_yCu_6$. This warrants a conclusion that the $La_{1-y}Gd_yCu_6$ system (with $y=0.02$) is far from the electron bottleneck point, and that the temperature dependence of the linewidth is determined solely by the Korringa relaxation of gadolinium ions. Presenting the Hamiltonian of s-f exchange interaction of the conduction-electron spin $\mathbf{S}_e$ with the impurity moment $\mathbf{J}$ in the form

$$H^{sf}=-\Gamma^{sf}_{Gd}\mathbf{J}_{Gd}\mathbf{S}_e, \tag{2}$$

we shall have for the constant b

$$b=b_0=\pi k_b\{\Gamma^{sf}_{Gd}N(\varepsilon_F)\}^2/g_{Gd}\mu_B. \tag{3}$$

Here Γ^{sf}_{Gd} is the integral describing exchange interaction of the conduction-electron spin with the impurity moment, $N(\varepsilon_F)$ is the density of states of conduction electrons per atom and per spin direction. The experimental value $b=7\pm 2$ Oe/K permits us to find the product $|\Gamma^{sf}_{Gd}N(\varepsilon_F)|=0.017\pm 0.004$. The sign of the exchange integral can be determined from the Knight electronic shift

$$\Delta g_N=\Gamma^{sf}_{Gd}N(\varepsilon_F). \tag{4}$$

The large error of resonance-line position measurement does not permit one to determine with a high accuracy the gadolinium EPR g factor. At any rate the shift of g relative to the value $g_0 = 2.00$ (the dashed line in Fig. 2) characteristic of the free gadolinium ion is negative, $\Delta g_{\exp} = -0.03 \pm 0.02$. It thus follows that the exchange integral for gadolinium has an antiferromagnetic character: $\Gamma^{sf}_{\mathrm{Gd}} < 0$. The experimental value of the conduction-band density of states at the Fermi level in $\mathrm{LaCu_6}$ derived[7] from electronic heat capacity measurements is $N(\varepsilon_F) = 0.24$ $(\mathrm{eV} \cdot \mathrm{spin} \cdot \mathrm{atom})^{-1}$. Knowing the value of $\Gamma^{sf}_{\mathrm{Gd}} N(\varepsilon_F)$, we come to $\Gamma^{sf}_{\mathrm{Gd}} \approx -0.07$ eV.

The main source of Gd^{3+} EPR line broadening in the $\mathrm{Ce}_{1-y}\mathrm{Gd}_y\mathrm{Cu}_6$ Kondo system compared to the $\mathrm{La}_{1-y}\mathrm{Gd}_y\mathrm{Cu}_6$ matrix is the indirect exchange interaction of Ce and Gd ions mediated by conduction electrons

$$H^{ex}_{\text{Ce-Gd}} = -\sum_j \Gamma^{ex}_{ij} \mathbf{J}^i_{\mathrm{Gd}} \mathbf{J}_{\mathrm{Ce}}. \tag{5}$$

In the RKKY model the exchange integral can be written

$$\Gamma^{ex}_{ij} = \Gamma^0_{\text{Ce-Gd}} v_0 \cos(2k_F r_{ij})/r^3_{ij}, \tag{6}$$

where v_0 is the volume per lattice site, k_F is the Fermi momentum, and the constant

$$\Gamma^0_{\text{Ce-Gd}} = \Gamma^{sf}_{\mathrm{Ce}} \Gamma^{sf}_{\mathrm{Gd}} N(\varepsilon_F)/8\pi. \tag{7}$$

The contribution of interaction (5) to gadolinium EPR linewidth comes from relaxation of the Gd^{3+} moment by spin fluctuations of the Ce ion. It can be written[2]

$$\Delta H_{fl} = A T \chi_{\mathrm{Ce}}(\Gamma^{(1)}_7)\tau, \tag{8}$$

where

$$A = 2k_B (g_{\mathrm{Ce}} - 1)^2 \sum_j (\Gamma^{ex}_{ij})^2 / g_{\mathrm{Gd}} g^2_{\mathrm{Ce}} \mu^3_B \hbar,$$

and $\chi_{\mathrm{Ce}}(\Gamma^{(1)}_7)$ is the static magnetic susceptibility of the cerium-ion ground state in the crystal field, which is a doubly degenerate Kramers level $\Gamma^{(1)}_7$. The quantity τ in Eq. (8) is the spin-fluctuation time of the cerium Kondo impurity. The dependence of the ΔH_{fl} contribution on temperature is determined by the temperature behavior of $\chi_{\mathrm{Ce}}(\Gamma^{(1)}_7)$ and of the $\tau(T)$ parameter of interest to us.

Besides the broadening of the Gd^{3+} EPR line, interaction (5) brings about its shift. This is due to the appearance in an external field of a nonzero polarization of cerium moments $\langle J^z_{\mathrm{Ce}} \rangle$, which is proportional to the magnetic susceptibility of cerium and creates a static exchange field at the gadolinium ion occupying the ith site on the cerium sublattice:

$$H^i = -\langle J^z_{\mathrm{Ce}} \rangle \sum_j \Gamma^{ex}_{ij}/2\mu_B. \tag{9}$$

Since in the regular $\mathrm{CeCu_6}$ system any two sites on the cerium sublattice are equivalent, the resonance-frequency shift associated with (8) does not have spatial dispersion and, while not producing additional inhomogeneous broadening of the Gd^{3+} EPR line of the type discussed in Ref. 8, shifts the g factor with respect to its value for $\mathrm{La}_{1-y}\mathrm{Gd}_y\mathrm{Cu}_6$ (Ref. 2):

$$\Delta g = \chi_{\mathrm{Ce}} \sum_j \Gamma^{ex}_{ij}/g^2_{\mathrm{Ce}} \mu^2_B. \tag{10}$$

The shift Δg is proportional to the static magnetic susceptibility $\chi_{\mathrm{Ce}}(T)$ of the cerium ion in $\mathrm{CeCu_6}$.

We thus obtain the following final equation for the temperature dependence of the Gd^{3+} EPR linewidth in $\mathrm{Ce}_{1-y}\mathrm{Gd}_y\mathrm{Cu}_6$:

$$\Delta H(T) = a + b_0 T + \Delta H_{fl}(T), \tag{11}$$

where the quantities b_0 and $\Delta H_{fl}(T)$ are defined by Eqs. (3) and (8), respectively. This equation can be used to estimate the spin fluctuation time τ of the cerium ion.

The temperature dependence of the static magnetic susceptibility of cerium ions, $\chi_{\mathrm{Ce}}(T)$, was found experimentally[5] as the difference between the magnetic susceptibilities of $\mathrm{CeCu_6}$ and of the matrix $\mathrm{LaCu_6}$. It was dominated by Stark splitting of the $J = 5/2$ state of the cerium ion in the orthorhombic crystal field into three doublets $\Gamma^{(1,2,3)}_7$ [the excited doublets $\Gamma^{(2)}_7$ and $\Gamma^{(3)}_7$ are separated from the ground-state doublet $\Gamma^{(1)}_7$ by energy gaps $\Delta^{(1,2)} \approx 60$ K and $\Delta^{(1,3)} \approx 120$ K, respectively (Ref. 5)], as well as by Kondo screening of the cerium ion spins. For $T \leqslant 100$ K, the temperature behavior of cerium-ion susceptibility is fitted well by the relation

$$\chi_{\mathrm{Ce}}(T) = C/(T + \theta), \tag{12}$$

where $C = 0.77 \pm 0.02$ CGSM units·K/mole Ce, and $\theta = 10 \pm 1$ K.

The static magnetic susceptibility of the cerium-ion ground state $\Gamma^{(1)}_7$ entering Eq. (8) is given by the expression

$$\chi_{\mathrm{Ce}}(\Gamma^{(1)}_7) = C^{(1)}/(T + \theta^{(1)}). \tag{13}$$

For temperatures ($T \leqslant 10$ K) substantially lower than the energy gap $\Delta^{(1,2)} \approx 60$ K, the susceptibility of the cerium ion is dominated by the Kramers doublet $\Gamma^{(1)}_7$. Therefore, in this temperature domain $\chi_{\mathrm{Ce}} \approx \chi_{\mathrm{Ce}}(\Gamma^{(1)}_7)$. Accepting this assumption, a comparison of Eq. (13) with $\chi_{\mathrm{Ce}}(T)$ measurements[5] yields $C^{(1)} = 0.77 \pm 0.02$ CGSM units·K/mole Ce, and $\theta^{(1)} = 10 \pm 1$ K.

The unknown in Eq. (11) is the parameter $\Sigma_j (\Gamma^{ex}_{ij})^2$, which is proportional to the square of the exchange integral $\Gamma^{sf}_{\mathrm{Ce}}$ of the cerium moment with the conduction-electron spin. We shall estimate it later using Mn^{2+} EPR data obtained for the $\mathrm{La}_{1-x}\mathrm{Ce}_x\mathrm{Cu}_{6-y}\mathrm{Mn}_y$ system. After this, having made an estimate of the above lattice sum, we will be able to determine from Eq. (11) the Ce^{3+} spin fluctuation rate in $\mathrm{Ce}_{1-y}\mathrm{Gd}_y\mathrm{Cu}_6$.

Let us turn now to Mn^{2+} EPR data for the $\mathrm{La}_{1-x}\mathrm{Ce}_x\mathrm{Cu}_{6-y}\mathrm{Mn}_y$ system (Fig. 3). The increase of the high- temperature slope $b = \delta(\Delta H)/\delta T$ with decreasing manganese impurity-probe content and increasing cerium content x, which acts as conduction-electron scatterer, indicates that the system is in the electron-bottleneck regime. In this case[6]

$$b^{-1}(x,y) = b_0^{-1} \left(\frac{\delta_{e\mathrm{Mn}}}{\delta_{eL} + \delta_{e\mathrm{Ce}}} + 1 \right), \tag{14}$$

where δ_{eL} is the spin-lattice relaxation rate for conduction electrons, and $\delta_{e\mathrm{Mn}}$ and $\delta_{e\mathrm{Ce}}$ are the Overhauser spin relaxation rates of conduction electrons caused by their scattering from magnetic moments of the Mn and Ce impurity ions, respectively. The Overhauser relaxation of conduction-electron spins by type *i* magnetic impurities (Mn, Ce) in the $La_{1-x}Ce_xCu_{6-y}Mn_y$ system can be written[6]

$$\delta_{ei}=\frac{2\pi}{21\hbar}(\Gamma_i^{sf})^2N(\varepsilon_F)J_i(J_i+1)c_i, \tag{15}$$

where c_i is the magnetic impurity concentration ($c_{\mathrm{Ce}}=x, c_{\mathrm{Mn}}=y$), and J_i is the total moment of the given impurity.

For $x=0$, spin-lattice relaxation of conduction electrons by their spin scattering from cerium ions does not exist in $La_{1-x}Ce_xCu_{6-y}Mn_y$, i.e., $\delta_{e\mathrm{Ce}}=0$. As the concentration of Mn^{2+} ions increases, the rate of the reverse relaxation of conduction-electron spins by the ion moments increases, $\delta_{e\mathrm{Mn}}\sim y$, and therefore $b(0,y)$, according to Eq. (14), decreases continually. The experimental values of the high-temperature slope $\delta(\Delta H)/\delta T=b$ of the Mn^{2+} EPR linewidth in $La_{1-x}Gd_xCu_{6-y}Mn_y$ can be fitted by the following relation as a function of manganese concentration:

$$b^{-1}(0,y)=0.012(\mathrm{K/Oe})+0.67y(\mathrm{K/Oe}). \tag{16}$$

A comparison of this relation with Eq. (14) yields $b_0=80$ Oe/K. Recalling Eqs. (3) and (15), we come to $|\Gamma_{\mathrm{Mn}}^{sf}|=0.24$ eV, $\delta_{e\mathrm{Mn}}(y)=0.55\times10^{14}y\ \mathrm{s}^{-1}$, $\delta_{eL}=1.0\times10^{12}\ \mathrm{s}^{-1}$.

Adding a small concentration of cerium into the sample increases the spin-lattice relaxation rate of conduction electrons through the appearance of an additional channel for their spin relaxation with a rate $\delta_{e\mathrm{Ce}}\sim x$. This results, for a given manganese concentration y_0, in a continuous increase of $b(x,y_0)$ with cerium content x in the system. The experimental values of the high-temperature slopes $b(x,0.14)$ for $La_{1-x}Ce_xCu_{6-y}Mn_y$ ($y_0=0.14$), as a function of cerium concentration ($x\leqslant0.05$), fit onto the relation

$$b/(b_0-b)=0.13+23.1x. \tag{17}$$

Equation (14) yields now $\delta_{e\mathrm{Ce}}(x)=1.79\times10^{14}x\ \mathrm{s}^{-1}$, whence, using Eq. (15), one comes to $|\Gamma_{\mathrm{Ce}}^{sf}|=0.4$ eV. When operating in the electron-bottleneck conditions, the shift of the Mn^{2+} EPR g factor relative to its magnitude for a free manganese ion, $g_0=2.00$, also depends on the ratio of the Overhauser and spin-lattice relaxation rates[6]:

$$\Delta g=\left(\frac{\delta_{e\mathrm{Mn}}}{\delta_{eL}+\delta_{e\mathrm{Ce}}}+1\right)^2\Delta g_N. \tag{18}$$

Since the experimental value of this g shift is negative, $\Delta g_{\mathrm{exp}}=-0.08\pm0.03$, we have $\Delta g_N<0$. Recalling Eq. (4), we come to a conclusion that the exchange integral for manganese has an antiferromagnetic character: $\Gamma_{\mathrm{Mn}}^{sf}<0$.

For $x\geqslant0.1$, no Mn^{2+} EPR signal is observed in $La_{1-x}Ce_xCu_{6-y}Mn_y$, because suppression by Ce^{3+} ions of the electron bottleneck broadens considerably the EPR linewidth. Therefore observation of a narrow Mn^{2+} EPR signal in the regular $CeCu_{6-y}Mn_y$ system (Fig. 3) was quite unexpected. The linewidth and its high-temperature slope $\delta(\Delta H)/\delta T$ (≈6 Oe/K for $y=0.02$) are substantially smaller than those for $LaCu_{6-y}Mn_y$ (≈40 Oe/K). Such a decrease in slope $b=\delta(\Delta H)/\delta T$ was observed[9,10] to occur in regular mixed-valence Ce systems $Ce_{1-x}La_xOs_2$ and $Ce_{1-x}La_xPd_3$. It was attributed[9,10] to the existence of a pseudogap in the density of states of conduction electrons at the Fermi level. Our Mn^{2+} EPR data suggest the existence of a similar pseudogap, possibly of hybridization origin, at lattice sites occupied by manganese ions. It is known that Al^{3+} ions destroy the Kondo lattice coherence and, therefore, they should destroy this pseudogap. Indeed, doping the $Ce_{1-y}Gd_yCu_6$ system lightly with aluminum increases the high-temperature slope $b\sim N(\varepsilon_F)$ ($b=23$ Oe/K for $z=0.1$, $y=0.02$ in $CeCu_{6-y-z}Mn_yAl_z$ (Fig. 5).

The main result of our Mn^{2+} EPR measurements on $CeCu_{6-y}Mn_y$ is that the broadening and shift of the magnetic resonance line indicating magnetic ordering of Mn^{2+} moments in this compound are observed at a substantially higher temperature ($\theta_{\mathrm{Ce}}\approx60$ K for $y=0.05$) than those in $LaCu_{6-y}Mn_y$ [$\theta_{\mathrm{La}}\approx10$ K (see Figs. 3 and 4)]. The small residual width and high magnetic ordering temperature imply enhanced RKKY interaction between Mn^{2+} moments in $CeCu_{6-y}Mn_y$ compared to $LaCu_{6-y}Mn_y$. This enhancement of nonlocal spin susceptibility of conduction electrons is apparently a consequence of the fine structure in conduction-band density of states at Fermi level originating from s-f hybridization.

The disappearance of the gap in the conduction-band density of states at the Fermi level observed when aluminum is injected into $CeCu_{6-y}Mn_y$ results in a weakening of RKKY exchange between manganese ions. This manifests itself in a shift of the magnetic ordering point of Mn^{2+} moments in $CeCu_{6-y-z}Mn_yAl_z$ ($\theta\approx20$ K for $y=0.02$, $z=0.02$) compared to $CeCu_{6-y}Mn_y$ ($\theta\approx40$ K for $y=0.02$) (see Figs. 5 and 6).

Let us estimate now the spin fluctuation time of the Ce^{3+} ion in $Ce_{1-y}Gd_yCu_6$, for which purpose Eq. (11) can be used. The unknown in this equation is the parameter $\Sigma_j(\Gamma_{ij}^{ex})^2$. On having estimated in Eq. (6) the Fermi momentum k_F in the free-electron approximation and calculated the corresponding lattice sums, we recall Eq. (7) and our previous estimates of $|\Gamma_{\mathrm{Ce}}^{sf}|$ and $|\Gamma_{\mathrm{Gd}}^{sf}|$ to obtain finally

$$\left|\sum_j \Gamma_{ij}^{ex}\right|=|\Gamma_{\text{Ce-Gd}}^0|\left|\sum_j v_0\cos(2k_Fr_{ij})/r_{ij}^3\right|\approx0.37\mathrm{K}, \tag{19}$$

$$\sum_j(\Gamma_{ij}^{ex})^2=(\Gamma_{\text{Ce-Gd}}^0)^2\left|\sum_j v_0^2\cos^2(2k_Fr_{ij})/r_{ij}^6\right|\approx0.9\mathrm{K}^2. \tag{20}$$

Since the experimental values of the Gd^{3+} EPR g factor shift $\Delta g(T)$ in $Ce_{1-y}Gd_yCu_6$ with respect to its value for $La_{1-y}Gd_yCu_6$ are positive (see Fig. 2), we obtain from Eq. (10) $\Sigma_j\Gamma_{ij}^{ex}>0$. The exchange integral $|\Gamma_{\text{Gd-Ce}}^0|\approx0.4$ K.

The temperature dependence of the Gd^{3+} EPR g factor obtained with the lattice sum estimated using Eq. (10), $\Sigma_j\Gamma_{ij}^{ex}>0$, and with experimental[5] values of the susceptibility $\chi_{\mathrm{Ce}}(T)$ [see Eq. (12)], is shown by a solid line in Fig. 2. This temperature dependence does not disagree with the corresponding experimental values of the Gd^{3+} EPR g factor for $Ce_{1-y}Gd_yCu_6$.

Although estimation of the parameter $\Sigma_j(\Gamma_{ij}^{ex})^2$ within the free-electron approximation has led us to results which

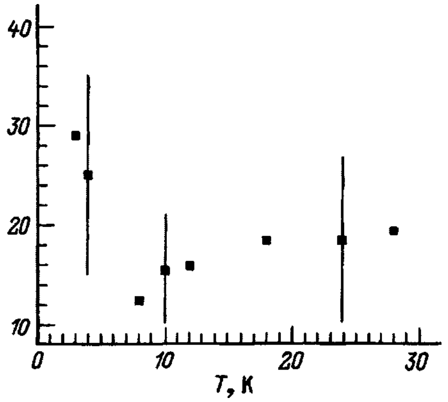

FIG. 7. Temperature dependence of cerium-ion spin fluctuation rate in $\text{Ce}_{1-y}\text{Gd}_y\text{Cu}_6$ for $y=0.02$.

agree semiquantitatively with experiment, the procedure employed to find this parameter cannot be considered satisfactory. Indeed, the fact that $\Sigma_j \cos(2k_F r_{ij})/r_{ij}^3<0$ implies that $\Gamma^0_{\text{Ce-Gd}}<0$ [see Eq. (6)], and, since $\Gamma^{sf}_{\text{Gd}}<0$, Eq. (7) yields $\Gamma^{sf}_{\text{Ce}}>0$. This result, however, is obviously at odds with the existence of the Kondo effect in the $\text{Ce}_{1-y}\text{Gd}_y\text{Cu}_6$ system, in other words, the exchange integral should have negative sign (antiferromagnetic interaction of cerium spins with conduction electrons).

The reason for this contradiction lies in the strongly oscillating character of the function $\cos(2k_F r_{ij})/r_{ij}^3$, as a result of which the estimate of the lattice sum should be very sensitive to the true form of the $\text{Ce}_{1-y}\text{Gd}_y\text{Cu}_6$ band structure, in particular, to the magnitude and anisotropy of k_F. Therefore the agreement with experiment obtained in terms of such a simple theory is to a certain extent accidental [although in order of magnitude the sum $\Sigma_j(\Gamma^{ex}_{ij})^2$ has certainly been estimated correctly], and the constants determined in this approach should be considered as parameters estimated empirically.

Having the values of the constants we need, the spin fluctuation rate can now be determined. Taking the experimental values of the Gd^{3+} EPR linewidth for $\text{Ce}_{1-y}\text{Gd}_y\text{Cu}_6$ and of susceptibility $\chi_{\text{Ce}}(T)$ for CeCu_6 (Ref. 5), we can use Eqs. (8), (11), and (13) to find the temperature dependence of the effective cerium-ion spin fluctuation rate τ^{-1} for the regular system $\text{Ce}_{1-y}\text{Gd}_y\text{Cu}_6$. Figure 7 presents the effective rate of cerium-ion spin fluctuations measured in units of temperature. The slight growth of $\tau^{-1}(T)$ in the high-temperature domain is due to the Korringa relaxation of local moments by thermal fluctuations of the conduction-electron spin density. As the temperature decreases, $\tau^{-1}(T)$ saturates because of the quantum Kondo fluctuations and tends to increasing with temperature approaching zero. The minimum value of the fluctuation rate, $\tau^{-1}\approx 13$ K, may serve as an estimate of the cerium-ion Kondo temperature in the $\text{Ce}_{1-y}\text{Gd}_y\text{Cu}_6$ alloy.

The temperature dependence of the Ce^{3+} spin-fluctuation rate calculated by us agrees with $\tau^{-1}(T)$ obtained[11] by NMR. In absolute magnitude, however, our values are smaller by at least a factor of 20. While the reason for this disagreement is unclear, it could be pointed out that our estimates of the fluctuation rate are substantially closer to the acceptable value[5] of the Kondo energy $T_K\approx 3$ K in CeCu_6.

Our estimates of the exchange integrals can be used to extract information on the RKKY interaction constant between the moments of nearest-neighbor Ce^{3+} ions in the CeCu_6 Kondo system: $\Gamma^{ex}_{\text{Ce-Ce}}=\Gamma^{ex}_{\text{Gd-Ce}}(\Gamma^{sf}_{\text{Ce}}/\Gamma^{sf}_{\text{Gd}})\approx -2.3$ K. The sign of this constant corresponds to the antiferromagnetic coupling between Ce^{3+} moments.

To conclude, our EPR study of the nonmagnetic Kondo system $\text{La}_{1-y}\text{Ce}_y\text{Cu}_6$ containing paramagnetic impurities Gd^{3+} and Mn^{2+} has yielded the exchange interaction parameters of gadolinium and manganese ions with conduction electrons and with one another, the Kondo temperature of cerium ions, and the temperature behavior of the cerium-ion spin fluctuation rate. A pseudogap in the density of states at the Fermi level has been found in the regular system CeCu_6, which is apparently due to s-f hybridization.

Support of the Russian Fund for Fundamental Research (Grant 97-02-16235) is gratefully acknowledged.

[1] P. Coleman and N. Andrei, J. Phys.: Condens. Matter **1**, 4057 (1989).

[2] M. Coldea, H. Schaeffer, V. Weissenberger, and B. Elschner, Z. Phys. B **68**, 25 (1987).

[3] M. Schlott, B. Elschner, M. Hermann, and W. Assmus, Z. Phys. B **72**, 385 (1988).

[4] S. A. Krivenko, A. G. Zenin, and G. G. Khaliullin, Zh. Éksp. Teor. Fiz. **100**, 1042 (1991) [Sov. Phys. JETP **73**, 576 (1991)].

[5] Y. Onuki, Y. Shimizu, M. Nishihara, Y. Machii, and T. Komatsubara, J. Phys. Soc. Jpn. **54**, 1964 (1985).

[6] S. E. Barnes, Adv. Phys. **30**, 801 (1981).

[7] A. Sumiyama, Y. Oda, A. Nagano, Y. Onuki, and T. Komatsubara, J. Phys. Soc. Jpn. **54**, 877 (1985).

[8] T. S. Al'tshuler, V. E. Kataev, and G. G. Khaliullin, Fiz. Tverd. Tela (Leningrad) **25**, 2154 (1983) [Sov. Phys. Solid State **25**, 1239 (1983)].

[9] M. Schlott, H. Schaeffer, and B. Elschner, Z. Phys. B **63**, 427 (1986).

[10] H. Schaeffer and B. Elschner, Z. Phys. B **53**, 109 (1983).

[11] T. Shimizu, M. Takigawa, H. Yasuoka, Y. Onuki, and T. Komatsubara, J. Phys. Soc. Jpn. **54**, 470 (1985).

Translated by G. Skrebtsov

Positron annihilation in polycrystalline metals

V. I. Grafutin, V. L. Grishkin, G. G. Myasishcheva, and Yu. V. Funtikov

Institute of Theoretical and Experimental Physics, Russian Academy of Sciences, 101000 Moscow, Russia

Yu. A. Novikov

Institute for General Physics, Russian Academy of Sciences, 117942 Moscow, Russia

(Submitted August 8, 1997; resubmitted November 18, 1997)
Fiz. Tverd. Tela (St. Petersburg) **40**, 600–602 (April 1998)

The empirical relation $\theta_p^6/I_p=aK$ (where θ_p is the limiting angle of the parabolic component in the angular distributions of annihilation photons in metals, I_p is the integrated contribution of this component, $K=1, 2, 3, \ldots$ is an integer, and a is a constant independent of the type of metal) observed earlier has been tested on magnesium, aluminum, copper, zinc, lead, and bismuth samples. The validity of this relation has been substantiated. The value of the dimensionless constant a has been determined and was found to coincide within experimental error with the result obtained in previous measurements. It is shown that the value of K for the same metal but for different samples may be different. It is conjectured that this may be due to different defect concentrations in samples. © *1998 American Institute of Physics.* [S1063-7834(98)00204-4]

Positron annihilation is presently enjoying wide use due to the simplicity of interpreting of the information it provides. For example, by measuring the angular distributions of annihilation photons one can determine the momentum distribution of electrons in a solid.[1,2] If the experiment is capable of detecting photons in parallel-slit geometry, the momentum density of electrons n_e is related to the angular distribution of annihilation photons $f(\theta)$ in the substance under study through

$$f(\theta)=A_\theta\int_{p_z-\frac{1}{2}\Delta p_z}^{p_z+\frac{1}{2}\Delta p_z}dp_z\int_{-\Delta p_y}^{+\Delta p_y}dp_y\int_{-\infty}^{+\infty}n_e(p_x,p_y,p_z)dp_x, \tag{1}$$

where A_θ is a normalization constant, Δp_y and Δp_z, the instrumental resolutions in electron momentum projections p_y and p_z, satisfy the conditions

$$\Delta p_y>>2p_{\max},\quad \Delta p_z<<p_{\max},$$

$p_{\max}$ is the maximum electron momentum in the substance, θ is the deviation of the annihilation photon escape angle from 180°

$$p_z=\theta mc,$$

m is the effective electron mass in the substance, and c is the velocity of light. Therefore the electron momentum density in an isotropic substance (z component) can be extracted from experimental data on the angular distributions of annihilation photons

$$n_e(p_z)=\frac{A_\theta}{\theta}\frac{df(\theta)}{d\theta}. \tag{2}$$

This can be illustrated most conveniently by considering positron annihilation in polycrystalline metals, where any anisotropy in electron distribution is absent (averaged out).

Electrons in metals[3] can be divided into two groups, viz. conduction (free) and core (bound) electrons.[3] Conduction electrons have the following momentum distribution

$$n_e(p)=\left[\exp\left(\frac{p^2/2m-\varepsilon_F}{k_BT}\right)+1\right]^{-1}, \tag{3}$$

where ε_F is the Fermi energy, k_B is the Boltzmann constant, and T is absolute temperature. At low temperatures this distribution is close in shape to rectangular. Therefore the angular distribution of annihilation photons $f(\theta)$ should contain a parabolic component

$$f_p(\theta)=\begin{cases}(3I_p/4\theta_p^3)(\theta_p^2-\theta^2), & \text{for } |\theta|\leq\theta_p\\ 0, & \text{for } |\theta|>\theta_p\end{cases}. \tag{4}$$

This is actually seen in the distributions obtained for all metals, even at room temperature. Figure 1 presents angular distributions of annihilation photons for some polycrystalline metals studied in this work. The dependence left after subtraction of the parabola, $f_g(\theta)$, is usually fitted quite well by a Gaussian

$$f_g(\theta)=(I_g/\sqrt{2\pi}\theta_g)\exp(-\theta^2/2\theta_g^2). \tag{5}$$

Therefore the angular distributions of annihilation photons in polycrystalline and amorphous metals are described by a sum of a parabola and a Gaussian

$$f(\theta)=f_p(\theta)+f_g(\theta).$$

Due to normalization

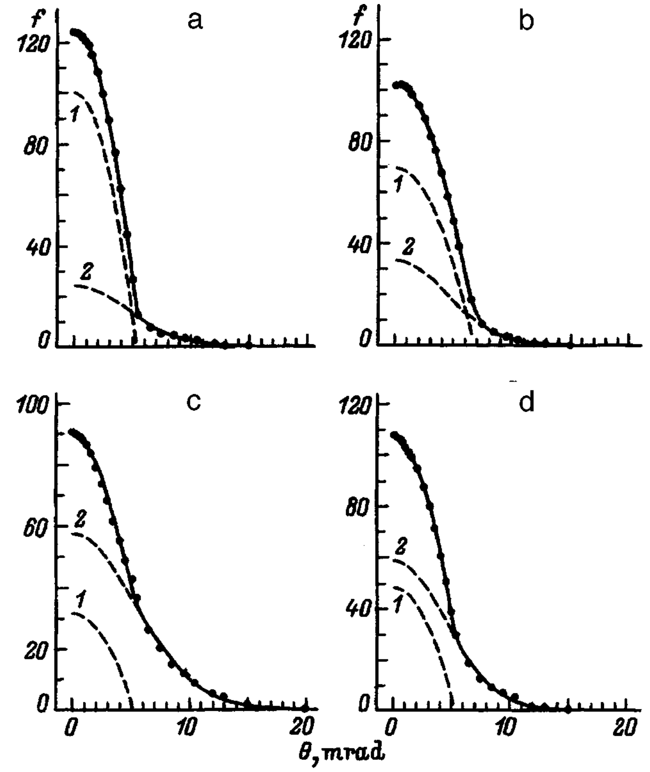

FIG. 1. Angular distributions of annihilation photons in samples of (a) magnesium, (b) aluminum, (c) copper, and (d) indium. The dashed lines show their deconvolution into a parabolic (*1*) and a Gaussian (*2*) component. The solid line is a sum of these components.

$$\int_{-\pi/2}^{\pi/2} f(\theta)d\theta=1$$

the condition

$$I_p+I_g=1\,,$$

relating the relative contributions of the parabolic and Gaussian components is met.

Using the parameter θ_p derived from experiment, one can obtain the Fermi momentum for a given metal, $p_F=\theta_p mc$, the Fermi energy

$$\varepsilon_F=\theta_p^2\frac{mc^2}{2}, \tag{6}$$

TABLE I. Specific number of free electrons Z_c and Fermi energies ε_F of the metals studied.

	Theory		Experiment	
Metal	Z_c	ϵ_F, eV	$Z_c\pm\Delta Z_c$	$\epsilon_F\pm\Delta\epsilon_F$, eV
Mg	2	7.12	2.107±0.012	7.37±0.03
Al	3	11.66	3.10±0.02 2.98±0.02(Ref. 4)	11.92±0.05 11.60±0.05(Ref. 4)
Cu	1	7.01	1.01±0.03 1.20±0.02(Ref. 4)	7.04±0.12 8.92±0.12(Ref. 4)
Zn	2	9.40	1.76±0.02	8.62±0.08
In	3	8.62	2.45±0.04	7.53±0.07
Sn	4	10.22	3.56±0.06	9.44±0.11
Pb	4	9.45	2.77±0.07	7.40±0.13
Bi	5	9.89	4.18±0.07	8.77±0.09

and the specific number of free electrons (number of conduction electrons per metal atom)

$$Z_c=\frac{8\pi}{3}\left(\frac{mc}{h}\right)^3\frac{A}{\rho N_A}\theta_p^3\,. \tag{7}$$

Here N_A is Avogadro's number, A is the mass number, ρ is the density of the substance, and h is Planck's constant.

It should be pointed out that the specific number of conduction electrons, according to current concepts, is determined by the number of the group of the periodic table, and the Fermi energy is a constant of a substance

$$\varepsilon_F=\frac{h^2}{8m}\left(\frac{3}{\pi}\frac{N_A}{A}\rho Z_c\right)^{2/3}. \tag{8}$$

Experiments showed, however, that the Fermi energy found from experiment differs strongly from its theoretical value (8). Besides, the specific number of conduction electrons varies from sample to sample. This is usually attributed to the fact that part of electrons (and positrons) are captured by defects in metals and, thus, do not contribute to the angular distributions of annihilation photons. This explanation appears reasonable and does not evoke any objections. Table I contains the values of Z_c and ε_F for the metals studied in this work.

TABLE II. Parameters of deconvolution of the annihilation-photon angular distributions of the studied metals into a parabolic and a Gaussian component.

	Parabola		Gaussian	
Metal	θ_p, mrad	I_p, %	θ_g, mrad	I_g, %
Mg	5.370±0.010	71.7±0.5	4.63±0.05	28.0±0.5
Al	6.830±0.015 6.738±0.015(Ref. 4)	62.9±1.3 85.1±0.6(Ref. 4)	4.36±0.05 6.4±0.4(Ref. 4)	36.6±1.3 14.9±2.4(Ref. 4)
Cu	5.25±0.04 5.566±0.025(Ref. 4)	22.0±0.8 38.4±0.9(Ref. 4)	5.36±0.04 6.31±0.16(Ref. 4)	77.2±0.8 59±5(Ref. 4)
Zn	5.81±0.03	34.0±1.3	4.64±0.04	65.7±1.3
In	5.43±0.03	34.7±0.9	4.43±0.03	65.0±0.9
Sn	6.08±0.03	53.6±2.1	4.77±0.11	45.8±2.0
Pb	5.38±0.05	25.2±1.4	4.23±0.04	74.6±1.4
Bi	5.86±0.03	38.3±1.8	4.33±0.05	61.1±1.8

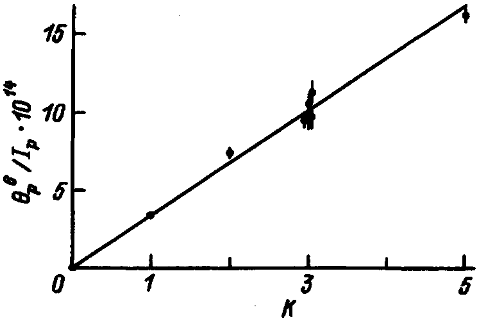

FIG. 2. Plot of Eq. (9). The straight line was drawn with $a=3.3\times 10^{-14}$. The experimental points for $K=3$ are shifted for convenience from their true positions.

TABLE III. Values of parameter K for the metals studied.

	$K\pm\Delta K$	
Metal	This work	Ref. 4.
Mg	1.00±0.08	
Al	4.8±0.4	2.94±0.06
Cu	2.8±0.3	2.06±0.08
Zn	3.4±0.3	
In	2.2±0.2	
Sn	2.8±0.3	
Pb	2.9±0.3	
Bi	3.2±0.3	

A recent study[4] revealed a new feature in positron annihilation in polycrystalline metals. Namely, the parameters of the parabolic component derived from experiment can be combined into a quantizable relation

$$\frac{\theta_p^6}{I_p}=aK, \tag{9}$$

where $K=1, 2, 3, \ldots$ are integers, and a is a parameter which does not depend on the type of metal. It was conjectured[4] that it is the quantity K rather than Z_c that governs the specific number of free electrons in a metal. This work is an attempt to check relation (9) on another setup and with other metal samples.

The angular distributions of annihilation photons were measured on a setup at the ITEP which detects annihilation photons in parallel-slit geometry. The setup was upgraded to computerize experiments and to provide counting the outputs of both detectors simultaneously with the coincidence rate[2], which permits one to introduce corrections into the angular distributions for photon absorption in the sample under study. The positron source was the isotope ^{22}Na with an activity of 100 mCi. The coincidence rate at the maximum was ~20000. The ~$10\times 20\times 10$-mm samples were cut from metal blocks and were not processed in any way. We chose for the study Mg, Al, Cu, Zn, In, Sn, Pb, and Bi. Two metals from this list (Al and Cu) were studied in Ref. 4, but with other samples.

Figure 1 shows angular distributions of annihilation photons measured in magnesium, aluminum, copper, and indium, and their deconvolution into a parabolic and a Gaussian component (dashed lines). The solid line is a sum of these components. It is seen to fit well to the experiment. Table II lists the parameters of this deconvolution, as well as data taken from Ref. 4 for aluminum and copper. Note that the values of θ_p, I_p, θ_g, and I_g obtained in this work and taken from Ref. 4 differ substantially both for aluminum and for copper. Since these two studies dealt with different samples of the metals, these differences can be attributed to different amounts of defects in the samples.

The data of Table II were used to check the validity of relation (9) (see Fig. 2). We see that θ_p^6/I_p does indeed fit well to a linear dependence on K. Figure 3 presents graphically the dimensionless parameter a from Eq. (9), which, as in Ref. 4, does not depend on the choice of the metal. Its average value $a=(3.3\pm 0.2)\times 10^{-14}$ coincides, within two measurement errors, with the value $a=(3.74\pm 0.05)\times 10^{-14}$ obtained in Ref. 4.

Table III presents the values of parameter K [see Eq. (9)] obtained in this work and the data of Ref. 4 for aluminum and copper. We see that all values of K are integers within experimental error. It was also found that for five metals (Cu, Zn, Sn, Pb, and Bi) out of eight $K=3$. Note that the values of Z_c for these metals lie within 1–5 (theory) and 1–4 (experiment).

Note also the different values of K for aluminum and copper obtained on different samples and different setups, although they are integers in both cases. This suggests that while the value of K may change with a change in properties of a given metal sample (e.g., in defect concentration), it always remains an integer.

Thus the experiments discussed in this work support the validity of the empirical relation (9). Its physical nature remains, however, unclear. This stresses the need of continuing the investigation of positron annihilation in metals, including samples with defects of different nature and present in different concentrations.

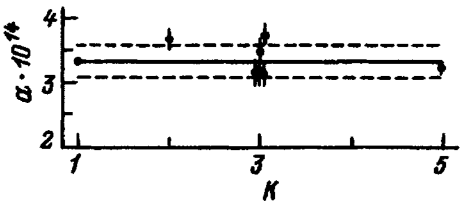

FIG. 3. The values of parameter a for different K. The experimental points for $K=3$ are shifted for convenience from their true positions. The solid line corresponds to the average value, and the dashed lines flank the error limits.

[1] *Positrons in Solids*, edited by P. Hautojärvi (Springer, Berlin, 1979), 255 pp.

[2] Yu. A. Novikov, M. K. Filimonov, and V. P. Shantarovich, Prib. Tekh. Eksp. No. **3**, 43 (1988).

[3] S. V. Vonsovskiĭ and M. I. Katsnel'son, *Quantum Physics of Solids* [in Russian], Nauka, Moscow, (1983), 336 pp.

[4] Yu. A. Novikov, A. V. Rakov, and V. P. Shantarovich, Fiz. Tverd. Tela (St. Petersburg) **36**, 1710 (1994) [Phys. Solid State **36**, 935 (1994)].

Translated by G. Skrebtsov

PHYSICS OF THE SOLID STATE VOLUME 40, NUMBER 4 APRIL 1998

Enhancement of fluctuation effects in superconductors with singularities near the Fermi surface. Paraconductivity

N. V. Shchedrina and M. I. Shchedrin

Volga State Academy of Water Transportation, 603600 Nizhniĭ Novgorod, Russia

(Submitted April 11, 1997)
Fiz. Tverd. Tela (St. Petersburg) **40**, 603–605 (April 1998)

It is shown that the existence of certain topological features on the equipotential surfaces of seed charge carriers near the Fermi level in a superconductor can have an effect on the character of the temperature anomalies in the fluctuation corrections. An expression is obtained for the fluctuation correction to the conductivity in a superconductor model, in which high values of the transition temperature are caused by an increase in the density of states of seed charge carriers in the region near the Fermi surface, where the interaction constant is nonzero. An anomaly in the density of states leads to nonanalyticity of the frequency dependence of the Cooper-pair propagator and to alteration of the fluctuation relaxation time relative to the classical value in the BCS theory. This situation is responsible for enhancement of the role of fluctuations in raising the power of the singularity in the temperature corrections. Possible interpretations of the experimental data available in the literature are discussed from this point of view. [S1063-7834(98)00304-9]

1. The significant role of fluctuation phenomena in understanding the processes occurring in the new class of superconductors known as high-T_c superconductors was pointed out already back in Ref. 1. The main contributions of the long-wavelength fluctuations near the transition temperature T_c are determined by the behavior of the vertex part Γ, which describes pairs with small values of the frequency Ω and the wave vector $\mathbf{k}$. In this region the spatial and temporal parameters characterizing the fluctuations are the correlation length ξ and the relaxation time τ. Their temperature dependence is specified by the quantity $\alpha(T)=\Gamma^{-1}(T,\ \Omega=0,\ \mathbf{k}=0)$, and T_c is determined by the condition $\alpha(T_c)=0$. The possible situations for the space-time evolution of fluctuations depend on the form of the quasiparticle energy spectrum, which is assigned by the poles of $\Gamma(\Omega,\ \mathbf{k})$, and, in particular, on whether the dependence on Ω and $\mathbf{k}$ is analytic in the region where they are small. The typical situation in the BCS theory is analyticity with respect to both Ω and $\mathbf{k}$, $\Gamma^{-1}\sim\alpha+\delta k^2+i\gamma_0\Omega$, $\xi=(\delta/\alpha)^{1/2}$, $\tau=\gamma_0/\alpha$, and $\tau=(\gamma_0/\delta)\xi^2$. In the general case the coefficients in such an asymptote are expressed in terms of the seed-particle Green's function $G^{-1}=i\omega+\mu-\varepsilon_k$ and the interaction g (ω is the frequency, which takes discrete values).[2–4] In the BCS theory Γ can be calculated exactly, $\gamma_0=\pi/8T$,[4] and the asymptote of Γ is actually a Landau–Ginzburg expansion. As for the classical result for the paraconductivity σ, it depends on the singularities of ξ and τ, as well as on the dimensionalities $d=3$, 2, and 1 in a varying manner: all the results are $\sim\tau$, but the power of ξ depends on d: $\sigma\sim\tau\xi^{2-d}$. The temperature anomaly is characterized by the appearance of integer powers of the ''smallest'' singularity $\alpha^{-1/2}$. In this context, the other fluctuation corrections also contain this parameter, although they behave differently with respect to τ and ξ. For example, in the low-temperature asymptote $\sigma_{\mathrm{LT}}\sim\tau^2\xi^{2-d}$ (Ref. 5) the impurity corrections to the paraconductivity $\sigma_{\mathrm{imp}}\sim\tau\xi^{4-d}$.[6] The corrections to purely thermodynamic quantities, such as the static susceptibility and the specific heat, do not contain τ in a lower order and are proportional to ξ^{4-d}.[1] The nonanalyticity of Γ can be a consequence of the specific form of both ε_k and $g(\mathbf{k},\ \mathbf{k}')$, the effects on $\mathrm{Re}\Gamma$ and $\mathrm{Im}\Gamma$ being different. We shall examine the situation in which a topological feature of ε_k leads to a singularity in the density of states, which primarily affects the dynamic part of Γ, while the static part remains analytic.

2. The energy spectrum of the Cooper pairs in the normal phase near T_c is specified by the poles of the vertex part (relaxor) $\Gamma=-g/(1+g\Pi)$ with $g>0$,[2] where

$$\Pi(\omega_n,\mathbf{q})=-T\sum\int d\mathbf{k}\,G(\omega,\mathbf{k})G(\omega_n-\omega,\mathbf{q}-\mathbf{k})$$
$$=\int d\mathbf{k}\,\tanh(\varepsilon_k-\mu)/2T[i\omega_n-(\varepsilon_{q-k}-\mu)-(\varepsilon_k-\mu)]^{-1},\quad \omega_n=2\pi nT. \tag{1}$$

The damping is given by the imaginary part of the retarded function $\Pi(\Omega,\ \mathbf{q})$. If we are not interested in the dispersion of the damping with respect to $\mathbf{q}$, the main contribution to the long-wavelength asymptote can be written simply as

$$\mathrm{Im}\Pi(\Omega)=-(i\pi/2)\tanh(\Omega/4T)N(\Omega/2), \tag{2}$$

where $N(\xi)$ is the density of states and $\xi=\varepsilon_k-\mu$. In this limiting case the damping is proportional to N, and the source of its nonanalyticity is the nonanalyticity of N. The real part of (1) is related to N in a more complicated manner through integration, which preserves the analyticity with respect to $\mathbf{q}$. When $N=\mathrm{const}$, we have the BCS result $\Pi=(-i\pi/2)N\tanh(\Omega/4T)\approx-iN(\pi/8T)\Omega$.

It is known that singularities can appear in the density of states for a definite topology of an isoenergy surface $\varepsilon_k = \text{const}$. Some of them have been studied in detail and have been the subject of a fairly large number of studies.[7–9] For example, the presence of flat or cylindrical areas points to the possibility of some of the charge carriers having one- or two-dimensional motion with root and logarithmic singularities, respectively. In the general case, the source of a singularity can be a deviation from the quadratic dependence of ε_k (''nonparabolicity'') in the vicinity of the Fermi energy μ (or a deviation from the linear dependence with respect to k relative to K_{F}). We note that the saddle points contained in the cosine dispersion for $d=2$ can also be attributed to violation of the parabolicity, since the energy surface has radii of curvature with different signs. In accordance with scaling ideas, a generalization of the form of these singularities is described by expressions of the form $N(\xi)=N_s(W/|\xi|)^s$ or $N(\xi)=N_e\ln|W/\xi|$,[10,11] where $0<s<1$, N_s and N_e are normalization factors, and W has the meaning of the effective width of the conduction band. After normalization to a whole number of states in the band, $N_s=(1-s)2^{-s}N_0$, and $N_e=\ln^{-1}(2e)N_0$, where $N_0=1/Wv_0$ and v_0 is the unit-cell volume of the crystal. The power of the density-of-states singularity s is related to the exponent of the deviation from parabolicity m, if the energy surface has, for example, a discontinuity of the form $\varepsilon_k \sim \mathrm{Sgn}\xi|\mathbf{k}|^m$ near μ. In this case s depends on both m and the dimensionality d. Since s is also related to the temperature singularity of the fluctuation correction, it might provide definite experimental information not only on the character of the density of states, but also on the structure of the energy surface near the Fermi energy.

For the coefficient in front of the linear power of Ω in $\mathrm{Im}\Pi$, we have from (2)

$$\gamma_s(\omega)=\gamma_0|2W/\Omega|^s \quad \text{or} \quad \gamma_e(\Omega)=\gamma_0\ln|2W/\Omega|. \tag{3}$$

The presence of a frequency dependence of γ alters the relaxation time of the long-wavelength fluctuations, for which Γ is now approximated by the expression $\Gamma^{-1}=\alpha_q-i\gamma(\Omega)\Omega$, where $\alpha_q=\alpha+\delta q^2$ and $\alpha=\Pi(T)-\Pi(T_c)$. The quadratic dependence of α_q is a consequence of the expandability of Π into a series in $\mathbf{q}$, and δ is written directly from (1) in terms of G:

$$\delta=(T/2)\sum\int d\xi[2N^{(1)}(\xi)G^3(\omega,\xi)+N^{(2)}(\xi)G^2(\omega,\xi)]G(-\omega,\xi), \tag{4}$$

where

$$N_{ij}^{(1)}=\int d\mathbf{k}(d\varepsilon_k/dk_i)(d\varepsilon_k/dk_j)\delta(\xi-\xi_k),$$

$$N_{ij}^{(2)}=\int d\mathbf{k}(d^2\varepsilon_k/dk_i dk_j),$$

and the $\delta(\xi-\xi_k)$ are weighted density of states. They are expressed in terms of N with the ξ_k indicated above. Since δ is nonsingular, the explicit expression for it is not written out here.

The value of γ depends only on the modulus of Ω, and Γ has poles in the lower half-plane of the complex plane of Ω:

$$\Omega=-i\alpha_q/\gamma(\Omega_0), \quad \alpha_q=\Omega_0\gamma(\Omega_0), \quad |\Omega|=\Omega_0. \tag{5}$$

The equation for ω_0 gives the fluctuation relaxation time $\tau_q=\Omega_0(\alpha_q)^{-1}$ in an implicit form. The temporal development of the process is given by the Fourier component $\Gamma(t)=\int d\Omega/2\pi\Gamma(\Omega)\exp(-i\Omega t)=-iR(\alpha_q)\exp(-t/\tau_q)$, where R is the residue of $\Gamma(\Omega)$ in its pole. Therefore, the main contribution to the evolution of a fluctuation is contained in the expression $\Gamma=R/(\Omega+i\Omega_0)$. This is a reflection of the fact that excitations are specified by the poles of the Green's function. We note that, in principle, the equation for Ω_0 can have more than one solution, in which case the temporal process is characterized by several parameters. We also note that such an approach is also used for Green's functions of a different nature, for example, in the description of excitations in an interacting Fermi gas.[2] In the case of a logarithmic singularity, the equation for Ω_0 is transcendental, $\alpha_q=\Omega_0\gamma_0\ln|2W/\Omega_0|$, and the analytic solution can be estimated approximately, if the logarithmic dependence is approximated by a power-law dependence with a suitable small exponent. For a power-law singularity, Eq. (5) gives

$$\Omega_0=(\alpha_q/\gamma_0)^{r+1}(2W)^{-r}, \quad R=(i/\gamma_0)(\alpha_q/2W\gamma_0)^r,$$
$$r=s/(1-s). \tag{6}$$

3. The correction to the electrical conductivity σ in the normal phase of a superconductor due to the fluctuation current of Cooper pairs can be found, as in Refs. 5 and 6, in terms of the current Green's function D. For the static electrical conductivity $\sigma=-\mathrm{Im}D(\Omega)/\Omega$ as $\Omega\rightarrow 0$. In the lower order, without consideration of the interaction of the fluctuations, we have

$$D(\omega_n)=-(4\delta e)^2T\sum\int d\mathbf{q}q_z^2\Gamma(\omega_n,\mathbf{q})\Gamma(\omega_n+\omega,\mathbf{q}). \tag{7}$$

Following Ref. 6, we obtain the general relation for σ

$$\sigma=2T(2\delta e/\gamma_0)^2(2W\gamma_0)^{-2r}\int d\mathbf{q}q_z^2\alpha_q^{2r}\Omega_0(\mathbf{q})^{-3}. \tag{8}$$

Equation (8) was derived using the high-temperature asymptote $\tau T\ll 1$, where

$$\tau=\tau(\mathbf{q}=0)=(\gamma_0/\alpha)^{r+1}(2W)^r. \tag{9}$$

The high-temperature asymptote was discussed in Ref. 5. In addition, the parameter δ, whose relationship to the spectrum is given by (4), appears instead of the mass of the seed carriers. For $d=3.2$ we present the results following from (8)

$$\sigma_3=(2A_3/3\pi^3)(e^2/h)T\tau\xi^{-1},$$
$$\sigma_2=(2A_2/\pi)(e^2/h)T\tau, \tag{10}$$

where the A_d are numerical multipliers, $A_d=\int du u^{1+d}\times(1+u^2)^{-(3+r)}$, and the limits of integration are from zero to infinity. Thus, the general form of the correction expressed in terms of the fundamental parameters τ and ξ remains classical to within numerical multipliers, as in the BCS theory, i.e., a scaling law appears, whereby significant variations are caused only by the nature of the behavior of the fundamental parameters themselves. In the present case this applies only to τ, whose temperature dependence (9) differs from the BCS result and transforms into the latter when $s=0$. As the dimensionality is lowered, the power of the temperature singularity increases by the same quantity, r: $\sigma_3 \sim \alpha^{-(1/2+r)}$, $\sigma_2 \sim \alpha^{-(1+r)}$, and $\sigma_1 \sim \alpha^{-(3/2+r)}$. This is clearly due to the fact that the temperature dependence $\xi(T)$ remains unchanged, i.e., $\xi \sim \alpha^{-1/2}$, but the relationship between τ and ξ is more complicated here: $\xi^2 = (\delta/\gamma_0)\tau^{1-s}(2W)^s$.

4. When experimental data are interpreted, the critical index n is found from the temperature dependence of the paraconductivity contribution: $\sigma \sim t^{-n}$, where $t = \Delta T/T_c$ and $\Delta T = T - T_c$. Some difficulty is associated with the width of the transition region (even without a magnitude field) δT_c, which produces a range for the estimate of T_c. The range of fluctuation effects ΔT should be small compared with T_c, but δT_c and ΔT are often of the same order of magnitude. We can utilize, for example, the results in Ref. 12, which presents the temperature dependence of the paraconductivity for two systems, viz., Tl–Ba–Ca–Cu–O and Er–Ba–Ca–O, on a logarithmic scale in Fig. 3. The classical exponent 1/2 is correct in the interval $0.8 < \Delta T < 9$ K for the former system and in the interval $0.5 < \Delta T < 7$ K for the latter. The value of δT_c is estimated as 10 K. Bearing in mind the departure from this range and taking into account the enhancement of the fluctuation effects in the model under consideration, we expand ΔT to $30-40$ K. Then, linearization is possible on the plots indicated for $n = 0.75$ and 0.65. This corresponds to the exponent values $s = 0.2$ and 0.13. In such an interpretation this attests to the three-dimensional character of the critical fluctuation in the presence of a weak singularity in the density of states of the seed charge carriers.

[1] L. N. Bulaevskiĭ, V. L. Ginzburg, and A. A. Sobyanin, Zh. Éksp. Teor. Fiz. **94** (7), 355 (1988) [Sov. Phys. JETP **67**, 1499 (1988)].

[2] A. A. Abrikosov, L. P. Gor'kov, and I. E. Dzyaloshinskiĭ, *Methods of Quantum Field Theory in Statistical Physics*, Prentice-Hall, Englewood Cliffs, N.J. (1963); Moscow (1962), 443 pp.

[3] P. G. de Gennes, *Superconductivity of Metals and Alloys* [W. A. Benjamin, New York–Amsterdam (1966); Mir, Moscow (1968), 280 pp.].

[4] A. A. Abrikosov, *Fundamentals of the Theory of Metals*, Elsevier, New York (1988); Moscow (1987), 520 pp.

[5] N. V. Shchedrina and M. I. Shchedrin, Sverkhprovodimost: Fiz. Khim. Tekh. **6**, 51 (1993) [Supercond., Phys. Chem. Technol. **6**, 38 (1993)].

[6] N. V. Shchedrina and M. I. Shchedrin, Sverkhprovodimost: Fiz. Khim. Tekh. **5**, 1614 (1992) [Supercond., Phys. Chem. Technol. **5**, 1562 (1992)].

[7] L. F. Mattheiss, Phys. Rev. Lett. **58**, 1028 (1987).

[8] V. N. Antonov, Vl. N. Antonov, V. E. Bar'yakhtar, A. I. Baglyuk, E. G. Maksimov, V. V. Nemoshkalenko, A. Ya. Perlov, S. Yu. Savrasov, and Yu. A. Uspenskiĭ, Zh. Éksp. Teor. Fiz. **95**, 732 (1989) [Sov. Phys. JETP **68**, 415 (1989)].

[9] V. A. Moskalenko, M. E. Palistrant, and V. M. Vakalyuk, Usp. Fiz. Nauk **159**, 621 (1989) [Sov. Phys. Usp. **32**, 1060 (1989)].

[10] C. C. Tsuei, C. C. Chi, D. M. Newns, P. C. Pattnaik, and M. Däumling, Phys. Rev. Lett. **69**, 2134 (1992).

[11] N. V. Shchedrina and M. I. Shchedrin, Fiz. Tverd. Tela (St. Petersburg) **36**, 2201, 3079 (1994) [Phys. Solid State **36**, 1200, 1637 (1994)]; Fiz. Tverd. Tela (St. Petersburg) **37**, 2238 (1995) [Phys. Solid State **37**, 1223 (1995)].

[12] N. E. Alekseevskiĭ, A. V. Mitin, E. P. Khlybov, G. P. Kuz'micheva, V. I. Nizhankovskiĭ, I. Varkhul'ska, and A. Gilevskiĭ, Zh. Éksp. Teor. Fiz. **97**, 263 (1990) [Sov. Phys. JETP **70**, 148 (1990)].

Translated by P. Shelnitz

^{61}Cu(^{61}Ni) and ^{133}Ba(^{133}Cs) Mössbauer emission spectroscopy of $Tl_2Ba_2Ca_{n-1}Cu_nO_{2n+4}$

V. F. Masterov, F. S. Nasredinov, N. P. Seregin, and P. P. Seregin

St. Petersburg State Technical University, 195251 St. Petersburg, Russia

(Submitted October 2, 1997)
Fiz. Tverd. Tela (St. Petersburg) **40**, 606–608 (April 1997)

The parameters of the electric-field gradient tensor at copper and barium sites in the $Tl_2Ba_2Ca_{n-1}Cu_nO_{2n+4}$ ($n=1,2,3$) lattice have been determined by ^{61}Cu(^{61}Ni) and ^{133}Ba(^{133}Cs) Mössbauer emission spectroscopy, and calculated in the point-charge approximation. The calculated parameters can be reconciled with experiment if one assumes that the holes produced as the valence state of a part of thallium atoms is lowered are localized predominantly on the oxygen sublattice lying in the same plane with copper atoms [in the Cu(2) plane in the $Tl_2Ba_2Ca_2Cu_3O_{10}$ lattice]. ^{133}Ba(^{133}Cs) Mössbauer emission spectroscopy data agree qualitatively with the proposed models of charge distribution in the $Tl_2Ba_2Ca_{n-1}Cu_nO_{2n+4}$ lattices.
[S1063-7834(98)00404-3]

$Tl_2Ba_2Ca_{n-1}Cu_nO_{2n+4}$ ($n=1, 2, 3$) compounds have high superconducting transition temperatures T_c, and therefore determination of the charge state distribution on atoms in these lattices is possible. This work reports on the use of Mössbauer emission spectroscopy on the ^{61}Cu(^{61}Ni) and ^{133}Ba(^{133}Cs) isotopes to determine the charge states of atoms in $Tl_2Ba_2Ca_{n-1}Cu_nO_{2n+4}$ (TlBaCaCuO).

$Tl_2Ba_2Ca_{n-1}{}^{61}Cu_nO_{2n+4}$ Mössbauer sources were prepared by diffusion doping of $Tl_2Ba_2Ca_2Cu_3O_{10}$ (2223) samples ($T_c \approx 120$ K), $Tl_2Ba_2CaCu_2O_8$ (2212) ($T_c \approx 60$ K), and $Tl_2Ba_2CuO_6$ (2201) ($T_c < 4.2$ K) by the technique described elsewhere[1]. The ^{133}Ba isotope was introduced into the above compounds during their preparation. ^{133}Ba(^{133}Cs) Mössbauer spectra were measured at 4.2 K with a ^{133}CsCl absorber, and ^{61}Cu(^{61}Ni) spectra, at 80 K with a $Ni_{0.86}V_{0.14}$ absorber. Typical spectra are displayed in Fig. 1, and the results of their treatment are given in Table I [quadrupole coupling constants C(Ni) and C(Cs) for the $^{61}Ni^{2+}$ and $^{133}Cs^{+}$ probes, respectively, where $C=eQU_{zz}, eQ$ is the quadrupole moment of the probe nucleus, and U_{zz} is the principal component of the electric-field gradient tensor (EFG) at the probe].

It was assumed that, during diffusion doping, the ^{61}Cu parent isotope occupies the copper sites in the lattice, and that the daughter isotope ^{61}Ni does not leave them. Since copper atoms occupy in the (2201) and (2212) lattices the only site available,[2,3] it was expected that ^{61}Cu(^{61}Ni) Mössbauer spectra would correspond to the only state of the $^{61}Ni^{2+}$ probe. Indeed, as evident from Fig. 1a and b, the ^{61}Cu (^{61}Ni) Mössbauer spectra of both ceramics are quadrupole multiplets that can be identified with the only state of the $^{61}Ni^{2+}$ center.

The spectrum of the (2223) sample was expected to be more complex. In its treatment, we used data obtained in a study of the (2223) compound by ^{67}Cu(^{67}Zn) Mössbauer emission spectroscopy,[4] where the experimental spectrum was a superposition of three quadrupole multiplets. Because copper atoms occupy in the (2223) lattice two crystallographically nonequivalent sites,[2] two multiplets (with the 1:2 ratio of the areas bounded by them) are due to two states of the Mössbauer probe at the Cu(1) and Cu(2) sites, and the third multiplet (its relative intensity was ~0.8) corresponds to the probe at the copper sites of the additional (2212) phase. This was taken into account when treating the ^{61}Cu(^{61}Ni) spectrum of the (2223) compound. Figure 1*c* shows the quadrupole triplets due to $^{61}Ni^{2+}$ centers sitting at the Cu(1) and Cu(2) sites of the (2223) lattice, and the quadrupole triplet corresponding to $^{61}Ni^{2+}$ centers at copper sites

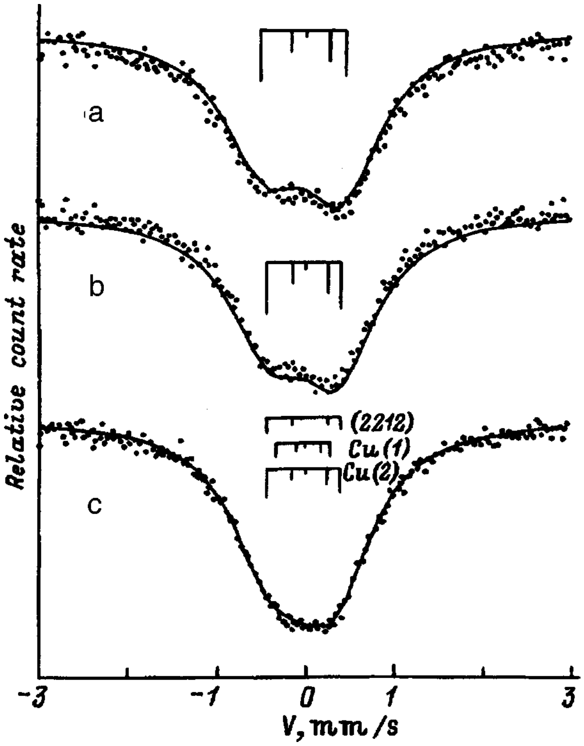

FIG. 1. ^{61}Cu(^{61}Ni) Mössbauer spectra of (a) (2201), (b) (2212), and (c) (2223) compounds. The position of the quadrupole multiplet components corresponding to $^{61}Ni^{2+}$ centers at copper sites in TlBaCasCuO ceramics is identified.

TABLE I. Parameters of ^{61}Cu(^{61}Ni) and ^{133}Ba(^{133}Cs) Mössbauer emission spectra for $Tl_2Ba_2Ca_{n-1}Cu_nO_{2n+4}$ compounds.

		Probe		
		$^{61}Ni^{2+}$	$^{133}Cs^{+}$	
Compound	Site	C(Ni), MHz	C(Cs), MHz	Γ, mm/s
$Tl_2Ba_2CuO_6$	Cu	−48(3)		
	Ba		<40	0.91(1)
$Tl_2Ba_2CaCu_2O_8$	Cu	−43(3)		
	Ba		<40	0.92(1)
$Tl_2Ba_2Ca_2Cu_3O_{10}$	Cu(1)	−30(5)		
	Cu(2)	−43(3)		
	Ba		<40	0.94(1)

Note: C(Ni) and C(Cs) are quadrupole coupling constants for the $^{61}Ni^{2+}$ and $^{133}Cs^{+}$ probes, respectively; Γ is the FWHM of the experimental ^{133}Ba(^{133}Cs) spectrum; for all centers, the EFG tensor asymmetry parameter $\eta < 0.2$

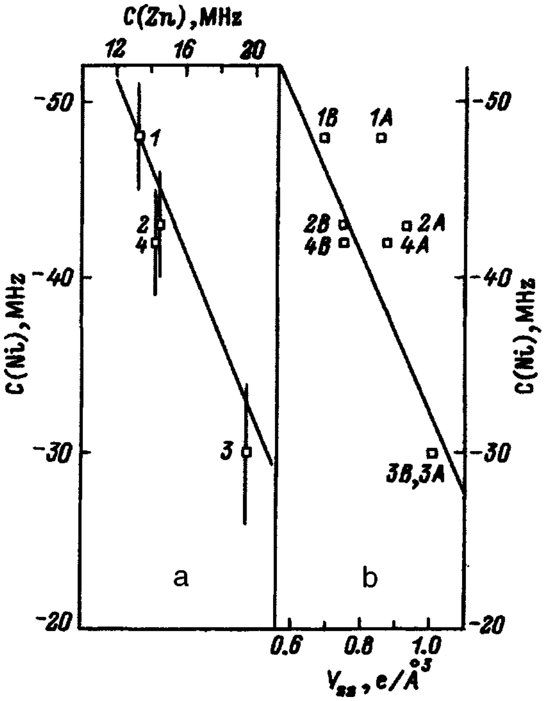

FIG. 2. (a) C(Ni)-vs-C(Zn) (b) C(Ni)-vs-V_{zz} diagrams for divalent copper compounds (solid lines). The points refer to: *1* — Cu in (2201), *2* — Cu in (2212), *3* — Cu(1) in (2223), *4* — Cu(2) in (2223). Indices A and B relate to the models used to calculate V_{zz}.

of the (2212) phase. The position of the lines of the latter triplet was prescribed based on the (2212) spectrum, and the ratio of the areas bounded by the spectra was taken as 1:2:0.8.

The $^{133}Cs^{+}$ probe occupies barium sites in the compounds studied and, since in all the above lattices barium atoms sit in the same site[2,3], the ^{133}Ba(^{133}Cs) Mössbauer spectra relate to the only probe state. The experimental spectra are single lines whose width Γ tends to increase in the order (2201)-(2212)-(2223) (see Table I).

To obtain information on the charge distribution in the cuprate lattices, we performed a combined analysis of Mössbauer emission spectroscopy data on the ^{61}Cu(^{61}Ni) and ^{67}Cu(^{67}Zn) isotopes. In a general case, the measured quantity C is a sum of two terms:

$$eQU_{zz} = eQ(1-\gamma)V_{zz} + eQ(1-R_0)W_{zz}, \qquad (1)$$

where U_{zz}, V_{zz}, W_{zz} are the principal components of the total, crystal-field, and valence-electron EFG tensor, and γ, R_0 are the Sternheimer coefficients for the probe atom.

The EFG at the $^{61}Ni^{2+}$ probe is generated by both the lattice ions and the valence electrons of the probe itself. At $^{61}Zn^{2+}$, the EFG is produced by the lattice ions only. Figure 2a shows a C(Ni)-vs-C(Zn) diagram constructed using the values of the quadrupole coupling constant for the $^{61}Ni^{2+}$ [C(Ni)] and ^{67}Zn [C(Zn)] probes at copper sites of the same cuprates, which were derived from Mössbauer emission spectroscopy data obtained with ^{61}Cu(^{61}Ni) and ^{67}Cu(^{67}Zn) isotopes.[5] Because the C(Ni)-vs-C(Zn) diagram in Fig. 2a is a straight line, this implies, according to Eq. (1), constancy of the valence-electron contribution to the quadrupole coupling constant C(Ni). Also presented in Fig. 2a are data obtained for the TlBaCaCuO compounds [the values of C(Zn) were taken from Ref. 4; we see a good agreement with the data for all known cuprates.

One can obtain additional information from the C(Ni)-vs-V_{zz} diagram (Fig. 2b). Plotted along the horizontal axis of this diagram are the calculated principal components V_{zz} of crystal-field EFG tensor for the copper sites for which C(Ni) was measured by ^{61}Cu(^{61}Ni) Mössbauer emission spectroscopy.[5] The C(Cu)-vs-V_{zz} relation is a straight line, and deviations from it may be due to errors in EFG tensor calculations stemming from a wrong choice of the ionic charges. Therefore the position of the corresponding points in the C(Ni)-vs-C(Zn) and C(Ni)-vs-V_{zz} diagrams drawn for the same copper site can be used to select the appropriate charge distribution versions in a lattice.

We calculated crystal-field EFG tensors for the copper and barium sites in TlBaCaCuO compounds, with the lattices represented as superpositions of several sublattices:

$[Tl_2][Ba_2][Cu][O(1)_2][O(2)_2][O(3)_2]$,

$[Tl_2][Ba_2][Ca][Cu_2][O(1)_4][O(2)_2][O(3)_2]$,

$[Tl_2][Ba_2][Ca_2][Cu(1)][Cu(2)_2][O(1)_2][O(2)_4][O(3)_2][O(4)_2]$.

In the (2201) and (2212) compounds, O(1) atoms lie in the same plane with copper atoms, and in (2223), O(2) and Cu(2) atoms share the same plane. The structural data needed for calculations were taken from Refs. 2,3. Figure 2b presents our results obtained with two models of crystal-field EFG tensor calculation. The data for TlBaCaCuO ceramics do not fit onto the C(Ni)-vs-V_{zz} straight line if V_{zz} was calculated assuming standard ionic charges (Tl^{3+}, Ba^{2+}, Ca^{2+}, Cu^{2+}, O^{2-}) (models A). The deviations of the TlBaCaCuO data from the linear relationship should be obviously attributed to a wrong choice of the model to calculate V_{zz}. To bring the data obtained for the (2201) and (2223) systems onto the linear relation in Fig. 2b, one has to localize holes at the oxygen atoms lying in the Cu-O plane. In the case of the (2223) ceramic, holes should be localized at the oxygen atoms in the Cu(2) plane. Holes may appear in these ceramics as part of thallium atoms become stabilized in univalent state.[6] As seen from Fig. 2b, models *B* assuming localization of holes at oxygen atoms provide satisfactory agreement with the linear relation [models *B* assume also that 10% of thallium atoms in the (2201) and (2223) compounds, and 12.5%, in the (2212) compound, are univalent].

^{133}Ba(^{133}Cs) Mössbauer emission spectroscopy data do not permit any quantitative conclusions on the parameters of the crystal-field EFG tensor at barium sites in the compounds under study. It should be stressed, however, that the small value of C and the tendency to an increase of Γ in the (2201)-(2212)-(2223) order obtained for the ^{133}Cs^{+} probe at barium sites are in agreement with the values of V_{zz} calculated for barium sites [models *B* yield $V_{zz}=0.01$, 0.03, and 0.07 e/Å^3 for the (2201), (2212), and (2223) ceramics, respectively].

Support of the Russian Fund for Fundamental Research (Grant 97-02-16216) is gratefully acknowledged.

[1] V. F. Masterov, F. S. Nasredinov, Ch. S. Saidov, P. P. Seregin, and O. K. Shcherbatyuk, Fiz. Tverd. Tela (Leningrad) **34**, 2294 (1992) [Sov. Phys. Solid State **34**, 1228 (1992)].

[2] K. Yvon and M. François, Z. Phys. B **76**, 413 (1989).

[3] A. W. Hewat, E. A. Hewat, Y. Brynestad, H. A. Mook, and E. D. Specht, Physica C **152**, 438 (1989).

[4] V. F. Masterov, F. S. Nasredinov, N. P. Seregin, and P. P. Seregin, Fiz. Tverd. Tela (St. Petersburg) **38**, 2331 (1996) [Phys. Solid State **38**, 1282 (1996)].

[5] F. S. Nasredinov, P. P. Seregin, V. F. Masterov, N. P. Seregin, O. A. Prikhodko, and M. A. Sagatov, J. Phys.: Condens. Matter **7**, 2339 (1995).

[6] Yu. I. Zhdanov, K. N. Mikhalev, B. A. Aleksashin, S. V. Verkhovskiĭ, K. A. Okulova, V. I. Voronin, L. D. Shustov, A. Yu. Yakubovskiĭ, and A. I. Akimov, Sverkhprovodimost' (KIAE) **3**, 194 (1990).

Translated by G. Skrebtsov

Features of the twin structure of $YBa_2Cu_3O_{7-x}$ epitaxial films

I. K. Bdikin

Institute of Chemical Physics, Russian Academy of Sciences, 142432 Chernogolovka, Moscow Region, Russia

A. D. Mashtakov, P. B. Mozhaev, and G. A. Ovsyannikov

Institute of Radio Engineering and Electronics, Russian Academy of Sciences, 103907 Moscow, Russia

(Submitted September 15, 1997; resubmitted November 18, 1997)
Fiz. Tverd. Tela (St. Petersburg) **40**, 609–611 (April 1998)

X-ray diffraction is used to investigate $YBa_2Cu_3O_{7-x}$ (YBCO) films on $NdGaO_3(110)$ and a (100) $CeO_2/(1102)$ Al_2O_3 heterostructure. Symmetric, asymmetric, and axial geometries for θ and $\theta/2\theta$ scans are used to obtain diffraction spectra from different crystallographic planes. The orientational and quantitative twinning characteristics of the films are determined. While the crystallographic parameters of these two types of film (the films are c-axis oriented with $c = 11.67$ Å) are similar, there are differences in the twin structure. In particular, the features of the $NdGaO_3$ structure lead to the appearance of an angle differing from 90° (90.20°) between the possible (110) and (110) twin planes in a YBCO film and a different number of twin components in each system of twins. It is concluded from an analysis of the broadening of reflections, which are sensitive to twinning, that there is not twinning in a 60% film of YBCO on Al_2O_3 with a CeO_2 buffer layer. *© 1998 American Institute of Physics.* [S1063-7834(98)00504-8]

The modern technology for depositing $YBa_2Cu_3O_{7-x}$ superconducting thin films permits the formation of films with a crystal structure differing only slightly from the single-crystal structure. Just as in single crystals, twinning occurs in the films according to a $\{110\}/\langle 110\rangle$ scheme with twinning angles of about 1°.[1,2] This paper presents the results of comparative investigations of twin structures for two c-axis oriented YBCO films with similar crystallographic parameters.

The $YBa_2Cu_3O_{7-x}$ films were grown by cathodic sputtering at a constant current.[3] Block-free $NdGaO_3(110)$ and R-plane oriented sapphire $[Al_2O_3(\bar{1}102)]$ served as substrates. The sapphire substrates were covered with a cerium oxide (CeO_2) buffer layer to prevent the superconductivity-suppressing diffusion of aluminum from the sapphire substrate into the film. The conditions for depositing cerium oxide were chosen to ensure the formation of a (001) oriented buffer layer. The YBCO film growth process was optimized by varying the substrate temperature, the pressure, and the discharge current.

The x-ray diffraction investigations were performed on Siemens D500 and DRON-3M diffractometers with Cu $K\alpha$ radiation. The symmetric, asymmetric, and axial recording geometries were used. To investigate twinning in c-axis oriented YBCO films, reflections from crystallographic planes inclined relative to the (001) plane must be obtained. In this work we recorded the (103) and (113) reflections in the axial geometry (see the inset in Fig. 1). These are among the most intense reflections in the YBCO structure.

The lattice constants of the films were determined from the (0 0 13), (3 0 10), and (0 3 10) reflections. The values for the films investigated were $a = 3.827(1)$ Å, $b = 3.889(1)$ Å, and $c = 11.674(2)$ Å and $a = 3.830(2)$ Å, $b = 3.880(2)$ Å, and $c = 11.670(2)$ Å for the films on $NdGaO_3$ and on (001) $CeO_2/(1102)$ Al_2O_3, respectively. The values of c point out a high degree of saturation of the film with oxygen for both films.[4]

The diffractogram obtained by scanning the sample about the ω axis with the detector in the position corresponding to the (113) reflection of the YBCO film (Fig. 1) reflects the characteristic picture of twinning in YBCO. Curves A and A' in this scan belong to different twin components relative to the (110) plane, and curve B belongs to two other twin components relative to the (110) plane; therefore, they do not have splittings. Curve C corresponds to the (020) plane of $NdGaO_3$. The relative positions of the peaks reflect the misorientation of the respective planes; therefore, the values of the twinning angle and the angle between the $NdGaO_3$ and YBCO atomic planes can be indicated on the basis of the diffractogram. These angles are determined using the relation

$$\delta = \alpha \cos(\gamma) + \beta \sin(\gamma), \tag{1}$$

where δ is the measured misorientation angle between film grains, α and β are the misorientation angles between the same grains in assigned mutually perpendicular planes, and γ is the angle between the planes corresponding to δ and α. In the present case $\beta = 0°$, $\delta = 1.39°$ (it is determined from the distance between peaks A and A' in the diffractogram in Fig. 1), $\gamma = 35°$ [the angle between the (113) and (110) planes in the YBCO structure], and α is twice the value of the twinning angle sought. This gives a twinning angle equal to 0.85°.

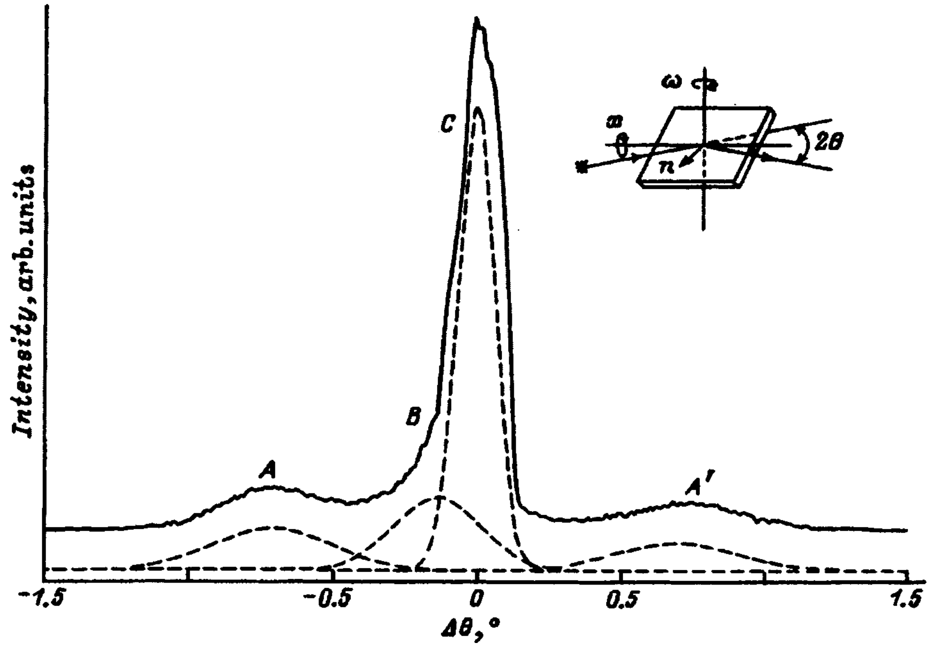

FIG. 1. Diffractogram obtained by scanning about the ω axis of the (113) reflection in the axial geometry for a c-axis oriented YBCO film on (110) $NdGaO_3$. Inset — diagram for recording x-ray diffraction in the axial geometry.

Similarly, Eq. (1) can be used to determine the angle between the twin planes of YBCO from the relative positions of peaks A, A', and B. This angle equals 90.20°. The presence of such an angle was also noted in Ref. 2 for a YBCO film on $NdGaO_3$. The appearance of an angle between twin planes that is not exactly equal to 90° does not contradict the symmetry of the $NdGaO_3$ lattice. Since the twin-structure components do not differ, the size of the A component is greater than the size of the A' component, because the magnitude of the mismatch between the positions of the film and substrate atoms is smaller for the A component. This is also observed experimentally.

The twinning in YBCO films on Al_2O_3 with a CeO_2 buffer layer is not manifested by characteristic splitting into twin components (Fig. 2). In addition, the diffraction lines have a smaller width than for the YBCO films on $NdGaO_3$. An analysis performed on the basis of diffraction orders from the same plane shows that the width of the reflections does not vary. This indicates that the broadening is related exclusively to misorientation, rather than the twin size or diffraction effects stipulated by the presence of defects in YBCO.[5]

The diffractograms obtained were analyzed on the basis of the assumption that there is a mixed state of twinned and untwinned YBCO phases in the film investigated. The relative quantities of the twinned and untwinned phases, the degree of misorientation of the film grains, and the degree of orthorhombism were varied. The best fit was obtained for the lattice constants $a = 3.830$ Å, $b = 3.880$ Å, and $c = 11.670$ Å, broadening of the reflections with misorientation amounting to 1.1° (this parameter also takes into account the instrumental broadening), and a concentration of the twinned phase equal to 40%. A decrease in the concentration of the twinned phase calculated in such a manner was observed for films containing an a-axis oriented component. This is easily attributed to the fact that in the mixed state with a- and c-axis oriented film components the contribution of the a-axis oriented component is the contribution of the untwinned phase.

The presence of an untwinned phase in a 100% c-axis oriented film can be attributed to the following reasons.

1) Extended twin boundaries, in which the transformation from one twin orientation into the other can occur through a phase with a small twinning angle.[6]

2) The grain size of CeO_2, which determines the size of the YBCO grains. The twinning of YBCO takes place in

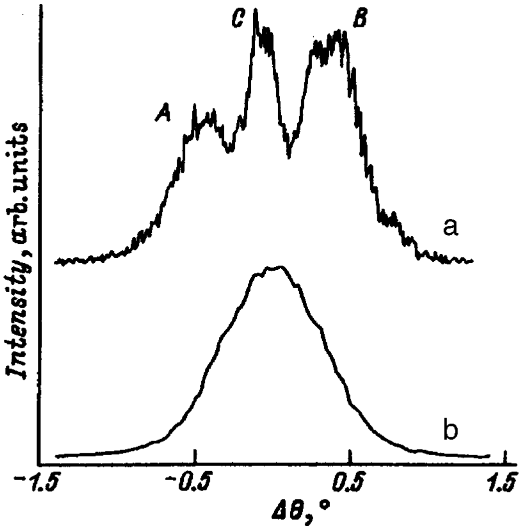

FIG. 2. Diffractograms obtained by scanning about the ω axis of the (103) reflection in the axial geometry for a c-axis oriented YBCO film on (110) $NdGaO_3$ (a), and a c-axis oriented YBCO film on (1102) Al_2O_3 with a (100) CeO_2 buffer layer (b). Peaks A and B correspond to two orientations of the twins in the (110) and (110) twin planes, and peak C corresponds to the position of the $NdGaO_3$ (112) plane.

grains with an already given size. The division of grains into twins may be energetically less favorable when the size of the grains is smaller than the characteristic size of the twins (500° Å).

We thank F. V. Komissinskiĭ for his assistance in depositing the high-T_c superconducting films and I. M. Kotelyanskiĭ for a useful discussion of the results of the work.

This work was partially financed by the Russian Fund for Fundamental Research (No. 95-02-06184) and the Superconductivity Section of the Russian Program ‘‘Current Trends in the Physics of the Condensed State.’’

[1] T. Schere, P. Marienhoff, R. Herwig, M. Neuhaus, and W. Jutzi, Physica C **197**, 79 (1992).
[2] T. Steinborn, G. Miehe, J. Wiesner, E. Brecht, H. Fuess, G. Wirth, B. Schulte, M. Speckmann, H. Adrian, M. Maul, K. Petersen, W. Blau, and M. McConnel, Physica C **220**, 219 (1994).
[3] P. B. Mozhaev, G. A. Ovsyannikov, S. N. Polyakov, É. K. Kovev, and N. P. Kukhta, Sverkhprovodimost: Fiz., Khim., Tekh., (in press).
[4] M. S. Osofsky, J. L. Cohn, E. F. Skelton, M. M. Miller, R. J. Soulen, Jr., S. A. Wolf, and T. O. Vanderah, Phys. Rev. B **45**, 4916 (1992).
[5] J. P. Gong, M. Kawasaki, K. Fujito, R. Tsuchiya, M. Yoshimoto, and H. Koinuma, Phys. Rev. B **50**, 3280 (1994).
[6] Yu. A. Osip'yan, N. S. Afonikova, T. K. Parsamyan, V. Sh. Shekhtman, and I. M. Shmyt'ko, JETP Lett. **47**, 587 (1988).

Translated by P. Shelnitz

PHYSICS OF THE SOLID STATE VOLUME 40, NUMBER 4 APRIL 1998

SEMICONDUCTORS AND INSULATORS

Investigation of dc hopping conduction in $TlGaS_2$ and $TlInS_2$ single crystals

S. N. Mustafaeva, V. A. Aliev, and M. M. Asadov

Institute of Physics, Azerbaidzhan Academy of Sciences, 370000 Baku, Azerbaidzhan

(Submitted May 22, 1997)
Fiz. Tverd. Tela (St. Petersburg) **40**, 612–615 (April 1998)

It is established that variable-range hopping conduction takes place between states localized near the Fermi level in layered $TlGaS_2$ and $TlInS_2$ single crystals both along and across their natural layers in a constant electric field at $T \leqslant 200$ K. The densities of states near the Fermi level and the hopping distances at different temperature are estimated. The occurrence of activationless hopping conduction is established in $TlGaS_2$ and $TlInS_2$ single crystals in the temperature range 110–150 K. © *1998 American Institute of Physics.* [S1063-7834(98)00604-2]

Single crystals of $TlGaS_2$ and $TlInS_2$ are layer-chain $A^{III}B^{III}C_2^{VI}$ semiconductors. This class of crystals has been investigated fairly thoroughly, but dc hopping conduction has not been studied in them, with the exception of $TlGaSe_2$ crystals.[1]

Layered single crystals of $TlGaS_2$ and $TlInS_2$ have a fairly high resistivity at room temperature ($\rho = 2\times10^7 - 7\times10^9$ and $5\times10^9 - 7\times10$ $\Omega\cdot$cm, respectively), as well as a small concentration of free charge carriers in the allowed band, and are also characterized by a high density of states in the band gap.[2,3] The observation of hopping conduction should be expected in just such materials. The ac hopping conduction in $TlGaS_2$ and $TlInS_2$ single crystals was studied in Refs. 2 and 3, and the density of states near the Fermi level was determined: $N_F = 9\times10^{18}$ $eV^{-1}\cdot cm^{-3}$ for $TlGaS_2$ single crystals[2] and $N_F = 6.5\times10^{18}$ $eV^{-1}\cdot cm^{-3}$ for $TlInS_2$.[3]

The purpose of the present work was to study the conduction between localized states in $TlGaS_2$ and $TlInS_2$ single crystals under dc conditions.

As we know, hopping conduction is observed in semiconductors at low temperatures, at which it is dominant over the conduction of thermally excited charge carriers in the allowed band.

The results of a study of the charge-transfer processes in layered $TlGaS_2$ and $TlInS_2$ single crystals in a constant electric field at low temperatures are presented below. The conductivity of the samples was determined both along ($\sigma_{\perp c}$) and across ($\sigma_{\parallel c}$) the layers of the crystals. The contact material used to prepare the samples in both configurations was fused indium, which provided an ohmic contact with $TlGaS_2$ and $TlInS_2$. The samples for the measurements had a thickness of the order of 40–50 μm for the $TlGaS_2$ single crystals and 80–130 μm for the $TlInS_2$ single crystals. The strength of the constant electric field applied to the samples ranged from 2×10^2 to 2.7×10^3 V/cm for different samples. The conductivity of the samples was measured in the temperature range 110–296 K. The samples for performing the measurements were placed in a UTREX helium cryostat with a temperature-stabilization system (the stabilization accuracy was within 0.02 K).

Figure 1 presents plots of the temperature dependence of the electrical conductivity of a $TlGaS_2$ single crystal. The dependence of $\sigma_{\perp c}$ on $10^3/T$ clearly exhibits the presence of a long exponential segment with a slope equal to 0.31 eV in the temperature range 200–293 K. As the temperature is decreased further below 200 K, a continuous decrease in the activation energy for $\sigma_{\perp c}$ is observed, and $\sigma_{\perp c}$ ceases to depend on the temperature in the range 115–150 K. The temperature dependence of $\sigma_{\perp c}$, which characterizes an activation energy that decreases monotonically with the temperature, has been replotted in $\log \sigma_{\perp c}$ versus $T^{-1/4}$ coordinates and is presented in Fig. 2. It is seen that all the experimental points lie close to a straight line in these coordinates. This allows us to state that charge transfer along the layers of a $TlGaS_2$ single crystal in this temperature range is effected by hopping conduction between states lying in a narrow energy band near the Fermi level:[4] $\log \sigma \sim T^{-1/4}$. The slope of the linear plot of $\log \sigma_{\perp c}$ versus $T^{-1/4}$ is $T_c = 2.7\times10^7$ K. We used the relation[4]

$$N_F = \frac{16}{T_0 \cdot k \cdot a^3}, \tag{1}$$

where k is Boltzmann's constant and a is the localization radius, to determine the density of localized states near the Fermi level in the $TlGaS_2$ single crystals: $N_F = 2.5\times10^{18}$ $eV^{-1}\cdot cm^{-3}$. The value taken for the localization radius was $a = 14$ Å (Ref. 5) in analogy to GaS single crystals.

The relation[4]

$$R(T) = \frac{3}{8} a T_0^{1/4} T^{-1/4} \tag{2}$$

was used to determine the hopping distance R of the charge carriers at different temperatures. The mean hopping distance in the temperature range studied was ~100 Å, which is 7 times greater than the mean distance between the localization centers of the charge carriers. The localization centers are

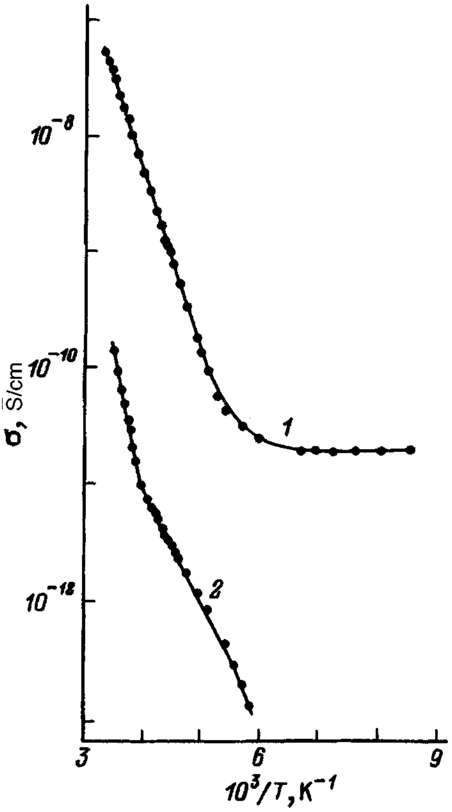

FIG. 1. Temperature dependence of the conductivity of a $TlGaS_2$ single crystal along (*1*) and across (*2*) its layers.

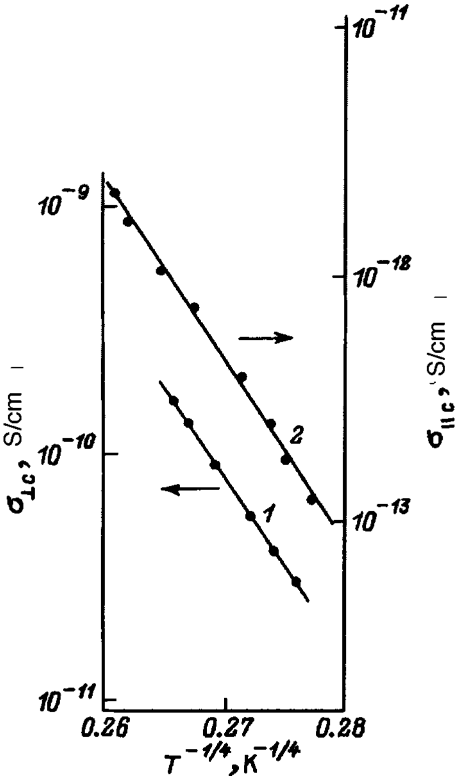

FIG. 2. Low-temperature conductivity of a $TlGaS_2$ single crystal along (*1*) and across (*2*) its layers in logσ versus $T^{-1/4}$ coordinates.

separated along the energy scale by ΔE. As the temperature is lowered, R increases, while ΔE decreases. As we have already noted, a temperature-independent conductivity $\sigma_{\perp c}$ is observed, i.e., ΔE becomes equal to zero, in the temperature range 115–150 K. This experimental finding attests to the occurrence of activationless hopping conduction along the layers of the $TlGaS_2$ single crystals, i.e., the hops of charge carriers within the localized band take place with phonon emission in the temperature range 115–150 K.[6]

Figure 1 also presents the temperature dependence of the conductivity across the layers of a $TlGaS_2$ single crystal. Two exponential segments with slopes equal to 0.5 and 0.25 eV, which cover the temperature range 220–284 K are displayed here. The experimental results on the conductivity below 220 K plotted in log $\sigma_{\|c}$ versus $T^{-1/4}$ coordinates are presented in Fig. 2. The slope of this dependence is $T_0 = 3.5\times10^7$ K. The value obtained for the density of localized states near the Fermi level is $N_F = 2\times10^{18}$ $\mathrm{eV}^{-1}\cdot\mathrm{cm}^{-3}$. The hopping distances of the charge carriers across the layers of a $TlGaS_2$ single crystal were $R = 105$ Å at 217 K and $R = 112$ Å at $T = 170$ K. Unfortunately, measurements of $\sigma_{\|c}$ could not be performed at lower temperatures due to the small values of the currents in the samples; however, oscillations and reversal of the current were observed.

It is noteworthy that the values of the density of localized states N_F calculated from the experimental results on the conductivity, both along and across the layers of the $TlGaS_2$ single crystals, practically coincide. As we know, the existence of localized states in the band gap is caused by the presence of structural defects, such as vacancies, interstitials, and dislocations, in the crystals. The coinciding values of N_F apparently provide evidence that the defects in the $TlGaS_2$ crystals are distributed in approximately the same way along and across the natural layers. In the $TlGaSe_2$ crystals the values of N_F along and across the C axis differed by almost an order of magnitude, i.e., the anisotropy was more pronounced in these crystals than in the $TlGaS_2$ crystals. Further evidence is provided by the fact that, while the maximum conductivity anisotropy $\sigma_{\perp c}/\sigma_{\|c}$ was $\sim5\times10^2$ in the $TlGaS_2$ crystals, $\sigma_{\perp c}/\sigma_{\|c}$ reached a value of 9×10^7 in the $TlGaSe_2$ crystals.

It is interesting to compare the values of N_F that we calculated from the results of measurements of the dc conductivity of $TlGaS_2$ with the value of N_F calculated from the results of measurements of the ac conductivity of these crystals.[2,7] As we have already noted above, a value of 9×10^{18} $\mathrm{eV}^{-1}\cdot\mathrm{cm}^{-3}$ was obtained for N_F in Ref. 2. However, Darvish *et al.*[2] set $a = 8$ Å in their calculation of N_F. Localization radius values of such an order are usually taken for amorphous materials,[4] but it is more prudent to use the value $a = 14$ Å, for a single crystal of $TlGaS_2$, which was obtained experimentally for gallium sulfide.[5] We used the relation[4]

$$N_F^2 = 6.4\times10^{49}\sigma(\omega)a^{-5}, \tag{3}$$

where $\sigma(\omega)$ is the conductivity at a frequency of 10^6 Hz, to calculate N_F from the experimental values of $\sigma(\omega)$ obtained in Ref. 2 for $TlGaS_2$ crystal crystals. Substituting the value $a = 14$ Å into this expression, we obtained 2.2×10^{18} eV^{-1}

$\cdot \mathrm{cm}^{-3}$ for N_F, which nearly coincides with the values obtained above $N_F = 2.0 \times 10^{18}$ and 2.5×10^{18} $\mathrm{eV}^{-1} \cdot \mathrm{cm}^{-3}$.

Thus, both ac[2,7] and dc hopping conduction take place in $TlGaS_2$ single crystals, and the results of these measurements are in good agreement with one another.

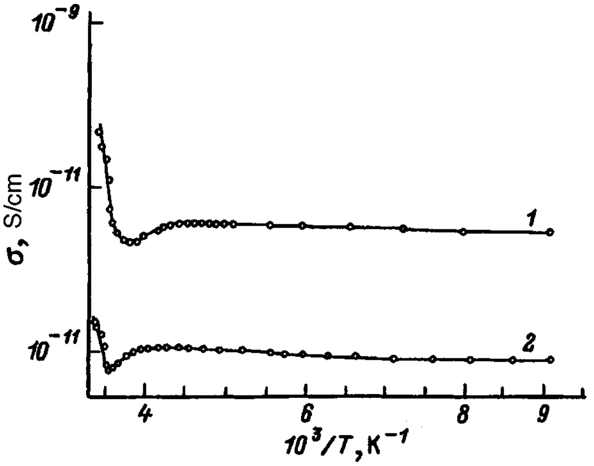

FIG. 3. Temperature dependences of $\sigma_{\perp c}$ (*1*) and $\sigma_{\parallel c}$ (*2*) for a $TlInS_2$ single crystal.

Figure 3 presents the temperature dependences of $\sigma_{\perp c}$ and $\sigma_{\parallel c}$ for a $TlInS_2$ single crystal. The high-temperature branches of these plots have an exponential character, and their slopes are equal to 0.7 and 0.4 eV, respectively. It is noteworthy that levels with an energy of 0.5–0.7 eV were also discovered in the band gap in the photocurrent spectra of $TlInS_2$ single crystals.[8,9] After the exponential decay, $\sigma_{\perp c}$ and $\sigma_{\parallel c}$ begin to increase and pass through a maximum at ~ 220 K. Such an anomalous course of $\sigma_{\perp c}$ and $\sigma_{\parallel c}$ is probably caused by a phase transition, whose occurrence in $TlInS_2$ single crystals at such a temperature was also established in Refs. 10 and 11. Both $\sigma_{\perp c}$ and $\sigma_{\parallel c}$ decay very slowly after the maximum. The approximate value of the activation energy ΔE in this temperature range is less than 10^{-2} eV. In the temperature range 110–140 K, the temperature dependence of $\sigma_{\perp c}$ and $\sigma_{\parallel c}$ vanishes entirely. The temperature-independent conductivity can be attributed to the tunneling of carriers in a strong electric field from localized states into the allowed band. However, in our case the experimental conditions (the relatively weak fields $F = 2.7 \times 10^3$ V/cm and the distance from the breakdown field) indicate that the activationless conduction in $TlInS_2$ in the temperature range 110–140 K is mediated by localized carriers, i.e., is essentially hopping conduction. To observe such conduction, the potential energy drop in an electric field over the hopping distance R, eFR, must be comparable to the energy spread ΔE of the localization centers.[6] Knowing that $N_F = 6.5 \times 10^{18}$ $\mathrm{eV}^{-1} \cdot \mathrm{cm}^{-3}$ in $TlInS_2$,[3] we evaluated the hopping distance of a charge carrier under dc conditions: for example, at $T = 110$ K the value of R was equal to 95 Å. The mean hopping distance in $TlInS_2$ under ac conditions is 117 Å.[3] Our evaluations showed that $eFR \approx 2.6 \times 10^{-3}$ eV, i.e., this value is comparable to the value of ΔE that we determined from the slope of the dependence of $\log\sigma$ on $10^3/T$ at low temperatures.

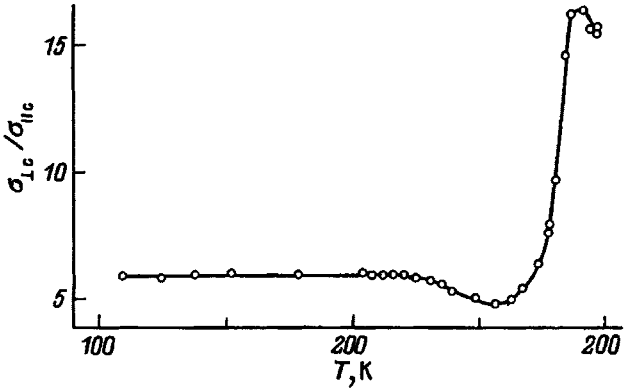

FIG. 4. Temperature dependence of the conductivity anisotropy in a $TlInS_2$ single crystal.

We note that the conductivity anisotropy was smaller in the $TlInS_2$ crystals than in the $TlGaS_2$ and $TlGaSe_2$ crystals. Figure 4 shows the temperature dependence of the conductivity anisotropy $\sigma_{\perp c}/\sigma_{\parallel c}$ in $TlInS_2$, whence it is seen that $\sigma_{\perp c}/\sigma_{\parallel c}$ does not depend on the temperature in the temperature range 110–220 K and that it increases sharply (by ~ 3 fold) at 260–293 K.

Thus, the experimental results obtained have shown that variable-range hopping conduction between states localized near the Fermi level takes place along and across the layers of $TlGaS_2$ and $TlInS_2$ single crystals at $T \leqslant 200$ K.

[1] S. N. Mustafaeva and S. D. Mamedbeili, in *Abstracts of the 9th International Conference on Ternary and Multinary Compounds, Yokohama, Japan (August 8–12, 1993)*, p. 281.

[2] A. M. Darvish, A. É. Bakhyshov, and V. I. Tagirov, Fiz. Tekh. Poluprovodn. **11**, 780 (1977) [Sov. Phys. Semicond. **11**, 458 (1977)].

[3] S. N. Mustafaeva, M. M. Asadov, and V. A. Ramazanzade, Fiz. Tverd. Tela (St. Petersburg) **38**, 14 (1996) [Phys. Solid State **38**, 7 (1996)].

[4] N. F. Mott and E. A. Davis, *Electronic Processes in Non-crystalline Materials* [Clarendon Press, Oxford (1971); Russ. trans., Mir, Moscow (1974), 472 pp.].

[5] V. Augelli, C. Manfredotti, R. Murri, R. Piccolo, and L. Vasanelli, Nuovo Cimento B **38**, 327 (1977).

[6] B. I. Shklovskiĭ, Fiz. Tekh. Poluprovodn. **6**, 2335 (1972) [Sov. Phys. Semicond. **6**, 1964 (1972)].

[7] A. É. Bakhyshov, S. R. Samedov, Safuat Bules, and V. I. Tagirov, Fiz. Tekh. Poluprovodn. **16**, 161 (1982) [Sov. Phys. Semicond. **16**, 98 (1982)].

[8] S. N. Mustafaeva and M. M. Asadov, *Inhomogeneous Electronic States* [in Russian], Inst. Neorg. Khim. Sib. Otd. Akad. Nauk SSSR, Novosibirsk (1991), pp. 198–199.

[9] S. N. Mustafaeva, M. M. Asadov, and V. A. Ramazanzade, Izv. Ross. Akad. Nauk, Neorg. Mater. **31**, 318 (1995).

[10] S. B. Vakhrushev, V. V. Zhdanova, B. E. Kvyatkovskiĭ, N. M. Okuneva, K. R. Allakhverdiev, R. A. Aliev, and R. M. Sardarly, JETP Lett. **39**, 291 (1984).

[11] K. R. Allakhverdiev, N. A. Bakhyshov, T. G. Mamedov, and A. I. Nadzhafov, Fiz. Tverd. Tela (Leningrad) **28**, 2243 (1986) [Sov. Phys. Solid State **28**, 1258 (1986)].

Translated by P. Shelnitz

Photoluminescence and multiphonon resonant Raman scattering in Ni- and Co-doped $Zn_{1-x}Mn_xTe$ crystals

Yu. P. Gnatenko, O. A. Shigil'chev, E. Rutkovskiĭ, G. Contreras-Puente, and M. Cardenas-Garcia

Institute of Physics, Ukrainian National Academy of Sciences, 252022 Kiev, Ukraine

(Submitted July 23, 1997)
Fiz. Tverd. Tela (St. Petersburg) **40**, 616–621 (April 1998)

Low-temperature photoluminescence, exciton reflection, and multiphonon resonant Raman scattering spectra of Ni- and Co-doped $Zn_{1-x}Mn_xTe$ crystals were investigated. Intense emission occurs in a broad spectral region (1100–17 000 cm^{-1}) in the crystals containing Ni atoms. It is caused by intracenter transitions involving Mn^{2+} ions and transitions between the conduction band and a level of the doubly charged acceptor. The features of the exciton photoluminescence and multiphonon resonant Raman scattering involving longitudinal-optical (LO) phonons at various temperatures are investigated. The insignificant efficiency of the localization of excitons on potential fluctuations in the $Zn_{1-x}Mn_xTe$:Co crystals is established. A temperature-induced increase in the intensity of the 5LO multiphonon resonant Raman scattering line due to the approach of the conditions for resonance between this line and the ground exciton state is observed in these crystals. *© 1998 American Institute of Physics.* [S1063-7834(98)00704-7]

Among II–VI semiconductors, ZnTe crystals are very promising materials for use as active elements in optoelectronics, since they have a high emission efficiency. The formation of substitutional solid solutions with Mn^{2+} ions markedly expands the scope of their practical application owing to the fundamentally new properties of such materials.

The $Zn_{1-x}Mn_xTe$ crystals investigated in the present work belong to a new class of materials, viz., semimagnetic semiconductors (SMSC's), which have been studied intensively in recent years. The most thoroughly investigated materials among these semiconductors are $Cd_{1-x}Mn_xTe$ crystals. As for $Zn_{1-x}Mn_xTe$ crystals, the literature contains information mainly on their magnetic and magneto-optical properties.[1–6] As far as we know, the investigation of the optical properties of these crystals has been the subject of a small number of papers,[7–11] which presented the results of low-temperature measurements of the intracenter absorption[7,8] and luminescence[8,9] spectra of the Mn^{2+} ions, as well as the exciton reflection,[8] absorption,[10] and IR absorption[11] spectra.

The physical properties of semiconductor crystals, especially their energy structure, are very sensitive to the presence of various crystal-structure defects in them. This permits regulation of their physical properties by introducing assigned sets of impurities into the crystals.

There is special interest in the study of impurity atoms of the iron group, which form deep levels in II–VI semiconductors, alter the number and type of intrinsic structural defects, and thereby control many optical, electrical, and photoelectric properties of the semiconductors.[12]

The study of the physical properties of semiconductors doped with the impurities indicated opens up the possibility for broader application as promising materials for photo- and optoelectronics. It is also noteworthy in the case that the investigation of the influence of impurity atoms on the basic physical properties of SMSC's is in its infancy.[13,14]

Low-temperature optical investigations are very effective in providing detailed information on the structure of the energy levels of impurities and defects, the mechanisms of radiative recombination, and the dynamic properties of elementary excitations in such materials.

For the purpose of obtaining information on the mechanisms of the luminescence of these crystals over a broad spectral range (11 000–20 000 cm^{-1}) at various temperatures (4.5–293 K), we investigated in the present work the exciton reflection, photoluminescence (PL), and multiphonon resonant Raman scattering (MPRRS) spectra of Ni- and Co-doped $Zn_{0.95}Mn_{0.05}Te$ SMSC's.

EXPERIMENTAL METHOD

We investigated single crystals of $Zn_{1-x}Mn_xTe$ ($x \approx 0.05$) grown by the Bridgman method in quartz ampules, which were evacuated to 1.3×10^{-3} Pa to eliminate the formation of impurity complexes containing oxygen in the crystals grown. The doping was carried out during crystal growth. The concentration of Ni and Co impurity atoms was calculated from the amounts introduced into the original mixture and amounted to 10^{19} cm^{-3}. To eliminate the interaction of the impurities with quartz and the wetting of quartz by the material being synthesized, a graphite coating was applied to the inner walls. Freshly cleaved surfaces were used to measure the photoluminescence and exciton reflection spectra.

The PL spectra were measured with excitation by an argon laser. The principal excitation line corresponded to $\lambda = 488.8$ nm. The PL spectra were recorded using a Spex

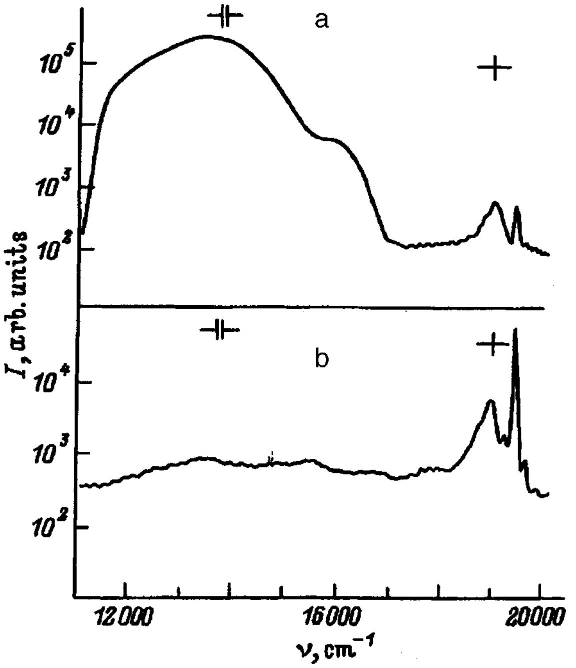

FIG. 1. Photoluminescence spectra of Ni- (a) and Co-doped (b) $Zn_{0.95}Mn_{0.05}Te$ crystals at $T=9.0$ K ($N=10^{19}$ cm^{-3}).

1403 double monochromator and an RCA C31034 photomultiplier operating in the photon-counting mode. The photomultiplier was cooled to improve the signal-to-noise ratio. The exciton reflection and photoluminescence spectra were measured in the exciton region of the spectrum using an SDL-1 spectrometer. The spectral slit width for these measurements did not exceed 2 cm^{-1}. The temperature measurements were performed using an UTREX system, which permits stabilization of the temperature to within 0.01 K.

EXPERIMENTAL RESULTS AND DISCUSSION

The PL spectra of Ni- and Co-doped $Zn_{1-x}Mn_xTe$ crystals at $T=9$ K are presented in Fig. 1. It is seen that the luminescence of these crystals covers a broad spectral region (11 000–20 000 cm^{-1}). In the case of $Zn_{1-x}Mn_xTe$:Ni crystals, the most intense emission, which consists of several overlapping broad bands, is located in the long-wavelength region (11 000–17 000 cm^{-1}), while the most intense emission for the $Zn_{1-x}Mn_xTe$:Co crystals is located in the short-wavelength region (18 000–20 000 cm^{-1}) of the spectrum.

The energy position of the emission line with the shortest wavelength in the PL spectra of the crystals investigated corresponds to $\lambda=514.5$ nm. The low-intensity satellites which are observed near this line in the case of the $Zn_{1-x}Mn_xTe$:Co crystals and are equidistant from it at distances equal to the energy of an LO phonon in a ZnTe crystal (205 cm^{-1}) attest to the appearance of MPRRS processes in these crystals.[15–18]

Figure 2 presents the emission (curves *1–6*) and reflection (curves *1′–6′*) spectra in the exciton region of the spectrum for $Zn_{1-x}Mn_xTe$:Co crystals at various temperatures ($T=4.5-70$ K). The inset in Fig. 2 presents the emission spectra of these crystals at $T=80$ and 100 K (curves *7* and *8*, respectively; the positions of the exciton reflection bands are marked by arrows). It is noteworthy that at $T=4.5$ K the line at $\lambda=514.5$ nm is almost in resonance with the ($n=1$) exciton transition. As we see from Fig. 2 (curves *1–3*), the long-wavelength wing of the laser line is protracted because of its overlap with the exciton I_L line, the position of whose maximum practically coincides with the position of the middle of the exciton reflection dispersion curve ($\lambda_{exc}=515.2$ nm). In addition, the PL spectrum recorded at $T\leqslant 20$ K also displays weak emission of a D^0X exciton-impurity complex, which is marked by arrows in Fig. 2 ($\lambda=516.2$ nm).

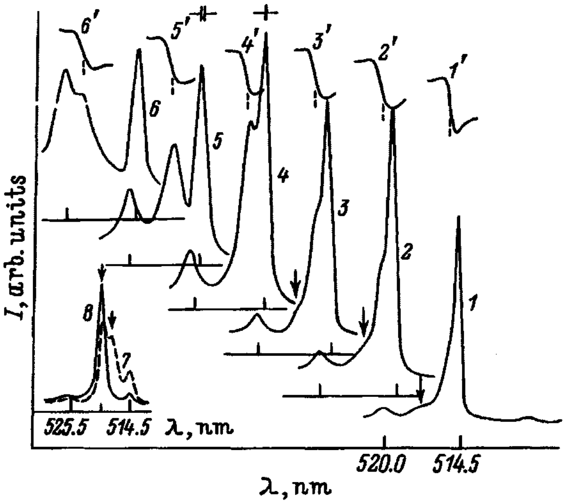

FIG. 2. Luminescence (*1–6*) and exciton reflection (*1′–6′*) spectra of Co-doped $Zn_{0.95}Mn_{0.05}Te$ crystals at $T=4.5$, 10.0, 20.0, 30.0, 50.0, and 70.0 K. The inset shows the luminescence spectra of these crystals at $T=80.0$ (*7*) and 100.0 K (*8*), on which the positions of the middle of the exciton reflection bands at the respective temperatures are marked by arrows.

An increase in temperature leads to an increase in the detuning of the line at $\lambda=514.5$ nm relative to excitonic resonance as a consequence of the long-wavelength shift of the exciton reflection band. The manifestation of the exciton I_L PL line, which is located between the line at $\lambda=514.5$ nm and the line at $\lambda=520.0$ nm becomes clearer at $T=50$ K (curve *5*). It is seen that an increase in temperature causes appreciable broadening of the I_L PL line, but its position relative to the exciton reflection band remains practically unchanged. It should also be noted that the intensity of the line at $\lambda=520.0$ nm undergoes a strong increase as the distance between this line and the exciton reflection band decreases with increasing temperature. For example, at $T=70$ K the intensity of this line is commensurate with the intensity of the line at $\lambda=514.5$ nm, while at $T=100$ K (curve *8* in the inset to Fig. 2), under the conditions of resonance between the line at $\lambda=520$ nm and the exciton transition to the ground state, this line becomes the most intense line in the PL spectrum. At $T=100$ K this line is superimposed on the I_L PL line.

The position of the exciton reflection band for the $Zn_{1-x}Mn_xTe$:Ni crystals at $T=9.0$ K corresponds to $\lambda_{exc}=512.9$ nm (Fig. 3). The difference between the positions of the exciton reflection line for the Co- and Ni-doped crystals

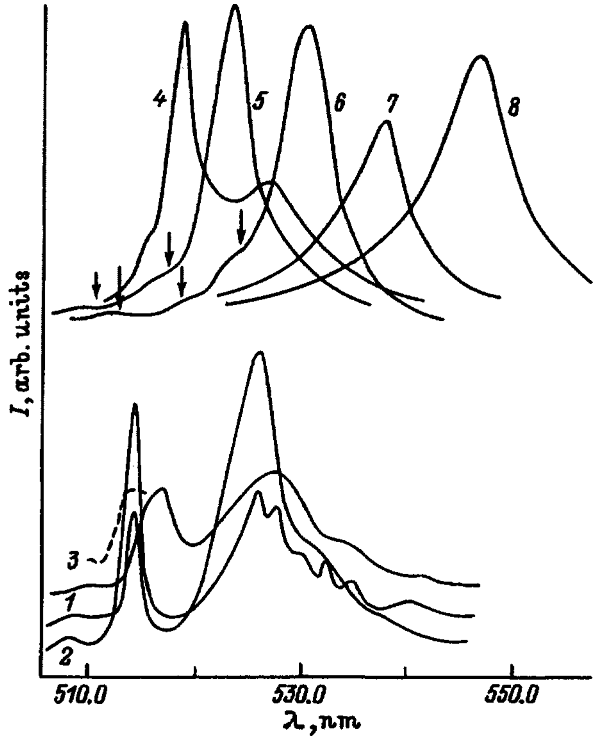

FIG. 3. Photoluminescence spectra of Ni-doped $Zn_{0.95}Mn_{0.05}Te$ crystals $T=4.5$ (*1*), 15.0 (*2*), 60.0 (*3*), 80.0 (*4*), 130.0 (*5*), 190.0 (*6*), 250.0 (*7*), and 293.0 K (*8*). The dashed curve corresponds to the exciton reflection band at $T=4.5$ K.

is due to the slight difference between the concentrations of Mn ions in the two crystals (the value $x=0.05$ was determined from the amounts of the components introduced into the original mixture). At low temperatures ($T \leqslant 60$ K) an intense line is seen at $\lambda=514.5$ nm in the region of excitonic resonance in the PL spectrum. At $T \leqslant 60$ K on the short-wavelength side of this line there is a weak line at the distance of an LO phonon, whose intensity decreases as the temperature rises. At $T>60$ K the most intense line in the PL spectrum is the I_L line, whose energy position is close to the maximum of the exciton reflection band. The exciton I_L line broadens appreciably at $T>80$ K. At $T \leqslant 130$ K it remains symmetric, but its short-wavelength wing then becomes strongly protracted at higher temperatures. It should be noted that an equidistant fine structure consisting of LO phonon replicas of the exciton PL band is displayed on the long-wavelength wing of the exciton band in the temperature range $80 \leqslant T \leqslant 190$ K (it is marked by arrows in Fig. 3).

As we see from Fig. 1, the PL spectra of the crystals investigated display a broad PL band on the long-wavelength side of the line at $\lambda=514.5$ nm. In the case of the $Zn_{1-x}Mn_xTe$:Ni crystals, this band has a fine structure at $T=4.5$ K (Fig. 3). An increase in the temperature to 15 K leads to obliteration of this fine structure, and the form of the band has a doublet character. A hump is observed on its long-wavelength wing at a distance of about 200 cm^{-1} from the position of the maximum. The intensity of this band decreases fairly rapidly in comparison with the exciton PL band as the temperature rises. For example, at $T=80$ K its intensity becomes less than that of the I_L line, and at $T=130$ K no such band is displayed in the PL spectrum. In the case of the $Zn_{1-x}Mn_xTe$:Co crystals the fine structure of the band just indicated is not observed in the PL spectrum even at $T=4.5$ K, and the temperature dependence of its intensity is similar to the dependence obtained for the $Zn_{1-x}Mn_xTe$:Ni crystals.

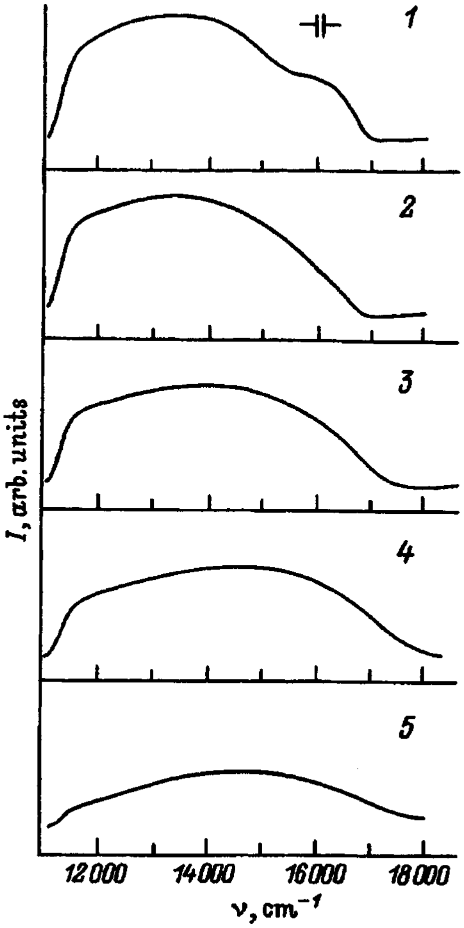

FIG. 4. Luminescence spectra of Ni-doped $Zn_{0.95}Mn_{0.05}Te$ crystals at $T=15.0$ (*1*), 60.0 (*2*), 130.0 (*3*), 220.0 (*4*), and 293.0 K (*5*).

Figure 4 presents the PL spectra of $Zn_{1-x}Mn_xTe$:Ni in the long-wavelength region of the spectrum (11 000–17 000 cm^{-1}) at various temperatures. The shape of the broad PL band observed and its temperature dependence are quite complicated: 1) on the long-wavelength wing of the band with a maximum at $\hbar\omega=13\,500$ cm^{-1} there is a hump at $\hbar\omega=16\,000$ cm^{-1}, which is clearly caused by overlap with another broad band of smaller intensity; 2) when the temperature is raised to 60 K, the hump on the short-wavelength wing of the band vanishes; 3) an increase in the temperature from 9 to 293 K causes displacement of the band maximum by 200 cm^{-1} toward shorter wavelengths; 4) at $T=293$ K the band becomes practically symmetric.

In the case of the $Zn_{1-x}Mn_xTe$:Co crystals the PL intensity in the long-wavelength portion of the spectrum is very weak (curve *2* in Fig. 2), and two broad bands can be identified here with maxima at $\hbar\omega=13\,500$ and 15 700 cm^{-1}. The intensity of these bands varies only slightly at $T \leqslant 50$ K, but at $T=100$ K they are scarcely observed in the PL spectrum.

The crystals investigated in this work are semiconductor solid solutions. Unlike ordinary binary compounds, semiconductor solid solutions are characterized by a chaotic potential-energy relief in the crystal lattice. The interaction of excitons with such a field determines the features of the exciton states and their appearance in the optical spectra.

According to Ref. 19, there is a characteristic exciton localization energy E_0, which depends on the parameters of the crystal and characterizes the obliteration of the spectrum at the bottom of the exciton band. The value of E_0 is a measure of the broadening of the exciton reflection bands. The long-wavelength maximum of the exciton reflection dispersion curve corresponds to the energy of localized excitons, while the middle of this curve corresponds to the energy of delocalized or free excitons.

The observed structure of the PL spectrum of the $Zn_{1-x}Mn_xTe$:Co crystals points out the effective role of the MPRRS processes involving longitudinal-optical phonons. In this case the PL spectra of the crystals investigated are excited by the line of an argon laser at $\lambda = 488.8$ nm. Thus, interband excitation of the crystal takes place under the experimental conditions indicated.

An analysis of the energy positions of the lines observed at low temperatures ($T < 70$ K) in the PL spectrum of the $Zn_{1-x}Mn_xTe$:Co crystals (Fig. 2) provides evidence that the very intense line at $\lambda = 514.5$ nm is the 5LO phonon replica of the exciting laser line at $\lambda = 488.8$ nm. The matching of the energy positions of this line and the argon laser line at $\lambda = 514.5$ nm is accidental and is characteristic of the crystals investigated in this work. The low-intensity satellites observed on the long- and short-wavelength sides of the line at $\lambda = 514.5$ nm correspond to the 6LO and 4LO phonon replicas of the laser line at $\lambda = 488.8$ nm. The strong increase in the intensity of the 5LO MPRRS line is a manifestation of its resonance with the ground exciton state, as was previously observed for $Zn_xCd_{1-x}Te$ crystals in the case of the 1LO and 2LO MPRRS lines.[16] As the temperature rises, especially in the range $T = 30 - 70$ K, where the measurement conditions (signal amplification and spectral slit width) remained unchanged, a decrease in the intensity of the 5LO MPRRS line and an increase in the intensity of the 6LO line are observed. They are unequivocally tied to changes in the resonance conditions of these lines with the exciton state as a result of the temperature-induced decrease in the band gap width and, accordingly, the displacement of the bottom of the exciton band toward lower energies. At $T = 100$ K, the 6LO line becomes the most intense line in the spectrum due to its resonance with the ground exciton state, as well as the exciton I_L PL line. Resonant enhancement of the 5LO MPRRS line is also observed for the $Zn_{1-x}Mn_xTe$:Ni crystals. An absence of the 6LO line is attributed to its weak intensity and overlap with the short-wavelength wing of the broad PL band.

It should be noted that the intensity of the 6LO MPRRS line in the case of cobalt-doped crystals is determined by two competing factors. The shortening of the exciton lifetime with increasing temperature should lead to a decrease, while the simultaneous decrease in the distance between the maximum of the I_L PL line and the position of the 6LO MPRRS line should lead to an increase in its intensity. Since a temperature-induced increase in the intensity of the 6LO line is observed experimentally, it must be assumed that the predominant factor in this case is the decrease in the detuning of the 6LO line and the maximum of the I_L PL line.

An analysis of the PL spectra of $Zn_{1-x}Mn_xTe$:Co crystals points out the weak influence of the localization of excitons on fluctuations of the crystal-field potential, since the maximum of the I_L PL line of such crystals at both helium and higher temperatures is near the middle of the exciton reflection dispersion curve, i.e., it corresponds to the emission of free or delocalized excitons. In semiconductor solid solutions, the I_L line is usually located near the maximum of the exciton reflection band and, at low temperatures, it is caused mainly by the radiative recombination of localized excitons. The insignificant role of the localization of excitons in these crystals is also evidenced by the appearance of the emission of excitons bound to neutral donors in the PL spectra at $T < 20$ K. The twofold broadening of the exciton reflection bands for the $Zn_{1-x}Mn_xTe$:Co crystals in comparison with the binary compound ZnTe at $T = 4.5$ K is clearly caused by the elastic scattering of free excitons on potential fluctuations, intrinsic defects, and impurity centers containing Co atoms. In the case of the $Zn_{1-x}Mn_xTe$:Ni crystals the efficiency of the localization of exciton states is significantly greater. This is indicated by the fact that the maximum of the exciton I_L PL line is near the maximum of exciton reflection band. The appreciable broadening of the exciton reflection band in comparison to the band for undoped or Co-doped crystals is inhomogeneous because of the formation of exciton density-of-states ''tails.''[20]

The presence of an equidistant fine structure on the short-wavelength wing of the highly broadened I_L PL line at $T = 80 - 190$ K (Fig. 3) attests to the effective role of the interaction involving several LO phonons in the radiative recombination processes of excitons. For example, only one LO phonon replica of the I_L line is observed at $T = 80$ K, while the emission of excitons involving three LO phonons is observed at $T = 190$ K. Thus, the interaction of localized excitons with LO phonons at $T < 80$ K is an effective mechanism for their transition to delocalized or free states. The strong short-wavelength asymmetry of the exciton band observed at $T > 200$ K (Fig. 3) is caused by such processes. The absence of an equidistant fine structure is attributed to its temperature-induced obliteration.

The PL spectrum of $Zn_{1-x}Mn_xTe$:Co crystals contains a relatively broad, intense band (Fig. 1). An analysis of the position of this band relative to the position of a free exciton and a comparison of the results obtained with the PL spectrum of ZnTe crystals[21] provides evidence that the emission in this region is caused by transitions involving the acceptor energy level at $E_v + 0.05$ eV and the donor energy level at $E_c - 0.01$ eV or the conduction band. Similar emission is also observed for $Zn_{1-x}Mn_xTe$:Ni crystals. The presence of a fine structure in this region of the spectrum (Fig. 3) is caused both by the appearance of these two types of optical transitions and by the presence of LO phonon replicas of the corresponding zero-phonon lines.

The appearance of an intense broad band in the PL spectrum with a maximum near $h\omega = 16\,000\ \mathrm{cm}^{-1}$ is characteristic of Mn-doped ZnTe crystals[8] and $\mathrm{Zn}_{1-x}\mathrm{Mn}_x\mathrm{Te}$ SMSC's.[9] The appearance of this band is associated with emission as a result of intracenter transitions between the $^4T_1$ and $^6A_1$ states of the Mn^{2+} ions.[8,9] As is seen from Fig. 1, the $\mathrm{Zn}_{1-x}\mathrm{Mn}_x\mathrm{Te{:}Ni}$ crystals exhibit a second band on the short-wavelength wing of the intense broad band ($h\omega_{\max} = 13\,500\ \mathrm{cm}^{-1}$), whose position on the energy scale provides evidence that it is caused by intracenter transitions of the Mn^{2+} ions. A broad PL band with a maximum near $h\omega = 13\,500\ \mathrm{cm}^{-1}$ and a symmetric shape was previously observed in ZnTe crystals.[22] Its appearance is associated with radiative transitions between the conduction band and the level of a doubly charged Zn vacancy ($E_v + 0.7$ eV).

The $\mathrm{Zn}_{1-x}\mathrm{Mn}_x\mathrm{Te{:}Co}$ crystals exhibit emission of weak intensity in the long-wavelength portion of the spectrum. It is clearly due to the fact that, like ZnTe:Co crystals,[23] these crystals are characterized by the appearance of intense absorption in the region $11\,00 - 17\,500\ \mathrm{cm}^{-1}$. Such absorption is caused by intracenter and photoionization transitions involving Co^{2+} ions. The weak intensity of the broad PL bands in the long-wavelength portion of the spectrum for the $\mathrm{Zn}_{1-x}\mathrm{Mn}_x\mathrm{Te{:}Co}$ crystals is caused by the intense reabsorption of radiation.

Thus, the results obtained in the present work provide evidence that the emission of the $\mathrm{Zn}_{1-x}\mathrm{Mn}_x\mathrm{Te{:}Ni}$ crystals ($x \sim 0.05$, $N_{\mathrm{Ni}} = 10^{19}\ \mathrm{cm}^{-3}$) observed over a broad spectral region ($11\,500 - 11\,700\ \mathrm{cm}^{-1}$) is caused by the superposition of two broad bands, which correspond to intracenter transitions of the Mn^{2+} ions (the band at $h\omega_{\max} \sim 16\,000\ \mathrm{cm}^{-1}$) and to transitions between the conduction band and a level of the doubly charged acceptor (the band at $h\omega_{\max} \sim 13\,500\ \mathrm{cm}^{-1}$). It has been established for the crystals investigated that the emission in the short-wavelength portion of the spectrum is due to exciton PL, MPRRS, and optical transitions between the conduction band or a shallow donor level and a level of the neutral acceptor. It has been shown that the optical transitions in this portion of the spectrum, which are caused by different emission mechanisms, occur with the effective participation of longitudinal-optical phonons.

An increase in the intensity of the 5LO MPRRS line as the temperature rises from 4.5 to 70 K has been discovered for the $\mathrm{Zn}_{1-x}\mathrm{Mn}_x\mathrm{Te{:}Co}$ crystals, for which the emission of delocalized and free excitons is observed at low temperatures. It has been attributed to the weak influence of the localization of excitons on fluctuations of the crystal-field potential and a decrease in the detuning of the exciting laser line relative to the maximum of the exciton I_L line as a result of temperature-induced displacement of the bottom of the exciton band. The broadening of the exciton reflection band for these crystals is mainly a result of elastic scattering by fluctuations in the crystal-field potential, defects, and impurity centers containing cobalt atoms. It has been established in the $\mathrm{Zn}_{1-x}\mathrm{Mn}_x\mathrm{Te{:}Ni}$ crystals that the exciton I_L line is determined by the emission of localized excitons and thus attests to their effective localization.

The research described in this paper was supported by the International Science Foundation (Grant No. UBJ000) and the Ukrainian State Fund for Fundamental Research (Project No. 2.4/327).

[1] T. M. Holden, G. Dolling, V. F. Sears, J. K. Furdyna, and W. Giriat, Phys. Rev. B **26**, 5074 (1982).

[2] A. Witlin, R. Triboulet, and R. R. Galazka, J. Cryst. Growth **72**, 380 (1985).

[3] Y. Shapira, S. Foner, P. Becla, D. N. Domingues, M. J. Naughton, and J. S. Brooks, Phys. Rev. B **33**, 365 (1986).

[4] A. V. Komarov, S. M. Ryabchenko, and N. I. Vitrikhovskiĭ, JETP Lett. **27**, 413 (1978).

[5] P. Swiderski and A. Twardowski, Phys. Status Solidi B **122**, K147 (1984).

[6] A. Twardowski, Phys. Lett. A **94**, 103 (1983).

[7] J. E. Morales Toro, W. M. Becker, B. I. Wang, U. Debska, and J. W. Richardson, Solid State Commun. **52**, 41 (1984).

[8] Yu. P. Gnatenko and A. I. Zhmurko, Ukr. Fiz. Zh. **30**, 843 (1985).

[9] E. Müller and W. Gebhardt, Phys. Status Solidi B **137**, 259 (1986).

[10] W. Giriat and J. Stankiewicz, Phys. Status Solidi B **124**, K53 (1984).

[11] A. Olszewski, W. Wojdowski, and W. Nazarewicz, Phys. Status Solidi B **104**, K155 (1980).

[12] Yu. P. Gnatenko, Doctoral thesis, Institute of Physics, Ukrainian National Academy of Sciences, Kiev (1992).

[13] J. K. Furdyna, J. Vac. Sci. Technol. A **4**, 2002 (1986).

[14] M. Cardenas-Garcia, G. Contreras-Puente, Yu. P. Gnatenko, and Y. H. Rutkowski, Bull. Am. Phys. Soc. **40**, 510 (1995).

[15] A. A. Klochikhin and A. T. Plyukhin, JETP Lett. **21**, 122 (1975).

[16] A. A. Klochikhin, A. T. Plyukhin, and L. T. Suslina, E. B. Shadrin, Fiz. Tverd. Tela (Leningrad) **18**, 1909 (1976) [Sov. Phys. Solid State **18**, 1112 (1976)].

[17] L. T. Suslina, A. T. Plyukhin, and D. L. Fedorov, Izv. Akad. Nauk SSSR, Ser. Fiz. **40**, 1994 (1976) [Izv. Akad. Nauk SSSR, Ser. Fiz. **40** (9), 193 (1976)].

[18] D. L. Fedorov, S. A. Permogorov, A. S. Nasibov, P. V. Shapkin, and Yu. A. Korostelin, Fiz. Tverd. Tela (St. Petersburg) **35**, 2142 (1993) [Phys. Solid State **35**, 1065 (1993)].

[19] S. D. Baranovskiĭ and A. L. Éfros, Fiz. Tekh. Poluprovodn. **12**, 2233 (1978) [Sov. Phys. Semicond. **12**, 1328 (1978)].

[20] P. I. Babiĭ, P. N. Bukivskiĭ, and Yu. P. Gnatenko, Fiz. Tverd. Tela (Leningrad) **28**, 3358 (1986) [Sov. Phys. Solid State **28**, 1890 (1986)].

[21] S. Nakashima and S. Yasuda, Phys. Status Solidi B **96**, 211 (1979).

[22] T. Taguchi, Phys. Status Solidi B **96**, K33 (1979).

[23] Yu. P. Gnatenko, A. I. Zhmurko, N. V. Potykevich, and I. A. Farina, Fiz. Tekh. Poluprovodn. **18**, 1105 (1984) [Sov. Phys. Semicond. **18**, 689 (1984)].

Translated by P. Shelnitz

PHYSICS OF THE SOLID STATE VOLUME 40, NUMBER 4 APRIL 1998

Microphase separation and magnetic Jahn–Teller polarons in LaSrAl$_{1-x}$Cu$_x$O$_{4-\delta}$

Yu. V. Yablokov, T. A. Ivanova, and A. E. Usachev

Kazan' Physicotechnical Institute, Russian Academy of Sciences, 420029 Kazan', Russia

(Submitted September 23, 1997)
Fiz. Tverd. Tela (St. Petersburg) **40**, 622–628 (April 1998)

An EPR study of the solid solutions LaSrAl$_{1-x}$Cu$_x$O$_4$, which are isostructural to La$_2$CuO$_4$, shows that microphase separation of the structure occurs already at small copper concentrations ($x \approx 0.01$). A phase enriched with Cu appears along with a phase of La$_2$AlO$_4$, which contains isolated CuO$_6$ centers. It is established that the nature of the states and the deformations of the CuO$_6$ centers is determined by internal Jahn–Teller factors. When $x \leqslant 0.1$, EPR signals are detected for new dynamic centers, which are identified as CuO$_6$ Jahn–Teller centers with a hole delocalized among the four in-plane oxygen ions (the total spin $S=1$). When $0.1 \leqslant x < 1$, local CuO$_6^-$ hole centers transform into magnetic Jahn–Teller polarons, which include five or more CuO$_6$ fragments, in the copper phase of the structure. Their transformations and the conditions for observing them are discussed. *© 1998 American Institute of Physics.* [S1063-7834(98)00804-1]

While investigating the EPR spectra of the ceramics LaSrAl$_{1-x}$Cu$_x$O$_4$, which are isostructural to La$_2$CuO$_4$, we discovered magnetic centers,[1] which were identified as CuO$_6$ centers with a hole delocalized among the four in-plane oxygen ions, i.e., CuO$_6^-$ Jahn–Teller centers with spin $S=1$. A microscopic model of these centers was proposed in Ref. 2, and they were compared to the magnetic quasiparticles studied in hole-doped La$_2$CuO$_4$.[3–6]

In this paper the results from Refs. 1 and 2 are developed and analyzed on the basis of further experimental investigations of the LaSrAl$_{1-x}$Cu$_x$0$_4$ system: the previously discovered effects are studied in other series of samples, and the EPR data are supplemented by the results of investigations employing other methods. The occurrence of microphase separation of the ceramics investigated into aluminum and copper microphases is established. The interrelationship between the electron-phonon properties of the hole centers in these phases is demonstrated.

1. EXPERIMENTAL RESULTS

Various series of the solid solutions LaSrAl$_{1-x}$Cu$_x$O$_{4-\delta}$, which were synthesized both by decomposing the nitrates[7] and by a solid-phase method from the metal oxides, were investigated. X-ray power diffraction analysis, which was performed on a DRON-2 diffractometer, showed that the samples belong to the K$_2$NiF$_4$ structural type at all copper concentrations ($0 \leqslant x \leqslant 1$). Figure 1 shows the variation of the unit-cell parameters a and c as the copper concentration increases. While a remains unchanged ($a=3.758$ Å at $x=0$ and $a=3.759$ Å at $x=1$) to within the experimental error (0.003 Å), c increases monotonically from 12.64 to 12.97 Å.

The diffuse reflectance spectra of the samples with $x=0.01-0.10$ were recorded on a Perkin-Elmer LAMDA9 spectrophotometer. The expected $d-d$ transitions could not be detected.

The oxidation state (the mean valence state) of copper in LaSrAl$_{1-x}$Cu$_x$0$_{4-\delta}$ was studied for several values of x by iodometric titrations The deviation of the oxygen content from stoichiometry δ was also determined. The values of the formal valence and δ are listed in Table I.

The EPR spectra of LaSrAl$_{1-x}$Cu$_x$0$_{4-\delta}$ were recorded in the X (ν=9.46 GHz) and Q (ν=37.1 GHz) bands in the temperature range 4.2–300 K on an ERS-230 radiofrequency spectrometer. The parameters of the experimental spectra were determined by optimizing model spectra.

Copper was introduced from a compound in the Cu^{2+} state. All the EPR signals observed should be assigned to this oxidation state of copper. A typical spectrum is shown in Fig. 2. It consists of signals of two types.

The signals of type I are typical of isolated Cu^{2+} centers in a polycrystalline matrix. They are described by a spin Hamiltonian of axial symmetry with the parameters $g_{\parallel}=2.320 \pm 0.002$, $g_{\perp}=2.069 \pm 0.003$, $A_{\parallel}=(150 \pm 1) \times 10^{-4}$

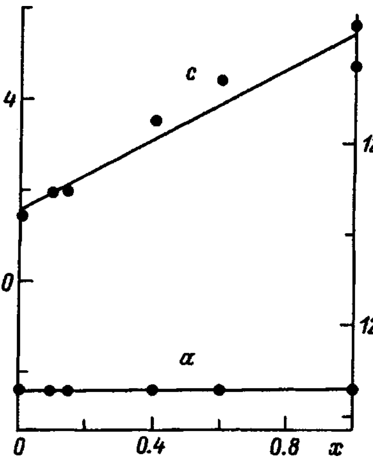

FIG. 1. Concentration dependence of the lattice constants a and c of LaSrAl$_{1-x}$Cu$_x$0$_4$ solid solutions.

TABLE I. Values of the formal valence of the Cu^{m+} ions in $\mathrm{LaSrAl}_{1-x}\mathrm{Cu}_x\mathrm{0}_{4-\delta}$ and deviation of the oxygen content δ from stoichiometry.

x	m	δ
0.2	2.47	0.05
0.4	2.46	0.11
0.6	2.46	0.16
0.8	2.46	0.22

cm^{-1}, and $A_\perp < 10\times10^{-4}$ cm^{-1}. For $x=0.01$ we have $\Delta H_\perp^{\mathrm{I}} = 6$ mT in the X band at $T=300$ K. In the parallel orientation of the constant magnetic field $\mathbf{H}$ and the OZ axis of the center, the linewidth $\Delta H_\parallel^{\mathrm{I}}$ equals 7 mT. The values of $\Delta H_\parallel^{\mathrm{I}}$ and $\Delta H_\perp^{\mathrm{I}}$ increase in the Q band and decrease as the temperature is lowered. Signals of type I are observed over the entire range of values of x up to $x\cong 0.8$. Their intensity reaches a maximum at $x=0.04$ and then decrease as the copper concentration is increased further (under a statistical distribution the largest number of these centers should be observed for $x=0.08$). The linewidth increases as x increases.

Signal II is observed at practically all concentrations of added copper. It is positively detected at $x\geqslant 0.02$, but it is also present in the spectra of the samples with $x=0.01$ in the form of a single, practically symmetric line with $g^{\mathrm{II}}=2.123\pm0.003$. Its width ΔH^{II}, measured in the Q band at $T=300$ K, increases successively from 18.5 mT for $x=0.01$ to 21 and 37 mT for $x=0.04$ and 0.60. The value of ΔH^{II} is smaller in the X band. For example, $\Delta H^{\mathrm{II}}=10$ mT for $x=0.02$ at $T=300$ K. The value of ΔH decreases somewhat as the temperature is lowered. The relative content of centers of type II in comparison with the content of the centers of type I (Kn) increases with increasing x (Fig. 3a). The total number of centers of types I and II is maximal for $x=0.04$ (Fig. 3b) and, in some series, for $x=0.02$. We note that signal II was also observed in the isostructural solid solutions $\mathrm{LaSrGa}_{1-x}\mathrm{Cu}_x\mathrm{0}_4$ with $x=0.02$ and 0.04, in which, unlike the series of the gallates $\mathrm{La}_{1+x}\mathrm{Sr}_{1-x}\mathrm{Ga}_{1-x}\mathrm{Cu}_x\mathrm{0}_4$ investigated in Ref. 10, the charge stoichiometry is violated.

The temperature dependence of the intensity of signal II in the samples with $x\leqslant 0.10$ (IIa) and $x>0.10$ (IIb) was unexpected. The intensity of signals IIb increases as the temperature is lowered, precisely as the intensity of signal I, obeying Curie's law. For example, for $x=0.4$ we obtained $K_{\mathrm{II}b}(293\ \mathrm{K})=0.61$ and $K_{\mathrm{II}}(4.2\ \mathrm{K})=0.68$. These values can be regarded as coinciding within the experimental errors. The intensity of signal IIa increases with decreasing temperature to $T\sim30$ K and then decreases sharply. For $x=0.10$, $K_{\mathrm{II}a}(>30\ \mathrm{K})=0.41$, while $K_{\mathrm{II}a}(4.2\ \mathrm{K})=0.09$. In the sample with $x=0.02$ signal IIa is scarcely detected at $T=4.2$ K.

The integrated intensity of the observed EPR spectrum was also measured. It was determined by a comparison with the signal of the reference BaMnF_4. The measurements revealed an unexpected result: EPR is observed for no more than 10% of the copper ions introduced into the matrix in the range $0.01\leqslant x\leqslant 0.1$. As x is increased, the fraction of Cu ions observed decreases. For example, when $x=0.6$, the number of centers detected in a sample weighing 50 mg is estimated as 10^{18} spins. We previously observed a similar picture for La,Sr aluminates with Ni^{3+} and Cr^{3+}.[8,9]

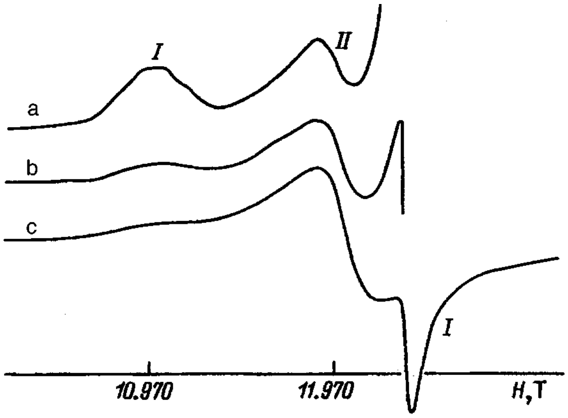

FIG. 2. EPR spectrum of $\mathrm{LaSrAl}_{1-x}\mathrm{Cu}_x\mathrm{0}_4$. $T=300$ K. $\nu=35.6$ GHz. $x=0.04$ (a), 0.10 (b), and 0.40 (c).

2. DISCUSSION OF RESULTS

The EPR parameters of the centers of type I are typical of Cu^{2+} ions in a tetragonally elongated, octahedral ligand environment. It hence follows that the Cu^{2+} ions in the $\mathrm{LaSrAl}_{1-x}\mathrm{Cu}_x\mathrm{0}_4$ solid solutions under discussion replace Al^{3+} ions and form oxygen octahedrons elongated along the [001] axis with nonlocal charge compensation.

The magnitude of the tetragonal component of the crystal field in the AlO_6 octahedra does not remain constant: it differs for different combinations of La and Sr ions along the [001] direction and reflects the changes in the lattice forces acting on the Me site as c/a increases (Fig. 1) due to increases in x.

These changes in the crystal fields at the site of the metal do not, however, lead to changes in the parameters of the copper EPR spectra. There is, in fact, no dependence of the g factors of Cu^{2+} on the copper concentration. No diversity is observed for the CuO_6 centers, although such diversity was

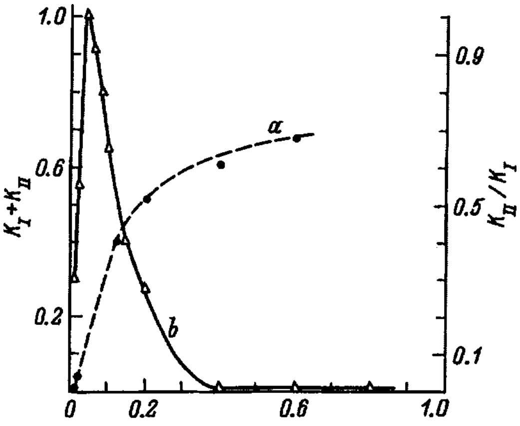

FIG. 3. Concentration dependence of the relative content of centers of type II in comparison to the content of centers of type I (a) and of the total number of centers of types I and II (b).

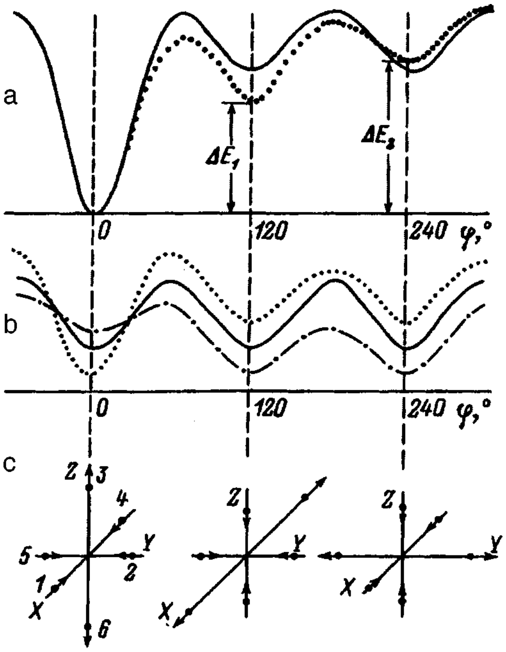

FIG. 4. Adiabatic potential of CuO_6 Jahn–Teller centers with small tetragonal and orthorhombic distortions in the Cu^{2+} site (a) and of dynamic CuO_6^- hole centers (b). The difference between the possible forms of the adiabatic potential is caused by the spread of local crystal fields in the Cu^{2+} site. c — Jahn–Teller deformations of complexes at the minima of the adiabatic potential.

observed for NiO_6 centers in a similar ceramic[8] as a consequence of statistical disordering of the La^{3+} and Sr^{2+} ions. It was also found that the EPR parameters of the centers of type I in $LaSrAl_{1-x}Cu_x0_4$ coincide to within the experimental accuracy with the parameters of the CuO_6 centers in the closely related solid solutions $La_{1+x}Sr_{1-x}Ga_{1-x}Cu_x0_4$,[10] while the values of a and c for the latter differ from the corresponding parameters for aluminates and vary from $a=3.84$ Å and $c=12.70$ Å for $x=0$ to $a=3.798$ Å and $c=13.154$ Å for $x=0.8$. The Cu(II) ions ''do not feel'' the accompanying changes in the crystal fields.

Such behavior, which is unusual for tetragonal centers, is easily explained within the Jahn–Teller effect for Cu^{2+} ions. As we know, the vibronic interactions in an octahedral Cu(II) complex results in spontaneous distortion of the octahedron along one of the fourth-fold axes. In the adiabatic approximation the three equivalent minima on the potential-energy surface separated by barriers of height 2β, where 2β is the anharmonicity parameter of the ligand vibrations (the solid line in Fig. 4b), correspond to tetragonally elongated configurations of the complexes. The magnitude of the deformations of the isolated Jahn–Teller complexes and the distortions of the crystal lattice in undiluted Jahn–Teller crystals are determined by the vibronic interactions.

If the site of a CuO_6 complex has small tetragonal or orthorhombic distortions, the minima of the adiabatic potential become energetically inequivalent with the energy differences between the minima $\Delta E_1=\Delta E_2$ or $\Delta E_1\neq\Delta E_2$, respectively (Fig. 4a). Experience and theoretical evaluations show that for $\Delta r=r_z-r_{x,y}\cong 0.01-0.15$ Å the distortions of the complexes in the ground and excited states are so close to the Jahn–Teller distortions that they are experimentally indistinguishable from them. The observed temperature dynamics of the complexes and their EPR spectrum depend on the magnitude of the distortion of the site and the temperature. If the energy differences between the minima ΔE_1 and ΔE_2 are so small that $kT>\Delta E_1,\Delta E_2$ over the entire measurement range, we have a pulsating configuration with $r_i=\langle r\rangle_{\mathrm{JT}}$ and $g_i=\langle g\rangle$. If $kT\lesssim\Delta E_1,\Delta E_2$, the parameters of the complex and its EPR spectrum depend on the temperature in accordance with the Boltzmann factor of the excited states: $r_i=r_i(T)$, $g_i=g_i(T)$.[11] If $kT\ll\Delta E_1,\Delta E_2$, the complex is stabilized in the lower state. Its distortions are enhanced in comparison to the distortions of the corresponding site in a crystal lattice (a Jahn–Teller complex). Variations of the tetragonal (or orthorhombic) component of the crystal field up to certain limits lead only to variation of the differences between the minima, but the degree of distortion of the complex and the parameters of the spectrum observed for the ground state do not depend on the magnitude of the deformation. In the linear approximation this limit $E_{\mathrm{tetr}}/2\beta<3$.[12]

The centers of type I clearly have a relationship between the tetragonal component of the crystal field and the vibronic constants for which the magnitude of the deformations of CuO_6 is determined by the interaction with e_g vibrations, and the magnitude of the ''tetragonal'' lattice component of the crystal field does not exceed 6β or $\sim 1500\ \mathrm{cm}^{-1}$ (~ 0.2 eV). Changes in this component lead only to changes in $\Delta E_{1,2}$ and have practically no influence on the magnitude of the distortions of the complex or the values of the g factors. Using the data for the Al–O distances in $LaSrAlO_4$ (2×1.997 Å and 4×1.898 Å, i.e., $\Delta r=0.099$ Å) and taking the linear vibronic coupling constant $V=10\,000\ \mathrm{cm}^{-1}/$Å, we find that $\Delta E\sim 1000\ \mathrm{cm}^{-1}$ in the CuO_6 Jahn–Teller complexes in $LaSrAl_{1-x}Cu_x0_4$. This means that there are excited $|y^2-x^2\rangle$ and $|z^2-x^2\rangle$ states corresponding to CuO_6 configurations that are elongated along the a and b directions of the crystal $\sim 1000\ \mathrm{cm}^{-1}$ above the ground $|x^2-y^2\rangle$ state. Under the influence of small deformations they can approach the ground state and have a significant influence on the processes taking place. A 0.01-Å change in a Me–O_z distance (here we are referring to the distance to an apical oxygen in the original matrix that has not yet been distorted by Jahn–Teller deformations) lowers these levels by $100\ \mathrm{cm}^{-1}$, and the replacement of La^{3+} by Sr^{2+} causes approximately the same change in the crystal field at a neighboring copper ion located on the same fourth-order axis as does axial compression of the complex by 0.015 Å.

Thus, the CuO_6 centers are Jahn–Teller complexes. In other words, the nature of their distortions is determined by the internal vibronic forces, and lattice perturbations are manifested only in the features of their dynamics. The conclusion that there is strong electron-phonon coupling in $LaSrAl_{1-x}Cu_x0_4$ suggests that such coupling exists in the cuprates $La_{1-x}Sr_xCuO_4$ as well. This would account for the significant elongation of the CuO_6 octahedrons along the [001] direction in these compounds: in La_2CuO_4 the Cu–O distances are equal to 2×2.46 Å and 4×1.905 Å, and in $La_{1.85}Sr_{0.15}CuO_4$ they are equal to 2×2.41 Å and 4×1.89 Å.[13,14]

Proceeding to an analysis of the nature of signal II, we bear in mind two points: the conditions for the appearance of the signal (it appears under the conditions of an electron deficiency in $Al_{1-x}Cu_xO_2$ layers) and its shape (it is a single symmetric signal).

The requirement for charge neutralization in $LaSrAl_{1-x}Cu_x0_{4-\delta}$ suggests the existence of either Cu^{3+} ions, O^- oxygen ions, or oxygen vacancies along with Cu^{2+} ions in the stable oxidation state. An iodometric titration confirmed this expectation by establishing that the effective charge state of copper is equal to $+2.47$. Oxygen vacancies can be encountered in various places in the structure: in the apical positions of AlO_6 and CuO_6 octahedrons when x is small, in an $Al(Cu)O_2$ layer, and in a La(Sr)O layer. Apical vacancies would preserve the axial symmetry of the EPR spectra of the centers, would leave these centers static, and would not disturb the antiferromagnetic character of the interactions in the CuO_2 layer. In the case of in-plane vacancies, CuO_5 centers with fairly strong orthorhombic distortions would appear, but they are not observed experimentally. Therefore, signal II cannot be associated with oxygen vacancies. Also, it cannot be assigned to Cu^{3+} ($3d^8$; $S=1$) ions. In this case a single EPR line can be observed only from cubic centers. There are no sites of cubic symmetry for copper ions in $LaSrAlO_4$. Only centers with O^- remain. At the same time, the experimental data allow us to conclude that the electron vacancy must be bound to a Cu^{2+} ion, since the observed value $g=2.123$ can be understood only in this case. In the matrix under consideration there are no other ions with a sufficiently large spin-orbit coupling constant. In the general case, the possibility of contamination of the nonstoichiometric solid solutions $LaSrAl_{1-x}Cu_x0_4$ by some foreign impurity that includes paramagnetic centers cannot be ruled out *a priori*. This impurity can go undetected by the fairly rough diffractometric method, but is manifested in EPR. However, the good reproducibility of the results in repeated syntheses with variation of the conditions allows us to disregard this possibility.

In Ref. 1 we assumed that an oxygen-ion electron vacancy is not localized on one site, but is distributed among the four in-plane oxygen sites of the CuO_6 octahedron. We shall utilize the scheme of molecular orbitals in a solitary, tetragonally deformed CuO_40_2 octahedron. The orbitals that are closest to the orbitals with e_g, b_{2g}, a_{1g}, and b_{1g} symmetry consisting predominantly of copper d orbitals are filled molecular orbitals formed from only the in-plane $a_{2g}(\pi)=(1/2)[py_1-px_2-py_3+px_4]$ and out-of-plane $b_{2u}(\pi)=(1/2)[pz_1-pz_2+pz_3-pz_4]$ oxygen $2p$ states. The $a_{2g}(\pi)$ and $b_{2u}(\pi)$ orbitals are written here in the coordinate system of a CuO_6 center. They are orthogonal to the a_{1g} and b_{1g} orbitals, which include the copper $|z^2\rangle$ and $|x^2-y^2\rangle$ states. The nonbonding $a_{2g}(\pi)$ and $b_{2u}(\pi)$ oxygen states are located in a free complex below the orbitals with a d character, but the interactions in the condensed matrix, particular the Madelung effects, render the bands of these states indistinguishable with respect to their energies, and we assume that the holes in the CuO_6 complexes in $LaSrAl_{1-x}Cu_x0_4$ occupy oxygen states of the $a_{2g}(\pi)$ and $b_{2u}(\pi)$ types.

The appearance of a hole delocalized over the in-plane oxygen ions of a CuO_6 octahedron in the immediate vicinity of the Cu^{2+}ion leads to a decrease in the tetragonal component of the crystal field to the point of possible reversal of its sign. It also leads to the appearance of spin-spin interactions between the unpaired electrons of $(O_4)^-$ and Cu^{2+}. When the exchange parameter J has the typical value in oxides $|J|\sim 10^3\ cm^{-1}$,[15] signal II can be observed only if the exchange interactions are ferromagnetic in nature. They should be such because of the orthogonality of the states of the interacting hole and Cu^{2+} spins. At the same time, these interactions do not disturb the orbital energy structure of the CuO_6^- center and do not suppress the vibronic effects inherent in it; the center is still a Jahn–Teller complex, but unlike a static CuO_6 center with a predominantly tetragonal deformation, a copper-hole center is dynamic.

Isolated CuO_6^- centers containing a hole have three approximately equally probable configurations with tetragonal axes parallel to the a, b, and c directions of the structure. Their adiabatic potential is shown in Fig. 4b. The crystal-field perturbations due to the statistically disordered arrangement of the La and Sr ions in distant coordination spheres of the Cu ions smooth the pattern of minima by an amount ΔE of the order of $\pm 100\ cm^{-1}$ and cause lowering of one (elongation of CuO_6 along the z axis) or two (elongation along x and y) minima of the adiabatic potential. Two stable positions for in-plane and apical oxygen ions, which are displaced by $\sim 0.2-0.4$ Å relative to the center, appear along each direction of the Cu–O bonds. At low temperatures the system is localized in one of these positions. In this case the EPR spectrum exhibits great anisotropy because of the presence of a fine structure, whose lines are broadened by the dispersion of the crystal fields and are not detected in the disordered samples. When the temperature is raised, the frequency of the jumps of the complex between the minima of the adiabatic potential increases. When this frequency $\nu > D/\beta h$ and $\Delta g \beta H/h$, a dynamic (single symmetric) signal of type IIa is observed. The appearance of this signal corresponds to a change in the wave function of the state and a change in the character of the motion of the oxygen ions of the complex. While these jumps between two stable positions occur with a frequency $<10^7$ Hz at low temperatures, the system is delocalized between these positions above a certain temperature.

Moving on to an analysis of the signals of type IIb, which are characteristic of the solid solutions with $x>0.1$ and do not vanish at helium temperatures, we first turn to the data from the measurements of the concentration of paramagnetic Cu^{2+} centers. There are two possible reasons for the observation in the EPR spectrum of only a small fraction of the copper ions introduced into the matrix: 1) either the bulk of the copper ions (>90%) in the Al^{3+} sites are in the $3+$ oxidation state, and the EPR signal is not observed because of the large zero-field splittings of the spin levels and because of the strong anisotropy of the spectrum of the powder and the broadening of the fine-structure lines; or 2) fairly large agglomerates of CuO_6 and CuO_6^- centers, whose paramagnetic resonance is not detected, appear already at small values of x as a result of the nonuniform distribution of the copper ions among the Al^{3+} sites (as is shown below, only weak EPR signals are observed in some defect sites). The x-ray structural data indicating an increase in the value of c for the structure of $\mathrm{LaSrAl}_{1-x}\mathrm{Cu}_x0_4$ with increasing x lead to a conclusion that the second hypothesis is correct. Moreover, the replacement of Al^{3+} by Cu^{3+} would not lead to an increase in c, because their ionic radii are close (0.54 and 0.535 Å, respectively). It can be attributed only to a continually increasing fraction of structural fragments containing $\mathrm{Cu}^{2+}\mathrm{O}_6$ octahedrons that are tetragonally elongated by the Jahn–Teller effect.

The early clustering of paramagnetic centers is not specific to Cu oxides. We also observed it in the solid solutions $\mathrm{LaSrAl}_{1-x}\mathrm{Me}_x\mathrm{O}_4$ with $\mathrm{Me}=\mathrm{Ni}^{3+}$ and Cr^{3+}, and it was demonstrated by direct observation of the corresponding EPR exchange signal in the case of Cr^{3+} ions in Ref. 9. The presence of one type of structure in the x-ray diffraction experiment attests to the microscopic character of the inhomogeneity appearing. It can be stated that aluminum phases (or microphases at large values of x) and copper microphases (or phases at large values of x) exist in the compounds investigated. In an aluminum phase, the Cu^{2+} ions form CuO_6 centers, which are observed as centers of type I, and CuO_6^- centers (centers of type II*a*). Taking into account the constancy of the structural type for all values of x in $\mathrm{LaSrAl}_{1-x}\mathrm{Cu}_x0_4$, which has been confirmed by x-ray diffraction, we can logically assign the formula $\mathrm{LaSrCuO}_4$ to the copper microphase. The presence of a microphase with a high copper concentration is also evidenced by the absence of observable $d-d$ transitions in the optical spectrum of $\mathrm{LaSrAl}_{1-x}\mathrm{Cu}_x0_4$ even at small values of x ranging from 0.01 to 0.1. In fact, according to Ref. 10, the optical spectra of the isostructural solid solutions $\mathrm{La}_{1+x}\mathrm{Sr}_{1-x}\mathrm{Ga}_{1-x}\mathrm{Cu}_x\mathrm{O}_4$ with $x\approx 0.01$ exhibit a charge-transfer band with an energy of $\sim 27\,000\ \mathrm{cm}^{-1}$. As x increases, this band shifts toward smaller energies, at $x\cong 0.4$ it reaches the region of $d-d$ transitions, and at $x=1$ it stretches to energies of $3000-4000\ \mathrm{cm}^{-1}$. The broad and intense charge-transfer band of the copper microphase suppresses the low-intensity $d-d$ transitions of the CuO_6 centers in the aluminum microphase of $\mathrm{LaSrAl}_{1-x}\mathrm{Cu}_x\mathrm{O}_4$.

As the copper concentration in $\mathrm{LaSrAl}_{1-x}\mathrm{Cu}_x\mathrm{O}_{4-\delta}$ increases, the fraction of the aluminum phase in the solid solutions decreases, while the fraction of the copper microphase increases. Accordingly, the content of solitary CuO_6 centers and isolated CuO_6^- hole centers (II*a*) decreases. As was noted above, this decrease outstrips the decrease expected for a statistically averaged distribution of the impurity Cu ions. At the same time, solitary centers of type I with a resolved hyperfine structure are observed up to $x\geqslant 0.4$. This is totally atypical of the EPR spectrum of solid solutions and directly points out the preservation of the Al microphase up to large values of x. As is seen from Fig. 3a, the relative content of the centers of type II increases in comparison to the content of the centers of type I as x increases, and while they are predominantly solitary hole centers of type II*a* up to $x\approx 0.10$, they are subsequently exchange clusters containing a hole center of type II*b* with different temperature-dependent properties.

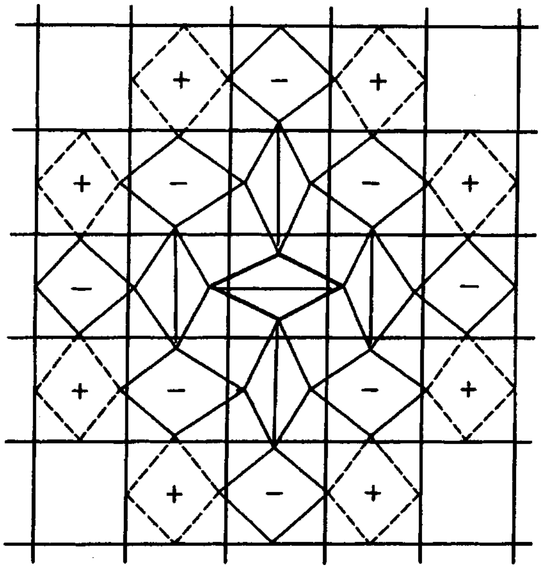

FIG. 5. Deformations of a fragment of a CuO_2 plane generated by Jahn-Teller distortions of a CuO_6^- center (which is shown as thick lines at the center of the figure). ''Snapshot'' of a magnetic Jahn–Teller polaron.

In $\mathrm{LaSrCuO}_4$ the concentration of holes is large, although it is less than the 47% of the copper introduced that would be expected for $\mathrm{Cu}^{2.47+}$, which was identified on the basis of the iodometric-titration data, since there are oxygen vacancies. As was noted above, the increase in c/a (Fig. 1) allows us to claim that the structure of $\mathrm{LaSrCuO}_4$ consists mainly of octahedra elongated along the c axis. Following the ideas developed, we can assume that holes in CuO_2 layers containing such octahedra will form in the broad band of oxygen $2p$ states,[16,17] which overlaps the region of the copper d states.[10] At the same time, the nonstatistical distribution of the heavy ions and oxygen vacancies leads to an inhomogeneous distribution of the holes in a layer. The regions depleted of Sr^{2+} are also depleted of holes; such a distribution of the Sr^{2+} ions is possible when a CuO_6^- fragment, in which delocalization of the hole is confined to the four in-plane oxygen ions, appears among the CuO_6 octahedra. With respect to the Jahn–Teller dynamics, such a CuO_6^- center in an environment of copper CuO_6 octahedra is similar to the hole centers in the aluminum phase of the structure. Their distortions in the ab plane become antiferrodistortive,[18] and ferromagnetic clusters containing 5–13 copper ions appear (Fig. 5).

The difference between the dimensions of the hole magnetic structures in the aluminum and copper phases is not the only difference between them. Other differences are related to the nature of the oxygen p states in which the hole is found and to the value of the total spin of the CuO_6^- fragment. In addition to the in-plane and out-of-plane oxygen p_π states there are also p_σ states in the p band of cuprates. According to Ref. 16, holes occupy in-plane oxygen p_π or p_σ orbitals in cuprates. X-ray photoelectron spectroscopy[16] did not permit lending preference to either of these orbitals. A theoretical treatment of the exchange coupling between the oxygen and copper electrons led to a singlet ground state.[19] These states have been termed Zhang–Rice singlets in the literature. However, it is important to stress that, regardless of whether the spin-spin coupling in the CuO_6^- fragment is ferromagnetic ($S=1$) or antiferromagnetic ($S=0$), this fragment remains a dynamic Jahn–Teller complex. Even when the spin of the CuO_6^- fragment has a zero value, the antiferrodistortive distortions of the neighboring CuO_6 octahedra preserve the ferromagnetic character of the interactions and the nonzero magnetic moment in the exchange cluster formed.

Thus, in the copper phase, along with the regions of octahedra containing holes in the oxygen $2p$ band that are elongated along the c axis there are also ferromagnetic clusters of finite dimensions in regions depleted of holes. As for their magnetic behavior, the regions of octahedra elongated along the c axis are characterized by short-term antiferromagnetic spin correlations, which prevent the observation of EPR in, for example, $LaSrCuO_4$ and La_2CuO_4. Ferromagnetic clusters should be observed in the EPR spectrum, and it would be natural to attribute the signals detected for $x \geqslant 0.2$ to the appearance of such clusters. At the same time, the ferromagnetic cluster appearing upon stabilization of the structure of the compound during its synthesis is essentially a magnetic Jahn–Teller polaron. Because of the equivalence of the copper sites, there is a finite probability that a hole will jump to another CuO_6 center, and the small differences in the crystal fields on the Cu ions up to a certain limit do not prevent this process. Migrating along a layer, a hole wanders together with lattice strains caused both by static Coulomb deformation and by deformation of vibronic origin. The effective mass of a Jahn–Teller polaron is large, and the frequency of walks does not exceed a time interval of the EPR scale, i.e., $<10^{10}$ GHz. Encountering other Jahn–Teller clusters or joining regions with the $LaSrCuO_4$ structure and holes in the oxygen $2p$ band, the magnetic Jahn–Teller polarons transform and do not produce an EPR signal.

As for the ferromagnetic Jahn–Teller clusters observed as signal II*b*, they are either located in regions of the structure from which it is less advantageous for them to diffuse (for example, regions where Sr^{2+} ions are surrounded by La^{3+}) or are associated with some structural imperfections of another nature. In general, the motion of a polaron is impeded by any structural defect which disturbs the dynamics of the central fragment. For example, the disturbances at the boundaries of microphases and crystals are systematic. Inducing an axial crystal-field component directed along the in-plane Cu–O bonds, a boundary or other defect isolates one of the minima of the adiabatic potential of the seed fragment and localizes a magnetic Jahn–Teller polaron.

The magnetic quasiparticles (ferrons) appearing as a result of the self-trapping of an electron in a ferromagnetic region within an antiferromagnet were predicted by Nagaev[20] back in 1967 and were investigated in subsequent years by him and others.[21] The magnetic quasiparticles in hole-doped La_2CuO_4 were treated theoretically by Hizhnyakov and Sigmund and were studied by Kremer *et al.* [3,5] The ferrons in antiferromagnetically ordered CuO_2 layers were investigated in connection with superconductivity by Gor'kov and Sokol,[22] and models of the magnetic clusters in La_2CuO_4 containing a hole and five or four Cu^{2+} ions were considered in Ref. 23. We assume that the model of a Jahn-Teller polaron proposed in our investigation (see also Ref. 2) reflects the real situation in LaSrAl cuprates and correlates with the magnetic centers having $g=2.120\pm0.02$ and $\Delta H=35$ mT (Ref. 6) observed in $La_2CuO_{4+\delta}$ under the conditions of the experiments in Ref. 5. The ambiguities in the appearance of the signal with $g=2.12$, which are associated with the conditions for creating holes in cuprates (by saturating them with oxygen or by replacing some of the La^{3+} ions by Sr^{2+} ions) and depend on the type of sample (a ceramic or a single crystal),[24] can be caused by structural imperfection of the material, a nonuniform distribution of the heavy-metal ions in the lattice, different conditions for diffusion and localization of the magnetic centers observed (Sr^{2+} ions, Sr^{2+} agglomerates, structural defects, boundary conditions, etc.).

Thus, the experimental investigation of $LaSrAl_{1-x}Cu_xO_{4-\delta}$ solid solutions has shown that the introduction of Cu^{2+} ions and several other ions of the iron group into $LaSrAlO_4$ leads to a sharply nonuniform distribution of the iron-group metal (Me) among the Al sites and is another illustration of the phenomenon of phase separation in magnetic materials, which has been studied intently in recent years.[4,25] Specific phenomena develop when Al^{3+} ions are replaced by divalent copper ions. The appearance of a copper microphase $LaSrCuO_{4-\delta}$ along with the aluminum phase occurs already at small copper concentrations. The aluminum phase contains CuO_6 centers that are tetragonally distorted by the Jahn–Teller effect without local charge compensation. The distortions of these centers, like the cooperative distortions in the copper phase, are specified by internal vibronic factors. Cooperative Jahn–Teller effects determine the structural parameters of $LaSrCuO_{4-\delta}$ and La_2CuO_4 and the strong electron-phonon interactions in them. On the other hand, restoration of the charge neutrality of the compound leads to the appearance of hole centers, i.e., copper octahedrons with a hole delocalized among the four in-plane oxygen ions (CuO_6^-), in both the aluminum and copper phases of the structure.

In the aluminum phase these CuO_6^- centers are isolated and have Jahn–Teller dynamics. The possibility of the existence of dynamic CuO_6^- Jahn–Teller centers in the copper phase depends primarily on the hole concentration and the character of the distribution of the heavy La and Sr ions. When the number of holes is not excessively great, a CuO_6^- center in the copper phase induces antiferrodistortive distortions of fragments of the CuO_2 layer near it which are at a distance of one to three coordination spheres from it, while remaining a dynamic Jahn–Teller complex. The ferromagnetic cluster formed is a magnetic Jahn–Teller polaron and can migrate within the crystal lattice. In $LaSrCuO_4$ the concentration of hole centers is large. Under these conditions the Jahn–Teller polarons are caused by the nonstatistical distribution of La and Sr and vanish by joining regions with the $LaSrCuO_4$ structure and holes in the $2p$ oxygen band. The EPR spectrum exhibits Jahn–Teller polarons stabilized on structural defects.

The single Jahn–Teller nature of the CuO_6 centers in all the cuprates with the K_2NiF_4 structure renders our investigation a model study and permits extrapolation of the phenomena discovered in $LaSrAl_{1-x}Cu_x0_4$ to the processes occurring in La_2CuO_4 when it is doped by Sr (Ba) or oxygen ions. Recognition and investigation of the conditions for generating hole centers in them, as well as the specific features of these centers, merit special attention.

We thank N. N. Kristofel' and V. V. Khizhnyakov for some useful discussions, as well as D. Reinen and U. Kesper for recording the diffuse reflectance spectra and determining the effective charges of the copper atoms by iodometric titrations.

This work was supported by the Russian Fund for Fundamental Research (Grants 94-02-03136 and 96-02-180075) and the George Soros Foundation (Grants RKD000 and RKD300).

[1] T. A. Ivanova, E. F. Kukovitskiĭ, É. N. Nabiullina *et al.*, JETP Lett. **57**, 63 (1993).
[2] Yu. V. Yablokov, T. A. Ivanova, A. E. Usachev *et al.*, JETP Lett. **60**, 785 (1994)].
[3] V. Hizhnyakov and E. Sigmund, Physica C **156**, 655 (1988).
[4] *Proceedings of the 2nd Workshop on Phase Separation in Cuprate Superconductors, Sept. 4–10, 1993, Cottbus, Germany*, E. Sigmund and K. A. Müller (Eds.), Springer-Verlag, Berlin–Heidelberg (1994) and references therein.
[5] R. K. Kremer, E. F. Sigmund, V. Hizhnyakov *et al.*, Z. Phys. B: Condens. Matter **86**, 319 (1992).
[6] G. Wübbeler and O. F. Schirmer, Phys. Status Solidi B **174**, K21 (1992).
[7] T. A. Ivanova, E. F. Kukovitskiĭ, A. E. Usachev *et al.*, Sverkhprovodimost: Fiz., Khim., Tekh. **5**, 860 (1992) [Supercond. Sci. Technol. **5**, 861 (1992)].
[8] Yu. V. Yablokov, T. A. Ivanova, S. Yu. Shipunova *et al.*, Appl. Magn. Reson. **2**, 547 (1990).
[9] Yu. V. Yablokov, T. A. Ivanova, S. Yu. Shipunova, I. A. Zvereva, and N. P. Bobrysheva, Fiz. Tverd. Tela (Leningrad) **34**, 338 (1992) [Sov. Phys. Solid State **34**, 182 (1992)].
[10] D. Reinen and J. Wegwerth, Physica C **183**, 261 (1991).
[11] V. E. Petrashen, Yu. V. Yablokov, and R. L. Davidovich, Phys. Status Solidi B **101**, 117 (1980).
[12] G. L. Bir, Fiz. Tverd. Tela (Leningrad) **6**, 1627 (1964) [*sic*].
[13] B. Grande, Hk. Müller-Buschbaum, and M. Schweizer, Z. Anorg. Allg. Chem. **428**, 120 (1977).
[14] J. D. Iorgensen, D. G. Hinks, and G. P. Felcher, Phys. Rev. B **35**, 5365 (1987).
[15] T. Thio, T. R. Thurston, N. W. Preyer *et al.*, Phys. Rev. B **38**, 905 (1988).
[16] N. Nücker, J. Fink, H. A. Romberg *et al.*, Physica C **153–155**, 119 (1988).
[17] Yu. A. Izyumov, N. M. Plakida, and Yu. N. Skryabin, Usp. Fiz. Nauk **159**, 621 (1989) [Sov. Phys. Usp. **32**, 1060 (1989)].
[18] M. V. Eremin, Yu. V. Yablokov, T. A. Ivanova *et al.*, Zh. Éksp. Teor. Fiz. **87**, 220 (1984) [Sov. Phys. JETP **60**, 128 (1984)].
[19] F. C. Zhang and T. M. Rice, Phys. Rev. B **37**, 3759 (1988).
[20] É. L. Nagaev, JETP Lett. **6**, 18 (1967)].
[21] E. L. Nagaev, *Physics of Magnetic Semiconductors*, Mir, Moscow (1983).
[22] L. P. Gorkov and A. V. Sokol, Physica C **159**, 329 (1989).
[23] M. Eremin and E. Sigmund, Solid State Commun. **90**, 795 (1994).
[24] O. F. Schirmer, G. Wübbeler, and T. Wahlbrink, in *Proceedings of the 2nd Workshop on Phase Separation in Cuprate Superconductors, Sept. 4–10, 1993, Cottbus, Germany*, E. Sigmund and K. A. Müller (Eds.), Springer-Verlag, Berlin–Heidelberg (1994), p. 133.
[25] É. L. Nagaev, Usp. Fiz. Nauk **165**, 529 (1995) [*sic*].

Translated by P. Shelnitz

PHYSICS OF THE SOLID STATE VOLUME 40, NUMBER 4 APRIL 1998

Features of charge-carrier recombination in amorphous molecular semiconductors doped with polymethine dyes

N. A. Davidenko and A. A. Ishchenko

T. G. Shevchenko Kiev State University, 252033 Kiev, Ukraine

(Submitted October 9, 1997)
Fiz. Tverd. Tela (St. Petersburg) **40**, 629–635 (April 1998)

The photogeneration and recombination of charge carriers in poly-N-epoxypropylcarbazole films with additions of a polymethine dye are investigated irradiation of films with blocking contacts by light both within and outside the absorption range of the dye. The kinetics of the accumulation and relaxation of electron-hole pairs, whose lifetimes exceed tens and hundreds of seconds, are studied. It is postulated that an increase in the recombination luminescence intensity occurs in an electric field as a result of an increase in the efficiency of the bimolecular radiative recombination stimulated by trapped electrons from photogenerated excitons. © *1998 American Institute of Physics.* [S1063-7834(98)00904-6]

Experimental investigations of the bimolecular recombination of charge carriers and the electroluminescence (EL) of amorphous molecular semiconductors (MS's) based on polymer films[1–3] usually employ samples of the ''sandwich'' type, in which the electrical contacts are selected so that there would be sufficiently efficient electric-field injection of charge carriers from the contacts into the bulk of the MS film. In the case of recombination electroluminescence[3] charge carriers which leave the contacts into an electric field and drift into the bulk of the MS film encounter recombination centers and recombine with the emission of light. In this case the recombination centers are molecules, which differ from the molecules among which transport of the charge carriers takes place. The efficiency of such recombination electroluminescence depends both on the conditions for the injection of carriers from the contacts and on the conditions for the passage of carriers from transport molecules to molecules which act as recombination centers, as well as on the ratio between the probabilities of radiative and nonradiative degradation of the energy of the excited state of the recombination center formed. In addition, recombination EL can be influenced by the history of the sample. In particular, as was discovered in the present work, recombination EL with the emission of visible light can be enhanced significantly by preliminary irradiation of the sample with light in the UV range.

Therefore, to understand the physical processes occurring upon EL in samples with MS films and to control these processes, it is important to separate the contact and bulk effects. For example, to investigate the bulk effects, the injecting contacts can be replaced by blocking contacts, and recombination EL can be simulated by creating a nonequilibrium concentration of charge carriers by photogenerating them in the bulk of the MS film.

In the present work we investigated the photogeneration, recombination, and enhancement of the radiative recombination of charge carriers in poly-N-epoxypropylcarbazole (PEPC) films doped with the cationic polymethine dye (PD) 1, 3, 3, 1′, 3′, 3′-hexamethylenedicarbocyanine tetrafluoroborate.[4] PEPC was selected as the hole transport layer, because effective hole transport takes place in it along the carbazole ring systems.[5] The selection of polymethine dye molecules as recombination and photogeneration centers is specified by the fact that dyes of this class have absorption and luminescence bands in the visible and near-IR regions of the spectrum, depending on their molecular structure, and the energies of upper valence orbitals of these dyes and of carbazole are close.[5] Therefore, holes can pass from carbazole ring systems in PEPC into valence molecular orbitals of the dye molecules and in the opposite direction.

1. SAMPLES AND EXPERIMENTAL METHOD

The samples were prepared either in the form of structures with a free surface, viz., quartz substrate–PEPC+N wt % PD and quartz substrate–PS+N wt % PD, or in the form of ''sandwich'' structures, viz., Al–PEPC+N wt % PD–SnO_2 and Al–PS+N wt % PD–SnO_2, where PS is a copolymer of styrene with butyl methacrylate, whose molecules have a high ionization potential and do not create a hole-transport energy band.[5] The concentration (N) of the polymethine dye was varied in the range $N=0.1-15$. For the MS films based on PEPC, the Al and SnO_2 contacts are blocking when the polarity of the voltage on Al is positive.[5] The MS films were obtained by drying solutions of PEPC $+N$ wt % PD or PS$+N$ wt % PD in dichloroethane, which were poured onto quartz substrates either with a layer of SnO_2 or without a layer of SnO_2. The thicknesses of the dried films were $L=0.5-2$ μm. The Al films were deposited by thermal sputtering in a vacuum chamber, and the Al thickness was 300−350 Å.

The samples with a free surface on the polymer film were used to record the optical spectra of the absorption coefficient $\varkappa$ and the photoluminescence intensity I_{PL} in the wavelength range $\lambda=400-1200$ nm. In the samples of the ''sandwich'' structures I_{PL}, the photocurrent density j_{PH}, the concentration Q of charge carriers which form in a short-

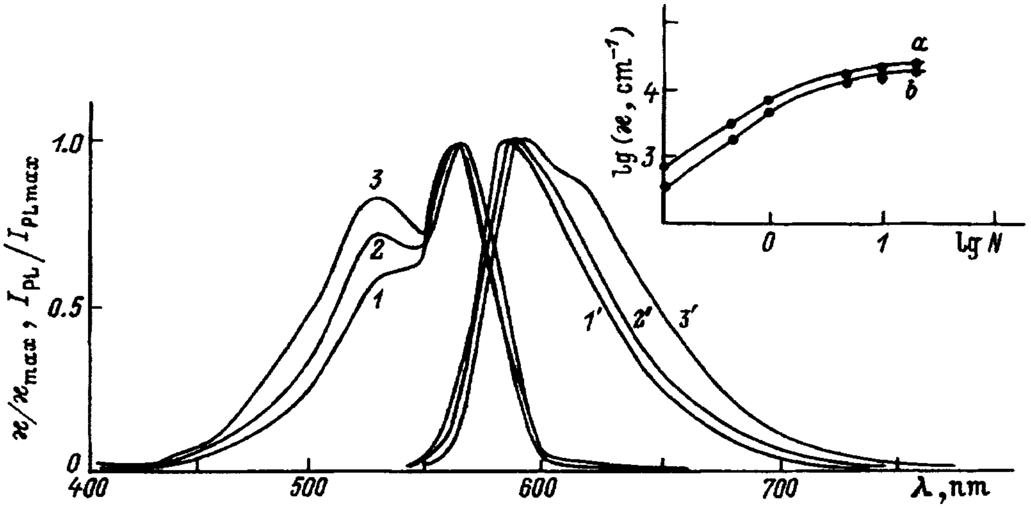

FIG. 1. Absorption (*1–3*) and photoluminescence (*1–3'*) spectra of PEPC+N wt % PD films for $N=0.1$ (*1, 1'*), 1(*2, 2'*), and 15 wt % (*3, 3'*).

circuited sample during a time t_1 of irradiation by monochromatic light and reach the collecting contacts upon the application of an electric field after a time interval t_2 following completion of the light pulse, and the intensity I_E of the recombination luminescence emitted from the sample during the measurement of Q were measured as functions of the electric field strength E and the intensities of the monochromatic light at the wavelengths $\lambda_1=380$ nm (the intensity I_1) and $\lambda_2=540$ nm (the intensity I_2).

A KSVIP-23 spectrum-computing system was used to measure $\varkappa$, I_{PL}, and I_E, but the value of I_E was recorded using an FÉU-100 photomultiplier without a monochromator. A hydrogen lamp with a glass filter served as the source of the light at λ_1, and an incandescent lamp with a glass filter served as the source of the light at λ_2. The light intensity was varied by neutral filters in the ranges $I_1=0.01-0.5$ W/m^2 and $I_2=0.2-20$ W/m^2. The electric field strength was varied in the range $E=1\times10^7-3\times10^8$ W/m. All the measurements were performed at $T=293$ K.

The steady-state photocurrent was recorded in a photoresistance regime using a storage oscillograph during irradiation of the sample by light from the side of the SnO$_2$ electrode. Along with j_{PL}, I_{PL} was measured simultaneously, and $\Delta I_{\mathrm{PL}}/I_{\mathrm{PL}}$, i.e., the relative change in I_{PL} in the field E, was determined from the relation $\Delta I_{\mathrm{PL}}/I_{\mathrm{PL}}=\{I_{\mathrm{PL}}(E)-I_{\mathrm{PL}}(0)\}/I_{\mathrm{PL}}(0)$, where $I_{\mathrm{PL}}(E)$ is the value of I_{PL} after the electric field is switched on, and $I_{\mathrm{PL}}(0)$ is the value of I_{PL} before the electric field is switched on.

The method for determining Q that was previously developed and described in Refs. 5 and 6 involves calculating Q from the relation

$$Q=\int_0^\infty dt\{i_2(t)-i_1(t)\}/qSL, \tag{1}$$

where the time $t=0$ corresponds to the moment when E is switched on, q is the charge of an electron, S and L are the area and thickness of the MS film between the contacts, $i_1(t)$ is the current for charging the electrical capacitance of the sample in the short-circuited state during the time t_1+t_2 in the dark, and $i_2(t)$ is the current for charging the electrical capacitance of the sample following preliminary irradiation in the short-circuited state by monochromatic light during the time t_1 followed by holding in the dark during the time t_2. In addition, the relation

$$Q_t(t)=\{i_2(t)-i_1(t)\}/qSL \tag{2}$$

was used to determine the variation of Q from the moment when the electric field is switched on.

2. EXPERIMENTAL RESULTS

Figure 1 presents plots of $\varkappa(\lambda)/\varkappa_{\max}$ (curves *1–3*) and $I_{\mathrm{PL}}(\lambda)/I_{\mathrm{PLmax}}$ (curves *1'–3'*) normalized to the maximum values in the range of λ investigated for PEPC+N wt % PD films. The electronic absorption spectra of the polymethine dye in liquid solvents contains the narrow intense band that is characteristic of this class of dyes with a vibrational structure on the short-wavelength edge of the spectrum. For example, in 1, 2-dichloroethane the values of the optical wavelengths of the vibrational (λ_v) and fundamental ($\lambda_{\max}$) maxima are equal to 518.5 and 550.5 nm. When the polymethine dye is introduced into PEPC and PS, its absorption bands undergo a bathochromic shift ($\lambda_v=528$ nm, $\lambda_{\max}=566$ nm) due to the larger values of the refractive indices of the polymers in comparison to 1, 2-dichloroethane. The values of λ_v and $\lambda_{\max}$ in PEPC and PS are equal to 528 and 566 nm and to 526 and 559 nm, respectively. As N is increased, the absorption increases more strongly at λ_v than at $\lambda_{\max}$. In the photoluminescence spectra an increase in N results in a bathochromic shift of the band and a decrease in I_{PL}. The Lambert–Beer law is not obeyed. These data attest to the formation of H aggregates of the polymethine dye, which absorb light at shorter wavelengths than do monomeric dye polymethine,[4] i.e., at λ_v. The $I_{\mathrm{PL}}(\lambda)/I_{\mathrm{PLmax}}$ curves for the samples irradiated at λ_1 are similar to the curves obtained for the samples irradiated at λ_2, but exhibit a slight hypsochromic shift. Similar laws are observed in PS+N wt % PD films.

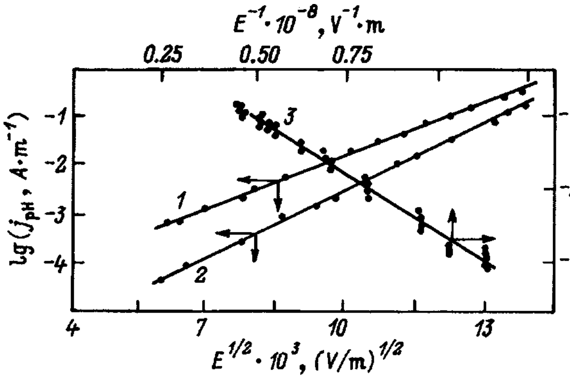

FIG. 2. Dependence of j_{PH} (*1, 2*) and I_{PL} (*3*) on E in an Al–PEPC+0.5 wt % PD–SnO$_2$ sample ($L=1.2$ μm) for $I_1=0.3$ W/m^2 (*1*) and $I_2=8$ W/m^2 (*2*).

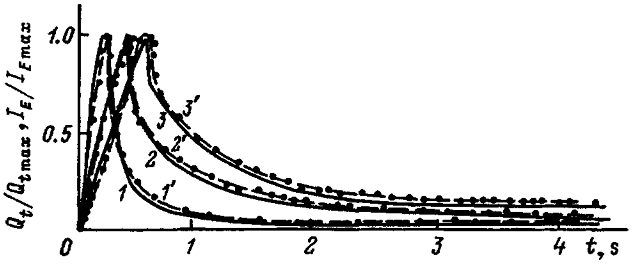

FIG. 3. Kinetics of the appearance of recombination luminescence (*1–3*) and kinetics of the escape of the photoinduced space charge into the contacts (*1′–3′*) for an Al–PEPC+N wt % PD–SnO$_2$ sample ($L=1.3$ μm) following irradiation at λ_2 for $t_1=30$ s, holding in the dark for $t_2=30$ s, and application of an electric field $E=2.8\times 10^8$ (*1, 1′*), 1.7×10^8 (*2, 2′*), and 7×10^7 V/m (*3, 3′*).

All the Al–PEPC+N wt % PD–SnO$_2$ films display photoconductivity at the wavelengths λ_1 and λ_2. The photocurrent exhibits sublinear dependences on I_1, I_2, and L. The plots of $j_{PH}(E)$ are linear in $\log j_{PH}-E^{1/2}$ coordinates (curves *1* and *2* in Fig. 2), and this dependence can be represented in an analytical form by the expression

$$j_{PH}(E)\sim\exp(-(W_{0PH}-\beta E^{1/2})kT_{\mathrm{eff}}), \quad (3)$$

which is similar to the expression for the photoconductivity characteristic of amorphous MS's,[5] where W_{0PH} is the activation energy for photogeneration when $E=0$, k is Boltzmann's constant, $1/T_{\mathrm{eff}}=1/T-1/T_0$, and T_0 is the characteristic temperature, which amounts to $T=490\pm 20$ K for PEPC. The slope of linear dependence *1* in Fig. 2 gives $\beta_1=(4.3\pm 0.2)\times 10^{-5}$ eV·m$^{1/2}$/V$^{1/2}$, and the slope of linear dependence *2* in Fig. 2 gives $\beta_2=(4.6\pm 0.2)\times 10^{-5}$ eV·m$^{1/2}$/V$^{1/2}$. These values of β_1 and β_2 are close to the corresponding values of β measured in other amorphous MS's based on PEPC.[5]

In the Al–PEPC+N wt % PD–SnO$_2$ samples, quenching of the photoluminescence of the polymethine dye is observed simultaneously with photoconduction at λ_1. As E is increased, the value of I_{PL} decreases. The plots of the dependence of $\Delta I_{PL}/I_{PL}$ on E can be approximated by straight lines in $\log(|\Delta I_{PL}/I_{PL}|)-E^{-1}$ coordinates, as follows from Fig. 2 (curve *3*). We note that the slope of linear dependence *3* in Fig. 2 equals $(1.95\pm 0.05)\times 10^8$ V/m. Photoconduction and an influence of E on I_{PL} were not detected in the Al–PS+N wt % PD–SnO$_2$ samples.

When an electric field was applied to the unirradiated samples investigated, $I_E=0$. After preliminary irradiation of these samples at λ_2 followed by application of an electric field, EL appeared. It also appeared after preliminary illumination at λ_1. However, if the sample was irradiated first at λ_1, the value of I_E after illumination at λ_2 increased by more than an order of magnitude in our experiments.

Figure 3 presents plots of the dependence of $I_E/I_{E\max}$ (curves *1–3*) and $Q_t/Q_{t\max}$ (curves *1′–3′*) on the time t after application of an electric field normalized to the corresponding maximum values for the particular value of E. It is seen that the $I_E(t)$ and $Q_t(t)$ curves correlate. An increase in L at a constant value of E or a decrease in E leads to the displacement of $I_{E\max}$ and $Q_{t\max}$ toward larger values of t and to an increase in the duration of the emission and the measurement of Q. No manifestations of EL were detected in the Al–PS +N wt % PD–SnO$_2$ samples, and under any experimental conditions $I_E=0$, and $Q=0$.

The experimental results presented in Fig. 3 were obtained on a sample which was first irradiated at λ_1 for 30 s and was used to measure I_E and Q with illumination at λ_2 only after the electric field was switched on and then switched off. The duration of the set of measurements with illumination at λ_2 following irradiation at λ_1 did not exceed an hour. After 24 h, the value of Q for this sample scarcely changed, but the value of I_E decreased by more than an order of magnitude.

In Fig. 4 curve *1* is a plot of the dependence of $\log I_{E\max}$ on E^{-1}, which was measured on a sample that had not been irradiated at λ_1 for more than 24 h. Curve *2* is a plot of the dependence of $\log I_{E\max}$ on E^{-1} for a sample which was irradiated at λ_1 before the electric field was switched on. Curve *3* is a plot of the dependence of $\log I_{E\max}$ on E^{-1} measured on the same sample after curve *2* was recorded, but with irradiation at λ_2. It is seen from Fig. 4 that preliminary irradiation of the samples at λ_1 provides for a significant increase in I_E for the subsequent cycles involving irradiation of the samples at λ_2 and the measurement of I_E. Here we note that the experimental plots of $I_E(E)$ in the coordinates selected can be approximated by straight lines. Figure 4 reveals the equality between the slopes of curves *1* and *3* [$(1.2\pm 0.05)\times 10^8$ V/m] and the small value of the slope of

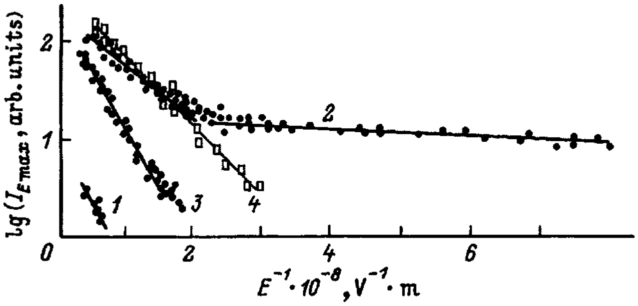

FIG. 4. Dependence of $I_E(E)$ in an Al–PEPC+0.5 wt % PD–SnO$_2$ sample ($L=1.1$ μm) for $t_1=30$ s and $t_2=10$ s.

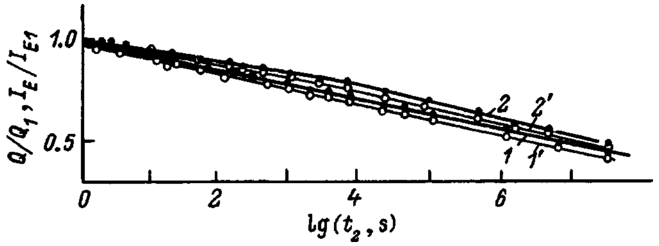

FIG. 5. Dependence of Q (*1, 2*) and I_E (*1', 2'*) on t_2 in an Al–PEPC+N wt % PD–SnO$_2$ sample ($L=1.3$ μm) following irradiation at λ_1 (*1, 1'*) and λ_2 (*2, 2'*).

curve *2*. At $E>5\times10^7$ V/m the slope of curve *2* is equal to $(5.65\pm0.05)\times10^7$ V/m, and at $E<3\times10^7$ V/m this plot can be approximated by a straight line with a slope equal to $(7.8\pm0.1)\times10^6$ V/m.

Figure 5 presents plots of the dependence of Q/Q_1 on $\ln t_2$ (curves *1* and *2*) and of $I_{E\max}/I_{E\max1}$ on $\ln t_2$ (curves *1'* and *2'*), where Q_1 and $I_{E\max 1}$ are the values of Q and $I_{E\max}$ for $t_2=1$ s. The experimental results can be approximated by straight lines in the coordinates selected, the slopes of these straight lines being close to one another. These dependences were measured for an irradiation time interval $t_1=30$ s, for which the $Q(t_1)$ and $I_E(t_1)$ curves have a saturation region. The $Q(t_1)$ and $I_E(t_1)$ curves are similar and can be described by a simple exponential function with a constant rise time for Q and I_E up to the saturation level $\tau=15\pm3$ s, and τ does not depend on I_1 and I_2. The experimental results presented in Fig. 5 were obtained on a sample which was preliminarily irradiated at λ_1.

3. DISCUSSION OF EXPERIMENTAL RESULTS

The possibility of approximating the $j_{\mathrm{PH}}(E)$ curves (Fig. 2) by the analytical expression (3) in interpreting the results allows us to use known models of the photogeneration of charge carriers in amorphous MS's[5] and to assume that electrostatically bound electron-hole pairs are photogenerated when the investigated samples with PEPC+N wt % PD films are irradiated at λ_2. In an external field, as E increases, the probability of dissociation of the electron-hole pairs increases due to the increase in the mobility of the holes, which move away from the electrons, leaving them in the photogeneration centers, j_{PH} increases (curve *2* in Fig. 2), and the probability of germinal recombination decreases. If geminate recombination is accompanied by the emission of light, the photoluminescence intensity can decrease (curve *3* in Fig. 2). However, it should be noted that the decrease in I_{PL} with increasing E can be associated not only with a decrease in the probability of geminate recombination, but also with an increase in the probability of the photogeneration of electron-hole pairs in the electric field, as was previously theorized in Ref. 7. Here we shall only point out the quenching of photoluminescence by an external electric field, and the nature of this phenomenon in PEPC+N wt % PD films will be additionally investigated in a separate study.

The sublinear nature of the photocurrent-intensity characteristics, the decrease in j_{PH} with increasing L, and the correlation between the $Q_t(t)$ and $I_E(t)$ curves (Fig. 3) indicate that not all the mobile holes formed as a result of dissociation of the photogenerated electron-hole pairs can reach the collecting contact and that the trapping and bimolecular recombination of charge carriers take place efficiently in the samples investigated.

The fact that photoconduction and EL are not observed in the samples with PS+N wt % PD films allows us to conclude that the electroluminescence effects induced by preliminary irradiation at λ_1 or λ_2 in the samples with PEPC +N wt % PD films have a recombination character and are not associated with the influence of E on the rate of intramolecular electronic transitions of the PC molecules. Since the spectral composition of the recombination luminescence (I_E) is similar to the spectral composition of the photoluminescence (Fig. 1), it can be concluded that the recombination centers are dye molecules.

However, as was discovered in the present work, the efficiency of the radiative recombination of the charge carriers photogenerated at λ_2 is enhanced in samples which were preliminarily irradiated at λ_1. There are at least five possible causes for this effect: 1) filling of deep trapping levels upon irradiation at λ_1 and photoinduced release of charge carriers from these levels upon irradiation at λ_2; 2) filling of deep trapping levels upon irradiation at λ_1 and recombination of these excess electrons with mobile holes upon irradiation at λ_2; 3) an increase in the probability of the photogeneration of electron-hole pairs by light with λ_2 following preliminary irradiation at λ_1; 4) an increase in the photogeneration of centers for the radiative recombination of charge carriers by light with λ_1; and 5) an increase in the probability of radiative recombination.

The repeated use of these samples for measuring increasing values of I_E becomes possible after they are irradiated at λ_1 and then subjected to an external electric field. The value of I_E does not vary significantly, if I_2, t_1, and t_2 are constant. Therefore, it can be assumed that the first of the possible causes just enumerated does not significantly influence the effects under discussion.

We found that prolonged irradiation of the samples at λ_1 with the application of an electric field leads to a decrease in the photoconductivity of these samples (see Fig. 6). The photoconductivity recovers when short-circuited samples are held in the dark, the recovery time being relatively insensitive to irradiation at λ_2. Therefore, there are no sufficient grounds to assume that the space charge accumulated during irradiation at λ_1 effectively recombines with the charge carriers photogenerated when these samples are irradiated by light with intensity I_2.

Since the measurements of Q and I_E following irradiation of the samples at λ_1 and λ_2 reveal that Q does not vary, while I_E increases, it can be assumed that after irradiation of the samples at λ_1 there is no increase in the number of charge carriers or recombination centers photogenerated at λ_2, but the radiative electronic transitions in the recombination centers are intensified. We attribute the enhancement of radiative recombination to the formation of new active centers in the MS film, which appear after irradiation of the samples at λ_1 and contain the electrons remaining after the decay or dissociation of the excitons photogenerated by that

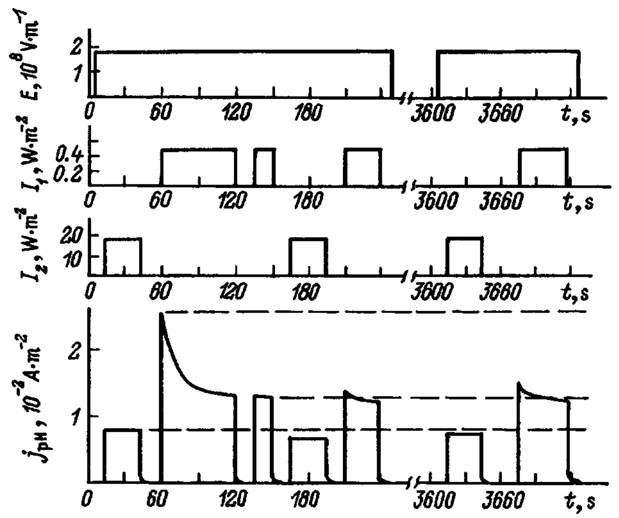

FIG. 6. Duration of the electric field and light pulses in photocurrent measurements in an Al–PEPC+0.5 wt % PD–SnO_2 sample ($L=1.1$ μm).

light. This hypothesis is based on the following experimental findings.

The wavelength λ_1 is in the transparency window of the dye and is close to the absorption edge of PEPC (400 nm). When films of the amorphous MS's investigated are irradiated at λ_1, mobile excitons are photogenerated. Diffusing among the carbazole fragments of PEPC, these excitons encounter monomeric molecules or aggregates of the dye. Exciton decay near monomers or aggregates of the dye is accompanied either by the transfer of energy to the dye and its degradation or the formation of free holes in an electric field and the appearance of a photocurrent (curve *1* in Fig. 2). However, even if $E=0$, after excitons decay, not all the holes and electrons recombine, and some of the charge carriers have a lifetime amounting to tens and hundreds of seconds (curve *1* in Fig. 5).

The linearity and identical slopes of the plots of Q/Q_1 and $I_{E\max}/I_{E\max 1}$ as functions of $\ln t_2$ (curves *1* and *1′* in Fig. 5) allow us to conclude that irradiation at λ_1 leads to the formation of electron-hole pairs in the MS films, in which the holes and electrons are distributed in the form of isolated pairs with the distances r between the charges and the distribution function $f(r)$. According to Refs. 8–10, the variation of their concentration with time is described by the equation

$$Q(t)/Q_1=\int_{r1}^{\infty} f(r)\exp(-\nu t\,\exp(-2r/\alpha))dr, \qquad (4)$$

where ν is the frequency factor for the passage of a mobile charge (hole) into a recombination center, α is the hole localization radius, and r_1 is the distance between the charges in the electron-hole pairs that recombine in the first second after light irradiation. If an electric field is applied to such a sample after a time interval t_2 following completion of the irradiation, the charge carriers in the electron-hole pairs become mobile and can recombine with the emission of light (curves *1* and *1′* in Fig. 5). Here it turned out that the radiative recombination process is similar to processes which take into account the tunneling of the charge carrier under the potential barrier ΔU_1, since the plots of the dependence of $\log I_E$ on E^{-1} can be approximated by straight lines (Fig. 4), and the variation of I_E in the field E can be represented, according to Refs. 3, 8, 9, and 11 in the analytical form

$$I_E\sim\exp\{-8\pi(2m^*)^{1/2}\Delta U_1^{3/2}/3qhE\}, \qquad (5)$$

where m^* is the effective mass of the charge carrier and h is Planck's constant. The linearity and identical slopes of the plots of Q/Q_1 and $I_{E\max}/I_{E\max 1}$ as functions of $\ln t_2$ (curves *2* and *2′* in Fig. 5) allow us to conclude that irradiation at λ_2 leads to the formation of long-lived electron-hole pairs in the amorphous MS's, in which the electrons and holes are distributed in space in the form of isolated pairs and that the variation of their concentration can be described by an equation similar to (4). In an external electric field the charge carriers in such pairs become mobile and can recombine with the emission of light. The dependence of the intensity of this emission on E can be described by an analytical expression similar to (5), but with a different value ΔU_2 for the height of the potential barrier.

Using the values of the slopes of linear dependences *2* and *3* in Fig. 4 for the $I_E(E)$ curves and relation (5), we find that $\Delta U_2/\Delta U_1=1.7\pm0.1$ for $5\times10^7<E<3\times10^8$ V/m and $\Delta U_2/\Delta U_1=6.2\pm0.1$ for $1\times10^7<E<3\times10^7$ V/m. These values allow us to presume that, upon the radiative recombination of charge carriers in an electric field in amorphous MS's which were preliminarily irradiated at λ_1, the holes pass into recombination centers by overcoming a lower potential barrier than in similar MS's which were subsequently irradiated at λ_2.

We do not rule out that the difference between ΔU_1 and ΔU_2 can be due to the difference between the energies of the upper valence orbitals of the H aggregate of the polymethine dye and the monomer. There is no contradiction here, since in our proposed recombination model holes pass from an upper valence orbital of a carbazole nucleus in PEPC to a valence orbital of a recombination center, in which there is already a trapped electron, and the valence orbital of an H aggregate of the polymethine dye is separated by a smaller energy gap from the analogous orbital of the carbazole nucleus than is the valence orbital of the monomeric dye molecule.[4] Therefore, it can be assumed that upon exciton decay the electrons pass more efficiently into free molecular orbitals of H aggregates of the polymethine dye than into monomeric dye molecules. However, we still consider this question open, and it calls for additional research.

To test the validity of the hypothesis regarding the accumulation of electrons in the bulk of an MS film during irradiation at λ_1 and their long lifetime, we performed special investigations of the influence of the prolonged irradiation of Al–PEPC+N wt % PD–SnO_2 samples at λ_1 on j_{PH} and I_E. The procedure used in these investigations is illustrated in Fig. 6, which shows the forms of the pulses of E, I_1, and I_2 and the photocurrent in a PEPC+0.5 wt % PD–SnO_2 sample, which was preliminarily held in the dark for a long time. As is seen from this figure, irradiation of the samples at λ_1 with an applied electric field leads to a decrease in the photoconductivity of the MS films, which does not recover for a long time. The recovery rate of j_{PH} does not depend on the polarity and strength of the electric field or irradiation of the samples at λ_2 following irradiation at λ_1.

However, irradiation of the samples at λ_1 with an applied electric field promotes a simultaneous increase in I_E with the decrease in the photoconductivity upon subsequent irradiation of the same samples at λ_2. Curve *4* in Fig. 4 is a plot of $I_E(E)$ measured on the same sample on which the dependence of $I_E(E)$ represented by curve *3* was measured, but after curve *3* was measured, an electric field ($E=2\times 10^8$ V/m) was applied to the sample and the sample was irradiated at λ_1 for 60 s ($I_1=0.5$ W/m^2). It is seen that the irradiation of MS films at λ_1 in an electric field leads to even greater enhancement of radiative recombination than in the absence of an electric field. This is because the mobility of the holes increases in an electric field[5,12] and the decay of the excitons that were photogenerated at λ_1 is accompanied by the escape of holes into the collecting contact and the accumulation of electrons in the MS film, which create negative space charge. The accumulation of considerable space charge, which diminishes the internal electric field in the MS film, is manifested both by a decrease in the photoconductivity of the MS films (Fig. 6) and by a decrease in the slope of the $I_E(E)$ curve (Fig. 4).

Refinement of the mechanism for the enhancement of recombination electroluminescence discovered in the present work following the irradiation of MS films by light in the UV range requires additional investigations of the causes of the formation of the long-lived electron-hole pairs, the mechanisms of the trapping of electrons following decay of the photogenerated excitons, and the influence of these electrons on the probability of radiative recombination of the charge carriers. However, even on the basis of the results of the present work, we can assume that the irradiation of PEPC$+N$ wt % PD films with light in the near UV range is followed by the formation of active centers which contain trapped electrons from photogenerated excitons and influence the probability of the bimolecular radiative recombination of the charge carriers. The mechanism of this influence can be associated with alteration of the rate of the singlet-triplet transitions in the recombining nongeminate pairs of charge carriers.[13] We shall now explain the grounds for such a hypothesis.

According to a generally accepted model[14] of the recombination of charge carriers, which takes into account the spin states of the pairs, four possible spin states of the charge carriers which approach to within the recombination distance, viz., one singlet state (S) and three triplet states (T_0, T_+, and T_-), are considered in the general case. If the recombination product is a particle in a singlet spin state, only pairs in the S state recombine, and recombination of the triplet pairs can occur only after alteration of the spin state. The rate constant of the $S-T$ transitions (k_{S-T}) can be influenced by external magnetic fields and the fields of paramagnetic particles. In particular, it was previously shown in amorphous MS's that k_{S-T} can increase when the recombining charges of electron-hole pairs interact with photogenerated excitons.[13] In the case of the germinal radiative recombination of charges in photogenerated singlet electron-hole pairs, an increase in the concentration of paramagnetic particles in the amorphous MS leads to reversible photoluminescence quenching.[15] In the case of bimolecular recombination of the charge carriers, all four spin states of the recombining pairs are populated with equal probabilities, but only the singlet pairs recombine. Therefore, an increase in k_{S-T} due to the presence of carriers trapped in deep traps should be accompanied by the enhancement of radiative recombination.

[1] J. H. Burroughes, D. D. C. Bradley, A. R. Braun, R. N. Marks, K. Mackay, R. H. Friend, P. L. Burn, and A. B. Holmes, Nature **343**, 539 (1990).

[2] D. Neher, M. Remmers, and V. Cimrova, in *Electrical and Related Properties of Organic Solids*, R. W. Munn *et al.* (Eds.), Kluwer, Netherlands (1997), pp. 79–99.

[3] J. Kalinowski, *ibid.*, pp. 167–206.

[4] A. A. Ishchenko, *Structure and Spectral Luminescence Properties of Polymethine Dyes* [in Russian], Naukova Dumka, Kiev (1994), 232 pp.

[5] N. G. Kuvshinskiĭ, N. A. Davidenko, and V. M. Komko, *Physics of Amorphous Molecular Semiconductors* [in Russian], Lybid', Kiev (1994), 176 pp.

[6] N. A. Davidenko and N. G. Kuvshinsky, J. Inf. Rec. Mater. **21**, 185 (1993).

[7] N. A. Davidenko and N. G. Kuvshinsky, J. Inf. Rec. Mater. **22**, 149 (1994).

[8] K. I. Zamaraev, R. F. Khaĭrutdinov, and V. P. Zhdanov, *Electron Tunneling in Chemistry* [in Russian], Nauka, Novosibirsk (1985), 317 pp.

[9] V. I. Gol'danskiĭ, L. I. Trakhtenberg, and V.N. Fleurov, *Tunneling Phenomena in Chemical Physics* [Gordon and Breach, New York (1989); Nauka, Moscow (1986), 296 pp.].

[10] A. K. Kadashchuk, N. I. Ostapenko, N. A. Davidenko, N. G. Kuvshinskiĭ, and N. V. Lukashenko, Fiz. Tverd. Tela (St. Petersburg) **39**, 1183 (1997) [Phys. Solid State **39**, 1047 (1997)].

[11] J. Gruner, P. J. Hamer, R. H. Friend, H.-J. Huber, U. Scherf, and A. B. Holmes, Adv. Mater. (Weinheim, Ger.) **6**, 748 (1994).

[12] M. Pope and C. E. Swenberg, *Electronic Processes in Organic Crystals*, Clarendon Press, Oxford (1982), 725 pp.

[13] N. A. Davidenko and N. G. Kuvshinskiĭ, Fiz. Tverd. Tela (St. Petersburg) **39**, 1020 (1997) [Phys. Solid State **39**, 916 (1997)].

[14] K. M. Salikhov, R. Z. Sagdeev, and A. L. Buchachenko, *Spin Polarization and Magnetic Effects in Radical Reactions*, Yu. N. Molin (Ed.) Elsevier, Amsterdam–New York; Akademiai Kiado, Budapest, Hungary (1984).

[15] N. A. Davidenko and G. N. Kuvshinsky, J. Inf. Rec. Mater. **22**, 612 (1994).

Translated by P. Shelnitz

PHYSICS OF THE SOLID STATE VOLUME 40, NUMBER 4 APRIL 1998

Influence of anisotropy on the dispersion of surface plasmon-phonon polaritons in silicon carbide

A. V. Mel'nichuk

Institute of Semiconductor Physics, Ukrainian National Academy of Sciences, 252650 Kiev, Ukraine

Yu. A. Pasechnik

National Pedagogic University, 252030 Kiev, Ukraine

(Submitted September 12, 1997; resubmitted November 18, 1997)
Fiz. Tverd. Tela (St. Petersburg) **40**, 636–639 (April 1998)

Surface plasmon-phonon polaritons (SPPP's) of types 3 and 4 are investigated in doped anisotropic single crystals of hexagonal silicon carbide (6H-SiC) in the orientation corresponding to $K\perp C$ and $xy\perp C$. It is shown that a dispersion dependence of the type-3 SPPP's bounded by K appears in 6H-SiC when the plasmon frequency increases to $\nu_{p\perp}\geqslant 350\ \mathrm{cm}^{-1}$. At $\nu_{p\perp}\geqslant 400\ \mathrm{cm}^{-1}$, $\nu_s(K)$ exists for type-4 SPPP's in the frequency range $\Omega_\parallel^+<\nu<\nu_\perp^+$. When the concentration of free charge carriers is increased, the dispersion curves are displaced toward higher frequencies. The conditions for the existence of type-3 and type-4 SPPP's in 6H-SiC are determined. © *1998 American Institute of Physics.* [S1063-7834(98)01004-1]

Optical investigations of the surface phonon polaritons of isotropic solids were begun back in the nineteen seventies (c.f. Refs. 1 and 2). Bryksin, Mirlin, Agranovich *et al.* shows that surface modes of type 1 appear in solids in the presence of long-range forces. In the monograph by Agranovich and Ginzburg,[2] all the kinds of surface excitations of type 1 are termed surface excitons. Surface modes whose amplitude decreases at distances from the surface close to the lattice constant are called type-2 surface modes.[1] Measurements of the dispersion of type-1 surface plasmon-phonon modes in an isotropic n-InSb single crystal by a modified attenuated total reflection (ATR) method were first reported in Ref. 3. The interaction leads to the appearance of two branches of surface plasmon-phonon modes. The first investigations of the spectra of surface phonon polaritons in anisotropic crystals were performed by Agranovich, Dubovskiĭ, Bryksin *et al.*[4] It was shown that anisotropy leads to the existence of surface modes in two cases. Type-1 surface phonon modes exist at any values of the wave vector, and type-2 polaritons are bounded by the frequency and the wave vector.

The surface plasmon-phonon polaritons (SPPP's) in a uniaxial semiconductor have dispersion relations, whose number depends on the concentration of charge carriers and on the orientation of the C optical axis of the crystal relative to its surface.[5] Gurevich and Tarkhanyan showed that the regions for the existence of SPPP's are determined by the anisotropy of the crystal and the strength of the electron-phonon interaction. However, the theory of SPPP's was developed without consideration of the anharmonicity and thus did not permit the investigation of the spectra of SPPP's. Experimental dispersion curves and spectra of SPPP's in highly doped hexagonal silicon carbide 6H-SiC were obtained in Ref. 6. The differences between these dependences are specified predominantly by the anisotropy of the electron effective mass in 6H-SiC.[7]

In the present work we investigated the dependences of the frequency $[\nu_s(K)]$ and the ATR spectrum of the SPPP's of hexagonal silicon carbide (the 6H-SiC polytype) on the wave vector K with variation of the electron concentration over a broad frequency range (plasmon frequencies equal to 180–2500 cm^{-1}) in the existence region of SPPP's of new types: type-3 and type-4. The mutually consistent parameters of the model of 6H-SiC in Ref. 8 were used.

Single crystals of 6H-SiC have the wurtzite structure with space group $C_{6V}^4(P6_3mc)$ and are characterized by strong anisotropy of the properties of the plasma subsystem, unlike ZnO.[9] The anisotropy of the effective electron mass and the phonon and plasmon damping coefficients has been thoroughly investigated for 6H-SiC.[7] However, investigations of the influence of the anisotropy of the plasma subsystem on the dispersion dependences of SPPP's and their number in 6H-SiC have not yet been performed.

The SPPP's observed in the orientation corresponding to $K\perp C$ and $xy\parallel C$ are characterized by a relation, under which the dispersion of the surface waves is determined by the dielectric function $\varepsilon_\perp(\nu)$. The x and y axis lie on the surface of the sample, $\varepsilon_\perp(\nu)$ is the dielectric function of 6H-SiC perpendicular to the C optical axis, and ν is the frequency of the radiation (in cm^{-1}). Only nonradiative surface plasmon-phonon polaritons for which $K>\omega/c$ (ω is the angular frequency) are considered in this paper. Two branches of SPPP's are observed. The high-frequency branch (ν^+) begins at the point $\nu=\nu_{t\perp}$, and the low-frequency branch (ν^-) begins at zero. As K increases ($K\to\infty$), the frequencies asymptotically approach the values of the frequencies of mixed surface plasmon-phonons $\nu_{\text{pl-ph}}^{+,-}$:

$$\nu^{+,-}_{\text{pl-ph}}=\sqrt{0.5}\{\tilde{\nu}^{\,2}_{t\perp}+\tilde{\nu}^{\,2}_{p\perp}\pm[(\tilde{\nu}^{\,2}_{t\perp}+\tilde{\nu}^{\,2}_{p\perp})-4\tilde{\nu}^{\,2}_{t\perp}\tilde{\nu}^{\,2}_{p\perp}]^{1/2}\}^{1/2},$$

$$\tilde{\nu}^{\,2}_{t\perp}=\nu^2_{t\perp}[(1+\varepsilon_{0\perp})/(1+\varepsilon_{\infty\perp})],$$

$$\tilde{\nu}^{\,2}_{p\perp}=\nu^2_{p\perp}[\varepsilon_{\infty\perp}/(1+\varepsilon_{\infty\perp})], \tag{1}$$

where $\varepsilon_{\infty\perp,\parallel}$ and $\varepsilon_{0\perp,\parallel}$ are the principal values of the high-frequency and static dielectric tensors in directions perpendicular and parallel to the C axis, $\nu_{t\perp,\parallel}$ and $\nu_{l\perp,\parallel}$ are the frequencies of the transverse- and longitudinal-optical phonons, and $\nu_{p\perp}$ and $\nu_{p\parallel}$ are the plasmon frequencies.

In the case of $K\perp C$ and $xy\perp C$, the SPPP's are characterized by the dispersion relation[5]

$$\chi_x^2=[\varepsilon_\parallel(\nu)-\varepsilon_\perp(\nu)\varepsilon_\parallel(\nu)]/[1-\varepsilon_\perp(\nu)\varepsilon_\parallel(\nu)],$$

$$\chi_x=Kc/\omega \tag{2}$$

and by the inequalities

$$\varepsilon_\perp<0,\quad K>\omega/c,\quad \varepsilon_\parallel(\chi_x^2-\varepsilon_\parallel)<0, \tag{3}$$

where $\varepsilon_\parallel(\nu)$ is the dielectric function of 6H-SiC parallel to the C axis. If $\varepsilon_\parallel(\nu)$ and $\varepsilon_\perp(\nu)$ are interchanged, the dependence $\nu_s(K)$ for the orientation corresponding to $K\parallel C$ and $xy\parallel C$ can be obtained using (2). These dependences correspond to extraordinary SPPP. Ordinary type-1 SPPP's appear in the orientation corresponding to $K\perp C$ and $xy\parallel C$, and (2) transforms when $\varepsilon_\parallel(\nu)$ is replaced by $\varepsilon_\perp(\nu)$. This case is characterized by two branches of $\nu_s(K)$: $\nu^{+,-}$. In contrast to the isotropic case, when $\varepsilon_\perp<0$ and $\varepsilon_\parallel>\chi_x^2$, new branches of SPPP's appear. Their number and ranges for existence depend on the electron concentration in the conduction band and on the relative positions of the frequencies $\nu_{t\perp,\parallel}$, $\nu_{l\perp\parallel}$, $\nu_{p\perp\parallel}$, $\nu^{+,-}_{\perp\parallel}$, and $\Omega^{+,-}_{\perp\parallel}$,[5] which are specified by the relations

$$\varepsilon_\perp(\nu^{+,-}_\perp)=0,\quad \varepsilon_\parallel(\nu^{+,-}_\parallel)=0,$$

$$\varepsilon_\perp(\Omega^{+,-}_\perp)=1,\quad \varepsilon_\parallel(\Omega^{+,-}_\parallel)=1,$$

$$\nu^{+,-}_{\perp\parallel}=\sqrt{0.5}\{\nu^2_{l\perp\parallel}+\nu^2_{p\perp\parallel}\pm[(\nu^2_{l\perp,\parallel}+\nu^2_{p\perp,\parallel})^2-4\nu^2_{t\perp,\parallel}\nu^2_{p\perp,\parallel}]^{1/2}\}^{1/2}, \tag{4}$$

$$\Omega^{+,-}_{\perp\parallel}=\sqrt{0.5}\{\tilde{\nu}^{\,2}_{t\perp\parallel}+\tilde{\nu}^{\,2}_{p\perp\parallel}\pm[(\tilde{\nu}^{\,2}_{t\perp\parallel}+\tilde{\nu}^{\,2}_{p\perp\parallel})-4\tilde{\nu}^{\,2}_{t\perp\parallel}\tilde{\nu}^{\,2}_{p\perp\parallel}]^{1/2}\}^{1/2},$$

$$\tilde{\nu}^{\,2}_{t\perp\parallel}=\nu^2_{t\perp\parallel}[(\varepsilon_{0\perp,\parallel}-1)/(\varepsilon_{\infty\perp\parallel}-1)],$$

$$\tilde{\nu}^{\,2}_{p\perp\parallel}=\nu^2_{p\perp\parallel}[\varepsilon_{\infty\perp\parallel}/(\varepsilon_{\infty\perp\parallel}-1)]. \tag{5}$$

The maximum number of the branches $\nu_i(K)$ corresponding to solutions of Eq. (2) is equal to four ($i=1-4$). The SPPP frequencies $\nu_i(K)$ lie in regions of the (ν, K) plane where condition (3) holds, and at $K\gg\omega/c$ they asymptotically approach the frequencies of the surface plasmon-phonon modes obtained by solving the equation $\varepsilon_\perp\varepsilon_\parallel=1$.

Figure 1 shows the dispersion curves $[\nu_s(K)]$ of the SPPP's in 6H-SiC obtained in a calculation for $K\perp C$ and $xy\perp C$ using parameters of 6H-SiC which faithfully describe the experimental data in Refs. 7 and 8.

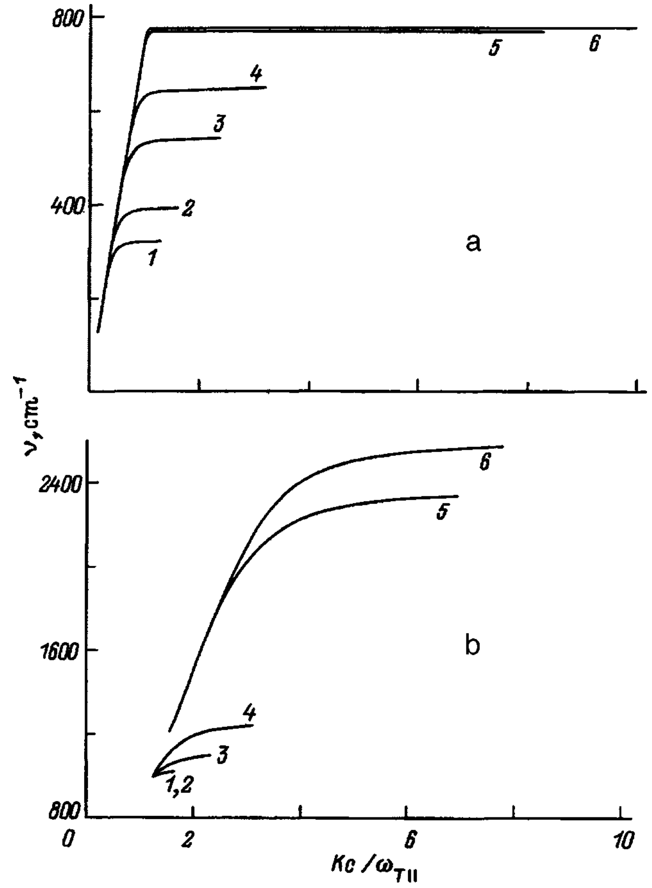

FIG. 1. Dispersion curves $[\nu_s(K)]$ of type-3 and type-4 SPPP's of 6H-SiC for $K\perp C$ and $xy\perp C$. a — type-3 SPPP's, b — type-4 SPPP's. Plasmon frequencies $\nu_{p\perp}=400$ (*1*), 500 (*2*), 740 (*3*), 1000 (*4*), 2250 (*5*), and 2500 cm^{-1} (*6*).

The inequalities $\nu_{t\parallel}<\nu_{t\perp}<\nu_{l\parallel}<\nu_{l\perp}$ are characteristic of 6H-SiC (Table I). The electron plasma frequencies $\nu_{p\perp}$ and $\nu_{p\parallel}$ of 6H-SiC are related by the expression $\nu_{p\parallel}=[(m^*_\perp\varepsilon_{\infty\perp})/(m^*_\parallel\varepsilon_{\infty\parallel})]^{1/2}\nu_{p\perp}$. For 6H-SiC we have $\nu_{p\perp}=2.682\nu_{p\parallel}$, since the effective electron mass perpendicular to the C axis $m^*_\perp=0.25m_e$, and $m^*_\parallel=1.75m_e$, where m_e is the mass of a free electron.[7] According to Ref. 5, $\nu_0=\nu_{p\perp}[\varepsilon_{\infty\perp}/m_\perp]^{1/2}$, and $\nu_1^2=\nu^2_{t\parallel}[\varepsilon_{\infty\perp}\nu^2_{t\parallel}-\varepsilon_{0\perp}\nu^2_{t\perp}]/[\mu_\perp(\nu^2_{t\perp}-\nu^2_{t\parallel})]$. For 6H-SiC $\nu_0=1.2767\nu_{p\perp}$, and $\nu_1=4766.3$ cm^{-1}, i.e., the inequality $\nu_0<\nu_1$ ($\nu^-<\nu_{t\parallel}$) holds, indicating the existence of surface modes in a bounded interval of K (Fig. 1a).

When there are no free charge carriers in 6H-SiC single crystals ($\nu_{p\perp}<10$ cm^{-1}), only the high-frequency branch $\nu_s^+(K)$ beginning at $\nu=\nu_{t\perp}=797$ cm^{-1} and asymptotically approaching the frequency of the plasmon-phonon modes $\nu^+_{\text{pl-ph}}=945.8$ cm^{-1} at $Kc/\omega_{t\parallel}=578.6$ is observed. The dependence $\nu_s^+(K)$ corresponds to extraordinary type-1 SP-

TABLE I. Parameters of the model of a 6H-SiC single crystal.[4]

6H-SiC	ε_0	ε_∞	ν_t, cm^{-1}	ν_l, cm^{-1}
$E\parallel C$	10.03	6.7	788	964
$E\perp C$	9.66	6.52	797	970

TABLE II. Results of a calculation of the parameters of the type-3 and type-4 SPPP's.

Sample number			PSE-3B	S-5	SC-1	
$\nu_{p\perp}$, cm^{-1}	400	500	740	1000	2250	2500
$\nu_{\perp}^{+}$, cm^{-1}	999.7	1018.9	1094.7	1234.7	2325.7	2566.8
$Kc/\omega_{t\parallel}$	1.323	1.594	2.280	3.0545	6.673	7.618
$\Omega_{\parallel}^{+}$, cm^{-1}	996.7	999.6	1009.3	1024.9	1207.8	1269.4
$Kc/\omega_{t\parallel}$	1.265	1.268	1.281	1.301	1.533	1.611
$\nu_{\parallel}^{+}$, cm^{-1}	968		977.9	990.2	1138.5	1190.8
ν^{+}, cm^{-1}	955	959.6	970.9	985.5	1135.8	1188
$Kc/\omega_{t\parallel}$	153	681.6	464.5	374.7	228.7	182.5
$\nu_{\perp}^{-}$, cm^{-1}	318.9	391.1	538.7	645.5	771	776
$Kc/\omega_{t\parallel}$	1.228	1.537	2.287	3.128	8.548	10.22
$\Omega_{\parallel}^{-}$, cm^{-1}	127.8	159.3	233.5	310.8	593.4	627.3
$Kc/\omega_{t\parallel}$	0.1622	0.2022	0.2964	0.3944	0.7530	0.7961
$\nu_{\parallel}^{-}$, cm^{-1}	121.4		222.3	296.7	580.6	616.8
ν^{-}, cm^{-1}	121.3	151.3	222.2	296.5	580.5	616.7
$Kc/\omega_{t\parallel}$	18.023	39.15	38.65	34.44	104.7	62.55

PP's. For the OZ-56 sample $\nu_{p\perp}=180$ cm^{-1}, and only two branches of $\nu_s(K)$ for type-1 SPPP's are displayed: $\nu_{\text{pl-ph}}^{+}=948$ cm^{-1} at $Kc/\omega_{t\parallel}=687.98$ and $\nu_{\text{pl-ph}}^{-}=54.7$ cm^{-1} at $Kc/\omega_{t\parallel}=9.1303$. A dispersion dependence of type-3 SPPP's with a bound on K begins to be displayed in 6H-SiC at $\nu_{p\perp}=350$ cm^{-1}. The cutoff frequencies are $\nu_{\text{pl-ph}}^{+}=953.3$ cm^{-1} and $\nu_{\text{pl-ph}}^{-}=106.2461$ cm^{-1}. The $\nu_s(K)$ curve for the type-3 SPPP's begins at $\Omega_{\parallel}^{-}=112$ cm^{-1} and $Kc/\omega_{t\parallel}=0.142$ and ends at $\nu_{\perp}^{-}=281.1$ cm^{-1} and $Kc/\omega_{t\parallel}=1.075$.

When $\nu_{p\perp}\geqslant 400$ cm^{-1} and $\nu_{p\perp}=2.682\nu_{p\parallel}$, 6H-SiC begins to display another dispersion curve (Fig. 1), which exists in a bounded interval of wave vector values. Its frequencies lie in the range $\Omega_{\parallel}^{+}<\nu<\nu_{\perp}^{+}$, and it lies above the high frequency $\nu_s(K)$ curve for the type-1 SPPP's. Curves *1–6* in Figs. 1a and 1b were obtained for the values of the plasmon frequency (modes perpendicular to the C axis) $\nu_{p\perp}=400$, 500, 740, 1000, 2250, and 2500 cm^{-1}. The frequencies 740, 1000, and 2190 cm^{-1} correspond to the parameters of the PSE-3B, S-5, and SC-1 samples. Figure 1a presents the $\nu_s(K)$ curve of the type-3 SPPP's, and Fig. 1b presents the $\nu_s(K)$ curve of the type-4 SPPP's. In the case of the type-3 SPPP's (Fig. 1a), when $\nu_{p\perp}=400$ cm^{-1}, $\nu_s(K)$ begins at 127.8 cm^{-1} and $Kc/\omega_{t\parallel}=0.1622$ and ends at 318.9 cm^{-1} and $Kc/\omega_{t\parallel}=1.2285$.

When $\nu_{p\perp}=400$ cm^{-1}, we have four dispersion curves, two of which have bounds on K (curves *1* in Fig. 1). For the type-1 SPPP's $\nu_{\text{pl-ph}}^{-}=121.3$ cm^{-1}, and $\nu_{\text{pl-ph}}^{+}=955.3$ cm^{-1} as $Kc/\omega_{t\parallel}\rightarrow\infty$ (Table II). The cutoff frequencies of the dispersion curves of the type-3 and type-4 SPPP's are equal to $\nu_{\perp}^{-}=318.9$ cm^{-1} at $Kc/\omega_{t\parallel}=1.2285$ and to $\nu_{\perp}^{+}=999.7$ cm^{-1} at $Kc/\omega_{t\parallel}=1.3231$, respectively.

Figure 2 presents modified internal reflection (ATR) spectra of the type-3 and type-4 SPPP's calculated using the parameters of the PSE-3B sample for the orientation of the 6H-SiC single crystal corresponding to $K\perp C$ and $xy\perp C$. Some of the parameters of the PSE-3B sample are presented in Table II. In addition, the values of the plasmon damping coefficients $\gamma_{p\perp}=155$ cm^{-1} and $\gamma_{p\parallel}=85$ cm^{-1} and the phonon damping coefficient $\gamma_{f\perp}=\gamma_{f\parallel}=15$ cm^{-1} were used. The spectra were calculated (Fig. 2a) with air gaps between the KRS-5 ATR element and the sample of thickness $d=90$ (curve *1*) and 4.32 μm (curve *2*) for the values of the angle of incidence α of the IR radiation in the ATR element indicated in the captions to the figure. The minima of the spectra correspond to $\nu_{\min}=524$ and 514 cm^{-1}, and the width of the spectra $\Gamma_s=22.5$ and 210 cm^{-1}.

Figure 2a (curve *3*) the experimental spectrum of the type-3 SPPP's of the PSE-3B sample is shown for the orientation of the 6H-SiC single crystal corresponding to $K\perp C$ and $xy\perp C$. The spectrum was recorded with an air gap between the KRS-5 ATR element and the sample of thickness $d=80$ μm for $\alpha=25°$ in the ATR element. The minimum of the spectrum is located in the region of the calculated spectra (525–515 cm^{-1}), but the width of the spectrum $3\Gamma_s\geqslant 600$ cm^{-1}, which is related to the significant damping coeffi-

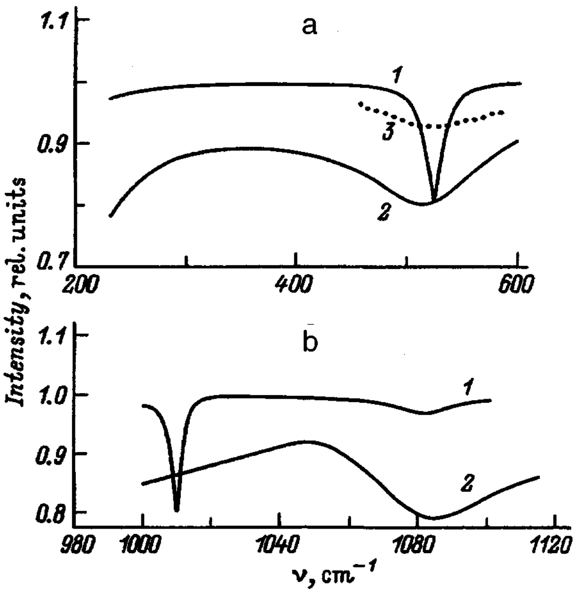

FIG. 2. ATR spectra of 6H-SiC for $K\perp C$, $xy\perp C$, and $\nu_{p\perp}=740$ cm^{-1}. α (μm) and α (°): a) *1* — 90 and 24.9, *2* — 4.32 and 35, *3* — 80 and 25 (experiment, sample PSE-3B); b) *1* — 33 and 25, *2* — 2.4 and 35.

cients of the type-3 SPPP's in the PSE-3B sample.

Figure 2b presents the calculated spectra of the type-4 SPPP's of this sample for $d=33$ μm (curve *1*) and $d=2.4$ μm (curve *2*). The minima of the spectra correspond to $\nu_{\text{min}}=1009.5$ and 1084 cm^{-1}, and the width of the spectra $\Gamma_s=4$ and 200 cm^{-1}. The ATR spectra of the type-3 and type-4 SPPP's (curve *2*) are characterized by radiation-induced broadening. We were unable to observe the spectra of type-4 SPPP's experimentally due to the significant damping coefficients of the plasmons in our samples.

Thus, investigations of the type-3 and type-4 surface plasmon-phonon polaritons in doped anisotropic 6H-SiC single crystals have been performed for orientations of the SPPP wave vector relative to the surface and the optical axis of the crystal corresponding to $K\perp C$ and $xy\perp C$. It has been shown that a dispersion dependence of the type-3 SPPP's bounded by K appears in 6H-SiC when the plasmon frequency increases to $\nu_{p\perp}\geqslant 350$ cm^{-1}. At $\nu_{p\perp}\geqslant 400$ cm^{-1}, there is a $\nu_s(K)$ curve for type-4 SPPP's in a bounded interval of wave vector values, whose frequencies lie in the range $\Omega_{\parallel}^{+}<\nu<\nu_{\perp}^{+}$ and which lies above the high-frequency $\nu_s(K)$ curve of the type-1 SPPP's. When the concentration of free charge carriers is increased, the beginning and end of the dispersion curves for the type-3 and type-4 modes are displaced toward higher frequencies. The conditions for the existence of type-3 and type-4 SPPP's in 6H-SiC have been determined. The spectrum of type-3 SPPP's has been obtained experimentally for the first time. The calculated ATR spectra of the type-3 and type-4 SPPP's demonstrate the possibility of detecting surface plasmon-phonon polaritons of the new types.

[1] V. V. Bryksin, D. N. Mirlin, and Yu. A. Firsov, Usp. Fiz. Nauk **113**, 29 (1974) [Sov. Phys. Usp. **17**, 305 (1974)].

[2] V. M. Agranovich and V. L. Ginzburg, *Crystal Optics with Spatial Dispersion, and Excitons*, 2nd ed., Springer-Verlag, Berlin–New York (1984), 432 pp.

[3] V. V. Bryksin, D. N. Mirlin, and I. I. Reshina, JETP Lett. **16**, 315 (1972).

[4] *Surface Polaritons: Electromagnetic Waves at Surfaces and Interfaces*, V. M. Agranovich and D. L. Mills (Eds.), North-Holland, Amsterdam (1982) [Russ. trans., Nauka, Moscow (1985), 526 pp.].

[5] L. É. Gurevich and R. G. Tarkhanyan, Fiz. Tverd. Tela (Leningrad) **17**, 1944 (1975) [Sov. Phys. Solid State **17**, 1273 (1975)].

[6] Yu. A. Pasechnik and E. F. Venger, Poverkhnost' **8**, 63 (1982).

[7] A. V. Mel'nichuk and Yu. A. Pasechnik, Fiz. Tverd. Tela (Leningrad) **34**, 423 (1992) [Sov. Phys. Solid State **34**, 227 (1992)].

[8] Yu. A. Pasechnik, O. V. Snitko, A. L. Bychkov, and V. F. Romanenko, Fiz. Tverd. Tela (Leningrad) **16**, 719 (1974) [Sov. Phys. Solid State **16**, 470 (1974)].

[9] A. V. Mel'nichuk, L. Yu. Mel'nichuk, and Yu. A. Pasechnik, Fiz. Tverd. Tela (St. Petersburg) **36**, 2624 (1994) [Phys. Solid State **36**, 1430 (1994)].

Translated by P. Shelnitz

Creation of excitons and defects in a CsI crystal during pulsed electron irradiation

E. S. Gafiatulina, S. A. Chernov, and V. Yu. Yakovlev

Tomsk Polytechnic University, 634004 Tomsk, Russia

(Submitted September 23, 1997)
Fiz. Tverd. Tela (St. Petersburg) **40**, 640–644 (April 1998)

Data presented on the influence of the temperature in the range 80–650 K on the spectral kinetics of the luminescence and transient absorption of unactivated CsI crystals under irradiation by pulsed electron beams ($\langle E\rangle = 0.25$ MeV, $t_{1/2} = 15$ ns, $j = 20$ A/cm^2). The structure of the short-wavelength part of the transient absorption spectra at $T = 80-350$ K exhibits features, suggesting that the nuclear subsystem of self-trapped excitons (STE's) transforms repeatedly during their lifetime until their radiative annihilation at $T \geqslant 80$ K, alternately occupying di- and trihalide ionic configurations. It is established that a temperature-induced increase in the yield of radiation defects, as well as F and H color centers, and quenching of the UV luminescence in CsI occur in the same temperature region (above 350 K) and are characterized by identical thermal activation energies (~ 0.22 eV). It is postulated that the STE's in a CsI crystal can have a trihalide ionic core with either an on-center or off-center configuration; the high-temperature luminescence of CsI crystals is associated with the radiative annihilation of an off-center STE with the structure $(\mathrm{I}^-(\mathrm{I}^0\mathrm{I}^- e^-))^*$.
[S1063-7834(98)01104-6]

The luminescence of unactivated CsI crystals under the action of ionizing radiations at temperatures near room temperature is characterized by a high intensity and a short decay time (~ 10 ns), making these crystals attractive for use in high-speed scintillation counters. The properties of the rapidly decaying luminescence of cesium iodide have been studied quite thoroughly, but the nature of the centers responsible for it remains unclear. In Ref. 1 this luminescence was assigned to an interaction between elementary excitations, while Nishimura *et al.*[2] attributed it to the thermal populating of a radiative triplet state of dihalide self-trapped excitons (STE's) with an ionic core having an on-center configuration. In the present work the structure of the luminescence centers is studied using optical absorption analysis, which permits studying the spectra and relaxation kinetics of transient absorption spectra induced in crystals upon irradiation by pulsed beams of accelerated electrons ($\langle E\rangle = 0.25$ MeV, $t_{1/2} = 10$ ns, $j_{\max} = 10^3$ A/cm^2) with nanosecond time resolution, along with the luminescence technique in the temperature range $80-550$ K and the range of photon energies $1.0-6.0$ eV.

1. EXPERIMENTAL RESULTS

1) Luminescence. The luminescence spectra of CsI measured at the moment of ending the electron irradiation pulses at various temperatures are illustrated by curves *1* in Figs. 1a–1d.

At 80 K (Fig. 1), the spectrum contains two bands of approximately equal intensity with maxima near 4.3 and 3.7 eV. The luminescence in the band at 4.3 eV decays rapidly ($\tau_f < 10$ ns), while the intensity of the band at 3.7 eV decreases considerably more slowly with a time constant $\tau_s = 1.0$ μs. According to experimental and theoretical studies,[1–5] these two bands should be assigned to the radiative annihilation of dihalide STE's with the structure $(\mathrm{I}_2^- e^-)^*$ from the singlet and triplet spin states, respectively.

As can be seen from a comparison of the spectra in Fig. 1, when the samples are heated above 80 K, the maximum of the high-energy band shifts toward longer wavelengths, the band becomes broader, and its contribution to the total spectrum increases with increasing temperature so that the spectrum at room temperature consists of a single broad nonelementary band with a maximum near 4.1 eV. As the temperature is increased further to 450 K, the form of the spectra remains unchanged.

The temperature evolution of the spectra just described is accompanied by the appearance of a high-energy band in the relaxation kinetics at $T > 90$ K along with a fast slow stage. The decay of the luminescence in this stage is described well by an exponential dependence of the intensity I on the time $I(t) = I_0 \exp(-t/\tau_s)$ with the time constant τ_s, whose values in the temperature range $90-200$ K coincide with the decay time of the triplet band at 3.6 eV.

As follows from the data presented in Fig. 2a, an increase in the temperature in this region results in identical decreases in the values of τ_s for both bands (curve *1*), an increase in the initial intensity of the slow component in the 4.3 eV band, which leads to a three- to fourfold increase in the integrated amplitude of the luminescence flash (curve *2* in Fig. 2a), and an approximately equal decrease in the luminescence intensity at the maximum of the triplet band at 3.6 eV (curve *3* in Fig. 2a).

These results are in good agreement with the data obtained for two-photon excitation[2] and clearly attest to the realization of thermally activated transitions between the STE states responsible for the luminescence bands at 3.6 and 4.3 eV. The temperature dependences of the integrated inten-

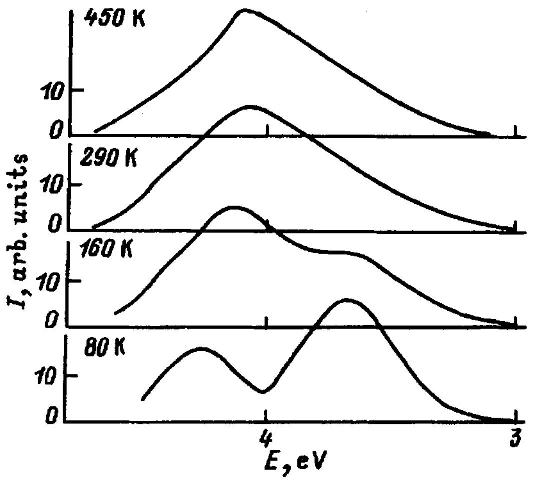

FIG. 1. Luminescence spectra of a CsI crystal measured at the moment of ending a pulse of accelerated electrons at various temperatures.

sity of the flashes in the bands at 3.6 and 4.3 eV, which characterize the redistribution of the populations of these two states, are illustrated by curves *1* and *2*, respectively, in Fig. 2b.

As the temperature rises further, the luminescence intensity decreases monotonically over the entire spectrum, the steepest (in Arrhenius coordinates) portion of the decrease in the luminescence yield lying in the region above 300 K.

2) Transient absorption. In the measurements of the transient absorption spectra of CsI, whose results were previously published in Ref. 6, we were forced to exclude the region of the spectrum with $h\nu > 3.0$ eV from the analysis because of the high brightness of the luminescence flash of the STE's, which is at a higher level than the brightness of the flashlamp installed in the spectrometer for transilluminating the samples. Using a more powerful probing light source, we were able to move into the region of shorter wavelengths and to discover an additional intense absorption band with a maximum at 3.4 eV. The general form of the absorption spectra measured with different delay times relative to the electron irradiation pulse at 80, 295, and 55 K is shown in Fig. 3.

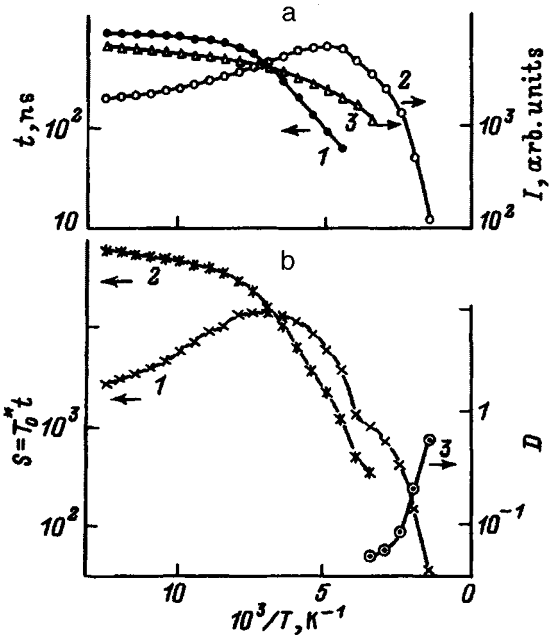

FIG. 2. Temperature dependence of the lifetime and luminescence intensity of STE's (a), the integrated luminescence intensity of STE's and the optical density in the *F* absorption band (b) in a CsI crystal. a) *1* — Relaxation time of the slow luminescence component at 4.3 eV, *2, 3* — amplitude values of the luminescence intensity at 4.3 and 3.6 eV, respectively; b) *1, 2* — integrated intensity of the flashes of slowly decaying luminescence at 4.3 and 3.6 eV, respectively, *3* — intensity of the *F* absorption band recorded 500 ns after the beginning of the irradiation pulse.

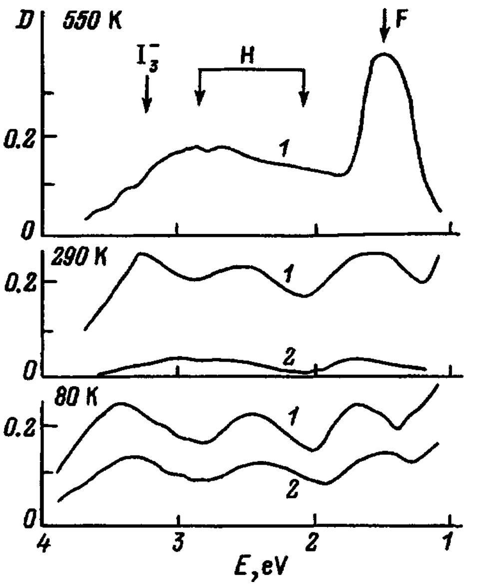

FIG. 3. Optical absorption spectra of a CsI crystal measured during a pulse of accelerated electrons of duration 15 ns (*1*) and 500 ns after its completion (*2*). The positions of the individual bands in the spectrum are marked by arrows.

It can be seen from this figure that in the temperature range 80–300 K, which corresponds to considerable changes in the spectral composition of the luminescence of the STE's, the structure of the absorption spectra (Fig. 3) remains practically unchanged. A typical finding for the transient absorption in this temperature range is that its intensity dropped following irradiation at the same rate in different parts of the spectrum, the characteristic relaxation times of the optical density at all the temperature values in this range coinciding with the decay times of the triplet luminescence. The set of properties indicated provides a sufficient basis to conclude that the transient absorption spectra appearing in this temperature range, like the luminescence spectra, are caused by STE's.

As the temperature was increased above room temperature, relatively long-lived absorption bands of *F* and *H* centers appeared, along with rapidly relaxing exciton bands, in the structure of the transient absorption spectra above ~350 K. The intensity of these bands increased rapidly with temperature, and, as can be seen from Fig. 3, the *F*-center band is the dominant feature in the spectrum at 550 K. The high-temperature ascending branch of the temperature dependence of the optical-density values at the maximum of the *F* band measured with a delay of 200 ns relative to the ending of the irradiation pulses is illustrated by curve *3* in Fig. 2b.

2. DISCUSSION OF RESULTS

As long as an STE exists, the molecular hole core in its composition and the electron bound to it can undergo optical excitation and move into a state of higher energy. The absorption then detected is characterized by a relaxation time which coincides with the decay time of the STE's in the radiative π state.[7,8] The form of the absorption spectrum is determined by the structure of the optical transitions in the electronic and nuclear subsystems of the STE in the lowest relaxed state.

The low-energy part of the spectra should correspond to transitions in the electronic subsystem of the STE: as was shown in Refs. 7–9, the maxima of the most intense long-wavelength peaks of STE's in most alkali-metal halide crystals are located between the absorption bands of the *F* and *M* color centers.[7] On this basis the most intense peak in the spectra of a CsI crystal might have been expected in the range between 1.7 and 1.05 eV. However, it follows from the data in Fig. 3 that it is apparently located beyond the red boundary of the range permitted by the spectrometer at $h\nu \leqslant 1.0$ eV. It is the first feature in the spectrum of the STE's in CsI.

According to existing theories, the structure of optical transitions in the nuclear subsystem of STE's is determined mainly by the internal structure of the electronic levels of the molecular hole ion forming the core of the STE.[10] Therefore, in particular, the short-wavelength transient absorption bands caused by dihalide STE's in alkali-metal halides[9] and crystals of alkaline-earth fluorides[11] are virtually identical, in their spectral characteristics to the bands of stable hole centers of the X_2^- family (where X is a halogen atom): *H* and V_k color centers.

The spectral kinetic characteristics of the new band in the short-wavelength part of the spectrum of the STE's in CsI with $E_m = 3.4$ eV take on special significance in this context. The intensity of this band drops following irradiation at all temperatures in the range 80−350 K synchronously with the absorption in other parts of the spectrum; therefore, it should unquestionably be assigned to self-trapped triplet excitons. The band is clearly expressed and is at a fairly large distance in the spectrum from the bands of the *H* and V_k centers of the I_2^- family (the maximum of the known absorption bands of the hole centers in a CsI crystal are marked with arrows in Fig. 3, according to the data in Refs. 12–15). At the same time, its position in the spectrum closely coincides with that of the absorption band of the V_2 color centers, which are among the simplest aggregate hole centers of the family of trihalide ions with an I_3^- structure. This is the second feature in the spectrum of the STE's in CsI.

The literature does not offer any information regarding the existence of centers of any other types that absorb in this region; therefore, the existence of bands corresponding to hole centers of the two families (both I_2^- and I_3^-) in the absorption spectra of the STE's in CsI should apparently be considered a weighty argument in support of the conclusion that the hole component of the self-trapped triplet excitons in this crystal is capable of being localized not only on two, but also on three halide ions.

Evidence of the existence of trihalide self-trapped holes in crystals of alkali-metal iodides is provided by data from femtosecond spectroscopy. It was shown in Ref. 16 that the trihalide self-trapped holes in KI are created after a time smaller than 1 ps and are unstable formations. It is possible that the trihalide self-trapped holes in a CsI crystal with a simple cubic lattice are more stable because of the small relative fraction of the ''empty space'' V_m [in ionic crystals of the NaCl type $V_m \sim 0.74$, and in crystals of the CsCl type $V_m \sim 0.52$ (Ref. 17)].

On the basis of the material presented, the processes of the formation and annihilation of self-trapped triplet excitons in a CsI crystal at 80 K can be described in the following manner.

After a conduction electron is trapped by a V_k center, dihalide STE's with the structure $(I^- I^0 e^-)^*$ form in the singlet ${}^1\Sigma_u^+$ or the triplet ${}^3\Sigma_u^+$ states.

The STE's in the singlet state have a centrosymmetric (on-center) core configuration and rapidly (with $\tau \approx 2$ ns) annihilate with the emission of σ luminescence [in CsI the maximum of the σ band is at 4.3 eV (Ref. 2)].

The relaxation of STE's to the lowest triplet state is accompanied, according to Ref. 18, by some displacement of the dihalide core along its axis with the formation of an off-center configuration. This displacement is unavoidably associated with a decrease in the distance between the I_2^- molecular ion and the neighboring I^- ion and the formation of a nearly trihalide geometric configuration of the type $(I^- - I^0 e)^* - I^-$ in a $\langle 100 \rangle$ chain of anions.

It can be expected that as a result of electron density fluctuations caused, for example, by thermal vibrations of the atoms, the nuclear subsystem of the STE's in CsI manages to transform repeatedly from the dihalide configuration to the trihalide configuration and vice versa during their lifetime before radiative annihilation. The structural formula of such a trihalide STE can be written in the form $(I^- \rightleftarrows (I^0 - I^- e))^*$.

With consideration of the results from the experimental and theoretical studies in Refs. 1–5, the transitions to the ground state of the STE's, in the period when the hole is localized on two halide ions, apparently should be considered responsible for the emission of luminescence in the 3.6 eV band at 80 K in cesium iodide.

At temperatures near room temperature, the luminescence in the 3.6 eV band is quenched and the main contribution to the luminescence spectrum of the STE's is made by transitions with an energy of 4.3 eV (Fig. 1). This luminescence is observed up to temperatures of the order of 500 K, and its quenching in the range 350–550 K is accompanied by alteration of the spectral composition of the transient absorption due to the appearance of bands belonging to *F* and *H* centers. The temperature dependence of the integrated intensity of the luminescence flash at 4.3 eV thus has the form of a curve with a maximum (curve *2* in Fig. 2b). The ascending branch of this curve in the range 100−160 K corresponds to a decrease in the luminescence intensity in the 3.6 eV band (curve *1* in Fig. 2b), and the descending branch in the region above 350 K corresponds to an increase in the yield of *F* color centers (curve *3* in Fig. 2b). In addition, this correspondence has not only a qualitative, but also a quantitative character: the values of the thermal activation energy found from the slopes of the intersecting curves in the low- and high-temperature regions are equal to ~50 meV and ~0.22 eV, respectively.

Thus, as a whole, the form of the families of curves presented in Fig. 2 attest to the occurrence of two successive configuration transformations of the STE's as the temperature is increased. The STE state responsible for the emission of luminescence at 4.3 eV should apparently be assumed to have a certain intermediate configuration between the configuration which the STE has at 80 K and the lattice configuration corresponding to a defect pair of *F* and *H* centers.

According to existing theoretical ideas, the displacement of the halide core of STE's, undergoing thermally activated transformation from the lowest relaxed state into *F*, *H* defect pairs, is associated with the formation of a certain quasistable state, i.e., an ''intermediate defect pair.''[19] For crystals with dihalide STE's such a state is usually represented as a pair of *F* and *H* centers located at neighboring lattice sites.[20] If an STE has a trihalide core, the structure of the intermediate defect state directly preceding the dissociation of the trihalide STE into *F* and *H* centers isolated from one another by a regular lattice site, clearly should be represented in the form of an *F* center and an I_3^- trihalide hole ion occupying two neighboring anion sites, which is an analog of an off-center STE of type III.[21,22]

According to data obtained a CsI crystal, the trihalide STE's, responsible for the high-temperature luminescence in the 4.1 eV band should have such an off-center configuration. In such a case, it is logical to assume that the state of a trihalide STE, which annihilates at low temperatures with the emission of luminescence in the 3.7 eV band and is capable of passing into an off-center state upon thermal displacement of the core, has an undisplaced trihalide core with a nearly on-center configuration.

The laws that we revealed in the temperature evolution of the luminescence and color centers in CsI together with the data on the luminescence properties at temperatures near 4.2 K in Refs. 2 and 4 can be described on the basis of the idea advanced in Ref. 23 that the lowest state of an STE and the ground state of an *F* center in an alkali-metal halide are related by a common adiabatic potential surface.

The form of a cross section of that surface, which, in our opinion, corresponds to the situation in CsI, is shown in Fig. 4. The generalized configuration coordinate *R*, which characterizes the relative position of the electron and hole components of an STE, is plotted along the horizontal axis. The cross section contains a series of minima corresponding to relaxed states of the STE+crystal system and the energy barriers separating them. The geometric configuration of each of the states is shown schematically at the bottom of Fig. 4.

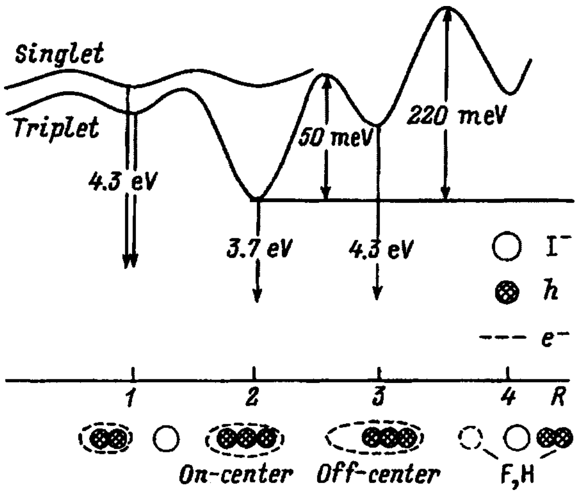

FIG. 4. Schematic representation of the luminescence of the lowest adiabatic potential surface joining the states of an STE and spatially separated *F* and *H* color centers in a CsI crystal.

According to the data in 2, the appearance of the characteristic luminescence band at 3.6 eV is a result of the thermally activated (with $E_a = 2$ meV) transformation of on-center dihalide STE's. If we take into account the foregoing ideas regarding the nature of the luminescence in CsI, the data from those studies can be interpreted as the resultant transitions of an on-center STE from the di- and trihalide configurations (this is the transition between the first and second minima in the diagram). The 2→3 and 3→4 transitions reflect the transformation of a trihalide STE from the on-center configuration to the off-center configuration and the subsequent dissociation of the trihalide STE into *F*, *H* defect pairs, respectively.

Thus, the set of data that we obtained and the data known from the literature on thermally activated luminescence and defect-formation phenomena in CsI crystals can be adequately described within a single approach on the basis of a fairly simple scheme as a consequence of a series of configuration transformations of an STE accompanied by a successive increase in the degree of spatial separation of the electronic and nuclear components of the STE with the temperature.

[1] A. N. Belsky, A. N. Vasil'ev, V. V. Mikhalin, A. V. Gektin, P. Martin, C. Pedrini, and D. Bouttet, Phys. Rev. B **49**, 13 197 (1994).
[2] H. Nishimura, M. Sakata, T. Tsujimoto, and M. Nakayama, Phys. Rev. B **51**, 2167 (1995).
[3] H. Lamatsch, J. Rossel, and E. Saurer, Phys. Status Solidi B **41**, 605 (1970).
[4] T. Iida, Y. Nakaoka, J. P. von der Weid, and M. A. Aegerter, J. Phys. C **13**, 983 (1980).
[5] L. Falco, J. P. von der Weid, M. A. Aegerter, T. Iida, and Y. Nakaoka, J. Phys. C **131**, 993 (1980).
[6] V. A. Kravchenko, V. M. Lisitsyn, and V. Yu. Yakovlev, Fiz. Tverd. Tela (Leningrad) **27**, 2181 (1985) [Sov. Phys. Solid State **27**, 1307 (1985)].
[7] R. G. Fuller, R. T. Williams, and M. N. Kabler, Phys. Rev. Lett. **25**, 446 (1970).
[8] R. T. Williams and M. N. Kabler, Phys. Rev. B **9**, 1897 (1974).
[9] R. T. Williams and K. S. Song, J. Phys. Chem. Solids **50**, 679 (1990).
[10] N. Itoh, Adv. Phys. **31**, 491 (1982).
[11] R. T. Williams, M. N. Kabler, W. Hayes, and J. P. Stott, Phys. Rev. B **14**, 725 (1976).
[12] J. Konitzer and H. Hersh, J. Phys. Chem. Solids **27**, 771 (1966).
[13] I. A. Parfianovich and É. É. Penzina, *Electronic Color Centers in Ionic Crystals* [in Russian], Vost.-Sib. Kn. Izd., Irkutsk (1977), 208 pp.

[14] V. V. Kolotilin and V. I. Shtan'ko, Fiz. Tverd. Tela (Leningrad) **26**, 236 (1984) [Sov. Phys. Solid State **26**, 138 (1984)].

[15] V. Yu. Yakovlev, Fiz. Tverd. Tela (Leningrad) **26**, 3334 (1984) [Sov. Phys. Solid State **26**, 2003 (1984)].

[16] S. Iwai, T. Tokizaki, A. Nakamura, T. Shibata, K. Tanimura, A. Shluger, and N. Itoh, J. Lumin. **60–61**, 720 (1994).

[17] C. Kittel, *Introduction to Solid State Physics*, 2nd ed., Wiley, New York (1956) [Russ. trans., Fizmatgiz, Moscow (1963)], 696 pp.

[18] R. T. Williams, K. S. Song, W. L. Faust, and C. H. Leung, Phys. Rev. B **33**, 7232 (1986).

[19] T. Toyozawa, J. Phys. Soc. Jpn. **44**, 482 (1978).

[20] N. Itoh, T. Eshita, and R. T. Williams, Phys. Rev. B **34**, 4230 (1986).

[21] K. Kan'no, K. Tanaka, and T. Hayashi, Rev. Solid State Sci. **4**, 383 (1990).

[22] T. Matsumoto, S. Kawata, A. Miyamoto, and K. Kan'no, J. Phys. Soc. Jpn. **61**, 4229 (1992).

[23] R. T. Williams, B. B. Craig, and W. L. Faust, Phys. Rev. Lett. **52**, 1709 (1984).

Translated by P. Shelnitz

PHYSICS OF THE SOLID STATE VOLUME 40, NUMBER 4 APRIL 1998

Calculation of the dielectric permittivity tensor for the surface layer of a cubic crystal

S. N. Latynin

Donbass State Academy of Construction and Architecture, 339023 Makeevka, Donetsk District, Ukraine

(Submitted September 30, 1997)
Fiz. Tverd. Tela (St. Petersburg) **40**, 645–647 (April 1998)

The dielectric permittivity tensor has been calculated by the effective-field method with inclusion of spatial inhomogeneities in the crystal surface layer. Cubic crystals have been shown to have natural optical activity within a layer a few lattice constants thick. © *1998 American Institute of Physics.* [S1063-7834(98)01204-0]

It was pointed out[1] that the dielectric permittivity tensor has to be calculated throughout the volume of a bounded crystal, including the near-surface region, since this would eliminate the need for deriving additional boundary conditions when studying the additional light waves[2]. For example, the additional boundary conditions were derived[3,4] from the constitutive relations within the dielectric approximation by calculating the nonlocal polarizability at the surface, which cannot be considered even approximately a homogeneous function in z. It was shown[5,6] that one can obtain the additional crystal-surface polarization within a microscopic approach with the use of the effective-field method[7]. The present work applies microscopic theory[5,6] to calculate the crystal polarization and dielectric permittivity tensor of a simple cubic lattice with a (100)-type surface plane.

We consider polarization of a semi-infinite lattice by a monochromatic wave $E^{(e)}(r,t)=E_0^{(e)}\exp(ik_0r-i\omega t)$, where $|\mathbf{k}_0|=(\omega a/c)$ (a is the lattice constant, and ω is frequency). As in Refs. 5 and 6, the dipole moment P^l of the lth atom of the crystal is determined in a self-consistent way from coupled equations

$$P^l(t)=\alpha(\omega)\{E^{(d)l}(t)+E^{(e)}(t)\}, \tag{1}$$

where $\alpha(\omega)$ is the atomic polarizability, and $E^{(d)l}$ is the field generated at the lth central atom by all the other atoms; its Fourier amplitudes were obtained for dipole moments in plane-wave representation in Ref. 5. For a simple cubic lattice, the position vector of the lth atom $l=(l_\perp,l_3)=(l_1,\,l_2,\,l_3)$, where $l_1,\,l_2,\,l_3$ are integers in units of the lattice constant, $l_3>0$, and symbol $\perp$ denotes projection onto the XY plane coinciding with the surface plane.

The dipole moment satisfying Eqs. (1) throughout the crystal, and with a zero remainder on the right-hand side, can be written in the following general form[5]

$$\begin{aligned}P^l={}&P_0\exp(ikl-i\omega t)\\&+\sum_{\substack{q_\perp\\q_\perp\neq 0}}B(q_\perp)\left[1+\sum_{n=1}^{l_3-1}\frac{1}{n!}\prod_{m=1}^{n}(l_3-m)\right]\\&\times\exp(-\gamma_q l_3+i(q_\perp+k_\perp)l_\perp-i\omega t),\end{aligned}\tag{2}$$

where $\gamma_q=\sqrt{(q_\perp+k_\perp)^2-k_0^2}$, $q_\perp$ is the reciprocal lattice vector (in units of $1/a$), and k is the wave vector multiplied by a. The second term in Eq. (2) determines the additional surface polarization of the crystal, which depends in a complicated way on l_3 (i.e. on the distance to the surface). Additional surface polarization is essential only at distances within a few lattice constants. The condition $q_\perp\neq 0$ in $\Sigma_{q_\perp}$ was introduced because of the absence in the bulk of the crystal of waves with $k=k_0$.

Using the generalization procedure of Ewald for 2D periodic structures,[5,6] and substituting into the Hertz vector the dipole moment in the form (2), the right-hand side of Eq. (1) transforms to a sum of two expressions:

$$\begin{aligned}E_\alpha^{(*)}(l,t)={}&\varphi_{\alpha\beta}(\omega,k)P_{0\beta}\\&\times\exp(ikl-i\omega t)+\sum_{\substack{q_\perp\\q_\perp\neq 0}}W_{\alpha\beta}(\omega,k,q_\perp)\\&\times B_\beta(q_\perp)\left[1+\sum_{n=1}^{l_3-1}\frac{1}{n!}\prod_{m=1}^{n}(l_3-m)\right]\\&\times\exp(-\gamma_q l_3+i(q_\perp+k_\perp)l_\perp-i\omega t),\end{aligned}\tag{3}$$

and

$$\begin{aligned}&E_{0\alpha}^{(e)}\exp(ik_0l-i\omega t)+\sum_{q_\perp}\rho^-_{\alpha\beta}(\omega,k_\perp,q_\perp)\\&\times\left[\frac{1}{1-\exp[-(ik_3+\gamma_q)}P_{0\beta}\right.\\&\left.+\sum_{\substack{q'_\perp\\q'_\perp\neq 0}}\frac{1}{2-\exp(-\gamma_q+\gamma_{q'})}B_\beta(q'_\perp)\right]\\&\times\exp(-\gamma_q l_3+i(q_\perp+k_\perp)l_\perp-i\omega t),\end{aligned}\tag{4}$$

where $\alpha,\ \beta=1,\,2,\,3$. The corresponding tensors in these expressions can be written

$$\varphi_{\alpha,\beta}(\omega,k)=\varphi^{\perp}_{\alpha\beta}(\omega,k_{\perp})+\sum_{q_{\perp}}\left[\rho^{-}_{\alpha\beta}(\omega,k_{\perp},q_{\perp})\frac{1}{1-\exp(\gamma_q+ik_3)}+\rho^{+}_{\alpha\beta}(\omega,k_{\perp},q_{\perp})\frac{1}{1-\exp(\gamma_q-ik_3)}\right], \tag{5}$$

$$W_{\alpha,\beta}(\omega,k_{\perp},q'_{\perp})=\varphi^{\perp}_{\alpha\beta}(\omega,k_{\perp})+\sum_{q_{\perp}}\left[\rho^{-}_{\alpha\beta}(\omega,k_{\perp},q_{\perp})\times\frac{1}{1-2\exp(\gamma_q-\gamma_{q'})}+\rho^{+}_{\alpha\beta}(\omega,k_{\perp},q_{\perp})\frac{2}{2-\exp(\gamma_q+\gamma_{q'})}\right], \tag{6}$$

$$\varphi^{\perp}_{\alpha\beta}(\omega,k_{\perp})=-\frac{2\pi}{a^3}\sum_{q_{\perp}}\frac{1-\Phi\left(\frac{\gamma_q}{2\sqrt{\pi}}\right)}{\gamma_q}\times[(q_{\perp}+k_{\perp})_{\alpha}(q_{\perp}+k_{\perp})_{\beta}-\gamma_q^2\delta_{\alpha3}\delta_{\beta3}-k_0^2\delta_{\alpha\beta}]-\frac{4\pi}{a^3}\sum_{q_{\perp}}\exp\left(-\frac{\gamma_q}{2\sqrt{\pi}}\right)\delta_{\alpha3}\delta_{\beta3}+\frac{1}{a^3}\left\{\frac{4\pi}{3}-2k_0^2\right\}\delta_{\alpha\beta}+\frac{2}{a^3\sqrt{\pi}}\times\sum_{\substack{l'_{\perp}\\ l'_{\perp}\neq l_{\perp}}}\exp[-ik_{\perp}(l_{\perp}-l'_{\perp})]\{k_0^2\delta_{\alpha\beta}f_0-2\delta_{\alpha\beta}f_2+4(l_{\perp}-l'_{\perp})_{\alpha}(l_{\perp}-l'_{\perp})_{\beta}f_4\},$$

$$\Phi(x)=2\pi\ 0x\ \exp(-t2)dt,$$

$$f_n=\int_{\sqrt{\pi}}^{\infty}x^n\exp[-x^2(|l_{\perp}-l'_{\perp}|)^2dx,$$

$$\rho^{\mp}_{\alpha\beta}=-\frac{2\pi}{\gamma_q a^3}\{(ik_{\perp\alpha}+iq_{\perp\alpha}\mp\gamma_q\delta_{\alpha3})\times(ik_{\perp\beta}+iq_{\perp\beta}\mp\gamma_q\delta_{\beta3})+k_0^2\delta_{\alpha\beta}\}.$$

Expression (3) is the refracted wave propagating in the crystal. The first term in Eq. (3) represents the bulk wave, where (5) can be recast in the form of a long-wavelength expansion

$$\varphi_{\alpha\beta}(\omega,k)a^3=-4\pi\frac{k_{\alpha}k_{\beta}-k_0^2\delta_{\alpha\beta}}{k^2-k_0^2}+\varphi'_{\alpha\beta}(\omega,k). \tag{7}$$

In contrast to the results of Ref. 8, the first term in Eq. (7), which is responsible for the macroscopic field, can always be isolated, both in a semi-infinite crystal and in a finite layer, down to monolayer thickness. $\varphi'_{\alpha\beta}(\omega,k)$ contains the same structural coefficients of the long-wavelength expansion in terms of order k^2, as in the case of a semi-infinite crystal (see Ref. 7).

The second term in Eq. (3) describes surface waves with amplitudes dying out with depth and propagating along the surface. In contrast to Eq. (7), the long-wavelength expansion of tensor (6) contains terms of order $ik_{\perp}$. This results in a natural optical activity of cubic crystals in a thin surface layer a few lattice constants thick.

The second term in Eq. (4) yields for $q_{\perp}=0$ the extinction theorem of Ewald–Oseen[5,6] which states that the incident wave is completely extinguished in the surface layer. If $q_{\perp}\neq 0$, we can obtain an expression relating the dipole moment amplitudes $B(q_{\perp})$ and P_0 by equating in Eq. (4) the coefficients of like exponentials:

$$B(q_{\perp})=V(\omega,k,q_{\perp})P_0, \tag{8}$$

where

$$V(\omega,k,q_{\perp})=\sum_{i=0}^{\infty}\frac{1}{2^{i+1}}\frac{1}{\exp[-(ik_3+\gamma_q^i)]-1}\times\prod_{j=1}^{i}\Phi^j(\omega,k_{\perp},q^j_{\perp});$$

$$\Phi^j(\omega,k_{\perp},q^j_{\perp})=\sum_{\substack{q^j_{\perp}\\ q^j_{\perp}\neq 0,\,q^{j-1}_{\perp}}}\frac{1}{\exp[-(\gamma_q^{j-1}-\gamma_q^j)]-1},$$

here $q^j_{\perp}$, $q^{j-1}_{\perp}$, $q^i_{\perp}$ denote separate reciprocal-lattice vectors in the ith or jth sum, and $q^0_{\perp}=q_{\perp}$.

Substituting Eq. (8) in Eq. (3) and using Eq. (7), we take the definition of the dielectric permittivity tensor[9] $\varepsilon_{\alpha\beta}$ to obtain

$$\varepsilon_{\alpha\beta}=\varepsilon_{\alpha\beta}(\omega,k,l_3)=\delta_{\alpha\beta}+4\pi A(\omega)T^{-1}_{\alpha\beta}(\omega,k,l_3), \tag{9}$$

where $A(\omega)=\frac{\alpha(\omega)}{a^3}$, and $T^{-1}_{\alpha\beta}$ is a tensor inverse to

$$T_{\alpha\beta}(\omega,k,l_3)=\delta_{\alpha\beta}-A(\omega)\times\left\{\varphi'_{\alpha\beta}(\omega,k)+\sum_{\substack{q_{\perp}\\ q_{\perp}\neq 0}}W_{\alpha\beta}(\omega,k_{\perp},q_{\perp})\times\left[1+\sum_{n=1}^{l_3-1}\frac{1}{n!}\prod_{m=1}^{n}(l_3-m)\right]V(\omega,k_{\perp},q_{\perp})\times\exp[-(\gamma_q+ik_3)l_3+iq_{\perp}l_{\perp}]\right\}. \tag{10}$$

To conclude, we have obtained, in a general form (9), the dielectric permittivity tensor including spatial inhomogeneity and optical anisotropy in the surface layer of a semi-infinite cubic crystal. As follows from Eq. (9), $\varepsilon_{\alpha\beta}$ is an inhomogeneous function in z varying very strongly with depth (the coordinate axis Z is directed into the bulk of the crystal and coincides with the translation vector a_3). The long-wavelength expansion (10) in k and, hence, of $\varepsilon_{\alpha\beta}$, will be unique for each layer and will contain, besides the quadratic terms, also terms of order $ik_\perp$, which assumes the existence of natural optical activity in the surface layer of a cubic crystal. At a depth of a few lattice constants and for a (100) type face, the long-wavelength expansion of $T_{\alpha\beta}$ and of $\varepsilon_{\alpha\beta}$ is the same as for an infinite crystal[10], because $T_{\alpha\beta}\rightarrow\delta_{\alpha\beta}-A(\omega)\varphi'_{\alpha\beta}(\omega,k)$ for $l_3\rightarrow\infty$.

[1] V. M. Agranovich and V. L. Ginzburg, *Spatial Dispersion in Crystal Optics and the Theory of Excitons* [Wiley, New York (1967); Nauka, Moscow (1986), 432 pp.].

[2] S. I. Pekar, *Crystal Optics and Additional Light Waves* [in Russian], Naukova Dumka, Kiev (1982), 296 pp.

[3] R. Zeyher, J. L. Birman, and W. Breng, Phys. Rev. B **6**, 4613 (1972).

[4] A. A. Maradudin and D. A. Mills, Phys. Rev. B **7**, 2787 (1973).

[5] S. N. Latynin and K. B. Tolpygo, Fiz. Tverd. Tela (Leningrad) **30**, 191 (1988) [Sov. Phys. Solid State **30**, 690 (1988)].

[6] S. N. Latynin, Fiz. Tverd. Tela (Leningrad) **33**, 2116 (1991) [Sov. Phys. Solid State **33**, 1191 (1991)].

[7] K. B. Tolpygo, Ukr. Fiz. Zh. **31**, 178 (1986).

[8] V. V. Rumyantsev and V. T. Shunyakov, Kristallografiya **36**, 535 (1991) [Sov. Phys. Crystallogr. **36**, 293 (1991)].

[9] M. Born and E. Wolf, *Principles of Optics* [Pergamon, Oxford (1964); Nauka, Moscow (1970), 856 pp.].

[10] V. V. Rumyantsev, Kristallografiya **36**, 1346 (1991) [Sov. Phys. Crystallogr. **36**, 763 (1991)].

Translated by G. Skrebtsov

PHYSICS OF THE SOLID STATE VOLUME 40, NUMBER 4 APRIL 1998

Structural characterization of opal-based photonic crystals in the visible range

V. N. Bogomolov, A. V. Prokof'ev, and A. I. Shelykh

A. F. Ioffe Physicotechnical Institute, Russian Academy of Sciences, 194021 St. Petersburg, Russia

(Submitted October 2, 1997)
Fiz. Tverd. Tela (St. Petersburg) **40**, 648–650 (April 1998)

For structural characterization of periodic three-dimensional systems with submicron-scale lattice parameters (optical photonic crystals), is analogous to the use of visible light of x-rays. It is shown that specular reflectance and transmittance spectra of opal do indeed yield information on the lattice period and structural perfection of photonic crystals. *© 1998 American Institute of Physics.* [S1063-7834(98)01304-5]

The optical properties of opals as systems whose lattice constant is comparable to the wavelength of visible light were studied in optically perfect samples prepared by us earlier[1,2]. We showed that opals are photonic crystals with a photonic band gap in the visible region. In these studies, the optical properties were considered in terms of band structure. At the same time investigation of the optical characteristics of opal also has another aspect.

The growing interest in opal-based three-dimensional periodic lattices witnessed in the recent two or three years provides motivation for a more detailed investigation of their structural properties. The parameter of the cluster lattice and its structural perfection are among the most important characteristics of nanocomposites. This work attempts to estimate these characteristics from an analysis of optical properties.

Since the optical properties of opals in the visible are dominated by interference effects accompanying the diffraction of visible light from a three-dimensional periodic lattice, these properties carry information on the structural characteristics of a sample. For opals, visible light is to a considerable extent analogous to x-radiation for conventional crystals, and optical diffraction analysis to that of x-ray diffraction analysis of ordinary crystals. Of the three goals of structure analysis, namely, establishment of the structure, determination of the lattice parameters and of crystalline perfection, only the latter two have significance for opal. It is known that synthetic opals have close-packed cubic structure, i.e., they have an fcc lattice. It is determination of the parameters of this lattice and of its perfection that is the goal of the optical diffraction analysis of opals.

Specular reflectance spectra from the opal surface may serve for the simplest structural characterization (curve *1* in Fig. 1). These spectra were obtained by measuring the signal reflected from the opal surface at the specular-reflection angle. The light was incident at 8° to the sample surface normal. The spectrum reveals several peaks. Also shown with dotted lines are the spectra of the same opal sample whose voids are filled by glycerine (*2*) and sulfur (*3*). We see that their peaks are shifted to longer wavelengths. The peaks are obviously of interference nature, and their shift is due to a change in the refractive index of the medium. The larger is the refractive index, the larger is the peak shift to longer wavelengths. The peak shift can be quantified using Bragg's relation describing diffraction phenomena.

Bragg's relation for the optical case should include the refractive index of the medium n:

$$2d\sin\alpha = k\lambda/n. \qquad (1)$$

Opal-based nanocomposites, which are optically inhomogeneous materials, can be conveniently characterized by an effective refractive index. We measured in this work effective refractive indices of various opal-based nanocomposites, namely, opals whose voids were filled by air (pure opal), water, and glycerine. The measurements were made by the prism method and borne out by the immersion technique. Measurements carried out in the wavelength region 500–600 nm yield $n_{\mathrm{eff}} = 1.27$ for the pure opal, 1.35 for opal filled by water, and 1.40 for opal filled by glycerine. We did not succeed in measuring the refractive index of the sulfur-filled opal because of the strong scattering due to the high optical contrast (the ratio of the refractive indices of opal spheres and sulfur-filled voids).

Calculations show that the law of additivity of the refractive indices of the components making up a composite is applicable to opal. Knowing the volume fractions of the components, one can readily calculate the effective refractive index. In the case of opal we have to take into account its complex structure, namely, the presence not only of voids between spheres which can be reached by a wetting liquid, but also of the array of voids inside the spheres themselves, which are inaccessible to a liquid.[3] The volume fractions of silica, liquid, and of the air remaining in the voids inaccessible to a liquid can be determined by measuring the sample density before and after void filling by the liquid.

Knowing the refractive indices of opal samples, we can now use Bragg's relation to assign the peaks in the reflectance spectra. Obviously enough, the various peaks result from Bragg reflections from various crystallographic planes in the opal lattice. We found that these peaks change position with a change of opal crystal orientation with respect to the incident beam.

Electron microscope studies of the opal sample whose spectrum is presented in Fig. 1 showed it to consist of

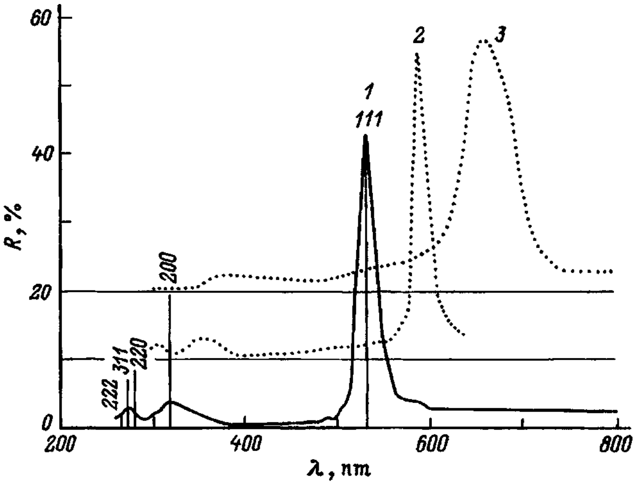

FIG. 1. Specular reflectance spectrum of opal (*1*). Vertical lines identify the reflection positions which were calculated from electron microscope data on the size of opal spheres using Eq. (1). Dotted lines show specular reflectance spectra from opal matrix filled by (*2*) glycerine and (*3*) sulfur.

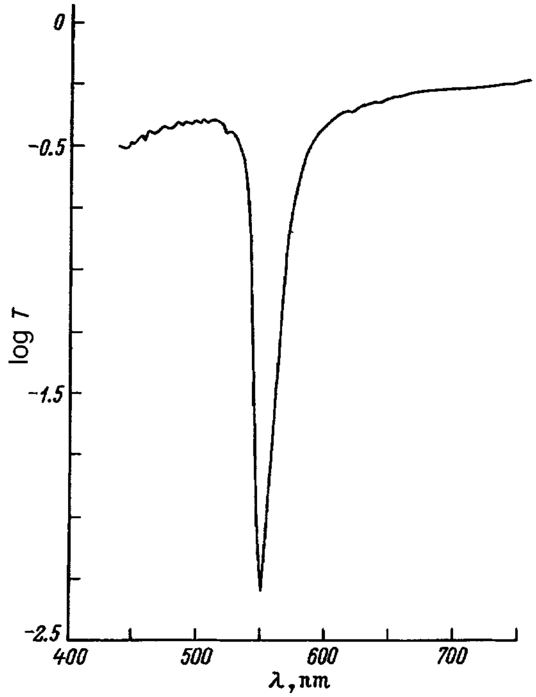

FIG. 2. Optical transmittance spectrum of opal with voids filled by water.

spheres about 250 nm in diameter. In the case of point contact between spheres, the fcc lattice constant for this sample is 354 nm, with a spacing of 205 nm between the (111) planes. Substituting these data and the value $n = 1.27$ into Eq. (1), we obtain that reflection from the (111) planes under nearly normal angle of incidence (82°) should produce a maximum at λ of about 520 nm. This agrees satisfactorily with the position of the main maximum in Fig. 1 (curve *1*). Thus the peak at $\lambda = 530$ nm is due to reflection from the sets of (111) planes.

The positions of peaks in the reflectance spectrum calculated using Eq. (1) for other planes of an fcc lattice is shown in Fig. 1 by vertical bars. We see that these bars coincide in position with the observed maxima in reflected intensity.

The peak positions for the opal filled by glycerine and sulfur (curves *2* and *3* in Fig. 1) coincide with the calculated positions of the intensity maximum, if the refractive indices for these samples are substituted in Eq. (1).

Thus a conventional reflectance spectrum offers a possibility of obtaining quantitative information on the lattice constant of an opal sample, as well as of orienting it (at least, of establishing the $\langle 111 \rangle$ direction).

The relative peak heights for the various fcc lattice planes in Fig. 1 was taken by analogy with the x-ray reflection-intensity ratio for the fcc copper lattice [100% for the (111) plane]. We see that the peak positions coincide well with those in the opal spectrum. Their intensity ratio, however, differs significantly from that of the copper x-ray reflections. The reflection intensities from planes other than (111) are considerably weaker. The reason for this lies probably in the geometry of the experiment. Bragg reflection maxima from planes other than (111) should obviously be detected with the highest intensity in other directions. It is only due to the strong diffuse light scattering that reflection from the (200), (220), (222), and others was detected. A more comprehensive optical diffraction analysis should obviously be performed in another, more complex arrangement. One should look for maxima in reflected intensity throughout the hemisphere. This requires making measurements with a position-sensitive detector.

There is a certain correspondence between the reflectance and transmittance spectra. The position of the main maximum in a reflectance can be identified with that of the minimum in the transmittance spectrum. Figure 2 presents a transmittance spectrum of an opal whose voids were filled by water to reduce the optical contrast, thus increasing light transmission through the sample (for this reason the minimum is slightly shifted away from $\lambda = 530$ nm). The dip in transmission is nothing else but the most direct manifestation of the photonic band gap[1].

Transmittance spectra can also be used for opal characterization. As already mentioned, opal samples can be separated into two classes. The first can be termed ''single crystals,'' in which a regular structure extends throughout the volume of the crystal. The second class combines ''polycrystalline'' opals having many regions with a regular arrangement of clusters, which are differently oriented with respect to one another. The difference between these two classes of samples can be established from optical spectra. From the depth of the dip in a transmission spectrum one can judge single-crystal perfection of the opal sample. The most structurally perfect opals prepared by us usually provide an attenuation of transmitted signal in the region of the minimum of about 2.5 orders of magnitude.

Thus optical diffraction analysis is similar in some respects to x-ray diffraction measurements. There is, however, a substantial difference, namely, the size of the region in a crystal involved in x-ray diffraction is usually substantially less than the x-ray wavelength, whereas in opal-based crystals they are comparable, in other words, we have in the latter case structural analysis of media with a spatially modulated refractive index.

Support of the Russian Fund for Fundamental Research (Grant 96-03-32460a) is gratefully acknowledged.

[1] V. N. Bogomolov, D. A. Kurdyukov, A. V. Prokof'ev, and S. M. Samoĭlovich, JETP Lett. **63**, 496 (1996).

[2] V. N. Bogomolov, A. V. Prokof'ev, and S. M. Samoĭlovich, Fiz. Tverd. Tela (St. Petersburg) **38**, 2722 (1996) [Phys. Solid State **38**, 1493 (1996)].

[3] V. N. Bogomolov, L. S. Parfen'eva, A. V. Prokof'ev, I. A. Smirnov, S. M. Samoĭlovich, A. Jezowski, J. Mucha, and H. Misiorek, Fiz. Tverd. Tela (St. Petersburg) **37**, 3411 (1995) [Phys. Solid State **37**, 1874 (1995)].

Translated by G. Skrebtsov

PHYSICS OF THE SOLID STATE VOLUME 40, NUMBER 4 APRIL 1998

Radiation-dose dependence of E_1' centers in samples of quartz containing uncharged oxygen vacancies

O. I. Shcherbina and A. B. Brik

Institute of Geochemistry, Mineralogy, and Ore Production, Ukraine Academy of Sciences, 252680 Kiev, Ukraine

(Submitted October 13, 1997
Fiz. Tverd. Tela (St. Petersburg) **40**, 651–652 (April 1998)

EPR is used to study the generation of E_1' centers (oxygen vacancies that have trapped one electron) in quartz samples containing uncharged oxygen vacancies as a function of irradiation dose. It is found experimentally that an irradiation dose of order 400 Gy is sufficient to allow every oxygen vacancy to trap two electrons apiece in essentially all such quartz samples. The linear segment of the dose dependences of E_1' centers in samples annealed at 300 °C for 15 minutes can be used to reconstruct prior radiation doses up to 60–70 Gy. If the concentration of oxygen vacancies in the original sample is larger than 10^{18} cm^{-3}, the signal intensity from E_1' centers in the sample can be used to detect radiation doses as low as 1–3 Gy, which is significantly lower than the minimum radiation dose detectable by other paramagnetic centers in quartz.
[S1063-7834(98)01404-X]

1. Despite the fact that the E_1' center[1] is one of the well-studied paramagnetic centers in quartz, its structure and formation mechanism are still in need of additional investigation (a review of papers dealing with the investigation of quartz by EPR is given in Ref. 2). It is believed that E_1' centers are created in strongly irradiated quartz samples after a brief anneal at 300 °C,[3] and that the dose dependence of the resulting signal from this center remains linear in the dose range from 0.01 MGy to 0.1 GGy.[3] These properties make the E_1' center ideal for dosimetry at these irradiation levels. However, we have found that E_1' centers in samples of quartz containing uncharged oxygen vacancies can be used to detect considerably lower irradiation doses.

2. In order to create a sample containing uncharged oxygen vacancies, we annealed a sample of quartz (a so-called morion) which had received a large irradiation dose under natural conditions at a temperature of 470 °C for 30 minutes. After the anneal, the EPR signal of the E_1' center disappeared in the sample. EPR signals from this center were detected using an ERS-231 spectrometer in the three-centimeter band. Then the sample was divided into portions, each of which was irradiated by an RUP-120 x-ray tube (2 mA, 65 kV). Irradiation for 60 minutes by this tube corresponds to a dose of approximately 290 Gy. The irradiated samples were kept at room temperature for a month in order to allow the short-lived centers in them to decay. After this, the signal intensity from the E_1' centers in them was measured. They then were annealed at a temperature of 300 °C for 15 minutes and the EPR signal measurement was repeated.

3. The values obtained of the EPR signal intensity were normalized such that that the saturation level for the EPR signal from the E_1' centers in the annealed samples was unity. Figure 1 shows the results of these measurements. The ordinate indicates the intensity of the normalized EPR signal I, while the abscissa gives the irradiation time t for the corresponding portion of the sample. It is noteworthy that the maximum value of the intensity of E_1' centers in irradiated samples is found to equal the intensity of these centers in the original morion, which was annealed at 300 °C for 15 minutes.

The dose dependences shown in Fig. 1 can be used to determine how the concentrations of E_1^0 (oxygen vacancy without electrons), E_1', and E_1'' centers (oxygen vacancies that have trapped 1 and 2 electron respectively) depend on irradiation dose. In fact, the distance from the straight line parallel to the abscissa and passing through the ordinate at $I = 1$ to plotted point near *2* is proportional to the concentration of E_1^0 centers, the distance between curves *1* and *2* is proportional to the concentration of E_1'' centers, and curve *1* shows the dose dependence of E_1' centers.

The dose dependences of E_1' centers remain linear for doses in the MGy range,[3] whereas EPR signals from $[\mathrm{AlO}_4]^0$ centers saturate.[4] The charge state of an $[\mathrm{AlO}_4]^0$ center can change as a result of trapping a free hole from the valence band and loss of an ion compensator. The presence of an ion compensator next to the paramagnetic aluminum center can be established unambiguously by studying electric-field effects arising from tunneling of paramagnetic holes in the double-well energy potential of the aluminum center.[5] The ion compensator distorts this double-well potential and makes tunneling of the hole and the accompanying electric-field effects impossible. The saturation of the dose dependences of $[\mathrm{AlO}_4]^0$ centers signals the saturation of electron traps, holes, and ion-compensators in the sample, and also that their excitation, trapping, and recombination have reached dynamic equilibrium. The linearity of the dose dependences of E_1' centers under these conditions is evidence that, under the experimental conditions discussed here,[3] irra-

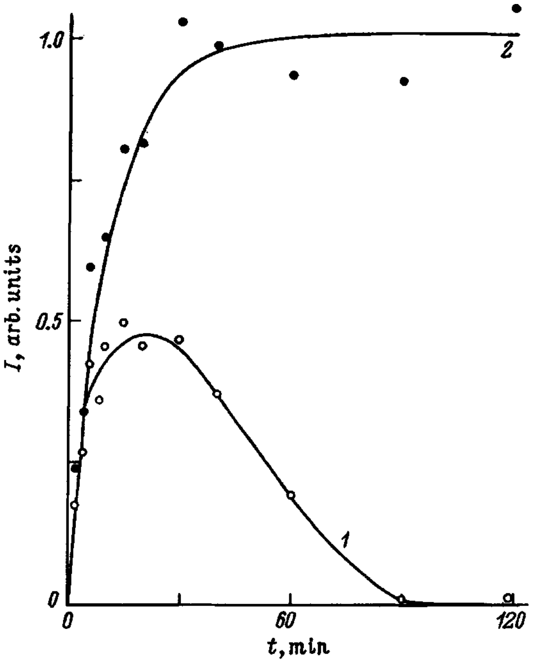

FIG. 1. Dose dependences of E_1' centers in quartz after irradiation (*1*) and after a subsequent anneal (*2*).

diation creates oxygen vacancies that trap free electrons created by the absorption of optical radiation (x rays).

In our experiment, the maximum intensity of E_1' centers in samples that were annealed and then irradiated coincides with the intensity of E_1' centers in the original sample after a brief anneal at 300 °C. Consequently, our laboratory irradiation does not create oxygen vacancies in the sample. Thus, in our experiments changes in the charge of oxygen vacancies present in the sample (that is, the dose dependences of the E_1' centers) are caused by trapping of free carriers generated by the absorption of x-ray energy. Trapping of electrons by oxygen vacancies takes place much more efficiently than the generation of the vacancies themselves, and therefore practically all the oxygen vacancies trap two electrons at radiation doses equal to approximately 400 Gy.

These experimental results are important for retrospective dosimetry using quartz.[6] Among the problems this dosimetry addresses are reconstruction of prior radiation doses at localities and buildings that have undergone undesirable irradiation due to accidents at atomic reactors or in manufacturing using radioactive materials. It is well known that retrospective dosimetry utilizes quartz extracted from structural building blocks. Experience shows that many of the quartz samples extracted from bricks and concrete blocks contain a large number of oxygen vacancies that have lost entirely their electrons in the course of preparing the building material. Consequently, such samples are analogous to those we have investigated. It must be kept in mind that in this case detecting an EPR signal from E_1' centers in these samples does not indicate a large radiation dose, but rather signals a high concentration of oxygen vacancies. If the concentration of oxygen vacancies in the sample is in the range $10^{17}-10^{18}$ cm^{-3}, then the linear portion of the dose dependence of E_1' centers in the sample can be used to reconstruct a prior radiation dose in the range 1–3 Gy.

This work was carried out under Project 2.4/689, financed by Minnauki, Ukraine.

[1] R. A. Weeks, J. Appl. Phys. **27**, 1376 (1956).
[2] J. A. Weil, Phys. Chem. Miner. **10**, 149 (1984).
[3] A. Wieser and D. F. Regulla, Appl. Radiat. Isot. **40**, 911 (1989).
[4] A. B. Brik, V. Ya. Degoda, Yu. A. Marazuyev, M. I. Samoĭlovich, and O. I. Shcherbina, Fiz. Tverd. Tela (St. Petersburg) **37**, 107 (1995) [Phys. Solid State **37**, 57 (1995)].
[5] A. B. Brik, Ferroelectrics **161**, 59 (1994).
[6] S. Toyoda, J. W. Rink, H. P. Schwarcz, and M. Ikeya, Appl. Radiat. Isot. **47**, 1393 (1996).

Translated by Frank J. Crowne

DEFECTS. DISLOCATIONS. PHYSICS OF STRENGTH

Electronic excitations of Sc^{3+} impurity in α-Al_2O_3 crystals

B. R. Namozov, R. I. Zakharchenya, and M. P. Korobkov

A. F. Ioffe Physicotechnical Institute, Russian Academy of Sciences, 194021 St. Petersburg, Russia

V. V. Mürk

Institute of Physics, Tartu, Estonia

(Submitted October 2, 1997)
Fiz. Tverd. Tela (St. Petersburg) **40**, 653–654 (April 1998)

Optical properties, including luminescence, of scandium-doped α-Al_2O_3 crystals have been studied in the VUV range. An absorption band associated with the scandium impurity was observed at the fundamental-absorption edge of crystalline corundum. A strong luminescence band peaking at 5.6 eV, which is most effectively excited within the 7.7–8.8-eV interval, was found. The kinetic and polarization characteristics of this luminescence were studied within the temperature range 6–500 K. An excitation model of the impurity complex and the mechanism of its relaxation are discussed. © *1998 American Institute of Physics.* [S1063-7834(98)01504-4]

The electronic structure of transition-metal impurities, A^{3+}, in white-sapphire (corundum) crystals has been studied in great detail.[1,2] Most of the A^{3+} cations have a nonzero magnetic moment, and therefore their structure was established by EPR. The Sc^{3+} impurity is not paramagnetic, because its outer electronic shell, $3p$, in the ground state $^1S_0$ is filled completely, which distinguishes the scandium ion from among elements in the first transition-metal row.

The Al_2O_3-Sc crystals were grown by Czochralski, Verneuill, and directed-crystallization methods. The typical residual impurities in corundum are the first-row transition metals (Ti through Cu).[3] These impurities were present in the crystals at a level of $10^{-4}-10^{-5}$ at. %.

These samples were used in the EPR studies. The measurements were performed on a Bruker ER220D spectrometer (X range) within the temperature range 4–300 K. Despite the high impurity concentration in the crystal, the EPR spectrum did not exhibit any features characteristic of a partially filled *d* shell, which supports the assumption of scandium being present in the trivalent state in the crystal.

A study was carried out of the optical properties of the Al_2O_3-Sc^{3+} crystals. Figure 1 shows an absorption spectrum of the corundum crystals with Sc concentration in Al_2O_3 of 0.0081 at. % (curve *1*). Shown for comparison (curve 2) is an absorption spectrum of a nominally pure Al_2O_3 sample. The samples with the Sc^{3+} impurity are seen to exhibit additional absorption at the transmission edge of the corundum crystal.

Steady-state excitation by 7.5–9-eV photons into the Al_2O_3-Sc^{3+} impurity band gives rise to a bright luminescence band peaking at 5.6 eV and having a halfwidth of about 1.0 eV. The room-temperature luminescence spectrum of Al_2O_3-Sc^{3+} is shown in Fig. 1 (curve *3*). At 300 K, the luminescence has a maximum at 5.55 eV. Within 6–100 K, the luminescence spectrum centers at 5.65 eV, with the halfwidth of the band remaining constant, which implies that the band shifts as a whole toward shorter wavelengths. The luminescence excitation spectrum is shown by the dotted curve *4* in Fig. 1. As the temperature is lowered, the short-wavelength edge of the excitation spectrum shifts toward higher energies, while the long-wavelength wing remains fixed. This shift coincides with the shift of the exciton Ohrbach tail in sapphire[4].

When excited to the impurity band, the steady-state luminescence intensity in the 5.6-eV band remains temperature independent up to 500 K. When excited by 8.47-eV photons (Xe resonant line), the luminescence quantum yield is close to one. Within the 300–500-K range, the degree of luminescence polarization, $P=(I_\parallel-I_\perp)/(I_\parallel+I_\perp)$ is constant and about 30%, and the polarization vector is perpendicular to the optical axis. The polarization P falls off gradually with decreasing temperature, so that, for instance, $P_{80\,\mathrm{K}}=70\%$, and $P_{6\,\mathrm{K}}=15\%$.

The independence of the luminescence band position from pump photon energy within the impurity absorption and excitation spectra implies that the electronic excitation relaxes from higher-lying levels to relaxed states, and it is from the latter that the radiative transition takes place. The high luminescence quantum yield and its temperature behavior warrant an assumption that despite the long lifetime ($\tau \approx 170\ \mu s$ at 80 K, see inset in Fig. 1) the electronic excitation energy does not migrate through the crystal. The anomalously large halfwidth of the luminescence band (of about 1 eV) and the Stokes shift of 2.5 eV evidence strong electron-phonon interaction of the electronic excitation. The fairly high polarization of the luminescence argues for the high stoichiometry of the luminescence centers in α Al_2O_3- Sc^{3+} crystals. The decrease of excitation efficiency in the short-wavelength region of the luminescence excitation spectra is

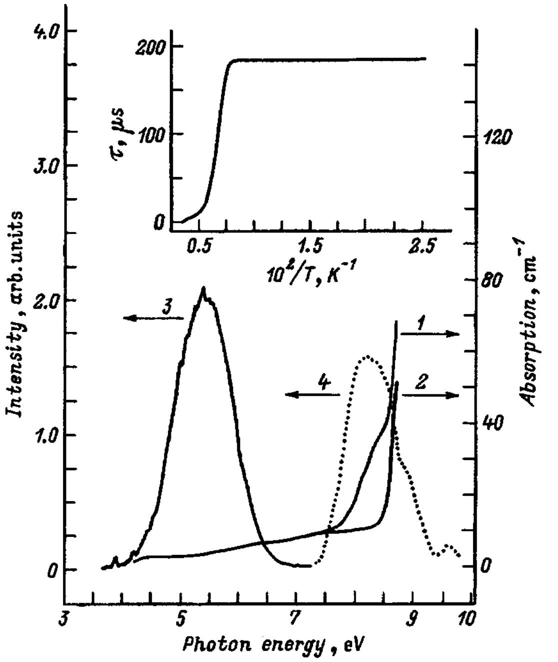

FIG. 1. Optical and luminescence spectra of Al_2O_3-Sc^{3+} crystals. *1* — absorption spectrum of α Al_2O_3 (0.0081 at. % Sc), *2* — Absorption spectrum of nominally pure *a* Al_2O_3, *3* — Room-temperature luminescence spectrum of *a* Al_2O_3 (0.0081 at. % Sc) at 300 K, *4* — Luminescence excitation spectrum of *a* Al_2O_3 (0.033 at. % Sc). The inset shows temperature behavior of the decay kinetics on the reciprocal-temperature scale.

due to the competition on the part of the matrix associated with the long-wavelength fundamental-absorption edge of α Al_2O_3 (the exciton-absorption Ohrbach tail).

Scandium ion substitutes isomorphically for aluminum in the α-Al_2O_3 lattice within distorted oxygen octahedra with local symmetry C_3. The radius of the free Sc^{3+} ion is 0.081 nm,[5] and the ionic radius of Al^{3+} in α Al_2O_3 is 0.057 nm (Ref. 6). Because of its larger size, the Sc^{3+} ion apparently tends to occupy a more symmetric position in the oxygen-ion octahedron than the Al^{3+} ion, thus distorting locally the lattice structure. One may assume, therefore, the appearance of a crystal-field perturbation in the vicinity of the impurity, which results in a local expulsion of the oxygen $2p$-orbital level from the valence band. The observed features in the luminescence excitation spectrum indicate electron transition from the split-off oxygen level to the conduction band, which involves hole formation. The electron is in the region of enhanced local density of states in the conduction band, which is formed by admixture of the $3p$ orbital of aluminum (and, possibly, of the $3d$ scandium orbital as well). Within this model, relaxation of an electronic excitation involves creation of a localized state formed by a hole in a bonding oxygen orbital and a conduction electron. One may envisage formation of several such states, localizing and relaxing over different configuration coordinates along the tetrahedral oxygen bonds. This process is similar to exciton localization near an impurity[7]. Radiative transition in such a center produces the observed luminescence, whose polarization and kinetic parameters depend on the actual radiative state of the complex.

The decrease of the luminescence decay time τ above 160 K at a constant light sum indicates the interplay of at least two states, which differ in τ by an order of magnitude but have the same polarization. As the temperature increases, the filling of the upper (faster) state increases too, and it is this state that dominates the luminescence kinetics. The activation energy of this process was found to be 0.03 eV. The temperature behavior of the polarization suggests that the lower state also contains two radiative levels with orthogonal polarizations. The spacing between these states was estimated to be less than 10 meV.

The authors are grateful to B. P. Zakharchenya for interest in the work. Particular thanks are due to I. G. Ozerov for EPR measurements.

Support of the Russian Fund for Fundamental Research (Grant 95-02-047760a) and of the R&D Program 5-15 of the Russian Federation is gratefully acknowledged.

[1] I. B. Bersuker, *Electronic Structure and Properties of Coordination Compounds* [in Russian] (Khimiya, Moscow, 1971), pp. 82–85.

[2] D. T. Sviridov, R. K. Sviridova, and Yu. F. Smirnov, *Optical Spectra of Transition Metals in Crystals* [in Russian] (Nauka, Moscow, 1976), pp. 115–133.

[3] R. J. Brook, J. Yee, and F. A. Kroger, J. Am. Ceram. Soc. **54**, 444 (1971).

[4] A. I. Kuznetsov, B. R. Namozov, and V. V. Mürk, Izv. AN ÉSSR, Ser. Fiz. Mat. **36**, 193 (1987).

[5] *Physical Quantities: A Handbook* [in Russian], edited by I. S. Grigor'ev and E. Z. Meĭlikhov (Énergoatomizdat, Moscow, 1991), 1232 pp.

[6] R. W. C. Wyckoff, in *Crystal Structures* (Interscience Publ., Vol. 1, Ch. V, New York, 1964), p. 4.

[7] Ch. B. Lushchik, in *Excitons*, Modern Problems in Condensed Matter Sciences, Vol. 2, edited by E. Rashba and M. Sturge (North-Holland, Amsterdam, 1982), p. 505.

Translated by G. Skrebtsov

PHYSICS OF THE SOLID STATE VOLUME 40, NUMBER 4 APRIL 1998

Phase competition in late stages of diffusive decomposition

V. V. Slezov, V. V. Rogozhkin, and A. S. Abyzov

Khar'kov Physicotechnical Institute, Ukraine Academy of Sciences, 310108 Khar'kov, Ukraine

(Submitted October 20, 1997)
Fiz. Tverd. Tela (St. Petersburg) **40**, 655–657 (April 1998)

The late stages of diffusive decomposition of a supersaturated solid solution into phases consisting of multicomponent stoichiometric compounds with a common element are investigated. It is shown that a competition is possible between phases for the common component, as a result of which only one of these phases survives. *© 1998 American Institute of Physics.* [S1063-7834(98)01604-9]

The majority of real materials are multicomponent supersaturated solid solutions. In the course of preparing and using these solid solutions, inclusions of various phases can appear, which significantly affects the properties of the materials. It is known that initially all the phases whose supersaturation is positive will precipitate out inclusions. However, at later stages, when the material available to generate inclusions becomes small, competition arises both between isolated regions of the same phase with different sizes and between different phases. As a result, only some of those phases that precipitate out at early stages of the decomposition can survive. In Refs. 1,2 Slezov et al. formulated a general theory for the evolution of inclusions of such phases. In this paper, the methods developed in these references are used to analyze the late stage of decay of a three-component solid solution.

1. PHASES WITH SIMPLE STOICHIOMETRY

Consider a three-component solid solution of atomic impurities A, B, and C in a chemically inert matrix, which can precipitate in two stoichiometric two-component phases containing a common component: $A_\mu C_\nu$ and $B_\eta C_\xi$. To start with, let us consider the simplest stoichiometric phases, where $\mu=\nu=\eta=1$. As shown in Ref. 1, at late stages when the excess impurity has primarily precipitated into inclusions and a redistribution has taken place between the phases and the precipitates of various size, the state of the system is determined by the law of mass action

$$c_a c_c = K_1, \quad c_b c_c = K_2, \tag{1}$$

and the equation of stoichiometry

$$q_a + q_b = q_c, \tag{2}$$

where c_i is the concentration of impurity i averaged over the volume (where $i=a,b,c$), $K_{1,2}$ are chemical reaction constants for the first and second phases respectively, and q_i is the relative number of impurities of type i in inclusions per unit volume. Moreover, the first phase will precipitate out when the following inequality is satisfied:

$$q_a > 0, \tag{3}$$

and the second when the condition

$$q_b > 0. \tag{4}$$

is satisfied. Taking Eq. (2) into account, we see that the condition $q_c>0$ is also necessary for the first and second phases to precipitate, whereas this takes place automatically when Eqs. (3) or (4) are satisfied.

The equation of balance for impurity type i takes the form

$$Q_i = q_i + c_i,$$

where Q_i is the total number of impurities in solution and in inclusions. Taking this relation into account, it is convenient to write Eq. (2) in the form

$$c_a + c_b - c_c + \delta Q = 0, \tag{5}$$

where

$$\delta Q = Q_a + Q_b - Q_c.$$

Note that, in general, Eq. (1) is satisfied exactly only for values of the concentration near the surface of an inclusion, and that the chemical reaction constant depends on the radius of the inclusion as well. However, at late stages of the decomposition the concentration near the surface is only slightly different from the average, and the distribution function of inclusions has a sharp peak so that the dependence of the chemical reaction constant on the radius can be neglected. This approximation, as shown in Ref. 1, is accurate to order of the square of the supersaturation. Thus, we will use the word ''concentration'' to mean its average value throughout the volume and we shall treat the quantities $K_{1,2}$ as constants.

The solution to the system (1), (5) gives the values of the impurity concentration at the late stage of the decomposition:

$$c_{a,b} = \frac{K_{1,2}}{2(K_1+K_2)}\left[\sqrt{(\delta Q)^2 + 4(K_1+K_2)} + \delta Q\right], \tag{6}$$

$$c_c = \frac{2(K_1+K_2)}{\sqrt{(\delta Q)^2 + 4(K_1+K_2)} + \delta Q}. \tag{7}$$

These expressions combined with Eqs. (3), (4) determine the conditions for existence of the phases. Thus, the first phase (AC) exists when

$$Q_b < Q_c + \frac{1}{Q_a}\left(\frac{K_1}{K_2} Q_a^2 - K_1\right) \tag{8}$$

while the second (BC) exists when

$$Q_a < Q_c + \frac{1}{Q_b}\left(\frac{K_2}{K_1} Q_b^2 - K_1\right). \tag{9}$$

A situation of interest in applications is one where the impurity precipitates strongly into inclusions, i.e., when $\delta Q \gg K_{1,2}$. Therefore, we will analyze the results for this case in particular. From Eqs. (6) and (7), we obtain for $\delta Q > 0$

$$c_{a,b} \approx \delta Q \frac{K_{1,2}}{K_1 + K_2}, \quad c_c \approx \frac{K_1 + K_2}{\delta Q}, \tag{10}$$

while for $\delta Q < 0$,

$$c_{a,b} \approx \frac{K_{1,2}}{|\delta Q|}, \quad c_c \approx |\delta Q|.$$

The conditions for existence of phases Eqs. (8), (9) take the form

$$Q_a > \frac{K_1}{K_2}(Q_b - Q_c), \tag{11}$$

$$Q_b > \frac{K_2}{K_1}(Q_a - Q_c). \tag{12}$$

It is easy to see that when $\delta Q > 0$ (i.e., the number of impurities of type C is less than the numbers of types A and B taken together) conditions (11) and (12) cannot be satisfied at the same time, i.e., the phases cannot coexist. In fact, from Eq. (10) it follows that in the final state $c_c \ll c_a, c_b$, i.e., impurity C is almost completely absorbed, while impurities A and B remain in solution. A competition then begins between inclusions of the first (AC) and second (BC) phases for the insufficient component C, as a result of which only one of the phases survives.

For $\delta Q < 0$ there is enough of impurity type C to prevent competition between the phases, and they exist independently of one another. All excess impurities A and B precipitate into inclusions, while the type C impurity remains partially in solution.

2. SEPARATION OF THREE PHASES

Consider the case where, in addition to the two binary compounds, it is possible for a third phase to precipitate out consisting of the pure components C, A, or B. As was shown above, when $\delta Q < 0$ the type-C impurity partially remains in solution, and consequently it can precipitate in the form of a pure phase. In this case, system (1) must satisfy the equation

$$c_c = c_{\infty,c}.$$

From this we find

$$c_{a,b} = K_{1,2}/c_{\infty,c}.$$

Here $c_{\infty,c}$ is the equilibrium concentration at the boundary plane. Stoichiometry (Eq. (2)) in this case determines the amount of precipitate of the third phase C:

$$q_c = (Q_c - c_c) - (Q_a - c_a) - (Q_b - c_b).$$

Taking into account that three phases precipitate for $q_c > 0$, it is easy to obtain the conditions for coexistence of all three phases:

$$Q_c > Q_a + Q_b + c_{\infty,c} - \frac{K_1 + K_2}{c_{\infty,c}},$$

$$Q_{a,b} > K_{1,2}/c_{\infty,c}.$$

When $\delta Q > 0$, the excess of type-C impurity is completely absorbed by inclusions of the new phases, and as we noted above, competition will allow only one of them to survive. The competition disappears if it is possible to precipitate a pure phase A (the case where phase B precipitates is entirely analogous). Adding the equation $c_a = c_{\infty,a}$ to system (1), we obtain, as before, the condition for coexistence of all three phases:

$$Q_a > Q_c - Q_b + c_{\infty,a}\left(1 + \frac{K_2}{K_1}\right) - \frac{K_1}{c_{\infty,a}},$$

$$Q_b > \frac{K_1}{K_2} c_{\infty,a}, \quad Q_c > \frac{K_1}{c_{\infty,a}}.$$

3. PHASES WITH ARBITRARY STOICHIOMETRY

Let us consider precipitation of two phases with arbitrary stoichiometries: $A_\mu C_\nu$ and $B_\eta C_\xi$. Equations (1), (2) in this case can be written in the form

$$c_a^\mu c_c^\nu = K_1,$$

$$c_b^\eta c_c^\xi = K_2, \tag{13}$$

$$\frac{q_a}{\mu} + \frac{q_b}{\eta} = \frac{q_c}{\nu + \xi}. \tag{14}$$

Let us introduce

$$\delta Q = \frac{Q_a}{\mu} + \frac{Q_b}{\eta} - \frac{Q_c}{\nu + \xi}, \tag{15}$$

and, as before, consider the case where the chemical reaction constant is small compared with δQ. Taking Eqs. (13) and (14) into account, let us rewrite Eq. (15) in the form

$$\delta Q = \frac{c_a}{\mu} + \frac{1}{\eta}(c_a)^{(\mu+\nu)/(\eta+\xi)}\left(\frac{K_2^\nu}{K_1^\xi}\right)^{1/(\eta+\xi)}.$$

This equation can be solved rather simply in two cases: when $\mu + \nu = \eta + \xi$ and $\mu + \nu = 2(\eta + \xi)$ (the case where $\mu + \nu = (\eta + \xi)/2$ obviously reduces to the previous cases by making the substitution $A \leftrightarrow B$). Note that this case, although restrictive, still includes a rather wide class of compounds: in the first case, AC_2 and BC_2, AC_2 and B_2C, A_2C_3 and B_2C_3, A_2C_3 and B_3C_2, etc., while in the second case, A_2C_2 and BC, A_3C and BC, etc.

In the first case

$$\delta Q = c_a\left[\frac{1}{\mu} + \frac{1}{\eta}\left(\frac{K_2^\nu}{K_1^\xi}\right)^{1/(\mu+\nu)}\right].$$

From this we obtain the condition for coexistence of the phase $A_\mu C_\nu$:

$$\kappa Q_a > Q_b - \frac{\eta}{\nu+\xi} Q_c \tag{16}$$

In phase $B_\eta C_\xi$:

$$\frac{1}{\kappa} Q_b > Q_a - \frac{\mu}{\nu+\xi} Q_c , \tag{17}$$

where $\kappa=(K_2^\nu / K_1^\xi)^{1/(\mu+\nu)}$.

Analogously, in the second case where $\mu+\nu=2(\eta+\xi)$, we find that phase $A_\mu C_\nu$ exists when the condition

$$\kappa Q_a^2 > Q_b - \frac{\eta}{\nu+\eta} Q_c , \tag{18}$$

is satisfied, and phase $B_\eta C_\xi$ when the condition

$$\frac{1}{\sqrt{\kappa}} Q_b^2 > Q_a - \frac{\mu}{\nu+\xi} Q_c . \tag{19}$$

is satisfied.

4. DISCUSSION OF RESULTS

At the initial stage of the decay all phases whose supersaturation is positive precipitate out. As the supersaturations decay, competition begins both between inclusions of the same phase but different sizes and between different phases, as a result of which one or several phases survive, depending on the sense of inequalities (8), (9), (16)–(19), and a universal size distribution of inclusions is generated.[3] We note the following interesting feature of the behavior of this system with time. The rate of precipitation of a phase depends not only on its supersaturation but also on the conditions for its nucleation, and the diffusion coefficients of the reagents. Therefore, a situation is possible where, at the initial stage of the decomposition, the phase that precipitates out most strongly is one that does not satisfy inequalities (8), (9), (16)–(19), while the phase that satisfies these inequalities precipitates out more slowly. Then (at the late stages), the first phase dissolves due to the competition, while the second phase survives. Thus, in this case, a replacement of precipitating phases takes place in the course of diffusive decomposition of a supersaturated solution. Note that a competition is possible, not only between different phases, but also between inclusions of the same phase under different conditions (for example, at a boundary and within the body of a grain). Although the location where the phase precipitates (in the body of a grain, at its boundaries, or at some nucleation centers) can affect the kinetics of the initial stage of the decay and the expression for the chemical reaction constant $K_{1,2}$, it does not alter the analysis given above qualitatively, nor the results obtained, since the only important factor is the diffusive exchange of material between phases.

This work was partially supported financially by the German Federation Ministry of Research and Technology (BMBF) (Grant ROS-1995B6) and the International Soros Fund for the Support of Science Education (ISSEP) (Grant ISSEPSPU 042062).

[1] V. V. Slezov and V. V. Sagalovich, Fiz. Tverd. Tela (Leningrad) **17**, 1497 (1958).
[2] V. V. Slezov and V. V. Sagalovich, J. Phys. Chem. Solids **38**, 943 (1977).
[3] I. M. Lifshits and V. V. Slezov, Zh. Éksp. Teor. Fiz. **35**, 1401 (1958) [Sov. Phys. JETP **8**, 980 (1959)].

Translated by Frank J. Crowne

Ion transport in the anion-deficient nonstoichiometric phases $La_{0.95}(Ba_{1-x}Sr_x)_{0.05}F_{2.95}$ $(0 \leqslant x \leqslant 1)$

N. I. Sorokin, M. V. Fominykh, E. A. Krivandina, Z. I. Zhmurova, and B. P. Sobolev

Institute of Crystallography, Russian Academy of Sciences, 117333 Moscow, Russia

O. I. Lyamina

Institute of General and Inorganic Chemistry, Russian Academy of Sciences, 101000 Moscow, Russia

(Submitted October 27, 1997)
Fiz. Tverd. Tela (St. Petersburg) **40**, 658–661 (April 1998)

The fluoride-ion conductivity of the nonstoichiometric tysonite phases $La_{0.95}(Ba_{1-x}Sr_x)_{0.05}Fe_{2.95}$ $(0 \leqslant x \leqslant 1)$ is investigated by impedance spectroscopy. Electrophysical measurements are performed in the frequency range $5-5\times10^5$ Hz and temperature range $300-700$ K. A discontinuity is observed in the temperature dependence of the conductivity at $T_c=410-430$ K. The behavior of the temperature dependence of the electrical conductivity is explained within a transport model taking into account the migration of fluoride ions between different inequivalent structural sites. The maximum value of the conductivity at room temperature (293 K) is $2\times10^{-4}\ \Omega^{-1}\ \text{cm}^{-1}$ for the solid solution $La_{0.95}Sr_{0.05}F_{2.95}$. The fluorine-ion conductivity in $La_{0.95}(Ba_{1-x}Sr_x)_{0.05}F_{2.95}$ single crystals is almost an order of magnitude larger than the value for the commercial solid electrolyte $La_{0.992}Eu_{0.008}F_{2.992}$ (a fluorine-selective membrane) having a tysonite structure. [S1063-7834(98)01704-3]

The trifluorides RF_3 with the rare-earth cations $R=La-Nd$, which have a tysonite structure (of the LaF_3 type), are high-temperature superionic fluorine-ion conductors.[1–3] The high mobility of the F^- ions in the tysonite structure is determined by the site disorder of the anion sublattice. As the temperature rises, thermal Schottky defects in the form of mobile fluorine vacancies and relatively immobile cation vacancies form in the compounds RF_3.

The list of fluoride materials with the tysonite structure also includes the anion-deficient nonstoichiometric phases $R_{1-x}M_xF_{3-x}$ (M=Ca, Sr, Ba; R=La−Yb, Y), which are mixed-valence two-component solid solutions with a variable number of atoms in the unit cell. The large isomorphous capacity of the tysonite matrix for divalent cations permits the synthesis of materials with a high concentration of structural defects. The charge appearing upon the replacement of rare-earth ions in the tysonite structure by alkali-earth ions is compensated by forming fluorine structural vacancies in the anion sublattice. In $R_{1-x}M_xF_{3-x}$ crystals the concentration of fluorine vacancies generated by the impurity MF_2 generally does not depend on the temperature and is several orders of magnitude larger than the concentration of anion vacancies of thermal origin formed by the Schottky mechanism.

In crystals of the tysonite compounds RF_3, ion transport takes place by a vacancy mechanism and the ion-current carriers are fluorine vacancies. Fluorine-ion transport processes have been found to be very sensitive to violations of the stoichiometry of tysonite phases. The anionic conductivity in the solid solutions $R_{1-x}M_xF_{3-x}$ is increased by two orders of magnitude in comparison to the RF_3 matrices.[2,3] The maximum values of the conductivity of the nonstoichiometric tysonite phases $La_{1-x}M_xF_{3-x}$ and $Ce_{1-x}M_xF_{3-x}$ (M=Ca, Sr, Ba) is observed at metal difluoride concentrations equal to 3–7 mol %.[3–7] For the purpose of studying the influence of mixed-valence isomorphism on the characteristics of anion transport in crystals of anion-deficient multicomponent tysonites, as well as finding the most conductive compositions of the tysonite phases, we performed an electrophysical investigation of single crystals of $La_{0.95}(Ba_{1-x}Sr_x)_{0.05}F_{2.95}$ $(0 \leqslant x \leqslant 1)$ and the commercial electrolyte $La_{0.992}Eu_{0.008}F_{2.992}$.

1. EXPERIMENTAL METHOD

Single crystals of $La_{0.95}(Ba_{1-x}Sr_x)_{0.05}F_{2.95}$ ($x=0$, 0.25, 0.5, 0.75, and 1 in the original mixture) were grown by to the Bridgman-Stockbarger method in the form of single-crystal boules with a diameter of 12 mm and a length of 16 mm. The crystals were grown in a KRF-1 two-zone apparatus (which was designed and fabricated by the Special Design Office of the Institute of Crystallography of the Russian Academy of Sciences) in a helium atmosphere. A multicell graphite crucible, which was lowered at the rate of 5.4±0.1 mm/h, was employed. The original reagents (chemically pure LaF_3 and ultrapure BaF_2 and SrF_2) were purified to remove any oxygen impurity by preliminary fluoridation of the compounds. The fluoridating agent (''cleanser'') used was ultrapure PbF_2, which was added to the mixture in an mount equal to 5 wt %. Lead fluoride was also added to the mixture as the crystals grew. The loss of material during the growth of the single-crystal boules amounted to no more than 2.5% of the mass of the mixture.

TABLE I. Chemical composition of $La_{0.95}(Ba_{1-x}Sr_x)_{0.05}F_{2.95}$ solid solutions from x-ray fluorescence analysis.

Composition of mixture	SrF_2		BaF_2	
	wt %	mol %	wt %*	mol %
$La_{0.95}Ba_{0.05}F_{2.95}$	0	0	4.50	0.0500
$La_{0.95}Ba_{0.0375}Sr_{0.0125}F_{2.95}$	0.87	0.0134	3.31	0.0367
$La_{0.95}Ba_{0.025}Sr_{0.025}F_{2.95}$	1.73	0.0266	2.07	0.0229
$La_{0.95}Ba_{0.0125}Sr_{0.0375}F_{2.95}$	2.44	0.0375	1.14	0.0126
$La_{0.95}Sr_{0.05}F_{2.95}$	3.26	0.0500	0	0

*Experimental error is 5%.

The tysonite of the single crystals tysonite structure was confirmed by x-ray power diffraction using an HZG-4 diffractometer (Cu $K\alpha$ radiation, Ni filter). The chemical composition of the $La_{0.95}(Ba_{1-x}Sr_x)_{0.05}F_{2.95}$ solid solutions were monitored by x-ray fluorescence analysis using the Sr $K\alpha$ and Ba $L\alpha$ lines and a VRA-33 x-ray analyzer (Cr tube, 40 kV and 35 mA). Deviations of the SrF_2 or BaF_2 content in the middle portions of the single-crystal boules from the composition of the original mixture did not exceed ± 0.2 mol % (Table I). The samples used to investigate the electrical properties were cut from the central portions of the single-crystal boules. Typical dimensions of the samples were 12 mm in diameter and 5 mm in length.

The electrical conductivity (σ) was determined from the impedance spectra of electrochemical cells with blocking electrodes (DAG-580 colloidal graphite). The measurements were performed in a vacuum with a residual pressure of $\sim 10^{-1}$ Pa in the temperature range $300-700$ K. The impedance was recorded in the frequency range $5-5\times 10^5$ Hz (Tesla BM 507 impedance meter). A detailed description of the conductometric apparatus and the method for determining the volume resistance were presented in Ref. 7. The experimental error in volume resistance was less than 5%.

Our investigations[7] and the literature data[3,4,8] show that the contribution of the electronic conductivity is negligible in comparison to the fluorine-ion conductivity in the tysonite solid solutions $La_{1-x}M_xF_{3-x}$ (M=Sr, Ba). All the electrophysical measurements were performed on unoriented single crystals under the assumption of pseudoisotropic behavior for σ, which holds quite rigorously for tysonite crystals of $R_{1-x}M_xF_{3-x}$ with $x \geqslant 0.05$.[5,7]

2. RESULTS AND DISCUSSION

Figure 1 shows plots of the temperature dependence of the fluoride-ion conductivity for $La_{0.95}(Ba_{1-x}Sr_x)_{0.05}F_{2.95}$ single crystals. For comparison, we also measured the anionic conductivity of a commercial fluorine-selective $La_{0.992}Eu_{0.008}F_{2.992}$ membrane (of pale green color, from the Pyshminskiĭ Chemical Concern), for which $\sigma = 3\times 10^{-5}$ Ω^{-1} cm^{-1} at 293 K. The values of σ for the $La_{0.95}(Ba_{1-x}Sr_x)_{0.05}F_{2.95}$ single crystals were almost an order of magnitude higher than the value for the commercial solid electrolyte $La_{0.992}Eu_{0.008}F_{2.992}$ having the tysonite structure.

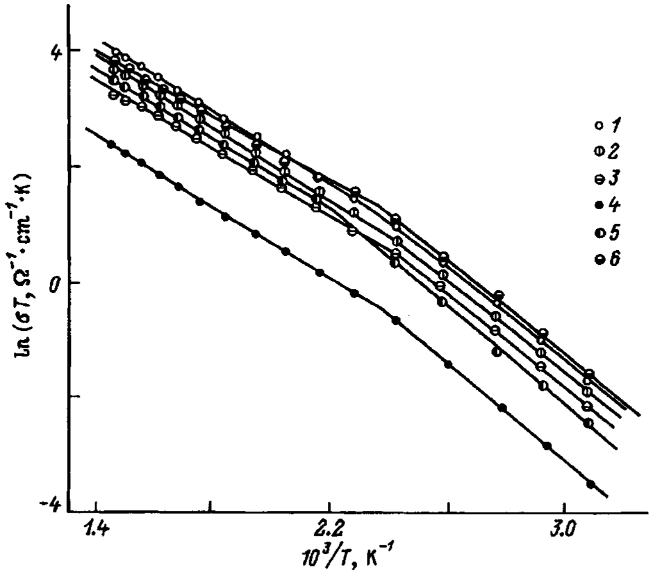

FIG. 1. Temperature dependence of the anionic conductivity for single crystals having the tysonite structure. *1* — $La_{0.95}(Ba_{0.25}Sr_{0.75})_{0.05}F_{2.95}$, *2* — $La_{0.95}(Ba_{0.5}Sr_{0.5})_{0.05}F_{2.95}$, *3* — $La_{0.95}(Ba_{0.75}Sr_{0.25})_{0.05}F_{2.95}$, *4* — $La_{0.992}Eu_{0.008}F_{2.992}$, *5* — $La_{0.95}Ba_{0.05}F_{2.95}$, *6* — $La_{0.95}Sr_{0.05}F_{2.95}$.

The plots of $\sigma(T)$ for $La_{0.95}(Ba_{1-x}Sr_x)_{0.05}F_{2.95}$ and $La_{0.992}Eu_{0.008}F_{2.992}$ exhibited a discontinuity at $T_c = 410-430$ K. In the temperature range studied the plots of the conductivity dependence on the reciprocal temperature consisted of two linear segments that satisfy the Arrhenius-Frenkel equation

$$\sigma T = \sigma_0 \exp[-\Delta H_{m,v}/kT],$$

where $\Delta H_{m,v}$ is the enthalpy of activation for the migration of anion vacancies. The enthalpy $\Delta H_{m,v}$ is determined by the height of the potential barriers overcome by the fluoride ions as they jump between vacancy sites in the anion sublattice. The values of $\Delta H_{m,v}$ and σ_0 for the crystals investigated are listed in Table II.

Lanthanum trifluoride, which is a progenitor of the tysonite-structure type, and the compounds RF_3 which are isostructural to them, crystallize in the trigonal system (space group $P\overline{3}c1$), and the number of formula units in the unit cell is equal to 6.[9–11] The unit cell of LaF_3 contains six La^{3+} ions, which are located in crystallographic sites labeled f, and 18 F^- ions, which are distributed among three fully occupied, structurally inequivalent sites labeled g, d, and a in the ratio $F_1(g):F_2(d):F_3(a) = 12:4:2$. The $F_1(g)$ atoms belong simultaneously to four La polyhedrons, and the $F_2(d)$ and $F_3(a)$ atoms belong to three; therefore, in interpreting the physical properties, the d and a fluorine sites are combined in a single subsystem $F_{2,3}(d+a) = F_2(d) + F_3(a)$. The ratio between the populations of the fluoride sites is $F_1(g):F_{2,3}(d+a) = 2:1$. The structural investigations of the anion-deficient solid solution $La_{0.85}Sr_{0.15}F_{2.85}$ in Ref. 12 confirmed that it belongs to the trigonal space group $P\overline{3}c1$ and that the fluorine vacancies form predominantly in the homogeneous $F_1(g)$ subsystem.

The results of ^{19}F NMR investigations of diffusion in stoichiometric LaF_3 and CeF_3 crystals[13–15] and anion-deficient $R_{1-x}M_xF_{3-x}$ crystals[16,17] point out the dynamic inequivalence of the fluorine atoms in the tysonite structure and the presence of a high-mobility $F_1(g)$ fluorine subsystem

TABLE II. Values of σ_0 and $\Delta H_{m,v}$ for the single crystals $La_{0.95}(Ba_{1-x}Sr_x)_{0.05}F_{2.95}$ $(0 \leqslant x \leqslant 1)$ and $La_{0.992}Eu_{0.008}F_{2.992}$.

	$T<T_c$		$T>T_c$	
Composition (x)	$\log(\sigma_0, \Omega^{-1}\cdot cm^{-1}\cdot K)$	$\Delta H_{m,v}$, eV	$\log(\sigma_0, \Omega^{-1}\cdot cm^{-1}\cdot K)$	$\Delta H_{m,v}$, eV
1	2	3	4	5
		$La_{0.95}(Ba_{1-x}Sr_x)_{0.05}F_{2.95}$		
0	4.49(7) [a]	0.356(5)	3.65(6)	0.284(6)
0.25	4.41(11)	0.343(8)	3.46(4)	0.266(4)
0.5	4.50(9)	0.341(7)	3.54(5)	0.261(5)
0.75	4.60(10)	0.343(7)	3.82(4)	0.277(4)
1	4.65(11)	0.344(8)	3.43(6)	0.244(6)
		$La_{1-x}Eu_xF_{3-x}$ (commercial solid electrolyte)		
0.008	4.08(8)	0.359(6)	3.02(2)	0.270(2)

[a] The standard deviations of the values are given in parentheses.

and a low-mobility $F_{2,3}(d+a)$ fluorine subsystem. A combined analysis of the temperature dependence of the fluorine-ion conductivity and the NMR data allows us to state that the transport of the fluorine vacancies V_F^+ takes place initially within the homogeneous $F_1(g)$ fluorine subsystem (in the range $T<T_c$). As the temperature is increased, fluoride-vacancy transport encompasses the entire anion sublattice as a consequence of the exchange of ion-current carriers between the homogeneous $F_1(g)$ and the combined $F_{2,3}(d+a)$ fluorine subsystems (in the range $T>T_c$). This leads to a decrease in the value of $\Delta H_{m,v}$ on the portion of the $\sigma(T)$ curve at $T>T_c$.

Figure 2 presents the concentration dependence of the isothermal conductivity for the solid solutions $La_{0.95}(Ba_{1-x}Sr_x)_{0.05}F_{2.95}$ $(0 \leqslant x \leqslant 1)$. As the SrF_2 content increases along the series of solid solutions, the anionic conductivity increases and reaches a maximum value of 2×10^{-4} $\Omega^{-1}\cdot cm^{-1}$ at 293 K for the crystal of $La_{0.95}Sr_{0.05}F_{2.95}$ $(x=1)$. The value of the conductivity for the two-component solid solution $La_{0.95}Sr_{0.05}F_{2.95}$ studied in the present work, which is an end member in the series of the three-component solid solutions $La_{0.95}(Ba_{1-x}Sr_x)_{0.05}F_{2.95}$, closely coincides with the value of σ for a crystal of the same composition previously grown during the investigations of the nonstoichiometric phases $La_{1-x}Sr_xF_{3-x}$ $(0 \leqslant x \leqslant 0.15)$.[18]

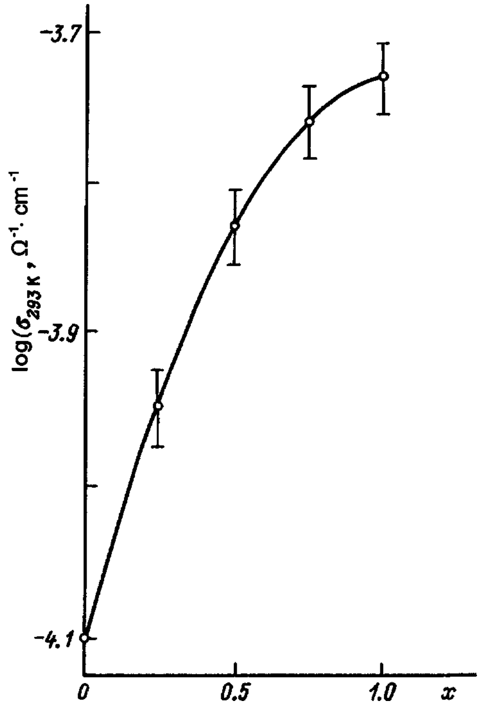

FIG. 2. Concentration dependence of the conductivity at 293 K for the single-crystal solid solutions $La_{0.95}(Ba_{1-x}Sr_x)_{0.05}F_{2.95}$.

The observed behavior of the concentration dependence of the anionic conductivity can be explained in the following manner. The concentration of V_F^+ structural vacancies generated by SrF_2+BaF_2 in the solid solutions investigated remained unchanged (5 mol %). However, the mixed-valence replacements of matrix La^{3+} ions by Sr^{2+} or Ba^{2+} ions lead to alteration of the geometry of the crystal lattice and to the appearance of structural and energetic distortions of the basic LaF_3 tysonite matrix. The replacement of La^{3+} ions by Sr^{2+} ions clearly causes smaller distortions of the tysonite crystal lattice than do $La^{3+}\rightarrow Ba^{2+}$ replacements. This is attributed to the closeness of the ionic radii $r_{La^{3+}}=0.13$ nm and $r_{Sr^{2+}}=0.14$ nm. For the barium ion $r_{Ba^{2+}}=0.156$ nm. The values of the ionic radii for a coordination number of 8 were taken from Ref. 19. This assertion is also consistent with the variation of the structural characteristics of the solid solutions studied. The unit-cell parameters for $La_{0.95}Ba_{0.05}F_{2.95}$ are $a=7.21$ Å and $c=7.38$ Å, while the parameters for $La_{0.95}Sr_{0.05}F_{2.95}$ are $a=7.18$ Å and $c=7.36$ Å. The increase in c upon $La^{3+}\rightarrow Ba^{2+}$ replacements, in comparison to $La^{3+}\rightarrow Sr^{2+}$ replacements, is accompanied by an increase in the distance between the fluorine ions of the homogeneous $F_1(g)$ subsystem, which leads to the generation of high potential barriers along the diffusion paths of the $F_1(g)$ fluorine subsystem (Fig. 3).

According to the value of the fluorine-ion conductivity, crystals of nonstoichiometric $La_{0.95}(Ba_{1-x}Sr_x)_{0.05}F_{2.95}$ are moderate-temperature solid electrolytes. An additional ad-

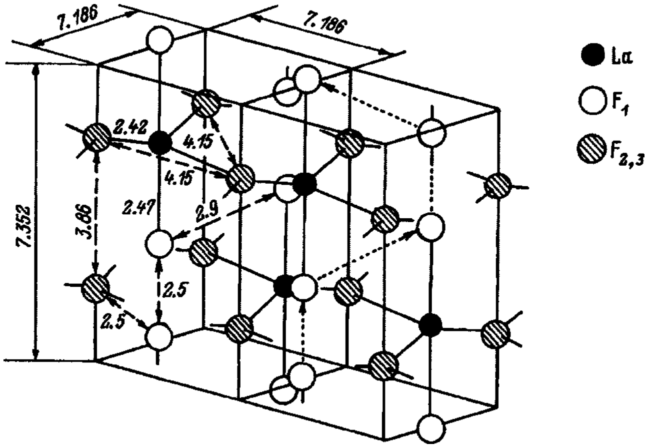

FIG. 3. Crystal structure of LaF_3. The distances between atoms and the unit-cell parameters are given in angstroms. The dotted line shows the direction of ion transport within the homogeneous $F_1(g)$ fluorine subsystem.

vantage of the solid solutions studied over the commercial membrane is the possibility of controlling the number of current carriers (V_F^+ structural vacancies) in the technology for producing the material using graphite crucibles. When $La_{1-x}Eu_xF_{3-x}$ single crystals are grown, the poorly controlled $Eu^{2+} \Leftrightarrow Eu^{3+}$ equilibrium is known to lead to irreproducibility of the final electrochemical characteristics of the material obtained. This allows us to recommend $La_{0.95}(Ba_{1-x}Sr_x)_{0.05}F_{2.95}$ as anionic solid electrolytes which are suitable for practical use in chemical sensors for fluorine and hydrogen fluoride, ion-selective membranes, electrochemical fluorine generators, etc.

Optimal geometric matching of the dopant cations ($M^{2+} + M'^{2+}$) and the matrix cation (R^{3+}) will be observed in the case of maximum proximity of the mean ionic radius of the divalent impurity cations to the ionic radius of the rare-earth cation. This calls for continuation of the investigations of ion-transport processes in tysonite phases using the single-crystal solid solutions $La_{0.95}(Ca_{1-x}Sr_x)_{0.05}F_{2.95}$, since the ionic radius of Ca^{2+} is equal to 0.126 nm.

[1] A. Sher, R. Solomon, K. Lee, and M. W. Muller, Phys. Rev. **144**, 593 (1966).

[2] L. E. Nagel and M. O'Keeffe, in *Fast Ion Transport in Solids*, W. van Gool (Ed.), North Holland, Amsterdam (1973), p. 165.

[3] T. Takahashi, H. Iwahara, and T. Ishikawa, J. Electrochem. Soc. **124**, 280 (1977).

[4] I. V. Murin, O. V. Glumov, and Yu. V. Amelin, Zh. Prikl. Khim. **53**, 1474 (1980).

[5] A. Roos, F. C. M. van de Pol, R. Keim, and J. Schoonman, Solid State Ionics **13**, 191 (1984).

[6] H. Geiger, G. Shon, and H. Strok, Solid State Ionics **15**, 155 (1985).

[7] N. I. Sorokin, M. V. Fominykh, E. A. Krivandina, Z. I. Zhmurova, and B. P. Sobolev, Kristallografiya **41**, 310 (1996) [Crystallogr. Rep. **41**, 292 (1996)].

[8] A. Roos and J. Schoonman, Solid State Ionics **13**, 205 (1984).

[9] M. Mansman, Z. Kristallogr. B **122**, 375 (1965).

[10] A. Zalkin and D. H. Templeton, Acta Crystallogr. B **41**, 91 (1985).

[11] B. Maximov and H. Schultz, Acta Crystallogr. B **41**, 88 (1985).

[12] S. F. Radaev, E. A. Krivandina, L. A. Muradyan, B. A. Maksimov, N. N. Bydanov, V. A. Sarin, B. P. Sobolev, and V. I. Simonov, Kristallografiya **36**, 369 (1991) [Sov. Phys. Crystallogr. **36**, 195 (1991)].

[13] K. Lee and A. Sher, Phys. Rev. Lett. **14**, 1027 (1965).

[14] M. Goldman and L. Shen, Phys. Rev. **144**, 321 (1966).

[15] G. A. Jaroszkiewicz and J. H. Strange, J. Phys. C: Solid State Phys. **18**, 2331 (1985).

[16] A. I. Livshits, V. M. Buznik, P. P. Fedorov, and B. P. Sobolev, Izv. Akad. Nauk SSSR, Neorg. Mater. **18**, 135 (1982).

[17] M. G. Izosimova, A. I. Livshits, V. M. Buznik, P. P. Fedorov, E. A. Krivandina, and B. P. Sobolev, Fiz. Tverd. Tela (Leningrad) **28**, 2644 (1986) [Sov. Phys. Solid State **28**, 1482 (1986)].

[18] N. I. Sorokin and B. P. Sobolev, Kristallografiya **39**, 889 (1994) [Crystallogr. Rep. **39**, 810 (1994)].

[19] R. D. Shannon, Acta Crystallogr. A **32**, 751 (1976).

Translated by P. Shelnitz

PHYSICS OF THE SOLID STATE VOLUME 40, NUMBER 4 APRIL 1998

Electric field of an isolated charged impurity in an ionic crystal

S. A. Prosandeev

Rostov-on-Don State University, 344090 Rostov-on-Don, Russia

(Submitted April 20, 1997)
Fiz. Tverd. Tela (St. Petersburg) **40**, 662–667 (April 1998)

The character of the behavior of the electric field created by a charged impurity in an ionic crystal is studied on the basis of both cluster and analytical approaches. In the cluster approach about 30 000 ions surrounding the impurity are taken into account. These ions are described in a model of polarizable sites. A direct calculation shows that the asymptote of the electric field of a charged impurity at lattice points can differ strongly from the one given by the Coulomb equation written for a homogeneous polarizable medium. The behavior of the electric field at intermediate distances, where the asymptotic behavior cannot yet be used, is studied in detail. It is found that the electric field is increased significantly in comparison to the Coulomb field in the region near the defect. The size of this (strongly polarized) region increases as the dielectric constant increases. These data are in qualitative agreement with the results obtained by Vikhnin *et al.* and account for the results of recent experiments designed to investigate polarization in reduced virtual ferroelectrics. © *1998 American Institute of Physics.* [S1063-7834(98)01804-8]

Charged impurities are easily obtained in ionic crystals by doping samples with atoms whose valence differs from the valence of the host elements. For example, the replacement of Ti^{4+} in $SrTiO_3$ by Fe^{3+} leads to the formation of a charged impurity with a charge equal to $1e$. Atomic vacancies can also be charged. For example, an oxygen vacancy can be singly or doubly charged. Finally, charged impurities can be found in an interstitial space.

The electrostatic field which a charged impurity creates is the sum of the field of the unscreened impurity and the field due to polarization of the medium. At small distances from an impurity the electric field due to polarization is essentially determined by the geometry of the crystal and the polarizability of the individual atoms. The local field in this region can be determined only by direct calculation. However, at large distances the electric field should apparently be given by some general asymptotic expression, which is determined only by the dielectric constant. Just such a hypothesis underlies the widely used Mott–Littleton model.

In this model, the crystal is divided into three regions. In the first region, which is near the defect, the local fields are determined in the framework of one of the exact calculation methods, viz., the density-functional formalism, the shell model, the model of polarizable point ions, etc. In the second, more distant region, the electric field of the charged impurity is given by the Coulomb equation written for a continuous medium. In the third, outer region, the continuum approximation is used, or it is assumed that there is no polarization in it.

At the same time, it has been found in investigations of dipolar impurities in oxides of the perovskite family[1,2] that a soft ferroelectric mode creates enormous electric fields at lattice points. The interaction of dipolar impurities with these fields leads to lowering of the total energy and, consequently, to phase-transition phenomena. These phenomena can be interpreted as results of the enhanced interaction between dipolar impurities and, therefore, as results of enhancement of the electric field of the dipole.

A similar effect with enhancement of the electrostatic field can also occur for monopolar impurities. In fact, it was shown in Refs. 3 and 4 that the asymptote of the electric field of a charged impurity in a simple cubic lattice is $(\varepsilon+2)/3$ times greater than the Coulomb field (here and below the Coulomb field refers to the field which appears in a uniformly polarizable medium with the same macroscopic dielectric constant). This assertion was based on several transformations of Coulomb sums, which have not hitherto been verified in a direct numerical calculation.

In the present work we calculate the local electric fields created by a charged impurity in a cluster consisting of $\sim$30 000 atoms. It is found that the asymptote of the electric field of the charge coincides exactly with the results of an analytical calculation. A new calculation scheme, which replaces the Mott–Littleton model, is proposed on this basis. General expressions, which describe the asymptote of the electric field of a charge in a crystal with arbitrary geometry, are obtained. The general laws governing the behavior of the electric field at short distances from an impurity are investigated. It is found that the local dielectric constant in that region exhibits nonmonotonic behavior. As a result, a region where the local electric fields are considerably stronger than the Coulomb fields forms near the impurity. Analytical expressions which permit estimation of the thickness of this region are derived. It is shown in the analytical and numerical approaches that the thickness of the polarized layer near a charged defect increases as the dielectric constant increases. For this reason, especially strong effects should be expected in ferroelectrics and virtual ferroelectrics. These data are in excellent agreement with the model of Vikhnin *et al.*,[5] which accounts for the results of experiments performed to study

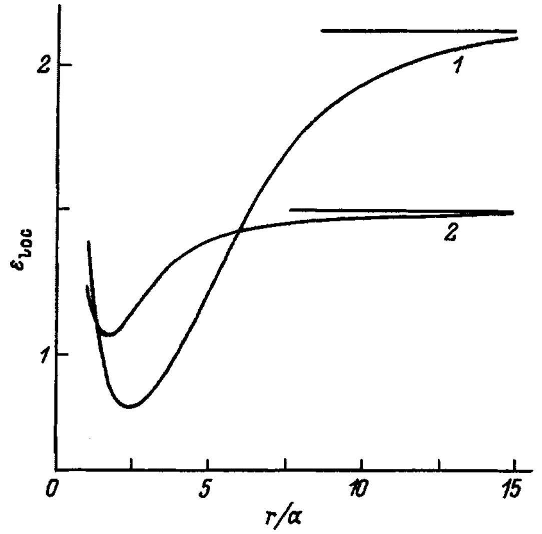

FIG. 1. Dependence of the local dielectric constant on the distance from an impurity. $\varepsilon = 5$ (*1*) and 2 (*2*).

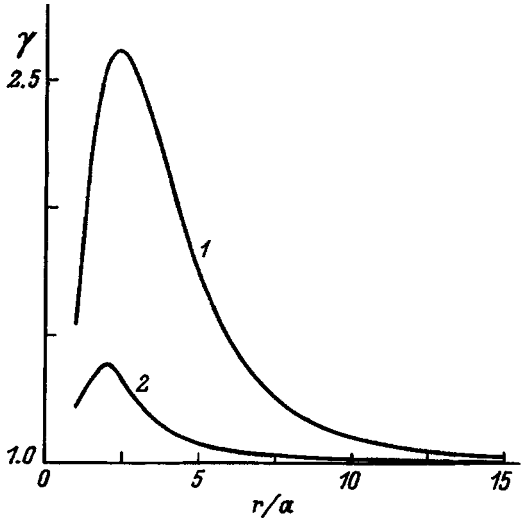

FIG. 2. Dependence of the electric field enhancement factor on the distance from an impurity. The notation is the same as in Fig. 1.

the polarization of virtual ferroelectrics in the low-temperature region.

1. RESULTS OF THE DIRECT CALCULATION

As in the Mott–Littleton model, we divided the crystal into three regions. In the first region the model of polarizable point ions was used. The equations of this model were solved numerically. The radius of this sphere was set equal to $15a$, where a is the lattice period. In the second region we used an analytical expression which describes the asymptotic behavior of the electric field (see Sec. 3). The radius of this region was set equal to $20a$. In the third region the polarization of the crystal was not taken into account. The radii of the spheres were chosen on the basis of a natural condition, which states that the final result should not depend on the values of the radii. It was found as a result of the numerical calculations that this condition holds with high accuracy for $\varepsilon = 2$ and 3.

The results of the calculation of the local electric fields on the (001) crystallographic axis are represented in the form

$$e_{nz} = \frac{q}{\varepsilon_{\mathrm{loc}}(na)^2}, \tag{1}$$

where q is the charge of the impurity, n labels the atoms on the z axis, and $\varepsilon_{\mathrm{loc}}$ is the local dielectric constant.

Figure 1 presents the values of the local dielectric constant obtained in the calculation. As we see, at small distances its value at first decreases and then increases. At large distances from the impurity it asymptotically approaches $3\varepsilon/(\varepsilon+2)$, which is $(\varepsilon+2)/3$ times smaller than the macroscopic dielectric constant. Thus, in accordance with the results of the analytical analysis performed by other investigators,[3,4] we found that the asymptotic behavior of the local electric field created by a charged impurity at the points of a simple cubic lattice is $(\varepsilon+2)/3$ times larger than the Coulomb field. We shall discuss this result in more detail in Sec. 6.

It is seen from Fig. 1 that the dip on the $\varepsilon_{\mathrm{loc}}(na)$ curve increases as ε increases. The width of the dip also increases in this case. It is shown in the next section that the same result can be obtained in the analytical approach. It is noteworthy that the minimum value of $\varepsilon_{\mathrm{loc}}(na)$ is less than 1 when $\varepsilon = 5$. This means that the local electric field at these sites is even larger than the unscreened electric field. Interpolating these results, we can theorize that at even larger values of ε it should expected that $\varepsilon_{\mathrm{loc}}(na)$ will have values close to 0 over a broad region. Several possible consequences of this hypothesis are discussed in Sec. 6.

For convenience, Fig. 2 presents the enhancement factor of the electrostatic field γ relative to its asymptotic behavior. In accordance with the foregoing presentation, this factor at first increases and then decreases, but it remains greater than unity over the entire range of values.

2. THICKNESS OF THE POLARIZED REGION

The following method is utilized to estimate the thickness of the polarized region. We expand the electric field of the charged impurity into a series in $1/R$ for large values of R. Here R is the distance from the impurity. We take the ratio of the second term in the expansion to the first, and from the condition that this ratio be equal to unity we find the characteristic thickness of the polarized region.

The field is expanded into a series in $1/R$ using several mathematical results obtained for the analogous expansion of the electric field potential in Ref. 6. We note that the electric field at a lattice point cannot be found by taking the derivative with respect to R, since R is not a continual variable in that case. The final result has the form

$$e_{nz} = \frac{\varepsilon+2}{3\varepsilon}\,\frac{1}{(na)^2}\left[1 + 2.110\frac{(\varepsilon-1)(\varepsilon-3/5)}{\varepsilon}\,\frac{1}{n^2} + \dots\right]. \tag{2}$$

As we see, the first term in the expansion coincides with the asymptote of the electric field which we obtained as a result of the numerical calculation and which was previously found analytically.[3,4] The second term in the expansion decreases as $1/R^4$ because of the centrosymmetric character of a cubic site; however, the expansion coefficient depends on ε in a more complicated manner. From the equality between the ratio of the second term to the first and unity we obtain

$$R=a\sqrt{2.110\frac{(\varepsilon-1)(\varepsilon-3/5)}{\varepsilon}}. \tag{3}$$

In particular, for large values of ε we have

$$R=a\sqrt{2.110\varepsilon}. \tag{4}$$

Thus, in accordance with the results of the numerical calculation, the thickness of the polarized region increases with increasing ε.

3. ASYMPTOTE OF THE ELECTRIC FIELD OF AN IMPURITY IN AN IONIC CRYSTAL WITH ARBITRARY GEOMETRY

The asymptotic behavior of the electric field created by a point charge in an ionic crystal is determined by inverse Fourier transformation. The unique feature of our treatment is that the result will be valid for crystals with an arbitrary geometry. To achieve this goal we take advantage of the fact that large distances in direct space correspond to small wave vectors in reciprocal space. As a result, the existing integrals over reciprocal space can be taken analytically, at least with respect to the modulus of the wave vector.

We find the Fourier transform of the electric field of a point charge

$$\mathbf{e}_{ni}(\mathbf{r})=\frac{1}{\Omega}\int_{\text{u.c.}} d^3k e^{-ik(r_{ni}+r)}\mathbf{e}_i(\mathbf{k},\ \mathbf{r}), \tag{5}$$

where Ω is the volume of the Brillouin zone, r_{ni} is the radius vector of the ith atom of the nth cell, the integration is carried out over a unit cell, and $\mathbf{e}_i(\mathbf{k},\ \mathbf{r})$ is the Fourier transform of the electric field in the ith sublattice, which can be found from the relation

$$\mathbf{e}_i(\mathbf{k,r})=\mathbf{e}_i^0(\mathbf{k,r})-\sum_{nj}\ \phi_{ij}(\mathbf{k,r})\chi_{jn}(\mathbf{k})\mathbf{e}_n^0(\mathbf{k},0). \tag{6}$$

Here $\mathbf{e}_i^0(\mathbf{k,r})$ is the Fourier transform of the unscreened field, $\phi_{ij}(\mathbf{k,r})$ is the Fourier transform of the dipolar interaction tensor, and $\chi_{jn}(\mathbf{k})$ is the susceptibility tensor defined by the equation

$$\sum_j\ [\alpha_j^{-1}\delta_{ij}+\phi_{ij}(\mathbf{k},0)]\chi_{jm}(\mathbf{k})=\delta_{im}\mathbf{I}, \tag{7}$$

where α is the atomic polarizability tensor.

At large distances from the impurity only small $\mathbf{k}$ make contributions to the integral (5). The following simplifications can accordingly be made. First, the dipolar interaction tensor can be replaced by the asymptotic expression for $\mathbf{k}\rightarrow 0$

$$\phi_{ij}=\frac{4\pi}{v}\hat{\mathbf{k}}\hat{\mathbf{k}}+\Lambda_{ij}, \tag{8}$$

where $\hat{\mathbf{k}}$ is a unit vector directed parallel to $\mathbf{k}$, and Λ_{ij} is a tensor, which gives the difference between the local field and the mean field (it is easily calculated by Ewald's method). We note that the tensor Λ_{ij} does not depend on $\mathbf{k}$. The susceptibilities, which can be found using this expression, correspond to the long-wavelength limit.

Now the integration in (5) can be partially eliminated using the relation

$$\int_{-1}^{1}\int_0^{\infty}\exp(-iklt)kf(t)dtdk=-i\frac{\pi}{l^2}f'(0). \tag{9}$$

We note that at large l the integration over the Brillouin zone in (5) can be replaced by integration over all reciprocal space.

The next difficulty involves finding the derivative of the integrand. To calculate it, we utilize the definition of susceptibilities, from which it follows that

$$\chi_t'=-\chi\phi_t'(\mathbf{k},0)\chi. \tag{10}$$

We note that the derivative of the dipolar interaction tensor does not depend on the labels of the sublattices.

The final result can now be represented in the form

$$\mathbf{e}_i(\mathbf{r})=\frac{1}{2\pi}\int_0^{2\pi}\mu_i^+(\varphi,\mathbf{r})F(\varphi)d\varphi, \tag{11}$$

where

$$\mu_i^+(\varphi,\mathbf{r})=\sum_m\ \left(\ \delta_{im}\mathbf{I}-\sum_j\ \phi_{ij}(\varphi,\mathbf{r})\chi_{jm}(\varphi)\right)_{\cos\theta=0}, \tag{12}$$

$$F(\varphi)=\frac{q}{l^2}\left(\hat{\mathbf{k}}_t'-\sum_{ij}\ \phi_t'\chi_{ij}\hat{\mathbf{k}}\right)_{\cos\theta=0}. \tag{13}$$

In the special case in which these tensors do not depend on φ (for example, in cubic crystals or in the direction of one of the principal axis of a rhombohedral crystal), the final result takes the form

$$\mathbf{e}_z\mathbf{e}_i(\mathbf{r})=\mathbf{e}_z\mu_i^+(\mathbf{r})\frac{\varepsilon_\perp^{-1}}{l^2}q. \tag{14}$$

Here

$$\varepsilon_\perp^{-1}=1-\frac{2}{v}\int_0^{2\pi}\left(\hat{\mathbf{k}}\sum_{ij}\ \chi_{ij}\hat{\mathbf{k}}\right)_{\cos\theta=0} d\varphi \tag{15}$$

is the reciprocal dielectric constant.

The result obtained has a simple interpretation. It is seen from (14) that the electric field of the charge at large distances from the defect is described by Coulomb's formula multiplied by μ_{zz}. We shall next discuss the nature of this multiplier.

At large distances from a defect the electric field in a small region near a lattice point can be considered uniform. When a crystal is polarized in a uniform external field, the Lorentz correction, which leads to enhancement of the polarization, must be taken into account. The Lorentz-Lorenz expression for a simple cubic lattice is known, and according to it

$$4\pi\frac{\alpha}{v}=3\frac{\varepsilon-1}{\varepsilon+2}. \tag{16}$$

As we see, the coefficient $(\varepsilon+2)/3$ produces enhancement of the atomic polarization and, consequently, of the local field at a lattice point due to the local effects.

Similarly, in our case, due to the deviation of the local field at a lattice point from the mean field, the resultant field created by a charge is larger than the Coulomb field. In a simple cubic lattice the enhancement factor is equal to $(\varepsilon+2)/3$ for the reasons cited above. In the general case μ_{zz} gives the ratio of the local field at a lattice point created by uniform polarization to the mean field. This factor is easily calculated by known methods. It is not even necessary to perform the complicated calculation of the electric fields created by a point charge for this purpose.

According to the determination made, the field enhancement factor has the following general properties:

$$\frac{4\pi}{v}\sum_i \alpha_i\mu_{izz}(0)=\varepsilon-1, \tag{17}$$

$$\frac{1}{v}\int_{\text{u.c.}}\mu_{izz}(\mathbf{r})d^3r=1. \tag{18}$$

The first property gives the general relationship between the enhancement factor and the macroscopic dielectric constant. The second, normalization condition shows that when the electric field is averaged over a unit cell, the resultant field coincides with the mean field, which, in turn, coincides with the Coulomb field.

4. CONSIDERATION OF RETARDATION EFFECTS

Back in the early nineteen sixties, Tolpygo[7] pointed out that an ambiguity appears in the determination of electric fields in the limit $\mathbf{k}\to 0$. In fact, uniform polarization leads to a macroscopic field of the form

$$\mathbf{E}=4\pi\frac{(\mathbf{Pk})\mathbf{k}}{k^2}. \tag{19}$$

When $k\to 0$, formula (19) gives different results, depending on whether the vector $\mathbf{k}$ is parallel or perpendicular to the field vector. It was proposed that this problem can be eliminated by utilizing retardation effects. When these effects are taken into account, we have

$$\mathbf{E}=4\pi\frac{(\mathbf{Pk})\mathbf{k}-\mathbf{P}(\omega^2/c^2)}{k^2-\omega^2/c^2}. \tag{20}$$

Now, allowing $\mathbf{k}$ to tend to zero, we obtain the correct result: $4\pi P$.

Disregarding the retardation effects can, in principle, lead to incorrect results, especially if everything occurs in the region of small $\mathbf{k}$, as in our case. This raises the problem of reformulating the problem for the case of a variable field. Let us consider one of the simplest cases, viz., a simple cubic lattice, in this context. Instead of tensor (8), we use the corresponding tensor obtained with the consideration of retardation

$$\phi_{\alpha,\beta}=\frac{4\pi}{v}\,\frac{k_\alpha k_\beta-\delta_{\alpha,\beta}(\omega^2/c^2)}{k^2-\omega^2/c^2}+\frac{4\pi}{3v}\,\delta_{\alpha,\beta}. \tag{21}$$

In the limit $\mathbf{k}\to 0$ we have

$$\phi_{\alpha,\beta}=\frac{4\pi}{v}\,\delta_{\alpha,\beta}-\frac{4\pi}{3v}\,\delta_{\alpha,\beta}=\frac{8\pi}{3v}\,\delta_{\alpha,\beta}. \tag{22}$$

This relation is valid for any direction of the vector $\mathbf{k}$. If Eq. (19) is used, a different result is obtained.

The use of (21) does not alter the conclusion drawn above: the asymptote of the electric field of a point charge is increased by a factor of $(\varepsilon+2)/3$ in comparison to the Coulomb field. However, the asymptote of the electric field of a dipole differs from the asymptote which was previously found by other investigators without taking into account retardation.[8]

It was shown in Ref. 8 that the asymptote of the electric field of a dipole is increased by a factor of $(\varepsilon+2)^2/9$ in comparison to the Coulomb field. However, in deriving this factor it was essentially assumed that the dipolar interaction tensor has different values for the longitudinal and transverse components. We are devoting a separate study to a discussion of this question, in which we shall examine the electric field created by a microscopic dipole in an ionic crystal.

5. CONSIDERATION OF THE FINITE DIMENSIONS OF THE ATOMS

Above we used the model of polarizable point ions. Actually, atoms have finite dimensions. This fact can be taken into account in a systematic quantum-mechanical or semiempirical approach.[9] An additional parameter appears in the latter approach, viz., the characteristic dimension of the electron cloud participating in electron polarization.

Let λ be the reciprocal of the characteristic dimension of an atom. Then the dipolar interaction tensor which takes into account the finite dimensions of an atom takes the form

$$\phi_{\alpha\beta}=\frac{4\lambda^3}{3\sqrt{\pi}}\delta_{\alpha\beta}-\frac{4\pi}{v}\sum_G\frac{(q_\alpha+G_\alpha)(q_\beta+G_\beta)}{|\mathbf{q}+\mathbf{G}|^2}\times\exp\left(-\frac{|\mathbf{q}+\mathbf{G}|^2}{4\lambda^2}\right). \tag{23}$$

When the value of λ is exceeds the lattice period in reciprocal space, the results of the calculation employing this relation differ from the results obtained in the model of polarizable point ions. If λ is smaller than the lattice period, the local effects vanish, and the final result does not differ from the equations of macroscopic electrostatics in media.

6. DISCUSSION OF RESULTS

A systematic study of the electrostatic field of a charged impurity in an ionic crystal was performed in this work. One of the simplest models, viz., the model of polarizable point ions, was used to obtain some highly general results. Within this model we were able to elucidate the general laws governing the behavior of the electrostatic field of an impurity at both small and large distances from the impurity.

At large distances, the electrostatic field tends to decrease to the asymptotic value previously found by other investigators in an analytical approach. This asymptotic value is $(\varepsilon+2)/3$ larger than the Coulomb field, i.e., the field obtained from the Coulomb relation written for a homogeneous polarizable medium. The factor $(\varepsilon+2)/3$ is valid only for cubic sites in cubic crystals. At other points in the unit cell (or in crystals with a different geometry) this factor can be arbitrary. The only restriction is that the factor averaged over a unit cell is equal to unity. This means that the mean electrostatic field in the cell coincides with the Coulomb field.

At short distances from the impurity we used a numerical cluster approach. It was found that the number of polarized lattice points which must be taken into account in the calculation should be very large. For example, the required number of lattice points reached 30 000 for the values of the macroscopic dielectric constant $\varepsilon=2$ and 5. The cluster must be even larger for larger values of the dielectric constant. However, there is an alternative approach based on integration in reciprocal space for these cases.[10]

As a result of the cluster calculations we discovered the nontrivial behavior of the electrostatic field of an impurity at small distances. It was found that this field has nonmonotonic behavior. The local dielectric constant at first decreases (at large values of ε it can even be less than unity) and then increases, smoothly approaching the asymptotic value. Such behavior indicates that there is a region in which the polarization is increased considerably in comparison to the Coulomb level near a charged impurity in an ionic crystal. We note that such behavior is a consequence of the inhomogeneous, cellular atomic structure of a crystal. In other words, it is a result of the deviation of the local field from the mean value.

One unexpected result is that the dip in the behavior of the local dielectric constant, as well as its width, increase as the macroscopic dielectric constant increases. Thus, the effect is strongest in polar crystals, for example, in ferroelectrics. This nontrivial finding was obtained here in both the direct numerical and analytical approaches. An expression relating the thickness of the polarized region to ε was obtained in the analytical approach.

Enhancement of the polarization near charged impurities can definitely lead to instability of the centrosymmetric position of an impurity. This can be manifested both by displacement of the impurity from the centrosymmetric point and by redistribution of the electron density. The former consequence is well known, but the latter is still inadequately understood. The case of a singly charged oxygen vacancy in oxides of the perovskite family can be cited as an example. It was shown in Ref. 9 that under certain conditions this defect can become a dipolar center. The reason for this is the interaction of an electron bound to the vacancy with polarization of the surrounding medium. It turns out that as a result of the polarization of the medium it is energetically more advantageous for the electron to be drawn away to one of the cations adjacent to the vacancy than to be delocalized equally among all the neighboring cations.

It was recently discovered by second-harmonic generation[5] that reduced strontium titanate contains of the order of 10^{18} dipolar impurities. These impurities form nanometer-scale polarized regions, which are forerunners of a phase transition of the crystal into the ferroelectric state. Vikhnin *et al.* attributed the results of these experiments to enhancement of the polarization of the crystal by impurities. Our data are in excellent qualitative agreement with these results.

One deficiency of the model used is that the displacement of atoms is described in the model of polarizable point ions, i.e., that the atomic polarizability contains both an electronic component and polarization caused by the displacement of ions. This approximation works well, if the displacements of the atoms are small. However, it has also proved itself in the description of ferroelectric phenomena, where the displacements can reach tenths of an angstrom. In describing real displacements it is better to use the shell model to take into account the interaction of the polarization with mechanical strains, but in this case it will hardly be possible to obtain analytical results. It is apparently better to use the shell model in the first region and to employ the results of the analytical calculation presented in this paper in the second region.

The deficiencies of the model used also include the fact that it does not take into account the Debye screening or the influence of the covalent component of the chemical bonding on the screening of the electrostatic field of an impurity. For this reason, the results obtained are valid for purely ionic crystals, which do not have free electrons. These factors must be taken into account when the theory is developed further. This approximation is correct only at very small impurity concentrations. If the polarized regions created by different impurity particles overlap, the polarization must be described in another way. In particular, the appearance of collective phenomena should be expected in such a case. Such behavior of dipolar impurities was previously studied in the soft-mode model.[1,2] In polar lattices, especially in ferroelectrics, impurities are apparently inclined to exhibit collective effects, but they are not included in the continuous medium model. Therefore, the development of a theory of impurities in polar lattices with consideration of the difference between the local field and the mean field should be considered promising.

We thank I. Osipenko and A. Ryabchinskiĭ for their assistance in performing the calculations.

[1] V. S. Vikhnin, Fiz. Tverd. Tela (Leningrad) **26**, 906 (1984) [Sov. Phys. Solid State **26**, 552 (1984)].

[2] B. E. Vugmeister and M. D. Glinchuk, Rev. Mod. Phys. **62**, 993 (1990).

[3] E. R. Smith, J. Phys. A: Math. Gen. **13**, L107 (1980).

[4] P. Wielopolski, J. Phys. A: Math. Gen. **14**, L263 (1981).

[5] V. S. Vikhnin, P. Voigt, and S. Kapphan, in *Seventh Europhysical Conference on Defects in Insulating Materials (EURODIM-94),* Abstracts,

Université Claude Bernard Lyon 1, Lyon (1994), 215 pp.
[6] G. D. Mahan and R. M. Mazo, Phys. Rev. **175**, 1191 (1968).
[7] K. B. Tolpygo, Usp. Fiz. Nauk **74**, 269 (1961) [Sov. Phys. Usp. **4**, 485 (1961)].
[8] G. D. Mahan, Phys. Rev. **153**, 983 (1967).
[9] S. A. Prosandeyev and I. A. Osipenko, Phys. Status Solidi B **192**, 37 (1995).
[10] S. A. Prosandeyev and A. I. Riabchinski, J. Phys.: Condens. Matter **8**, 505 (1996).

Translated by P. Shelnitz

Formation mechanism for nanodefects on surfaces of loaded metals

V. I. Vetergren', V. L. Gilyarov, S. Sh. Rakhimov, and V. N. Svetlov

A. I. Ioffe Physicotechnical Institute, Russian Academy of Sciences, 194021 St. Petersburg, Russia

(Submitted October 9, 1997)
Fiz. Tverd. Tela (St. Petersburg) **40**, 668–671 (April 1998)

Tunneling profilometry is used to investigate the shape and orientation of defects that form at the surfaces of Cu, Au, Mo and Pd under loading. The defects have the shape of an indented prism. The value of the angles at the tip of the defects coincide with the angles between glide planes, while the orientation of the walls coincide with the orientation of these planes. At the edges of the defects there exist ''swellings'' caused by expulsion of material at the surface. Based on these results, the creation of these defects is explained by the exit of dislocations as they burst through barriers formed at intersecting glide planes. © *1998 American Institute of Physics.* [S1063-7834(98)01904-2]

In Refs. 1 and 2 we used tunneling and interference microscopy to begin a systematic study of defects that form under loading at the surfaces of Cu, Au, Mo and Pd. We observed that the shallowest of these have the form of the imprint of a prism with nanometer dimensions. With time, the dimensions of the defect increase and attain values of several μm before rupture of the metal. This process is discontinuous in nature: for a certain time, Δt, the dimensions of the defect are practically unchanged and then within a time $\approx 0.1\Delta t$ they change by several tens of nm. This allows us to classify all defects in two groups, with quasistationary, i.e., long-lived defects in the first group and short-lived defects in the second. It turns out that the ''depth'' H of the quasistationary defects is smaller than the depth H_0 of defects which, for convenience, we will refer to as ''primary defects'': $H = nH_0$. The question that interests us is: what is the formation mechanism of the primary defects?

In order to answer this question, we carried out a detailed investigation of the shape, orientation and dimensions of primary defects.

We used a scanning tunneling profilometer RTP-1, developed at the the Institute of Physics, St. Petersburg State University[3] and manufactured by the industrial cooperative ''Era.''

We studied the surfaces of rolled foils of 99.99% pure Au and 99.96% pure Cu, Mo, and Pd. The thicknesses of these foils ranged from 30 to 60 μm. The samples were cut along the direction of rolling using curved knives. In order to localize the points of rupture, we made semicircular cuts of radius 1.5 mm at the edges of strips of width 6 mm. The length of a working portion of the sample was 12 mm. The samples were polished using GOI paste and washed in acetone and alcohol. To load the samples we used a spring-loaded apparatus[1] constructed in our laboratory.

The chemical structure of the surfaces before and after the measurements was monitored by Auger spectroscopy, with spectra recorded by a LH-10 spectrometer. It turned out that the surfaces of Cu, Mo, and Pd were coated by oxide layers and carbon to a thickness of 1–2 nm, while atoms of carbon and oxygen were present on the surfaces of the Au samples, which remained after washing with acetone and alcohol.

Topograms of the surfaces of Cu, Au and Pd reveal that two walls of the defects (ABG and CDF, Fig. 1a) were parallel to the axis of elongation and perpendicular to the sample surface. The dihedral angle at the tip of the defects (i.e., the angle between planes $ACFG$ and $DBGF$, Fig. 1a) was equal to $70 \pm 10°$, while the angle between their axes (the lines FG, Fig. 1a) and the direction of extension of the sample was $\approx 60°$. The defects can be separated into two groups. For the first, one of the walls ($DBFG$, Fig. 1a) formed an angle $\approx 90°$, while the opposite wall ($ACFG$, Fig. 1a) formed an angle of $\approx 20°$ with the plane of the surface. For the other group of defects, the corresponding angles were ≈ 70 and $\approx 40°$.

At the surfaces of loaded foils of Mo we also observed two groups of defects with dihedral angles at the tips of ≈ 50 and $\approx 90°$. In contrast to Cu, Au and Pd, we were unable to observe the primary orientation of the defect walls at the surface of Mo relative to the elongation axis of the sample.

The lengths (distances between walls AGB and CDF, Fig. 1a), the widths (distance between lines AC and BD), and depth (the length of lines DB and BG) of the primary defects are given in Table I.

Previously, analogous ''triangular'' defects with dimensions 60–100 nm were observed on the rupture surfaces of single crystals of MgO by Keh,[4] Aller,[5], and Landford using scanning tunneling microscopy.[6]

It is known that the shape and dimensions of defects on topograms can be quite distorted due to the shape and dimensions of the measuring tip.[7] Therefore, rather than continuing our discussion of the experimental results, let us address the question of how much correspondence there is between the geometric parameters revealed by topograms and the true parameters of the primary defects.

As an example, we show schematically in Fig. 1b the cross section of the prism imprint obtained using a point in the shape of a conical column with a dome-shaped tip. It is clear that the geometric parameters of the defect in the illustration are smaller than the true dimensions, the angle at the

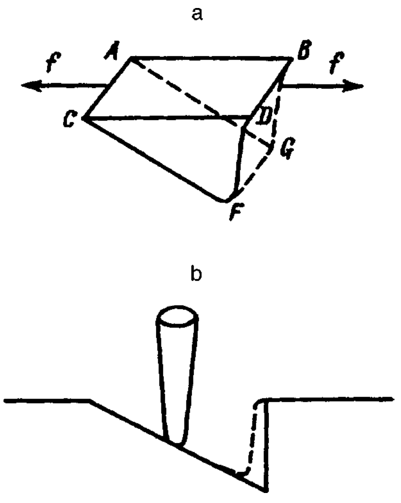

FIG. 1. Schematic illustration of a defect (a) and the distortion in its shape (b) caused by the shape of the probe tip.

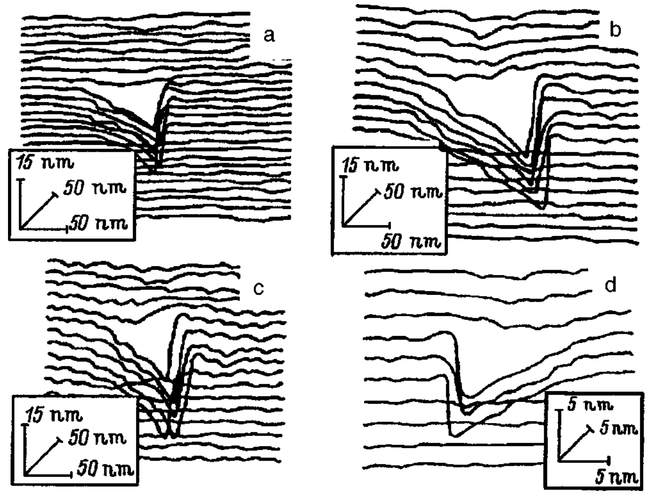

FIG. 2. Sections of topograms with isolated defects at the surfaces of Cu (a), Au (b), Mo (c) and Pd (d).

vertex of the defect is smoothed out, and the vertical wall is converted into a sloped wall. The slope angle of the latter equals the apex angle of the cone, i.e., the tip, while the radius of curvature of the curve described as we sweep around the right angle at the intersection of the right wall of the defect on the surface equals the radius of curvature of the dome of the probe tip.[7]

Unfortunately, the shape of the tip depends on the uncontrollable conditions under which it was prepared[8,9] and changes continuously in the course of the trial.[1,10] Therefore, it has not been possible previously to take into account distortions caused by the shape and dimensions of the tip. However, we can estimate these parameters based on the shape and dimensions of defects in the topograms.[7] As an example, consider the illustration of a primary defect at the surface of Cu (Fig. 2a). Having measured the slope of the right-hand wall in the illustration, and its height and radius of curvature at the intersection of the defect with the surface plane, we find that the radius of curvature of the tip is 60–100 nm, the apex angle of the column—the tip—is less than 10°, and the width of the tip is more than 15 nm.

Using these parameters, we can estimate the true dimensions of a defect from its image. It turns out that the width and length of a defect at the surface of Cu is ≈ 60 nm, the depth is ≈ 17 nm, and the angle at the vertex is smaller by $\approx 5°$ than it is on the topogram.

Analogous calculations show that true length and width of primary defects at the surfaces of the other metals we studied were 5–10 nm larger, the depth was 2–3 nm larger, and the angle at the vertex approximately 5° smaller than in the images. These values are smaller than the random scatter of dimensions and angles at the vertex for the images of defects and, in what follows, we will not take them into account.;

As time passes, the dimensions of the defects increase,[1,2] and before rupture we observe ''large- scale'' defects, which for Cu, Au and Pd most often resemble trenches, at the surface in addition to the shallow primary defects (Fig. 3). Their length exceeds 10 μm, their width is ≈ 2 μm, and their depth is 500–700 nm. In a cross section parallel to the axis of extension of the sample, the form of the ''trenches'' is similar to the form of primary defects and is a triangle with an angle of $70 \pm 10°$ at the vertex. This similarity leads us to assert that the mechanism for formation of ''large-scale'' and ''shallow-primary'' defects are identical.

In order to bring their nature to light, we turn to Fig. 4, which demonstrates the evolution of two defects on the surface of a Au sample under a load of 350 MPa. One of the

TABLE I. Dimensions of primary defects in loaded metals

Metal	Length, nm	Width, nm	Depth, nm
Cu	50±10	50±10	15±3
Au	60±10	100±10	22±3
Pd	≈20	≈10	5±3
Mo	60±10	50±10	18±3

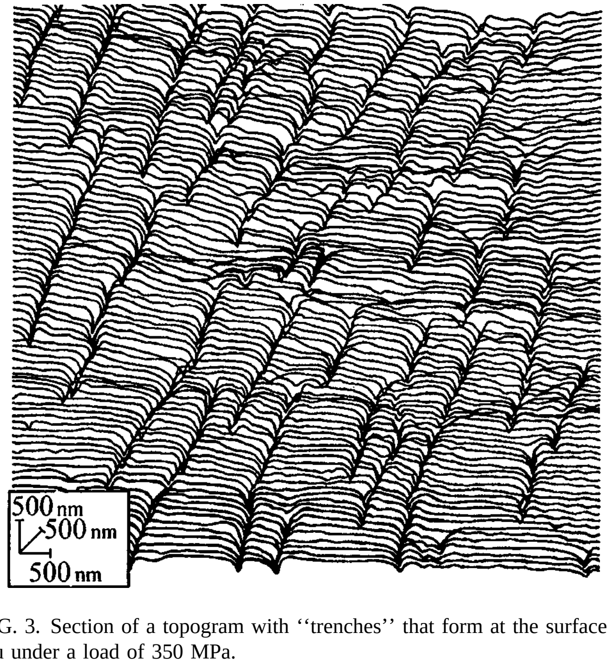

FIG. 3. Section of a topogram with ''trenches'' that form at the surface of Au under a load of 350 MPa.

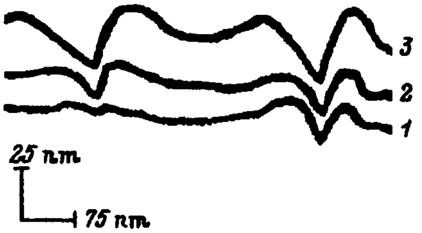

FIG. 4. Cross section of the profile of an Au surface at different times under a load of 350 MPa. $t(s)$: *1*—20, *2*—600, *3*—1400. The measurements began 70 hours after the load was applied.

defects (the left one) grows, while the second (the right one) relaxes. It is clear that, during the time the defects are growing, the surface of the metal swells out at their edges, while as they are re-absorbed the ''swelling'' disappears. Analogous ''swellings'' are observed at the edges of defects at the surfaces of Cu, Mo and Pd. Their height increases as the depth of the defect increases and decreases when they are re-absorbed. Consequently, during the generation of defects the metal is carried out of the volume onto the surface, and during their re-absorption it enters back in.

As is well known,[7] Cu, Mo and Pd have the FCC lattice, and the angle between easy-glide planes (111) and (111) in these metals is ≈70.5°. The angle at the vertex of defects formed at the surface of these metals has the same value. Therefore, the expulsion of material at a surface can be explained by the exit of dislocations along easy glide planes.

This explanation agrees with the orientation of walls of the defect with respect to the axis of elongation. Actually, as we already noted above, the metal foils we studied were subjected to cold rolling, and then were loaded along the rolling direction. It is well known from the literature[12] that a texture is formed in cold-rolled samples of metals with FCC lattices in which the direction ⟨112⟩ is parallel to the direction of rolling, while the plane (110) is parallel to the plane of rolling. The angles between families of (111) and (110) planes are 35.3 and 90°. The values of the angles we measured between the surface plane and defect walls (≈40 and 90°, see above) are close to these. The angle between the direction ⟨112⟩ and the line of intersection of the planes (111) is 54.7°. This value is also close to the angle between the axis of the dihedral angle and the direction of extension of the sample (≈60°).

These coincidences show that the orientation of the defect walls is given by the orientation of easy glide planes in cold-rolled samples of Cu, Au and Pd.

On the other hand, in metals with BCC lattices, one of which is Mo, the glide planes are {110} and {112}. The angles between them are ≈48.2, ≈54.7 and 90°.[11] These values are also close to the angles at the tips of primary defects on the surface of Mo (≈ 50 and ≈90°). Probably the defects are formed by the exit of dislocations in this metal as well.

However, in metals with this type of crystal lattice there are no well-defined easy glide planes. It is probable that for this reason the ''large-scale'' defects at the surface of Mo have the shape of formless clusters (Fig. 5) in contrast to the ''triangular trenches'' oriented along the axis of extension at the surfaces of Cu, Au and Pd.

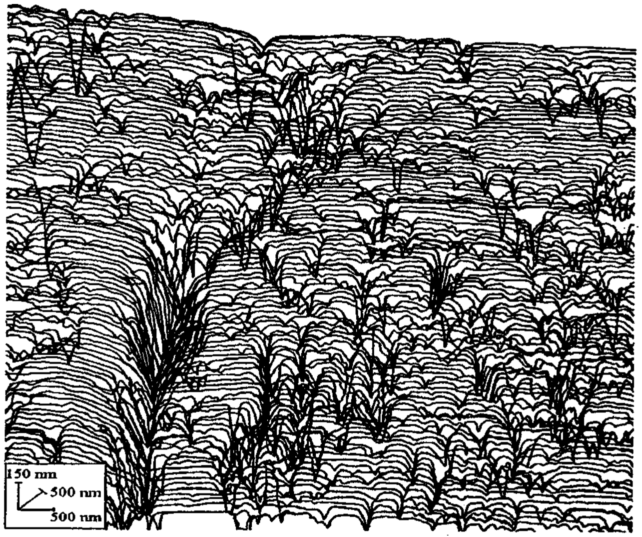

FIG. 5. Section of a topogram with clusters of defects that form at the surface of Mo 80 hours after application of a load of 800 MPa.

The model we are proposing for formation of defects is qualitatively illustrated by Fig. 6. Under the action of an applied stress, dislocations exit at the surface along intersecting glide planes. In this process, as head dislocations merge a new dislocation *A* forms, which hinders the motion of the remaining dislocations.[11,13,14]After the dislocation punches through the surface a primary defect forms. This model is analogous to models for the formation of cracks proposed previously by Cottrell,[13] Vladimirov,[14] and Keh.[4]

The energy advantage of this latter mechanism, in our view, is due to the closeness of the source of generation of the defects to the metal surface. In fact, as follows from the topogram, the distance from the surface at which the vertices

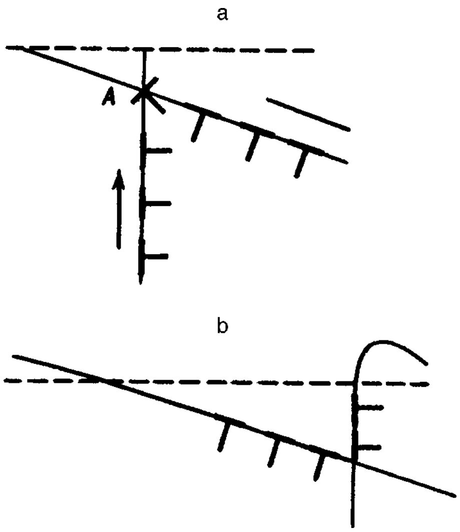

FIG. 6. Sketch of the mechanism for formation of defects at the surface of metals under a load. a—dislocation moving towards the surface, b—cross section of defect. The dashed line shows the position of the surface before formation of the defect , the arrows indicate the direction of motion of the dislocation.

of the primary defects are located is $\approx 5-25$ nm, i.e., $\approx(10-100)|b|$, where $|b|$ is the magnitude of the Burgers vector. Near the surface in loaded metals, the concentration of dislocations is considerably larger than in the bulk.[15] Furthermore, at small distances x from the surface an image force acts on the dislocation $\approx Db^2/2x = D/20$,[14] which draws it toward the surface, and make it possible to penetrate the barrier, creating ''sessile'' dislocations.

It is also known that in the surface layer the intensity of thermal motion of atoms is increased compared to the bulk, along with the probability of large thermal fluctuations,[16–18] which can punch through a potential barrier.

This work was supported by the Russian Fund for Fundamental Research (Grant No. 96-02-16874).

[1] V. I. Vettergren', S. Sh. Rakhimov, and V. N. Svetlov, Fiz. Tverd. Tela (St. Petersburg) **37**, 913 (1995) [Phys. Solid State **37**, 495 (1995)]; Fiz. Tverd. Tela (St. Petersburg) **37**, 3635 (1995) [Phys. Solid State **37**, 2001 (1995)]; Fiz. Tverd. Tela (St. Petersburg) **38**, 590 (1996) [Phys. Solid State **38**, 323 (1996)]; Fiz. Tverd. Tela (St. Petersburg) **38**, 1142 (1996) [Phys. Solid State **38**, 632 (1996)]; Fiz. Tverd. Tela (St. Petersburg) **39**, 2256 (1997) [*sic*].

[2] V. I. Vettergren', S. Sh. Rakhimov, and E. A. Bakulin, Fiz. Tverd. Tela (St. Petersburg) **37**, 3630 (1995) [Phys. Solid State **37**, 1998 (1995)].

[3] B. K. Adamchuk, Instrum. Exp. Tech. **5**(4), 182 (1989) [in Russian].

[4] A. S. Keh, J. C. M. Li, Y. T. Chou, Acta Metall. **7**, 694 (1959).

[5] W. F. Adler and T.W. James, in *Fracture Mechanics for Ceramics, Rocks, and Concrete*, Freiman and E.R. Fuller (Eds.), (American Society for Testing and Materials, Philadelphia, PA, USA, 1981) p. 271–290.

[6] S. C. Landford, Ma Zhenyi, I. C. Jensen, J. T. Dickinsen, J. Vac. Sci. Technol. A **8**, 447 (1990).

[7] J. E. Griffith and D. A. Grigg, J. Appl. Phys. **74**(9), R83 (1993).

[8] D. K. Biegeisen, F. A. Ponce, and J. C. Tramontarna, Appl. Phys. Lett. **50**, 696 (1987).

[9] J. P. Ibe, P. P. Bey, S. L. Brandow, R. A. Brizzolara, N. A. Burnham, D. P. Dipsila, K. P. Lee, S. R. K. Marrian, and R. J. Coftan, J. Vac. Sci. Technol. A **8**, 3570 (1990).

[10] J. Tersoff, Phys. Rev. B **39**, 1052 (1989).

[11] I. I. Novikov, *Defects in the Crystallographic Structure of Metals* (Metallurgiya, Moscow, 1975) [in Russian], 220 pp.

[12] M. C. Smith, *Principles of Physical Metallurgy* (Harper & Brother, N.Y., 1957), 453 pp.

[13] A. H. Cottrell, *The Mechanical Properties of Matter* (John Wiley, N.Y.–London–Sidney, 1958), 350 pp.

[14] V. I. Vladimirov, *The Physical Nature of the Rupture of Metals* (Metallurgiya, Moscow, 1975) [in Russian], 280 pp.

[15] V. P. Alekhin, *The Physics of Hardness and Plasticity of the Surface Layers of Materials* (Nauka, Moscow, 1983) [in Russian], 283 pp.

[16] V. E. Korpsukov, S. A. Knyazev, A. S. Luk'yanenko, R. R. Nazarov, B. A. Obidov, E. V. Stepin, and V. N. Svetlov, Fiz. Tverd. Tela (St. Petersburg) **38**, 113 (1996) [Phys. Solid State **38**, 60 (1996)].

[17] V. E. Korpsukov, Fiz. Tverd. Tela (Leningrad) **25**, 3250 (1983) [Phys. Solid State **25**, 1873 (1983)].

[18] R. R. Nazarov, V. E. Korpsukov, A. S. Luk'yanenko, M. Shermatov, Surfaces No. 5, 27 (1987) [in Russian].

Translated by Frank J. Crowne

PHYSICS OF THE SOLID STATE VOLUME 40, NUMBER 4 APRIL 1998

Evolution of dislocation structures having various orientations in strained single crystals of the alloy Ni_3Ge

V. A. Starenchenko, Yu. V. Solov'eva, Yu. A. Abzaev, and E. V. Kozlov

Tomsk State Academy of Architeture and Construction, 634003 Tomsk, Russia

V. V. Shpeĭzman, V. I. Nikolaev, and B. I. Smirnov

A. I. Ioffe Physicotechnical Institute, Russian Academy of Sciences, 194021 St. Petersburg, Russia

(Submitted October 29, 1997)
Fiz. Tverd. Tela (St. Petersburg) **40**, 672–680 (April 1998)

The dislocation structure of strained single crystals of Ni_3Ge with various orientations is investigated by electron microscopy. The evolution of the dislocation structure parameters is studied as a function of the degree of strain, temperature, and orientation of the single crystals. Analysis of the experimental dependences of the yield stress on the density of dislocations leads to certain conclusions about how various mechanisms for dislocation drag make temperature-dependent contributions to the deforming stress, and about the nature of the thermal hardening of Ni_3Ge. © *1998 American Institute of Physics.* [S1063-7834(98)02004-8]

Ni_3Ge alloys belong to the class of intermetallic compounds having the $L1_2$ superstructure, which exhibit changes in mechanical properties with increasing temperature that are unusual compared to pure FCC metals: in the majority of cases, the yield limit, yield strength, and coefficient of strain hardening increase in temperature ranges that differ for different alloys.

Mechanical properties as a function of orientation of the strain axis in different alloys with the $L1_2$ superstructure as a function of orientation of the strain axis are rather fully treated in the scientific literature.[1–7] However, experimental studies of the dislocation structures in these alloys are inadequate. Despite the obvious success of the authors of Refs. 8–12 in their studies of the fine structure of individual dislocations, the systematic studies of the evolution of dislocation structures with temperature and strain that are needed to understand the nature of mechanical phenomena are lacking, nor are there quantitative data on the changes of various parameters of the dislocation structure. Such studies have been made for the alloy Ni_3Fe, which possesses a low ordering energy,[13] and single crystals of Ni_3Ge with high-energy antiphase boundaries oriented in the [001] direction.[14] The subject of this paper is a comparative analysis, both qualitative and quantitative, of the dislocation structure of single crystals of Ni_3Ge with three orientations: [001], [234] and [139]. The choice of this alloy is not accidental, since this material possesses clearly marked anomalies in its mechanical properties (the yield point τ_0 increases by more than a factor of 10 with increasing temperature) and, in contrast to other alloys with the $L1_2$ superstructure, it exhibits strong orientational dependence of its thermal hardening.[15]

1. EXPERIMENTAL METHOD

Our methods for fabricating single crystals and carrying out mechanical trials were described in detail in our paper Ref. 16. Using a spark cutter with a goniometer, we cut out sheets 0.3–0.4 mm thick from strained samples along planes of type {100}, {110}, and {111}, from which we made foils to study in a UEMB-100K electron microscope. For each orientation we studied the evolution of the dislocation structure as a function of the strain ε and temperature. We chose five temperatures (77, 293, 523, 673, and 873 K), for each of which we performed a qualitative and quantitative analysis of the dislocation structure with respect to the degree of strain (up to approximately 5% relative strain according to the yield curve).

Due to its high resolution, diffraction electron microscopy is the most effective way to investigate the dislocation structure in detail. However, there are ambiguities regarding the degree to which the dislocation structure observed in the electron microscope corresponds to the structure of the strained material. With regard to the materials we studied, we can say the following. The primary reasons why the dislocation structure could differ strongly from the original structure are a thinning strained crystal region and redistribution of the dislocations which may occur after it is unloaded. We expect that in both situations, the more significant the resistance to dislocation motion and the lower the field of long-range stresses are, the smaller these changes must be. The alloys we studied are in this sense ideal objects, since very large frictional stresses cause a high degree of stability of the dislocation structure. The absence of pileup and the high degree of resistance to dislocation motion should ensure minimum redistribution of dislocations during unloading and thinning of the samples. Nevertheless, we took measures to avoid errors that arise due to some possible change in the position of the dislocations in the foil. In the [234] orientation, we studied the dislocation structure at each point corresponding to a fixed value of temperature and degree of strain in three cross sections (approximately (001), (111), (011)), each oriented differently with respect to the glide elements. Once we had sufficient observation statistics,

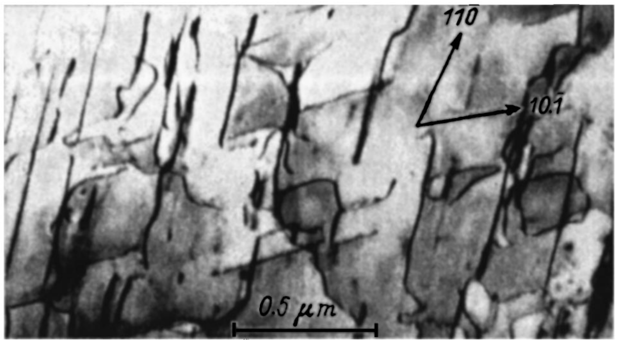

FIG. 1. Dislocation structure of Ni_3Ge alloy with [$\bar{2}34$] orientation. $T=77$ K. (111) foil cross section, $\varepsilon=10\%$.

we were able to monitor some of the effects of redistribution and exit of dislocations at the surface connected with tapering of the crystal, since these phenomena manifest themselves differently at different cross sections for dislocations of different types. In the [139] orientation we studied the dislocation structure in foils parallel to the slip planes.

2. QUALITATIVE REGULARITIES IN THE EVOLUTION OF A DISLOCATION STRUCTURE

Based on information on the crystal-geometric peculiarities of the deformation of single crystals of Ni_3Ge with orientation [234] obtained from analysis of surface and shape changes in samples,[17] we customarily divide the temperature range into segments over which the crystal deforms via octahedral ($T=77$–293 K) and cubic ($T=293$–953 K) slip.

Let us first consider the qualitative features of a dislocation structure observed at $T=4.2$–77 K. At the very beginning of the strain we identify two systems of dislocations in various cross sections on the electron-microscope patterns (Fig. 1). It will be clear from our analysis of the patterns of slip traces and changes in crystal shape that these correspond to the following coplanar slip systems: [101](111) and [110](111). For sufficiently large strains ($\varepsilon>10\%$), three systems of dislocations appear in the structure, which are a sign that a latent glide system is acting.

According to Ref. 18, the dislocation structure can be classified qualitatively as mesh-chaotic. The basic elements of the dislocation structure are edge dislocations which extend along close-packed directions such as ⟨110⟩. Along the dislocations are many kinks and reacting segments. Also observed are dipoles with various configurations, although the fraction of these is comparatively small. As a whole, the evolution of the dislocation structure with strain in the temperature range 4.2–77 K differs from what is observed at higher temperatures. We have remarked that the fraction of edge dislocations at cryogenic temperatures has a tendency to increase with increasing strain, whereas at 293 K and higher, as already noted in Ref. 19, the fraction of edge dislocations decreases strongly as the strain develops. In the 4.2–77 K temperature range, just as for the [100] orientation at 77 K, there is a preferred development of one system of long edge dislocations as the strain increases, which are located along one primary direction. This behavior probably indicates that the nature of edge dislocations formed at cryogenic temperatures may be different from what is observed at higher temperatures.

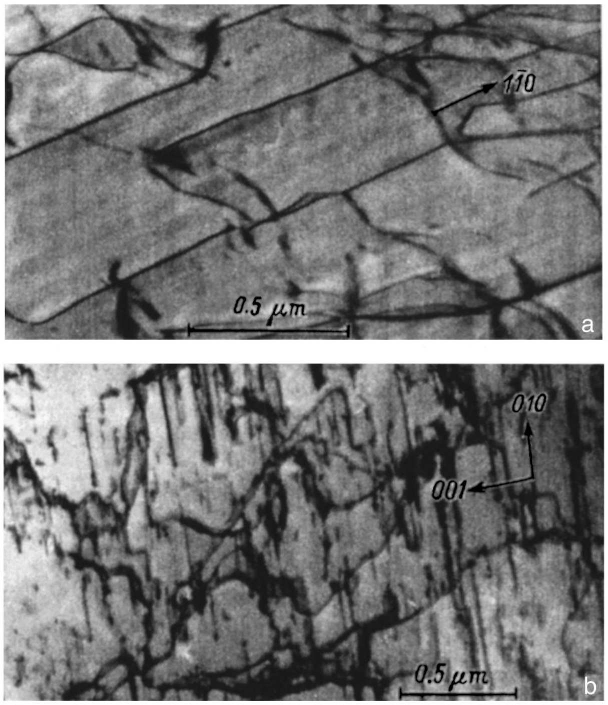

FIG. 2. Dislocation structure of Ni_3Ge alloy with orientation [$\bar{2}34$]. $T=293$ K. a—(111) foil cross section, $\varepsilon=7\%$, b—(001) foil cross section, $\varepsilon=10\%$.

Room temperature corresponds to the descending portion of the first peak in the temperature dependence $\tau_0(T)$, at which a mixed slip is observed along both octahedral and cubic planes.[2] Figure 2 shows images of dislocation structures obtained at 293 K in foils cut parallel to the acting slip planes. There is an observable difference between dislocations of a cubic glide system and dislocations that lie within the planes of the primary octahedron: long rectilinear threading segments of superdislocations whose splitting cannot be resolved are characteristic for an octahedral slip system, whereas superdislocations of a cubic system are strongly split and warped. It should be noted that even though room temperature corresponds to the descending portion of the first peak of the anomaly, cubic slip is less developed than octahedral slip. This is evidence that a replacement of the slip system is taking place gradually throughout a certain temperature range in the neighborhood of the first peak. We observed the first dislocations of the cubic slip system at room temperature.

Further increases in temperature lead to complete disappearance of the octahedral slip system, and at temperatures $T=523$, 673, 953 K the strain takes place exclusively through the cubic slip system. In order to obtain a clear picture of the distribution of dislocations throughout the crystal, we observed the orientation of screw and edge dislocations separately. Distinctive features of the geometry of a cubic slip system for crystals with this orientation allowed us to obtain images of the dislocation structure with preferred resolution of dislocations of either edge or screw orientation.

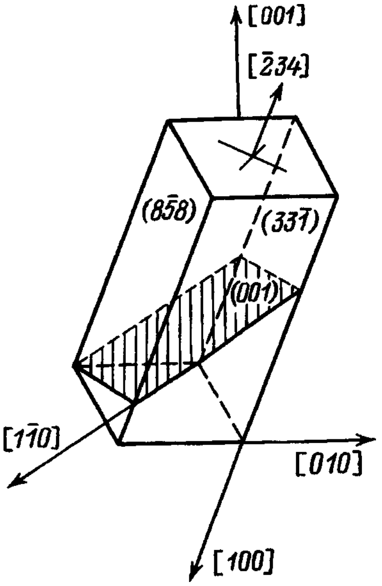

FIG. 3. Sketch of positions of primary cubic glide system (001)$[1\bar{1}0]$ in a crystal with strain axis [234] and faces (858), (331).

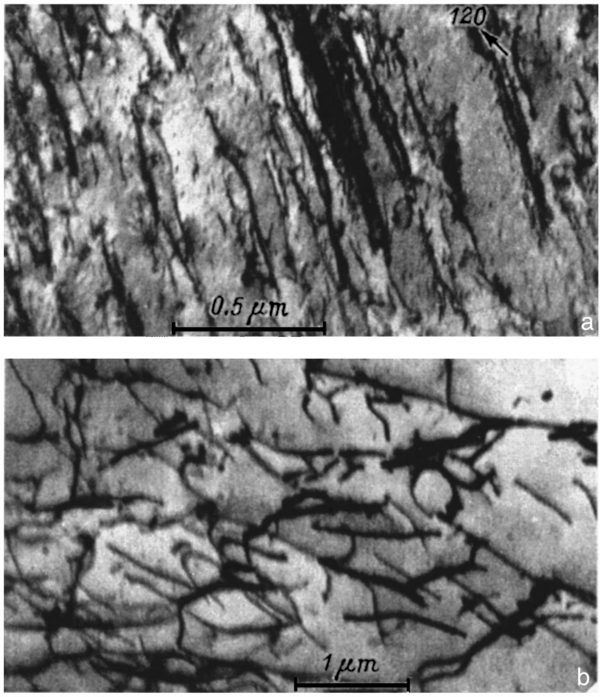

FIG. 4. Dislocation structure of Ni_3Ge alloy with orientation $[\bar{2}34]$. Foil cross section (858), $\varepsilon=15\%$. $T=523$ (a) and 953 K (b).

The sketch in Fig. 3 shows quite clearly that foils cut parallel to the (858) facet contain primarily edge dislocations (since the direction of shear is approximately perpendicular to the plane of the facet), while in foils parallel to the (331) facet we expect screw dislocations (since the plane of the facet is close to the plane where the shear vector [110] lies). We isolated the screw and edge components of a dislocation loop according to the method we have described at trial temperatures of 523, 673, and 953 K. At 523 K we observed a layerlike dislocation structure: long dislocations whose orientations are close to that of the edge cause bunches separated by rarefied regions with low dislocation density (Fig. 4a). This dislocation distribution is now maintained until the rupture strain is reached (i.e., $\varepsilon\approx20\%$). A similar structure is encountered at a temperature of 673 K as well. However, the layerlike quality described above is here less marked. As the temperature increases to 953 K, the dislocation structure undergoes significant qualitative changes. As can be seen from Fig. 4b, the dislocations are practically unconnected with their glide planes. It is probable that diffusion processes are so intense that superdislocations, even as they mediate creep, may themselves become the mechanism for plastic flow. In cross sections cut so as to reveal screw dislocations we observe protruding dislocations or very short dislocation segments.

In the $[\bar{1}39]$ orientation we studied the evolution of dislocation structures at five temperatures (77, 293, 523, 673, 873 K) in planes close to the slip planes for various degrees of strain. The orientations we studied were characterized by a sharp peak in the temperature anomaly[29] at a temperature of ~ 620 K. Therefore, we will analyze the distinctive features of the dislocation structure individually for $T<620$ K and $T>620$ K.

We investigated three temperatures in the temperature range 77–620 K: 77, 293, and 523 K. The structure we observed at a temperature of 77 K was similar to the structures observed at this temperature in other orientations. In keeping with our choice of orientation, the development took place preferentially for one slip system, although traces of a second less-developed system were present. The fundamental elements of the dislocation structure were edge dislocations with density ρ_l, which made up roughly half of the structure when $\varepsilon=5\%$. We also observed bent dislocations, narrow dipoles and dislocation loops. The fraction of linear dislocations increased with strain. As we mentioned previously in discussing the orientation [234], this is atypical at higher temperatures.

At room temperature the dislocation structure in the $[\bar{1}39]$ orientation has a number of features that distinguish it from the corresponding structure in [001] orientation, notably a high density of dislocations but relatively small fraction of linear dislocations compared to the [001] orientation (Fig. 5). Glide along a latent system is obviously in evidence:

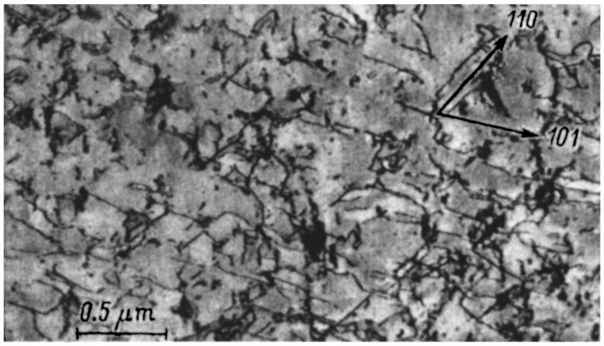

FIG. 5. Dislocation structure of Ni_3Ge alloy in $[\bar{1}39]$ orientation. (111) foil cross section. $T=293$ K, $\varepsilon=7\%$.

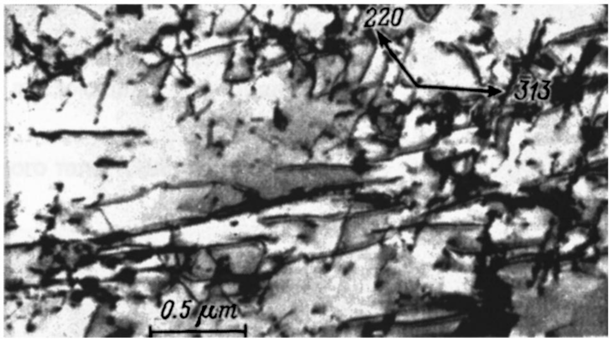

FIG. 6. Dislocation structure of Ni_3Ge alloy in orientation $[\bar{1}39]$. (111) foil cross section. $T=673$ K, $\varepsilon=2.5\%$.

despite the fact that glide in the primary octahedral planes dominates, practically all the microphotographs we observed showed dislocations of two other glide systems. We assume that the deformation starts with primary octahedral slip, but because of the strong hardening of the first glide system the hidden glide system begins to act even at 5% deformation. This is probably why a tendency to form a cell-like substructure is observed for strains that are pre-rupture ($\varepsilon \approx$ 20%). An analogous picture applies at $T=523$ K. Here the dislocation structure is even more dense, and once again two more systems of dislocations are observed although the dominant glide system is in the primary octahedral plane. Further increases in the deformation lead to enhancement of glide along hidden systems. Characteristic elements of the dislocation structure linear dislocations, whose fraction decreases with increasing strain.

At temperatures 673 and 873 K, along with dislocations of the octahedral glide system we observe strongly split dislocations, which are probably dislocations belonging to the cubic glide system as it enters into the strain process (Fig. 6). It is characteristic that the cubic glide replaces the octahedral glide gradually, as it does in the case of the [234] orientation. The glide is mixed in character both at 673 K and at 873 K. The dislocation structure becomes noticeably nonuniform as the temperature increases to 873 K. Qualitatively different structures are observed on microphotographs obtained from various places on the film, both patterns that are typical of low-temperature octahedral glide and patterns that qualitatively recall the structure of high- temperature cubic and octahedral glides. A similar structural nonuniformity may be the origin of the complicated hardening curves obtained at $T=873$ K.[16]

3. CHANGES IN THE DISLOCATION PARAMETERS OF THE STRUCTURE WITH TEMPERATURE AND STRAIN FOR NI$_3$GE CRYSTALS WITH VARIOUS ORIENTATIONS

In Figs. 7a and 7b we plot the change in average dislocation density ρ versus temperature and strain for Ni_3Ge single crystals with [139] and [234] orientations. Comparison of plots of $\rho(\varepsilon)$ obtained for the different orientations shows that the microstructural parameters of the alloy under study are senistive to a considerable degree to changes in the orientation of the strain axis.

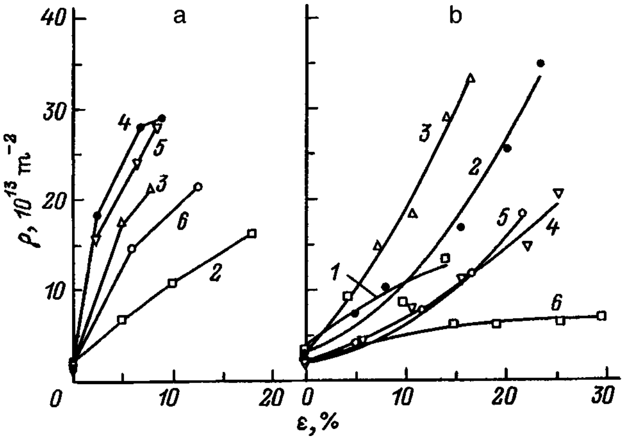

FIG. 7. Dependence of the average dislocation density on degree of strain for orientations [139] (a) and [234] (b). T (K): *1*— 4.2, *2*— 77, *3*— 293, *4*— 523, *5*— 673, *6*— 873.

For the $[\bar{2}34]$ orientation, the curves that describe the dependence of the dislocation density on strain have a common outline and shape (with one exception at 953 K, which we discuss in more detail below): at all the temperatures we studied, these functions can be described by quadratic parabolas both for octahedral and cubic glides, i.e., $\rho=k_0\varepsilon^2+k_1$, where k_0 depends on temperature. The exception is the high-temperature region, where the dislocation density (at $T=953$ K) saturates even at $\varepsilon=10\%$, remaining unchanged (or even decreasing) as the strain is increased further. This is obviously related to activation and intense evolution of the processes that annihilate dislocations at these temperatures. The way these curves $\rho(\varepsilon)$ change with temperature correlates with the behavior of the hardening curves $\tau(\varepsilon)$,[16] allowing us to assert that the shape of the yield curve is determined by the change in the dislocation component of the shear stresses. Nevertheless, the curves $\rho(\varepsilon)$ obviously behave differently for octahedral and cubic glide: increasing the temperature while other conditions are kept the same, leads to an increase in the dislocation density for octahedral glide, whereas the reverse is observed under cubic shear, i.e., a decrease in the dislocation density. The intensity of dislocation pileup is anomalous in its temperature dependence for octahedral glide: instead of the expected decrease in dislocation pileup intensity occurring in pure metals, increasing the temperature causes the pileup intensity to increase (Fig. 7b), whereas cubic glide exhibits the normal dependences that are characteristic of pure metals. A common feature of all the orientations is the fact that, despite the considerable effect temperature has on the magnitude of the dislocation density, the overall strain dependence of the density and rate of dislocation pileup over various temperature ranges intervals is described by curves $\rho(\varepsilon)$ that vary with temperature in a similar manner, although the rates of change of these curves (as well as the hardening curves; see Ref. 16) depend strongly on orientation. Under octahedral glide, the most rapid change in the curves $\rho(\varepsilon)$ is observed for the [139] orientation (Fig. 7a).

There is a traditional point of view that associates thermal hardening with interlocking of screw dislocations, which

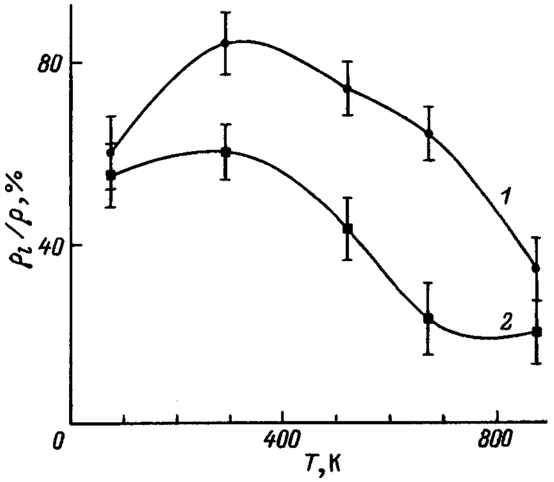

FIG. 8. Temperature dependences of the fraction of rectilinear dislocations for orientation [001] (*1*) and [139] (*2*). $\varepsilon=5\%$.

is accompanied by the creation of edge dislocations. A distinctive feature of dislocation structures of strained ordered alloys is long interlocked edge segments with screw orientation. Let us compare the distinctive features of pileup of edge dislocations in [001]-oriented Ni_3Ge single crystals with pileup in single crystals of the same alloy oriented for a single slip (the [139] orientation). In the [234] orientation this kind of measurement is not made, because cubic glide is present even at 293 K; we only observed pure octahedral glide in this case at 4.2 and 77 K, when the formation of edge dislocations is probably unrelated to the generation of Kira–Wilsdorf barriers. In Fig. 8 we plot the fraction of rectilinear dislocations versus temperature for 5% strain and crystals oriented along the directions [001] and [139]. It is clear that the fraction of edge dislocations in the [139] orientation is approximately twice as small as in the [001] orientation. For both orientations, plots of the fraction of edge dislocations versus temperature share a common feature: the presence of a maximum at roughly room temperature, followed by a decrease, despite the fact that shear stresses and the yield limit continue to grow.

The way the length l of edge dislocations varies with strain also has its peculiarities under conditions of single or multiple glide. In Fig. 9 we plot the dependence of the length of edge dislocations versus strain for single crystals with the orientations under discussion at $T=523$ K. Measurements of the length of edge dislocations were made using 15 to 20 photographs of dislocation structures obtained from foils parallel to the glide planes. It turned out that the rate of decrease of the length of edge dislocations in orientations with multiple glide was considerably higher than for single glide, which can be related to the fact that the length of interlocking screw segments is determined by the length of free dislocation segments bounded by obstacles formed by interdislocation interactions.

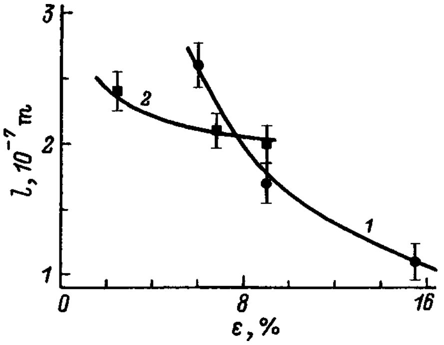

FIG. 9. Dependence of the average length of edge dislocations on the degree of strain for orientations [001] (*1*) and [139] (*2*). $T=523$ K.

4. ANALYSIS OF CONTRIBUTIONS OF VARIOUS MECHANSIMS TO THE RESISTANCE TO STRAIN

A multitude of experimental data show that the connection between the shear stress τ for a given rate of strain and the density of dislocations ρ can be described satisfactorily by the expression

$$\tau=\tau_F+\alpha G b \rho^{1/2}, \qquad (1)$$

where τ_F is a frictional stress unrelated to dislocations and α is the interdislocation interaction parameter. Relation (1) can be used to analyze how various mechanisms that arise during strain contribute to the yield stress. Changes in the yield stress can be due to several factors.

1) A change in the resistance to motion of dislocations that is unrelated to interdislocation interactions which, in turn, can be written as two terms:

$$\tau_F(T)=\tau_F^0(T)+\tau_F^s(T), \qquad (2)$$

where $\tau_F^0(T)$ is the dislocation-independent friction resistance, connected with intrinsic lattice friction (the depth of the Peierls valley), interaction of gliding dislocations with atomic impurities, antiphase domain boundaries, antiphase boundaries of strain-related origin, and nonuniformities of the crystal structure related to it, while $\tau_F^s(T)$ is the self-braking stress of superdislocations defined by specific mechanisms that are characteristic of the $L1_2$ superstructure. The first group of mechanisms has a negative (normal) temperature dependence, while the second has a positive dependence (anomalous).

2) A change in $\alpha(T)$, which can occur for several reasons. The first of these is traditionally associated with a decrease in the thermally activated component of the interaction with the dislocation ''forest.'' The second, which is not so obvious, is connected with entrainment of other systems of the cubic and octahedral glide during plastic strain and, accordingly, with changes in the spectrum of the interdislocation interaction. The latter, in principle, can lead to a nonmonotonic variation of the parameter $\alpha(T)$. Finally, anomalous effects on the parameter $\alpha(T)$ maybe possible connected with the creation of Kira–Wilsdorf barriers. Let us clarify this with more detail. Kira–Wilsdorf barriers can appear and disappear during strain, creating an additional resistance to dislocation motion. The number of places at which thermal activation can occur is proportional to the number of obstacles generated by dislocations of the ''forest'' in the shear zone (i.e., the number of lengths of free segments of a moving dislocation that appear on it as it ''hovers'' at ob-

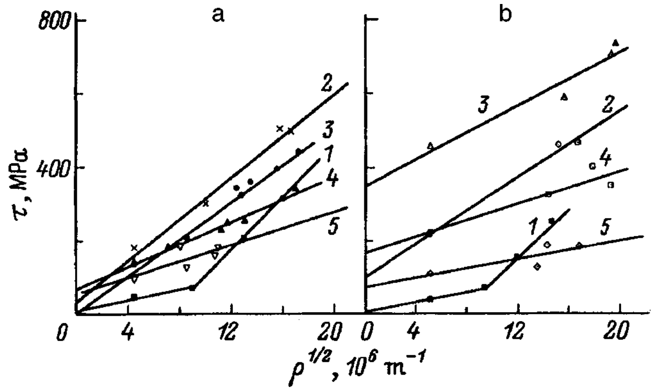

FIG. 10. Dependence of the reduced shear stresses τ on the square root of the average dislocation density $\sqrt{\rho}$ for deformations with the following axis orientations: $[\bar{2}34]$ (a) and $[\bar{1}39]$ (b). T, (K): *1*—77, *2*—293, *3*—523, *4*—673, *5*—873.

stacles), $N \cong (D/\rho^{-\frac{1}{2}})\ (D/\rho^{-\frac{1}{2}}) = D^2\rho$, where D is the size of the shear zone and ρ is the dislocation density. The number of successful activations that lead to the appearance of a virtual barrier (i.e., one that appears and then is destroyed) will be proportional to $D^2\rho\ \exp(-u/kT)$. In this case the work that the external stress will do is $\delta A \cong D^2\rho\ \exp(-u/kT)\Delta U\omega\rho^{-\frac{1}{2}}$, where ΔU is the energy to destroy a unit length of Kira–Wilsdorf barrier, u is the activation energy for generating the Kira–Wilsdorf barrier, and $\omega\rho^{-\frac{1}{2}}$ is the length of the Kira–Wilsdorf barrier. The shear $\Delta a \cong D^2 b$; consequently, the resistance to destruction of Kira–Wilsdorf barriers $\tau = (\delta A/\Delta a) \cong \rho^{-\frac{1}{2}} \times \exp(-u/kT)\Delta U/b$. A component of the resistance to motion of superdislocations appears that is proportional to the square root of the dislocation density, which leads to an effective anomalous increase with temperature of the parameter α. The other component of the shear resistance, which is not associated with the density of the dislocation ''forest'' (the appearance of Kira–Wilsdorf barriers and their destruction by free superdislocations), gives a contribution to the change of τ_F.

3) The shear modulus G decreases linearly with temperature, and its change does not exceed 25% in this temperature range.

4) Finally, a contribution that turns out to be important is one connected with the pileup of dislocations, which in contrast to the case of pure metals can be anomalous.

The plots of the experimental shear stresses versus the square root of the dislocation density $\tau(\rho^{1/2})$ shown in Fig. 10 for various temperatures other than cryogenic turn out to be linear with reasonable accuracy. At cryogenic temperatures the function $\tau(\rho^{1/2})$ can be approximated by two line segments, indicating the presence of two stages of strain hardening in this case.

Equation (1) allows us to separate the contributions of these mechanisms using the following considerations. Let the temperature change from T_i to T_{i+1}. Then neglecting the change in the shear modulus, the change in deforming stresses for a preset strain can be approximately written (keeping the first terms of the expansion in a Taylor series) in the form

$$\Delta\tau_i = \Delta\tau_{iF} + \frac{1}{2}\alpha(T_i)Gb\,\frac{\Delta\rho}{\rho^{\frac{1}{2}}(T_i)} + \Delta\alpha Gb\rho^{\frac{1}{2}}(T_i), \tag{3}$$

where $\Delta\tau_{iF}$ is the change in frictional stress, the second term $\Delta\tau_\rho$ is the contribution connected with changes in the intensity of dislocation pileup, and the third term $\Delta\tau_\alpha$ is the change in stress caused by changes in the interdislocation interaction parameter. These contributions can be determined from the experimental function $\tau(\rho^{1/2})$. Then the resistance to strain can be written as

$$\tau = \tau(T_0) + \sum_i \Delta\tau_i = \tau(T_0) + \sum_i \Delta\tau_{iF} + \sum_i \frac{1}{2}\alpha(T_i)Gb\frac{\Delta\rho}{\rho^{\frac{1}{2}}(T_i)} + \sum_i \Delta\alpha_i Gb\rho^{\frac{1}{2}}(T_i). \tag{4}$$

Figure 11a shows the results of this analysis for the $[\bar{2}34]$ orientation. As a starting temperature we used $T_0 = 77$ K; the strain for this analysis was 5%.

Consider a diagram of how the contributions to the deforming stress change with temperature (Fig. 11a). All three of the abovementioned contributions increase in the temperature range 77–293 K, i.e., they exhibit an anomalous temperature dependence. The largest change in the resistance to dislocation motion ($\approx$80%) comes from the increase in the parameter α, while the remaining $\approx$20% of the increase in deforming stresses is connected with an increase in the frictional stress ($\approx$15%) and the rate of dislocation pileup ($\approx$5%). Increasing the temperature up to values that exceed room temperature qualitatively changes the temperature dependence of these contributions: up to a temperature of 550–570 K, they all decrease with increasing temperature. Increasing the temperature further decreases the contribution connected with the dropoff in interdislocation interaction parameter and the rate of dislocation pileup, whereas the frictional stress (τ_F) increases, reaching values of $\approx$150 MPa. Because of this anomalous increase in τ_F, the total function $\tau(T)$ exhibits a second washed-out extremum in the neighborhood of the cubic glide.

By analyzing the contributions to the deforming stresses as we did for the $[\bar{1}39]$ orientation, see Fig. 11b, we can establish the following facts. In the temperature range where anomalous increases in the deforming stresses are observed, the contributions connected with changes in the frictional stresses and intensity of dislocation pileup increase anomalously. In this case the main contribution comes from changes in the frictional stress, which greatly exceed the contribution from changes in the rate of dislocation pileup. Changes in the contribution connected with the temperature dependence of the parameter α are also nonmonotonic; however, their maximum value does not coincide with the maximum of the anomaly and occurs at room temperature. The parameter α, and accordingly the contributions connected with it to the deforming stresses, increase only in the range 77–293 K and decreases when the temperature is increased

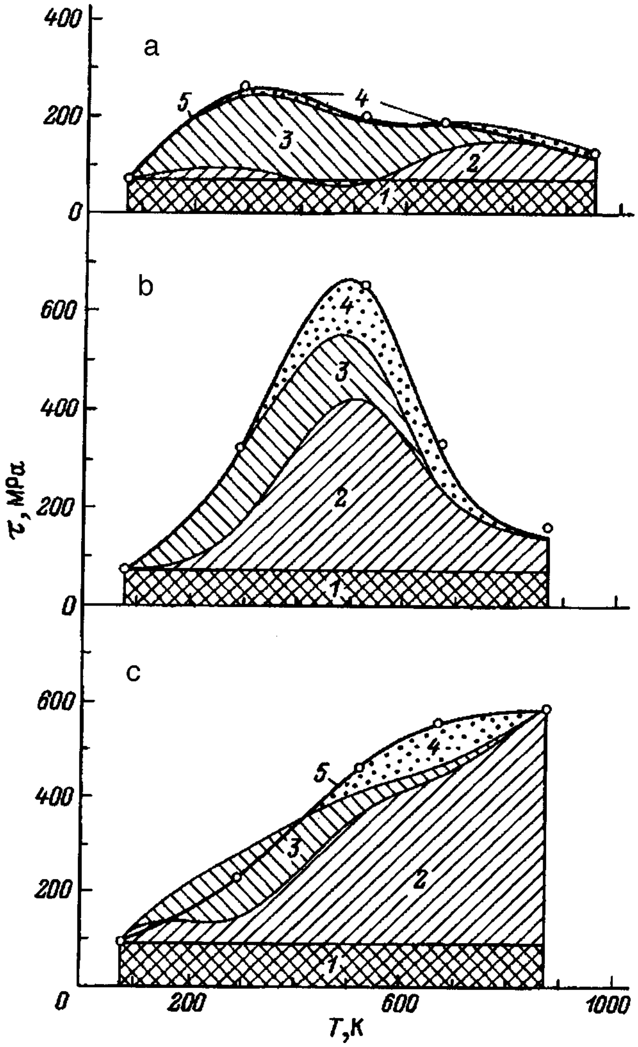

FIG. 11. Diagram of the temperature variation of contributions to the deforming stresses for various orientations of the strain axis: [234] (a), [139] (b), and [001] (c). *1*—shear stresses corresponding to the temperature of boiling nitrogen (the temperature-independent part of the shear stresses) $\tau_\varepsilon(T_0)$, $\varepsilon=5\%$, *2*—contribution caused by changes in the friction stress $\Delta\tau_F$, *3*— contribution connected with the temperature variation of the interdislocation interaction parameter $\Delta\tau_\alpha$, *4*—contribution connected with the change in dislocation pileup intensity $\Delta\tau_\rho$, *5*—total resistance to strain $\tau_\Sigma=\tau_\varepsilon(T_0)+\Delta\tau_F+\Delta\tau_\alpha+\Delta\tau_\rho$. The points indicate the experimental dependences of the deforming stresses on temperature.

further. A part of the decreasing function $\alpha(T)$ falls within the region where octahedral glide takes place (T=293–600 K), while the rest falls within the region of cubic glide (T>600 K).

Note in particular that in this case $\tau_F(T)$ has no maximum. The reason for this is that the temperature of the second maximum is close to that of the first, so the two maxima are not resolved. This probably is correct, since at a temperature of 973 K the quantities $\Delta\tau_F$ approximately coincide in the [234] and [139] orientations under conditions of cubic glide.

We did not investigate the [001] orientation in this work; however, the data given in Ref. 14 are enough for us to analyze by analogy with what was said above (Fig. 11c). A distinctive feature of the experiments in Ref. 14 is that the deformation was mediated by octahedral glide over the entire temperature range studied (T=77–293 K). Under these conditions, the thermal hardening is related primarily to anomalous changes in the friction stress, which increase monotonically in all temperature intervals (77–963 K). For the intensity of dislocation pileup anomalies appear beginning only at room temperature, and in the temperature range 77–293 K the pileup intensity decreases only slightly or does not increase. The parameter α is anomalous at the initial stage (as it is in other orientations) only at temperatures below room temperature, whereas at temperatures above room temperature a normal decrease with temperature is observed. The second peak in the function $\tau_F(T)$ is not observed, and in the temperature range 600–700 K the curvature of the function $\tau_F(T)$ is observed to decrease, which could indicate the hidden presence of a second peak and its indirect effect on the function $\tau_F(T)$.

The regularities we have observed in our study of the dislocation structure of Ni_3Ge single crystals with various orientations, and their analysis, lead us to certain conclusions and assumptions regarding the mechanisms for thermal hardening in alloys with $L1_2$ superstructure.

Most importantly, this involves the Kira-Wilsdorf mechanism, which is traditionally assumed to be the primary and most often the only mechanism for thermal hardening. The facts we have observed require critical examination of this mechanism. First of all, there is the impossibility of understanding the evolution of a dislocation structure in the regime of high-temperature thermal hardening, where the anomalies produce their strongest effects even as the edge dislocation configurations that are characteristic of Kira-Wilsdorf barriers are being displaced by bent dislocations: in some cases, the fraction of linear dislocations does not exceed 5% in the range where the temperature anomaly has its maximum. This compels us to view arguments that the Kira-Wilsdorf mechanism plays the decisive role in the high-temperature region skeptically. In contrast, the low-temperature region of thermal hardening, and also the range of medium temperatures where diffusion processes have not yet developed, give evidence that effects connected with the formation of Kira-Wilsdorf barriers are operating. Here an increase in the density of linear dislocations is observed, along with an anomalous change in the interdislocation interaction parameter, and the intensity of dislocation pileup can be explained by the process of forming Kira-Wilsdorf barriers.

In order to understand the evolution of a dislocation structure in the high-temperature region it is necessary to take into account the effect of temperature as a factor that activates the processes of diffusion and self-diffusion, and consequently the processes of interaction of point defects with dislocations. Only by viewing the processes of edge dislocation creep as processes of diffusive self-interlocking of superdislocations can we understand such facts as the absence of linear dislocations in the neighborhood of the high-temperature peak of the anomalies, the low mobility of edge dislocations under cubic glide, and the anomalous dependence of the yield stress and dislocation pileup intensity under cubic glide in the high- temperature range.

The regularities we have identified in this paper allow us to assert that thermal hardening is determined by at least two kinds of mechanisms: those connected with the transverse glide of screw superdislocations which, in the final analysis, are a consequence of changes in the structure of the superdislocation core brought about by temperature, and those connected with the creep of edge superdislocations due to their interaction with point defects of various kinds.

This does not imply that mechanisms belonging to other classes, e.g., the appearance of long-range order, relaxation of antiphase boundaries, the formation of an atmosphere, etc., do not occur in thermal hardening. However, the majority of the features of dislocation-structure evolution that we have identified in the present work can be understood by postulating the existence of mechanisms in just two classes, which are manifest to different degrees in various temperature ranges.

[1] C. Lall, S. Chin, and D. P. Pope, Metall. Trans. A **10**, 1323 (1979).

[2] D. P. Pope and S. S. Ezz, Int. Met. Rev. **29**, 136 (1984).

[3] S. Takeuchi and E. Kuramoto, J. Phys. Soc. Jpn. **31**, 1282 (1971).

[4] F. E. Heredia and D. P. Pope, Acta Metall. **39**, 2027 (1991).

[5] M. S. Kim, S. Hanada, S. Watanabe, and O. Isumi, Acta Metall. **36**, 2967 (1988).

[6] Y. Liu, T. Takasugi, and O. Isumi, Philos. Mag. **59**, 401 (1989).

[7] V. A. Starenchenko, V. S. Kobytev, L. A. Teplyakova, and L. E. Popov, Fiz. Met. Metalloved. **47**, 188 (1979) [in Russian].

[8] R. J. Taunt and B. Ralph, Philos. Mag. **30**, 1379 (1974).

[9] D. Caillard, N. Clement, and A. Court, Philos. Mag. **58**, 263 (1988).

[10] A. Korner, H. P. Karntaler, and C. Hitzenberger, Philos. Mag. **56**, 73 (1987).

[11] Y. Liu, T. Takasugi, and O. Isumi, Philos. Mag. **59**, 437 (1989).

[12] A. E. Staton-Bevan, and R. D. Rawlings, Philos. Mag. **32**, 787 (1975).

[13] N. A. Koneva, V. F. Esipenko, E. V. Kozlov, and A. S. Taĭlashev, Izv. vuzov. Fizika No. 11, 118 (1975) [in Russian].

[14] Yu. A. Abzaev, V. A. Starenchenko, N. A. Koneva, Izv. vuzov. Fizika No. 3, 65 (1987) [in Russian].

[15] K. Aoki and O. Izumi, J. Mater. Sci. **13**, 2313 (1978).

[16] V. A. Starenchenko, Yu. V. Solov'eva, Yu. A. Abzaev, V. I. Nikolaev, V. V. Shpeĭzman, and B. I. Smirnov, Fiz. Tverd. Tela (St. Petersburg) **38**, 3050 (1996) [Phys. Solid State **38**, 1668 (1996)].

[17] V. A. Starenchenko, Yu. A. Abzaev, Yu. V. Solov'eva, and E. V. Kozlov, Fiz. Met. Metalloved. **79**(5), 23 (1995) [in Russian].

[18] E. V. Kozlov and N. A. Koneva, *Structural Levels of Plastic Deformation* (Nauka, Novosibirsk, 1990) [in Russian], 255 pp.

[19] P. Veyssiere and G. Saada, *The Nabarro series ''Dislocations in Solids''* V. 10 (1996), p. 154.

Translated by Frank J. Crowne

PHYSICS OF THE SOLID STATE VOLUME 40, NUMBER 4 APRIL 1998

Changes in the discontinuous creep of a polymer composite brought on by weak stress and magnetic fields

N. N. Peschanskaya, P. N. Yakushev, and A. B. Sinani

A. I. Ioffe Physicotechnical Institute, Russian Academy of Sciences, 194021 St. Petersburg, Russia

(Submitted October 23, 1997)
Fiz. Tverd. Tela (St. Petersburg) **40**, 681–683 (April 1998)

Using precision interferometric methods, we were able to record changes in the characteristics of discontinuous creep of glassy polymers brought on by preliminary treatment with weak external fields. For the example of a polymer composite we have shown that the long-period application of small loads and a constant magnetic field greatly reduces the nonuniformity of the creep rate at large stresses, i.e., it decreases the suddenness of abrupt deformations. After separating the effects of the magnetic and force fields, we concluded that the effects resulting from not only stress but also magnetic fields have partially reversible character. Our data confirm that a constant magnetic field affects the local potential barriers that inhibit strain in nonmagnetic materials. © *1998 American Institute of Physics.* [S1063-7834(98)02104-2]

In recent years interest has revived in the question of how constant magnetic fields affect the mechanical properties of nonmagnetic materials such as polymers.[1] Such effects are explained by the high anisotropy of the diamagnetic susceptibility of polymer chains. In Refs. 2–4 it was demonstrated that a constant magnetic field can affect the creep-rate characteristics of linear polymers at temperatures below the glass temperature $T<T_g$. The results of Ref. 2 imply that at $T=300$ K, when relaxation processes in polymers are slow, the magnitude of the creep rate $\dot{\varepsilon}$ changes under the action of a weak magnetic field (2 kOe) only if the magnetic field acts on the sample for a long time. For some polymers the most sensitive characteristic is the nonuniformity of the rate h, i.e., its degree of scatter under small strain increments. When other conditions of the test are kept the same, the effect of a constant magnetic field on the degree of rate scatter is different for different polymers and depends on the magnetic susceptibility of the material.[2,4] It is assumed that the constant magnetic field smooths out local magnetic fields at those physical lattice sites which interrupt the motion of defects, thereby giving rise to discontinuous creep or a scatter of creep rates.[3] As a rule, a constant magnetic field acts to suppress the nonuniformity of the creep rate. A similar effect is observed, especially for large bodies, after preliminary exposure to small mechanical stresses. It is reasonable to assume that any decrease in suddenness of strain jumps in a sample caused by fields of any nature corresponds to smaller scatter in the hardness and longevity of the material.

In previous studies of the effect of a magnetic field on creep, the systems investigated were linear polymers in the glassy state.[2–4] However, the systems that find most widespread application in practice, composites based on hardened resins with a network-like structure, are more complicated. In such systems, a large role is played by adhesive layers between the bonding (resin) material and the filler. These materials are distinguished by nonuniform structure both at the molecular and premolecular levels.

The goal of this paper is to estimate the degree to which weak stress and magnetic fields change the discontinuous creep of a polymer composite.

1. SAMPLES AND METHOD

We studied changes in the creep rate under uniaxial compression of a composite consisting of epoxy resin and diabase powder. The average diameter of a diabase grain was 0.315 mm. The samples had a height of 6 mm and a diameter of 3 mm. The test temperature of 290 K lies in the relaxation range, which is most sensitive to changes in the structure of the adhesive layers in analogous composites.[5] We recorded the creep process using laser interferometers.[2–7] By applying a strain having a sinusoidal time dependence, we can measure the creep rate based on the beat frequency and its change, with an accuracy up to ~1% on a base strain of 0.3 μm. Before being loaded, i.e., before the creep begins, the sample is compressed by a die, which is used to test how preliminary exposure to a weak stress field σ_0 along with the constant magnetic field affects the creep. A DC magnet is incorporated into the apparatus such that a sample placed under the die is located between the magnetic poles. The axis of the sample was perpendicular to the direction of the magnetic field intensity **H**. Creep was observed when the composite was loaded by a large stress σ for a certain time ($t=20$ or 10 min); the overall deformation did not exceed 3.5%. The last 20 beats on the diagram were used to calculate the rate, and then the rate function $\dot{\varepsilon}$ was constructed from successive 0.3 μm strain increments $\Delta\varepsilon$.

Previous work has established that polymer creep is discontinuous in character, connected with the nonuniformity of the supramolecular structure.[3–7] In this paper, $\varepsilon-\Delta\varepsilon$ plots are used to calculate one of the characteristics of discontinuous creep: $h=\Sigma_{n=1}^{m}(\dot{\varepsilon}_n^{\max}/\dot{\varepsilon}_n^{\min}/m)$, where $\dot{\varepsilon}^{\max}$ and $\dot{\varepsilon}^{\min}$ are the maximum and minimum values of the rate within the n-th period of its change. The value of h is defined as the average of various trials over five periods on the same strain

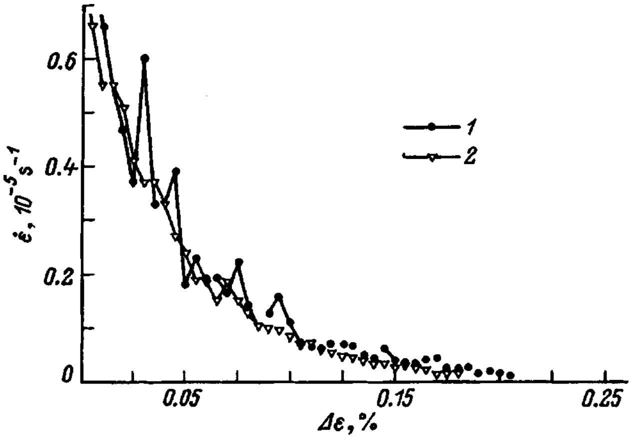

FIG. 1. Dependence of the creep rate $\dot{\varepsilon}$ on the strain increment $\Delta\varepsilon$ for the composite ED + diabase, σ=47 MPa, ε=3%, t=20 min. *1*— H=0, σ_0=0. *2* — H=2 kOe, σ_0=0.4 MPa, t_0=4 days.

interval. The value of h is investigated for creep under stresses of σ=47 and 60 MPa after various times t_0 for preliminary exposure to constant magnetic (**H**=2 kOe) and stress fields (σ_0=0.4 MPa).

2. RESULTS AND DISCUSSION

Figure 1 shows dependences of the creep rate on strain for an initial composite sample and for a sample subjected to σ_0 and **H**. It is clear from Fig. 1 that although the average creep rates of the two samples are roughly the same the original sample exhibits strong oscillations in the creep rate.

The effects of the constant magnetic field and σ_0 were further examined in more complicated tests and at larger stresses σ, sometimes on the same sample in order to exclude random differences in the rate. Creep was observed in the initial stages of the strain, where damage to the structure takes place only in local volumes and a large part of the strain (to accuracy of 0.1%) is reversible upon unloading. In Fig. 2 (curve *1*) the change in the creep rate is plotted as a function of strain for loading after 17 days exposure to a constant magnetic field and σ_0. It is clear that the scatter in the rate is small. After this test, the samples were unloaded and the procedure was repeated for the same σ but a different exposure time t_0 during which the sample was without a magnetic field ($H=0$) but still subjected to σ_0. Curve *2* in Fig. 2 shows that the rate is more nonuniform than on curve *1*, which indicates relaxation, i.e., partial recovery of the rate nonuniformity after the constant magnetic field is removed. Curve *3* in Fig. 2 corresponds to creep after the material has relaxed for a day without either the magnetic field or σ_0: the nonuniformity of the rate has become even more marked than for the original composite (Fig. 1). We used curves such as those shown in Figs. 1 and 2 obtained over the same time periods and on the same strain intervals to calculate the average value h, which characterizes the degree of rate scatter quantitatively.

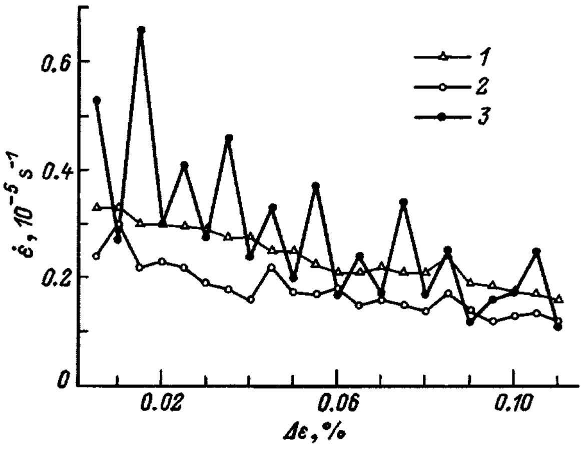

FIG. 2. Dependence of the creep rate $\dot{\varepsilon}$ on the strain increment $\Delta\varepsilon$ for the composite ED + diabase: σ=60 MPa, $\varepsilon\simeq$ 3.5%, t=10 min. *1* — H=2 kOe, σ_0=0.4 MPa, t_0=17 days, $h\simeq$ 1.15, *2* — H=0, σ_0=0.4 MPa, t_0= 20 days, h=1.35, *3* — H=0, σ_0=0, t_0=1 day, h=2.2. *2* is after regime *1*, *3* is after regimes *1* and *2*.

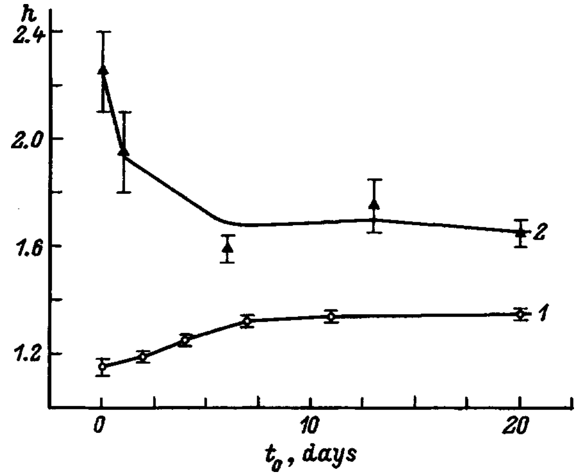

FIG. 3. Dependence of the degree of nonuniformity of the rate h on the time t_0 after removal of **H** and σ_0=0.4 MPa (*1*) and on the time t_0 in which only σ_0 acts (*2*). σ=60 MPa, ε=3.5%, t=10 min. *1* is for preliminary exposure to the constant magnetic field (17 days). The scatter in values of h is deduced from 5 measurements

It is clear from Fig. 3 (curve *1*) that during the time in which the sample is kept at **H**=0 after exposure to the constant magnetic field (but with $\sigma_0\neq 0$), the value of h first increases and then saturates, i.e., the magnetic field reduces, although slightly, the scatter in the rates. Preliminary exposure to only the stress σ_0 for a long time also decreases the nonuniformity of the rate h (curve *2*), but not as much as the combined effect of the two fields does Fig. 3, $t_0=0$).

Thus, curves *1* and *2* in Fig. 3 can be used to distinguish the effects of the fields, and allow us to conclude that both the constant magnetic field and $\sigma_0\ll\sigma$ decrease the nonuniformity of the strain rate under subsequent loading ($\sigma\gg\sigma_0$) and that the effect of both σ_0 and the constant magnetic field is relaxational in character.

The structure of the composite is nonuniform not only at the micro- but at the macroscopic level, due to granularity, the presence of pores, and defectiveness of the diabase-resin boundaries. It is possible that the mechanism by which the fields **H** and σ_0 affect the composite structure are different. For example, a long preliminary exposure to small stresses that do not cause growth of harmful cracks can result in ''healing'' of microcracks and pores as a result of local shears, whereas the magnetic field acts to smooth out and decrease the nonuniformity of local magnetic fields that make up part of the strain potential barriers. In both cases, loading with a large stress causes motion of defects according to a mechanism whereby physical sites are replaced by more uniform sites, and consequently the strain discontinuities become less sharp.[2–4] It is assumed that strain processes take place essentially in the adhesive layers of the polymer.[5]

The changes we have discussed in the creep rate affect not only strain but also crack formation during creep, which is slowed by preliminary loading. In fact, the longevity of a composite loaded with 60 MPa without preliminary exposure to either $\mathbf{H}$ or σ_0 was 50 minutes, whereas the total longevity of a sample loaded by the same stress of 60 MPa was 170 minutes after a preliminary loading with small stresses. Previous studies of the longevity of polymers have yielded similar results.[6,8] Hence, a preliminary loading with stresses that are roughly a hundred times smaller than the rupture stress significantly increases the longevity of the material due to its hardening in local volumes. An analogous effect on the material can be expected after exposure to a constant magnetic field as well.

Thus, our data confirm the possibility, in principle, that not only small stresses but also magnetic fields can affect the generation of kinetic features in the deformation of macroscopically nonmagnetic polymeric materials. In our tests the strain in the composites did not exceed 3–3.5%, i.e., within the reversible viscoelastic region. Since viscoelastic deformation is connected to localized plastic shears which do not interact with one another, our results prove experimentally that local potential barriers at the initial stage of deformation are changed by the influence of a magnetic field and that the kinetics of local shears can affect mechanical characteristics at the macroscopic level.

The authors are grateful to Yu. Khristova (Bulgarian Academy of Sciences) for providing the samples.

[1] Yu. P. Rodin, Mechanics of Composite Materials No. 3, 490 (1991) [in Russian].

[2] N. N. Peschanskaya, V. Yu. Surovova, and P. N. Yakushev, Fiz. Tverd. Tela (Leningrad) **34**, 2111 (1992) [Sov. Phys. Solid State **34**, 1127 (1992)].

[3] N. N. Peschanskaya, Fiz. Tverd. Tela (St. Petersburg) **35**, 3019 (1993) [Phys. Solid State **35**, 1484 (1993)].

[4] N. N. Peschanskaya and P. N. Yakushev, Fiz. Tverd. Tela (St. Petersburg) **39**, 1690 (1997) [Phys. Solid State **39**, 1509 (1997)].

[5] N. N. Peschanskaya, P. N. Yakushev, Yu. Khristova, and A. Toplĭska, High Molecular Weight Compounds A **35**, 1493 (1993) [in Russian].

[6] V. A. Stepanov, N. N. Peschanskaya, and V. A. Shpeĭzman, *Hardness and Relaxation Phenomena in Solids* (Leningrad, 1984) [in Russian], 245 pp.

[7] N. N. Peschanskaya, P. N. Yakushev, L. P. Myasnikova, V. A. Marikhin, A. B. Sinani, and M. Yakobs, Fiz. Tverd. Tela (St. Petersburg) **38**, 2582 (1996) [Phys. Solid State **38**, 1416 (1996)].

[8] V. V. Zhitkov, N. N. Peschanskaya, and V. A. Stepanov, Polymer Mechanics *1*, 176 (1972) [in Russian].

Translated by Frank J. Crowne

PHYSICS OF THE SOLID STATE VOLUME 40, NUMBER 4 APRIL 1998

Thermal effects and anomalies in the low-temperature plasticity of crystals

G. A. Malygin

A. I. Ioffe Physicotechnical Institute, Russian Academy of Sciences, 194021 St. Petersburg, Russia

(Submitted October 31, 1997)
Fiz. Tverd. Tela (St. Petersburg) **40**, 684–689 (April 1998)

This paper discusses theoretically the mechanism that causes the temperature dependences of the yield point and yield stress, along with their rate coefficients, to deviate from behavior characteristic of thermally activated plastic strain at low temperatures (<30 K). At this time the existence of such deviations, e.g., anomalous decreases in the values of these characteristics in this temperature range, is explained by arguing that the process whereby dislocations overcome local barriers has inertia. It is shown that the observed anomalies can be caused by the development of thermal instability in the plastic strain at low temperatures. In contrast to inertia-related effects, thermal effects allow us to explain the plasticity of crystals at low temperatures without contradiction and within the framework of a single mechanism, including the unstable, discontinuous character of plastic strain that is characteristic of these temperatures. [S1063-7834(98)02204-7]

Studies of plastic strain in crystals at low temperatures (<30 K) have found that the temperature dependences of yield stresses τ and yield points,[1–4] along with their rate coefficients $\partial\tau/\partial\ln\dot{\varepsilon}$,[5–7] are often anomalous when compared to normal plots of thermally activated plastic strain (curves *1* and *1′* in Fig. 1). Observed deviations from the standard Arrhenius form of these functions have been used as evidence[2–7] that the plateaulike anomalies (curves *2* and *2′*) on these curves are signs that dislocations are using athermal quantum mechanisms[2–6] to overcome local barriers, whereas inertia of the process by which dislocations overcome obstacles with short-range forces can explain only the sharp dropoffs that appear on these curves (curves *3* and *3′*)[8]. Like the quantum effects, inertia gives rise to a rate of plastic deformation that is higher than that associated with thermal fluctuations, and a corresponding decrease in the deforming stresses.

Although these phenomena can, in principle, be invoked to explain the anomalous form of the temperature dependences of the yield stress at low temperatures, there exist a number of factors which cast doubt on whether these mechanisms are actually present in an experiment, thereby giving rise to controversy. The doubt is based on the following facts.

Athermal plateaus are observed in the temperature dependences of yield points, but are absent in samples stressed below the yield point.[9] The situation is analogous for anomalies such as the abrupt decrease in the magnitude of the yield point as the temperature is decreased starting with some critical value of the temperature (curve *3* in Fig. 1). In Ref. 10 the authors compared the temperature dependences of the macroscopic yield point[11] and shear stresses at small plastic strain ($<10^{-4}$, trials based on internal friction[10]) in single crystals of aluminum. The temperature dependence of the shear stresses has a normal form, whereas the macroscopic yield point exhibits an anomalous decrease below 20 K.

It is clear that if they existed, quantum and inertia effects would have to appear even at the earliest stages of plastic strain, when individual dislocations interact with obstacles, but experiment shows that they are not found in the microstrain range. It is the temperature dependences of the yield point and yield stress that exhibit anomalies, i.e., regimes of intense multiplication of dislocations and the formation of slip lines and slip bands in the crystal, .

Another important fact that challenges the proposed quantum athermal character (and dislocation-induced inertial character) of plastic strain in crystals at low temperatures is the unstable nature of the strain at these temperatures: strain discontinuities develop within precisely those temperature ranges where athermal plateaus[6,12–14] or anomalous dropoffs[5,7,15,16] are observed in the temperature dependences of the yield stress and its rate coefficients. At present, there is convincing experimental[13,17,18] and theoretical[18–21] proof that the instability of low- temperature strain is caused by thermal instability as the crystal is heated by moving dislocations. This fact is not very compatible with proposed quantum athermal mechanism for the appearance of plateau-shaped segments on the temperature dependences of the yield point in the temperature range under discussion.

In discussing inertia effects as the cause of anomalies, like the sharp dropoff in the magnitude of the yield stress as the temperature decreases, it should be noted that the magnitude of this dropoff observed in experiments is tens of percent.[1,11,15,16] In quantitative terms this is in poor agreement with, e.g., the decrease in the yield stress as a result of a transition of a metal from its normal to its superconducting state, which is well studied today and known to be connected with dislocation inertia, since the magnitude of this decrease does not exceed one percent.[1]

These facts compel us to look for other mechanisms to explain the appearance of anomalies in the low-temperature plasticity of crystals. The goal of this paper is to clarify the role of thermal effects arising from heating of the strained

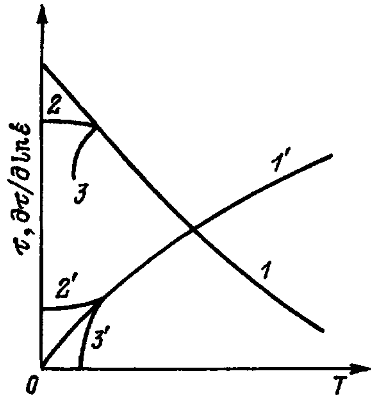

FIG. 1. Low-temperature anomalies in the temperature dependences of the yield stress τ (*2* and *3*) and sensitivity coefficient of the yield stress to the strain rate $\partial\tau/\partial \ln \dot\varepsilon$ (*2*′ and *3*′) (sketch).

crystal by plastic strain as a possible reason why the temperature dependences of the yield stress and its rate coefficients exhibit deviations such as the rapid decrease in their values after a certain critical temperature is reached (curves *3* and *3*′ in Fig. 1). In this paper we show that these deviations could be caused by thermal instability of the low- temperature strain. Previously it was demonstrated[22] that the appearance of plateau-shaped segments in the temperature dependences of the yield point and its rate coefficients (Fig. 1, curves *2* and *2*′) is connected with heating at places where the strain is localized (slip lines and slip bands). This heating does not lead to the appearance of thermally unstable strain, but it anticipates its appearance once the deforming stresses have increased further.[12]

1. THERMAL INSTABILITY OF THE STRAIN

The usual objection to the idea that thermal effects play any significant role in the appearance of low-temperature anomalies in the hardness properties is that the average bulk heating of crystals strained at low temperatures, as measured by any experimental method, are quite small. Figure 2 shows experimental data on the heating $\Delta T = T - T_0$ of single crystals of Zn[23] and Al[24] strained at different rates $\dot\varepsilon$ in liquid He^3 at temperatures $T_0 \approx 0.8 - 1.2$ K. The magnitude of the heating is determined from the shift of the critical transition temperature of the deformed crystal from superconducting to normal state with respect to the critical temperature of an unloaded sample. In the case of CsI crystals[25] strained at 4.2 K in liquid He^4, the magnitude of the heating was measured by a thermocouple. The straight lines in Fig. 2 bound the scatter region of the experimental points. Their slope is unity, which agrees with the theoretical estimate of the magnitude of steady-state heating of a sufficiently thin crystal strained with a constant rate $\dot\varepsilon$:

$$\Delta T = \frac{\beta\tau\dot\varepsilon d}{2h}. \tag{1}$$

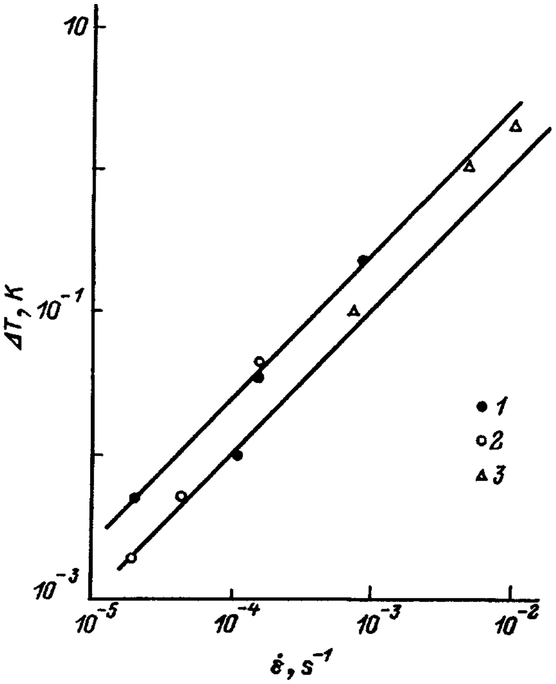

FIG. 2. Dependence of the bulk heating ΔT of the crystal on the rate of plastic strain $\dot\varepsilon$ for 0.8–4.2 K. *1* — Zn (Ref. 23), *2* — Al (Ref. 24), *3* — CsI (Ref. 25).

In accordance with the equation of heat balance

$$c\frac{\partial T}{\partial \xi} = -\frac{2h}{d}(T - T_0) + \beta\tau\dot\varepsilon, \tag{2}$$

the heating of such a crystal depends significantly on the deforming stress τ and the coefficient of surface heat transfer h as well.[25] In Eqs. (1) and (2), T and T_0 are the temperatures of the crystal and the cooling medium respectively, ξ is time, c is the heat capacity, β is the conversion coefficient of the work of plastic strain into heat, and d is a characteristic transverse dimension of the working portion of the crystal.

The magnitude of the steady-state heating of the crystal ΔT is determined by the equilibrium between the rate of dissipation of energy of plastic strain and the rate of relaxation of heat into the cooling medium. For a thermally activated type of strain, violation of this balance leads to thermal instability,[18–21] which affects the thermal activation parameters for low-temperature strain determined in the experiment and can change the form of their temperature dependences.

The criterion for thermal instability of the strain is a negative value of the effective coefficient for rate sensitivity of the yield stress[18]

$$\left(\frac{\partial \tau}{\partial \ln \dot\varepsilon}\right)_{T_0} = \frac{kT}{V}\left[1 - \left(\frac{\partial \ln T}{\partial \ln \dot\varepsilon}\right)\ln\frac{\nu}{\dot\varepsilon}\right], \tag{3}$$

where $V = -dH/d\tau^*$ is the activation volume, $H(\tau^*)$ is the activation energy, $\tau^* = \tau - \tau_0$ and τ_0 are respectively the thermal and athermal components of the yield stress, and ν is the pre-exponential factor in the expression for the rate of thermally activated plastic strain $\dot\varepsilon = \nu\,\exp(-H/kT)$. The dependence of the activation energy on the effective stress τ^* can be written in the following very general form:[26]

$$H(\tau^*)=H_c[1-(\tau^*/\tau_c)^p]^q, \tag{4}$$

where the constants H_c and τ_c and exponents p and q depend on the magnitude and nature of the local barriers that control the rate of thermally activated dislocation motion.

When the temperature of the crystal T is independent of the strain rate $\dot{\varepsilon}$, according to Eq. (4) the temperature dependences of the yield stresses and coefficient of rate sensitivity of the stresses are given by the expressions

$$\tau=\tau_0+\tau^*, \quad \tau^*=\tau_c[1-(T/T_c)^{1/q}]^{1/p}, \quad T_c=\frac{H_c}{k\ \ln(\nu/\dot{\varepsilon})}, \tag{5}$$

$$\left(\frac{\partial(\tau/\tau_c)}{\partial \ln \dot{\varepsilon}}\right)=\frac{kT}{V\tau_c}=\frac{1}{pq\ \ln(\nu/\dot{\varepsilon})}\left(\frac{T}{T_c}\right)^{1/q}\left[1-\left(\frac{T}{T_c}\right)^{1/q}\right]^{\frac{1-p}{p}}. \tag{6}$$

Whenever $\dot{\varepsilon}$ depends on T, i.e., whenever the crystal is heated by plastic strain, thermal softening of the crystal can exceed its rate hardening Eq. (6). This will lead to a negative value of the effective coefficient of rate sensitivity Eq. (3) and to a relaxation of the deforming stresses, i.e., to the appearance of a jump in the load on the stress-strain diagrams.

Taking into account the heating instability, the condition for loss of strain and thermal stability Eq. (3) can be written in the form[18]

$$\left(\frac{\partial\tau}{\partial \ln \dot{\varepsilon}}\right)_{T_0}=\frac{kT}{V}\,\frac{h/h_k+c/c_k-1}{h/h_k},$$

$$c_k=\frac{\beta\tau}{K+\chi}\left(-\frac{\partial\tau}{\partial T}\right)_{\dot{\varepsilon}}, \quad h_k=\frac{\beta\tau\dot{\varepsilon}d}{2T}\ \ln\left(\frac{\nu}{\dot{\varepsilon}}\right). \tag{7}$$

Here $\chi=d\tau/d\varepsilon$ is the coefficient of strain hardening and K is the effective modulus of the system crystal-loading apparatus. According to Eq. (7), the rate coefficient becomes negative if

$$\frac{h}{h_k}+\frac{c}{c_k}<1. \tag{8}$$

Condition (8) for thermal instability of the strain is well confirmed by experiment.[17–20]

2. THERMAL ANOMALIES OF HIGH-TEMPERATURE PLASTICITY IN CRYSTALS

For a quantitative analysis of the temperature dependence of the coefficient Eq. (7), it is more convenient to express it in the form

$$\left(\frac{\partial\tau}{\partial \ln \dot{\varepsilon}}\right)_{T_0}=\frac{kT}{V}\left[1-\left(1-\frac{c}{c_k}\right)\frac{h_k}{h}\right]. \tag{9}$$

It is also necessary to include the temperature dependences of the heat capacity and heat transfer coefficients:

$$c=\gamma_e T+c_m(T/T_D)^3, \quad h=h_m T^r, \tag{10}$$

where γ_e and c_m are the coefficients of the electronic and phonon components of the heat capacity, respectively, and T_D is the Debye temperature. The coefficient h_m and the exponent r depend on the phase state of the cooling medium. According to Eq. (7), the temperature dependences of the parameters c_k and h_k are determined by Eq. (5), the change of the stress τ with temperature, and the coefficient of temperature sensitivity of the stresses

$$\left(-\frac{\partial\tau}{\partial T}\right)_s=\frac{\tau_c}{qpT_c}\left(\frac{T_c}{T}\right)^{\frac{q-1}{q}}\left[1-\left(\frac{T}{T_c}\right)^{1/q}\right]^{\frac{1-p}{p}}. \tag{11}$$

With no loss of generality in the results, and in order to compare them with experimental data of Ref. 7, in what follows we will assume that in Eqs. (4)–(6) and (11) we have $q=3/2$, $p=1$.

In that case, substituting Eqs. (5), (6), (10), and (11) into Eq. (9), we obtain the dependence of the coefficient of rate sensitivity of the yield stresses on the crystal temperature $t=T/T_c$ in the form

$$\left(\frac{\partial(\tau/\tau_c)}{\partial \ln \dot{\varepsilon}}\right)_{T_0}=\frac{2t^{2/3}}{3\ \ln(\nu/\dot{\varepsilon})}\times\left\{1-\left[1-\frac{a_e t+a_m t^3}{1-t^{2/3}}t^{1/3}\right]\frac{(1-t^{2/3})}{a_h t^{1+r}}\right\}. \tag{12a}$$

The dimensionless parameters

$$a_e=\frac{3\gamma_e T_c^2}{2\beta\tau_c}\left(\frac{K+\chi}{\tau_c}\right), \quad a_m=\frac{3c_m T_c}{2\beta\tau_c}\left(\frac{T_c}{T_D}\right)^3\left(\frac{K+\chi}{\tau_c}\right),$$

$$a_h=\frac{2h_m T_c^{1+r}}{\beta\tau_c\dot{\varepsilon}d\ \ln(\nu/\dot{\varepsilon})} \tag{12b}$$

determine the characteristic temperature at which the temperature dependence of the rate coefficient first deviates from its normal form, and the magnitude of the deviation. The normal form of this dependence is shown by the curve *1* in Fig. 3a, which is plotted using the expression inside the curly brackets in Eq. (12a) at $T=T_0$. Curve *2* in Fig. 3a shows (for $T\approx T_0$) how the character of this dependence changes according to Eq. (12) if, at temperatures below point d, the heat capacity of the crystal c becomes smaller than a critical value c_k and begins to satisfy the adiabatic criterion $c<c_k$ for thermal instability of the strain according to Eqs. (8) and (9).

A consequence of the rate coefficient's deviation from the normal temperature dependence is the appearance of anomalies in the temperature dependences of the activation volume V and the parameter $H/kT_0=\ln(\nu/\dot{\varepsilon})$. The temperature independence of the latter results from the thermally fluctuating nature of dislocation motion. In a thermal-activation analysis of plastic strain,[26] the activation energy H

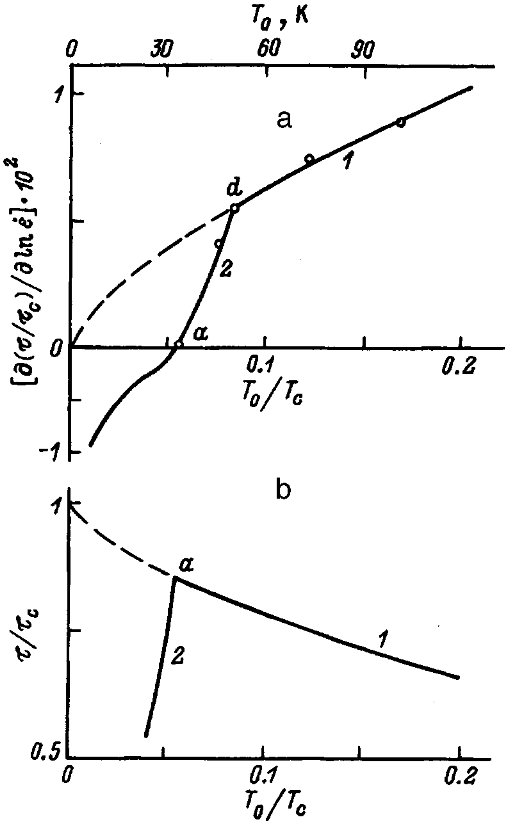

FIG. 3. Temperature dependences of the rate coefficient (*a*) and yield stress (*b*) under conditions of stable (*1*) and thermally unstable (*2*) strain. Experimental points—data from Ref. 7

and activation volume V are found from expressions whose denominators contain the coefficient for rate sensitivity of the yield stress Eq. (9). Therefore, the sharp decrease in the value of this coefficient due to heating causes an anomalous increase in the experimental values of these parameters, as the temperature at which the strain occurs decreases.[7]

The next critical point is point a on curve *2* in Fig. 3a where, according to Eqs. (8) and (9), the kinetic criterion for thermal instability of the strain $h<h_k$ begins to be satisfied. For temperatures to the left of this point the coefficient of sensitivity of the yield stress to the rate of strain becomes negative, and the strain becomes unstable and discontinuous in character. According to Eqs. (8)–(10) and (12) the critical temperature for the onset of unstable strain equals

$$T_c=\left(\frac{\beta\tau\dot{\varepsilon}d}{2h_m}\ln\frac{\nu}{\dot{\varepsilon}}\right)^{\frac{1}{1+r}}. \tag{13}$$

From relation (13) it follows that the value of the yield stress τ at which plastic deformation ceases to be stable should decrease with decreasing temperature

$$\tau=\left(\frac{2h_mT_0}{\beta\dot{\varepsilon}d\ \ln(\nu/\dot{\varepsilon})}\right)^{1+r}. \tag{14}$$

Curve *2* in Fig. 3b illustrates the deviation of the deforming stresses from the normal course of the temperature dependence of the yield stress (curve *1*) due to this fact ($r=0$).

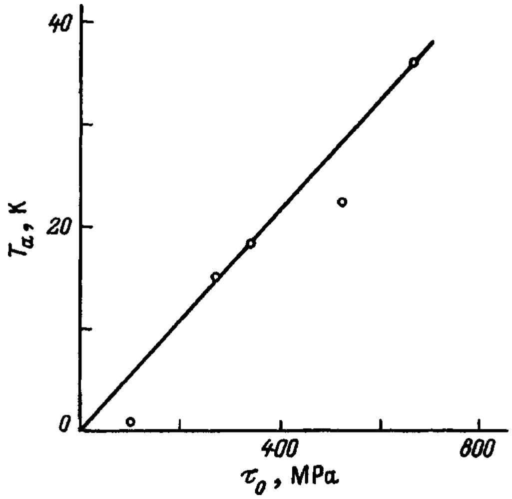

FIG. 4. Dependence of the temperature T_a of the onset of discontinuous strains in Ti–O solid solutions (Ref. 7) on the yield point τ_0 as the oxygen content increases.

3. COMPARISON WITH EXPERIMENT

The points in Fig. 3a show experimental results for the coefficient of rate sensitivity of the yield point in polycrystalline titanium containing 0.96 at. % oxygen.[7] According to Eq. (12a), with the following parameter values: $a_e=1.1$ and $a_m=3.2\times10^3$ ($\gamma_e=3.6\times10^2$ J$\cdot$m$^{-3}\cdot$K^{-2}, $c_m=2.1\times10^8$ J$\cdot$m$^{-3}\cdot$K^{-1}, $T_D=415$ K[27], $T_c=600$ K, $\tau_c=660$ MPa, $\chi \ll K$, $K=1.6\times10^3$ MPa, $\beta=0.6$), the critical temperature $T_k=0.082\ T_c$ at which this dependence deviates from its normal course (point d in curve *1*, Fig. 3a) is primarily determined by the phonon component of the heat capacity, $T_k/T_c\approx a_m^{-3/10}\sim\tau_c^{3/5}$. A decrease in the content of oxygen atoms lowers the value of the stress τ_c,[7] which causes a corresponding decrease in the critical temperature down to $T_k\approx1$ K and oxygen concentrations of 0.06 at. %.[7] At these low temperatures, the critical temperature $T_k/T_c=a_e^{-3/4}\sim\tau_c^{3/2}$ depends on the electronic component of the heat capacity.

Curve *2* (Fig. 3a) was plotted using Eq. (12) and the parameter value $a_h=11$ corresponding to values $\dot{\varepsilon}=1.4\times10^{-4}$ s^{-1}, $d=4\times10^{-3}$ m, $r=0$, $h=50$ W$\cdot$m$^{-2}\cdot$K^{-1} (helium gas blowing over the sample, see Ref. 28). The values of the remaining parameters are the same as above. Clearly the agreement between the thermal mechanism and experiment is quite satisfactory. Unfortunately, no data was given in Ref. 7 for negative values of this coefficient, but the existence of an unstable discontinuous strain in the temperature range where the latter becomes negative is specifically mentioned in the paper.

From Eq. (13) it follows that when $r=0$ the temperature at which the rate coefficient becomes zero (point a on curve *2*) should increase linearly as the deforming stress τ increases. Figure 4 shows that within the scatter of experimental data this does in fact happen. The increase in deforming stress (the yield point τ_0) is caused by an increase in the concentration of oxygen atoms contained as interstitial impurities in Ti.[7] Up to a coefficient of order unity, the slope of

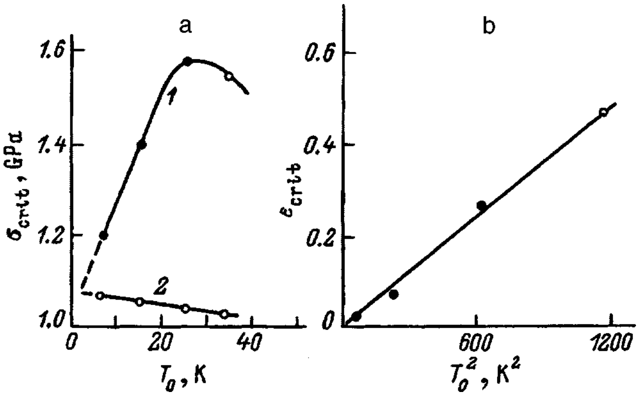

FIG. 5. Temperature dependences of critical stresses (*1a*), yield points (*2a*), and critical strains (*b*) for the onset of strain discontinuity in 326LN steel (Ref. 29).

the line coincides with the low-temperature strain parameters given above.

As a further illustration of the agreement between the thermal mechanism and experiment, Fig. 5 shows the results of processing the data of Ref. 29 on discontinuous strain in 316LN stainless steel in the temperature range 7–35 K. Curve *1* (Fig. 5a) shows that a decrease in the strain temperature causes a strong decrease in the stress σ_k at which the strain begins to be unstable as the steel is stretched, in agreement with the theoretical curve in Fig. 3b. The open circles on curve *1* indicate the temperature and corresponding stress for which no jumps in the deforming stresses are present on the tensile diagram up to rupture of the sample. The dashed continuation of curve *1* shows that further decreases in temperature should lead to the appearance of unstable strain at stresses close or equal to the yield point $\sigma_{0.2}$. Curve *2* shows the temperature dependence of this stress in the steel referred to above.[29] It is clear that when curves *1* and *2* are extrapolated into the low-temperature range, they intersect at a temperature where cooling of the sample requires liquid helium. Since the coefficient of heat transfer in liquid helium is higher than in the vapor form, this should lead to a strong increase in the stress at the beginning of the thermal strain instability. Such falloffs and rises in the deforming stresses as the temperature varies in the range 1–30 K are actually observed.[1,15,16]

It is also interesting to note that, according to the criterion for thermal instability Eq. (14), for parabolic hardening $\sigma \sim \varepsilon^{1/2}$ which is characteristic of polycrystalline samples the critical strain ε_{crit} at which the discontinuity occurs should vary with temperature like $\varepsilon_k \sim T_0^2$. It is clear from Fig. 5*b* that this actually happens.

Thus, the results of this work show that deviations from the normal Arrhenius behavior of the temperature dependence of the yield stress and its rate coefficients (and also the activation volumes V and the parameter $\ln(\nu/\dot{\varepsilon})$) observed in experiments at very low temperatures can be explained by a thermal mechanism, and do not require the inclusion of specifically inertia-related effects for this. In addition, a natural explanation has been found for the close connection between the anomalous decrease in deforming stresses, along with their rate coefficients in the temperature interval <30 K, and the development of unstable strain at these temperatures.

[1] V. I. Startsev, V. Ya. Il'ichev, and V. V. Pustovalov, *Plasticity and Hardness of Metals and Alloys at Low Temperature* [in Russian], Metallurgiya, Moscow (1975), 327 pp.

[2] E. Kuramoto, Y. Aono, K. Kitajima, K. Maeda, and S. Takeuchi, Philos. Mag. A **39**, 717 (1979).

[3] T. Suzuki, and H. Koizumi, *Dislocations in Solids. Proc. 9th Yamada Conf.*, H. Suzuki (Ed.) (Univ. Press, Tokyo, 1985), p. 159.

[4] V. V. Pustovalov, Fiz. Nizk. Temp. **15**, 901 (1989) [Sov. J. Low Temp. Phys. **15**, 497 (1989)].

[5] V. Isaev, V. V. Pustovalov, V. S. Fomenko, and S. E. Shumilin, Fiz. Nizk. Temp. **20**, 832 (1994) [Sov. J. Low Temp. Phys. **20**, 653 (1994)].

[6] V. D. Natsik, G. I. Kirichenko, V. V. Pustovalov, V. P. Soldatov, and S. E. Shumilin, Fiz. Nizk. Temp. **22**, 965 (1996) [Low Temp. Phys. **22**, 264 (1996)].

[7] V. A. Moskalenko, V. N. Kovaleva, V. D. Natsik, V. V. Pustovalov, and S. E. Shumilin, Fiz. Nizk. Temp. **22**, 1459 (1996) [Low Temp. Phys. **22**, 1108 (1996)].

[8] A. I. Landau, Phys. Status Solidi A **65**, 119 (1989).

[9] O. V. Klyavin, *Physics of the Plasticity of Crystals at Helium Temperatures* [in Russian], Nauka, Moscow (1987), 257 pp.

[10] A. B. Lebedev, J. Physique IV. Suppl. J. Physique III **6**(12), C8-255 (1996).

[11] D. A. Didenko and V. V. Pustovalov, Sov. J. Low Temp. Phys. **11**(1/2), 65 (1973).

[12] V. S. Bobrov and M. A. Lebedkin, Fiz. Tverd. Tela (Leningrad) **35**, 1881 (1993) [Phys. Solid State **35**, 939 (1993)].

[13] O. V. Klyavin, G. A. Malygin, and Yu. M. Chernov, Fiz. Tverd. Tela (St. Petersburg) **38**, 191 (1996) [Phys. Solid State **38**, 105 (1996)].

[14] G. A. Malygin, Fiz. Tverd. Tela (St. Petersburg) **39**, 1392 (1997) [Phys. Solid State **39**, 1235 (1997)].

[15] E. D. Tabachnikova, A. M. Dolgin, V. Z. Bengus, and Yu. V. Efimov, Fiz. Met. Metalloved. **88**(3), 571 (1984).

[16] S. Saji, S. Senda, and S. Hori, *Dislocations in Solids. Proc. 9th Yamada Conf.*, H. Suzuki (Ed.) (Univ. Press, Tokyo, 1985), p. 471.

[17] S. N. Komnik and V. V. Demirskii, Cryst. Res. Technol. **19**, 863 (1984).

[18] G. A. Malygin, Fiz. Met. Metalloved. **40**(3), 642 (1975); Fiz. Met. Metalloved. **63**(5), 864 (1987).

[19] L. P. Kubin and Yu. Estrin, Cryst. Res. Technol. **19**(6), 853 (1984).

[20] G. A. Malygin, Fiz. Met. Metalloved. **81**(3), 5 (1996).

[21] M. Zaiser and P. Hahner, Phys. Status Solidi B **199**, 267 (1997).

[22] G. A. Malygin, Fiz. Tverd. Tela (St. Petersburg) **39**, 2019 (1997) [Phys. Solid State **39**, 1806 (1997)].

[23] I. V. Gektina, F. F. Lavrent'ev, V. V. Pustovalov, and S. E. Shumilin, Fiz. Nizk. Temp. **13**, 1025 (1987) [Sov. J. Low Temp. Phys. **13**, 583 (1987)].

[24] I. N. Kuzmenko, O. A. Palagina, and V. V. Pustovalov, Phys. Status Solidi A **74**, 51 (1982).

[25] A. V. Nikiforov and O. V. Klyavin, Fiz. Tverd. Tela (Leningrad) **18**, 1167 (1976) [Sov. Phys. Solid State **18**, 672 (1976)].

[26] U. F. Kocks, A. S. Argon, and M. F. Ashby, Prog. Mater. Sci. **19**, 159 (1975).

[27] *Handbook of Physical Quantities* [in Russian], Energoatomizdat, Moscow (1991), 1232 pp.

[28] Yu. Estrin and K. Tangri, Scr. Metall. **15**, 1323 (1981).

[29] B. Obst and A. Nyilas, Mater. Sci. Eng., A **137**, 141 (1991).

Translated by Frank J. Crowne

PHYSICS OF THE SOLID STATE VOLUME 40, NUMBER 4 APRIL 1998

Nonmonotonic creep in LiF crystals containing Mg

V. V. Shpeĭzman, N. N. Peschanskaya, and B. I. Smirnov

A. I. Ioffe Physicotechnical Institute, Russian Academy of Sciences, 194021 St. Petersburg, Russia

(Submitted November 3, 1997)
Fiz. Tverd. Tela (St. Petersburg) **40**, 690–693 (April 1998)

Precision measurements of the creep rate using interferometric recording of the process in LiF crystals containing 0.002 to 0.03 wt % Mg using interferometric recording of the process show that nonmonotonic episodes in the form of alternating segments with relatively high and low creep rates periodically appear against a background of overall creep attenuation. The accumulation of creep strain takes place mostly on the segments with increased rates, which causes kinks to appear in the creep curve that are noticeable when shifts are resolved at a level of fractional microns. Measurements were made of the height of steps L based on ''rate-strain increment'' curves for stresses smaller and closer to the yield point. Increasing the stresses causes the value of L to fall off, while increasing the Mg content causes it to increase. It is proposed that the nonmonotonic behavior of creep is connected with structural nonuniformity of the material, which is determined by the impurity content and the nonuniformity of the strain process itself. For small strains in the neighborhood of the yielding area, where strain comes about as a result of a broadening of a pre-existing slip band, the impurity atoms enhance the nonuniformity of the strain (L increases). As the strain (stress) increases, L decreases, which corresponds to a smoothing out of the nonuniformities. It is emphasized that the step-like character of the strain accumulation is a general property. © *1998 American Institute of Physics.* [S1063-7834(98)02304-1]

The well-known nonuniformity of plastic strain observed in a multitude of microscopic studies is caused by nonuniformity of the material structure and of the strain process itself. Traditional methods for recording strain curves or creep usually do not reveal the localized character of the generation of displacements (other than cases of macrolocalization, for example, at helium temperatures, high loading rates, etc.), thereby contradicting the view that the process evolution is significantly nonuniform.[1] In recent years papers have begun to appear in which the nonuniformity of the strain is demonstrated by using high-resolution apparatus to measure its macroscopic characteristics. In Ref. 2, we observed a manifestation of strain nonuniformity at its initial stages in the form of kinks on the loading curves (peaks in the rate) for various materials at stresses considerably below the yield point. Here the strain rate turns out to be nonmonotonic both at the yield area and close to it in the range of plastic flow. In Refs. 3 and 4, Peschanskaya *et al.* demonstrated the discontinuous character of the accumulation of overall creep strain in polymers, while in Ref. 5 Gol'denberg *et al.* observed a strain nonuniformity in studies of the relaxation of stresses in whisker NaCl crystals. By using laser interferometry, we were able to record in Refs. 2–4 small translations, thereby revealing the nonuniformity at the micron level, and study regularities in the development of strain discontinuities in polymers.[3,4]

In this paper we investigate strain nonuniformity of short-time creep in LiF single crystals. The measurements were made by interferometry, allowing us to analyze the strain at the mesoscopic level, i.e., strains that are close in value to the local shears that may describe a single translation of a mesostructural defect (slip bands, grain boundaries or blocks, and also any other stable dislocation clusters). Defects of this kind and their contribution to the strain are suitable for observation in an optical microscope. We studied how the characteristics of strain nonuniformity are affected by the magnitude of stresses and the impurity concentration. For information about the latter, we studied the behavior of LiF single crystals with varying concentrations of Mg.

1. EXPERIMENTAL METHOD

In this paper we used three LiF single crystals differing in their Mg concentration ($c = 0.002$, 0.007, and 0.03 wt %). The single crystals were grown by the Kiropoulos method and annealed at a temperature of 1020 K for 48 hours with subsequent cooling at a rate of 5 K/hour. From these crystals we extracted samples with dimensions $4 \times 4 \times 10$ mm along the $\{100\}$ cleavage planes. The samples were loaded in uniaxial compression along the $[001]$ direction, and the experiments were done at room temperature.

The interferometric method used in this paper, in which the time history of the strain is recorded in the form of successive beats,[3,4] makes it possible to measure the strain rate based on small increments of sample length l with an error of less than 5%. One beat on the interferogram equals a strain increment $\Delta l_0 = 0.3\ \mu$m. Figure 1a shows an example of a creep curve, whose ordinate $\varepsilon = \Delta l / l$ corresponds to the number of oscillations on the interferogram. In order to clarify the periodic change in the creep rate, i.e., the strain steps, we chose a certain segment of the creep on which the rate was measured at successive equal-strain increments Δl_0

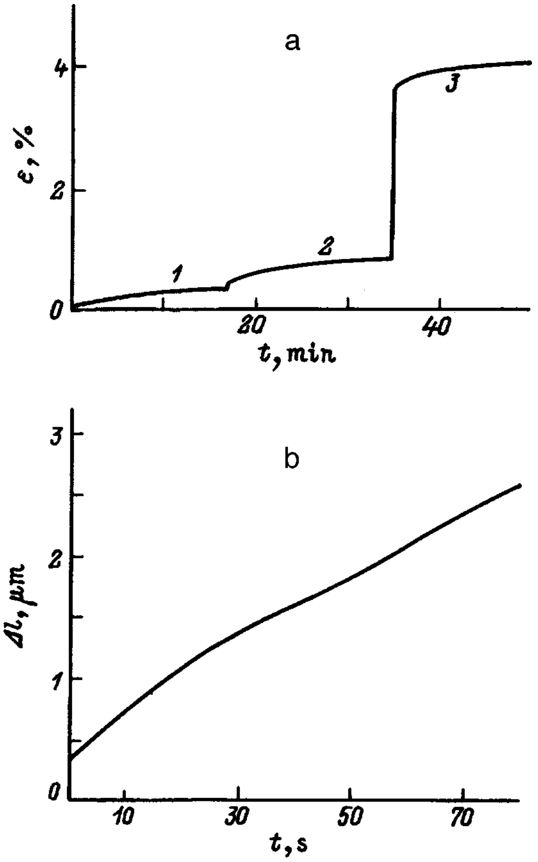

FIG. 1. Creep curve for the LiF sample with 0.007 wt % Mg for stresses $\sigma = 6$ (*1*), 7 (*2*) and 12 MPa (*3*) (a) and the initial segment of the creep in region (*1*) (b).

equal to 0.15 or 0.3 μm. Then dependences of the rate are plotted from the strain increments (multiples of Δl_0). In Refs. 3 and 4 the periods L of oscillations in the rate as functions of the strain equal the magnitudes of the strain discontinuities (heights) defined as the product $L = n\Delta l_0$, where n is the number of measurements of the rate within the given period. In this paper we take twice the average deviation of the experimental points from a curve found by least-squares fitting the creep behavior, i.e., the mean-statistical strain step, as the strain characteristic of the nonuniformity. This step is the elementary discontinuity of the deformation at the mesolevel.

2. RESULTS OF EXPERIMENTS AND DISCUSSION

The creep curves $\varepsilon - t$ taken for one sample (LiF with 0.007% Mg) at three different stresses σ and plotted using the ''macroscale'' that is customary for creep, where t is the time, do not exhibit any strain nonuniformity (Fig. 1a). In Fig. 1b the initial part of segment *1* of the creep curve is shown on a scale that allows us to resolve micron translations. It is clear that the accumulation of strain does not decay smoothly, but rather decreases in a stepwise manner with differing rates; segments with increased rate appear against a background of overall slowing-down of the creep. This effect is even more marked when we consider the strain or temporal dependences of the strain rate $\dot{\varepsilon}$.

In Fig. 2 we show examples of segments of the creep curves for various stresses in crystals with varying Mg content in the form of ''strain rate ($\dot{\varepsilon}$)—strain magnitude (Δl)'' plots. The results offer striking evidence of the nonequilib-

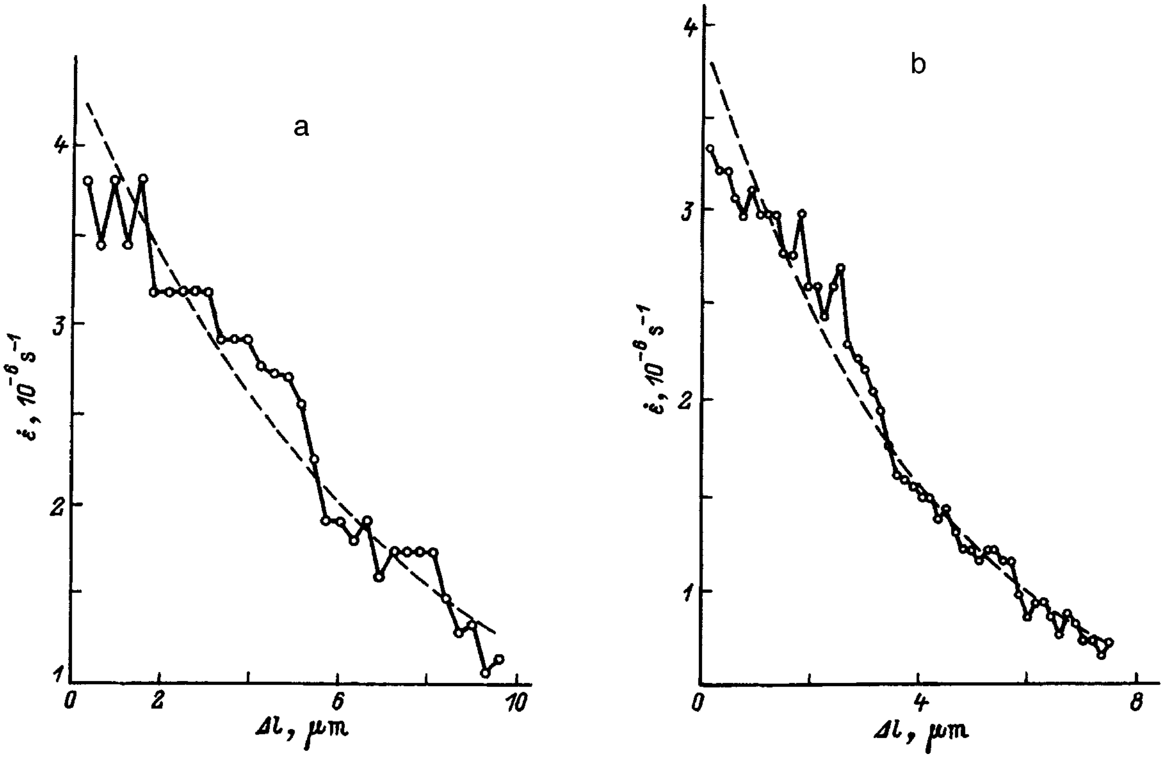

FIG. 2. Dependence of the creep rate on strain for LiF with 0.007% Mg at a stress of 7 MPa (a) and LiF with 0.002% Mg at a stress of 6 MPa (b). The open circles are experimental data; the dashed curve is averaged.

TABLE I. Values of the coefficient B in (2)

Mg content, wt %	Stress, MPa 6	7	12	42
0.002	2300	2830	3270	–
0.007	1310	1310	1590	–
0.03	–	–	–	1470

rium nature of the strain, i.e., nonmonotonic changes in the rate and discontinuous time dependences of the strain magnitude and strain rate. Note that the jumps in the strain rate considerably exceed the measurement error, so that their appearance is not due to methodological causes. We used the method of least squares to calculate and plot an analytic dependence based on these experimental points (a linear relation between $\ln\dot{\varepsilon}$ and ε or Δl), which is equivalent to the assumption that the creep attenuation follows a logarithmic law. In fact, if we follow a multitude of studies of low-temperature creep (see, e.g., Ref. 6), and use a logarithmic function for the time dependence of the creep strain

$$\varepsilon\approx\varepsilon_0+\alpha\,\ln(\beta t+1), \tag{1}$$

where ε_0, α, and β are constants, then it is not difficult to obtain

$$\ln\dot{\varepsilon}=A-B\varepsilon \tag{2}$$

(here $A=\ln(\alpha\beta)+\varepsilon_0/\alpha$, $B=1/\alpha$). Our calculations show that A changes only slightly as the stress and Mg content are varied, while the coefficient B regularly increases with increasing stress and decreases with increasing Mg concentration (see Table I).

In dislocation models of creep, a dependence of the strain rate on strain magnitude appears when we treat the activation energy for creep U as a function of stress, and replace the latter by the product $h\varepsilon$, where h is the hardness coefficient. In this case it turns out that $B=hV/kT$ (where V is the activation volume, k is Boltzmann's constant, and T is the temperature). The increase of B with increasing stress can be connected with an increase in the mean free path of the dislocations and consequently an increase in V (we can neglect changes in h for small strain increments). Impurities probably decrease this range. Without insisting on the explanations we propose, we note that a general inadequacy of such treatments is the use of a picture of some ''average'' dislocation whose properties determine the macroscopic strain in the sample. And although the quantity B listed in Table I corresponds to appropriate values of h and V and agrees with those given in the literature,[6] a creep analysis that uses characteristics at the microlevel is in this case not very informative. In particular, we do not find in it any reflection of the oscillations in the strain rate during the creep process.

Let us introduce the following characteristic of the creep nonuniformity: $L=(2/m)\,\Sigma_{l=1}^{m}|\Delta l_{\mathrm{exp}}-\Delta l_{\mathrm{cal}}|_i$, where the summation runs over all m points on the curve $\dot{\varepsilon}(\Delta l)$, while Δl_{exp} and Δl_{cal} are the experimental values of the strain and those calculated from the smooth curve respectively. Figure 3 shows the dependence of L on the stress σ for LiF with 0.002 and 0.007% Mg. Since we have chosen segments of the creep curves with roughly equal rates, the increase in the stress shown in Fig. 3 also corresponds to an increase in the strain (from 1.5% at 6 MPa to 7.1% at 15 MPa). The decrease of L with increasing stress (or strain) attests to equalization of the creep rates, which is probably associated with the high uniformity of the strained structure and a decrease in the degree of localization of the strain, i.e., the inclusion of a larger and larger number of locations in the strain. Thus, strain hardening leads, as shown in Fig. 3, to a decrease in the value of L. We obtained the opposite result when we analyzed how doping affects the strain nonuniformity parameter L in the case of hardening (Fig. 4). The change in L with Mg content was plotted under single-variable experimental conditions: identical strain (around 4%) and stresses close to the yield point (7, 12, and 42 MPa for LiF crystals with 0.0024, 0.007, and 0.03% Mg, respectively). The increase of L with increasing Mg concentration is probably related to the fact that the distribution of Mg in the crystal causes an additional nonuniformity of the strain and enhances its localization. Our picture is that depending on the type of impurity, the way it is introduced, and the thermal processing, the

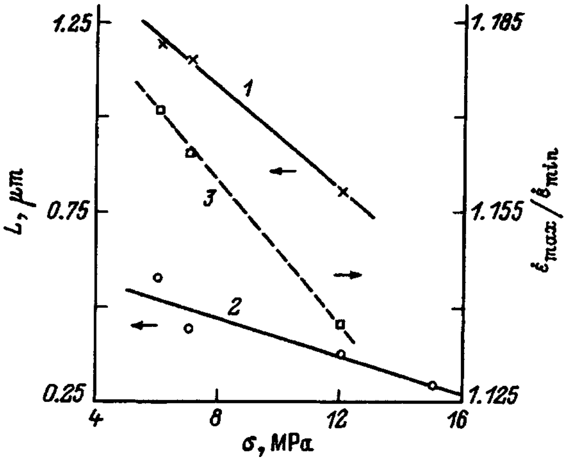

FIG. 3. Dependence of the mean-statistical characteristics of the strain nonuniformity L (*1, 2*) and ratio of maximum to minimum strain rates at a step (*3*) on stress for LiF with 0.007% Mg (*1, 3*) and 0.002% Mg (*2*).

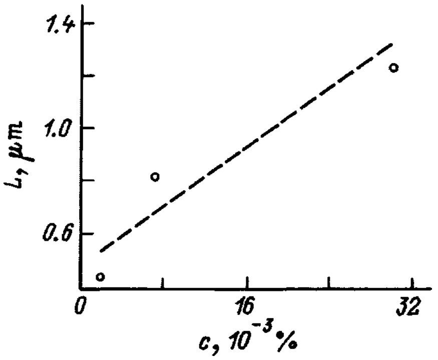

FIG. 4. Effect of Mg content on the nonuniformity of the strain at stresses close to the yield point (7, 12, and 42 MPa for LiF with 0.002, 0.007, and 0.03% Mg respectively).

value of L will change and consequently we can judge from it how nonuniform the impurity distribution is and how it affects the strain.

The values of L obtained in this paper lie in the range 0.4–1.2 μm. For LiF single crystals this number is close in value to the width of the boundary of the slip band.[1] We can assume that the strain is determined by processes in these near-boundary zones (for example, broadening of the slip band). In Ref. 1, Smirnov showed within the range of variation of experimental conditions that the strain takes place by motion of the edge of the slip band (widening of the band) while keeping the magnitude of the shear in the band constant. The size of the boundary zone for these experiments did not exceed 2 μm in the interference microscope, which does not contradict the treatment of the results given here. Our new strain characteristic, which describes its nonuniformity, allows us to construct a model of the strain and thereby identify the boundary itself or some part of it as an individual element of the structure and treat its translation as a whole.

Since the shear γ is constant in the slip band at the initial stages of the strain,[1] the value of the axial translation Δl resulting from motion of the boundary of the band can be defined as $\gamma s/\sqrt{2}$, where s is the average displacement of the boundary in the direction perpendicular to its plane. Using this expression we can try to explain why L increases with doping. In fact, γ increases linearly as we increase the yield point by adding Mg, with a coefficient of proportionality of 1×10^{-3} MPa^{-1}.[1] For the crystals used in this work the yield points (axial stresses) were 7, 12, and 42 MPa; taking this into account, we find that L increases with increasing yield point with a coefficient of 2×10^{-2}MPa^{-1} (Fig. 4). Consequently, we cannot explain the increase in L with doping by only one increase in the value of the shear in the slip band. Thus, the decrease in L with increasing stress (strain) and the increase of L with Mg addition (if the comparison is made at the yield point for similar values of the strain) must be connected with changes in the magnitude of the elementary displacement of the boundary of the shear band. The influence of the degree of strain can be explained by the convergence of neighboring bands and by equalization of the local shears along the length of the sample, whereas impurities obviously enhance the nonuniformity of the strain by creating additional obstacles for nucleation and development of slip bands.

Note that the changes in the strain rate within a single strain jump were rather small: the change in the ratio $\dot{\varepsilon}_{\max}/\dot{\varepsilon}_{\min}$ did not exceed 1.65, while its dependence on stress and degree of doping repeated the analogous dependences for L (see curve *3* in Fig. 3). These results are a consequence of the good match between the data and the logarithmic-law approximation in our case. In other cases, for example for creep steady-state, where our method of estimating L is presumably unsuitable, we can use the methods described in Refs. 3 and 4 to analyze the nonequilibrium nature of the rate, which give independent values of the ratio of rates and the strain-induced characteristic of the strain nonuniformity.

Thus, in this paper we have proposed a new method for analyzing the strain at the mesoscopic level and a new characteristic for it—the time dependent nonuniformity of the strain L. The latter is introduced as the average swing of the strain oscillations as they deviate from the presumed linear dependence $\ln\dot{\varepsilon}-\varepsilon$. As a result, we have shown that in LiF crystals with Mg impurities the value of L decreases with increasing strain (stress) and increases with increasing Mg content. We have assumed that L, whose value changes in our experiments from 0.4 to 1.2 μm, is determined by the displacement of slip-band boundaries as they grow broader. This process, which is well known from data on structural investigations, gives the primary contribution to the strain at its initial stages.

[1] B. I. Smirnov, *Dislocation Structure and Hardness of Crystals* [in Russian], Nauka, Leningrad (1981), 235 pp.

[2] V. A. Shpeĭzman, N. N. Peschanskaya, and V. A. Stepanov, Fiz. Tverd. Tela (Leningrad) **26**, 2387 (1984) [Sov. Phys. Solid State **26**, 1446 (1984)].

[3] N. N. Peschanskaya and P. N. Yakushev, Fiz. Tverd. Tela (Leningrad) **30**, 2196 (1988) [Sov. Phys. Solid State **30**, 1264 (1988)].

[4] N. N. Peschanskaya, High Molecular Weight Compounds A **31**, 1181 (1989) [in Russian].

[5] S. U. Gol'denberg and O. D. Khlebnikov, Fiz. Tverd. Tela (Leningrad) **32**, 1226 (1990) [Sov. Phys. Solid State **32**, 720 (1990)].

[6] J. Weertman and J. R. Weertman, in *Physical Metallurgy*, Vol. 3, R. W. Cahn (Ed). (North-Holland Publ. Co., Amsterdam, 1965) [Russ. trans., *Physical Metallography*, Vol. 3, Mir, Moscow, 1968].

Translated by Frank J. Crowne

PHYSICS OF THE SOLID STATE VOLUME 40, NUMBER 4 APRIL 1998

MAGNETISM AND FERROELECTRICITY

Effect of stabilization processes on NMR signals from 180° domain boundaries in cubic ferrite-garnet crystals

I. V. Vladimirov, R. A. Doroshenko, S. V. Seregin, and R. S. Fakhretdinova

Institute of the Physics of Molecules and Crystals, Russian Academy of Sciences, 450075 Ufa, Russia

(Submitted September 15, 1997)
Fiz. Tverd. Tela (St. Petersburg) **40**, 694–698 (April 1998)

Numerical methods were used to study the effect of stabilization processes on the line shape of NMR signals from 180° domain walls in cubic ferrite-garnet crystals, taking into account the structural change of the boundaries as they shift quasistatically in a magnetic field. The dependences of the amplitude of absorption maxima on the induced anisotropy constants and the amplitude of the external magnetic field are analyzed. *© 1998 American Institute of Physics.* [S1063-7834(98)02404-6]

Up to now, analysis of NMR signals from nuclei localized within domain walls in magnetically ordered crystals has been done only for materials with spatially uniform parameters determining the structure of the boundary. In this case it is assumed[1,2] that the domain boundary structure does not change as it moves in the radio-frequency AC magnetic field, and coincides with the structure of a domain boundary at rest. However, stabilization of domain boundaries, i.e., pinning of domain boundaries at defects in the crystal structure which disrupt the spatial uniformity, leads to a dependence of the domain wall structure on its position in space.

In this paper we investigate the effect of stabilization processes on the line shape of NMR signals from 180° Bloch domain walls in cubic crystals with mixed magnetic anisotropy. We discuss the dependence of the domain-wall NMR line shape on the value of the induced anisotropy constant and the amplitude of the AC magnetic field. NMR signals from domain walls are calculated numerically, taking into account the change in domain wall structure as the wall moves quasistatically in the magnetic field.

The presence of stabilization makes it necessary to include terms in the energy density of the domain wall that explicitly depend on the spatial coordinates. Therefore, it is impossible to describe the structure of a stabilized domain wall by an analytic expression. In order to calculate the structure of a domain wall we used the method proposed in Ref. 3. The essence of this method is to expand the equation that describes rotation of the magnetization vector in a one-dimensional magnetic nonuniformities

$$\varphi'' - f(y,\varphi,\varphi') = 0 \tag{1}$$

in a Taylor series near its approximate solution in the form

$$\varphi''_{n+1} - \left(f(y,\varphi_n,\varphi'_n) + \frac{\partial f(y,\varphi_n,\varphi'_n)}{\partial \varphi}(\varphi_{n+1}-\varphi_n) \right) = 0, \tag{2}$$

where φ_n is an approximate solution to the equation. Representing derivatives in the form of finite differences, we obtain a system of linear algebraic equations with a tridiagonal matrix, which is solved by the method of cyclic reduction. The solution obtained is a distribution of directions for the magnetization vector in the domain wall. The directions of the magnetization within the domains coincide with the [111] and [111] directions respectively, i.e., the boundary conditions for the problem have the form $\varphi(-\infty)=0$, $\varphi(+\infty)=\pi$, and $\varphi'(\pm\infty)=0$. Since the domain wall is (110), we must include the following terms in the energy density of the domain wall: the cubic anisotropy energy ($K_1 < 0$) and the uniaxial anisotropy (K_u), which lifts the degeneracy of the cubic axes (with an axis of symmetry along [111]), the exchange energy (A), the energy of the external magnetic field that translates the domain wall (h^*), and the induced anisotropy energies (F, G):

$$\begin{aligned} e_{DW}/K_u = & -q\left(\frac{\sin^4\varphi}{4} + \frac{\cos^4\varphi}{3} - \frac{\sqrt{2}}{3}\sin^3\varphi\cos\varphi \right) \\ & + \sin^2\varphi - h\cos\varphi + a(\varphi')^2 \\ & - f\sum_i \alpha_i^2\beta_i^2 - g\sum_{i\neq j}\alpha_i\alpha_j\beta_i\beta_j , \end{aligned} \tag{3}$$

where $q=|K_l|/K_u$, $h=h^*/K_u$, $a=A/K_u$, $f=F/K_u$, $g=G/K_u$, α_i are the direction cosines of the magnetization vector, β_i are direction cosines of the magnetization vector in the original domain wall (i.e., before stabilization), and φ is the angle measured from the direction [111] and describing rotation of the magnetization vector in the domain wall.

The solutions obtained allow us to determine the effect of induced anisotropy and magnetic field on the domain wall structure. We will discuss two limiting cases: 1) the cubic anisotropy is small compared to uniaxial, i.e., $q\rightarrow 0$ (a pseudo-uniaxial crystal), and 2) the uniaxial anisotropy is small compared to the cubic ($q \gg 1$). In addition to the dependences on q, the component of induced anisotropy with

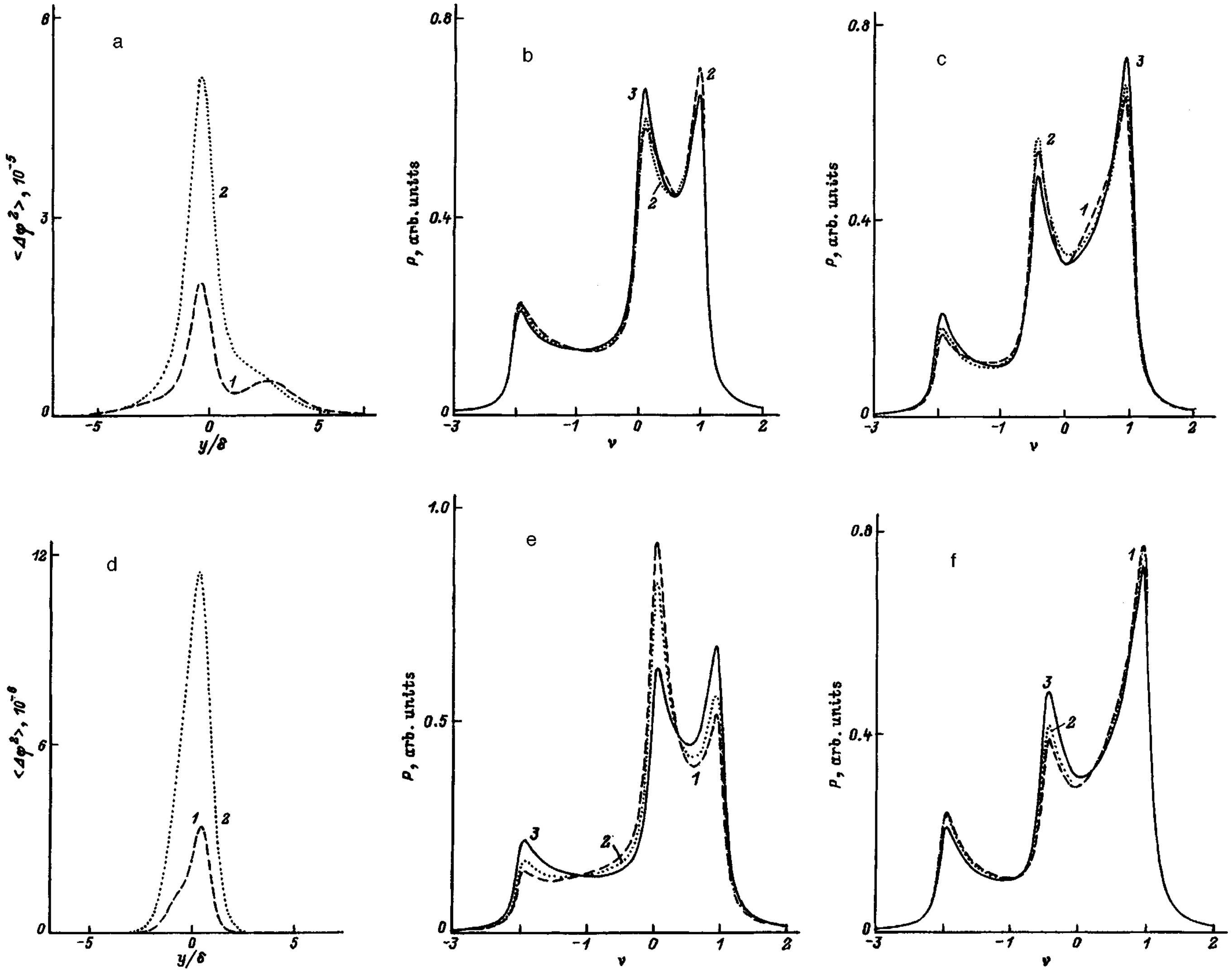

FIG. 1. Change in the square of the enhancement coefficient $\langle \Delta\varphi^2 \rangle$ over the thickness of the domain wall (a,d) and NMR absorption line shape of a domain wall for $q=0$, $h=0.01$ in the octahedral positions (b,e) and tetrahedral positions (c,f). Curves a–c were computed when $g=0$ for $f=5$ (*1*), 3 (*2*), and 0.1 (*3*), curves d–f when $f=0$ for $g=10$ (*1*), 5 (*2*), 0.1 (*3*).

constant F leads to pinning of segments of the boundary with spin direction along the crystallographic directions $\langle 100 \rangle$ and to a lesser extent $\langle 110 \rangle$ during stabilization of the domain wall. Analogously, the induced anisotropy component with constant G leads to pinning of segments of the boundary along the direction $\langle 111 \rangle$. In the first case $(q \to 0)$ segments appear in the domain wall structure where the direction of the magnetization vector changes more slowly. As F and G increase, the dissimilarity in the changes of individual segments of the domain wall becomes evident, as is clear from Figs. 1a and 1d. In the second case $(q \gg 1)$, the structure of the original (unstabilized) domain wall already includes a region where the orientation of the magnetization vector changes slowly near the direction $\mathbf{M} \| [111]$. The induced anisotropy is the primary source of change in this region. The component of induced anisotropy with constant F decreases it, while that with constant G increases it. In this case the nature of the time-dependent displacement of the domain wall by a magnetic field differs strongly from the previous case. A 180° boundary can be decomposed into two components at 71 and 109°, which, depending on the component of induced anisotropy, will translate differently under the action of the field. In this case the maximum change occurs at segments of the domain wall corresponding to centers of the corresponding components of the 180° domain wall.

We now discuss the line shape of the domain-wall NMR signal domain wall for three groups of nuclei with orientations of the anisotropy axis of the local magnetic field along the edges of a cubic crystal lattice and for four groups with orientations of the axis along the diagonals of a cube (iron atoms in the d and a positions of a ferrite garnet). Absorption on a domain wall segment $[y, y+dy]$ is proportional to the square of the amplitude of the AC component of the local magnetic field at the nucleus. The NMR absorption line shape, in this case, will have the form

$$P(\nu)=N\sum_i \int_{-\infty}^{+\infty} \langle \Delta\varphi^2 \rangle dy / [\Delta^2 + (\nu_i(\varphi)-\nu)^2], \qquad (4)$$

where $i=1, 2, 3, 4$ (1, 2, 3) for the a-position (d- position),

N is a normalizing coefficient ($\int P d\nu = 1$) , $\Delta = 10^{-1}$, ν is the frequency of the rf field h^*, and $\langle \Delta\varphi^2 \rangle$ is the squared change in the orientation angle of the magnetization vector averaged over an oscillation period during quasistatic translation of the domain wall caused by the field h^*. The anisotropic component of the local magnetic field is small, which allows us to describe the dependence of the NMR frequency on the orientation of the magnetic moment in the form $\nu_i(\varphi) = 1 - 3\cos^2\Phi_i$, where Φ_i is the angle between the i-th local anisotropy axis at the nucleus and the direction of the magnetization in the domain wall, and $\nu_i(\varphi)$ is the reduced frequency.

It is known[4] that the main contribution to a maximum in the NMR absorption at a domain wall comes from segments of the boundary having maximum spectral density, i.e., those for which $d\nu_i(\varphi)/dy = 0$. For the a positions of the iron nuclei, the primary contribution to the maximum at frequency $\nu = -2$ occurs on segments whose direction of the magnetization is close to $\langle 111 \rangle$, at frequency $\nu = 0$ on segments where the direction is close to $\langle 100 \rangle$, and at frequency $\nu = 1$ on segments where the direction is close to either $\langle 011 \rangle$ or $\langle 112 \rangle$. For the d position of the iron nuclei the primary contribution to the maximum at frequency $\nu = -2$ occurs on segments with the direction of the magnetization close to $\langle 100 \rangle$, at frequency $\nu = -0.5$ on segments with the direction of the magnetization close to $\langle 011 \rangle$, and at frequency $\nu = 1$ on segments with the direction of the magnetization close to either $\langle 100 \rangle$ or $\langle 011 \rangle$.

We have established that stabilization processes lead to a change in the domain wall structure and to nonuniform changes in segments of the domain wall in a magnetic field. Increasing the induced anisotropy constant leads to an absolute decrease in the NMR absorption of the domain wall at all frequencies and to a change in the ratio of amplitudes of the absorption maxima. The absolute intensity of the signal increases with increasing amplitude of the external magnetic field; the frequencies of maximum absorption in this case do not change and are respectively equal to -2, 0, 1 for the a-position and -2, -0.5, 1 for the d-position.

1) $q = 0$.

a positions. Figures 1b and 1e show the NMR absorption line shape for iron nuclei in a positions of the garnet crystal lattice. It is easy to see that an increase of F leads to a change in the ratios of the amplitudes of absorption maxima at frequencies $\nu =$ 0, 1 and -2 (a decrease at frequency $\nu = 0$ and an increase at frequencies $\nu =$ 1 and -2; see Fig. 1b). An increase in G (see Fig. 1e) brings about an increase in the amplitude of the absorption maximum at frequency $\nu =$ 0 and suppression at frequencies $\nu = -2$ and 1.

d positions. A relative decrease is observed in the amplitude of the NMR absorption line shape of iron nuclei in d positions with increasing F at frequencies $\nu =$ 1 and -2 (see Fig. 1c). At a frequency $\nu = -0.5$, the amplitude of the maximum first increases and then decreases, which is connected with the creation of segments with slower variation of the direction of the magnetization vector on the domain wall structure (curve *1* in Fig. 1a). As G increases, the amplitude of the absorption maxima at frequencies $\nu = 1$ and -2 increases insignificantly, and decreases strongly at frequency $\nu = -0.5$ (see Fig. 1f).

At fixed values of F and G ($F = \text{const}$ and $G = 0$, $G = \text{const}$ and $F = 0$), increasing the amplitudes of the applied external field leaves the ratio of amplitudes of the absorption maxima practically unchanged. An exception is the case of large values of the parameter F ($f \sim 10$) and large shifts in the domain wall ($> \delta$). In this case, at a position of domain wall stabilization, magnetic nonuniformities of the 0° domain wall type appear,[3] which can significantly change the NMR spectrum. However, this case is a subject for a separate investigation, and will not be treated in this paper.

2) $q = 100$.

a positions. As in the pseudo-uniaxial case, increasing the induced anisotropy constants F and G for a fixed value of the magnetic field changes the ratio of the absorption maxima amplitudes. For small values of the induced anisotropy constant, changes in the shape of the absorption line have the same character: the amplitude at frequency $\nu = 0$ first increases and then decreases with increasing constants F or G. Despite the fact that the induced anisotropy components produce similar effects, the mechanisms for their activity are different. As we already mentioned above, the change in the value of the absorption maximum is determined by the spectral density of the spins and the local enhancement coefficient. For small values of F there is an insignificant increase in the number of spins with directions close to [100]. The boundary is pinned weakly, i.e., the change in orientation of the spins of a domain wall segment with directions close to [100] is large. All this leads to an increase in the amplitude of the absorption maximum at frequency $\nu = 0$. Increasing F increases the spectral density of spins at frequency $\nu = 0$, but the pinning effect for this domain wall segment is stronger, which leads to a decrease in the amplitude of the absorption maximum at this frequency. The induced anisotropy component with constant G decreases the number of spins with directions close to [100], but in this case it destabilizes the segment of domain wall with the corresponding spin directions (i.e., it increases the local enhancement coefficient). In the small-G range, increasing G leads to a slight decrease in the spectral density at frequency $\nu = 0$. More important is the manifestation of a destabilization of this segment of the domain wall, which also leads to an increase in the amplitude of the absorption maximum at $\nu = 0$. At larger values, increasing G strongly decreases the spectral density, in which case the amplitude of the absorption maximum at frequency $\nu = 0$ decreases.

Increasing both F and G leads to a monotonic growth in the amplitude of the maximum at frequency $\nu = -2$. The amplitude of the maximum at frequency $\nu = 1$ strongly increases as F increases, and is practically unchanged as G increases.

In contrast to the pseudo-uniaxial case, increasing the external field at fixed values of F and G ($F =$ const and $G = 0$, $G =$ const and $F = 0$) changes the ratio of amplitudes of the absorption maxima. We considered the effect of the field on the NMR absorption line shape for various values of the induced anisotropy constants (f or g vary within the range 1–100). From the obtained spectra we arrive at the following conclusions: increasing the amplitude of the external magnetic field leads to a relative decrease in the amplitude of the absorption maximum at frequency $\nu=-2$. For the amplitude of the absorption maximum at frequency $\nu=0$ a tendency to decrease with increasing field is also characteristic. The exception is the case $G=10$ and $F=0$, for which we observed a nonmonotonic change in the amplitude of the maxima (a rather small increase and then a decrease). This is connected with the fact that in small fields the center of a stabilized domain wall (with magnetization direction [111]) changes less than the segment of domain wall with magnetization directions close to [100], which corresponds to effective growth of the enhancement coefficient for this segment. With increasing field, the domain wall shifts as a whole, which leads to effective decrease of the enhancement coefficient on this segment of domain wall. In the NMR absorption spectrum this corresponds to a rather small increase and than a decrease in the amplitude $P_{\nu=0}$. The amplitude of the absorption maximum at frequency $\nu=1$ changes insignificantly, except for the case of large values of the parameters $F=100$, $G=0$, when an increase is observed in the amplitude $P_{\nu=1}$.

It is also necessary to note the differences in the NMR absorption spectra of domain walls stabilized by different components of the induced anisotropy. At small values of the constants G and F, the NMR absorption line shapes coincide, and the largest maximum corresponds to frequency $\nu=0$. The agreement of the absorption line shapes is due to the unimportance of the changes in the domain wall structure. However, even at values of the induced anisotropy constants that are 10% of the magnitude of the cubic anisotropy constant, the differences in absorption spectrum become appreciable. The spectrum of a domain wall stabilized by the induced anisotropy component with constant F has its largest maximum at a frequency $\nu=1$, while for a domain wall stabilized by the induced anisotropy component with constant G the maximum is observed for $\nu=0$.

d positions. The individual changes in the absorption maxima amplitudes have the following characteristics: with increasing constants F or G, the amplitude at frequency $\nu=1$ first increases and then decreases; at frequency $\nu=-0.5$ it increases strongly with increasing F and insignificantly with increasing G; at frequency $\nu=-2$ it first increases and then strongly decreases with increasing F and insignificantly decreases with increasing G. The causes of the nonmonotonic change in the amplitudes of the absorption maxima, which are connected with peculiarities in the changes of the domain wall structure during stabilization and the action of the magnetic field, were explained previously.

At small values of the constants G and F, the changes in the domain wall structure are insignificant, and the shape of the NMR absorption lines coincide. The largest maximum corresponds to a frequency $\nu=1$. As the induced anisotropy constants increase, the differences in the absorption spectra become appreciable. The spectrum of a domain wall stabilized by the induced anisotropy component with constant F ($f=60$) has its largest maximum at a frequency $\nu=-0.5$, while for a domain wall stabilized by the induced anisotropy component with constant G ($g=60$) it is at $\nu=1$.

For a constant values of F ($F=\text{const}$, $G=0$) or G ($G=\text{const}$, $F=0$) increasing the amplitude of the external magnetic field leads to a relative decrease in the absorption maxima amplitudes against a background of absolute growth in the signal intensity. An exception is the case $F=10$, $G=0$ and $G=100$, $G=0$, where the change in the amplitude of the absorption maxima at frequency $\nu=-0.5$ is insignificant. The basic tendency of the amplitudes of the absorption maxima to decrease relative to an increasing field is connected with a decrease in the enhancement coefficient of the domain wall segments that make the primary contribution to the absorption maxima compared to the enhancement coefficient at the center of the domain wall.

Thus, our studies of how processes that stabilize domain walls affect the NMR line shape show the need to include changes in the domain wall structure as it moves from its stabilization position. In the NMR absorption spectra, three maxima form at frequencies -2, 0, 1 for the *a* position and -2, -0.5, 1 for the *d* position, which coincides with the conclusions of Ref. 5 where spectra were obtained for domain walls with analytically defined structure. Increasing the induced anisotropy constants leads to an absolute decrease in the intensity of the absorption over the entire absorption band and to a relative change in the amplitudes of the absorption maxima. The difference in the way the induced anisotropy components with constants F and G affect the relative change of the amplitudes of absorption maxima is most clearly evident for the case of a pseudo-uniaxial crystal ($q=0$). For the *a* position an increase in the constant F leads to a decrease in the absorption amplitude at frequency $\nu=0$ and an increase in the amplitude of the maxima at frequencies $\nu=-2$ and 1. An increase in G gives the opposite effect: the amplitude of the absorption at $\nu=0$ increases, while at $\nu=-2$ and 1 it falls off. For the *d* position, increasing F leads to a relative decrease in the amplitudes at frequencies $\nu=1$ and -2. At frequency $\nu=-0.5$ the amplitude of the maximum first increases, and then decreases, which is connected with the formation of segments with a slower variation of the direction of the magnetization vector in the domain wall structure. As G increases, the amplitudes of the absorption maxima at frequencies $\nu=1$ and -2 increase only slightly, and decrease strongly at a frequency $\nu=-0.5$.

In crystals with mixed cubic and uniaxial anisotropies ($q=100$), the domain wall structure incorporates a region with slower change in the orientation of the magnetization vector with directions close to $\mathbf{M}\parallel[111]$. The induced anisotropy acts to change this region: the component of induced anisotropy with constant F decreases it, and that with constant G increases it. For small values of F and G, these features of the induced anisotropy components are barely detectable; however, increasing the induced anisotropy constants leads to an appreciable change in the domain wall structure and consequently to differences in the NMR absorption spectra. In this case the various domain wall segments are not affected in the same way by the magnetic field, which leads to a change in the ratio of amplitudes of the absorption maxima and to a dependence on the magnetic amplitude unrelated to saturation effects.

These results allow us to explain qualitatively the photoinduced changes in nuclear magnetic resonance from domain walls experimentally observed in yttrium-ferrite-garnet[6] and yttrium orthoferrite.[7]

This work was carried out with the financial support of the Russian Fund for Fundamental Research (96-02-19255).

[1] G. A. Murray and W. Marshall. Proc. Phys. Soc. **86**, 315 (1965).
[2] E. A. Turov, A. P. Tankeev, and M. I. Kurkin, Fiz. Tverd. Tela (Leningrad) **28**, 385 (1969) [*sic*], Fiz. Tverd. Tela (Leningrad) **29**, 747 (1970) [*sic*].
[3] V. G. Veselago, I. V. Vladimirov, and R. A. Doroshenko, Trans. IOFAN on Photomagnetism **44**, 92 (1993) [in Russian].
[4] R. A. Doroshenko, S. V. Seregin, and R. S. Fakhretdinova, in *Statics and Dynamics of Ordered Media* (Ufa, 1994) [in Russian], 54 pp.
[5] R. A. Doroshenko, S. V. Seregin, and R. S. Fakhretdinova, Fiz. Tverd. Tela (St. Petersburg) **38**, 3642 (1996) [Phys. Solid State **38**, 1985 (1996)].
[6] S. V. Seregin, R. A. Doroshenko, V. A. Timofeeva, and R. S. Fakhretdinova, JETP Lett. **50**, 130 (1989).
[7] S. Nadolski IEEE Trans. Magn. **14**, 5, 912 (1971).

Translated by Frank J. Crowne

Investigation of spin-reorientation phase transitions in single-crystal $DyFe_{11}Ti$

I. S. Tereshina, I. V. Telegina, and K. P. Skokov

M. V. Lomonosov State University at Moscow, 119899 Moscow, Russia

(Submitted October 10, 1997)
Fiz. Tverd. Tela (St. Petersburg) **40**, 699–700 (April 1998)

[S1063-7834(98)02504-0]

In this paper we study the phenomenon of spin reorientation in the compound $DyFe_{11}Ti$, which has a tetragonal crystal structure of $ThMn_{12}$ type. We experimentally measured curves for the mechanical torque that acts on single-crystal samples placed in a magnetic field. Literature data on the spin-reorientation transition temperatures in this compound and on the character of the spin reorientation are quite contradictory.[1–6] Thus, for example, Hsu *et al.*[2] observed that a second-order spin-reorientation transition takes place in $DyFe_{11}Ti$ at $T_1 = 200$ K and a first-order spin-reorientation transition at $T_2 = 58$ K, whereas Kudrevatykh *et al.* [1] reported that the second transition occurs at $T_2 = 120$ K. Only one spin-reorientation transition was observed in Ref. 3. Analysis of the other papers[4–6] also results in contradictory information, since the measurements (primarily studies of the temperature dependence of the magnetic susceptibility and magnetization) were most often made on oriented powder samples by methods that do not allow an unambiguous answer to the question about the nature of the spin-reorientation transition. This prompted us to investigate the spin-reorientation transition in $DyFe_{11}Ti$ single crystals.

The technology for obtaining single crystals and the method for making measurements were described previously in Refs. 7,8. For the magnetic measurements we took samples whose crystallographic axes in single-crystal blocks were misoriented by no more than 3°. Samples cut along the crystallographic planes (010) and (110) had a weight of around 30 mg; they had the shape of disks with diameter ~4 mm and thickness ~ 0.5 mm. Curves of the mechanical torque $L(\theta)$, where θ is the angle between the crystallographic direction [001] and the field **H**, were plotted for a $DyFe_{11}Ti$ single crystal on a torque magnetometer in the temperature range 78–300 K for magnetic fields up to 13 kOe. Although a magnetic field $H = 13$ kOe is insufficient for saturation far from the easy magnetization axis, near this axis the magnetization curves[2] and mechanical torques both saturated in this field. The use of stronger magnetic fields leads to such undesirable effects as disruption of the collinearity of the magnetic moments of the dysprosium and iron sublattices, which hinders the analysis of the experimental data.

Figure 1 shows experimental curves for $L(\theta)$ measured in the (010) plane at various temperatures in a field $H = 13$ kOe. At $T = 300$ K the crystallographic directions [001] ($L = 0$ and $\partial L/\partial\theta < 0$) and [100] ($L = 0$ and $\partial L/\partial\theta > 0$) are easy-magnetization and difficult-magnetization axes respectively. As the temperature decreases, a spin-reorientation transition takes place at $T_1 = 250$ K, and then the curves exhibit rather small additional maxima and minima along the direction [001]. From the observed curves of $L(\theta)$ we can determine the position of the easy magnetization axis (the angle θ_0 which the magnetization I_s makes with the **c** axis), having studied the point of intersection on the abscissa. In the temperature range 125–250 K the value of the angle $\theta_0(T)$ (Fig. 2) varies smoothly and the angle θ_0 varies with the reduced temperature like $\theta_0 = \chi(T - T_c)^{1/2}$, where $\chi = 0.075\ \mathrm{K}^{-1/2}$. The maximum value of the angle $\theta_0 = 45°$ is reached at $T_2 = 122$ K. From our results it follows that as the temperature decreases a second-order spin- reorientation transition occurs in the compound $DyFe_{11}Ti$ from an easy-magnetization-axis state to an easy-magnetization-axis-cone state. When $T < 122$ K the angle θ_0 changes discontinuously, which indicates a jump of the magnetic moment of the compound in the basal plane. Similar temperature dependence of $L(\theta)$ is also obtained for samples cut along the (110) plane.

It is known that the torque is related to the magnetic anisotropy energy by the following expression: $L(\theta) = -\partial E(\theta)/\partial(\theta)$. Values of the magnetic anisotropy energy for the (010) plane were obtained by integrating the experi-

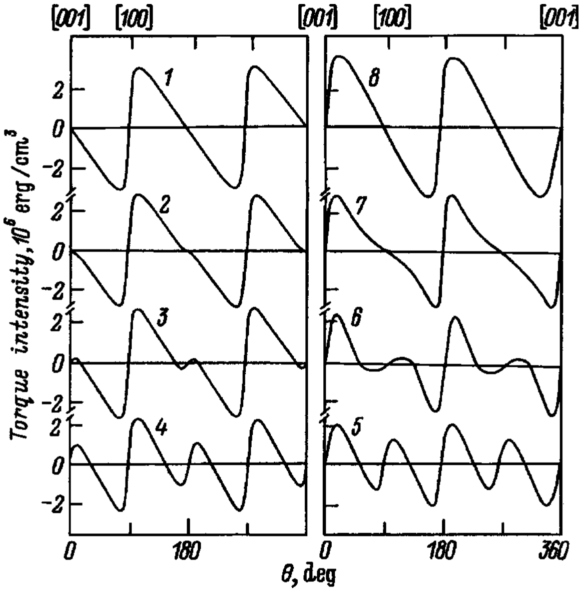

FIG. 1. Experimental curves of the torque for $DyFe_{11}Ti$ single crystals at various temperatures. T (K): *1* — 300, *2* —250, *3* — 235, *4* — 205, *5* — 165, *6* — 125, *7* — 118, *8* — 78.

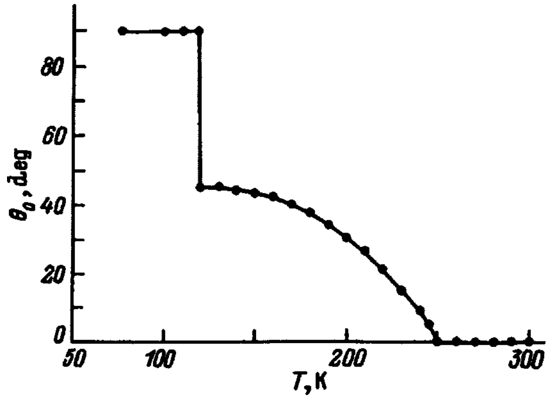

FIG. 2. Temperature dependence of the angle θ_0 of deviation of the magnetic moment from the crystallographic *c* axis in single-crystal $\mathrm{DyFe_{11}Ti}$.

mental curves for the torque $L(\theta)$. Figure 3 shows the angular dependences of the energy at various temperatures from 118 to 300 K. It is clear from Fig. 3 that the curve for the function $E(\theta)$ has minima on it. In the temperature range 300–125 K these are located symmetrically relative to the ordinate and gradually approach one another as the temperature decreases, which indicates a smooth ''opening'' of the easy magnetization axis cone below a temperature $T_1 = 250$ K. However, for $T < 125$ K one minimum appears discontinuously, which indicates the presence of a first-order phase transition near $T_2 = 122$ K.

Thus, our investigation of single-crystal samples by analyzing the temperature dependence of $L(\theta)$ allows us to clarify the complicated temperature behavior of the magnetocrystalline anisotropy, and lead us to the following conclusions.

1) A spin-reorientation transition takes place as a result of a competition between the magnetic anisotropy of the two sublattices (the Dy and Fe sublattices). At high temperatures ($T > 250$ K) the effective magnetic anisotropy field of the Fe sublattice dominates, which orients I_s along the **c** axis; at low temperatures the effective anisotropy field of the Dy sublattice dominates, which orients I_s in the basal plane.

2) In the compound $\mathrm{DyFe_{11}Ti}$ there is a smooth spin-reorientation transition of easy magnetization axis–easy magnetization axis cone type at $T_1 = 250$ K, for which the magnetic moment of the compound rotates under cooling away from the **c** axis to the plane (010), reaching a value of $\theta_0 = 45°$.

3) At $T_1 = 122$ K a discontinuous reorientation of the magnetic moment takes place in the basal plane (a first-order phase transition).

In conclusion the authors are grateful to S. A. Nikitin and V. V. Zubenko for helpful discussions of the results.

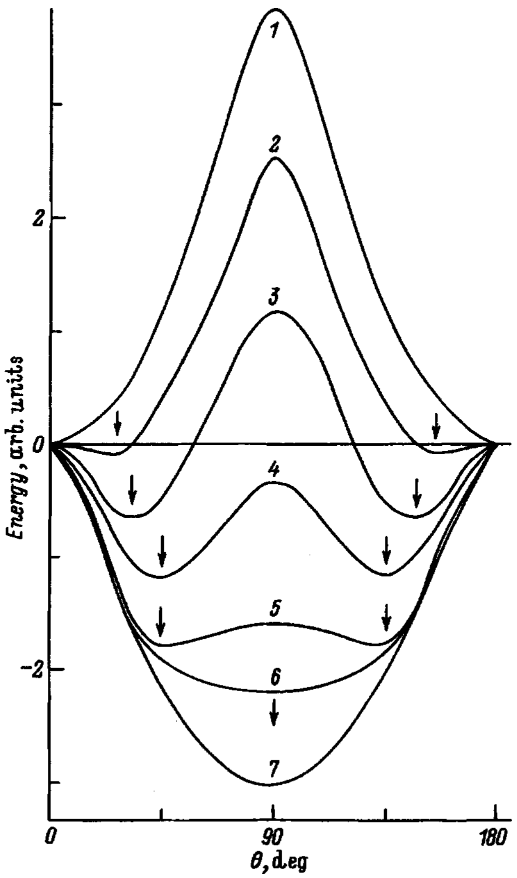

FIG. 3. Experimental angular dependences of the magnetic anisotropy energy of a $\mathrm{DyFe_{11}Ti}$ single crystal in the (010) plane at 300 (*1*), 235 (*2*), 205 (*3*), 165 (*4*), 125 (*5*), 121 (*6*) and 118 K (*7*).

This work was supported by grants from the Russian Fund for Fundamental Research Nos. 96-02-18271 and 3/97-52.

[1] N. V. Kudrevatykh, M. I. Bartashevich, V. A. Reĭmer, S. S. Sigaev, and E. N. Tarasov, Fiz. Met. Metalloved. **70**, *11*, 53 (1990).

[2] B.-P. Hu, H.-S. Li, and J. M. D. Coey, Phys. Rev. B **41**, 2221 (1990).

[3] P. H. Quang, N. H. Luong, and N. P. Thuy, J. Magn. Magn. Mater. **128**, 67 (1993).

[4] K. Yu. Guslienko, X. C. Kou, and R. Grossinger, J. Magn. Magn. Mater. **150**, 383 (1995).

[5] B.-P. Hu, H.-S. Li, J. P. Gavigan, J. M. D. Coey, J. Phys.: Condens. Matter **1**, 755 (1989).

[6] X. C. Kou, T. S. Zhao, R. Grossinger, H. R. Kirchmayr, X. Li, and F. R. de Boer, Phys. Rev. B **47**, 3231 (1993).

[7] O. A. Zolotukhin, V. V. Zubenko, T. I. Ivanova, S. A. Nikitin, V. V. Sergeev, I. V. Telegina, and I. S. Tereshina, Bull. Moscow State Univ., Ser. 3: Physics and Astronomy **34**, *5*, 80 (1993)[in Russian].

[8] K. P. Skokov, M. B. Lyakhova, Yu. G. Pastushenkov, T. I. Ivanova, I. V. Telegina, and V. V. Zubenko, in Sci. Ann. Tver' State Univ. (1996) [in Russian], Vol. 1, p. 138.

Translated by Frank J. Crowne

PHYSICS OF THE SOLID STATE VOLUME 40, NUMBER 4 APRIL 1998

Effect of mechanical stresses on the magnetoelastic properties of $TmVO_4$

Z. A. Kazeĭ

M. V. Lomonosov State University at Moscow, 119899 Moscow, Russia

(Submitted October 28, 1997)
Fiz. Tverd. Tela (St. Petersburg) **40**, 701–705 (April 1998)

In this paper the influence of mechanical stress on magnetoelastic properties, i.e., magnetostriction and thermal expansion in the neighborhood of a structural phase transition of the Jahn-Teller crystal $TmVO_4$ is investigated experimentally and theoretically. It is shown that the magnetoelastic properties of $TmVO_4$ for a magnetic field $H\|[001]$ do not change the domain structure of the sample, which is rather well described when mechanical stresses in the crystal are taken into account using the parameter $\overline{P}\sim 0.5\ \mathrm{cm}^{-1}$. Conversely, for magnetic fields along the direction of spontaneous strain [110] the magnetoelastic properties are primarily caused by reorientation of the Jahn-Teller domains and short-range order effects. It is shown that the ''true'' magnetostriction of a single-domain crystal for $H\|[110]$ diverges at the phase transition point $T_c = 2.15$ K in the absence of mechanical stresses and is strongly decreased by these stresses. © *1998 American Institute of Physics.* [S1063-7834(98)02604-5]

Rare-earth elastic materials undergoing structural phase transitions of Jahn-Teller type are characterized by exceptional sensitivity to various external perturbations—magnetic and electric fields, external pressures, etc. This is because the spectra of rare-earth ions contain low-lying quasidegenerate levels with large quadrupole moments, on which external fields can act efficiently. The effect of a magnetic field on the structural phase transition and order parameter in rare-earth compounds having the zircon structure has been studied in considerable detail.[1] Much less work has been done to study the effect of an electric field, and especially mechanical stresses, on the magnetoelastic characteristics of Jahn-Teller elastic materials. The large electron-deformation coupling constant in Jahn-Teller elastic materials leads us to expect that mechanical stresses will perturb these systems strongly, at least for the rare-earth zircons investigated in this paper.

It is well known that the strong electron-phonon interaction in rare-earth compounds having the zircon structure RXO_4 (where R is a rare-earth ion, and $X=V,\ P)$[2] leads to structural phase transitions which cause large strictive effects in these crystals.[3,4] In this case the strictive characteristics are qualitatively distinguished depending on whether a magnetic field enhances ($DyVO_4$, $TbVO_4$, $TmPO_4$) or suppresses ($TmVO_4$, $TmAsO_4$) the Jahn-Teller correlations. For $TmVO_4$ a large value of the striction is predicted only for fields oriented along the tetragonal axis at temperatures and fields below their critical values, i.e., in the distorted rhombic phase.[3]

Our experimental investigation of magnetostriction in $TmVO_4$,[5] revealed a number of effects that cannot be described by a simple model of the Jahn-Teller effect for an isolated doublet, notably the large values of the striction for field orientations along [110], and also for $H\|[001]$ in fields and at temperatures above critical. This implies that a quantitative description of the magnetoelastic properties of $TmVO_4$ must include mixing of the first excited singlet into the ground state doublet in a magnetic field and in the presence of external and/or internal mechanical stresses. In Ref. 6, Vekhter and Kaplan estimated the influence of mechanical stress on the magnetostrictive properties of $TmVO_4$, including experimental data for $H\|[110]$. However, in our view their approach is not entirely justified, because it implies that the magnetoelastic properties are determined primarily by reorientation of Jahn-Teller domains. On the other hand, it can be predicted that when H is oriented along the tetragonal axis the domain state of the crystal does not change, and the magnetoelastic characteristics reflect the behavior of the order parameter of the phase transition. Therefore, the goal of this paper is to present a model that describes all the magnetoelastic properties of $TmVO_4$ for a field $H\|[001]$ with sufficiently good quantitative accuracy, taking into account mechanical stresses and the demagnetization effect, which plays an important role at low temperatures.

1. SAMPLES AND METHODS OF MEASUREMENT

In this paper we present the results of studies of the thermal expansion and magnetostriction of $TmVO_4$ single crystals in a range of temperatures around the structural phase transition. $TmVO_4$ crystals were grown from a solution in a melt and had an average dimension $1\times1\times2$ mm. The thermal expansion and magnetostriction are defined respectively as $\Delta l(T)/l_0=[l(T)-l_0]/l_0$ and $u=\Delta l(T,H)/l_0$, where l_0 is the length of the crystal along the measurement direction when $H=0$ and $T=6$ K, i.e., in the undistorted tetragonal phase.

For these measurements we used a setup with a capacitive strain detector, which was included in the tank circuit of a cryogenic oscillator (frequency $\sim$ 1.5 MHz).[7] Temperatures in the range 1.7–6 K were measured by angular resistance thermometry. The external magnetic field was created by two superconducting magnetic systems, which allowed us to apply fields parallel ($H \leqslant 40$ kOe) or perpendicular ($H \leqslant 25$ kOe) to the strain being measured.

2. THEORETICAL TREATMENT

In most theoretical papers, the magnetoelastic properties of $TmVO_4$ are calculated using only wave functions for the ground-state, non-Kramers doublet of the Tm^{3+} ion as a basis, because the distance to the first excited singlet state $\Delta \sim 50\ cm^{-1}$, i.e., much larger than the value $kT_c = 1.5\ cm^{-1}$. The interaction of localized strains of B_{2g} symmetry via the phonon field leads to a tetragonal-orthorhombic phase transition. In a magnetic field $H \| [001]$, the doublet is split ($g_\perp = 0$, $g_\| = 10$), which decreases the orthorhombic strain $u(H)$ and the critical temperature $T_c(H)$. At each temperature $T < T_c$ there exists a critical field $H_c(T)$ at which the strain reduces to zero, i.e., the tetragonal phase is recovered; $H_c \approx 6$ kOe for $T = 0$ and decreases with increasing temperature. Note that for a basis consisting of a non-Kramers doublet there is no striction in a transverse field $H \perp [001]$, because the matrix elements of the Zeeman interaction with $H_\perp$ are zero. Since considerable striction is observed experimentally in a field $H_\perp$, as well as in the unordered phase when $H \| [001]$ ($T > T_c(H)$ and $H > H_c(T)$), an adequate description of $TmVO_4$ must take into account the admixture of first excited singlet and the presence of external and/or internal mechanical stresses.

For the extended ($E + A$) basis, the single-site Hamiltonian of the $TmVO_4$ crystal in the molecular field approximation has the form

$$H = -A\bar{\sigma}\sigma + \Delta\tau - \bar{P}\sigma - \frac{1}{2}g_\|\mu_B H_z S_z - \frac{1}{2}g_\perp\mu_B \times (H_x S_x + H_y S_y), \qquad (1)$$

where

$$\sigma = \begin{pmatrix} 1 & 0 & 0 \\ 0 & -1 & 0 \\ 0 & 0 & 0 \end{pmatrix}, \quad \tau = \begin{pmatrix} 0 & 0 & 0 \\ 0 & 0 & 0 \\ 0 & 0 & 1 \end{pmatrix},$$

$$S_z = \begin{pmatrix} 0 & i & 0 \\ -i & 0 & 0 \\ 0 & 0 & 0 \end{pmatrix}, \quad S_x = \begin{pmatrix} 0 & 0 & 1 \\ 0 & 0 & 0 \\ 1 & 0 & 0 \end{pmatrix},$$

$$S_y = \begin{pmatrix} 0 & 0 & 0 \\ 0 & 0 & i \\ 0 & -i & 0 \end{pmatrix}.$$

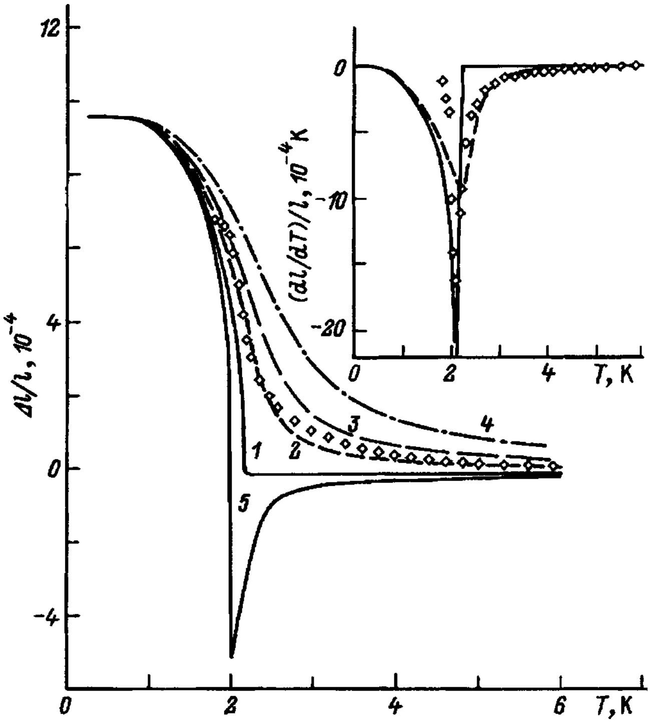

FIG. 1. Thermal expansion of a $TmVO_4$ crystal along the [110] axis for $H = 0$. The dots are experimental values, the curves are calculated for the mechanical stress parameter $\bar{P} = 0$ (*1*), 0.05 (*2*), 0.1 (*3*), 0.2 (*4*) and $-0.02\ cm^{-1}$ (*5*). The inset shows the temperature dependence of the coefficient of thermal expansion $\alpha_c = (dl/dT)/l$ in the neighborhood of the phase transition for the same values of the parameter $\bar{P}$.

The first term of the Hamiltonian (1) describes the correlation of localized Jahn-Teller distortions having B_{2g} symmetry, the second describes the interaction with the crystal field, and the last two terms are the Zeeman interaction with a magnetic field along and perpendicular to the tetragonal axis. In order to include external and/or internal elastic stresses in the Hamiltonian (1) we shall introduce a term similar to the Hamiltonian for Jahn-Teller correlations with parameter $\bar{P} \equiv [(V_s/C_0)P + \delta]$, where P is the external pressure induced by the strain having B_{2g} symmetry, V_s is the electron-strain coupling constant, C_0 is the elastic modulus, and δ is the parameter of the random stresses.

For a quantitative description of the experiments we calculated the function $\bar{\sigma}(H,T)$ numerically at various temperatures and magnetic fields using Hamiltonian (1) and the values $A = 2.1$ K, $\Delta = 51\ cm^{-1}$, $g_\| = 10$, and $g_\perp = 5.3$.[8] The results of these calculations are in rather good agreement with experimental data if we assume that the crystal is subjected to rather small elastic stresses, whose constant $\bar{P}$ was estimated from data on the thermal expansion of $TmVO_4$ in the absence of a field.

3. EXPERIMENTAL RESULTS

We first consider the results of measuring the thermal expansion $\Delta l(T)/l_0$ of $TmVO_4$ in the neighborhood of the phase transition. Figure 1 shows the function $\Delta l(T)/l_0$ for a $TmVO_4$ crystal along the [110] axis—the direction of the spontaneous rhombic distortion of the B_{2g} type— when $H = 0$. It is clear that the function $\Delta l(T)/l_0$ exhibits an anomaly; defining the critical temperature to be the temperature at which the coefficient of linear expansion $\alpha_c = [d\Delta l(T)/dT]/l_0$ of the sample is a maximum (see the inset) gives $T_c = (2.15 \pm 0.05)$ K. This value is in good agreement with the value of T_c determined previously in Refs. 8–10 by different methods.

Above T_c, up to $T \approx 3T_c$, the function $\Delta l(T)/l_0$ in $TmVO_4$ exhibits a considerable ''tail,'' indicating the presence of considerable rhombic strain of the lattice having B_{2g} symmetry. Since short-range order effects, in $TmVO_4$ are unimportant,[8] in our view the observed tail of $\Delta l(T)/l_0$ is connected with strains of B_{2g} symmetry induced by mechanical stresses. These strains could be caused by rather small uniaxial stresses, both external, arising as a result of gluing the crystal into the measurement capacitor, and internal, generated during crystal growth. Actually, even insignificant mechanical stresses applied to the sample near T_c can strongly affect the physical properties of Jahn-Teller crystals due to the pronounced softening of the elastic moduli.[10]

The sign of the anomaly in $\Delta l(T)/l_0$ and its magnitude depend on the nature of the breakup below T_c of the sample into structural (Jahn-Teller) domains. These domains consist of regions in which the tensile strain is directed along the two-fold axes $[110]$ or $[1\overline{1}0]$, which are equivalent in the tetragonal unit cell of the crystal (a' or b', $a' < b'$). In the sample whose measurement results are shown in Fig. 1, the b' axis for the domains was predominantly oriented along the direction of measurement of Δl. Because the domain state of the crystal does not change in the absence of a field $H \| [110]$, the temperature dependence of $\Delta l(T)/l_0$ reflects the behavior of the order parameter. Note that reorientation of the domains is accompanied as a rule by an abrupt and irreversible change in the thermal expansion and magnetostriction curves (see curve *5* in Fig. 1). Thus, the thermal expansion curves in zero field, or in a field $H \| [001]$, allow us to estimate the magnitude of mechanical stresses in the $TmVO_4$ crystal. From Fig. 1 it is clear that the more the parameter $\overline{P}$ characterizing the magnitude of the mechanical stresses increases, the more washed out the function $\Delta l(T)/l_0$ becomes above T_c. For the crystal whose data is shown in Fig. 1, the mechanical stresses were $\overline{P} = 0.05$ cm^{-1}; this value varies somewhat (by roughly a factor of 1.5–2) from crystal to crystal. Uniform stresses in the crystal were assumed in the calculation; nonuniform internal stresses δ, for example with a Gaussian distribution, lead to additional washing out of the thermal expansion curves.

The effect of mechanical stresses on the suppression of the structural phase transition by an external magnetic field $H \| [001]$ is illustrated by Fig. 2. It is clear that the field decreases the magnitude of the lattice strain in $TmVO_4$ considerably near T_c and lowers the phase transition temperature, in agreement with data from measurements of the magnetic[8] and elastic[10] properties. A comparison of the dependences for $\overline{P} = 0$ (dashed curves) and 0.05 cm^{-1} (solid curves) at various values of the magnetic field reveals that mechanical stresses give rise to considerable strain of B_{2g} symmetry above $T_c(H)$. The calculated curves shown in Fig. 2 are for a real $TmVO_4$ crystal with a finite demagnetizing factor $N \approx 4\pi/3$. In fact this implies that in the constant external field in which the measurements are made, the internal field decreases with decreasing temperature due to magnetization of the sample, and the suppression of the phase transition by an external field is weakened. Thus, the primary effect of mechanical stresses is to suppress the long ''tail'' of the thermal expansion for $T > T_c$, and the effect on the demagnetizing field reduces to increasing the strain compared to the state with $\overline{P} = 0$ and $N = 0$ at low temperatures. In light of the nonuniformity of the mechanical stresses in a real crystal and the indeterminacy connected with demagnetizing effects, the agreement between experimental and calculated data in Fig. 2 may be regarded as entirely satisfactory.

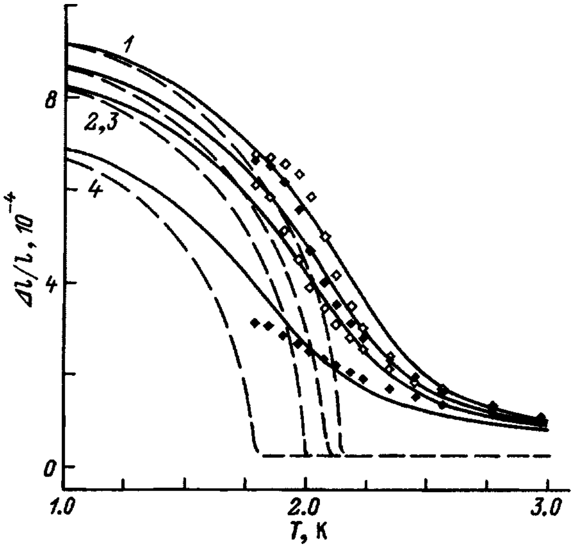

FIG. 2. Thermal expansion of a $TmVO_4$ crystal along the $[110]$ axis in a constant magnetic field $H \| [001]$ for a sample with demagnetizing factor $N \approx 4\pi/3$. The points are experimental, the curves are calculated in the absence (dashed) and in the presence (solid) of mechanical stresses $\overline{P} = 0.05$ cm^{-1}. H (kOe): *1* — 0, *2* — 3, *3* — 4, *4* — 6 kOe.

Mechanical stresses can also be expected to have an analogous effect on the magnetostriction of $TmVO_4$. Figure

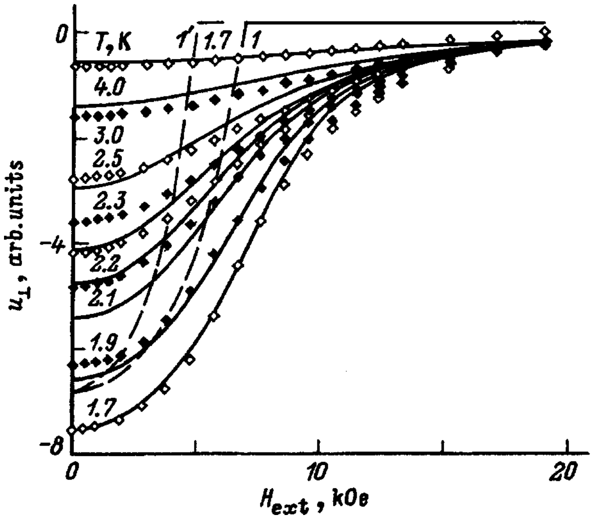

FIG. 3. Isotherms of the transverse magnetostriction of $TmVO_4$ ($H \| [001]$, $\Delta l \| [110]$) for a sample with demagnetizing factor $N \approx 4\pi/3$. The points are experimental, the curves are calculated for $\overline{P} = 0.1$ cm^{-1} (solid curves) and 0 (dashed) ($N = 0$ (*1*) and $4\pi/3$ (*1'*). The change of $u_\perp$ with temperature for $H = 0$ reflects the thermal expansion of the sample.

3 shows isotherms of the transverse magnetostriction $u_\perp$ for $H\|[001]$ and $\Delta l\|[110]$. For $T<T_c$ in an abrupt increase in $u_\perp$, is observed in the isotherms, which is connected with recovery of the tetragonal phase in a magnetic field $H_c(T)$. Note that the signs of the jump in magnetostriction, as H increases, and in the thermal expansion, as the crystal is cooled below T_c, are different, i.e., the magnetic field causes the reverse rhombic- tetragonal phase transition.

It is clear from Fig. 3 that the phase transition in a magnetic field is washed out and differs considerably from the behavior predicted by theory for the function $u_\perp(H)$ in the absence of mechanical stresses[3] (see the dashed curves *1* and *1'* in Fig. 3). In particular, for $T<T_c$ this theory predicts that the magnetostriction coefficient $D_\perp=du_\perp/d(H^2)$ diverges as $H\to H_c$ and $D_\perp=0$ for $H>H_c$ and $T>T_c$. Thus, experimental data both on magnetostriction and on thermal expansion point to the existence of strain in TmVO_4 crystals induced by mechanical stresses. The calculated curves for $u_\perp(H)$ with parameter $\overline{P}=$ 0.1 cm^{-1} and demagnetizing factor $N\approx 4\pi/3$ describe the experiment rather well; a rather small discrepancy is observed only at temperatures corresponding to the knee point on the thermal expansion curve. Note that demagnetizing effects shift the critical field $H_c(T)$ at $T=1.7$ K by roughly 2 kOe, as can be seen from a comparison of curves *1* ($N=4\pi/3$) and *1'* ($N=0$) for $\overline{P}=0$ in Fig. 3. Thus, inclusion of elastic stresses gives us a rather good quantitative description of both magnetostriction isotherms and thermal expansion of TmVO_4 for the field orientation $H\|[001]$ and reasonable values of the parameter $\overline{P}$.

For fields along the [110] axis the magnetoelastic properties of TmVO_4 are determined primarily by reorientation of the Jahn-Teller domains. We observed that a magnetic field $H\|[110]$ has a strong effect on the thermal expansion of TmVO_4: cooling the crystal in a field $H\|[110]\|\Delta l$ decreases the magnitude of the positive anomaly in $\Delta l(T)/l_0$, while cooling in a field $H\|[\overline{1}10]\perp\Delta l$ increases the anomaly, i.e., a longitudinal magnetic field aligns the short axes of the a' domains along the direction of measurement of Δl (for TmVO_4 below T_c, $\chi_{a'}>\chi_{b'}$). The longitudinal striction of TmVO_4 in the geometry $H\|[110]\|\Delta l$ attains the large value $u_\|\sim 10^{-3}$ in a field $H=$ 40 kOe for $T\approx$ 1.7 K, decreases as the temperature increases, and has a tendency to saturate below T_c.

Various mechanisms can be invoked to explain the magnetostriction $u_\|$ in TmVO_4 when $H\|[110]$. First of all, there is reorientation of Jahn-Teller domains in a magnetic field, whose cause is the anisotropy of the magnetic susceptibility χ in the basal plane arising from the phase transition. Since the magnitude of χ in the basal plane is not large for TmVO_4 (at 4 K we have $\chi_a=\chi_b\approx 0.025\chi_c$, see Ref. 8), the field needed to reorient the domains is considerably larger than, e.g., in DyVO_4,[11] and for $H=$ 40 kOe the sample has not yet reached the single-domain state. In our view, it is this reorientation of the Jahn-Teller domains that makes the largest contribution to the magnetostriction of TmVO_4 when $H\|[110]$, since the striction is large only in the range of temperatures where a lattice distortion exists, and the function $u_\|(H)$ below T_c has a tendency to saturate, which is characteristic of domain-induced magnetostriction.

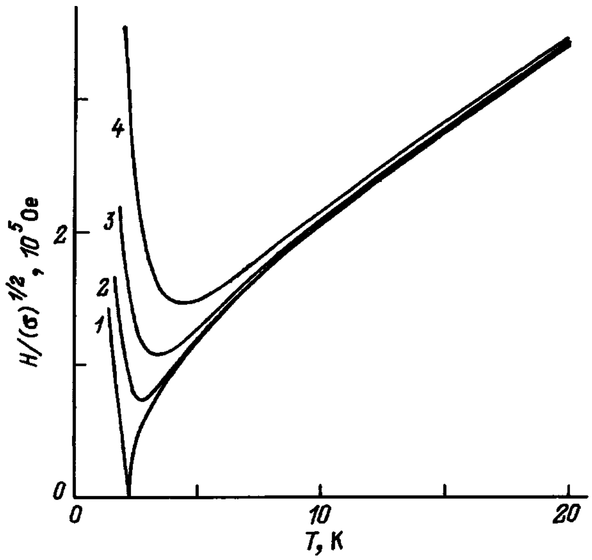

FIG. 4. Temperature dependence of the inverse magnetostriction coefficient $(D_\|)^{-1/2}=H/(\sigma)^{1/2}$ for TmVO_4 when $H\|[110]$ in the neighborhood of the structural phase transition in the absence and in the presence of mechanical stresses. $\overline{P}$ (cm^{-1}): *1* — 0, *2* — 0.2, *3* — 0.5, *4* — 1.

The "intrinsic" striction $u_\|$ of a single-domain TmVO_4 crystal when $H\|[110]$ arises only when we take into account the mixing of the doublet with the excited singlet state located a distance Δ above it. In Ref. 6 it was shown that, although the gap $\Delta=51\ \text{cm}^{-1}$ is rather large, the striction $u_\|\sim H^2/\Delta(T-T_c)$ that appears should be quite significant near the phase transition when $T\sim T_c=A/k$. For $T<T_c$ the striction falls off rapidly with decreasing temperature, since the effect of the external magnetic field on the strain is weakened as the internal molecular field is enhanced. Thus, the temperature dependence of "single-domain" striction $u_\|$ directly contradicts what is observed in experiment, confirming our conclusions that the latter is caused primarily by reorientation of Jahn-Teller domains.

Eliminating domain-related effects in the experiment is rather difficult; therefore, the "intrinsic" striction and the effect of mechanical stresses on it can be investigated only in the tetragonal phase when $T>T_c$. It is known that during a structural phase transition of Jahn-Teller type, the magnetostriction coefficient $D_\|=du_\|/d(H^2)$ along the direction of spontaneous strain diverges at the phase transition point. However, this divergence is never seen in experiment, and one of the reasons for this is probably the influence of mechanical stresses. Actually, our calculations show that in the presence of mechanical stresses the value of the magnetostriction coefficient $D_\|$ for TmVO_4 near the critical temperature is significantly decreased (Fig. 4). This decrease is observed for the majority of rare-earth zircons,[11] both with enhanced and suppressed Jahn-Teller correlations in a magnetic field, implying that both external and internal mechanical stresses are always present in real crystals, due to theconditions of the experiment, whose role near the phase transition is enhanced by the strong softening of the corresponding elastic constant.

In conclusion we note that experimental data on thermal expansion and magnetostriction of $TmVO_4$ admit an adequate interpretation within the framework of the theory of the cooperative Jahn-Teller effect, generalized by including an excited state and the presence of weak mechanical stresses. The strong influence of mechanical stresses on the magnetoelastic properties of Jahn-Teller elastic systems, which are characterized by anomalously large elastic susceptibility to various external probes near the phase transition, is not unexpected. The influence of mechanical stresses monitored during the experiment on crystals having different types of Jahn-Teller ions and different types of strains at the phase transition merits more detailed investigation.

[1] E. Pytte, Phys. Rev. **9**, 932 (1974).

[2] W. G. Wyckoff, *Crystal Structure* (Interscience, N.Y., 1965), Vol. 3.

[3] B. G. Vekhter and M. D. Kaplan, Fiz. Tverd. Tela (Leningrad) **16**, 1630 (1974) [Sov. Phys. Solid State **16**, 1064 (1974)].

[4] B. G. Vekhter and M. D. Kaplan, Zh. Éksp. Teor. Fiz. **87**, 1774 (1984) [Sov. Phys. JETP **60**, 1020 (1984)].

[5] Z. A. Kazeĭ and V. I. Sokolov, Zh. Éksp. Teor. Fiz. **91**, 1799 (1986) [Sov. Phys. JETP **64**, 1065 (1986)].

[6] B. G. Vekhter and M. D. Kaplan, Fiz. Nizk. Temp. **14**, 395 (1988) [Sov. J. Low Temp. Phys. **14**, 218 (1988)].

[7] Z. A. Kazeĭ, M. V. Levantsov, and V. I. Sokolov, Instrum. Exp. Tech. **1**, 196 (1982) [in Russian].

[8] A. H. Cooke, S. J. Swithenby, and M. R. Wells, Solid State Commun. **10**, 265 (1972).

[9] A. Segrmuller, R. L. Melcher, and H. Kinder, Solid State Commun. **15**, 101 (1974).

[10] R. L. Melcher, E. Pytte, and B. A. Scott, Phys. Rev. Lett. **31**, 307 (1973).

[11] B. G. Vekhter, Z. A. Kazeĭ, M. D. Kaplan, and V. I. Sokolov, Zh. Éksp. Teor. Fiz. **43**, 287 (1986) [*sic*].

Translated by Frank J. Crowne

PHYSICS OF THE SOLID STATE VOLUME 40, NUMBER 4 APRIL 1998

Magnetic properties of iron nitride films obtained by reactive magnetron sputtering

L. A. Chebotkevich, Yu. D. Vorob'ev, and I. V. Pisarenko

Far-East State University, 690600 Vladivostok, Russia

(Submitted August 8, 1997; resubmitted November 18, 1997)
Fiz. Tverd. Tela (St. Petersburg) **40**, 706–707 (April 1998)

[S1063-7834(98)02704-X]

1. In recent years directed ion implantation of nitrogen in metals has become an effective method for creating metal nitrides at room temperature. The inclusion of a rather small amount of nitrogen in Fe-based films makes them polycrystalline, which greatly improves their magnetic softness properties, increases the saturation induction B_s, and increases their resistance to corrosion.[1–5]

In this paper we investigate the dependence on the nitrogen content of the crystal structure, saturation inductance, and coercive field of thin (40 nm) films of Fe-N in the working gas $Ar+N_2$, the working gas pressure, and the substrate temperature T_s.

2. The films were obtained by reactive magnetron sputtering of Fe targets in an atmosphere consisting of a mixture of the gases $Ar+N_2$. The pressure of the working gas mixture during the sputtering varied from 1.3×10^{-4} to 1×10^{-2} Torr. The content of nitrogen in the mixture varied in the range 0–20%. The films were sputtered onto glass substrates and cleaved faces of NaCl. During the sputtering T_s varied from 20 to 300 °C.

The thickness of the film was monitored according to the sputtering time. B_s was measured on an automated vibrating magnetometer. The coercive field H_c was determined by inductance and magnetooptic methods; the structure of the film was investigated by transmission electron microscopy and electron microdiffraction.

3. Investigation of the dependence of B_s and H_c on the pressure of operating gas for various C_N in the working mixture showed that the value of B_s is a maximum and the value of H_c a minimum when $P=2.3\times10^{-4}$ Torr.

Figure 1 plots the quantities B_s and H_c for a Fe-N film deposited on a substrate at room temperature versus C_N in the working gas. It is clear that B_s does not begin to decrease until $C_N>10\%$. H_c behaves otherwise. A minimum in H_c is observed when C_N for the working gas is in the range 7–12%. The decrease in B_s for $C_N>10\%$ is caused by the formation of a nonmagnetic phase. Electron microdiffraction patterns show that as nitrogen is added to the working gas diffraction rings appear that are characteristic of various phases of iron nitride. When $C_N\geqslant15\%$ in the working gas, the only phase that was reliably identified in the films obtained was the phase Fe_2N. It was not possible to identify ferromagnetic phases ($Fe_{16}N_2$, Fe_4N, Fe_3N) that form at small nitrogen contents due to the overlap of the diffraction rings. However, the increase of B_s as T_s increases (curve *1* in Fig. 2) is evidence that ferromagnetic phases of iron nitride form. The decrease of H_c (Fig. 1) is related to the decreasing grain size from 7 nm (in pure iron) down to 3–4 nm (in Fe-N films). The increase of H_c for $C_N>10\%$ is caused by internal stresses and magnetostatic fields of the growing phases of iron nitride.[6] The electron-microscope images of the film structure reveal ''pleats'' which attest to the presence of internal stresses. The lattice strain for α phases increases with increasing nitrogen content and for $C_N=19\%$ it equals 1.3%.

The dependence of B_s and H_c on substrate temperature for Fe–N films obtained at $C_N=10\%$ is shown in Fig. 2.

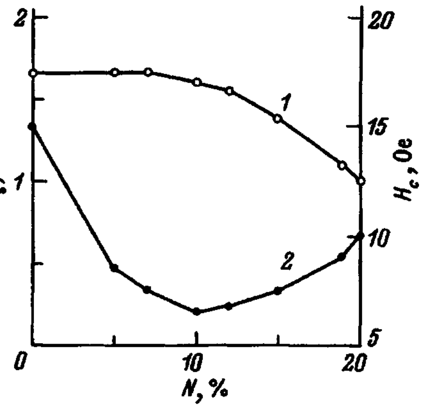

FIG. 1. Dependence of the magnetic induction B_s (*1*) and coercive field H_c (*2*) of Fe–N films on nitrogen content in the working gas. The substrate temperature equals 20°C.

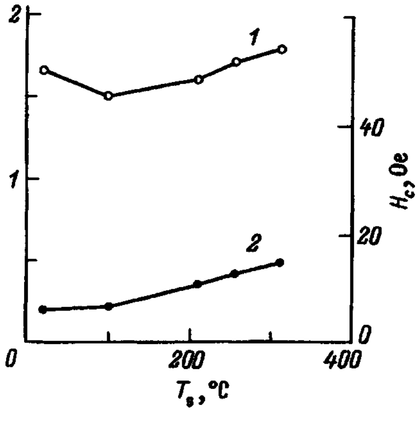

FIG. 2. Dependence of B_s (*1*) and H_c (*2*) of Fe–N films on substrate temperature. The working gas pressure was 2.3×10^{-4} Torr. The nitrogen content in the working gas was 10%.

1063-7834/98/40(4)/2/$15.00

When the films are deposited on heated substrates, B_s increases and at $T_s = 300$ °C it equals 1.9 T. The increase in B_s is connected with the formation of ferromagnetic phases of iron nitrides with inductions that exceed that of pure iron. Since the formation of chemical compounds of the sputtered materials is possible only at the substrate surface, increasing its temperature leads to an increase in the reactivity of the components, and an increase in the relative quantities of magnetic nitride phases in the bulk of the film, and consequently an increase in the magnetic induction. On the other hand, increasing T_s leads to an increase in the grain size and in the final analysis to an increase in H_c.

4. Thus, Fe–N films obtained by reactive magnetron sputtering are multiphase and contain both ferromagnetic and nonmagnetic phases. Nanocrystalline films of Fe–N deposited with $C_{\mathrm{N}} = 10\%$ in the working gas have the minimum value of H_c. Increasing T_s in the process of condensation allows us to obtain Fe–N films with higher B_s than for films of pure Fe.

[1] K. Terunuma, M. Miyazaki, H. Kowashima, and K. Terazono, J. Magn. Soc. Jpn. **14**, 257 (1990).

[2] E. Ma, B. X. Liv, X. Chen, and H. D. Li, Thin Solid Films **147**, 49 (1987).

[3] Y. Hoshi and M. Naoe, J. Appl. Phys. **69**, 5622 (1991).

[4] M. Kume, T. Tsujioka, K. Matsuura *et al.*, IEEE Trans. Magn. **MAG-23**, 3633 (1990).

[5] S. Kh. Karpenko, Foreign Electron. **6**, 3 (1993) [in Russian].

[6] V. E. Osukhovskiĭ, Yu. D. Vorob'ev, L. A. Chebotkevich *et al.*, Fiz. Met. Metalloved. No. 3, 543 (1986) [in Russian].

Translated by Frank J. Crowne

PHYSICS OF THE SOLID STATE VOLUME 40, NUMBER 4 APRIL 1998

Metal-insulator transition induced by a magnetic field in the compounds $Eu_{0.7}A_{0.3}MnO_3$ (A = Ca, Sr)

Ya. M. Mukovskiĭ and A. M. Ionov

Moscow State Institute of Steel and Alloys, 117935 Moscow, Russia

(Submitted December 8, 1997)
Fiz. Tverd. Tela (St. Petersburg) **40**, 708–712 (April 1998)

The temperature $R(T)$ and field $R(H)$ dependences of the electrical resistance in the compound $Eu_{0.7}A_{0.3}MnO_3$ (A = Ca, Sr) are investigated in the temperature range 4.2–200 K in magnetic fields up to 14 T. Above the antiferromagnetic transition temperature T_a, the function $R(T)$ is semiconducting in character. Application of a magnetic field H that exceeds a certain critical value H_c changes the character of the function $R(T)$ for $Eu_{0.7}Sr_{0.3}MnO_3$ to metallic $(dR/dT>0)$. For $T<T_a$ and $H<H_c$ a jump in the resistance is observed indicating instability of the electronic state caused by competition between charge and spin ordering of the Mn ions of different valences. © *1998 American Institute of Physics.* [S1063-7834(98)02804-4]

Rare-earth manganite compounds doped with group-II elements $A_{1-x}A'_xMnO_{3+\delta}$, where A is a rare-earth and A' is Ca, Sr, Ba, or Pb, exhibit gigantic magnetoresistance, which has attracted much attention recently not only due to the possibility of extensive applications, but also because of multitude of other physical effects that accompany or are caused by the giant magnetoresistance effect.

These compounds have the perovskite structure in which the Mn atoms occupy the B position in an octahedral environment of oxygens, while atoms A and A' are located at the A positions between the octahedra. The Mn atoms in these compounds have mixed valence, and the ratio Mn^{3+}/Mn^{4+} depends on the degree of doping element A' and on the actual content of oxygen $(3+\delta)$. The ratio of ionic radii of the component elements is expressed as a tolerance factor $t=d_{A-O}/\sqrt{2}d_{Mn-O}$, where d_{A-O} is the average distance between ions A, A', and O, and d_{Mn-O} is the distance between Mn^{3+}, Mn^{4+}, and O. This factor determines the stability of the perovskite structure and the strength and direction of the Mn–O bonds.[1,2] In compounds with $t>0.91$ and $0.15<x<0.5$, a transition is observed to a ferromagnetic state upon cooling[3,4] with a change in the character of the conductivity from semiconducting to metallic. In compounds with $t<0.91$ or with $x<0.15$, the usual transition observed is to an antiferromagnetic state, in which case the temperature dependence of the conductivity remains activated.

Although this class of compounds has been studied for a long time,[1] and a qualitative explanation has been given for the changes in the character of temperature dependence of the conductivity as the compound enters the ferromagnetic state, based on the theory of double exchange,[5,6] more detailed study of the properties of these compounds has further shown that this explanation is incomplete. In particular, a single ferromagnetic transition cannot quantitatively provide the change in conductivity observed.[7] Recently, it has been observed that the ferromagnetic transition is accompanied by a structural transition.[8,9]

The anomalously strong effect of rather weak magnetic fields on the resistance in these compounds at fairly high temperatures ($\Delta R/R(H)=$ 17% in a field of 1 kOe at $T=190$ K,[10] or $\Delta R/R(H)=$ 60% in a field of 1.3 kOe for $T=100$ K,[11] for the compound $La_{0.7}Ca_{0.3}MnO_3$) also cannot be described quantitatively by the simple model of double exchange.[5,6]

Studies of the compounds $(La_{1-x}Tb_x)_{2/3}Ca_{1/3}MnO_3$,[4] $La_{0.7-x}Pr_xCa_{0.3}MnO_3$[12] reveal that cooling causes a transition to take place from paramagnetic insulator to ferromagnetic metal when $t>0.91$ and a transition to a state that is a ferromagnetic insulator or to a state of a spin glass[4] when $t<0.91$. In the compound $Pr_{0.7}Ca_{0.3}MnO_3$, which is an insulator over the entire temperature range, an applied magnetic field causes the value of the resistance to fall by 8–10 orders of magnitude.[13]

There is interest in studying the properties of compounds based on other previously uninvestigated rare-earth elements, in particular those which possess intrinsic magnetic moments caused by the $4f$ states of the A ions and which can also have valences different from +3 in compounds.

In this paper we study the temperature $R(T)$ and field $R(H)$ dependences of the electrical resistance and magnetic susceptibility $\chi(T)$ of the compound $Eu_{0.7}A_{0.3}MnO_3$, where A — Ca, Sr, in magnetic fields up to 14 T.

We find that these compounds undergo a magnetic transformation in which the character of the temperature dependence of the resistance changes. Application of an external magnetic field at temperatures below the magnetic conversion temperature leads to a significant decrease in the resistivity of the compound $Eu_{0.7}Sr_{0.3}MnO_3$.

1. EXPERIMENTAL METHOD

Ceramic samples of $Eu_{0.7}Ca_{0.3}MnO_3$ and $Eu_{0.7}Sr_{0.3}MnO_3$ were obtained by sintering powders of these compounds synthesized previously at $T=1300$ °C in air for 12 hours with an intermediate grinding and sintering at $T=1100$ °C for 12 hours. Subsequently, the samples undergo an additional stay in vacuum at $T=1300$ °C for 12 hours or in oxygen at

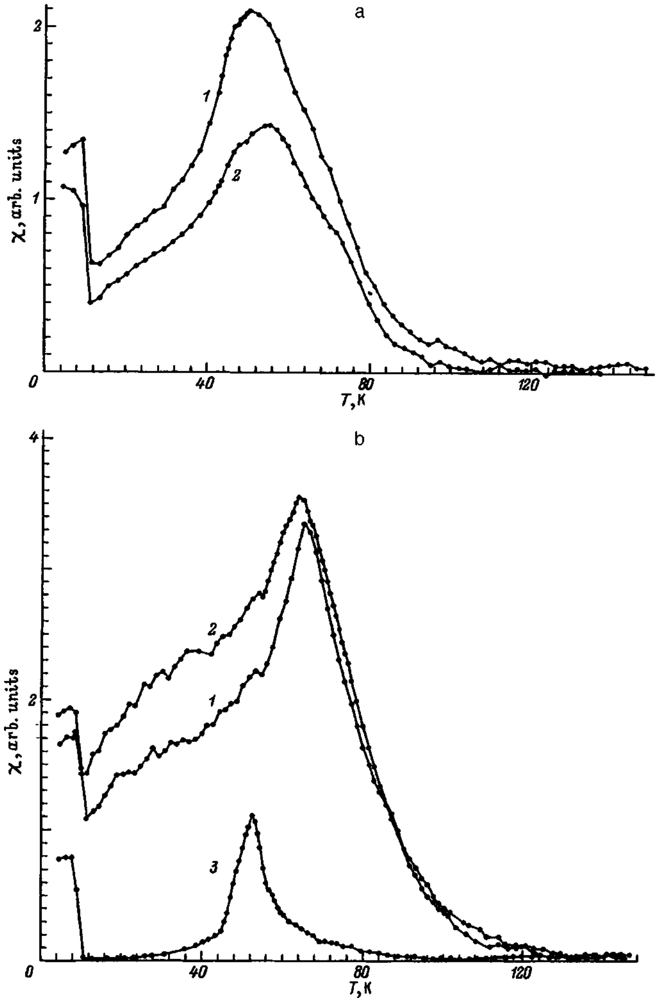

FIG. 1. Temperature dependence of the magnetic susceptibility $\chi(T)$ of samples of the compounds $Eu_{0.7}Sr_{0.3}MnO_3$ (a) and $Eu_{0.7}Ca_{0.3}MnO_3$ (b). *1*—original state, *2*—annealed in oxygen, *3*—annealed in vacuum.

$T = 800$ °C for 48 hours. Based on data from x-ray analysis, the samples have a distorted perovskite structure with less than 5% admixture of phases of the original components.

The resistance was measured by a four-probe method, while the magnetic susceptibility was measured by a modulation method.

2. EXPERIMENTAL RESULTS AND DISCUSSION

Measurement of the functions $\chi(T)$ in the samples revealed an antiferromagnetic transition in the temperature range $T_a =$ 40–60 K and a jump in the susceptibility for $T < 10$ K, which in all likelihood corresponds to a ferromagnetic transition (Fig. 1).

In the original state, the temperature dependence of the resistance $R(T)$ in the absence of a magnetic field was activated in all the samples at temperatures higher than T_a (Fig. 2). For $T < T_a$ the resistance falls, and in the range $\sim 20\text{K} < T < T_a$, abrupt jumps in the resistance are observed that indicate instability of the state that forms. Annealing the samples in vacuum leads to a significant increase in the resistance, which makes it impossible to carry out low-temperature measurements of $R(T)$. The antiferromagnetic

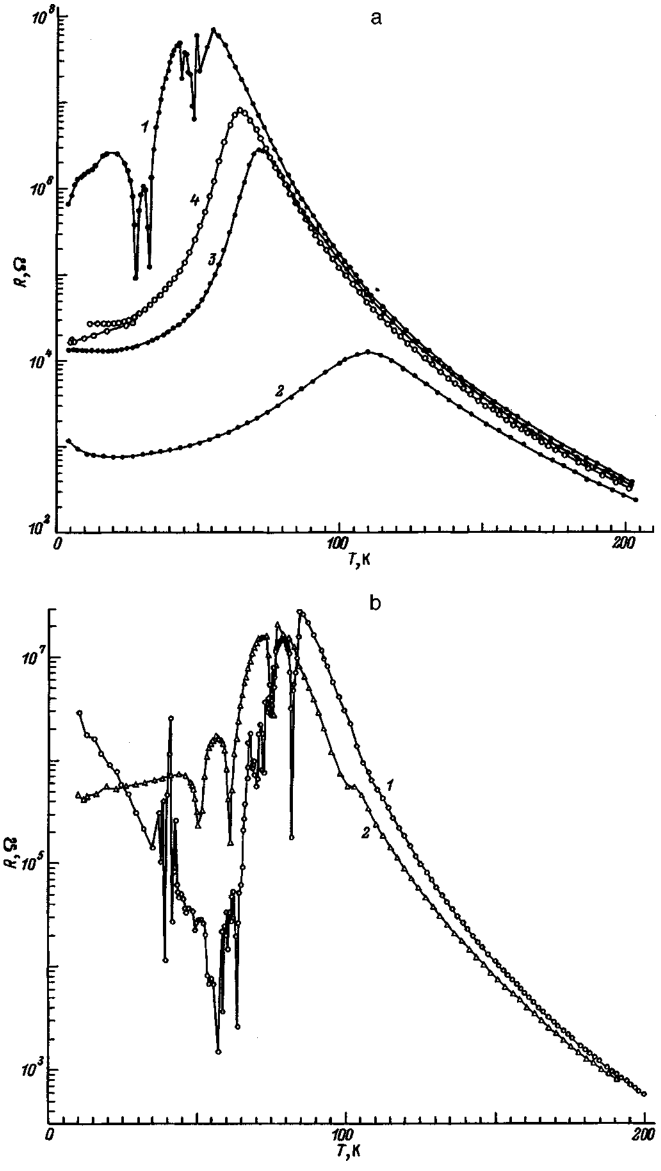

FIG. 2. Temperature dependence of the resistance $R(T)$ of samples of the compound $Eu_{0.7}Sr_{0.3}MnO_3$ (a) and $Eu_{0.7}Ca_{0.3}MnO_3$ (b). $H(T)$: a): *1*—0 (cooled), *2*—14 (heated), *3*—3 (cooled), *4*—1.7 (heated); b): *1*—0 (cooled), *2*—11 (cooled).

transition in this case is shifted to lower temperatures and becomes more pronounced (Fig. 1b). Annealing in oxygen leads to a negligible decrease in the resistance (and activation energy for $T > T_a$) and to a certain washing-out of the antiferromagnetic transition (Fig. 1).

Applying a magnetic field H decreases the resistance both below and considerably above T_a (Fig. 2). When $H > H_c$ (where H_c is a certain critical value of magnetic field at which the instability in $R(T)$ below T_a disappears) for the compound $Eu_{0.7}Sr_{0.3}MnO_3$ the function $R(T)$ beccomes metallic in character ($dR/dT > 0$) (Fig. 2a). Increasing H leads to a further decrease in the resistance, such that in a field of 14 T at $T = 50$ K the ratio of the resistances $R(0)/R(14)$ reaches 10^5; however, at $H = 14$ T a segment is observed below 10 K with $dR/dT < 0$ (curve *2* in Fig. 2a). Jumps are observed in the field-dependent resistances $R(H)$ for $T < T_a$ like those for $R(T)$ (Fig. 3).

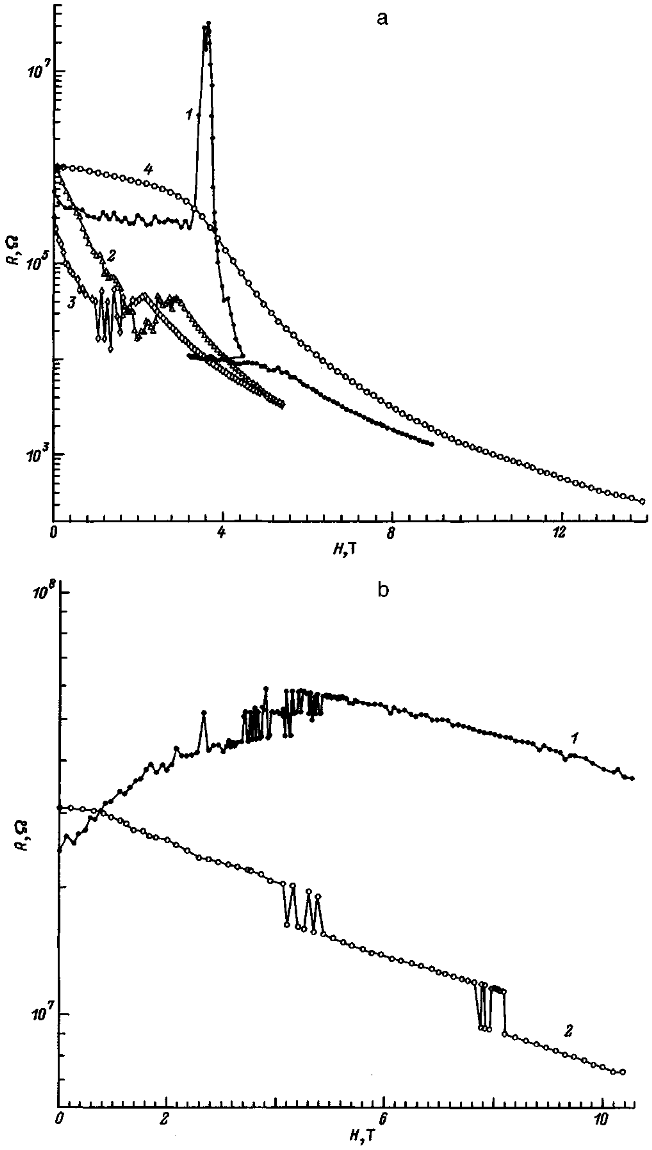

FIG. 3. Field dependence of the resistance $R(H)$ of samples of the compounds $Eu_{0.7}Sr_{0.3}MnO_3$ (a) and $Eu_{0.7}Ca_{0.3}MnO_3$ (b). $T(K)$: a): *1*—4.2 (H increasing), *2*—41 (H increasing), *3*—41 (H decreasing), *4*—77 (H increasing); b): *1*—84 (H increasing), *2*— 87 (H decreasing).

The low-temperature state ''freezes out'' in a magnetic field and, in this case, the function $R(T)$ for $H > H_c$ is reversible when this state is approached from the high-temperature region ($T > T_a$). When H varies in the low-temperature region we observed a hysteresis in $R(T)$ (Fig. 2a).

For the compound $Eu_{0.7}Ca_{0.3}MnO_3$, the critical value of magnetic field was not reached; thus $H_c > 11$ T. However, when $H = 11$ T, the jumps in resistivity in the unstable range became more orderly in character (Fig. 2b). The decrease in the resistance in a magnetic field is considerably smaller for this compound than it is for $Eu_{0.7}Sr_{0.3}MnO_3$ (Fig. 2a).

The behavior of $R(T)$ in the compound $Eu_{0.7}Sr_{0.3}MnO_3$ when $H > H_c$ is, to a considerable degree, similar to the behavior of $R(T)$ in $Pr_{0.7}Ca_{0.3}MnO_3$.[12,13] We can assume that there is a ferromagnetic component to the antiferromagnetic state in these compounds (i.e., the antiferromagnetic transition is of the ''spin canted'' type), which leads to manifestation of the double-exchange mechanism for $T < T_a$. Applying a magnetic field leads to enhancement of the polarization of the spin system, and possibly, when $H > H_c$, to a completely polarized ferromagnetic state. In contrast to compounds based on Pr, the decrease in resistance observed in these compounds below T_a in the absence of an external magnetic field can be due to the absence of charge ordering taking place in $Pr_{0.7}Ca_{0.3}MnO_3$.[12] Jumps in the resistance in the unstable range ($20\text{K} < T < T_a$) in $Eu_{0.7}Sr_{0.3}MnO_3$ and $Eu_{0.7}Ca_{0.3}MnO_3$ could be due either to a competition between charge and spin ordering or to possible nonuniformity of the samples under study, including the presence of magnetically ordered regions [states of a spin glass observed in the compound $(La_{1-x}Tb_x)_{2/3}Ca_{1/3}MnO_3$, see Ref. 4], in which case we may see percolation effects manifested in the behavior of $R(T)$. The observed increase in resistance at $H = 14$ T below 10 K in $Eu_{0.7}Sr_{0.3}MnO_3$ can be a manifestation of the interaction of charge carriers with magnetic moments of the Eu.

The studies we have begun of fully single-crystal samples of these compounds, including neutron-diffraction analysis in a magnetic field, could lead to a more complete understanding of the nature of the processes that occur in $Eu_{0.7}Sr_{0.3}MnO_3$ and $Eu_{0.7}Ca_{0.3}MnO_3$.

The authors are grateful to G. K. Strukova for help in preparing samples and A. E. Kovalev for help in making the measurements in high-magnetic fields.

This work was supported financially by grants No. 95-0-7.4-142 in the area of fundamental natural science from the State Education Department of the Russian Federation and No. 95-1.14 for State Program 012 on ''Surface atomic structures.''

[1] G. H. Jonker and J. H. van Santen, Physica **16**, 337 (1950).

[2] J. B. Goodenough, Phys. Rev. **100**, 564 (1955).

[3] H. Y. Hwang, S. W. Cheong, P. G. Radaelli, M. Marezio, and B. Batlogg, Phys. Rev. Lett. **75**, 914 (1995).

[4] J. M. de Teresa, M. R. Ibarra, and J. Garcia, Phys. Rev. Lett. **76**, 3392 (1996).

[5] C. Zener, Phys. Rev. **82**, 675 (1951).

[6] P. W. Anderson and H. Hasegawa, Phys. Rev. **100**, 675 (1955).

[7] A. J. Millis, P. B. Littlewood, and B. I. Shraiman, Phys. Rev. Lett. **74**, 5144 (1995).

[8] P. G. Radaelli, D. E. Cox, M. Marezio, S.-W. Cheong, P.E. Shiffer, and A. P. Ramiez, Phys. Rev. Lett. **75**, 4488 (1995).

[9] H. Kuwahara, Y. Tomioka, A. Asamitsu, Y. Moritomo, and Y. Tokura, Science **270**, 961 (1995).

[10] S. Jin, T. H. Tiefel, M. McCormack, R. A. Fastnacht, R. Ramesh, and L. H. Chen, Science **264**, 413 (1994).

[11] V. A. Kozlov, Ya. Mukovskii, and A. M. Ionov, Phys. Low-Dimens. Struct. **10/11**, 13 (1995).

[12] H. Yoshizawa, H. Kawano, Y. Tomioka, and Y. Tokura, J. Phys. Soc. Jpn. **65**, 1043 (1996).

[13] Y. Tomioka, A. Asamitsu, Y. Moritomo, and Y. Tokura, J. Phys. Soc. Jpn. **64**, 3626 (1995).

Translated by Frank J. Crowne

PHYSICS OF THE SOLID STATE VOLUME 40, NUMBER 4 APRIL 1998

Electrostriction soliton as a cluster model in the high-temperature phase of a hydrogen-containing ferroelectric

M. B. Belonenko and V. V. Kabakov

Volgograd State University, 400062 Volgograd, Russia

(Submitted September 15, 1997)
Fiz. Tverd. Tela (St. Petersburg) **40**, 713–715 (April 1998)

The polarization clusters observed experimentally in the high-temperature phase of ferroelectrics are interpreted as solitons in the microscopic pseudospin formalism. These solitons are the result of modulation of the pseudospin interaction constant by acoustic vibrations, which represents an electrostriction interaction from the phenomenological point of view. The influence of higher-order nonlinearities present in the pseudospin subsystem and the damping of acoustic modes on a soliton is analyzed. © *1998 American Institute of Physics.* [S1063-7834(98)02904-9]

1. In recent experiments on the physical properties of the paraelectric phase of ferroelectrics and ferroelastics[1,2] anomalous behavior has been observed on the part of the complex dielectric permittivity in the paraelectric phase of a ferroelectric crystal at low frequencies. This behavior was attributed to the existence of polarization clusters in the nonpolar ferroelectric phase, providing a means for explaining at the qualitative level the observed strong dependence of the permittivity not only on external parameters (the low-frequency field and the temperature of the crystal), but also on the sample history and, hence, on the equilibrium characteristics of the ferroelectric itself. The explanation given in several other papers[3,4] for the experimentally determined relations, based on the model of ''pulsing'' dipoles, ignores all the specific attributes of the dynamics of ferroelectrics with hydrogen bonds and, moreover, requires additional assumptions for its justification. Thus, one can infer from the pulsing-dipole model, in particular, the existence of a second superionic phase transition and a conductivity that increases with the temperature, neither of which is observed in experiments.[1]

2. In our opinion, all the significant characteristics of the anomalous behavior of the permittivity can be described by the pseudospin formalism widely used in the theory of ferroelectrics.[5,6] The Hamiltonian of a hydrogen-bonded ferroelectric in the pseudospin formalism has the form of the Ising Hamiltonian in crossed fields:

$$H-\Omega\sum_j S_j^x-(1/2)\sum_{i,j} J_{ij}S_i^zS_j^z+H_{s-a}, \tag{1}$$

where Ω and J_{ij} are the tunneling and exchange integrals of the ith and jth ferroelectric cells, respectively, S_j^x is the proton tunneling operator of the jth ferroelectric cell, S_j^z is the dipole moment operator of the jth ferroelectric cell, and H_{s-a} is the Hamiltonian of interaction of the pseudospin and acoustic subsystems. We propose to investigate the acoustic modes in the classical setting, i.e., assume that an acoustic mode is completely determined by the displacement vector u_α ($\alpha=\zeta,\eta$ indicate axes of the sample), and we assume that a transverse acoustic wave having a single nonzero component $\mathbf{u}=[0,u(\zeta,\eta),0]$ propagates in the ζ. The Hamiltonian H_{s-a} can now be written in the form

$$H_{s-a}=-d\sum_j\frac{\partial u(\zeta,\eta)}{\partial\zeta}S_j^z-h\sum_{j,i}\frac{\partial u(\zeta,\eta)}{\partial\zeta}S_j^zS_i^z, \tag{2}$$

where d is an appropriate piezoelectric strain constant, and the second term reflects the modulation of the exchange integral J_{ij} by the field of the acoustic wave[6] and corresponds to electrostriction from the phenomenological standpoint. The Heisenberg equations of motion for the average values of the pseudospin operators $\langle S^a\rangle$ (in the random-phase approximation and in the continuum limit) with phenomenologically introduced longitudinal and transverse pseudospin relaxation times T_1 and T_2 then have the form

$$\begin{aligned}\langle S^x\rangle_t&=(J\langle S^z\rangle+A\langle S^z\rangle_{\zeta\zeta}+B\langle S^z\rangle_{\eta\eta}+du_\zeta+hu_\zeta\langle S^z\rangle)\langle S^y\rangle\\&\quad-(\langle S^x\rangle-\langle S^x\rangle_0)/T_1,\\\langle S^y\rangle_t&=\Omega\langle S^z\rangle-(J\langle S^z\rangle+A\langle S^z\rangle_{\zeta\zeta}+B\langle S^z\rangle_{\eta\eta}+du_\zeta\\&\quad+hu_\zeta\langle S^z\rangle)\langle S^x\rangle-\langle S^y\rangle/T_2,\\\langle S^z\rangle_t&=-\Omega\langle S^y\rangle-\langle S^z\rangle/T_2,\end{aligned} \tag{3}$$

where $J=\Sigma_{i,j}J_{ij}$, $A=Ja^2$, a is the distance between consecutive cells in the direction of wave propagation (ζ direction), $B=Jb^2$, b is the distance between consecutive cells in the direction perpendicular to the direction of wave propagation (η direction), $\langle S^z\rangle_{\zeta\zeta}=\partial^2\langle S^z\rangle/\partial\zeta^2$, $\langle S^a\rangle_t=\partial\langle S^a\rangle/\partial t$, u is the effective component of the displacement vector, and $\langle S^x\rangle_0$ is the equilibrium average value of the tunneling operator. Note that the system (3) takes into account the fact that real hydrogen-containing ferroelectrics are quasi-two-dimensional and that normally $A\gg B$ (a good example is CsH_2PO_4).

The system of equations (3) must be augmented with an equation describing the dynamics of the nonzero component of the displacement vector u (Refs. 7 and 8):

$$\begin{aligned}&u_{tt}-v^2u_{\zeta\zeta}-v_1^2u_{\eta\eta}+\tilde{d}\langle S^z\rangle_\zeta+\tilde{h}\langle S^z\rangle_\zeta^2+\gamma u_t=0,\\&\tilde{d}=d/\rho,\quad \tilde{h}=h/\rho,\end{aligned} \tag{4}$$

where ρ is the density of the crystal, γ is the decay rate of the acoustic wave, and v and v_1 are the acoustic wave velocities in the ζ and η directions, respectively.

3. The above-derived complete system of equations (3), (4) is a system of partial differential equations, for which there is no known solving algorithm. We therefore use the method of multiscale expansions,[9] noting at the outset that the times T_1 and T_2 do not exceed 10^{-9}s, and the characteristic period of the acoustic wave is not more than 10^{-4}s, so that Eqs. 3) can be solved in the approximation $\langle S^a\rangle_t=0$, which enables us to express all pseudospin averages in terms of derivatives of the displacement vector u. This approximation has the physical significance that the pseudospin subsystem adiabatically tracks the variations in the acoustic subsystem of the ferroelectric. In this case

$$\langle S^z\rangle = z^{(1)}+z^{(2)}+z^{(3)},$$

$$z^{(1)}=B_1du_\zeta,\quad B_1=\langle S^x\rangle_0 \Bigg/ \left(\Omega+\frac{1}{\Omega T_2^2}-J\langle S^x\rangle_0\right),$$

$$z^{(2)}=B_1^2d(Au_{\zeta\zeta\zeta}+Bu_{\zeta\eta\eta}+h(u_\zeta)^2),$$

$$z^{(3)}=c_1u_{\zeta\zeta\zeta\zeta\zeta}+c_2u_\zeta u_{\zeta\zeta\zeta}+c_2(u_\zeta^2)_{\zeta\zeta}+c_3(u_\zeta)^3,$$

$$c_1=B_1^3A^2d,\quad c_2=B_1^3Adh,$$

$$c_3=B_1^3dh^2-\frac{B_1^2d^3T_1}{\Omega\langle S^x\rangle_0T_2}(JB_1+1)^2. \tag{5}$$

On the basis of (5), Eq. (4) then has the form

$$\begin{aligned} &f_{tt}+(B_1d\tilde{d}-v^2)f_{\zeta\zeta}-v_1^2f_{\eta\eta}+\gamma f_t+D_1f_{\zeta\zeta\zeta\zeta}+D_2(f^2)_{\zeta\zeta}\\ &\quad+D_3f_{\zeta\zeta\eta\eta}+D_4f_{\zeta\zeta\zeta\zeta\zeta\zeta}+D_5(f^2)_{\zeta\zeta\zeta\zeta}+D_6(ff_{\zeta\zeta})_{\zeta\zeta}\\ &\quad+D_7(f^3)_{\zeta\zeta}=0,\end{aligned}$$

$$f=u_\zeta,\quad D_1=Ad\tilde{d}B_1^2,\quad D_2=2hd\tilde{d}B_1^2,\quad D_3=Bd\tilde{d}B_1^2,$$

$$D_4=A^2d\tilde{d}B_1^3,\quad D_5=Ad\tilde{d}hB_1^3,\quad D_6=3Ad\tilde{d}hB_1^3,$$

$$D_7=3d\tilde{d}h^2B_1^3-\frac{d^3\tilde{d}B_1^3T_1}{\Omega\langle S^x\rangle_0T_2}(JB_1+1)^2. \tag{6}$$

To describe the dynamics of pulse propagation in the ferroelectric, we formally introduce a small parameter ε characterizing the departure of our system from equilibrium, and we seek a solution for f in the form

$$f=\varepsilon^2U(\varepsilon^{1/2}X,\varepsilon^{3/2}T,\varepsilon Y),$$

$$X=\zeta-\tilde{v}t,\quad T=t,\quad Y=\eta, \tag{7}$$

where v is the velocity at which the wave packet propagates. As is customary in the method of multiscale expansions,[10,11] the condition that first-order secular terms in ε vanish gives

$$\tilde{v}^2=v^2-d\tilde{d}\langle S^x\rangle_0 \Bigg/ \left(\Omega+\frac{1}{\Omega T_2^2-J\langle S^x\rangle_0}\right). \tag{8}$$

In the next-higher order of the expansion in ε, after integration we readily obtain

$$-2\tilde{v}U_T+Ad\tilde{d}B_1^2U_{XXX}+4\tilde{h}d^2B_1^2UU_X=v_1^2\partial_X^{-1}U_{YY}. \tag{9}$$

Making the change of coordinates $t=\gamma T$, $x=\alpha X$, $y=\rho Y$, $r=\xi U$, where

$$\gamma=-1/2\tilde{v},\quad \alpha=(Ad\tilde{d}B_1^2)^{-\frac{1}{3}},$$

$$\zeta=24\tilde{h}d^2B_1^2\alpha,\quad \rho^2=-\alpha\beta/v_1^2,$$

we can transform Eq., (9) to the classical form of the Kadomtsev–Petviashvili (KP) equation[12]

$$\partial_x(r_t+6rr_x+r_{xxx})+\beta r_{yy}=0. \tag{10}$$

It is a well-known fact that for $\beta=-1$ this equation has a stable solution representing a two-dimensional soliton, i.e., a lump that decays as $O(1/x^2,1/y^2)$ as $|x|$, $|y|\to\infty$ and moves with a velocity $v_x=P_R^2+P_l^2$, $V_y=-2P_R$,

$$r=\frac{4[-(x'+P_Ry')+P_I^2y'^2+(3/P_I^2)]}{[(x'+P_Ry')+P_I^2y'^2+(3/P_I^2)]^2}, \tag{11}$$

where $x'=x-(P_R^2+P_I^2)t$ and $y'=y+2P_Rt$.

The particular form of the above solution (11) is dictated by the presence of a quadratic nonlinearity in the KP equation [the nonlinearity, in turn, is a consequence of the inclusion of the electrostriction term proportional to h in the Hamiltonian (2)] and can therefore be interpreted as an electrostriction soliton. We note that, owing to its nonexponential decay, the lump has a far greater localization length than ordinary solitons, and it can be associated with the experimentally observed[1,2] clusters in the nonpolar phase of a ferroelectric. By virtue of the properties of the KP equation the lump solutions are stable and do not interact, so that the clusters in the proposed approach are stable as well.

4. The inclusion of intrinsic ferroelectric nonlinearities in the next-higher order of the expansion in ε and the allowance for damping of the acoustic wave imparts a time dependence to the lump parameters P_R and P_I. The perturbation of the KP equation to make the lump parameters depend on the time in the next-higher order of the expansion in ε has the form

$$\begin{aligned}\Pi=M_1r+M_2r_{xyy}+M_3r_{xxxxx}+M_4(r^2)_{xxx}+M_5(rr_{xx})_x\\ +M_6(r^3)_x+M_7\partial_x^{-1}r_{tt},\end{aligned} \tag{12}$$

where

$$M_1=-\gamma\tilde{v},\quad M_2=D_3\alpha^2\rho^2,\quad M_3=D_4\alpha^5,$$

$$M_4=D_5\zeta\alpha^3,\quad M_5=D_6\zeta\alpha^3,\quad M_6=D_7\zeta^2\alpha,\quad M_7=\gamma^2/\alpha.$$

To take the influence of the perturbation into account, we make use of the fact that the KP equation has integrals of motion P_x and P_y that can be interpreted as the lump momentum components:

$$P_x=\frac{1}{2}\int r^2dxdy,\quad P_y=-\frac{1}{2}\int r_xr_ydxdy. \tag{13}$$

Under the influence of the perturbation the integrals of motion now begin to depend on the time as

$$(P_x)_t=\int u\Pi d^2r,$$

$$(P_y)_t=-\frac{1}{2}\int (u_y\Pi_x+u_x\Pi_y)d^2r. \qquad (14)$$

Invoking the method of integrals of motion[9] to analyze the evolution of the lump parameters and substituting the solution (11) into (13) and (14), we obtain

$$(P_I)_t=2M_1P_I,$$

$$(P_RP_I^3)_t=2M_1P_RP_I^3 \qquad (15)$$

and, therefore, $P_I=P_I(0)\exp(\{2M_1t\}$ and $P_R=P_R(0)\times\exp\{-4M_1t\}$. Consequently, the dynamics of the parameters of the lump solution is determined entirely by the acoustic decay rate (associated with the constant M_1) and does not depend on the perturbations associated with the inclusion of intrinsic ferroelectric nonlinearities in the next-higher order of the expansion in ε. We can conclude from these considerations that the clusters are stable against pseudospin nonlinearities, in the proposed approach, and their properties are determined mainly by the damping of acoustic waves.

5. To summarize, on the basis of the above-described elementary model taking electrostriction into account (or taking into account the modulation of the exchange integral by acoustic vibrations in the pseudospin formalism) we have obtained soliton solutions that can be interpreted as the experimentally observed polarization clusters in the nonpolar phase of hydrogen-containing ferroelectrics. The principal advantage of the proposed approach is that the solutions are obtained strictly within the framework of the pseudospin formalism without recourse to additional assumptions of any kind. On the other hand, the treatment here leaves open the question of how electrostriction solitons can be excited in a ferroelectric. We note that the most effective techniques appear to be one that involves heating and cooling (thermal shock) and one that involves x irradiation. Electrostriction solitons can be excited in thermal shock, in particular, by virtue of the different heating and cooling rates of different parts of the sample. Under the influence of x irradiation the unpinning of defects actually present in the sample can produce local acoustic strains, which, in turn, can lead to the generation of electrostriction solitons by virtue of the piezoelectric effect. We also note, in conclusion, that the above-proposed electrostriction solitons, in particular, can also attach to local defects in the crystal structure.

The authors are deeply grateful to A. V. Shil'nikov for valuable consultations and access to experimental data.

[1] A. V. Shil'nikov, E. G. Nadolinskaya, V. A. Fedorikhin, and S. V. Rodin, Kriostallografiya **39**, 84 (1994) [Crystallogr. Rep. **9**, 74 (1994)].
[2] A. V. Shil'nikov, E. G. Nadolinskaya, V. M. Varikash, and S. V. Rodin, in *Proceedings of the Russian Scientific-Technical Conference ''Diélektriki-93''* [in Russian], Part 1 (St. Petersburg, 1993), p. 127.
[3] N. D. Gavrilova and A. M. Lotonov, Izv. Ross. Akad. Nauk, Ser. Fiz. **57**, 123 (1993).
[4] Yu. R. Zabrodskiĭ, V. M. Koshkin, and Yu. B. Reshetnyak, Izv. Akad. Nauk SSSR, Ser. Fiz. **54**, 1207 (1990).
[5] R. Blinc and B. Žekš, *Soft Modes in Ferroelectrics and Antiferroelectrics* (North-Holland, Amsterdam, 1974; Mir, Moscow, 1975).
[6] V. G. Vaks, *Introduction to the Microscopic Theory of Ferroelectrics* [in Russian], Nauka, Moscow, 1973.
[7] M. B. Belonenko and M. M. Shakirzyanov, Zh. Éksp. Teor. Fiz. 99, 860 (1991) [Sov. Phys. JETP **72**, 477 (1991)].
[8] L. D. Landau and E. M. Lifshitz, *Theory of Elasticity*, 3rd ed. (Pergamon Press, New York, Oxford, 1986) [Russ. original, Nauka, Moscow, 1986].
[9] G. L. Lamb, Jr., *Elements of Soliton Theory* (Wiley, New York, 1980; Mir, Moscow, 1983).
[10] R. K. Dodd, J. C. Eilbeck, G. D. Gibbon, and H. C. Morris, *Solitons and Nonlinear Wave Equations* (Academic Press, New York, 1983).
[11] A. H. Nayfeh, *Introduction to Perturbation Techniques* (Wiley, New York, 1981) [Russ. trans., Mir, Moscow, 1984].
[12] V. G. Bakurov, *Candidate's Dissertation* [in Russian], Inst. Teor. Fiz., Chernogolovka (1990), p. 93.

Translated by James S. Wood

PHYSICS OF THE SOLID STATE VOLUME 40, NUMBER 4 APRIL 1998

Chaotic behavior of triglycine sulfate crystals containing radiation defects

A. Yu. Shchekotov and S. N. Drozhdin

Voronezh State University, 394693 Voronezh, Russia

(Submitted October 14, 1997)
Fiz. Tverd. Tela (St. Petersburg) **40**, 716–718 (April 1998)

The temperature-amplitude region of existence of chaotic oscillations in a resonant circuit containing a triglycine sulfate crystal shifts toward higher amplitudes of the repolarization field when the crystal is irradiated with small x-ray doses. This trend is attributed to a change in the kinetics of the domain structure of the crystal in a strong electric field in the presence of radiation defects. *© 1998 American Institute of Physics.* [S1063-7834(98)03004-4]

It has been shown[1–3] that chaotic oscillations are observed in a triglycine sulfate (TGS) crystal in the temperature range corresponding to the ferroelectric phase of this crystal when it is connected as a nonlinear capacitance in a series resonant circuit. The transition from single-period to random oscillations after a change in any of the control parameters (crystal temperature T, amplitude E_0 and frequency f of the repoling field, or strength of the static bias field $E_=$) takes place through a sequence of period doublings. Chaos sets in upon application of a field whose amplitude is two or three times the coercive field of the sample E_c (Ref. 2). It has been hypothesized[3] that the mechanism underlying the onset of chaotic oscillations in the circuit is associated with irregular dynamics of the domain structure of the crystal when it is switched in a strong electric field.

The properties of ferroelectrics are governed to a large extent by various kinds of defects present in them, including radiation defects. Previous studies[4] have been concerned with the influence of small x-ray doses on the form and temporal behavior of the region of random oscillations of a circuit containing a TGS crystal in coordinates of the amplitude and frequency of the repoling field.

The behavior of the domain structure of a crystal during repolarization depends significantly on the temperature. In the present study, therefore, we have investigated the influence of small x-ray doses applied to nominally pure TGS crystal samples on the amplitude-temperature region of existence of chaotic oscillations in a circuit containing this crystal.

The investigated samples were plane-parallel, Y-cut wafers of thickness 0.6 mm and area 25 mm^2 with sprayed-on silver electrodes.

For all the samples, the temperature dependences of the coercive and internal (E_i) fields were measured prior to irradiation from the dielectric hysteresis loop at a frequency of 2.8 kHz. None of the samples selected for investigation had an internal field before irradiation. We then used the same procedure as in our earlier work[2–4] to observe the phase portrait and Poincaré maps of a circuit containing the investigated sample as a nonlinear capacitance. These observations were made in the temperature range from room temperature to the Curie point T_c. At each fixed temperature we traced the variations of the form of the phase portrait and the Poincaré map as the amplitude E_0 during slow variation of the external repoling field. From the critical values of T and E_0, at which the nature of the oscillations in the circuit exhibited a qualitative changed, we reconstructed a diagram on the (T,E_0) coordinate plane, representing the behavior of the system in these control variables and, on the diagram, we identified the region of chaotic oscillations.

The samples were irradiated with x rays (Cu $K\alpha$, $W = 30$ keV) at room temperature in successive dose increments of 20 kR each. For each dose the entire set of measurements was repeated on all samples both immediately following irradiation and again at 140 h after irradiation.

Figure 1 shows the regions of chaotic behavior in coordinates (T, E_0) for a TGS crystal sample before irradiation (region *1*) and after irradiation at doses of 40 kR and 80 kR (regions *2* and *3*). It is evident that irradiation causes the region of chaotic behavior to shift toward higher amplitudes, which become especially pronounced beginning with a dose of 80 kR. In addition, as the dose is increased, the high-temperature limit T_x of the chaos region shifts slightly toward the low-temperature end (see the inset to Fig. 1). Here the values of the internal field generated by radiation defects at these doses are low, amounting to 20–50 V/cm for our investigated samples. The values of the coercive field also increase slightly after irradiation, approximately from 200 V/cm to 300 V/cm; this change is an order of magnitude smaller than the shift of the lower amplitude limit E_{0x} of the chaos region. As a result, the relation $E_{0x} \cong (2-3)E_c$ found in Ref. 3 for nominally pure TGS no longer holds for the irradiated crystal.

The observed behavior of the $T-E_0$ region of chaotic behavior with variation of the dose can be explained as follows. Radiation defects formed in the crystal impede the repolarization process, influencing all of its stages, because irradiation is accompanied by the disappearance of low-energy centers of both initial and wall nucleation.[5] It is impossible for the nucleation of new domains and the motion of domain walls to take place in fields below a certain threshold E', which increases in proportion to the radiation dose.[5] Under these conditions the switching process must go to completion in higher fields than would account for the shift of the chaos region toward higher amplitudes. Moreover, in the presence of defects, the noncoordination of the initial

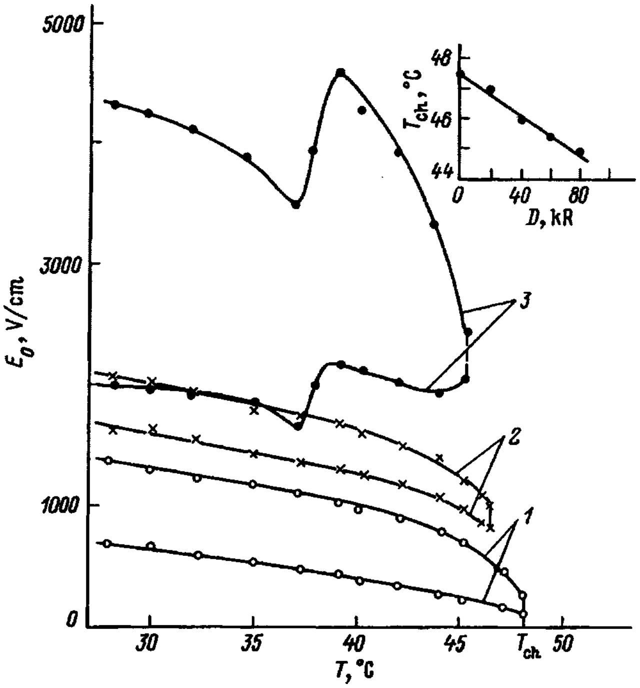

FIG. 1. Amplitude-temperature regions of chaotic behavior of a resonant circuit containing a triglycine sulfate crystal sample. *1*) Before irradiation; *2, 3*) after irradiation with doses of 40 kR and 80 kR, respectively. Frequency $f = 2.8$ kHz. Inset: High-temperature limit of the chaos region versus radiation dose.

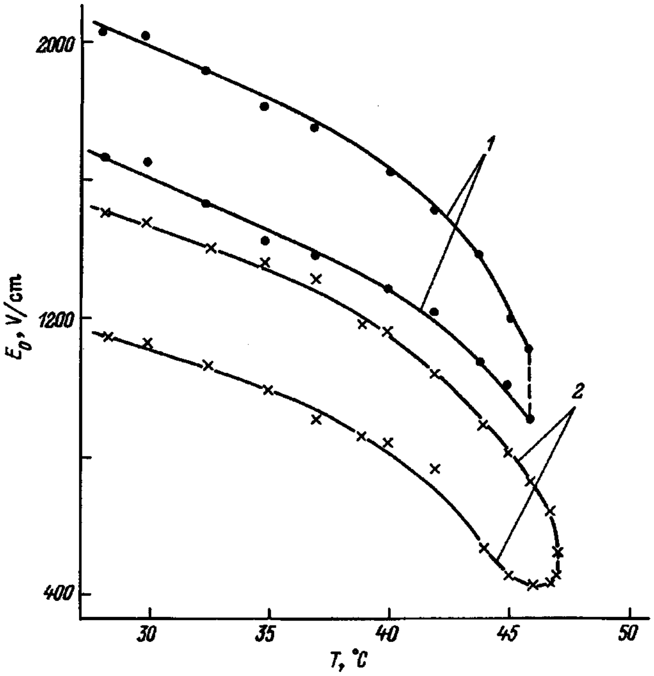

FIG. 2. Amplitude-temperature regions of chaotic behavior of a resonant circuit containing irradiated TGS. *1*) 20 h after irradiation; *2*) 140 h after irradiation. $D = 40$ kR.

nucleation processes with processes involving the motion of domain walls is intensified, and this effect most likely broadens the amplitude range of the existence of chaos.

Only near T_c does the presence of an internal field of radiation origin become significant. Like an external static electric field,[3] it specifically limits the region of chaotic behavior on the T_c side, increasing as the dose increases and, hence, as E_i increases (inset to Fig. 1).

With a time lapse following irradiation, as is evident from Figs. 2 and 3, the chaos regions are observed to shift toward their initial position, the most interesting case corresponding to a dose of 80 kR.

Immediately after radiation a very distinct anomaly is observed on the $T-E_0$ region of chaotic behavior at a temperature ~38 °C, at which the entire region moves sharply upward along the amplitude scale (region *1* in Fig. 3). This anomaly can be attributed to the abrupt increase in the number of domain walls when the domain structure of the TGS crystal is transformed near this temperature.[6] The increase in the number of oscillators, i.e., domains interacting with radiation defects and, as a result, entering into irregular oscillations, produces the effect observed in the experiment.

After 140 h following irradiation, the entire region of chaotic behavior shrinks drastically (essentially because its lower boundary rises; region *2* in Fig. 3), the anomaly at the temperatures of domain structural transformation vanishes, and the high-temperature boundary of the region shifts even farther to the left.

The above-described behavior can be attributed to the fact that the radiation defects migrate toward positions of stable equilibrium and consolidate with the passage of time, so that the repolarization process becomes more difficult than immediately after irradiation and requires the application of a stronger field. Consequently, the lower amplitude limit of the region of chaotic oscillations rises even higher in amplitude. Some of the domain walls, becoming attached to these defects, are totally excluded from the repolarization process, causing the amplitude interval of chaos to diminish. The downward temperature shift of the chaos region is prob-

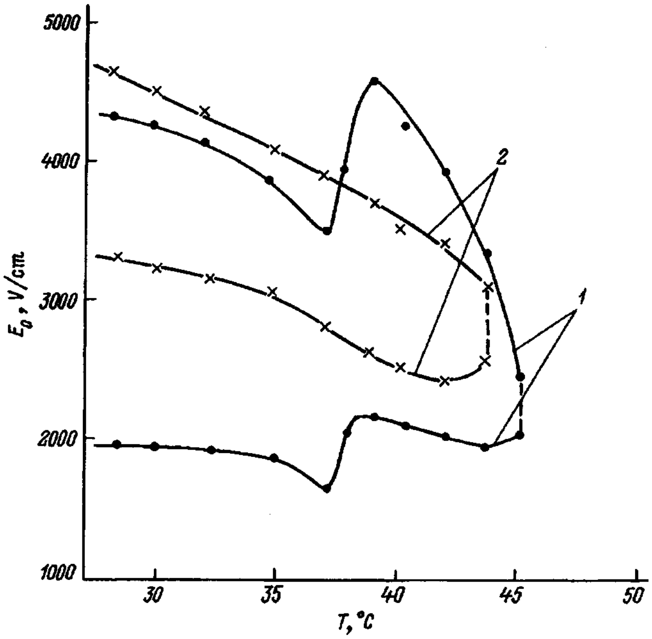

FIG. 3. Amplitude-temperature regions of chaotic behavior of a resonant circuit containing irradiated TGS. *1*) 20 h after irradiation; *2*) 140 h after irradiation. $D = 80$ kR.

ably associated with an increase and, as time passes, stabilization of the internal field created by radiation defects.

[1] H. Beige, M. Diestelhorst, R. Forster, J. Albers, and H. Musser, Ferroelectrics **104**, 355 (1990).

[2] S. N. Drozhdin and L. N. Kamysheva, Kristallografiya **36**, 925 (1991) [Sov. Phys. Crystallogr. **36**, 519 (1991)].

[3] S. N. Drozhdin and L. N. Kamysheva, Fiz. Tverd. Tela (Leningrad) **34**, 2797 (1992) [Sov. Phys. Solid State **34**, 1496 (1992)].

[4] S. N. Drozhdin, L. N. Kamysheva, and O. M. Golitsyna, Ferroelectrics **175**, 119 (1996).

[5] L. I. Lontsova, Author's Abstract of Doctoral Dissertation [in Russian], Voronezh (1991), 36 pp.

[6] V. P. Konstantinova, N. N. Minyushkina, V. S. Rumyantsev, and V. M. Rudyak, Kristallografiya **20**, 1296 (1975) [Sov. Phys. Crystallogr. **20**, 780 (1975)].

Translated by James S. Wood

Anomalously high photovoltages in terbium molybdate

B. K. Ponomarev, V. D. Negriĭ, G. M. Vizdrik, and B. S. Red'kin

Institute of Solid-State Physics, Russian Academy of Sciences, 142432 Chernogolovka, Moscow Province, Russia

I. A. Kornev

Novgorod State University, 173003 Novgorod, Russia

(Submitted October 22, 1997)
Fiz. Tverd. Tela (St. Petersburg) **40**, 719–721 (April 1998)

In terbium molybdate $Tb_2(MoO_4)_3$ at room temperature, a laser beam of wavelength $\lambda_1=4880$ Å induces an electric polarization that lasts for several days after the irradiation is turned off. The photoinduced polarization has the same sign as the spontaneous polarization. At a laser power of 0.5 W and an exposure time of 4.5 h, the photoinduced polarization exceeds the spontaneous polarization by an order of magnitude. The corresponding electric field is 2.5×10^6 V/cm. Under the influence of radiation with $\lambda_1=4880$ Å, terbium molybdate luminesces in the green part of the spectrum near $\lambda_2\approx5425$ Å. The luminescence quantum yield is 20%. © *1998 American Institute of Physics.* [S1063-7834(98)03104-9]

The phenomenon of anomalously high photovoltages (AHP effect) has been observed experimentally in a number of ferroelectrics: $SbSi_{0.35}Br_{0.65}$, $BaTiO_3$, $LiNbO_3$, $SbNbO_3$, $KNbO_3$, and α-$LiIO_3$ (Refs. 1–6). The highest photoinduced field $E\approx10^5$V/cm was obtained in $LiNbO_3$ (Ref. 3).

Here we report an investigation of the AHP effect in the metastable, orthorhombic, ferroelectric β' phase of terbium molybdate $Tb_2(MoO_4)_3$. A $Tb_2(MoO_4)_3$ single crystal was grown by the Czochralski method described in Ref. 7. The samples comprised polished $3\times3\times2$ mm^3 rectangular parallelepipeds. The square faces of the samples were perpendicular to the polar [001] axis, which was the direction of spontaneous electric polarization. The edges of the square faces were parallel to the [110] and [110] axes. The potential difference between the (001) faces was measured. The measurements were performed by means of a Cary 31 electrometer. The latter had a dc input resistance of at least 10^{14} Ω. To safeguard against electrometer overload, the sample was shunted by an additional capacitance. For a sample capacitance $C_{\mathrm{sam}}=0.36\times10^{-12}$ F, the additional capacitance was $C_{\mathrm{add}}=6.46\times10^{-9}$ F. The photoinduced potential difference decreased 18000-fold in this case. The time constant of the electrometer input circuit was of the order of 10^2 h. Spring-loaded brass and sprayed-on aluminum contacts were used in the measurements.

Prior to the measurements the sample was made a single domain by a procedure described in Ref. 8. The room-temperature value of the spontaneous polarization P_s and the profile of its temperature curve $P_s(T)$ agreed with published data.

During the measurements the sample was contained in a double-walled copper container. The container served the dual role of electrostatic shield and thermostat. A heater was enclosed in the container. The container walls had openings for the passage of a laser beam. This structure was suitable for electric polarization measurements in the temperature range from room temperature to 220 °C. The temperature was measured by means of a Chromel-Alumel thermocouple. The laser had an output power of 0.5 W and an emission wavelength of 4880 Å. The latter corresponded to the intrinsic absorption of $Tb_2(MoO_4)_3$ due to the dipole-forbidden transitions $^7F_6\Rightarrow{}^5D_4$ (Ref. 9). The laser beam was parallel to the orthorhombic [110] axis and passed through the middle of the sample at various distances from the (001) faces. The polarization plane of the laser radiation was perpendicular to the (001) faces. At the given radiation power level and wavelength the equilibrium temperature of the sample in the container with the heater off was approximately 40 °C. The equilibrium temperature was determined experimentally prior to the start of the photoinduced voltage measurements.

Before the measurements the temperature of the shorted sample was raised to 40 °C by the heater without radiation. Once this temperature had been established, the laser was turned on, the heater was turned off, the shorting contact was opened, and the sample was connected to the electrometer. The measurements were thus performed in thermal equilibrium between the sample and the laser beam. This condition eliminated any contribution from the pyroelectric effect. The measured potential difference $V(t)$ at time t was proportional to the photoinduced electric polarization of the sample $P_{\mathrm{ind}}(t)=P(t)-P(t_0)$. Here P is the electric polarization, and t_0 is the start time of the measurements. The measurement results are shown in Fig. 1. The various curves were measured at the same temperature of 40 °C but with different shapes of the laser beam cross section.

Curve *1* was measured while the sample was illuminated with an unfocused beam having a circular cross section of diameter ≈1 mm. We see that the illumination of the sample creates a potential difference $V(t)$ between its (001) faces that increases with time. The average photoinduced electric polarization $P_{\mathrm{ind}}(t)$ over the volume of the sample is deter-

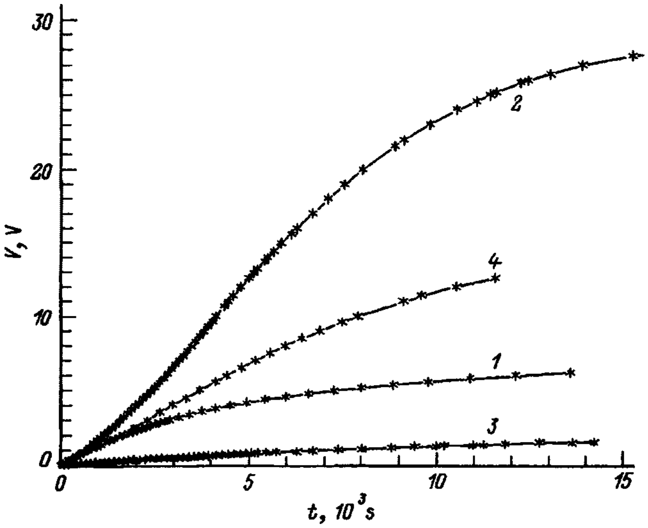

FIG. 1. Photovoltage in $Tb_2(MoO_4)_3$ versus time for various laser beam cross sections. *1*) Circular cross section of diameter 1 mm; *2*) stripe of width 0.1 mm and length 2 mm, parallel to the [001] axis of the crystal; *3*) the same cross section as for curve *2*, but with the stripe perpendicular to the [001] axis; *4*) the same cross section as for curve *2*, but from later measurement.

mined from the measured quantity $V(t)$ according to the relation $P_{\text{ind}}(t)=[V(t)\cdot C_{\text{sam}}+C_{\text{add}})]/S$. Here $S=0.09\ \text{cm}^2$ is the area of the (001) faces of the sample, between which the potential difference $V(t)$ was measured. The rate of increase of the potential difference decreases with time. The voltage after four-hour illumination of the sample is 6.2 V. It corresponds to $P_{\text{ind}}=445\times10^{-9}\ \text{C/cm}^2$, which is two and a half times the room-temperature spontaneous polarization of $Tb_2(MoO_4)_3$: $P_s=187.5\times10^9\ \text{C/cm}^2$ (Ref. 10). The photoinduced polarization has the same sign as the spontaneous polarization. The potential difference $V(t)$ remains almost constant after removal of the laser beam, decreasing by a few percent after 24 h. After shorting of the photopolarized sample the temperature dependence of its spontaneous polarization $P_s(T)$ does not differ more than a few percent from the initial value. In $Tb_2(MoO_4)_3$ radiation at the wavelength $\lambda_1=4880$ Å stimulates strong luminescence in the green part of the spectrum near $\lambda_2\approx5425$ Å. The luminescence quantum yield is $\approx20\%$.

For the measurements in curve *2*, the laser beam was focused by a cylindrical lens. The beam cross section was in the shape of a narrow stripe approximately 0.1 mm wide and approximately 2 mm long, oriented along the polar [001] axis of the crystal and passing through the middle of the (110) face, its ends almost touching the (001) faces of the sample. Clearly, when the beam is focused in this way, P_{ind} increases more rapidly than without focusing. The electrometer input voltage after 4.5-h illumination of the sample is 28 V. This voltage corresponds to $P_{\text{ind}}\approx2\times10^{-6}\ \text{C/cm}^2$, which is an order of magnitude higher than the spontaneous polarization.

For the measurements in curve *3*, the beam formed a stripe parallel to the (001) faces of the sample and was directed onto the middle of the (110) face of the sample. It is evident that for this orientation of the laser spot P_{ind} increases far more slowly with time than in the two preceding cases.

For the measurements corresponding to curve *4*, the laser spot was oriented as in the curve-*2* measurements. A comparison of curves 2 and 4 shows that the effect depends on the previous irradiations of the sample.

The values of the photocurrent can be determined from the curves in the figure by means of the relation $i(t)=-(C_{\text{sam}}+C_{\text{add}})(dV/dt)$. The values of the current at the start of illumination are $i\approx10^{-11}$ A. The current depends on the distance between the illuminated spot and the electrodes: The larger the distance, the lower is the current.

The value attained by us for the photoinduced field $E_{\text{ind}}=2.5\times10^6$ V/cm is two orders of magnitude higher than the value $E_{\text{ind}}=1.05\times10^4$ V/cm for $SbSi_{0.35}Br_{0.65}$ in Ref. 1 and is an order of magnitude higher than the value $E_{\text{ind}}=10^5$V/cm for $LiNbO_3$ in Ref. 3. In Ref. 3 E_{ind} was evaluated by direct measurements. In the present study and in Ref. 1 it was determined from measurements of the photopolarization P_{ind} according to the relation $E_{\text{ind}}=4\pi P_{\text{ind}}/\varepsilon$. The values of ε are 10 for $Tb_2(MoO_4)_3$ (Ref. 11) and 2×10^3 for $SbSi_{0.35}Br_{0.65}$ (Ref. 1).

According to Fridkin,[12] there are two possible causes of the onset of anomalously high photovoltages: 1) the photovoltaic effect; 2) transition photocurrents.

The photovoltaic effect refers to the generation of a steady current (the photovoltaic current) in a single-domain ferroelectric single crystal when it is uniformly illuminated; the induced current can be attributed to the asymmetry of the potential distribution of impurity centers. As a result of this asymmetry the photoexcitation of an impurity center causes an electron to be ejected into the conduction band, producing a steady current. In our case the role of such centers can be filled by Tb^{3+} ions. The asymmetric potential distribution of these centers also causes them to move when ionized (Franck–Condon relaxation). This mechanism also contributes to the steady photovoltaic current.

The AHP effect in ferroelectrics can be identified not only with the steady photovoltaic current, but also with transition photocurrents. According to Fridkin,[12] transition photocurrents can be induced as a result of shielding the spontaneous polarization by nonequilibrium carriers and from the influence of nonequilibrium carriers on the magnitude of the spontaneous polarization.

The presence of transition photocurrents in our experiment is obvious from the $V(t)$ curves. The derivative dV/dt, which is proportional to the photocurrent, decreases after long times t. This behavior is typical of a transition current. However, the nature of the transition current is vague. If the observed values of $V(t)$ were associated with the influence of nonequilibrium carriers on the spontaneous polarization $P_s(T)$, the long persistence of $V(t)$ on the irradiated, unshorted sample after the removal of illumination would indicate that the photoinduced polarization P_{ind} was equal to the change $\Delta P_s(T)$ induced in the spontaneous polarization by nonequilibrium carriers. In that event, however, the curve obtained from measurements of the temperature dependence of the spontaneous polarization of the sample after it had been illuminated and shorted would have the form

$P_{sind}(T)=P_s(T)+\Delta P_s(T)=P_s(T)+P_{\text{ind}}$, which would differ from the initial $P_s(T)$ curve by an amount equal to the photoinduced polarization $\Delta P_s(T)=P_{\text{ind}}$. As mentioned, P_{ind} is an order of magnitude larger than $P_s(T)$. Our measurements of the temperature dependence of the spontaneous polarization of the sample after its illumination and shorting have shown that the $P_{sind}(T)$ curve does not differ more than a few percent from the initial $P_s(T)$ curve. Consequently, $\Delta P_s(T)\ll P_{\text{ind}}$, and the measured effect is not related to the influence of nonequilibrium carriers on the spontaneous polarization.

Shielding of the spontaneous polarization P_s cannot produce the observed values of P_{ind}, for two reasons: 1) the shielding of P_s cannot alter the polarization of the sample by an amount in excess of P_s; 2) the sign of P_{ind} must be opposite that of P_s when the latter is shielded. It follows, therefore, that the nature of the transition currents in our experiment is not the same as that described in Ref. 12. The solution of the steady-current problem will require additional measurements, which are now in the preparation stage.

The authors are indebted to V. V. Kveder and V. V. Sinitsyn for valuable discussions.

This work has received financial support from the International Association for the Promotion of Cooperation with Scientists from the Independent States of the Former Soviet Union (INTAS Project No. 94-0935), from the International Science Foundation (ISF) in collaboration with the Russian government (Project No. JET100), and from the Stipend Fund of the President of the Russian Federation.

[1] A. A. Grekov, M. A. Malitskaya, V. D. Spitsyna, and V. M. Fridkin, Kristallografiya **15**, 500 (1970) [Sov. Phys. Crystallogr. **15**, (1970)].

[2] T. R. Volk, A. A. Grekov, N. A. Kosonogov, and V. M. Fridkin, Fiz. Tverd. Tela (Leningrad) **14**, 3214 (1972) [Sov. Phys. Solid State **14**, 2740 (1972)].

[3] A. M. Glass, D. von der Linde, and T. J. Negran, Appl. Phys. Lett. **25**, 233 (1974).

[4] K. A. Verkhovskaya, A. N. Lobachev, B. N. Popov, V. I. Popolintov, V. F. Peskin, and V. M. Fridkin, JETP Lett. **23**, 476 (1976).

[5] V. M. Fridkin, B. N. Popov, and K. A. Verkhovskaya, Phys. Status Solidi A **39**, 193 (1977).

[6] A. R. Pogosyan, E. M. Uyukin, A. P. Levanyuk, and G. F. Dobrzhanskiĭ, Fiz. Tverd. Tela (Leningrad) **23**, 3280 (1981) [Sov. Phys. Solid State **23**, 1906 (1981)].

[7] B. S. Red'kin, V. N. Kurlov, I. S. Pet'kov, and S. N. Rossolenko, J. Cryst. Growth **104**, 77 (1990).

[8] B. K. Ponomarev, S. A. Ivanov, B. S. Red'kin, and V. N. Kurlov, JETP Lett. **55**, 356 (1992).

[9] B. K. Ponomarev, J. Zeman, G. Martinez, A. G. M. Jansen, P. Wyder, A. K. Zvezdin, V. D. Negrii, and B. S. Red'kin, in *Magnetoelectric Interaction in Crystals, Third International Conference* (Novgorod, 1996), p. 39.

[10] H. J. Borchard and P. E. Bierstedt, J. Appl. Phys. **38**, 2057 (1967).

[11] E. T. Keve, S. C. Abrahams, K. Nassau, and A. M. Glass, Solid State Commun. **8**, 1517 (1970).

[12] V. M. Fridkin, *Photoferroelectrics*, Springer-Verlag, Berlin–New York (1979) [Russ. original, Nauka, Moscow, 1979].

Translated by James S. Wood

PHYSICS OF THE SOLID STATE VOLUME 40, NUMBER 4 APRIL 1998

Self-trapped carrier states and dielectric hysteresis in disordered dipole systems

M. D. Glinchuk

Institute for Materials Sciences, National Academy of Sciences of Ukraine, 252680 Kiev, Ukraine

V. A. Stefanovich

Institute for Semiconductor Physics, National Academy of Sciences of Ukraine, 252650 Kiev, Ukraine

L. Jastrabik

Institute of Physics, Academy of Sciences of the Czech Republik, 18040 Prague 8, Czech Republik

(Submitted October 31, 1997)
Fiz. Tverd. Tela (St. Petersburg) **40**, 722–727 (April 1998)

Theory of self-trapped free-carrier states (fluctuons) at polarization fluctuations in $KTaO_3$:Li,Nb-type disordered ferroelectrics has been developed. The main characteristics of the fluctuon, viz. its energy, localization length, effective mass, and mobility have been calculated as functions of impurity-dipole concentration and temperature. The theory predicts the appearance of stable fluctuon states both in the ferroelectric–dipole-glass mixed phase and in the dipole glass state of disordered ferroelectrics. The possible participation of fluctuons in conduction and other transport phenomena in disordered ferroelectrics is discussed.

Self-trapped carrier states, such as polarons[1] and fluctuons[2], play an essential part in the physics of semiconductors and insulators. It is known that the fluctuon is a carrier trapped close to a fluctuation in crystal polarization.[2,3] Therefore fluctuons result from carrier interaction with both longitudinal and transverse lattice vibrations. The latter is particularly important for ferroelectrics, where spontaneous polarization is connected with transverse phonons. Physics of self-trapped states was being developed primarily for polarons (see, e.g., Refs. 1,4), whereas information on fluctuon states is very scarce. A theory of fluctuons in conventional ferroelectrics was put forward in Ref. 5, where domain walls were considered as the main source of polarization fluctuations. At the same time disordered dipole systems residing in the dipole glass state or in a mixed ferroelectric-glass phase contain only polar clusters with short-range order, or coexisting short- and long-range order (see, e.g., Ref. 6 and references therein). Obviously enough, polarization fluctuations should be a characteristic feature of such systems. Taking into account that many systems with random electric dipoles exhibit noticeable electrical conduction[7–9], one may expect that fluctuon formation is more probable in such systems than in conventional ferroelectrics.

This work develops a theory of self-trapped fluctuon states of carriers in systems with random electric dipoles, which are capable of inducing dipole-glass–ferroelectric-glass–ferroelectric-phase transitions.

The calculations are performed for a model disordered system with electric dipoles, $K_{1-x}Li_xTaO_3$ (KLT), with $x<0.05$, where off-center Li^+ ions act as randomly located and oriented electric dipoles in the incipient ferroelectric $KTaO_3$. It is known that lithium dipoles in KLT induce a ferroelectric phase transition for $x>0.05$ and dipole-glass–ferroelectric-glass phase transitions for $x\leqslant 0.05$ at low temperatures $T<50$ K.[10] We are going to show that due to large polarization fluctuations in the above two phases, the fluctuon states of self-trapped carriers are stable, and that they produce very shallow local carrier states in the crystal's energy gap.

1. GENERAL EQUATIONS

The fluctuon energy functional for the case of strong coupling with polarization in a dielectric containing dipole impurities can be written in the effective-mass approximation[1)] similarly to the way this was done by Pekar (see, e.g., Ref. 1):

$$W=\frac{\hbar^2}{2m^*}\int|(\nabla\psi)^2|d^3r-\int \mathbf{P}\mathbf{D}d^3r+\int fd^3r, \tag{1}$$

where m^*,ψ, and $\mathbf{D}$ are, respectively, the effective mass, wave function, and electric field induction of the carrier, $\mathbf{P}$ is polarization, and f is the free-energy density of a disordered dielectric with dipole impurities[11]. The simplest expression for f is obtained in the case of eight possible impurity-dipole orientations[11]

$$f=\frac{C}{2}(\nabla P)^2+\frac{4\pi}{C_1}\left[\frac{1}{2}P^2-\frac{d^{*2}}{V_0^2\beta}\int_0^\infty\frac{[1-\cos(\rho P_1E_0(\rho))]\exp[F_1(\rho)]}{\sinh(\pi\rho/2\beta)\rho E_0(\rho)}d\rho\right],$$

$$C_l=(1/\varepsilon_\infty)-(1/\varepsilon_0), \tag{2}$$

where $d^*=\gamma_0d\varepsilon_0/3$ is the effective impurity dipole moment, γ_0 is the Lorentz factor, ε_0 and ε_∞ are the low- and high-frequency dielectric permittivities, respectively, the functions

$E_0(\rho)$ and $F_1(\rho)$ characterize, respectively, the mean field and halfwidth of the random-electric-field distribution function in the system[11], $P_1 = PV_0/d^*$, V_0 is the unit cell volume, and $\beta \equiv 1/kT$. Vector **D** is the electric-field induction of the carrier (electron):[1]

$$\mathbf{D}(\mathbf{r}) = -e\int |\psi(\mathbf{r}_1)|^2 \frac{(\mathbf{r}-\mathbf{r}_1)}{|\mathbf{r}-\mathbf{r}_1|^3} d^3r_1 . \tag{3}$$

For definiteness, we are going to assume below that **P** and **D** are oriented along the z axis, i.e. that $\mathbf{P} = P\mathbf{i}_z$ and $\mathbf{D} = D\mathbf{i}_z$.

Equation (1), combined with Eqs. (2) and (3), determines the static properties of the fluctuon. By applying to Eq. (1) independent variations in ψ and P, we obtain the following equations for the fluctuon structure[2)]

$$-D[\psi] - C\Delta P + \frac{4\pi}{C_1}\left[P - \frac{d^{*2}}{V_0^2\beta}\int_0^\infty \frac{\sin(\rho P_1 E_0(\rho))\exp[F_1(\rho)]}{\sinh(\pi\rho/2\beta)} d\rho\right] = 0 ,$$

$$-\frac{\hbar^2}{2m^*}\Delta\psi - eP(\psi)\int \psi(\mathbf{r}_1)\frac{(z-z_1)}{|\mathbf{r}-\mathbf{r}_1|^3} d^3r_1 = 0 . \tag{4}$$

Equations (4) have to be solved subject to an additional normalization condition

$$\int |\psi|^2 d^3r = 1 \tag{5}$$

The coupled partial integro-differential equations (4) represent the main result of this theoretical work. They are extremely complex and have many classes of solutions, with one of them describing the carrier trapped at various nonuniformities in **P** of domain-wall type. Many physically important conclusions can be drawn by analyzing the case of macroscopically uniform polarization, i.e. the case of $\Delta\mathbf{P} = 0$. In this case the expression relating **D** and **P** becomes algebraic rather than differential, so that

$$D = \frac{4\pi}{C_1}\left[P - \frac{d^{*2}}{V_0^2\beta}\int_0^\infty \frac{\sin(\rho P_1 E_0(\rho))\exp[F_1(\rho)]}{\sinh(\pi\rho/2\beta)\rho E_0(\rho)} d\rho\right]. \tag{6}$$

It should be pointed out that for $P_1 = L$, i.e., at equilibrium, the bracketed expression in Eq. (6) is zero, so that $D = 0$, and the fluctuon does not exist. This means that despite our neglecting the term with ΔP the fluctuon remains to be an essentially nonlinear phenomenon. Moreover, inclusion of ΔP would only introduce unjustifiable complications, since the most essential fluctuations in disordered systems arise as a result of disorder, and they are described by Eq. (6).

Equations (4)–(6) make up a fairly general system. It can be applied to investigation of the effect of carriers on polarization in disordered dielectrics. This effect turns out to be essential in the compounds under study[12] and is typical of photoferroelectrics[13]. This system is still, however, too complex, and we have not been able to find an analytical solution to it. Therefore we are going to study the properties of the fluctuon by direct variational techniques. To do this, we have to substitute Eq. (6) into (1) with due account of Eq. (3), and to minimize the expression thus obtained using Eq. (5) with some trial function.

We shall have first to investigate the relation between polarization and induction, which is important also for description of dielectric hysteresis in the systems of interest here for the case where D is the induction of an external electric field. We are turning now to a study of this phenomenon.

2. DIELECTRIC HYSTERESIS

Equation (6) can be recast in dimensionless variables

$$\mathscr{D} = P_1 - 4\pi\nu\tau\int_0^\infty \sin(2\pi P_1 g_2(x))\frac{\exp[-2\pi\nu g_1(x)]}{\sinh(2\pi^2\nu\tau x)} dx, \tag{7}$$

where $\mathscr{D} = C_1V_0D/4\pi d^*$, $\nu = nr_c^3$, $\tau = T/T_{cMF}$, $k_BT_{cMF} = 4\pi n d^{*2}/3\varepsilon_0$, $x = \rho d^{*2}/\varepsilon_0 r_c^3$, and the functions $g_1(x)$ and $g_2(x)$ are related to functions $F_1(\rho)$ and $E_0(\rho)$ written in dimensionless variables. In the mean-field approximation Eq. (7) allows simplification to

$$\mathscr{D} = P_1 - \tanh\left(\frac{P_1}{\tau_1}\right). \tag{8}$$

The $P_1(\mathscr{D})$ relation (8) is plotted in Fig. 1 for different values of τ. This relation is seen to be s-shaped for $\tau < 1$ ($T < T_{cMF}$), i.e., in the ferroelectric phase. As this will be shown later, part of the $P_1(\mathscr{D})$ curve, where $dP_1/d\mathscr{D} < 0$, corresponds to the maximum of energy (rather than to its minimum, where $dP_1/d\mathscr{D} > 0$), i.e., to the unstable fluctuon. Thus the dependence of P_1 on external electric field in ferroelectric phase (in our case it is electric induction $\mathscr{D}$) has the form of conventional hysteresis. A qualitatively similar situation is obtained also beyond the mean-field approximation (Fig. 1b).

Note that if one considers $\mathscr{D}$ as a function of external electric field, the hysteresis dependences $P(E)$ can be used to describe the experimentally observed dielectric hysteresis loops in KTN and other incipient ferroelectrics with dipole impurities (see, e.g., Refs. 10,12,14,15).

3. FIXED FLUCTUON

The $P_1(\mathscr{D})$ relations (Fig. 1) permit an important conclusion, namely, that both stable and unstable parts of the hysteresis curve can be approximated by straight lines, with the deviation being the largest at the points where $dP_1/d\mathscr{D} = 0$. This approximation does not affect the qualitative results while at the same time permitting a straightforward analysis of the fluctuon structure similar to the case of Pekar's polaron[1].

Approximation of the hysteresis relation (7) by straight lines can be achieved by expanding it in the vicinity of $P_1 = P_0$, $\mathscr{D}(P_0) = 0$ to first order in $\mathscr{D}$:

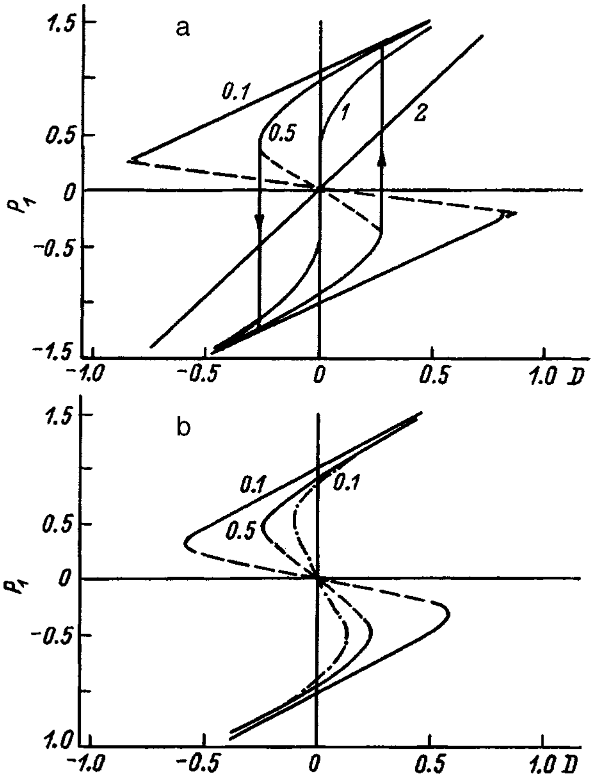

FIG. 1. Hysteresis relation $P_1(\mathscr{D})$. The numbers at the curves relate to the values of τ. (a) Mean-field approximation. Dashed line corresponds to the ''unstable'' part of the hysteresis curve, as well as to its approximation with straight lines. Vertical bars with arrows identify motion along the hysteresis curve. (b) Analysis beyond the mean-field approximation; $nv_c^3=1$ - solid lines, $nv_c^3=0.05$ - dot-and-dash lines.

$$P_1=P_0+\frac{\mathscr{D}}{\Phi(\nu,\tau)},\quad \Phi(\nu,\tau)=\left(\frac{dP_1}{d\mathscr{D}}\right)\Bigg|_{P=P_0},\tag{9}$$

where P_0 is given by the equation

$$P_0=4\pi\nu\tau\int_0^{\infty}\sin(2\pi P_0 g_2(x))\frac{\exp[-2\pi\nu g_1(x)]}{\sinh(2\pi^2\nu\tau x)}dx.\tag{10}$$

The relation can be recast in an explicit form

$$\Phi(\nu,\tau)=1-8\pi^2\nu^2\tau\int_0^{\infty}xg_1(x)\cos(2\pi P_0 g_2(x))\times\frac{\exp[-2\pi\nu g_1(x)]}{\sinh(2\pi^2\nu\tau x)}dx.\tag{11}$$

This expansion for the ''stable'' part of the hysteresis can be readily made by setting $P_0=0$ in Eq. (11).

Note that the mean-field approximation yields the following explicit expressions for the above expansion

$$P_1=P_0+\mathscr{D}\frac{\tau\cosh^2 P_0/\tau}{\tau\cosh^2 P_0/\tau-1}\tag{12}$$

for the stable, and

$$P_1=\frac{\tau}{\tau-1}\mathscr{D}$$

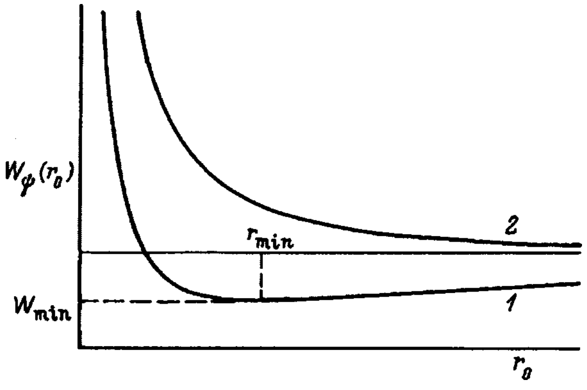

FIG. 2. Schematic representation of $W_\psi(r_0)$ [Eq. (16)] for the ''stable'' (*1*) and ''unstable'' (*2*) parts of the hysteresis curve.

for the unstable parts of the hysteresis curve.

Using Eqs. (9)–(11), the fluctuon energy functional assumes the following simple form

$$W=\frac{\hbar^2}{2m^*}\int|(\nabla\psi)^2|d^3r-\frac{2\pi d^{*2}}{C_1V_0^2\Phi(\nu,\tau)}\int\mathscr{D}^2d^3r,\tag{13}$$

with $\Phi(\nu,\tau)$ given by Eq. (11). We readily see that for $D=D_z$ Eq. (3) for a spherically symmetric function $\psi=\psi(r)$ can be identically rewritten

$$D(\mathbf{r})=4\pi\cos\theta\frac{e}{r^2}\int_0^r r_1^2|\psi(r_1)|^2dr_1.\tag{14}$$

To obtain the fluctuon ground-state energy, we choose a one-parameter trial function in Pekar's form[1]. With this choice, this function gives the lowest ground-state energy compared to all other one-parameter trial functions. It can be written as

$$\psi=\frac{1}{\sqrt{7\pi r_0^{3/2}}}\left(1+\frac{r}{r_0}\right)\exp\left(-\frac{r}{r_0}\right),\tag{15}$$

where r_0 is the variational parameter.

Substituting Eqs. (14) and (15) into Eq. (13) yields

$$W_\psi=\frac{3\hbar^2}{14m^*r_0^2}-0.428332\frac{e^2C_1}{6\Phi(\nu,\tau)r_0}.\tag{16}$$

It can be easily shown that within the unstable part of the hysteresis, the energy W_ψ has a maximum (Fig. 2), whereas within the stable one it passes through a minimum, so that

$$r_{\min}=\frac{6\hbar^2\Phi(\nu,\tau)}{m^*e^2C_1},\quad W_{\min}=-0.0054946\frac{m^*e^4C_1^2}{\hbar^2\Phi^2(\nu,\tau)}.\tag{17}$$

The relations $\Phi(\nu,\tau)$ (dimensionless localization length) and $1/\Phi^2$ (absolute value of the dimensionless ground-state energy) are shown graphically in Fig. 3 for different ν for the paraelectric, ferroelectric, and dipole-glass phases in a disordered ferroelectric (the phase diagram is described, for example, in Refs. 11, 15). We see that in the ferroelectric phase the localization length follows a temperature behavior which is qualitatively similar to that of spontaneous polarization. This is a typical manifestation of the fluctuon (and not of the

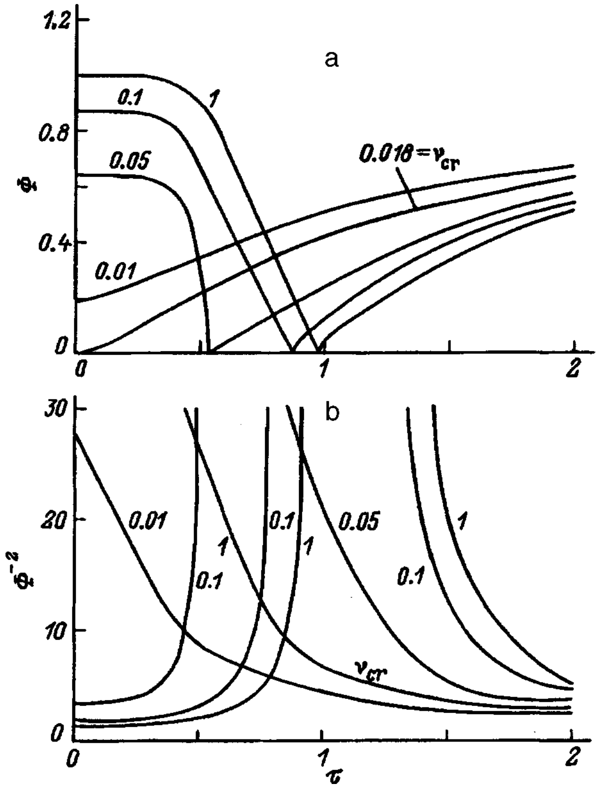

FIG. 3. (a) Dimensionless localization length Φ and (b) absolute value of fluctuon ground-state energy Φ^{-2} *vs* dimensionless temperature τ. The numbers at the curves specify the values of nr_c^3.

polaron) nature of carrier localization in disordered ferroelectrics. Indeed, the growth of spontaneous polarization with decreasing temperature implies depression of fluctuations, which, in its turn, reduces the probability of fluctuon formation. The same behavior follows also from Eq. (17) and Fig. 3, because $|W_{\min}| \propto 1/r_{\min}^2$. The points where $\Phi(\nu,\tau)=0$ correspond to the ferroelectric transition temperature.[11] At these points, $r_{\min}\rightarrow 0$, and $W_{\min}\rightarrow -\infty$. This implies that the fluctuon collapses at the phase transition point, but has a finite radius in the para- and ferroelectric phases. In the paraelectric phase there is no spontaneous polarization, and carrier localization can occur due to both polarization fluctuations induced by random electric fields and the conventional polaron effect. In the limit as $\nu\rightarrow 0$, only the polaron effect can produce carrier localization. This follows from Eqs. (9) and (16), where for $\tau\rightarrow\infty$ and/or $\nu\rightarrow 0$ we obtain $\Phi=1$, which corresponds to Pekar's polaron[1].

Since the asymptotic behavior with $\nu\rightarrow 0$ is valid also for the dipole-glass phase setting in for $\nu<\nu_{cr}\approx 0.0184$ (Ref. 11), we again have here Pekar's polaron. For $\nu\approx\nu_{cr}$ and low temperatures, however, the polaron contribution is essential for the dipole-glass state as well.

4. EFFECTIVE MASS AND MOBILITY OF THE FLUCTUON

As usual, the effective mass of the fluctuon can be calculated from its energy when it moves with a low velocity. Since the fluctuon is coupled to the impurity subsystem, its motion will have a dissipative character.

The equations of motion for the fluctuon can be readily derived using the free energy (2) in the form of Landau-Khalatnikov equations

$$\frac{dP_1}{dt}=-\Gamma\frac{\delta F}{\delta P_1}, \tag{18}$$

where F is the free energy (2) taken at $C=0$, and Γ is a kinetic coefficient connected with the polarization relaxation time[16].

Equation (18) can be written in an explicit form

$$\frac{dP_1}{dt}=\Gamma\frac{4\pi d^{*2}}{C_1V_0^2}\left[\mathscr{D}-P_1+\int_0^\infty \sin(2\pi P_1 g_2(x))\right.$$
$$\left.\times\frac{\exp[-2\pi\nu g_1(x)]}{\sinh(2\pi^2\nu\tau x)}dx\right]. \tag{19}$$

The linearization procedure in the vicinity of P_0 can be applied also to Eq. (19). Assuming $P=P_0+\delta P$, we obtain

$$\frac{d\,\delta P}{dt}=-\Gamma\frac{4\pi d^{*2}}{C_1V_0^2}[-\mathscr{D}+\Phi\,\delta P], \tag{20}$$

where Φ is defined by Eq. (11). Equation (20) has the following solution

$$P_1-P_0=\gamma\,\exp(-\gamma\Phi t)\int_{-\infty}^{t}\mathscr{D}(t_1)\exp(\gamma\Phi t_1)dt_1,$$

$$\gamma=\Gamma\frac{4\pi d^{*2}}{C_1V_0^2}. \tag{21}$$

This solution is valid for an arbitrary fluctuon velocity. Investigation of fluctuon motion with an arbitrary velocity (for instance, in an external electric field) is of interest because it can be applied to description of transport phenomena (such as photoconductivity[9]) in the compounds under study. Such an investigation could be performed similar to the way this was done for Pekar's polaron[17]. We shall restrict ourselves here, however, to studying fluctuon motion with low velocities.

Let the fluctuon move along the x axis. In this case $\mathscr{D}=\mathscr{D}(x-vt,y,z)$, where v is the velocity. For small v, Eq. (21) yields

$$P_1(\xi,y,z)-P_0\simeq\frac{1}{\Phi}\left(\mathscr{D}+\zeta\left(\frac{\partial\mathscr{D}}{\partial\xi}\right)+\zeta^2\left(\frac{\partial^2\mathscr{D}}{\partial\xi^2}\right)+\cdots\right),$$

$$\xi=x-vt,\quad \zeta=\frac{v}{\gamma\Phi}. \tag{22}$$

To obtain Eq. (22) from (21), we have set $t-t_1=t_2$ in Eq. (21) and expanded the resultant expression in t_2, taking into account that $\partial/\partial t=-v\,\partial/\partial\xi$.

As seen from Eq. (22), for $v=0$ we obtain as the result Eq. (9) for a fixed fluctuon. Substitution of Eq. (20) into Eq. (1), followed by some straightforward algebra, yields an expression for the energy of the low-velocity fluctuon

$$W_v=\frac{\hbar^2}{2m^*}\int|(\nabla\psi)^2|d^3r-\frac{2\pi d^{*2}}{C_1V_0^2}\times\left[\frac{1}{\Phi(\nu,\tau)}\int\mathscr{D}^2d^3r-\frac{u^2}{\gamma^2\Phi^3}\int\left(\frac{\partial\mathscr{D}}{\partial x}\right)^2d^3r\right]. \qquad (23)$$

The next step consists, as usual, in substitution into Eq. (23) of $\psi_v=\psi_0+v^2\psi_1$, followed by finding the coefficient of v^2 in the energy W_v. This yields

$$\mathscr{M}=\frac{C_1V_0^2}{4\pi d^{*2}\Gamma^2\Phi^3}\int\left(\frac{\partial\mathscr{D}}{\partial x}\right)^2d^3r, \qquad (24)$$

where $\mathscr{M}$ is the fluctuon effective mass we are looking for. To calculate it, we can use the wave function ψ_0 of the polaron at rest (15) (see, e.g., Refs. 1, 18).

In the low-velocity limit, the fluctuon mobility can also be calculated. It can be shown that in an external electric field $\mathscr{E}$ (we assume it to be directed along the x axis) the equation of motion of the fluctuon has the form

$$e\mathscr{E}v=\frac{dW_t}{dt}, \qquad (25)$$

where W_t is the energy of the moving fluctuon. For small v, $dW_t/dt\simeq W_t/\tau_0$, where τ_0 is the polarization relaxation time. Since for low v, $W_t-W_0\simeq\mathscr{M}v^2/2$, where W_0 is the mass of the fluctuon at rest, and $\mathscr{M}$ is the effective mass (24), we obtain for the mobility $\mu=v/\mathscr{E}$

$$\mu=\frac{2e\tau_0}{\mathscr{M}}. \qquad (26)$$

Expression (26) for the fluctuon mobility is formally identical with the relation for the mobility of a band carrier in a semiconductor (see, e.g., Ref. 19). It implies that for low velocities the mobility of the fluctuon is inversely proportional to its effective mass.

Using Eqs. (14) and (17), we substitute the trial function (15) into (24) to obtain

$$\mathscr{M}=2.719\times10^{-7}\frac{C_1^6V_0^4e^8m^{*3}}{\Gamma^2d^{*4}\hbar^6}\frac{1}{\Phi^6}(g). \qquad (27)$$

The dimensionless effective mass and mobility of the fluctuon are shown in Fig. 4a, b, respectively. We see that at the phase transition point the effective mass goes to infinity, and the mobility vanishes. This means that at phase transition points the fluctuation contribution to mobility vanishes. The fluctuon contribution is seen to be the largest at $T=0$ in the ferroelectric phase. This indicates that thermal and spatial fluctuations in the impurity subsystem depress the fluctuon contribution to conduction.

It should be pointed out that the mobility behaves with temperature and concentration qualitatively similarly to the localization length (compare Figs. 3a and 4b), so that all the effects discussed above manifest themselves in mobility as well.

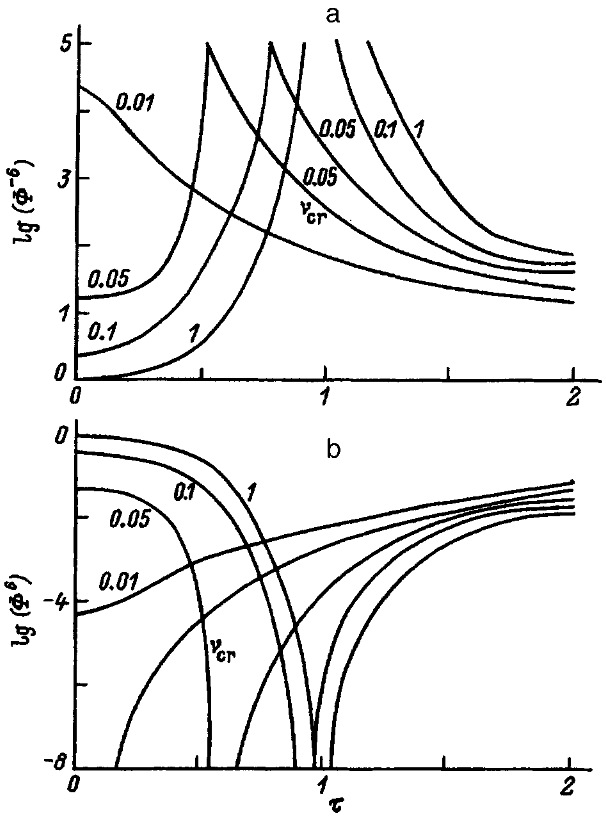

FIG. 4. (a) Fluctuon dimensionless effective mass Φ^{-6} and (b) fluctuon mobility Φ^6 *vs* dimensionless temperature τ. The numbers at the curves specify the values of nr_c^3.

Let us make some numerical estimates. Regrettably, the experimental data (see Refs. 10, 14, 15 and references therein) available for disordered dielectrics are not sufficient for making a more or less accurate calculation of the fluctuon parameters. We shall therefore restrict ourselves here to order-of-magnitude estimates only. Equation (17) yields

$$r_{\min}=3.18\frac{\Phi}{\alpha C_1},(\text{Å}), \quad W_{\min}=-0.16\frac{\alpha C_1^2}{\Phi^2},(\text{eV}), \qquad (28)$$

where $\alpha=m^*/m_0$, and m_0 is the free-electron mass. For the effective-mass approximation used here to be valid, $r_{\min}$ should be large enough that $r_{\min}/a\geqslant3-4$, where $a\simeq4$ Å is the lattice constant of $KTaO_3$. Assuming in Eq. (28) $r_{\min}=3a$, we obtain $\Phi/\alpha C_1\simeq3.8$, which yields

$$W_{\min}\simeq-\frac{0.01}{\alpha},(\text{eV}).$$

It is known that the effective-mass approximation is valid for $|W_{\min}|\leqslant0.01$ eV. In this case $\alpha\sim1$, i.e. for the fluctuon to exist, the bare carrier should be heavy. This conclusion is limited, however, to the effective-mass approximation employed here.[3)]

Estimates of the effective mass and mobility likewise turn out to be rather crude because of the lack of reliable information on Γ. Assuming $\Gamma\sim V_0/W_{\min}\tau_0$, we come to $\mathscr{M}\sim10^3m_0$. This estimate makes the fluctuon contribution to conduction very small, but one should bear in mind that more accurate values of Γ and m^* could change this value by orders of magnitude.

Partial support of ISSEP Foundation (Grant SPU072012) is gratefully acknowledged.

[1] We neglect here the anisotropy in carrier effective mass, which does not affect qualitatively the properties of the fluctuon.

[2] It should be kept in mind that for the fluctuon ground state ψ is a real function.

[3] Our method permits one to go beyond the effective-mass approximation. In this case the periodic potential of the host crystal lattice should be included into the fluctuon functional (1).

---

[1] S. I. Pekar, *Collection of Papers* [in Russian], Naukova Dumka, Kiev (1987), 380 pp.

[2] M. A. Krivoglaz, Usp. Fiz. Nauk **111**, 617 (1973) [Sov. Phys. Usp. **16**, 856 (1974)].

[3] M. I. Klinger, Usp. Fiz. Nauk **146**, 105 (1985) [Sov. Phys. Usp. **28**, 391 (1985)].

[4] Yu. A. Firsov, *Polarons* [in Russian], Nauka, Moscow, 1975.

[5] B. V. Egorov, I. B. Egorova, and M. A. Krivoglaz, Fiz. Tverd. Tela (Leningrad) **26**, 3112 (1984) [Sov. Phys. Solid State **26**, 1874 (1984)].

[6] M. D. Glinchuk and R. Farhi, J. Phys.: Condens. Matter **8**, 6985 (1996).

[7] A. I. Lebedev and I. A. Sluchinskaya, Fiz. Tverd. Tela (St. Petersburg) **35**, 629 (1993) [Phys. Solid State **35**, 321 (1993)].

[8] K. Woicik, J. Blaszczak, and J. Handerek, Ferroelectrics **70**, 3946 (1986).

[9] R. S. Klein, G. E. Kugel, M. D. Glinchuk, R. O. Kuzian, and I. V. Kondakova, Phys. Rev. B **50**, 9721 (1994).

[10] B. E. Vugmeister and M. D. Glinchuk, Rev. Mod. Phys. **62**, 993 (1990).

[11] V. A. Stephanovich, Ferroelectrics **192**, 29 (1997).

[12] B. E. Vugmeister and M. D. Glinchuk, Usp. Fiz. Nauk **146**, 459 (1985) [Sov. Phys. Usp. **28**, 589 (1985)].

[13] V. M. Fridkin, *Photoferroelectrics* [Springer, Berlin (1979); Vysshaya Shkola, Moscow (1976), 257 pp.].

[14] W. Kleemann, Int. J. Mod. Phys. B **7**, 2469 (1993).

[15] U. T. Höchli, K. Knorr, and A. Loidl, Adv. Phys. **39**, 405 (1990).

[16] R. Blinc and B. Žekš, *Soft Modes in Ferroelectrics and Antiferroelectrics* (North-Holland, Amsterdam, 1974, 342 pp.).

[17] A. S. Davydov and V. Z. Énol'skiĭ, Zh. Éksp. Teor. Fiz. **81**, 1088 (1981) [Sov. Phys. JETP **54**, 577 (1981)].

[18] Yu. G. Semenov and V. A. Stefanovich, Zh. Éksp. Teor. Fiz. **101**, 1024 (1992) [Sov. Phys. JETP **74**, 549 (1992)].

[19] A. I. Ansel'm, *Introduction into the Physics of Semiconductors* [in Russian], Nauka, Moscow (1978), 832 pp.

Translated by G. Skrebtsov

PHYSICS OF THE SOLID STATE VOLUME 40, NUMBER 4 APRIL 1998

LATTICE DYNAMICS. PHASE TRANSITIONS

Identification of biphonons from prominent features of the angular and energy dependences of the inelastic-scattering cross section of biphonon-splitting neutrons

O. A. Dubovskiĭ and A. V. Orlov

Physics and Power Institute, 249020 Obninsk, Kaluga Province, Russia

(Submitted October 8, 1997)
Fiz. Tverd. Tela (St. Petersburg) **40**, 728–734 (April 1998)

The dispersion relations and wave functions of biphonon and dissociated two-phonon states of anharmonic crystals are used to determine the cross section of inelastic scattering of neutrons that split biphonons into unbound phonons, which scatter each other as a result of their anharmonicity. Prominent features are found of the angular and energy dependences of the cross section, useful for analyzing experimental data to identify biphonons; it is possible that these features can also be used for subsequent, potentially major modification of the system of existing criteria, based solely on energy-balance considerations for the classification of series of spectral resonances, supposedly corresponding to bound multiphonon states of various multiplicities. For a fixed, large loss of neutron energy, the cross section is a maximum in a ''nonhead-on'' neutron-biphonon collision with a lobe-shaped angular scattering diagram; for intermediate energy losses the cross section has the largest of all possible values at all collision angles; and, for small energy losses, the cross section is a maximum for ''head-on'' collision in a narrow range of angles. For a fixed angle the energy dependence of the cross section has a resonance peak, which exists at the low-energy edge of a finite energy band for large angles and, as the angle decreases, gradually increases as it shifts toward the high-energy edge of the band, which becomes narrower and shifts into the low-energy region. However, when the angle decreases below a critical value, the still-increasing resonance maximum changes direction and shifts back toward the low-energy edge. It is shown that, despite strong oscillations of the biphonon wave function in the presence of negative phonon dispersion, the cross section does not depend on the sign of the dispersion, i.e., the universal law of independence from this sign, established previously for the dispersion relation and the biphonon damping constant, appears to carry over to the cross section. [S1063-7834(98)03304-8]

Experimental and theoretical studies are currently in progress on the spectra of nonlinear coupled multiexciton excitations and multiphonon vibrational modes involving biexcitons, biphonons, triphonons, etc.[1–5] These excitations and modes are investigated in various crystalline materials — semiconductors, metal hydrides, and ionic crystals — by a variety of methods: slow-neutron scattering, optical excitation by lasers in the visible and infrared regions, and electron scattering.[6–10] The narrow peaks observed in the inelastic neutron and photon scattering spectra in the vicinity of broad bands of dissociated two-phonon and three-phonon states are identified as corresponding to biphonons and triphonons. Only the first few components of multiplets of 2, 3, 4, 5, ... fold multiphonon coupled modes, with the additional inclusion of multiplets of terms of excited bound states within the spectral region corresponding to each individual multiplicity, have been found experimentally.[4–13] The identification of the narrow resonance peaks near the broad bands of dissociated modes as biphonons and triphonons is based at the present time on general energy-balance considerations. Suppose that a band of, say, optical vibrations with wave vector $\mathbf{k}$ and energy $\mathbf{E}_1 = E(\mathbf{k})$ is observed in the one-phonon region of the spectrum, and a narrow peak with energy $E_{\mathrm{bp}} = E_{2,min} - 2A$ is observed in the high-frequency region of binary states below the minimum of a two-phonon vibrational band $E_2 = E(\mathbf{k}_1) + E(\mathbf{k}_2)$; when the one-phonon region of the spectrum does not have any prominent feature at the energy $E_{1,min} - A$, the narrow peak E_{bp} can be attributed to anharmonicity of the vibrations, i.e., the possibility that the energy of the two phonons that decreases by the amount of the binding energy $2A$ when they combine to form a biphonon. Apart from energy considerations, at the present time there is no direct proof that the given peak corresponds to a bound biphonon or triphonon. As a result, other versions of the existence of local states associated with various types of defects, or anomalies in the density of states of (e.g.) diamond,[1] etc., have been advanced in addition to the above-stated prevalent explanation to account for the nature of the indicated peaks in the interpretation of the results of myriad experiments reported to date. We note for future consideration that the anharmonicity constant A in vanadium hydride is negative,[6] and in diamond the narrow, hypothetically biphonon line is situated above the band of dissociated two-phonon states.[1]

In the present article we propose to identify the peaks supposedly associated with bound multiphonon states by analyzing prominent features of the angular and energy dependences of the cross section of inelastic neutron or photon scattering leading to the splitting of biphonons, triphonons, etc. We note that the detailed biphonon structure has only a slight influence on the angular dependence of the cross section of inelastic neutron scattering with the generation of biphonons and the corresponding release of the total biphonon energy E_{bp} by a neutron, because this dependence is linked, in terms of Feynman diagrams for example, to the interaction of two emitted phonons in the final state. In such scattering, of course, the rates of generation of a biphonon as an integral bound two-phonon complex and generation of a single phonon differ, for example, as a result of the large effective mass of the biphonon; in either case, however, a single quasiparticle is generated, albeit one that is more complicated in the case of a biphonon. A more significant difference should be expected when the incident neutron in inelastic scattering splits a biphonon into free modes, where only the biphonon binding energy $2A$ is released by the neutron, or (as the reverse process) the neutron gains the biphonon binding energy when two free modes collapse into a biphonon. Here, for example, when energy is gained, not only the final biphonon state, but also the initial dissociated two-phonon state depends significantly on the corresponding form of the anharmonic interaction potential, i.e., on the anharmonicity constant A, because in such interaction the dissociated two-phonon states have the form of interacting, mutually scattering one-phonon modes. Consequently, the form of the phonon-phonon interaction potential is doubly manifested, and it will be shown below that this duality produces prominent features in the spectra of inelastic neutron scattering with the splitting of a biphonon or capture of the biphonon binding energy. In the present article we discuss the first process, where the anomalies of the scattering cross section have the following character.

For a fixed high neutron energy loss, the cross section is a maximum in a nonhead-on collision of a neutron and a biphonon with a lobe-shaped angular scattering diagram; for intermediate energy losses the cross section has the minimum possible value at all collision angles; and for low losses the cross section is a maximum in head-on collision in a narrow angular range. The resonance peak of the energy dependence of the cross section for a fixed angle is situated at the low-energy edge of a finite energy band; as the angle decreases, the cross section gradually increases while shifting toward the high-energy edge of the band, which constantly narrows and shifts into the low-energy region. However, when the angle decreases below a critical value, the resonance maximum, continuing to grow, begins to shift in the opposite direction toward the low-energy edge of the band. Here we show that, despite the strong oscillations of the biphonon wave function in the presence of negative phonon dispersion and the monotonic behavior for positive dispersion, the cross section does not depend on the sign of the dispersion, i.e., the universal law of independence from this sign, having been established previously only for the biphonon dispersion relation and damping constant,[1,3] appears to be preserved here.

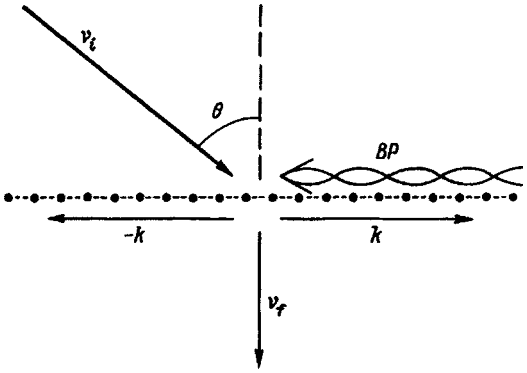

FIG. 1. Geometry of neutron-biphonon inelastic scattering.

One problem encountered in the experimental implementation of the processes of biphonon splitting or the capture of its binding energy, of course, is how to create first a sufficiently high population of biphonon (two-phonon) states that can subsequently be broken (bound) in interaction with neutrons. However, this problem can be solved, as before in optical experiments, for example, by preliminary high-intensity laser irradiation, which leads to the generation of biphonons having a wave vector corresponding to the laser frequency, owing to direct vertical transitions from some low-lying band of local states having weak dispersion. Recently fabricated new-generation devices having a high neutron flux and interfaced with high-resolution neutron spectrometers could possibly be used to run experiments analogous to those performed nowadays in nonlinear optics involving the preliminary production of a macroscopic density of excitons, which then serve as light scatterers. We note that the theory developed below can be used in studying not only relatively high-frequency multiphonon modes with energies $\sim 200-700$ meV (Refs. 6 and 7), but also low-frequency acoustic biphonons with energies ~ 10 meV (Ref. 14), for which the population problem is easier to treat.

We consider the scheme of inelastic scattering of two-dimensional neutron waves by a plane, homogeneous system of crystal chains in the geometry shown in Fig. 1. Note that such a scheme of the phenomenon is amenable to analysis and subsequent elaboration. For example, it is fully applicable to real crystals because experimental data have been published on the introduction of quasi-one-dimensional, chain-configured hydrogen and deuterium atoms in hydrides of transition metals such as (e.g.) lutetium hydride.[15] Shown schematically in the upper half of Fig. 1 above the crystal chain is the initial state: a high-energy neutron ν_i (the long, bold arrow) incident at angle θ relative to the normal and, colliding with it [at the angle $(\pi/2)-\theta$], a biphonon BP with wave vector K. We consider an inelastic scattering geometry that is entirely feasible with neutron spectrometers, where a lower-energy neutron ν_f (the short, fine arrow) departing in the direction perpendicular to the chain is fixed in the final state represented in the lower half of Fig. 1. Here the angle θ is such that the sign of the projection of the wave vector of the incident neutron ν_i onto the axis of the chain is opposite to that of the biphonon wave vector, and the moduli of these quantities are equal or differ by a finite number of reciprocal-lattice vectors. Inasmuch as the total wave vector along the axis of the chain in the initial state departs along the perpendicular to the chain, this projection is also equal to zero, and the splitting of the biphonon is accompanied by the generation of two unbounded phonons having oppositely directed wave vectors $\pm k$. The theory developed below to describe the inelastic scattering of neutrons with the splitting of biphonons in the given geometry can be used for appropriate generalization to more complex experimental conditions (e.g., involving the oblique departure of neutrons, filling of the entire band of biphonon states, the investigation of capture of the biphonon binding energy with the initial and final states inverted, etc.).

According to the general theory,[1,3] the Hamiltonian H_{ph} of the subsystem of optical phonons, taking into account the anharmonicity of the vibrational modes, i.e., phonon-phonon interaction, has the following form in second-quantization site representation:

$$H_{\text{ph}}=\sum_n E_0 B_n^+ B_n+\sum_{nm} V_{nm} B_n^+ B_m - A\sum_n B_n^+ B_n^+ B_n B_n, \tag{1}$$

where E_0 is the optical phonon energy without regard for the band component V_{nm} characterizing the transfer of phonons, B_n^+ and B_n are the corresponding Bose operators of vibrational excitations at site b, and A is the anharmonicity constant of contact phonon-phonon interaction. When the interaction of nearest neighbors $V_{nm}=V\delta_{n,m\pm1}$ is taken into account, one-phonon states with the wave vector k have energy $E(k)=E_0+2V\cos|k|$ (from now on all wave vectors will be tacitly given in units of $1/a$, where a is the ''lattice constant'' of the crystal chain). The two-phonon states of the system are sought in the form[1,3]

$$|2\rangle=\sum_{nm}\Psi_{nm}B_n^+B_m^+|0\rangle, \tag{2}$$

where Ψ_{nm} is a wave function, and $|0\rangle$ is the ground state. The wave function Ψ_{nm} and the energy E of the two-phonon states are found by the solution of the Schrödinger equation

$$H_{\text{ph}}|2\rangle=E|2\rangle. \tag{3}$$

The substitution of Eq. (2) into (3) yields the system of equations for Ψ_{nm} and E

$$(E-2E_0)\Psi_m=V(\Psi_{n+1,m}+\Psi_{n-1,m}+\Psi_{n,m+1}+\Psi_{n,m-1}) -2A\Psi_{nm}\delta_{nm}. \tag{4}$$

The solution of the system of equations (4) for a bound biphonon state with wave vector K and energy $E=E_{\text{bp}}(K)$ has the form[1,3]

$$\Psi_{nm}=\Psi_{nm}^{\text{BP}}(K)=\frac{1}{\sqrt{N}}\sqrt{\tanh\chi}\left(-\frac{V}{|V|}\right)^{n-m} \times\exp\left(i\frac{K}{2}(n+m)-\chi|n-m|\right), \tag{5a}$$

$$E=E_{\text{BP}}(K)=2E_0-\sqrt{(2A)^2+[4V\cos(K/2)]^2}, \tag{5b}$$

$$\chi=\chi(K)=\text{Arsh}\,(A/[2|V|\cos(K/2)]), \tag{5c}$$

where N is the number of sites in the main volume, $\chi=\chi(K)$ characterizes the spatial attenuation rate of the amplitude of the biphonon state, and $1/\chi$ therefore determines the radius of this bound state. We note that for a given $A>0$ the biphonon wave function as a function of $|n-m|$ decays uniformly for $V<0$ but for $V>0$ it decays with rapid oscillations. On the other hand, the $E=E_{\text{bp}}(K)$ and $\chi(K)$ curves are identical in both cases. For $A<0$ the signs of V for the two types of decay are inverted. A slight modification of the theory developed here fully validates it for determining the cross section for a neutron to capture the binding energy of a biphonon with $A<0$ after it interacts with the neutron and splits into free phonons. It is possible that for diamond, in particular, the postulated biphonon splitting experiment could lead to resolution of a controversial issue, long debated in the literature, as to whether the above-mentioned line observed in the energy spectrum does in fact correspond to a biphonon.[1] We note that the question of the sign of V, i.e., the sign of phonon dispersion, has not been adequately studied for metal hydrides, owing to the difficulty of single-crystal preparation.

The solution of the system of equations (4) for the dissociated state, i.e., two mutually scattering phonons with wave vectors $\pm k$ and energy $E=2E(k)$, has the form

$$\Psi_{nm}^{\text{dis}}(k)=(2/N^2)(\cos[k(n-m)]+T\exp(ik|n-m|)), \tag{6a}$$

$$E=2E(k)+4V\cos|k|, \tag{6b}$$

$$T(k)=[-1+i(2V/A)\sin|k|]^{-1}, \tag{6c}$$

where the second term on the right-hand side of Eq. (6a) represents the scattered wave in the two-body problem reduced to single-particle formulation, and $T(k)$ is the corresponding scattering amplitude.

In calculating the neutron inelastic scattering cross section, we use the approximation of direct contact interaction of particles for the neutron-phonon interaction Hamiltonian:

$$H_{\text{int}}=\sum_n W\nu_n^+\nu_n B_n^+ B_n, \tag{7}$$

where W is the interaction energy, and ν_n^+ and ν_n are the corresponding second-quantization neutron operators. In site representation on the chain model the operators ν_n form a subspace of neutron operators $\nu_{\mathbf{n}}$ on the corresponding two-dimensional crystal grid $\mathbf{n}=(n_1,\,n_2)$, which includes the chain $n_1=n$, $n_2=0$. The transformation from $\nu_{\mathbf{n}}$ to the secondary-quantization neutron operators ν in the representation of two-dimensional wave vectors $\mathbf{q}=(q_1,\,q_2)$ is given by the relations

$$\nu_{\mathbf{n}}=\sum_{\mathbf{q}}\nu_{\mathbf{q}}\varphi_{\mathbf{n}}(\mathbf{q}),\qquad \varphi_{\mathbf{n}}(\mathbf{q})=(1/N)^2\exp(i\mathbf{q}\cdot\mathbf{n}).$$

For the scattering of neutrons in metal hydrides, the interaction Hamiltonian H_{int} in Eq. (7) depends explicitly on direct neutron-proton interaction. To calculate this interaction in detail using a representation of the form (7), including transformation from the operators $\nu_{\mathbf{q}}^{+}$, $\nu_{\mathbf{q}}$, and x_n, where x_n is the proton shift translation operator,[12] to the operators $\nu_{\mathbf{n}}^{+}$, $\nu_{\mathbf{n}}$, and B_n^{+}, and B_n in (7), would serve no purpose at this stage of the calculations. In the first Born approximation, which is customarily used in the study of neutron scattering,[16] the double differential cross section of the given inelastic process is defined as

$$\sigma''(\varepsilon,\theta)=\frac{d^2\sigma}{d\varepsilon d\theta}=\sigma_0\sum_f |\langle f|H_{\text{int}}|i\rangle|^2\delta(\varepsilon_f-\varepsilon_i), \qquad (8)$$

where σ_0 is a constant factor, whose exact value is not essential to our investigation of the general laws governing the energy and angular dependence of σ''. In Eq. (8) $|i\rangle$ and $|f\rangle$ are the initial and final states (Fig. 1) with corresponding energies ε_i and e_f, defined by the equations

$$|i\rangle=\sum_{nm\mathbf{p}}\Psi_{nm}^{\text{bp}}(-K)\varphi_{\mathbf{p}}(\mathbf{q}_i)\,B_n^{+}B_m^{+}\nu_{\mathbf{q}_i}^{+}\,|0\rangle,$$

$$\varepsilon_i(K)=(\hbar^2\mathbf{q}_i^2/2M)+E^{\text{BP}}(K), \qquad (9a)$$

$$|i\rangle=\sum_{nm\mathbf{p}}\Psi_{nm}^{\text{dis}}(k)\varphi_{\mathbf{p}}(\mathbf{q}_f)\,B_n^{+}B_m^{+}\nu_{\mathbf{q}_f}^{+}\,|0\rangle,$$

$$\varepsilon_f(k)=(\hbar^2\mathbf{q}_f^2/2M)+2E(k), \qquad (9b)$$

where M is the neutron mass. To simplify the calculations, we assume that the neutron transfers much of its energy to the lattice, so that the energy and wave vector of the departing neutron are small in comparison with the incoming quantities ($|\mathbf{q}_i|\gg|\mathbf{q}_f|$). In this case, for a fixed energy loss to the lattice

$$\varepsilon=(\hbar^2/2M)(|\mathbf{q}_i|^2-|\mathbf{q}_f|^2) \qquad (10)$$

the biphonon wave vector and the sine of the angle of incidence are linearly related: $K=\sin\theta(2M\varepsilon/\hbar^2)^{1/2}$, so that the dependence of the cross section σ'' on K is easily transformed into the angular dependence $\sigma''(\theta)$. In normal incidence $K=\theta=0$, and in the opposite limit of tangential incidence the value of the wave vector at the boundary of the Brillouin zone $K=\pi/a$ corresponding to the limiting angle $\theta\approx\pi/2$ for an energy loss $\varepsilon\approx20$ meV and a chain lattice constant $a\approx1$ Å; this result is fully admissible from the viewpoint of methodological capabilities in experimental work. To transform from the biphonon wave vector K to the scattering angle θ, we use the relation

$$Ka=\sin\theta\sqrt{2M\varepsilon a^2/\hbar^2}. \qquad (11)$$

The substitution of Eqs. (5), (6), and (9) into (8) gives the following relation for the double differential scattering cross section:

$$\sigma''=\sigma_0\int dk\left|\sum_{nm}\Psi_{nm}^{*\text{BP}}(K)\Psi_{nm}^{\text{dis}}(k)S(\mathbf{q}_i,\mathbf{q}_f)\right|^2$$

$$\times\delta[\varepsilon_f(k)-\varepsilon_i(K)], \qquad (12a)$$

$$S(\mathbf{q}_i,\mathbf{q}_f)=\varphi_n^{*}(\mathbf{q}_i)\varphi_n(\mathbf{q}_f)+\varphi_m^{*}(\mathbf{q}_i)\varphi_m(\mathbf{q}_f). \qquad (12b)$$

Detailed calculations involving the substitution of the explicit forms of Ψ^{BP}, Ψ^{dis}, and φ after partial summations, which naturally yield the condition of conservation of the projection of the total wave vector onto the axis of the chain, lead to the following relation for $\sigma''(\varepsilon,\theta)$:

$$\sigma''(\varepsilon,\theta)=\sigma_0\tanh\chi\int dk|R(K,k)|^2\delta[\varepsilon_f(k)-\varepsilon_i(K)], \qquad (13)$$

where

$$R(K,k)=\sum_m\left(-\frac{V}{|V|}\right)^m\exp\left(-i\frac{K}{2}m-\chi(K)|m|\right)$$

$$\times[\cos(km)+T(k)\exp(ik|m|)].$$

The sums involved in Eq. (13) are equal to

$$\sum_m(-V/|V|)^m\cos(km)\exp[-i(K/2)m-\chi|m|]$$

$$=\alpha(K,k)/\beta(K,k), \qquad (14a)$$

$$\sum_m(-V/|V|)^m\exp[ik|m|-i(K/2)m-\chi|m|]$$

$$=\gamma(K,k)/\beta(K,k), \qquad (14b)$$

where

$$\alpha(K,k)=\sinh\chi[\cosh\chi+\cos k\cos(K/2)], \qquad (15a)$$

$$\beta(K,k)=[\cosh\chi+\cos k\cos(K/2)]^2$$

$$-\sin^2 k\sin^2(K/2), \qquad (15b)$$

$$\gamma(K,k)=\gamma'(K,k)+\gamma''(K,k)$$

$$=\sinh(\chi-ik)[\cosh(\chi+ik)\mp(K/2)]. \qquad (15c)$$

With regard to the symbol $\mp$ in relations (15), the minus sign is used for $V<0$, and the plus sign for $V>0$. After integration over k in Eq. (13) with allowance for Eqs. (15) and (16) we finally obtain the relation for the double differential cross section of inelastic scattering

$$\sigma''(\varepsilon,\theta)=\sigma_0\frac{\tanh\chi}{\sin k_0}\frac{[\alpha_0+T_0'\gamma_0'-T_0''\gamma_0'']^2+[T_0'\gamma_0''+T_0''\gamma_0']^2}{\beta_0^2},$$

$$\alpha_0\equiv\alpha(K,k_0),\qquad \beta_0\equiv\beta(K,k_0),$$

$$\gamma_0\equiv\gamma(K,k_0),\qquad T_0\equiv T(K,k_0), \qquad (16)$$

where the wave vector $k_0=k_0(K)$ is determined from the energy conservation law

$$4V\cos k_0=\varepsilon-\sqrt{(2A)^2+[4V\cos(K/2)]^2}, \qquad (17)$$

and T_0' and T_0'' are the real and imaginary parts of the scattering amplitude T_0 defined in Eq. (6c).

A remarkable fact emerges here. The change of sign in Eqs. (15) in transition from $V<0$ to $V>0$ does not alter the cross section σ''. The reason is that a change of sign of V in the energy conservation law (17) leads to the transformation $k_0\rightarrow\pi-k_0$, with $\cos k_0$ changing sign. For real-valued α_0 and β_0 in Eq. (15a), therefore, the change of sign is canceled, and for the complex-valued γ_0 in (15b), when the change of sign is compensated in the real part, the imaginary part changes sign, i.e., the quantity goes over to its complex

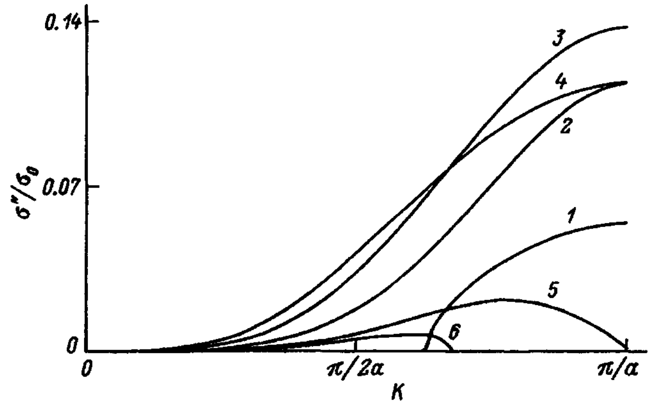

FIG. 2. Neutron scattering cross section versus the biphonon wave vector.

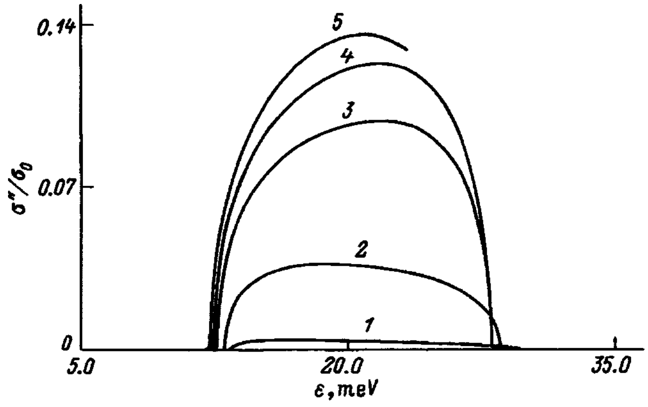

FIG. 4. Neutron scattering cross section versus neutron energy loss at fixed scattering angles.

conjugate γ_0^*, so that, in accordance with (12), σ'' is left unchanged. Consequently, even though for $V>0$ the biphonon wave function Ψ_{nm}^{BP} (5a) oscillates strongly as $(n-m)$ changes and might appear at first glance to contribute nothing to σ'' in integral relations of the type (12); the same universal law of independence from V, which applies to the biphonon dispersion relation and the damping constant χ in Eqs. (5b) and (5c), still holds in this case as well, where σ'' is also independent of the sign of V.

Figures 2–4 show graphs of $\sigma''(\varepsilon, \theta)$ for fixed energy losses ε, representing the angular dependence of the cross section, and also for fixed angles θ, representing the resonance energy dependence of the cross section. An analysis of Figs. 2–4 shows that the angular and energy curves of the inelastic scattering cross section has specific features that can serve as special identifiers of the participation of biphonon states in the inelastic scattering of neutrons in the presence of vibrational anharmonicity.

To illustrate the general form of the angular and energy dependences of the cross section in the given geometry (Fig. 1), Fig. 2 shows the cross section as a function of the neutron energy loss. The values of the parameters are chosen close to their experimental values observed for biphonon modes of hydrogen atoms in metal hydrides. In various transition-metal hydrides the anharmonicity constant varies from ~5 meV to ~20 MeV (Refs. 6, 7, and 15). The widths of the one-phonon band of optical modes of hydrogen are ~5 −15 meV. To highlight the biphonon band of uncoupled two-phonon modes, the values of the parameters $A=10$ meV and $V=-2$ meV, which are fully consistent with experimental data, are used in the calculations. We use specific values of A and V for clarity, although the results of the calculations can be given for a fixed dimensionless parameter A/V, and the energy dependence (Fig. 4) can be given with ε/V as the independent variable. The bands of dissociated two-phonon states, the splitting-off of biphonons from this band, and the biphonon band proper are determined for these values of the parameters. Figure 2 shows the behavior of $\sigma''(K)$ for six successively incremented energy losses in the interval $\varepsilon_1-\varepsilon_9$ ranging from $\varepsilon_1=2A+4V=12\,\mathrm{meV}$ to $\varepsilon_9=[(2A)^2+(4V)^2]^{1/2}-4V=29.5\,\mathrm{meV}$, where only zeros of the δ function in (12) and (17) exist. When the energy loss increases from the lower limit ε_1 to $\varepsilon_3=[(2A)^2+(4V)^2]^{1/2}=13.5\,\mathrm{meV}$ near the boundary of the Brillouin zone $K=K_{\mathrm{B}}\equiv\pi/a$, there appears a narrow, gradually broadening region of K where the cross section, having a maximum at $K=K_{\mathrm{B}}$, increases as ε is increased (curve *1*, $\varepsilon=\varepsilon_2=12.5\,\mathrm{meV}$). Then for $\varepsilon>\varepsilon_3$ inelastic scattering takes place in the entire Brillouin zone $0<K<K_{\mathrm{B}}$ with a maximum at $K=K_{\mathrm{B}}$, along with an overall increase in the cross section as ε is increased (curve *2*, $\varepsilon=\varepsilon_4=15\,\mathrm{meV}$). The maximum value of the cross section is observed for $\varepsilon=\varepsilon_5=2A=20\,\mathrm{meV}$ (curve *3*). With a further increase in ε the cross section begins to decrease, but with a relative increase in the wing of σ'' for small K (curve *4*, $\varepsilon=\varepsilon_6=25\,\mathrm{meV}$). As ε approaches the energy $\varepsilon_7=2A-4V=28\,\mathrm{meV}$, a maximum emerges in the Brillouin zone, exceeding the value of $\sigma''(K=K_{\mathrm{B}})$ at the boundary. At the energy $\varepsilon=\varepsilon_7$ (curve *5*) we have $\sigma''(K=K_{\mathrm{B}})=0$, and the maximum occurs at $K\cong(3/4)K_{\mathrm{B}}$. With a further increase in ε in the interval $\varepsilon_7<\varepsilon<\varepsilon_9$ this maximum decreases and shifts into an interval of wave vectors that closes in around $K\cong0$, where only zeros of the δ function in Eqs. (12) and (17) exist (curve *6*, $\varepsilon=\varepsilon_8=28.4\,\mathrm{meV}$). All these features of the $\sigma''[\varepsilon, \theta(K)]$ curve can be obtained analytically from the functional relations (14)–(16) and, at the same time, clarify the physical significance of the features. For example, the fact that $\sigma''=0$ for $K=0$ follows from the relation $\alpha T^{-1}=-\gamma$, which is

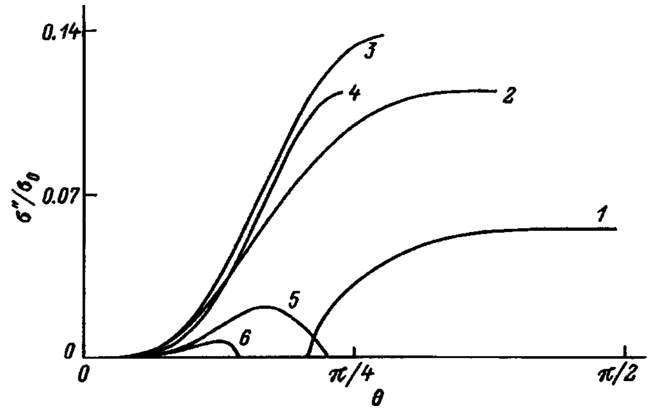

FIG. 3. Inelastic neutron scattering cross section versus the neutron scattering angle at fixed neutron energy losses.

readily verified in this case. As $K \rightarrow K_B$ and $\varepsilon \rightarrow \varepsilon_7$, it follows from (17) that $\sin k_0 \rightarrow 0$, $\chi \rightarrow \infty$, $T \rightarrow -1$, $\alpha\beta \cong \gamma\beta 1$, $(\alpha + T\beta)/\gamma \rightarrow 0$, and it is necessary to expand the corresponding indeterminacy in Eq. (16).

To obtain the angular dependence $\sigma''(\theta)$ directly for fixed values of the energy loss, we assume that the lattice constant has a value close to actual, $a = 1.5$ Å, and that Eq. (11) relating K to θ has the form

$$Ka = \pi \sin \theta \sqrt{\varepsilon/\varepsilon_1}, \tag{18}$$

so that the angle $\theta = \pi/2$ at $\varepsilon = \varepsilon_1$ corresponds to the limiting value of K at the boundary of the Brillouin zone.

Figure 3 shows the dependence of the cross section on θ for the same energy losses as in Fig. 2 and with the same interpretation of the numbering of the curves. It is evident that as the energy loss increases, the biphonon splits initially in a narrow but expanding interval of θ close to $\pi/2$, and σ'' has an increasing maximum at $\theta = \pi/2$, i.e., for a ''head-on'' neutron-biphonon collision (curve *1*, $\varepsilon = \varepsilon_2$). Then as the energy loss $\varepsilon = \varepsilon_5$ is approached, the cross section reaches a maximum, which exists at $\theta \geqslant 0$, increasing as θ is increased (curve *2*, $\varepsilon = \varepsilon_4$; curve *3*, $\varepsilon = \varepsilon_5$). With a further increase in the energy loss the cross section decreases, its maximum shifting into a narrowing interval close to small angles $\theta \rightarrow 0$ (curve *4*, $\varepsilon = \varepsilon_6$; curve *5*, $\varepsilon = \varepsilon_7$; curve *6*, $\varepsilon = \varepsilon_8$). Consequently, the angular scattering diagram for large energy losses comprises a lobe with zero-valued minima at $\theta = 0$ and $\theta = \theta_0(\varepsilon)$, where $\theta_0(\varepsilon \rightarrow \varepsilon_9) \rightarrow 0$, and an increasing maximum at $\theta_{\max}$, $0 < \theta_{\max} < \theta_0$. Curves *2–4* in Fig. 3 cut off at finite angles of incidence, because for large angles and the fixed energy losses for these curves condition (18) is not satisfied for the biphonon and neutron wave vectors in the first Brillouin zone, and the terms $\pm 2mK_B a$ must be introduced on the right-hand side of (18) to account for umklapp processes. Certainly the procedure for taking such processes into account is an important consideration, but will not be pursued in the present article. Their inclusion amplifies the results obtained here.

Figure 4 shows the energy dependence of the cross section $\sigma''(\varepsilon, \theta)$ at fixed angles of incidence. Curves *1–5* correspond to successively incremented values of θ. At small angles (curve *1*, $\theta = \pi/16$) we observe a broad band with a weak resonance at the low-energy edge of this band. As the angle is increased, the entire band of nonzero-cross sections shrinks and shifts toward the low-energy region; it is interesting, however, that the increasing maximum of the resonance initially shifts, contrarily, into the high-energy part of the band (curve *2*, $\theta = \pi/8$, curve *3*, $\theta = \pi/5$). However, at angles exceeding a critical value $\theta \geqslant \pi/5$, the shift of the maximum changes direction and the maximum, continuing to grow, shifts toward the low-energy edge of the band (curve *4*, $\theta = \pi/4.5$; curve *5*, $\theta = \pi/4$). Curve *5* cuts off after the maximum passes a certain point, where condition (18) no longer holds, as discussed in connection with Fig. 3 above. With a further increase in θ the calculations yield ascending low-energy parts of the resonance, which shift into the low-energy region.

If future experimentally observed prominent features of the angular and energy dependences of the inelastic neutron scattering cross section exhibit the same general attributes as those found in the present study, this information appended to general energy considerations can amply serve as critical proof of the involvement of bound biphonon states in processes of inelastic neutron scattering. The further expansion of research in this direction will possibly lead to a major modification of the system of existing criteria, based solely on energy-balance considerations, for the classification of series of spectral resonances corresponding prevalently to bound multiphonon states of various multiplicities. The values assigned to the parameters of the scattering geometry, etc., in the present study provide guideposts for such investigations.

In closing, the authors are obliged to express their heartfelt appreciation to V. M. Agranovich for helpful comments.

This work has received support from the Russian State Scientific-Technical Program ''Critical Directions in the Physics of Condensed Media'' on the topic ''Neutron Examination of Matter.''

[1] V. M. Agranovich and I. Ĭ. Lalov, Usp. Fiz. Nauk **146**, 267 (1985) [Sov. Phys. Usp. **28**, 484 (1985)].
[2] V. M. Agranovich and S. Mukamel, Phys. Lett. **147**, 155 (1990).
[3] V. M. Agranovich and O. A. Dubovsky, *Optical Properties of Mixed Crystals* (North-Holland, Amsterdam, 1988), p. 297.
[4] O. A. Dubovskiĭ and A. V. Orlov, Fiz. Tverd. Tela (St. Petersburg) **39**, 163 (1997) [Phys. Solid State **39**, 141 (1997)].
[5] O. A. Dubovskiĭ and A. V. Orlov, Fiz. Tverd. Tela (St. Petersburg) **39**, 542 (1997) [Phys. Solid State **39**, 472 (1997)].
[6] S. Ikeda and N. Watanabe, KEK Preprint 66 (National Laboratory for High Energy Physics, Tsukuba Science City, Japan, 1986).
[7] I. S. Anderson, J. J. Rush, T. Uvodic, and J. M. Rowe, Phys. Rev. Lett. **57**, 2822 (1986).
[8] A. I. Kolesnikov, M. Prager, J. Tomkinson, I. O. Bashkin, V. Yu. Malyshev, and E. G. Ponyatovskii, J. Phys.: Condens. Matter **3**, 5297 (1991).
[9] R. Bini, P. R. Salvi, and V. Schettino, J. Chem. Phys. **98**, 164 (1993).
[10] L. J. Richter, T. A. Germer, J. P. Sethna, and W. Ho, Phys. Rev. B **38**, 10403 (1988).
[11] V. M. Agranovich, O. A. Dubovsky, and A. V. Orlov, Phys. Lett. A **119**, 83 (1986).
[12] V. M. Agranovich, O. A. Dubovsky, and A. V. Orlov, Solid State Commun. **72**, 491 (1989).
[13] O. A. Dubovskiĭ and A. V. Orlov, Fiz. Tverd. Tela (Leningrad) **32**, 2407 (1990) [Sov. Phys. Solid State **32**, 1397 (1990)].
[14] O. A. Dubovskiĭ and A. V. Orlov, Fiz. Tverd. Tela (St. Petersburg) **36**, 3131 (1994) [Phys. Solid State **36**, 1663 (1994)].
[15] T. J. Uvodic, J. J. Rush, I. S. Anderson, J. N. Daou, P. Vajda, and O. Blaschko, Phys. Rev. B **50**, 3696 (1994).
[16] V. F. Turchin, *Slow Neutrons* (Israel Program for Scientific Translations, Jerusalem, 1965) [Russ. original, Atomizdat, Moscow (1963), 372 pp.].

Translated by James S. Wood

Vibrations of hydrogen atoms in amorphous $PrNi_2H_{3.6}$

P. P. Parshin, M. G. Zemlyanov, and A. V. Irodova

Russian Science Center ''Kurchatov Institute,'' 123182 Moscow, Russia

V. V. Sumin

Joint Institute for Nuclear Research, 141980 Dubna, Moscow Province, Russia

(Submitted October 24, 1997)
Fiz. Tverd. Tela (St. Petersburg) **40**, 735–737 (April 1998)

The atomic dynamics of hydration-amorphized $PrNi_2H_{3.6}$ are investigated by the incoherent inelastic scattering of neutrons, and the spectrum of vibrations of hydrogen atoms is reconstructed. It is shown that the spectral distribution of thermal excitations can be conceived as consisting of two bands, whose average energies coincide with the vibrational energies of the hydrogen atoms in the binary hydrides NiH and PrH_x. The final results agree with a previously proposed structural model of hydrogen amorphization. *© 1998 American Institute of Physics.* [S1063-7834(98)03404-2]

Although the phenomenon of amorphization of certain intermetallic compounds in reaction with hydrogen has been known for some time,[1] its nature and mechanism have remained unclear to the present day. It is obvious that progress must be sought through investigations of the structure and dynamics of amorphous hydrides formed by such reactions, because information can be obtained both on the atomic structure of these systems and on the characteristics of interatomic interaction in them. We have previously investigated the structural aspects of hydrogen amorphization.[2,3] We previously[2] employed x-ray diffraction to study the sequence of phase transformations in the system $PrNi_2$–H in transition from the crystalline to the amorphous state. In Ref. 3 we investigated the atomic structure of the amorphous hydride $PrNi_2D_{3.6}$ by neutron diffraction and proposed a model of the hydrogen amorphization of hydrides. In this paper we give the results of a study of the dynamics of hydrogen atoms in $PrNi_2H_{3.6}$ by the inelastic scattering of neutrons.

A sample weighing 40 g was prepared by a procedure similar to that used in Ref. 2 at a temperature of 300 K. The hydrogen constituency was determined form the quantity of gas absorbed during reaction. The x-ray pattern of the sample (Fig. 1) is completely devoid of Bragg peaks, and only a slight background modulation is observed. Inelastic neutron-scattering experiments were carried out at room temperature on a KDSOG-M inverted-geometry spectrometer[4] mounted on an IBR-2 pulsed reactor. Energy analysis of the scattered neutrons was performed in a high-transmission modification with only a nitrogen-cooled polycrystalline beryllium filter used as the analyzer. Under these conditions the energy resolution of the instrument was 16% (19 meV) at an energy of 120 meV. The measured time-of-flight spectra for four different scattering angles (after subtraction of the sample cassette background and correction for the spectrum of the incident neutrons) were processed in the incoherent one-phonon approximation, and the contribution of multiphonon scattering processes was taken into account in the Gaussian approximation.[5] A correction for the Debye–Waller factor was made by a self-consistent iterative procedure using the experimentally determined spectrum. As a result, a generalized (neutron-weighted, Ref. 6) spectrum of the vibrational states of the lattice was reconstructed for amorphous $PrNi_2H_{3.6}$: $G(T) \sim \Sigma\sigma_i/M_i g_i(E)$, where σ_i, M_i, and g_i are the neutron scattering cross section, the atomic mass, and the partial spectrum of the vibrations for the ith atomic species, and the summation is carried out over all atoms in the formula unit. Owing to the very large cross section of incoherent scattering of neutrons by hydrogen (80 b, as opposed to the typical values for metals, of the order of a few barns) and the low mass of the hydrogen atoms, the function $G(E)$ essentially represents the spectral distribution of the vibrations of hydrogen atoms in the investigated sample.

The vibration spectrum (Fig. 2) consists of two parts: a low-energy part (up to 30 meV) associated predominantly with hydrogen atom vibrations in phase with the vibrations of the heavier metal atoms (acoustic branches), and a high-energy part mainly associated with hydrogen atom vibrations in antiphase with the metal atoms (optical branches). The low density of vibrational states in the acoustic part of the spectrum indicates the weak participation of hydrogen in vibrations at these energies. The most interesting object from the standpoint of exposing the characteristics of Me-H interaction is the high-energy vibrational band. In discussing the results below, we address only the optical part of the spectrum, whose average energy is 121 meV.

We call attention to the considerable width of the optical band, 96 meV, which is significantly greater than the typical widths for hydrides of crystalline Laves phases. For example, the bandwidth is 60 meV for $ZrV_2H_{3.37}$ and 74 meV for $ZrV_2H_{4.23}$ (Ref. 7) and is the result of anisotropy of the nearest-neighbor environment and appreciable H-H interaction. A major increase in the width of the optical spectrum of hydrogen atoms also occurs in conventional amorphous hy-

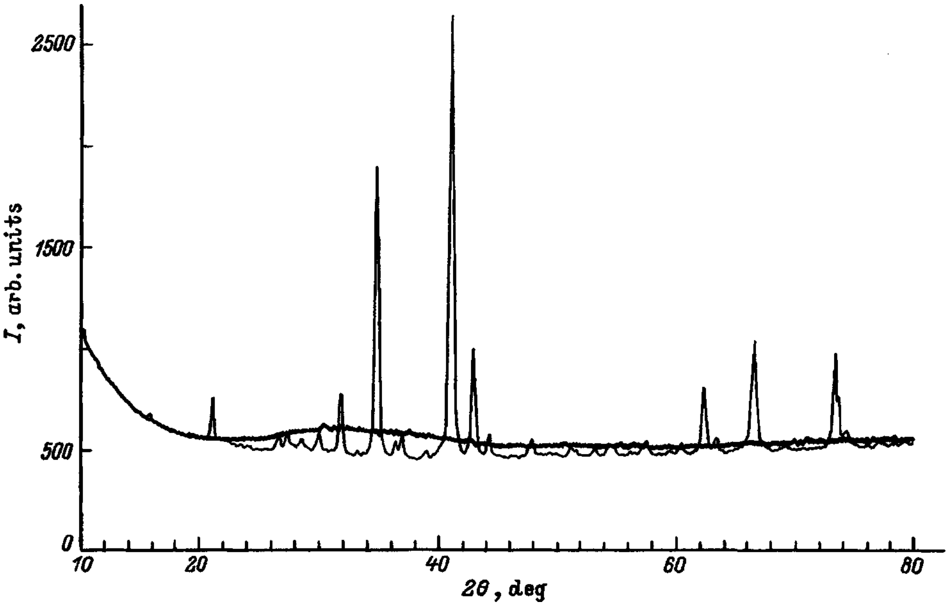

FIG. 1. X-ray pattern of the hydride $PrNi_2H_{3.6}$ after subtraction of the incoherent background (see Ref. 3). The bold curve represents the x-ray pattern of the original intermetallic $PrNi_2$.

drides (see, e.g., Ref. 8), where the initial amorphous alloy is obtained by quenching from the melt. Such a large width is attributable, on the one hand, to the spread of interatomic spacings in amorphous systems and, on the other, to H-H interaction, possibly more so than in crystalline systems.

In the simplest case, the dynamic behavior of hydrogen atoms in the investigated system can be conceptualized in one of two ways: 1) Hydrogen on the average interacts identically with Pr and Ni atoms (a ''gray'' metal atom); 2) the interactions with Pr and Ni atoms differ. Accordingly, in the first model the optical band can be expected to consist of a single maximum, and in the second it should have two maxima corresponding to the interaction of hydrogen with Pi and with Ni. The experimental spectrum of the optical vibrations of hydrogen atoms is approximated by one and two (Fig. 2) Gaussian curves, where three parameters (amplitude, position, and width) are varied for each curve. The approximation results are summarized in Table I, which also shows the values of the profile (R_p) and weighted profile (R_{wp}) uncertainty factors.[9] The two Gaussian curves ($R_{wp}=4.8\%$) provide a significantly better description of the optical spectrum than the single curve ($R_{wp}=10.08\%$), so that the spectrum can be regarded as consisting of two bands. The average energy of the first band, $E_1=97$ meV (see Table I), is close to the average energy of the optical vibrations of hydrogen atoms in the octahedral interstices of binary crystalline nickel hydride [$E=94$ meV for $NiH_{0.8}$ (Ref. 10) and $E=100$ meV for $NiH_{0.4}$ (Ref. 11)], and the energy of the sec-

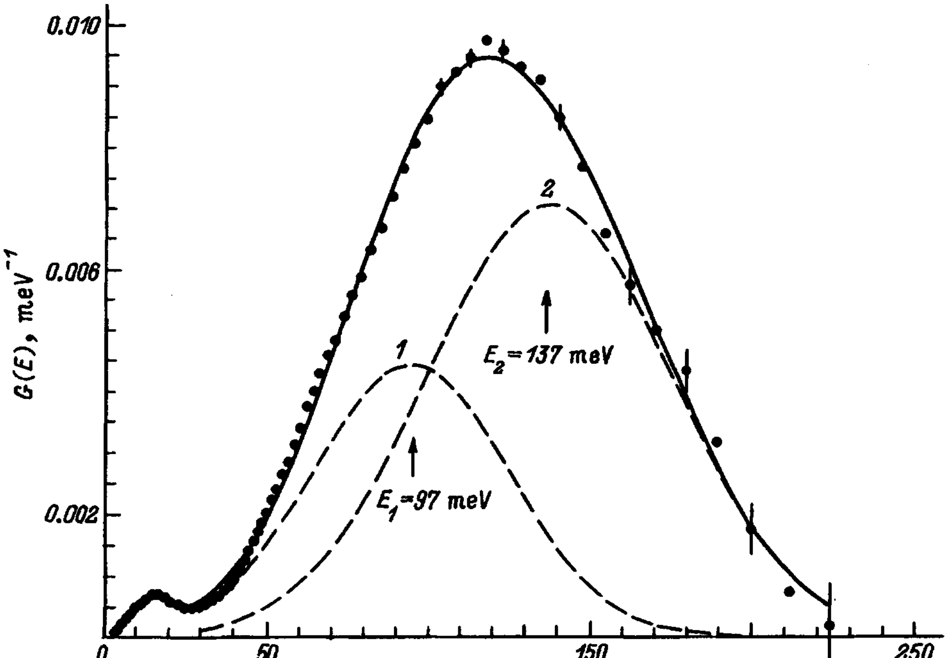

FIG. 2. Spectrum of hydrogen-atom vibrations in amorphous $PrNi_2H_{3.6}$ (dots) and approximation of the optical part of the spectrum by two Gaussian curves (solid curve). The dashed curves represent the bands of the optical vibration spectrum.

TABLE I. Parameters of the bands of the spectrum of optical vibrations of hydrogen atoms in amorphous $PrNi_2H_{3.6}$.

Approximation by one Gaussian curve					Approximation by two Gaussian curves							
E_1	ΔE_1	S_1	$\langle E\rangle$	$\langle u^2\rangle$	E_1	ΔE_1	E_2	ΔE_2	S_1	S_2	$\langle E\rangle$	$\langle u^2\rangle$
121±2	96±4	0.99±0.02	62±2	0.035±0.002	97±2	72±3	137±3	89±4	0.34±0.02	0.67±0.04	63±2	0.030±0.002
$R_p=6.18\%$, $R_{wp}=10.08\%$					$R_p=3.78\%$, $R_{wp}=4.82\%$							

Note: Here E_1 and E_2 are the average energies (meV), ΔE_1 and ΔE_2 are the full widths at half maximum (meV), $S_{,1}$ and S_2 are the areas under the spectral bands, and R_p and R_{wp} are the profile and weighted profile uncertainty factors. Integral characteristics of the spectrum of hydrogen-atom vibrations at $T=293$ K: $\langle E\rangle$ is the average vibrational energy (meV), and u^2 is the mean-square value of the thermal displacements (Å^2).

ond band, $E_2=137$ meV is close to the average energy of hydrogen vibrations in the tetrahedral interstices of the hydride $PrH_{2.8}$ [$E=130\pm5$ meV (Ref. 12)]. Consequently, the first band corresponds to the interaction of hydrogen with nickel atoms, and the second band corresponds to interaction with praseodymium atoms. It can be inferred from the ratio of the areas under these spectral bands $S_2/S_1=1.97$ (see Table I) that almost one fourth more hydrogen atoms are localized near praseodymium atoms than near nickel atoms, consistent with the difference in the hydride-forming properties of praseodymium (maximum constituency of the hydride PrH_3) and nickel (maximum constituency of the hydride NiH).

It has been shown[2,3] that the amorphized hydride $PrNi_2H_{3.6}$ can be regarded structurally to be an interstitial solid solution incorporating the highly distorted lattice of the original intermetallic $PrNi_2$. The hydrogen atoms are localized in it in such a way as to preserve the same Me-H spacings as in the binary hydrides PrH_x and NiH. The bonds between Pr and Ni atoms are broken, and in fact binary hydrides are formed at the atomic level.

The correlation between the Me-H spacing and the average energy of the optical vibration band of hydrogen in crystalline hydrides is well known.[13,14] We assume that the same correlation occurs in amorphous hydrides as well. The coincidence of the average energies of the optical bands in amorphous $PrNi_2H_{3.6}$ with the vibrational energies of the hydrogen atoms in binary praseodymium and nickel hydrides indicates that the average Pr-H and Ni-H spacings in $PrNi_2H_{3.6}$ are close to the spacings in the corresponding binary hydrides. The results obtained in the present study therefore confirm the previously developed[2,3] structural model of hydrogen amorphization at the interatomic bonding level.

In closing, the authors are grateful to G. V. Laskova for performing the x-ray analysis of the samples and to V. G. Fedorov for assistance in setting up the inelastic neutron-scattering experiment.

This work has received financial support from the Russian Fund for Fundamental Research (Project 94-02-05988) and the State Scientific-Technical Program ‘‘Critical Directions in the Physics of Condensed Media’’ on the topic ‘‘Neutron Examinations of Condensed Media’’ (Project 96102).

[1] D. Shaltiel, J. Less-Common Met. **62**, 407 (1978).

[2] A. V. Irodova, O. A. Lavrova, G. V. Laskova, P. P. Parshin, and A. L. Shilov, Fiz. Tverd. Tela (St. Petersburg) **38**, 277 (1996) [Phys. Solid State **38**, 156 (1996)].

[3] A. V. Irodova, I. N. Goncharenko, P. P. Parshin, and R. Bellisan, Fiz. Tverd. Tela (St. Petersburg) **38**, 1679 (1996) [Phys. Solid State **38**, 927 (1996)].

[4] G. Baluka, A. V. Belushkin, S. I. Bragin, T. Zaleski, M. Z. Ishmukhametov, I. Natkanets, V. Oleyarchik, and Ya. Pavelchik, Preprint OIYaI-R13-84-242 [in Russian] (Joint Institute for Nuclear Research, Dubna, 1984).

[5] V. F. Turchin, *Slow Neutrons* [Israel Program for Scientific Translations, Jerusalem (1965); Atomizdat, Moscow (1963), 372 pp.].

[6] W. Marshall and S. Lovesey, *Theory of Thermal Neutron Scattering* (Clarendon Press, Oxford, 1971).

[7] P. P. Parshin and M. G. Zemlyanov, Z. Phys. Chem., Neue Folge **164**, 1095 (1989).

[8] J. J. Rush, J. M. Rowe, and A. J. Maeland, J. Phys. F **10**, L283 (1980).

[9] J. Rodriguez-Carvajal, Physica B **192**, 55 (1993).

[10] J. Eckert, C. F. Majkzrak, L. Passell, and W. B. Daniels, Phys. Rev. B **29**, 3700 (1984).

[11] R. Wisniewski, R. Dimitrova, I. Natkaniec, and J. Wasicki, Solid State Commun. **54**, 1073 (1985).

[12] P. P. Parshin, M. G. Zemlyanov, M. E. Kost, A. Yu. Rumyantsev, and N. A. Chernoplekov, Fiz. Tverd. Tela (Leningrad) **22**, 472 (1980) [Sov. Phys. Solid State **22**, 275 (1980)].

[13] P. P. Parshin, M. G. Zemlyanov, M. E. Kost, A. Yu. Rumyantsev, and N. A. Chernoplekov, Izv. Akad. Nauk SSSR, Neorg. Mater. **14**, 1653 (1978).

[14] D. K. Ross, P. F. Martin, W. A. Oates, and R. Knoda Bakhsh, Z. Phys. Chem., Neue Folge **114**, 221 (1979).

Translated by James S. Wood

PHYSICS OF THE SOLID STATE VOLUME 40, NUMBER 4 APRIL 1998

Ordering of V–H hydrides near the $\beta-\delta$ transition

N. L. Arabadzhyan, V. I. Serdobintsev, and V. M. Tavkhelidze

Institute of Physics, Academy of Sciences of Georgia, 380077 Tbilisi, Georgia

(Submitted September 25, 1997)
Fiz. Tverd. Tela (St. Petersburg) **40**, 738–740 (April 1998)

Low-frequency acoustics is used to study the $\beta-\delta$ phase transition in the vanadium hydride $VH_{0.73}$. It is established that the nature of the transition depends significantly on the degree of perfection of the crystal structure of the hydride. It is shown that such behavior can be attributed to long-period ordering in the investigated system. © *1998 American Institute of Physics.* [S1063-7834(98)03504-7]

Problems in the kinetics of the order parameter are an important part of the theory of phase transitions. Among the most widely used investigation methods are measurements of the dielectric dispersions and absorption, neutron scattering, Raman and Brillouin light scattering, magnetic resonance, and the dispersion and absorption of ultrasound.[1,2]

All of these methods can be used to investigate fast relaxation processes with $\tau^1 \sim 10^6-10^{12}$ Hz (τ is the relaxation time of the order parameter).

Recently, however, there has been major interest in transitions to phases characterized by a modulated order parameter, where the modulation period is much larger than the period of the original structure. Such long-period structures are characterized by lower excitation frequencies ($\tau^{-1} \sim 1-10^4$ Hz) and, hence, are successfully investigated by methods of low-frequency acoustics.

Vanadium-hydrogen solid solutions are known to form a series of ordered and disordered phases, in which hydrogen occupies both tetrahedral and octahedral sites.[3] It has been found that the ordered β phase corresponds to V_2H stoichiometry.[3] At lower temperatures (<210 K) another ordered phase has been found with the composition V_3H_2 (δ phase), which has been investigated previously.[4]

In this paper we report a low-frequency ($\sim 10^3$ Hz) acoustics investigation of the kinetics of the $\beta-\delta$ phase transformation ($T_c \sim 208$ K) in the system $VH_{0.73}$.

1. SAMPLES AND EXPERIMENTAL PROCEDURE

Samples were prepared by spark cutting from single-crystalline vanadium hydride $VH_{0.73}$ in the form of having two notches which enabled thin plates clamping the sample in a massive support block, while the strip between them, with dimensions $12\times 3\times 0.8$ mm, functioned as the acoustic resonator proper.

A quarter-wave flexural mode was excited electrostatically. A metal electrode situated near the free end of the vibrator served simultaneously as the vibration source and detector.

Measurements were performed by the regenerative excitation of normal modes of the sample by means of an apparatus described in Ref. 5.

In the graphs the temperature dependence of the elasticity is given in units of the vibrator natural frequencies squared, ν^2, and the absorption of vibrational energy is given in units of the reciprocal Q factor of the vibrator, Q^{-1}.

The absorption of energy in the presence of large damping ($\sim 10^{-1}$) is shown in the figures in units of the vibration driving voltage U.

In addition, measurements of in-phase and quadrature signals using vector voltmeters[6] were performed as a means of directly determining the real part χ' and imaginary part χ'' of the complex vibrator amplitude.

2. EXPERIMENTAL RESULTS

Figure 1 shows the results of measurements on an as-prepared $VH_{0.73}$ sample. The measurements were carried out during slow heating of the sample ($\sim 0.5-1.0$ K/min). It is evident from the figure that the behavior of the elastic modulus near 208 K corresponds to a phase transition, as attested by the kink in the curve at $T=208$ K (Ref. 7). A doubled central peak is observed on the damping curve at the transition temperature, along with two lower peaks to the left and to the right of T_c.

To investigate the nature of the satellite peaks, the real (χ') and imaginary (χ'') components of the complex susceptibility were measured by means of a vector voltmeter.

The result of measuring χ' for the right satellite is shown in the inset to Fig. 1. It is evident that the χ' dispersion curve corresponds to damping of the resonance type rather than the nonresonance type.[1]

Measurements of the diffuse scattering of x rays were also performed on the sample. The results are shown in Fig. 2. It is evident from this figure that above the transition temperature in the temperature interval 210–240 K the principal Bragg reflections are flanked by nearby satellites representing diffuse scattering maxima, indicating a periodic modulation of the metallic vanadium lattice.[8] The distances from the satellites to the principal Bragg peaks in reciprocal space must be equal to the reciprocal of the period of the modulated structure. Calculations show that the modulation period is ~ 70 Å.

During cooling–heating cycles the resonance damping peaks of the $VH_{0.73}$ samples gradually vanish, the central

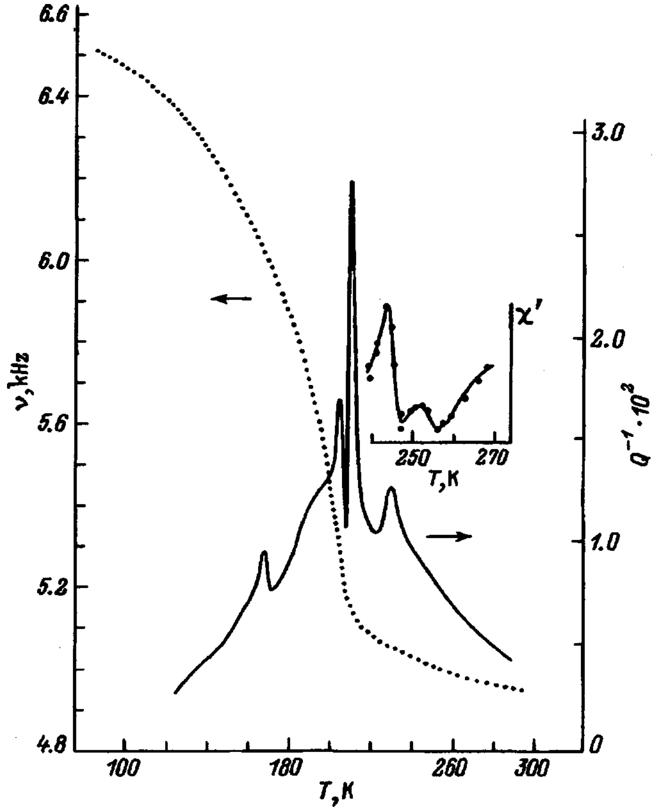

FIG. 1. Damping of elastic vibrations (Q^{-1}) and elastic modulus (ν^2) versus temperature for the hydride $VH_{0.73}$ in the vicinity of the $\beta-\delta$ transition (after the first cooldown). Inset: Elastic dispersion χ' versus temperature in the vicinity of the first satellite.

relaxation peak becomes narrower, and its middle trough becomes smoother. The diffuse satellites in the x-ray scattering spectra also vanish at the same time, suggesting a relationship between the observed features.

Figure 3 shows the temperature spectra of the elastic modulus and damping after multiple thermal cycling of the sample. It is evident that the damping curve represents a classical λ-shaped peak characteristic of second-order phase transitions, and the inflection point of the elastic modulus curve coincides exactly with the maximum of the damping peak at the phase transition temperature.

3. DISCUSSION OF THE RESULTS

The foundation of acoustical methods for the investigation of phase transitions is the work of Landau and Khalatnikov,[9] who have shown that the ultrasound absorption coefficient α (which is proportional to the reciprocal Q factor of the vibrator, Q^{-1}), increases in the vicinity of phase transition according to the expression

$$\alpha \sim \frac{\omega^2 \tau}{1+\omega^2\tau^2},$$

where ω is the acoustic frequency, and τ is the order-parameter relaxation time, which exhibits critical slowing according to the law

$$\tau \sim (T-T_c)^{-1}, \quad T \to T_c .$$

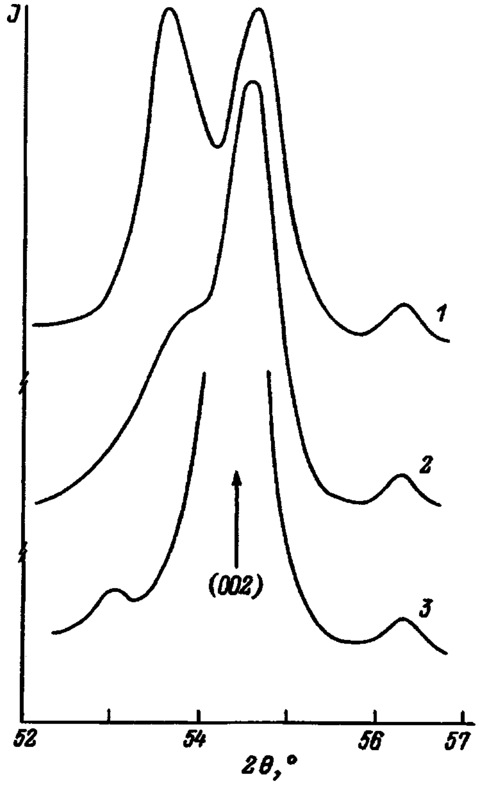

FIG. 2. X-ray diffraction patterns of the hydride $VH_{0.73}$ at three temperatures above the $\beta-\delta$ transition temperature T_c (J denotes the scattering intensity). *1)* $T=210$ K; *2)* 220 K; *3)* 240 K.

It is evident from Fig. 1 that the temperature dependence of the vibration damping of $VH_{0.73}$ in the vicinity of T_c is not at all similar to the classical λ-shaped curve characteristic of continuous phase transitions. The occurrence of the double

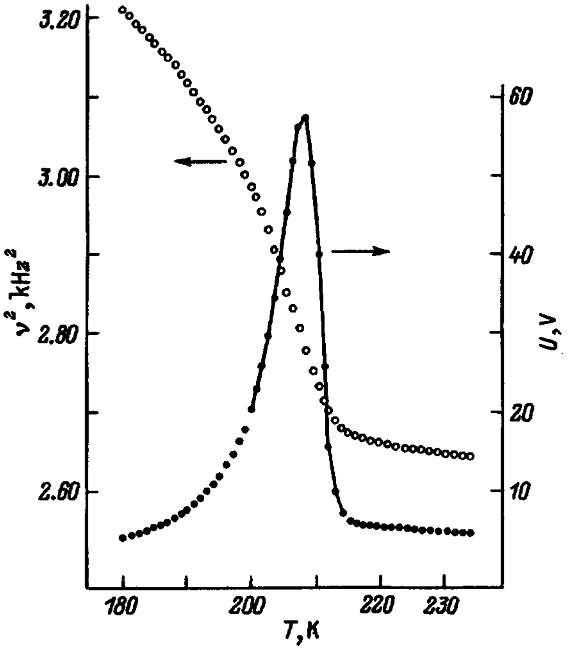

FIG. 3. Elastic modulus (in units of the driving frequency squared ν^2) and energy damping of the sample vibrations (in units of the driving voltage U) versus temperature in the vicinity of the $\beta-\delta$ phase transition in the hydride $VH_{0.73}$. The excitation voltage $U \sim 60$ V corresponds to a reciprocal Q factor $Q^{-1} \sim 10^{-2}$.

absorption peak near T_c requires the fulfillment of two conditions: 1) The acoustic wave must interact with ''soft'' excitations of the order parameters in the low-temperature and high-temperature phases; 2) the reciprocal relaxation time τ^{-1} must become lower than the sample vibration frequency ω. In this case the condition of the absorption maximum $\omega\tau=1$ is satisfied twice, once for $T<T_c$ and once for $T>T_c$.

The presence of resonance damping peaks in addition to the relaxation peaks in the damping spectrum shows that the response function for coordinates descriptive of ordering is determined by the behavior of the harmonic oscillator coupled by interaction with certain internal degrees of freedom characterized by the Debye relaxation time τ (Ref. 2).

This form of the order-parameter response function was first observed in $SrTiO_3$ (Ref. 10) in the vicinity of phase transition at $T=105$ K at frequencies of the order of 10^{11} Hz. In contrast with the cited example, the extremely slow critical dynamics observed by us ($\omega\sim 10^3$ Hz) can be linked only to long-period structures characterized by ''ultrasoft'' excitations.[11]

Inasmuch as phase transitions associated with hydrogen ordering in hydrides are accompanied by distortion of the metal matrix, the emergence of order with a long period should induce diffuse satellites near certain Bragg reflections,[8] as is indeed demonstrated in Fig. 2.

We can assume in regard to the evolution of the damping spectrum in thermal cycling that the structural defects formed during thermal cycling suppress long-range order, thereby setting the phase of the order parameter. The stabilizing influence of the defects is manifested in the system dynamics, inhibiting the growth of pretransition ordering clusters and subsequent frequency reduction of ''soft'' modes. This assumption is confirmed by the disappearance of the resonance absorption peaks of the vibrations together with the disappearance of the diffuse satellites in the x-ray scattering spectrum, and also by the substantial narrowing of the relaxation absorption peak, which acquires the shape of the classical ''λ'' curve (Fig. 3).

Our investigations of the phase-transformation kinetics in $VH_{0.73}$ at $T_c=208$ K have thus shown that the unusual form of the low-frequency acoustic absorption anomaly is attributable to long-period modulation accompanied by a $\beta-\delta$ transition in the hydride $VH_{0.73}$.

[1] R. Blinc and B. Žekš, *Soft Modes in Ferroelectrics and Antiferroelectrics* (North-Holland, Amsterdam, 1974) [Russ. trans., Mir, Moscow (1975), 398 pp.].

[2] A. D. Bruce and R. A. Cowley, *Structural Phase Transitions* (Taylor and Francis, Philadelphia, 1981) [Russ. trans., Mir, Moscow (1984), 407 pp.].

[3] *Hydrogen in Metals II: Application-Oriented Properties*, edited by G. Alefeld and J. Völkl (Springer-Verlag, Berlin-New York, 1978) [Russ. trans., Mir, Moscow (1981), Vol. 2, 430 pp.].

[4] H. Asano and M. Hirabayashi, Phys. Status Solidi A **16**, 69 (1973).

[5] V. A. Melik-Shakhnazarov and I. A. Naskidashvili, Pribory Tekh. Éksp., No. 1, 181 (1967).

[6] F. S. Crawford, Jr., *Waves and Oscillations* (*Berkeley Physics Course*, Vol. 3), 2nd ed. (McGraw-Hill, New York, 1973) [Russ. trans., Nauka, Moscow (1976), 527 pp.].

[7] W. Rehwald, Adv. Phys. **22**, 721 (1973).

[8] A. G. Khachaturyan, *Theory of Phase Transitions and Structure of Solid Solutions* [in Russian], Nauka, Moscow (1974), 384 pp.

[9] L. D. Landau and I. M. Khalatnikov, Dokl. Akad. Nauk SSSR **96**, 469 (1954).

[10] T. Riste, E. J. Samuelsen, K. Otnes, and J. Feder, Solid State Commun. **9**, 1455 (1971).

[11] V. A. Golovko and A. P. Levanyuk, Zh. Éksp. Teor. Fiz. **81**, 2296 (1981) [Sov. Phys. JETP **54**, 1217 (1981)].

Translated by James S. Wood

PHYSICS OF THE SOLID STATE VOLUME 40, NUMBER 4 APRIL 1998

Phase transitions in a system of unstable particles

V. I. Sugakov

Institute for Nuclear Research, National Academy of Sciences of Ukraine, 252028 Kiev, Ukraine

(Submitted October 8, 1997)
Fiz. Tverd. Tela (St. Petersburg) **40**, 741–745 (April 1998)

A study is reported of phase separation in a system of particles created at a constant rate and having a finite lifetime. It is shown that (1) phase separation is possible if the particle lifetime exceeds a certain critical value, (2) the particle-density difference between the phases depends on particle lifetime, and (3) the correlation function in the two-phase region oscillates (with damping) as a function of spatial coordinates, which implies correlation between the phase locations. © *1998 American Institute of Physics.* [S1063-7834(98)03604-1]

Phase transitions are usually observed and studied in systems of particles whose lifetime is infinite. In physics, however, there exist a large number of phenomena where external pumping creates unstable particles (or quasi-particles in crystals) having a finite lifetime. Among such systems are: (1) the electron-hole liquid in semiconductors,[1,2] (2) the dielectric exciton liquid in crystals,[3,4] (3) a strongly excited gas whose excited atoms (molecules) become attracted by resonant interaction to unexcited ones, which may give rise to formation of a new phase,[5–7] (4) the system of vacancies and interstitials in a crystal,[8,9] and others. In cases (1)–(3), the particles (electrons and holes, excitons, excited molecules) are created by external light pumping, and in case (4) (vacancies and interstitials) a high concentration of particles can be produced by a flux of energetic particles (protons, neutrons, ions etc.), processes which can be accompanied by vacancy coalescence (pore formation) and phase separation in multicomponent systems. In all the above cases the particles (quasi-particles) live a finite time; for example, excited molecules and excitons have a natural lifetime and, besides, can be destroyed in various interactions, electrons and holes, as well as vacancies and interstitials, are captured by traps and sinks and can recombine.

If the particle generation rate is independent of time, a steady state sets in in the system, with the number of particles created per unit time equal to that of annihilated particles. The above systems are usually considered to be in equilibrium, with the concentration equal to its steady-state value generated by external irradiation. If the particle concentration is high enough, and they are subject to attraction, such a system can support different phases, and its phase state will change with changing particle concentration, i.e. actually with the changing rate of their creation. Within a certain region of particle concentration, the total number of particles may not be high enough for a new phase to form throughout the volume of the system. In this case the system breaks up into regions of different phases. The problem of the properties of such a system is similar to that of spinodal decomposition in a system of stable particles. A typical phase diagram (in the temperature-concentration coordinates) for spinodal decomposition is presented in Fig. 1. In region 1 there is one phase, and in region 2, two phases exist. A system with a uniform particle distribution that resides in a certain state at a high temperature (for instance, at point A), can be rapidly cooled to a state (point B) where two phases can coexist. The system separates subsequently into phases whose state is determined by points C_1 and C_2. The dynamics of the system undergoing spinodal decomposition, first considered in Refs. 10–13, was studied in detail in Refs. 14–17. For $t \rightarrow \infty$, a steady state sets in, and the system separates into infinitely large regions of different phases, with concentration fluctuations occurring in each of them as they do in the given phase of infinite size.

In our problem of phase formation in a system of unstable particles continually created by an external source one also starts with a uniform particle distribution, which corresponds, for instance, to the state of the system at point B. As in spinodal decomposition, phase separation likewise sets in here, and the system moves toward the state with phases C_1 and C_2. Because the particle lifetime is finite, however, phase separation may either progress to a lesser extent or not at all, i.e., the steady state thus formed is nonequilibrium, it should depend substantially on particle lifetime, and can dif-

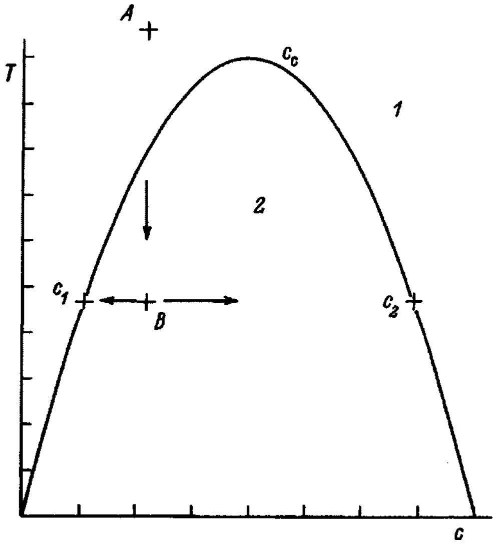

FIG. 1. Typical temperature-concentration phase diagram for stable particles.

fer strongly from the steady state obtained in spinodal dynamics for stable particles. This work studies characteristics of a state (distribution function, correlation function) in a system with unstable particles. Obviously enough, the part played by the instability depends on the relation between the particle lifetime and the time required for equilibrium to obtain. The time needed to attain equilibrium can be divided into the time required for local equilibrium to set in and the time required for equilibrium to extend in space. The latter is longer than the former, and it plays an essential role in the concentration domain where phase separation exists (i.e., in the so-called diffusion-dominated region between points C_1 and C_2 in Fig. 1). In this domain, the finiteness of the lifetime can play an important part, and we shall investigate it later. Since the phase states under study here exist only in nonequilibrium conditions (in the presence of an external factor creating the particles), they are, by the terminology of Prigogine[18], dissipative structures.

1. DETERMINATION OF THE PARTICLE DISTRIBUTION DEPENDENCE ON CONCENTRATION

Thus we consider a system of particles which interact with one another, are created continually by an external source, and exist for a finite time. The state of the system in a general case is described by a distribution function $\rho[c(\mathbf{r})]$ depending on particle concentration $c(\mathbf{r})$, which turns out to be an order parameter. To find $\rho[c(\mathbf{r})]$, one has to solve a kinetic equation whose form depends on the actual type of particle interaction. To consider the problem in a more general way in terms of a model that was studied comprehensively in various applications, we shall present the dependence of free energy on fluctuating fields $c(\mathbf{r})$ in the Landau-Ginzburg form. The functional equation of Focker-Planck can be written

$$\frac{\delta\rho}{\delta t}=-\int d\mathbf{r}\,\frac{\delta(j_d+j_\tau)}{\delta c(\mathbf{r})}, \tag{1}$$

where j_d is the probability flux due to diffusion processes,

$$j_d(\mathbf{r})=M\Delta\left(\frac{\delta F}{\delta c(\mathbf{r})}+kT\frac{\delta\rho}{\delta c(\mathbf{r})}\right), \tag{2}$$

M is the mobility, F is the free energy in the Ginzburg-Landau representation

$$F(c)=\int d\mathbf{r}\left[\frac{1}{2}K(\boldsymbol{\nabla}c)^2+f(c)\right], \tag{3}$$

j_τ is the probability flux associated with particle creation and annihilation, which is introduced here into the equation of spinodal decomposition dynamics,

$$j_\tau=-\frac{c(\mathbf{r})-c_0}{\tau}-\frac{1}{2}\,\frac{\delta\left[\left(G+\dfrac{c(\mathbf{r})}{\tau}\right)\rho\right]}{\delta c(\mathbf{r})}, \tag{4}$$

τ is the particle lifetime, $c_0=G\tau$ is the average particle number, and G is the particle generation rate, i.e., the number of particles created per unit time in a unit volume; we shall assume in what follows that G is coordinate independent, i.e., that the sample is so thin that the pump intensity does not vary within it.

Relation (4) can be obtained in the creation-annihilation model for a system with a large number of particles. We neglect here the term quadratic in concentration, which accounts for two-particle recombination. This term can be essential in the case of a high particle concentration, and we shall analyze its role later.

Introduce a quantity characterizing order-parameter fluctuations

$$u(\mathbf{r})=c(\mathbf{r})-c_0. \tag{5}$$

Equation (1) corresponds to the following stochastic equation for the field u:

$$\frac{\partial u}{\partial t}=M\Delta\frac{\delta F}{\delta u(\mathbf{r})}-\frac{u}{\tau}+\eta(\mathbf{r},t), \tag{6}$$

where $\eta(\mathbf{r},t)$ is the fluctuation term.

Introduce a correlator

$$S(\mathbf{r}-\mathbf{r}',t)=\langle u(\mathbf{r})u(\mathbf{r}')\rangle$$

and its Fourier component

$$S(\mathbf{k})=\int d\mathbf{r}S(\mathbf{r})\exp[-i\mathbf{k}\mathbf{r}]. \tag{7}$$

Multiplying Eq. (1) by $u(\mathbf{r})u(\mathbf{r}')$, and integrating over the function space u yields an equation for $S(\mathbf{k})$

$$\frac{dS(\mathbf{k})}{dt}=-2M\left[\left(k^2\left(Kk^2+\frac{\partial^2 f}{\partial c_0^2}\right)+\frac{1}{\tau}\right)S(\mathbf{k})+\frac{1}{2}\frac{\partial^3 f}{\partial c_0^3}S_3+\frac{1}{6}\frac{\partial^4 f}{\partial c_0^4}S_4+\cdots\right]+2\left(\frac{c_0}{\tau}+MkTk^2\right), \tag{8}$$

where

$$S_n(\mathbf{r}-\mathbf{r}')=\langle u^{n-1}(\mathbf{r})u(\mathbf{r})\rangle. \tag{9}$$

To carry out the calculations to the end, we shall use subsequently an approximation of the two-particle distribution function ρ_2 in terms of the one-particle one, ρ_1, proposed in Ref. 14

$$\rho_2(u(\mathbf{r}),u(\mathbf{r}'))=\rho_1(u(\mathbf{r}))\rho_1(u(\mathbf{r}'))\times\left[1+\frac{S(\mathbf{r}-\mathbf{r}')}{\langle u^2\rangle^2}u(\mathbf{r})u(\mathbf{r}')\right]. \tag{10}$$

The further calculations are similar to those made in Ref. 14 [one has only to take into account the term j_τ in Eq. (1)]. We finally obtain

$$\frac{dS(\mathbf{k})}{dt}=-2M\left[k^2(Kk^2+A)+\frac{1}{\tau}\right]S(\mathbf{k})+2\left(\frac{c_0}{\tau}+MkTk^2\right), \tag{11}$$

where

$$A=\frac{\left\langle u\dfrac{\partial f(c_0+u)}{\partial u}\right\rangle}{\langle u^2\rangle}. \tag{12}$$

Thus determination of $S(\mathbf{k})$ reduces to calculation of a certain mean value with a one-particle distribution function. The equation for the one-particle distribution function in the cell model is obtained in the way this was done in Ref. 14. Dropping the calculations similar to those in Ref. 14, we come to

$$\frac{\partial\rho_1}{\partial t}=\frac{\partial}{\partial u}\left\{\left[D\left(\frac{\partial f}{\partial u}-\left\langle\frac{\partial f}{\partial u}\right\rangle-\frac{u\left\langle\frac{\partial f}{\partial u}\right\rangle}{\langle u^2\rangle}\right)-W-\frac{u}{M\tau}\right]\rho_1+\frac{1}{l^2}\frac{\partial\left[kTD-\frac{1}{2M}\frac{2c_0+u}{\tau}\right]\rho_1}{\partial u}\right\}, \tag{13}$$

where l is the linear size of the cell, d is the dimension of the system,

$$\langle u^2\rangle=S(0)=\int du u^2\rho_1(u), \tag{14}$$

$$\left\langle\frac{\partial f}{\partial u}\right\rangle=\int du\frac{\partial f}{\partial u}\rho_1(u), \tag{15}$$

$$W=\frac{l^d}{(2\pi)^d}\int d\mathbf{k}S(\mathbf{k})(Kk^2+A), \tag{16}$$

D is the diagonal element of the operator which is an analog of the Laplacian in the cell representation defined by the relation

$$\Delta\psi(\mathbf{r})|_{\mathbf{r}=\mathbf{n}}\rightarrow\sum_{n'}D_{\mathbf{nn}'}\psi(\mathbf{n}'),$$

$$D_{\mathbf{nn}'}=-\frac{l^d}{(2\pi)^d}\int d\mathbf{k}k^2\exp(i\mathbf{k}(\mathbf{n}-\mathbf{n}')).$$

The integration is performed here over the Wigner-Seitz cell.

Present function f in the form

$$f=\frac{a}{2}(\Delta c+u)^2+\frac{b}{4}(\Delta c+u)^4, \tag{17}$$

where $\Delta c=c_0-c_c$, and c_c is the critical concentration.

Introduce dimensionless variables

$$\tilde{u}=\frac{u}{(-a/b)^{1/2}},\quad \tilde{\mathbf{r}}=\frac{\mathbf{r}}{\xi},\quad \tilde{T}=\frac{\kappa b}{a^2l^d}T,\quad \tilde{\tau}=\frac{l^{d-2}Ma^2}{[b(-a)]^{1/2}}\tau, \tag{18}$$

where $\xi=(k/-a)^{1/2}$ is the correlation length.

The size of the cell we shall choose close in order of magnitude to the boundaries of the transition layer separating the phases (l is of order ξ, Refs. 14,16). The quantity u in the last term of Eq. (13) is dropped compared to $2c_0$ (as we shall see later, at the maxima of the distribution u is small for not too large τ, while for large τ the term $2c_0+u$ is insignificant altogether).

We obtain for the stationary solution to Eqs. (11) and (13)

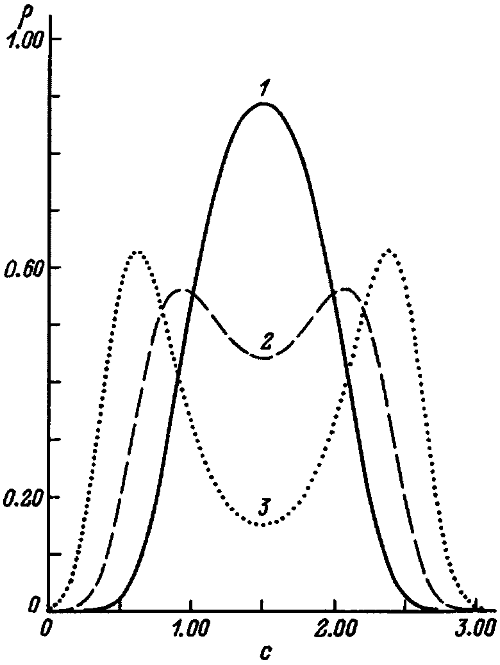

FIG. 2. One-particle distribution function *vs* particle concentration for $\tilde{T}=0.1$, $\tilde{c}_0=\tilde{c}_c=1.5$ for different lifetimes $\tilde{\tau}$: *1* — 10, *2* — 30, *3* — 1000 (3D case).

$$S(\tilde{\mathbf{r}})=\frac{1}{(2\pi)^d}\int\frac{\left(\frac{\tilde{c}_0}{\tilde{\tau}}+\tilde{T}\tilde{k}^2\right)\exp(i\tilde{\mathbf{k}}\tilde{\mathbf{r}})}{\left(\tilde{k}^4+A\tilde{k}^2+\frac{1}{\tau}\right)}d\tilde{\mathbf{k}}, \tag{19}$$

$$\rho_1=\rho_0\ \exp\left\{-\frac{f(\tilde{u})-\tilde{u}\left\langle\frac{\partial f}{\partial\tilde{u}}\right\rangle-\frac{\tilde{u}^2}{2}\left(A-\frac{\tilde{T}+\tilde{c}_0/\tilde{\tau}\tilde{D}}{\langle\tilde{u}^2\rangle}\right)}{\tilde{T}+\tilde{\tau}_0/\tilde{\tau}\tilde{D}}\right\}, \tag{20}$$

where $\tilde{D}=|D|/l^2$, in the one-dimensional case $\tilde{D}=\pi^2/3$, and in three dimensions $\tilde{D}=3(3\pi^2)^{2/3}$.

The parameters of the distribution function (20) are found by the following algorithm. The quantity $\langle\tilde{u}^2\rangle=S(0)$ is expressed with the use of Eq. (19) through A. After this, the one-particle distribution function contains two parameters: A and $\langle\partial f/\partial\tilde{u}\rangle$. Substitution of the distribution function ρ_1 [Eq. (20)] in explicit form reduces Eqs. (12) and (15) to coupled transcendental equations in two unknowns, A and $\langle\partial f/\partial\tilde{u}\rangle$. The system thus obtained was solved numerically.

2. CALCULATIONS, ANALYSIS, DISCUSSION

The above algorithm was used to calculate $\rho_1(\tilde{u}),S(\tilde{\mathbf{r}})$, and $S(\tilde{k})$ as functions of $\tilde{\tau},\tilde{T}$, and $\tilde{c}_0$. The existence of phase transitions in the system was established from the appearance (disappearance) of maxima in the $\rho_1(\tilde{u})$ relation.

Figure 2 shows a one-particle distribution function in the three-dimensional case calculated for different values of $\tilde{\tau}$ and for a pump intensity such that $\Delta c=0$, i.e,. a pump intensity producing a concentration which for an infinite quasi-

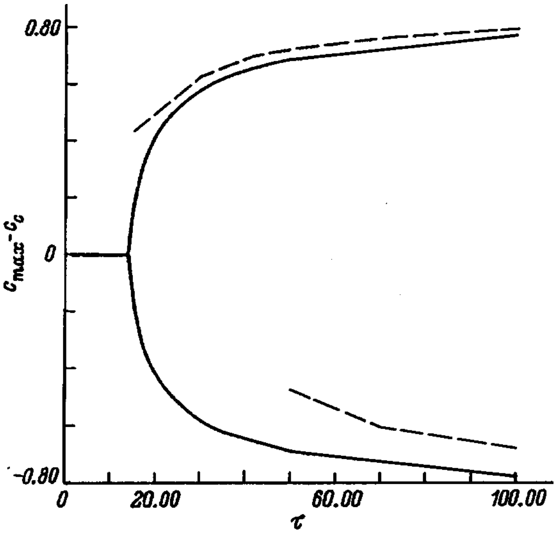

FIG. 3. Positions of the maxima in the one-particle distribution function for the three-dimensional case *vs* particle lifetime for $\tilde{T}=0.1$ calculated for different steady-state concentrations: $\tilde{c}_0=1.5$ (solid line) and $\tilde{c}_0=1.8$ (dashed line).

particle lifetime would be critical ($c_0=c_c$, see Fig. 1). For small $\tilde{\tau}$ the distribution function has one maximum, and no phase separation occurs in the system (curve *1* in Fig. 2). As $\tilde{\tau}$ increases, two maxima appear in the distribution function for some $\tilde{\tau}>\tilde{c}$ (curves *2* and *3* in Fig. 2), whose separation increases and whose positions tend to $\tilde{u}_{\max}\approx\pm 1$ for $\tau\rightarrow\infty$. The appearance of two maxima implies separation of the system into phases. Thus phase separation is possible only in the case where the lifetime of quasi-particles exceeds a certain value. The finiteness of the lifetime narrows considerably the concentration region within which phase separation sets in. The critical value of $\tilde{\tau}$ at which phase separation takes place depends on Δc (3D case, Fig. 3). This value is the smallest at $\Delta c=0$. Besides, the particle concentration in the phases differs from the equilibrium value ($\tilde{u}\approx\pm 1$) and does not depend on the lifetime. As seen from Fig. 3, after the separation the concentration in the phases depends on $\tilde{\tau}$, strongly in the beginning, to weaken gradually. One also sees that irrespective of the pumping (C_0) the particle concentrations in the phases tend for $\tau\rightarrow\infty$ to the same (equilibrium) values. Very long lifetimes are needed, however, to reach the equilibrium values.

Figure 4 illustrates the variation of the distribution function for a fixed $\tilde{\tau}$ with increasing pumping (particle concentration), i.e., as one moves from point c_1 to c_2 (Fig. 1). At low pumping levels, there is only one maximum in the distribution function (curve *1*), then a second maximum appears, its amplitude grows with pumping, until at a certain pump intensity the first maximum disappears to leave only one in place (curve *5* in Fig. 4).

The correlation function $S(z)$ oscillates in the phase separation region to damp out with increasing z (Fig. 5). This means that the phase locations are correlated. For a given τ the oscillation period depends on pumping. It is the smallest for pump intensities such that $\Delta c=0$. The period grows with τ and tends to infinity. The onset of periodicity for spinodal decomposition in a system of stable particles was demonstrated by Cahn and Hillert.[10–13] Subsequent rigorous analysis[14–17] showed that for $t\rightarrow\infty$ a system of stable particles tends to a state with infinitely large domains, and that periodicity can exist only in some stages of spinodal decomposition. At the same time in the system of unstable particles studied here large domains do not have time enough to form, and a periodic phase arrangement in steady state sets in. For $\tau\rightarrow\infty$, we come to a system of stable particles, for which there is no periodicity. The onset of periodicity in steady state in a system of continually created unstable particles

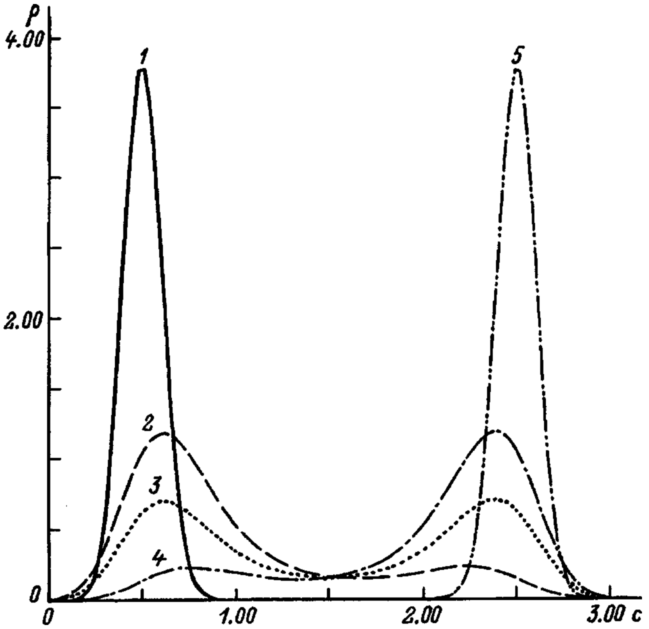

FIG. 4. One-particle distribution function *vs* particle concentration for $\tilde{T}=0.1$ and $\tilde{\tau}=1000$ calculated for different concentration $\tilde{c}_0$ (pump intensity): *1* — 0.5, *2* — 1.0, *3* — 1.5, *4* — 2.0, *5* — 2.5 (3D case).

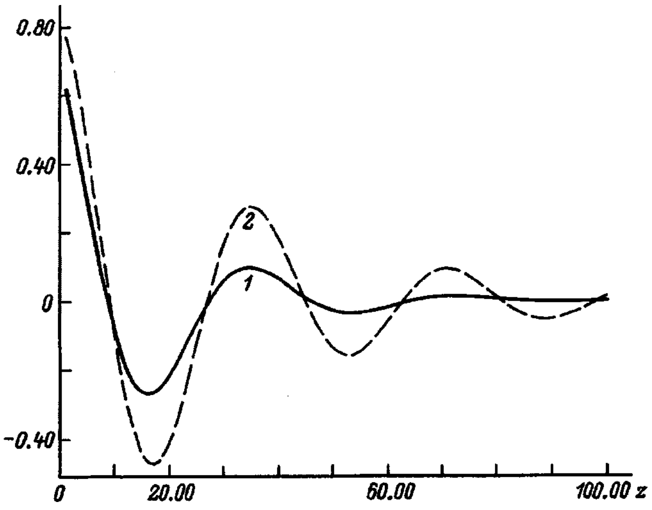

FIG. 5. Coordinate dependence of the correlation function for a given steady-state concentration $\tilde{c}_0=\tilde{c}_c=1.5$, $\tilde{\tau}=1000$ in a one-dimensional system calculated for different temperatures $\tilde{T}$: 0.05 (dashed line) and 0.1 (solid line).

(excitons under light excitation,[19] vacancies and interstitials in a crystal irradiated by penetrating radiation[20]) was considered earlier neglecting fluctuations. Taking fluctuations into account results in a damping out of the correlation function. The damping decreases with decreasing temperature. The $S(z)$ dependence for a one-dimensional system is shown in Fig. 5 for two temperatures.

Partial support of State Foundation for Fundamental Research of the Ministry of Science of Ukraine and of USA CRDF is gratefully acknowledged.

[1] L. V. Keldysh, in *Proceedings of the IX International Conference Physics of Semiconductors* (Nauka, Moscow, 1969), Vol. 2, 1384 pp.
[2] T. M. Rice, J. C. Hensel, T. G. Phillips, and G. A. Thomas, *The Electron-Hole Liquid in Semiconductors* (Academic, New York, 1977; Mir, Moscow, 1980).
[3] A. P. Silin, Fiz. Tverd. Tela (Leningrad) **19**, 134 (1977) [Sov. Phys. Solid State **19**, 77 (1977)].
[4] I. S. Gorban, M. M. Biliy, I. M. Dmitruk, and O. A. Yeshchenko, Solid State Commun. **98**, 489 (1996).
[5] V. N. Mal'nev and S. I. Pekar, Zh. Éksp. Teor. Fiz. **51**, 1811 (1966) [Sov. Phys. JETP **24**, 1220 (1966)].
[6] Yu. A. Vdovin, Zh. Éksp. Teor. Fiz. **54**, 445 (1968) [Sov. Phys. JETP **27**, 242 (1968)].
[7] I. R. Yuchnovskii, O. V. Derzhko, and K. K. Levitskii, Physica A **203**, 381 (1993).
[8] K. C. Russell, Prog. Mater. Sci. **28**, 229 (1984).
[9] G. Martin, Phys. Rev. B **21**, 2122 (1980).
[10] J. W. Cahn and J. E. Hillard, J. Chem. Phys. **28**, 258 (1958).
[11] J. W. Cahn, Acta Metall. **9**, 795 (1961).
[12] M. A. Hillert, Acta Metall. **9**, 525 (1961).
[13] J. W. Cahn, Acta Metall. **10**, 179 (1962).
[14] J. S. Langer, M. Bar-on, and H. D. Miller, Phys. Rev. A **11**, 1147 (1975).
[15] K. Bidner, Phys. Rev. B **15**, 4425 (1977).
[16] G. F. Mazenko, O. T. Valls, and M. Zannetti, Phys. Rev. B **38**, 520 (1988).
[17] G. F. Mazenko, Phys. Rev. B **43**, 5747 (1991).
[18] G. Nicolis and I. Prigogine, *Self-Organization in Nonequilibrium Systems* (Wiley, New York; Mir, Moscow, 1979).
[19] V. I. Sugakov, Fiz. Tverd. Tela (Leningrad) **28**, 2441 (1986) [Sov. Phys. Solid State **28**, 1365 (1986)].
[20] V. I. Sugakov, in *Effects of Radiation on Materials: 14th International Symposium ASTM STP 1046* (Philadelphia, 1989), edited by N. H. Packan, Vol. 1, pp. 510–527.

Translated by G. Skrebtsov

PHYSICS OF THE SOLID STATE VOLUME 40, NUMBER 4 APRIL 1998

Phase transitions in silicon single crystals resulting from directional plastic deformation

I. M. Shmyt'ko, A. N. Izotov, and N. S. Afonikova

Institute of Solid-State Physics, Russian Academy of Sciences, 142432 Chernogolovka, Moscow Province, Russia

S. Vieira and G. Rubio

Instituto Universitario de Ciencia de los Materiales Nicolás Cabrera, Laboratorio de Bajas Temperaturas C-III, Universidad Autónoma de Madrid, 28049 Madrid, Spain

(Submitted October 31, 1997)
Fiz. Tverd. Tela (St. Petersburg) **40**, 746–749 (April 1998)

The formation of polytypic modifications is observed in dislocation-free silicon single crystals under directional plastic deformation. It is shown that the deformation-stimulated phase appears on the surface of the sample in the form of small grains ranging from several hundred to several thousand angstroms in size. A twin structure in the individual grains is observed. © *1998 American Institute of Physics.* [S1063-7834(98)03704-6]

A special modification in its own right among the ten phases of silicon known to exist at the present time is the hexagonal, lonsdaleite type first synthesized in 1963 (Ref. 1) by annealing high-pressure-treated polycrystalline blocks. It was identified as a simple wurtzite lattice with parameters $a = 0.38$ nm and $c = 0.628$ nm. More recently, several research groups[2–5] have observed a hexagonal phase with the same parameters after the indentation of single-crystal samples at room temperature and above, indicating the important role of plastic deformation in the formation of the wurtzite modification. However, the mechanism of this transformation has not been studied in detail.

Based on zinc sulfide,[6,7] we have proposed a structural mechanism for the transformation of the sphalerite (cubic) and wurtzite (hexagonal) modifications into various polytipes phases as a result of the correlated motion of partial dislocations during plastic deformation, and we have studied experimentally the mutual structural transformations of polysynthetic twins of the sphalerite phase, where the results corroborate the postulated mechanism.

In the present study we report the observation of structural transformations of a diamond lattice into new polytypic formations during plastic deformation in silicon.

We have investigated dislocation-free single-crystal silicon samples prepared in the form of $2.5 \times 3.0 \times 10.0$-mm rectangular bars with faces parallel to (541), (111), and (1 2 3), respectively. The choice of orientation of the samples was made so that only one glide plane of the type {111} would be active in the deformation process. The deformation temperature was 900 °C, and the rate of deformation was 5 μm/min for one series of tests and 20 μm/min for another series. The total deformation did not exceed 2–3%.

X-ray analysis and atomic-force microscopy (AFM) were used for the investigations. For the x-ray examinations an oscillation camera was built on the base of a DRON-2.0 diffractometer, utilizing monochromatized Ag $K\alpha$ radiation from the monochromator of a GUR-5 goniometer. The voltage on the tube did not exceed 40 kV, and the current was 30 mA. The voltage had to be limited to exclude radiation having wavelengths in multiples of Ag $K\alpha/n$ from the diffraction.

Atomic-force microscopy was used for topographic visualization of new phase formations and for studying the true structure of these formations at the level of atomic resolution. A cantilever-reflected laser beam was used as the recording signal. Images of the silicon surface were obtained in the topographic regime and in the friction regime. The experiment was performed on a microscope constructed in the Low-Temperature Laboratory at the Autonomous University of Madrid.

To remove all surface oxide films, the samples designated for the AFM investigations were first boiled in deionized water for 10 min and then rinsed consecutively 10–15 times in a 1% HF solution and boiling water for 30 s each time. The samples, cooled down from this treatment in deionized water at room temperature, were blown with dry nitrogen gas and were immediately placed on the sample holder of the microscope. The total adjustment time did not exceed a few minutes.

X-ray oscillation patterns about the ⟨110⟩ and ⟨112⟩ axes were recorded for structural identification of the deformed samples. An example of an oscillation pattern about the ⟨110⟩ axis of a crystal deformed at a rate of 5 μm/min is shown in Fig. 1. In addition to the strong reflections from the cubic matrix, a series of secondary, weak reflections is also visible in the x-ray pattern (Fig. 1b), presenting clear-cut evidence of the formation of a new phase in the silicon. The dotted appearance of the reflections of this phase indicate that it takes up fairly large dimensions in the sample (>1000 Å). An analysis of x-ray patterns obtained from different parts of the crystal show that the new phase forms on the surface of the sample within the active deformation zone. We conclude from the positions of the secondary reflections relative to the reflections associated with the original cubic structure and relative to the zero order for both oscillation diagrams that the observed structure is not of the wurtzite

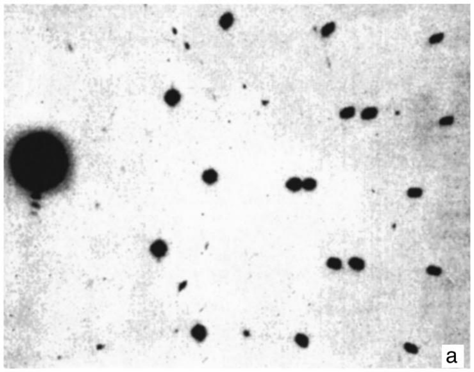

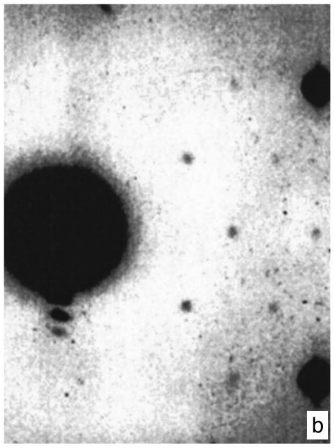

FIG. 1. Oscillation diagrams of a silicon single crystal deformed at the rate of 5 μm/min. a) Overall view of the x-ray pattern; b) magnified section of the x-ray pattern near the zero-order beam (axis of rotation [110]).

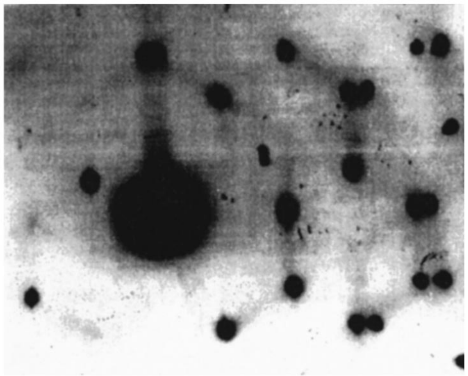

FIG. 2. Oscillation diagram of a silicon single crystal deformed at the rate of 20 μm/min (axis of rotation [112]).

type. Indeed, it is evident from the figure that a layer line of secondary reflections is present between the zero and first layer lines of the as-prepared diamond modification. This means that the lattice period of the new phase is twice the period of the matrix along the oscillation axis (for the derivative-phase indices published in Refs. 2–5, this change corresponds to doubling of the period along the *a* direction of the postulated hexagonal form). The periods of the new phase simultaneously double in layers perpendicular to the rotation directions, creating secondary reflections along the layer lines. The doubling of the lattice periods along the rotation axis and in the perpendicular layers is a departure from the lonsdaleite structure; hence, the phase induced by plastic deformation differs from the wurtzite modification of silicon obtained in Refs. 1–5.

The phase initiated by plastic deformation does not always appear in the form of reflections on the oscillation x-ray patterns. More often the secondary reflections appear as diffuse streaks, connecting reflections of the cubic matrix. Figure 2 shows an oscillation pattern about the [112] axis for one of the samples deformed at a rate of 20 μm/min. In contrast with Fig. 1, it does not have any isolated superstructure; rather, it has strong diamond-modification reflections joined by streaks. Diffuse reflections are perceived only in zones where such streaks intersect. Only the positions of certain ones coincide with the positions of secondary reflections on the x-ray pattern corresponding to this rotation axis for a sample deformed at a rate of 5 μm/min. The latter result indicates that the plastic deformation-induced phases differ in these samples.

The broad, diffuse streaks indicate that a new phase has evolved in the form of thin, interstratified layers. An analysis of x-ray patterns recorded from different faces of a sample show that the layers of the new phase have extended dimensions along a surface at which dislocations emerge, and they are thin in the interior of the sample. At the present time it has not been determined whether the small dimensions of the new phase inclusions are attributable to the deformation rate or to the dopant concentration. It has been established, however, that the broad, diffuse streaks are formed in both *n*-type and *p*-type crystals.

The topography of the allocation of the new phase formations in the cubic matrix has been investigated by atomic-force microscopy. Figure 3 shows examples of AFM topograms obtained from different scanned zones of the same sample. The new-phase outcroppings appear as regions of diminished intensity. It is evident from the scales shown in the figures that the dimensions of the outcroppings vary from hundreds to thousands of angstroms. The abrupt change in contrast obtained in the friction regime indicates that the properties of the newly-emerged outcroppings differ markedly from those of the host matrix (e.g., in the coefficient of friction).

The new-phase outcroppings form on the surface of the matrix after the etching of bumps with heights up to several hundred angstroms. This also indicates that the structure of the new outcroppings differs considerably from the matrix, specifically in terms of the etching rate in this case. A three-dimensional image of one such bump is shown in Fig. 4a. Figure 4b shows an atomic image of the top of this bump. Clearly, the new-phase outcropping consists of two grains with pronounced lattice disorientation in the plane of the image. Because the starting single crystal was free of dislocations, the only way a new orientation could be formed is through the formation of a new phase in plastic deformation. The low level of deformation in our experiment could not have formed grains with pronounced disorientation in the matrix. This inference is confirmed by original scanning-x-ray topograms, in which the disorientation of parts of the

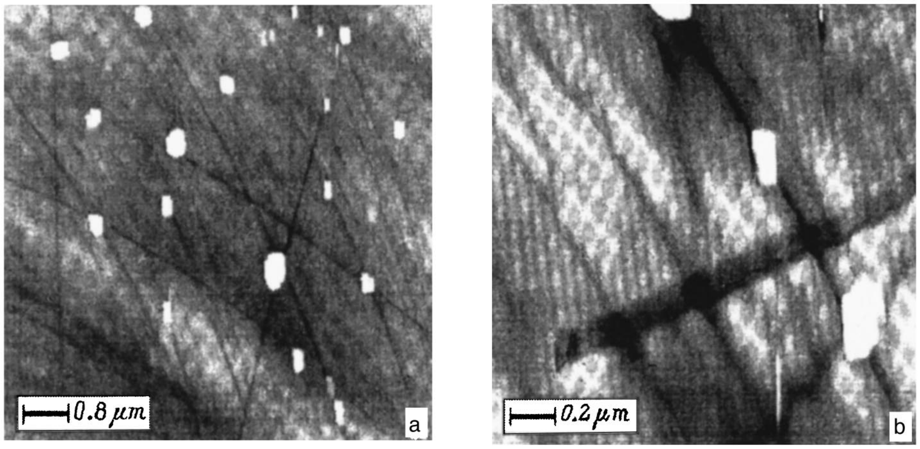

FIG. 3. Atomic-force microscopy topograms obtained in the friction regime for different scanned zones.

matrix does not exceed a few minutes of angle. It is more natural to assume that different dislocation glide planes of the crystal create different orientations of the newly emerged phase and, hence, that Fig. 4b exhibits growth twins.

It is evident from the figure that the distance between rows of atoms for one twin orientation is ~7 Å (unfortunately, the microscope had approximately 10% calibration error limits), which exceeds the interatomic spacings in the diamond structure of pure silicon and is close to twice the interplanar spacing along $\langle 111\rangle$. The row spacing for the other orientation is larger than for the first one. We postulate that these distances exceed the long-period structure, which is a polytypic phase of silicon (by analogy with zinc sulfide). It is impossible to determine the structure of these phases unambiguously by AFM. It is proposed that high-resolution electron-microscopy be used for their identification.

The mechanism underlying the formation of polytypes in a diamond structure under plastic deformation is based on the correlated motion of partial dislocations along $\langle 112\rangle$ directions in the $\{111\}$ glide plane.[6–8] This process requires a large number of dislocations. In the dislocation-free sample deformation-related dislocations are formed only on the crystal surface, so that new phases are formed only on the surface as well. In particular, the source of dislocations responsible for polytypic structural transformations could be scratches formed on the surface during mechanical polishing. This conjecture is confirmed by the displayed AFM topograms. In fact, all the different-phase outcroppings in Fig. 3 are situated along lines of enhanced contrast running in random directions. Considering that such lines are also observed on the as-prepared, undeformed samples and that their contrast diminishes as the depth of chemical polishing is increased, they can be confidently ascribed to surface scratches.

One might assume that the zones of diminished intensity on the AFM topograms were inadequately etched islands of oxide film in the aftermath of chemical polishing in the HF solution. However, a control test of undeformed samples did not expose any such zones (after surface cleaning by the same procedure as for the deformed samples). A comparison of the image contrast levels obtained for the same sample before and after surface cleaning also fails to corroborate the model of under-etched oxide-film zones.

Finally, we have observed an interesting process that confirms the mechanism of formation of polytypic phases as being due to the correlated motion of partial dislocations. Along with the polytypic outcroppings, Fig. 3b also reveals a narrow band of enhanced contrast relative to the background, running through a large region of the crystal. Such bands disappear every time after repeated scanning of exactly the same region of the sample. We assume that this contrast represents zones containing irregularly distributed stacking faults formed after the passage of partial dislocations. Since

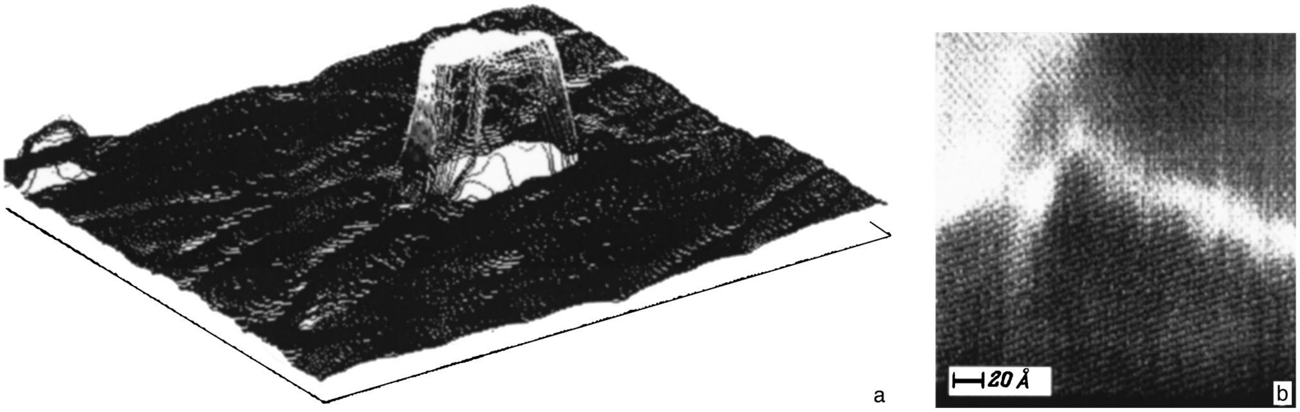

FIG. 4. Three-dimensional view of a new-phase outcropping (a) and its AFM image (b).

stacking faults have excess energy, they are nonequilibrium defects and, under mechanical loading induced by the needle while the image is being recorded, they leave the crystal, restoring the diamond-structure matrix. When a polytypic phase is formed, the total energy of the correlated-position stacking faults falls below the total energy of randomly distributed stacking faults (an effect analogous to dislocations in low-angle boundaries), but is higher than the energy of the matrix. This process is confirmed by the disappearance of the polytypic outcroppings a few months after deformation.

In closing, we note that the results obtained for silicon clearly corroborate the initiating influence of plastic deformation in the formation of polytypic structures in a diamond lattice. The correlated motion of partial dislocations results in the formation of bulk phase outcroppings, which are relatively stable in the as-prepared cubic matrix. The randomly distributed stacking faults formed by the motion of the partial dislocations are unstable in this case and, under small mechanical loading, emerge at the surface of the crystal.

This work has received support from the International Association for the Promotion of Cooperation with Scientists from the Independent States of the Former Soviet Union (INTAS Grant N 93-3230-ext) and the Russian Fund for Fundamental Research (RFFI Grant No. 96-02-17482-a).

[1] R. H. Wentorf and J. S. Kasper, Science **139**, 338 (1963).
[2] V. G. Eremenko and V. I. Nikitenko, Phys. Status Solidi A **14**, 317 (1972).
[3] T. Y. Tan, H. Foll, and J. M. Hu, Philos. Mag. A **44**, 127 (1981).
[4] P. Pirouz, R. Chaim, and J. Samuels, Izv. Ross. Akad. Nauk, Ser. Fiz. **51**, 753 (1987).
[5] S. F. Levitan, A. V. Prikhod'ko, and Yu. V. Sokolov, Ukr. Fiz. Zh. **35**, 1537 (1990).
[6] V. Sh. Shekhtman, I. M. Shmyt'ko, V. V. Aristov, and B. A. Abdikamalov, Fiz. Tverd. Tela (Leningrad) **18**, 1358 (1976) [Sov. Phys. Solid State **18**, 781 (1976)].
[7] I. M. Shmyt'ko, L. A. Matveeva, S. I. Bredikhin, V. Sh. Shekhtman, and S. Z. Shmurak, Fiz. Tverd. Tela (Leningrad) **26**, 2033 (1984) [Sov. Phys. Solid State **26**, 1233 (1984)].
[8] C. W. Allen and K. C. Liao, Phys. Status Solidi A **74**, 673 (1982).

Translated by James S. Wood

PHYSICS OF THE SOLID STATE VOLUME 40, NUMBER 4 APRIL 1998

Low-temperature structural phase transition in a monoclinic KDy$(WO_4)_2$ crystal

V. P. D'yakonov, V. I. Markovich, V. L. Kovarskiĭ, and A. V. Markovich

Donetsk Physicotechnical Institute, National Academy of Sciences of Ukraine, 340114 Donetsk, Ukraine

M. Borowiec, A. Jedrzejczak, and H. Szymczak

Institute of Physics, Polish Academy of Sciences, 02-668 Warsaw, Poland

(Submitted July 17, 1997; resubmitted November 4, 1997)
Fiz. Tverd. Tela (St. Petersburg) **40**, 750–758 (April 1998)

The low-temperature thermal and magnetic-resonance properties of a monoclinic KDy$(WO_4)_2$ single crystal are investigated. It is established that a structural phase transition takes place at $T_c = 6.38$ K. The field dependence of the critical temperature is determined for a magnetic field oriented along the crystallographic a and c axes. The initial part of the $H-T$ phase diagram is plotted for $H \| a$. The prominent features of the structural phase transition are typical of a second-order Jahn–Teller transition, which is not accompanied by any change in the symmetry of the crystal lattice in the low-temperature phase. The behavior of $C(T)$ in a magnetic field shows that the transition goes to an antiferrodistortion phase. An anomalous increase in the relaxation time (by almost an order of magnitude) following a thermal pulse is observed at $T > T_c(H)$, owing to the structural instability of the lattice. A theoretical model is proposed for the structural phase transition in a magnetic field, and the magnetic-field dependence of T_c is investigated for various directions of the field.
[S1063-7834(98)03804-0]

Phase transitions, including structural phase transitions, are among the most pervasive phenomena in nature. They are intriguing in that structural phase transitions manifest connections and interactions in a substance that determine the structure and properties of its stable states. Structural phase transitions, whether spontaneous or induced, can be used to establish the basic laws governing the formation of phase states and symmetry in real crystals.

Accordingly, the investigation of structural phase transitions induced by the cooperative Jahn–Teller effect is of major importance. As a rule, structural phase transitions of the Jahn–Teller type take place in high-symmetry crystals. In rare-earth compounds strong spin-orbit coupling stabilizes the symmetry configuration. If the energy of interaction of Jahn–Teller centers is lower than or comparable with the splitting of energy levels of the ground state of a rare-earth ion, a Jahn–Teller structural phase transition does not occur.

A detailed study of structural phase transitions due to the cooperative Jahn–Teller effect has shown that they take place in compounds of rare-earth ions whose ground term represents a system of closely spaced energy levels.[1] Consequently, even in the case of low symmetry of the local environment of Jahn–Teller centers, structural phase transitions can occur as a result of lifting of the pseudodegeneracy of lower electron levels. For example, in rare-earth double molybdates MRe$(MoO_4)_2$, where M=K, Rb, Cs, and Re denotes a rare-earth ion,[2–7] a structural phase transition is observed only in compounds containing Dy^{3+}. The structural phase transition temperatures in MDy$(MoO_4)_2$ crystals are equal to 38 K, 20 K, and 14 K for M=Cs, Rb, and K, respectively. The transition takes place from a high-temperature D_{2h}^3 phase to a phase with the lower symmetry C_{2h}^3.

Whereas cooperative effects in rare-earth double molybdates have been well studied, they have been almost completely ignored in related compounds, double tungstates in particular. Investigations of the optical and Raman spectra and the dielectric permittivities of KRe$(WO_4)_2$ crystals (Re =Y, Gd, Dy) have been published so far. Shifts of the maxima in the absorption bands and an increase in the energy state between lowest doublets of the ground term $^6H_{15/2}$ of the Dy^{3+} ion close to $T=10$ K have been observed in KDy$(WO_4)_2$. The changes in the energy spectrum are characteristic of the Jahn–Teller phase transition mechanism and indicate strong electron-phonon coupling.[8,9] Prominent features of the Raman spectrum, associated with electron transitions in the Dy^{3+}, and an anomalous increase in the permittivity have been observed[10,11] in a KDy$(WO_4)_2$ single crystal at low temperatures ($T \approx 10$ K). The authors have interpreted the observed effects as a manifestation of Jahn–Teller phase transition. Anomalies associated with structural phase transition have not been observed in KRe$(WO_4)_2$ compounds (Re=Y, Gd).

In this paper we report investigations of a KDy$(WO_4)_2$ single crystal with a view to conducting a comprehensive examination of the structural phase transitions and ground state of the Dy^{3+} ion in phase transition.

The investigation of this compound in a magnetic field is important for understanding the nature of phase transitions in crystals containing Jahn–Teller ions and having a crystal lattice of low symmetry. Such an investigation also affords the possibility of plotting the phase diagram and obtaining information on magnetic anisotropy.

Interest in the study of double tungstates is further stimulated by their potential applications as solid-state lasers.[12,13]

1. SAMPLES AND EXPERIMENTAL PROCEDURE

Potassium dysprosium tungstate $\mathrm{KDy(WO_4)_2}$ belongs to the class of double tungstates of alkali and rare-earth elements $\mathrm{MRe(WO_4)_2}$ (Refs. 14 and 15). The investigated $\mathrm{KDy(WO_4)_2}$ crystal belongs to the monoclinic system with space group $C^6_{2h}(C2/c)$. The ground state of the dysprosium ion is $^6H_{15/2}$. In the $\mathrm{KDy(WO_4)_2}$ crystal the Dy^{3+} ion is surrounded by an octahedron of oxygen ions, with local symmetry C_2. In the crystal field of monoclinic symmetry a multiplet splits into eight Kramers doublets. Investigations of the spectra of absorption bands[8,9] and Raman scattering[10] give estimates of the energy intervals between the quasidegenerate lowest doublets of the $^6H_{15/2}$ term of the Dy^{3+} ion, $W_1 \approx 10.5\ \mathrm{cm}^{-1}$ in the high-temperature phase and $W_2 \approx 18\ \mathrm{cm}^{-1}$ in the low-temperature phase. The unit cell of $\mathrm{KDy(WO_4)_2}$ contains four formula units. The lattice parameters are $a = 8.05$ Å, $b = 10.32$ Å, $c = 7.52$ Å, and the monoclinic angle is $\beta = 94°13'$ (Refs. 9 and 10). The Dy^{3+} cations are situated on two-fold axes ($L2$) (which coincide with the crystallographic [010] directions) inside the distorted octahedra of oxygen atoms, wherein two DyO spacings are longer than the other six, which are close to each other.

Single crystals of $\mathrm{KDy(WO_4)_2}$ were grown by two methods from a potassium ditungstate ($\mathrm{K_2W_2O_7}$) melt: a modified Czochralski method on an oriented seed (the crystals attained dimensions of $20 \times 20 \times 60$ mm) and the method of spontaneous crystallization by slow temperature diminution from 950 °C at the rate of 3 °C/h. The crystals obtained by the second method, having a maximum dimension of 3 mm, were placed without further processing in the cavity of an EPR spectrometer. The density of the $\mathrm{KDy(WO_4)_2}$ crystals was 7.47 g/cm^3.

Here we give the results of an investigation of the thermal, magnetic, and resonance properties of $\mathrm{KDy(WO_4)_2}$ as part of a comprehensive research program on the rare-earth double tungstate series.

Magnetic measurements were performed on single crystals of dimensions $1.5 \times 1.5 \times 5$ mm by means of an EG&G/PAR Model 450 vibrating-sample magnetometer in the temperature interval $T = 4.2 - 50$ K and in magnetic fields up to 1 T. The thermal expansion was measured by a four-probe method using heat sensors in an EG&G/PAR Model 155 magnetometer. The samples had dimensions $6 \times 5 \times 4$ mm. The heat capacity was measured by means of a quasiadiabatic calorimeter in the temperature interval 4.2–25 K and in magnetic fields up to 3 T on a $\mathrm{KDy(WO_4)_2}$ sample of dimensions $5 \times 5 \times 0.6$ mm with a mass of 0.0796 g. The magnetic field was generated by a superconducting solenoid. Once a near-zero temperature run had been established, a train of three thermal pulses was applied to the sample with preprogrammed times of the initial and final temperature runs (before and after input of a thermal pulse). The recorded temperature runs were then processed to determine the temperature difference, the average temperature, and the heat increment ΔQ, from which the values of the molar heat capacity were calculated at three points. The time to record the final temperature run depended on the nature and time of the heat distribution in the calorimeter after the thermal pulse and varied from 40 s to 360 s in the given experiments. We also recorded magnetic-field cooling and heating thermograms in the temperature interval 4–10 K in the vicinity of structural transition. The temperature scanning rate was varied between 0.05 K/min and 0.2 K/min. The EPR spectra were analyzed in a 3-cm spectrum with rf modulation. The magnetic component of the rf field was perpendicular to the external magnetic field. The sample was rotated in the cavity in a single plane. The temperature was varied by blowing with cooled gaseous helium; the temperature could be varied over a wide range ($T = 4.2 - 300$ K) by this method.

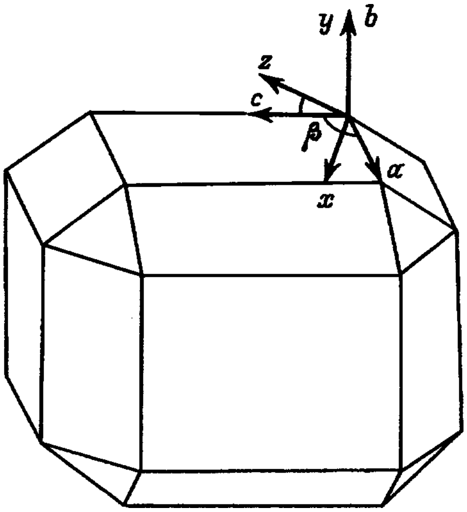

FIG. 1. The $\mathrm{KDy(WO_4)_2}$ crystal. a, b, c) Crystallographic axes; x, y, z) magnetic axes.

The magnetic-resonance and thermal properties were measured along the principal crystallographic axes. The samples were oriented both by external crystal faces and by x-ray alignment.

2. EXPERIMENTAL RESULTS AND DISCUSSION

Figure 1 shows an external view of the $\mathrm{KDy(WO_4)_2}$ crystal along with the crystallographic (a, b, c) and magnetic (x, y, z) axes. The crystal structure consists of $\mathrm{DY(WO_4)_2}$ layers perpendicular to the b axis. They are connected only by K ions, which accounts for the perfect cleavage along the ac plane.

Figure 2 shows the temperature dependence of the magnetization of $\mathrm{KDy(WO_4)_2}$ in the temperature interval 4.2–45 K, measured along the c axis. In the vicinity of $T = 7$ K the $M(T)$ curve is observed to have a kink associated with a structural phase transition in $\mathrm{KDy(WO_4)_2}$. This conjecture is confirmed by the graph of dM/dT as a function of the temperature in the inset to the figure. The magnetization along the b and c axes at low temperatures is almost an order of magnitude higher than the magnetization along the a axis, which is essentially independent of the temperature at temperatures below T_c. The difference in the magnetizations is

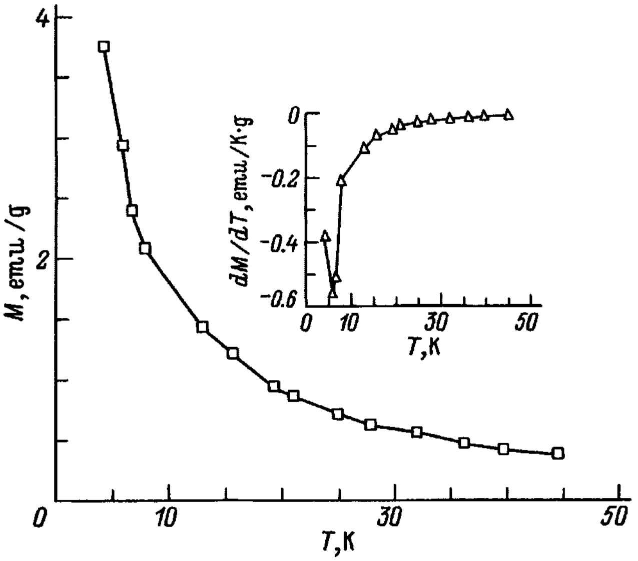

FIG. 2. Temperature dependence of the magnetization of $KDy(WO_4)_2$ along the c axis.

indicative of large anisotropy of the magnetic properties in different crystallographic directions, resulting from the low symmetry of the crystal field of the ligands. A magnetic field $H=1$ T intensifies the kink on the $M(T)$ curve, but has scarcely any influence on the temperature at which it occurs.

The variation of the thermal expansion of a $KDy(WO_4)_2$ single crystal at low temperatures is shown in Fig. 3, which gives the temperature dependence of the relative elongations along the a and c axes. The relative change in length of the sample $\Delta l/l$ in the temperature interval 4.2–80 K is $(1.5-2.5)\times10^{-4}$. The $\Delta l(T)/l$ curve along the a axis has a minimum at $T\approx7$ K, where the coefficient of thermal expansion changes sign. The temperature curve $\Delta l(T)/l$ along the c axis has a broad minimum and a slight anomaly near $T\approx7$ K. The absence of sharp anomalies of the thermal expansion indicates that the symmetry of the lattice remains unchanged in structural phase transition, but the ratio of the lattice parameters changes. This pattern is consistent with the results of Ref. 10. The observed anomalies of $\Delta l(T)/l$ and the change of sign of the coefficient of thermal expansion are most likely attributable to the escalation of magnetoelastic interactions at low temperatures ($T<12$ K), which, in turn, is a consequence of a change in the spectrum of the ion in the low-temperature phase.

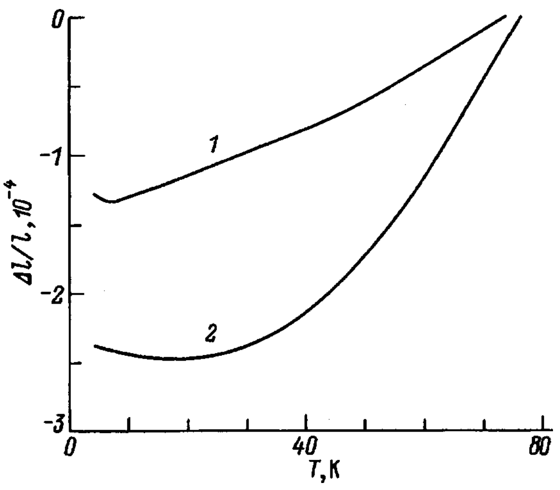

FIG. 3. Temperature dependence of the linear coefficient of thermal expansion of $KDy(WO_4)_2$. 1) Along the a axis; 2) along the b axis.

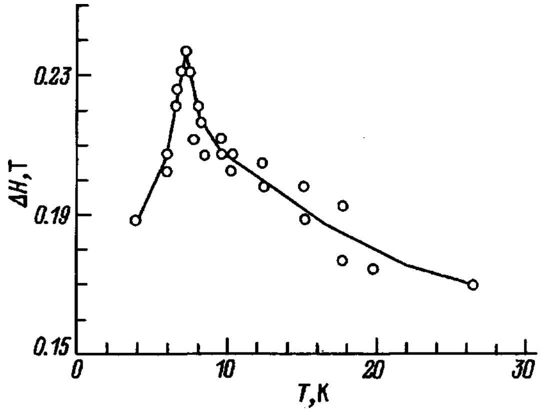

FIG. 4. Absorption linewidth versus temperature. The static magnetic field is directed along $g_{\max}$.

An EPR spectrum consisting of one line has been observed between the components of the lowest Kramers doublet. An absorption line has been observed both above and below T_c. It has been determined from the angular dependences of the EPR lines that the g factors in the high-temperature phase ($T>12$ K) have the values $g_{\min}\approx0$, $g_b=0.82$, and $g_{\max}=3.13$. The direction in which the g factor is a maximum lies in the ac plane and deviates 20° from the c axis. In the low-temperature phase ($T=4.2$ K) the directions of the principal axes of the g tensor coincide with the directions in the high-temperature phase. However, the components have different values: $g_{\min}\approx0$, $g_b=1.19$, and $g_{\max}=1.98$. The transition region in the vicinity of T_c has a broad temperature interval ~8 K, in which $g_{\max}$ is observed to decrease smoothly. It is interesting to look at the temperature variation of the absorption linewidth. According to Fig. 4, the linewidth, which is equal to 0.17 T far from the transition point, increases with decreasing temperature, attaining a maximum value ~0.24 T at a temperature ~7 K. The broadening of the absorption line is probably associated with a variation of the parameters of the crystal field acting on the dysprosium ion. A further reduction in the temperature is accompanied by narrowing of the line to 0.19 T. It is evident that the λ-shaped temperature dependence of the absorption linewidth accurately pinpoints the structural phase transition temperature in $KDy(WO_4)_2$. The observed smooth variation of the absorption linewidth with a peak at the phase-transition point is attributable to the specific characteristics of the structural phase transition in $KDy(WO_4)_2$.

Our experimental investigation of the temperature dependence of the heat capacity of a $KDy(WO_4)_2$ single crystal in the temperature interval 4.2–20 K reveals an anomaly with a peak at $T_c=6.38$ K, associated with a structural phase transition. Figure 5 shows a part of the anomaly of the heat capacity in the vicinity of the structural phase transition. We note that the temperature curves of the heat capacity and the

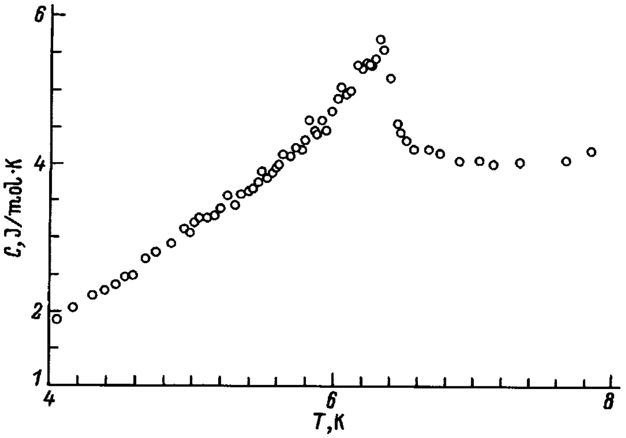

FIG. 5. Temperature dependence of the molar heat capacity of $KDy(WO_4)_2$ in the vicinity of structural phase transition.

absorption linewidth in the EPR spectrum are qualitatively similar in the vicinity of the structural phase transition in $KDy(WO_4)_2$.

The hypothesis that the observed structural phase transition in $KDy(WO_4)_2$ is a transition of the Jahn–Teller type is supported by the significant energy reduction of the lower doublet as a result of an increase in the splitting between the ground and first excited electronic states in the low-temperature phase ($T<T_c$). The broad temperature interval of the transition, the absence of abrupt changes in the parameters of the EPR spectra in the transition region, the absence of plateaus in the heating and cooling thermograms, the deviation from a cubic law at the transition point ($T>15$ K), and the kink of the $M(T)$ curve constitute evidence of a second-order phase transition. According to EPR spectra, which disclose an absence of nonequivalent sites and preservation of the directions of the principal axes of the g tensor, the symmetry of the initial high-temperature phase does not change in structural phase transition, but a smooth distortion of the lattice takes place. The difference in the values of T_c determined from the heat-capacity measurements and by spectroscopic methods (≈ 10 K) can be attributed to the fact that the point at which the temperature dependence of the positions of the lines in the spectrum begins to acquire anomalies has been interpreted as the structural phase transition temperature in spectroscopic methods, and this approach might be inconsistent with the establishment of the low-temperature phase. Experimental proof of the active role of the electronic system in a structural phase transition of the Jahn–Teller type lies in the magnetic-field dependence of the structural phase transition temperature; data on this dependence are reported for the first time in the present article.

Figures 6 and 7 show the temperature dependence of the heat capacity of a $KDy(WO_4)_2$ single crystal in the interval 4–10 K in magnetic fields parallel to the a and c axes, respectively. When the magnetic field is oriented along the a axis, the position of the peak at T_c shifts toward lower temperatures as the field is increased, and at the same time the anomaly becomes smoother until it is scarcely perceptible at $H=1.3$ T. When the field is oriented along the c axis, the heat-capacity anomaly also shifts toward lower temperatures and is gradually smoothed out as the field is increased, and at $H=3$ T it is no longer perceptible on the $C(T)$ curve. The variations of T_c along the a and c axes are highly anisotropic; for example, a field $H=1$ T along the c axis leaves the position and magnitude of the peak at T_c almost totally unchanged (Fig. 7), whereas the same field in the direction of the a axis shifts the peak at T_c (Fig. 6) by approximately 1.5 K. We have used the results of the measurements of $C(T)$ in a magnetic field $H\|a$ to plot the initial segment of

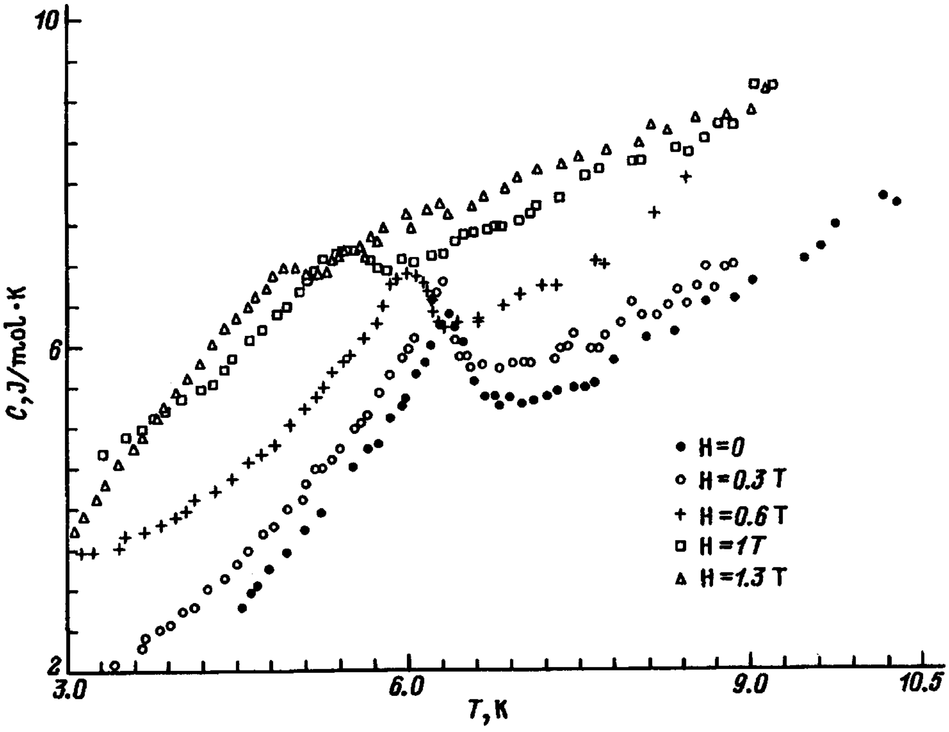

FIG. 6. Temperature dependence of the molar heat capacity of $KDy(WO_4)_2$ for various values of the magnetic field $H\|a$.

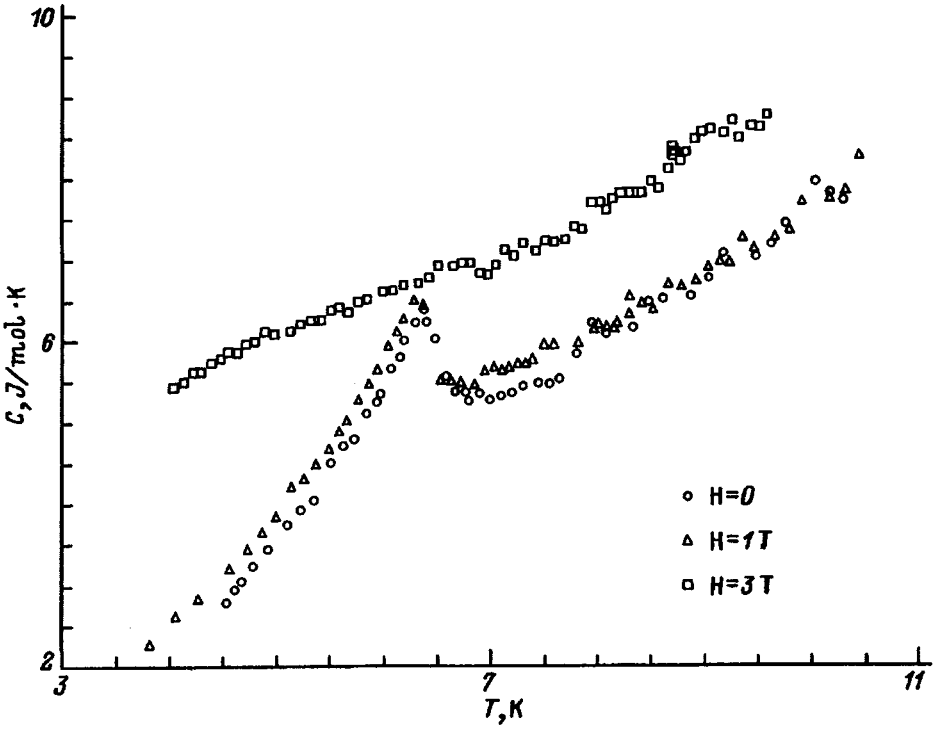

FIG. 7. Temperature dependence of the molar heat capacity of $KDy(WO_4)_2$ for various values of the magnetic field $H \| c$.

the $H-T$ phase diagram. The heating and cooling thermograms reveal monotonic behavior on the part of $T(t)$ and lack the characteristic plateau associated with the presence of latent heat of transition. In the recorded thermogram the transition temperature is seen only as a change in the curvature of the $T(t)$ curve in the vicinity of T_c. This result actually indicates that structural phase transition in a magnetic field takes place as a second-order transition. The high magnetic-field sensitivity of T_c in low fields (Fig. 8) is probably associated with the lower symmetry of the crystal field in comparison with molybdates. The similarly constituted compound $KDy(MoO_4)_2$ exhibits antiferrodistortion-type ordering. In this case a field of several teslas must be applied to achieve any appreciable shift of the structural transition temperature.[15–17]

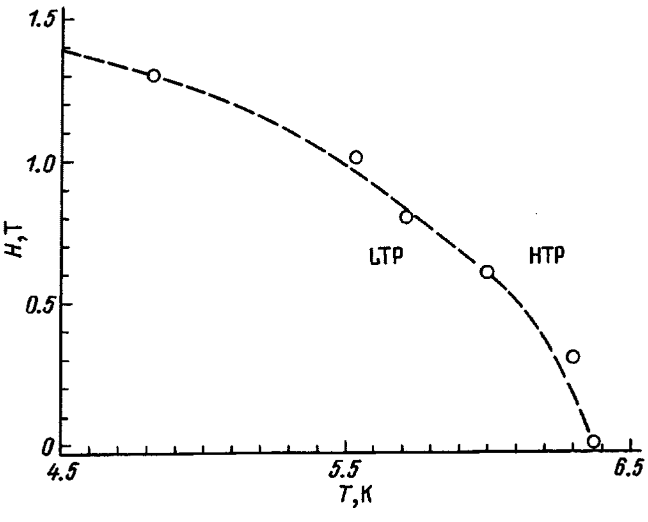

FIG. 8. H–T phase diagram for $H \| a$.

A theoretical analysis[16] has shown that T_c depends weakly on the magnetic field in the case of an antiferrodistortion-ordered crystal. Anisotropic antiferroelastics exhibit a weak dependence on the magnetic field in low fields, and only as H_c is approached does T_c begin to change significantly, dropping abruptly at $H \approx H_c(0)$. The experimental phase diagram for $KDy)MoO_4)_2$ confirms this dependence.[17] Antiferrodistortion ordering is usually encountered in compounds for which the g factors of Jahn–Teller rare-earth ions are high ($g_{\max} \sim 10$). In $KDy(WO_4)_2$ the maximum value of the g factor in the high-temperature phase, $g_{\max} \approx 3.13$, occurs in the ac plane, and in the low-temperature phase we have $g_{\max} \approx 1.98$ (Ref. 18).

It should be mentioned that the scatter of the experimental values increased considerably in measurements of the heat capacity of $KDy(WO_4)_2$ above the structural transition temperature $T_c(H)$. The increase is attributable to a multiple increase (by almost an order of magnitude) in the relaxation time τ of the system to equilibrium at $T > T_c(H)$ after the thermal pulse. For example, at $T < T_c(H)$ the relaxation time to thermal equilibrium (and, hence, to linear temperature behavior) after the pulse was 5–15 s, whereas at $T > T_c(H)$ it increased to 150–200 s. Accordingly, the temperature dependence following the thermal pulse was measured at $T < T_c(H)$ for 40–60 s and at $T > T_c(H)$ for 300–360 s.

We now discuss the possible causes of this trend. The structural phase transitions in the alkali rare-earth double molybdates $KDy(MoO_4)_2$ and $CsDy(MoO_4)_2$ have a complex character and are accompanied by specific anomalies. The transition from the high-temperature to the low-temperature phase in $KDy(MoO_4)_2$ and $CsDy(MoO_4)_2$ takes place through an intermediate phase.[17,19,20] The intermediate phase is assumed to represent an incommensurate superstructure. The range where the incommensurate superstructure exists in $\mathrm{CsDy(MoO_4)_2}$ is around 20 K, and heat-capacity measurements over a wide range of temperatures (40–100 K) exhibit the anomalous nature of the shift of $C(T)$ in different series of experiments, owing to the structural instability of the crystal lattice.[21] The structural phase transition in $\mathrm{CsDy(MoO_4)_2}$ at $T_c=42$ K is accompanied by a sudden drop in the thermal conductivity, where the thermal conductivity of the high-temperature phase is several times lower than that of the low-temperature phase.[20] This behavior of the thermal conductivity, possibly elicited by a substantial change in the phonon spectrum in phase transition, cannot help but drastically increase the relaxation time at $T>T_c(H)$. The existence of a modulated structure is confirmed by the behavior of a great many characteristics, as evinced by the results of the heat-capacity, permittivity, and EPR measurements. An estimate of the effective mean free path of phonons for $\mathrm{CsDy(MoO_4)_2}$ gives a value ~ 80 Å at $T\approx 40$ K (Ref. 19). This quantity is related to the scale of microinhomogeneities that emerge in the vicinity of the phase-transition point and form an additional source of phonon scattering.[19,20] Not to be ruled out is the possibility that the specific anomalies of the behavior of the thermal properties of the rare-earth double molybdates $\mathrm{KDy(MoO_4)_2}$ and $\mathrm{CsDy(MoO_4)_2}$ are similar in nature to those in $\mathrm{KDy(WO_4)_2}$, or that the structural transition at $T_c(H)$ in $\mathrm{KDy(WO_4)_2}$ is also accompanied by a sudden drop in the thermal conductivity, leading to a multifold increase in τ at $T>T_c(H)$.

In the double molybdates $\mathrm{KDy(MoO_4)_2}$ and $\mathrm{CsDy(MoO_4)_2}$ the incommensurate phase occurs as an intermediate phase between two phase transitions: a first-order phase transition with T_{c1} and a second-order transition with T_{c2}, where $T_{c1}=11.5$ K and 42 K, $T_{c2}=14.5$ K and 59 K for $\mathrm{KDy(MoO_4)_2}$ and $\mathrm{CsDy(MoO_4)_2}$, respectively. The conditions for the onset of the incommensurate phase and several examples of its occurrence in crystals with different lattice symmetries, specifically in crystals of the monoclinic system, are given in Ref. 22.

Our heat-capacity measurements in the temperature interval 4.2–25 K yield only one anomaly of the heat capacity, with a peak at $T_c\approx 6.38$ K (Fig. 5). It is essential to note that two additional lines at frequencies of 10 $\mathrm{cm^{-1}}$ and 135 $\mathrm{cm^{-1}}$ appear in the optical Raman spectrum below 78 K and become more pronounced as the temperature is further decreased. Comparative investigations of the optical Raman spectrum of the isostructural compound $\mathrm{KY(WO_4)_2}$, whose room-temperature spectrum is similar to that of $\mathrm{KDy(WO_4)_2}$, have not disclosed any additional lines in cooling down to 4.2 K (Ref. 10). It is conceivable that the transition from the high-temperature to the low-temperature phase is achieved through an intermediate incommensurate phase and that the emergence of the additional lines in the Raman spectrum corresponds to a second structural phase transition. Careful x-ray analysis over a wide range of temperatures and measurements of the thermal conductivity $\mathrm{KDy(WO_4)_2}$ in the vicinity of T_c and at $T>T_c$ will be a necessary part of future studies.

In molecular field theory, which describes phase transitions due to the cooperative Jahn–Teller effect, the functional relation $W_1/W_2=\tanh(W_1/2kT_c)$ is obtained for the case of two nondegenerate electronic states interacting with one-dimensional distortion.[4] The application of this equation and the above values of W_i gives a structural transition temperature ≈ 11.5 K. The fact that the experimental value is much lower than the calculated value indicates that the proposed model affords only a very crude description of the structural phase transition in the low-dimensional $\mathrm{KDy(WO_4)_2}$ crystal. Skorobogatova and Savchenko[9] have used data on the absorption spectra in $\mathrm{KDy(WO_4)_2}$ and postulated a ferrodistortion type of ordering. They showed that the structural phase transition can be described by the Ising model in a transverse field. Here the Ising variables σ_x and σ_z describe the effects of the crystal field and Jahn–Teller deformation of dysprosium complexes, respectively. In general, a magnetic field induces forced deformation of the Jahn–Teller mode and eradicates the structurally disordered state.[23] Consequently, the occurrence of structural phase transition in a magnetic field attests to the nonferrodistortion character of the low-temperature phase and requires appropriate modification of the model.

It has been shown earlier[23,24] that only the two lowest Kramers doublets need to be included in the energy structure of the $\mathrm{Dy^{3+}}$ ion. The model Hamiltonian is then written in the form

$$\hat{H}=-\frac{1}{2}\sum_{i,j} J_{ij}\hat{\sigma}_{iz}\hat{\sigma}_{jz}-\frac{1}{2}\Delta\sum_i \hat{\sigma}_{ix}, \tag{1}$$

where Δ is the crystal field parameter, J_{ij} denotes the pair quasiinteraction constants of the Kramers doublets at the ith and jth sites. Assuming the simplest type of nonferrodistortion ordering, we consider a two-sublattice model. In the molecular field approximation the free energy per unit cell in this model is given by the expression

$$f=-\frac{1}{2}J_s(\sigma_{1z}^2+\sigma_{2z}^2)-J_i\sigma_{1z}\sigma_{2z}-\frac{1}{2}\Delta(\sigma_{1x}+\sigma_{2x})$$
$$+\frac{1}{2}kT[\varphi(1+\sigma_1)+\varphi(1-\sigma_1)+\varphi(1+\sigma_2)+\varphi(1-\sigma_2)]-2kT\ln 2, \tag{2}$$

where

$$\varphi(x)=x\ln x,\quad \sigma_{1,2}^2=\sigma_{1,2x}^2+\sigma_{1,2z}^2, \tag{3}$$

J_s and J_i are the in-sublattice and intersublattice pair interaction constants of the complexes, respectively, and σ_{ix} and σ_{iz} are the average values of the operators $\hat{\sigma}_{ix}$ and $\hat{\sigma}_{iz}$. The one-site effective Hamiltonians at type 1 and type 2 sites have the form (respectively)

$$\hat{H}_1=-(J_s\sigma_{1z}+J_i\sigma_{2z})\hat{\sigma}_{1z}-\frac{1}{2}\Delta\hat{\sigma}_{1x},$$
$$\hat{H}_2=-(J_i\sigma_{1z}+J_s\sigma_{2z})\hat{\sigma}_{2z}-\frac{1}{2}\Delta\hat{\sigma}_{2x}, \tag{4}$$

which leads to corresponding expressions for the splitting between the Kramers doublets at sites 1 and 2:

$$W_1=\sqrt{4(J_s\sigma_{1z}+J_i\sigma_{2z})^2+\Delta^2},$$

$$W_2=\sqrt{4(J_i\sigma_{1z}+J_s\sigma_{2z})^2+\Delta^2}. \tag{5}$$

The conditions for minimization of the free energy (2) with respect to the variables σ_{1x}, σ_{2x}, σ_{1z}, and σ_{2z} are satisfied, in particular, by a nonvanishing solution of the antiferrodistortion type $\sigma_{1z}=-\sigma_{2z}$, $\sigma_{1x}=\sigma_{2x}$. The equations of state for σ_{1z} and σ_{1x} now coincide exactly with the corresponding results of Ref. 9. The splittings of the Kramers doublets also coincide in this case, and their behavior is analogous to the case of a ferrodistortion structure, including the validity of the well-known relation

$$W_\infty=W_0\ \tanh\frac{W_\infty}{2kT_c}, \tag{6}$$

which relates the splittings of the doublets W_0 at $T=0$ and $W_\infty=\Delta$ at $T>T_c$ to the structural phase transition temperature T_c. Consequently, the antiferrodistortion structure is thermodynamically and spectroscopically indistinguishable from the ferrodistortion structure, and our hypothesis as to the structure of the low-temperature phase does not conflict with published results.[9]

The situation changes significantly in a magnetic field, because every Kramers doublet splits. In this case the one-site state of the Dy^{3+} ion is described by 4×4 matrices. The Jahn–Teller deformations are now represented by $\hat{1}\otimes\hat{\sigma}_z$ and $\hat{1}\otimes\hat{\sigma}_x$ matrices, and the magnetic moment[23] is written in the form

$$\hat{m}_{x;y}=\hat{\sigma}_{x;y}\otimes\frac{\hat{1}\pm\hat{\sigma}_z}{2}. \tag{7}$$

It is now required to add a magnetic term to the Hamiltonian (1):

$$\hat{H}_m=-\Lambda J\mu_0\mathbf{B}\cdot\mathbf{m}, \tag{8}$$

where $J=15/2$ is the maximum value of the total angular momentum, $\Lambda=4/3$ is the Landé factor, and **B** is the induction vector of the magnetic field. The vector **B** lies in the *ac* plane of the crystal, and the Cartesian *x* and *y* coordinate axes of this plane are the symmetry axes of the undistorted local environment of the Dy^{3+} ion. The structural phase transitions in such systems under the influence of a magnetic field have been investigated previously for ferrodistortion[23] and antiferrodistortion[5,16] ordering. However, the topic of interest to us — the dependence on the direction of **B** — has not been studied in detail. Making use of the nonequilibrium density matrix,[24,25] we find the free energy per unit cell in the two-sublattice model in the multiplicative approximation:

$$\begin{aligned}f=&\frac{1}{2}J_s(\sigma_{1z}^2+\sigma_{2z}^2)-J_i\sigma_{1z}\sigma_{2z}-\frac{1}{2}\Delta(\sigma_{1x}+\sigma_{2x})\\&-\frac{1}{2}J\mu_0\mathbf{B}\cdot(\mathbf{m}_1+\mathbf{m}_2)+kT\sum_{\alpha=1}^{4}\sum_{i=1}^{2}\varphi(1+\lambda_{i\alpha})\\&-2kT\ \ln 4,\end{aligned} \tag{9}$$

where $\lambda_{i\alpha}$ are the roots of the equation

$$(\sigma_{ix}^2+\sigma_{iz}^2-\lambda^2)^2-m_x^2(\sigma_z+\lambda)^2-m_y^2(\sigma_z-\lambda)^2+m_x^2m_y^2=0. \tag{10}$$

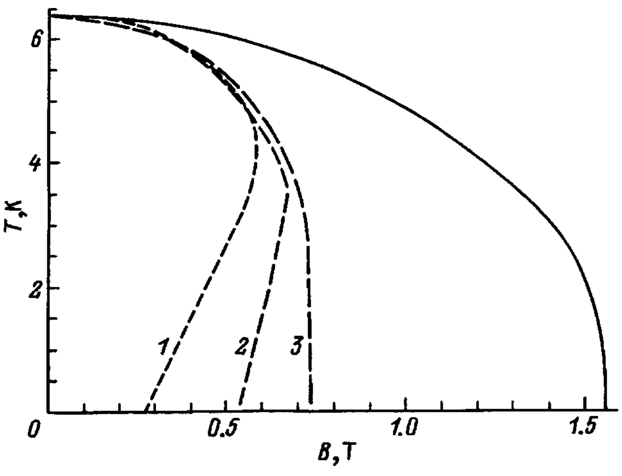

FIG. 9. Stability threshold of the high-temperature phase. The solid curve corresponds to $\mathbf{B}=B(\pm 1/\sqrt{2}\ ;\ \pm 1/\sqrt{2})$, and the dashed curves correspond to $\mathbf{B}=B(\pm 1;\ 0)$ [or $\mathbf{B}=B(0;\ \pm 1)$]: *1)* $J_s+J_i=5.5$ K; *2)* 4.5 K; *3)* 3.5 K

The minimum of the free energy (9) corresponds to a solution of the ferrodistortion type $\sigma_{1z}=\sigma_{2z}\neq 0$ for the high-temperature phase and to a solution of the general type $\sigma_{1z}\neq\pm\sigma_{2z}$ for the low-temperature phase. Structural phase transition takes place through an antiferrodistortion parameter of the order of $\sigma_{z-}=\sigma_{1z}-\sigma_{2z}$ and is determined by the loss of stability of the solutions under the second derivative $\partial^2 f/\partial\sigma_{z-}^2$. Figure 9 shows the lines of loss of stability of the ferrodistortion phase

$$\partial^2 f/\partial\sigma_{z-}^2|_{\sigma_{1z}=\sigma_{2z}}=0.$$

The value of $T_c=6.38$ K is taken from the heat-capacity experiment, and $\Delta=W_\infty=14.4$ K from spectroscopic data,[9] whereupon Eq., (6) can be used to calculate $2(J_s-J_i)=W_0=W_\infty=W_\infty\coth(W_\infty/2kT)=17.76$ K. There is a noticeable consistency of the theoretical results with experiment: T_c decreases as B increases; the induction has a critical value B_c at which $T_c=0$; the curves behave differently for different orientations of the vector **B**. The bending of curves *1* and *2* implies, most likely, the existence of a critical point and the possibility of first-order transitions. Such bending has not been observed, and neither has a first-order transition, suggesting that J_s+J_i has definite bounds:

$$0\leqslant J_s+J_i\leqslant 3\ \text{K},$$

from which we obtain the estimates

$$4.5\leqslant J_s\ (\text{K})\leqslant 6\ \text{K},\quad -4.5\leqslant J_i\ (\text{K})\leqslant -3\ \text{K}. \tag{11}$$

A comparison of Fig. 9 with the experimental results (Figs. 6–8) leads to the assumption that the crystallographic *c* axis is closer to the bisector of the angle *xOy*, while the *a* axis is closer to the *x* or *y* axis.

The following conclusions can be drawn from the results of the study.

1) It has been shown by four independent experimental methods that a structural phase transition takes place (at $T_c=6.38$ K) in a monoclinic $KDy(WO_4)_2$ single crystal.

2) The low-temperature phase transition exhibits anomalies typical of a Jahn–Teller transition.

3) The investigated transition is second-order. A magnetic field does not change the order of the transition.

4) It is impossible to draw from the experimental data an unambiguous conclusion as to the symmetry of the crystal lattice in the low-temperature phase, but it can be assumed on the basis of the data that in structural phase transition the symmetry of the initial high-temperature phase does not change, and the lattice undergoes a smooth distortion in the ac plane.

5) The replacement of the complex $(\mathrm{MoO}_4)_2^{2-}$ in $\mathrm{KDy(MoO_4)_2}$ by the complex $(\mathrm{WO}_4)_2^{2-}$ leads to a significant drop in the structural phase transition temperature.

6) An abrupt increase in the relaxation time of the system after a thermal pulse at $T>T_c(H)$ has been observed, possibly attributable to structural instability of the system and the existence of an incommensurate phase.

7) A portion of the H–T phase diagram has been plotted for $H\|a$.

8) A theoretical model of structural phase transition in a magnetic field has been proposed, and the dependence of the transition temperature on the direction and modulus of the induction vector **B** has been investigated.

We have shown that the antiferrodistortion model of the low-temperature phase is consistent with the behavior of the thermodynamic and spectroscopic properties.

The authors are grateful to A. A. Pavlyuk for growing the high-quality $\mathrm{KDy(WO_4)_2}$ crystals, to V. I. Kamenev for orienting the crystals, and to B. Ya. Sukharevskiĭ for a useful discussion of the results.

The work of authors M. Borowiec, A. Jedrzejczak, and H. Szymczak has received partial support from the State Committee for Scientific Research of Poland (Komitet Badan Naukowych) (KBN Contract N 2 PO3B 071 08).

[1] G. A. Gehring and K. A. Gehring, Rep. Prog. Phys. **38**, 5 (1975).
[2] A. I. Zvyagin, E. D. El'chaninova, T. S. Stetsenko, L. N. Pelikh, and E. N. Khats'ko, Fiz. Nizk. Temp. **1**, 79 (1975) [Sov. J. Low Temp. Phys. **1**, 39 (1975)].
[3] A. H. Cooke, M. M. Davidson, N. J. England, M. J. M. Leask, J. B. Lewry, A. C. Tropper, and M. R. Wells, J. Phys. C **9**, 573 (1976).
[4] I. V. Skorobogatova and E. M. Savchenko, Fiz. Nizk. Temp. **6**, 112 (1980) [Sov. J. Low Temp. Phys. **6**, 55 (1980)].
[5] M. J. M. Leask, A. C. Tropper, and M. R. Wolls, J. Phys. C **13**, 3481 (1981).
[6] E. N. Khats'ko, A. C. Chernyĭ, and A. I. Kaplienko, Fiz. Nizk. Temp. **7**, 1048 (1981) [Sov. J. Low Temp. Phys. **7**, 509 (1981)].
[7] D. Mihailovic, J. F. Ryan, and M. C. K. Wiltshire, J. Phys. C **20**, 3047 (1987).
[8] I. V. Skorobogatova and A. I. Zvyagin, Fiz. Nizk. Temp. **4**, 800 (1978) [Sov. J. Low Temp. Phys. **4**, 381 (1978)].
[9] I. V. Skorobogatova and E. M. Savchenko, Fiz. Nizk. Temp. **6**, 240 (1980) [Sov. J. Low Temp. Phys. **6**, 115 (1980)].
[10] Yu. A. Popkov, V. I. Fomin, and L. N. Pelikh, Fiz. Nizk. Temp. **8**, 1210 (1982) [Sov. J. Low Temp. Phys. **8**, 614 (1982)].
[11] L. N. Pelikh and A. A. Gurskas, Fiz. Tverd. Tela (Leningrad) **21**, 2136 (1979) [Sov. Phys. Solid State **21**, 1223 (1979)].
[12] A. A. Kaminskiĭ, P. V. Klevtsov, L. Li, and A. A. Pavlyuk, Phys. Status Solidi A **5**, K79 (1971).
[13] A. A. Kaminskiĭ, G. R. Verdún, V. Koechner, F. A. Kuznetsov, and A. A. Pavlyuk, Kvantovaya Élektron. **19**, 941 (1992) [Sov. J. Quantum Electron. **22**, (1992)].
[14] S. V. Borisov and R. F. Klevtsova, Kristallografiya **13**, 517 (1968) [Sov. Phys. Crystallogr. **13**, 420 (1968)].
[15] P. V. Klevtsov and L. P. Kozeeva, Dokl. Akad. Nauk SSSR **185**, 571 (1969) [Dokl. Akad. Nauk SSSR **14**, 185 (1969)].
[16] M. D. Kaplan, Fiz. Tverd. Tela (Leningrad) **26**, 89 (1984) [Sov. Phys. Solid State **26**, 51 (1984)].
[17] Yu. N. Kharchenko, Fiz. Nizk. Temp. **22**, 394 (1996) [Low Temp. Phys. **22**, 306 (1996)].
[18] M. Borowiec, V. P. Dyakonov, A. Nabialek, A. Prokhorov, S. Piechota, and H. Szymczak, Physica B (in press).
[19] E. E. Anders, I. V. Volchok, A. I. Zvyagin, V. B. Kokshenev, and S. V. Startsev, Izv. Akad. Nauk SSSR, Ser. Fiz. **50**, 369 (1986).
[20] E. E. Anders and S. V. Startsev, Fiz. Tverd. Tela (Leningrad) **34**, 812 (1992) [Sov. Phys. Solid State **34**, 434 (1992)].
[21] E. E. Anders and S. V. Startsev, Fiz. Nizk. Temp. **18**, 774 (1992) [Sov. J. Low Temp. Phys. **18**, 548 (1992)].
[22] J. Kosinski, *Commensurate and Incommensurate Phase Transitions* (Elsevier Sci. Publ., Amsterdam, 1990).
[23] E. Pytte, Phys. Rev. **9**, 932 (1974).
[24] C. J. Elliot, Proc. R. Soc. London, Ser. A **328**, 217 (1972).
[25] V. L. Kovarskiĭ and B. Ya. Sukharevskiĭ, Ukr. Fiz. Zh. **36**, 266 (1991).

Translated by James S. Wood

PHYSICS OF THE SOLID STATE VOLUME 40, NUMBER 4 APRIL 1998

Diffusion and solubility of helium in lead fluoride single crystals in the superionic transition region

A. G. Dudorov and A. Ya. Kupryazhkin

Ural State Technical University, 620002 Ekaterinburg, Russia

(Submitted September 30, 1997; resubmitted November 10, 1997)
Fiz. Tverd. Tela (St. Petersburg) **40**, 759–760 (April 1998)

Temperature curves of the diffusion coefficients and solubilities of helium in pure and holmium-doped lead fluoride crystals are obtained in the superionic phase-transition range. Possible mechanisms of the interaction of helium with ions are discussed, along with mechanisms of the solubility and diffusion of helium in a crystal. © *1998 American Institute of Physics.* [S1063-7834(98)03904-5]

We have investigated the diffusion and solubility of helium in PbF_2, using two types of single crystals. The total impurity content of sample No. 1 did not exceed $1\times 10,^{-3}$ wt %. In sample No. 2 HoF_3 was introduced in concentrations up to 0.5 wt % during growth. The investigations were carried out by desorption of helium from crystals presaturated in the gaseous phase in an apparatus employing mass-spectrometric detection of the liberated helium.[1,2]

The experimental data from measurements of the solubility of helium in PbF_2 are shown in Fig. 1. For both samples the temperature dependence has four discernible intervals, in each of which the behavior of their solubilities is identical. In the first, low-temperature interval, the effective solubility of helium in PbF_2 increases according to the exponential law $C_{\mathrm{eff}}=C_0\exp(-E^p_{\mathrm{eff}}/kT)$. The data for both samples agree within the experimental error limits. The value of the preexponential factor is $C_0=(3.5^{+1.7}_{-1.2})\times 10^{18}\ \mathrm{cm}^{-3}$, and the effective energy of solution is $E^p_{\mathrm{eff}}=0.36\pm 0.30$ eV.

In the second and third temperature intervals, the helium solubility passes through a minimum and, owing to large errors, is not amenable to approximation. In the fourth interval, the helium solubility decreases exponentially. For the pure sample we have $C_0=(3.1^{+6.3}_{-2.1})\times 10^{14}\ \mathrm{cm}^{-3}$ and $E^p_{\mathrm{eff}}=-(0.28\pm 0.08)$ eV; for the holmium-doped sample $C_0=(9.2^{+19.1}_{-6.2})\times 10^{14}\ \mathrm{cm}^{-3}$ and $E^p_{\mathrm{eff}}=-(0.16\pm 0.07)$ eV.

The temperature dependence of the effective diffusion coefficient D_{eff} is shown in Fig. 2. In contrast with the solubility data, D_{eff} does not have any singular anomalies, exhibiting instead a simple variation of the activation energy E^D_{eff} and the preexponential factor D_0 in the transition region and obeying the exponential law $D_{\mathrm{eff}}=D_0\exp(-E^D_{\mathrm{eff}}/kT)$ in the low-temperature and high-temperature ranges. At low temperatures the diffusion coefficients of helium in the pure crystals are lower than in the doped crystals. The values of the parameters of D_{eff} for the pure sample are $D_0=(1.2^{+2.3}_{-0.8})\times 10^4\ \mathrm{cm}^2\cdot\mathrm{s}^{-1}$ and $E^D_{\mathrm{eff}}=1.58\pm 0.07$ eV; for the holmium-doped crystals $D_0=(1.3^{+4.1}_{-0.9})\times 10^4\ \mathrm{cm}^2\cdot\mathrm{s}^{-1}$ and $E^D_{\mathrm{eff}}=1.39\pm 0.06$ eV. In the high-temperature range the temperature curves of the helium diffusion coefficient for both samples coincide: $D_0=(1.7^{+3.4}_{-1.1})\times 10^4\ \mathrm{cm}^2\cdot\mathrm{s}^{-1}$ and $E^D_{\mathrm{eff}}=0.87\pm 0.07$ eV.

The mechanism of the recorded behavior of the transport coefficients of helium in PbF_2 can be portrayed as follows. The temperature of the solubility minimum for the pure sample, $T_c=783$ K, coincides with the transition temperature determined from the maximum of the specific heat in Ref. 3, so that the recorded variations in the helium transport coefficients are associated with disordering of the anionic sublat-

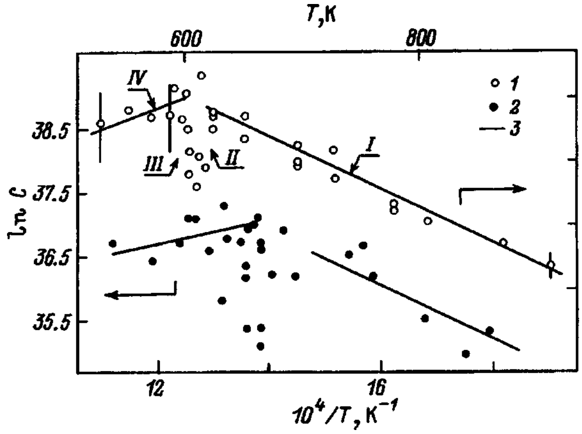

FIG. 1. Solubility of helium in PbF_2 crystals versus temperature. *1*) PbF_2; *2*) $PbF_2+0.5$ wt % HoF_3; *3*) (solid lines) approximations.

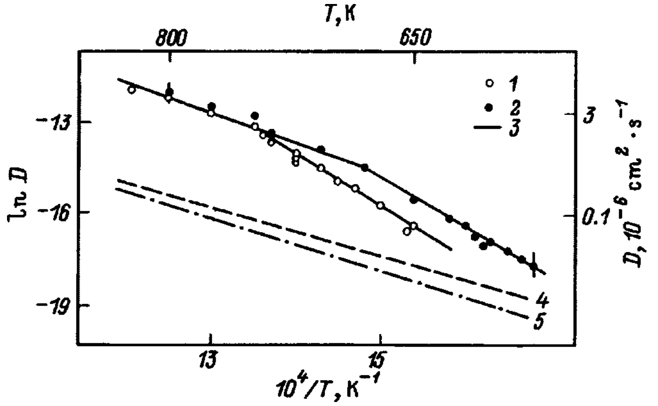

FIG. 2. Solubility of helium in PbF_2, SrF_2, and BaF_2 crystals versus temperature. *1*) PbF_2; *2*) $PbF_2+0.5$ wt % HoF_3; *3*) (solid lines) approximations; *4, 5*) interstitial diffusion of helium in BaF_2 and SrF_2, respectively.[4]

tice. The shift of T_c toward lower temperatures for the holmium-doped crystals can be attributed to the presence of Ho^{3+} ion compensators, whose interaction with anions occupying sites of the fluorine sublattice can cause them to shift from the main sties and lower the ''melting point'' of the sublattice.

The energy of solution for the low-temperature (first) interval lies between the energies of interstitial solution of helium in SrF_2 and BaF_2 (Ref. 4), implying that the solubility is basically interstitial in this interval. In the high-temperature interval the sublattice of fluorine anions is annealed, so that the number of thermal vacancies is constant and, accordingly, the recorded negative energy of solution (the average value for the two samples is $\overline{E_{\text{eff}}^{p}} = -0.22$ eV) corresponds to the solution of helium at anion vacancies. Estimates of the contribution of fluorine anions to the energy of interaction of helium with lattice ions, based on the undeformed lattice model and the values of the He–F pair potential,[1,5] show that it is negligible. Consequently,[1] the energy of solution of helium is equal to the energy of interaction of helium with four nearest-neighbor Pb^{2+} cations. The latter energy, referred to the Pb^{2+}–He pair, is almost an order of magnitude higher than the van der Waals interaction energy and indicates the chemical nature of the interaction of helium with lead cations.

A comparison of the above-determined diffusion coefficients of helium in PbF_2 with data on the interstitial diffusion of helium in SrF_2 and BaF_2 (Fig. 2) shows that the expected value of the interstitial diffusion coefficient of helium in PbF_2 in the given temperature interval is substantially lower than the recorded values for both temperature ranges. The latter result could conform to a mechanism of migration of highly mobile helium-containing defect clusters (diffusion in the annealed sublattice), this mechanism becoming dominant above the phase transition temperature. At low temperatures, because of the abrupt drop in the number of free defects, the diffusion of helium most likely takes place by a ''trapping'' mechanism.[6] In this case the low-temperature increase of the diffusion coefficient in the doped samples can be attributed both to oxygen-vacancy compensation of the Ho^{3+} impurity ion (Ref. 7) (and, accordingly, a large number of impurity vacancies) and to the possible involvement of F^{-}–He pairs in the diffusion process in the presence of fluorine compensation.

This work has received support from the Fundamental Research Foundation (Grant No. 95-02-03649).

[1] A. Ya. Kupryazhkin, A. U. Kurkin, O. V. Semenov *et al.*, J. Nucl. Mater. **208**, 180 (1994).

[2] A. G. Dudorov and A. Ya. Kupryazhkin, in *Collected Scientific Papers on Metastable States and Phase Transitions* [in Russian], UrO RAN, Ekaterinburg (1997), 242 pp.

[3] I. V. Murin and O. V. Glumov, Fiz. Tverd. Tela (Leningrad) **23**, 624 (1981) [Sov. Phys. Solid State **23**, 35 (1981)].

[4] A. Ya. Kupryazhkin and E. V. Popov, Fiz. Tverd. Tela (Leningrad) **26**, 160 (1984) [Sov. Phys. Solid State **26**, 94 (1984)].

[5] A. Ya. Kupryazhkin and A. Yu. Kurkin, Fiz. Tverd. Tela (St. Petersburg) **35**, 3003 (1993) [Phys. Solid State **35**, 1475 (1993)].

[6] A. Ya. Kupryazhkin, I. R. Shein, and E. V. Popov, Zh. Tekh. Fiz. **53**, 1578 (1983) [Sov. Phys. Tech. Phys. **28**, 970 (1983)].

[7] A. Ya. Kupryazhkin, A. Yu. Kurkin, and A. G. Dudorov, Fiz. Tverd. Tela (St. Petersburg) **38**, 1272 (1996) [Phys. Solid State **38**, 703 (1996)].

Translated by James S. Wood

PHYSICS OF THE SOLID STATE VOLUME 40, NUMBER 4 APRIL 1998

LOW-DIMENSIONAL SYSTEMS AND SURFACE PHYSICS

Electronic state confinement in a Hubbard chain

A. N. Kocharyan and A. S. Saakyan

Yerevan Institute of Physics, 375000 Yerevan, Armenia;
State University for Engineering, 375009 Yerevan, Armenia

(Submitted November 4, 1997)
Fiz. Tverd. Tela (St. Petersburg) **40**, 761–763 (April 1998)

Electron redistribution over a 1D sublattice resulting from Hubbard repulsion leads to an effective two-particle interaction with a potential linear in coordinate difference. Two-particle wave functions and a narrow-band electron spectrum have been found. © *1998 American Institute of Physics.* [S1063-7834(98)04004-0]

1. Studies of high-T_c superconductivity have stimulated recently interest in the two-particle problem as applied to low-dimension finite and infinite lattices within models of the type of Refs. 1–3. This is motivated by attempts to go beyond the weak-coupling limits and to use nonperturbative methods in theory. This work reports on a solution of a similar problem with the use of exact two-particle 1D Hubbard wave functions and on finding the effective two-electron interaction potential, which turns out to be linear in the difference between their coordinates. The Schrödinger equation for two electrons interacting via this potential has been solved. The wave functions are expressed through Bessel functions, and the energy spectrum has an equidistant character.

In an analysis[4] of a similar problem, the wave functions were found by drawing an analogy between the Schrödinger equation and the recurrence relations for Bessel functions; whereas the considerations leading to the equation for the eigenfunctions of the problem, they appear doubtful. Another study[5] comes to a correct conclusion of the equidistant character of the spectrum. We have used here a modification of the method of Lifshits[6] to find the eigenfunctions of the problem.

2. The excess charge density created by redistribution of electrons on a chain can be written

$$\Delta\rho=-|e|\int_0^{p_F}[|\Psi(n_1,n_2)|^2-|\Psi_0(n_1,n_2)|^2]dp, \qquad (1)$$

where $\Psi(n_1,n_2)$ is the two-particle 1D Hubbard wave function, $\Psi_0(n_1,n_2)$ is the wave function of two free singlet electrons, and p_F is the Fermi quasi-momentum.

We choose the Hubbard wave function in the form[7]

$$\Psi(n_1,n_2)=\exp\left[i\frac{Q}{2}(n_1+n_2)\right]\cos(p|n_1-n_2|-\delta), \qquad (2)$$

where Q is the center-of-mass quasi-momentum, p is the relative quasi-momentum of two electrons, n_1 and n_2 are vectors of a 1D lattice (we set the lattice constant subsequently equal to one), δ is the scattering phase defined as

$$\delta=\arctan\frac{\eta}{\sin p}, \quad \eta=\frac{U}{4t\cos\frac{Q}{2}}, \qquad (3)$$

and U is the Hubbard interaction energy.

The effective interaction was calculated for the simplest case of $U=+\infty$. Substituting Eq. (2) into Eq. (1) and integrating in p yields ($\delta=\pi/2$)

$$\Delta\rho=|e|\frac{\sin 2p_Fn}{2n}, \quad n=|n_1-n_2|. \qquad (4)$$

The potential of the excess charge distribution field (4), found by solving Poisson's difference equation

$$\Delta^2\varphi=-2\pi|e|\frac{\sin 2p_Fn}{n}, \qquad (5)$$

has the form

$$\varphi(n)=-2\pi|e|p_Fn+\frac{\pi|e|}{\sin^2p_F}\frac{\sin(2p_Fn-2p_F)}{2n}. \qquad (6)$$

The first term in Eq. (6) is dominant. In solving the Schrödinger equation, it is only this term that we shall take into account. Thus electron redistribution should result in confinement of electronic states. The two-electron interaction energy can be written

$$U(n)=\alpha n, \quad \alpha=2\pi e^2p_F. \qquad (7)$$

The quantity α can be estimated from the relation of p_F with electron concentration by assuming electrons to consitute 1D ideal gas. Then close to half filling $\alpha\sim 12\pi^2\varepsilon_0x$, where ε_0 is the energy of Coulomb interaction between adjacent lattice sites, and x is the electron concentration.

3. The Schrödinger equation for two particles on a chain can be written

$$\begin{aligned}-T[\Psi(n_1+1,n_2)]+T[\Psi(n_1-1,n_2)+\Psi(n_1,n_2+1)\\+\Psi(n_1,n_2-1)]+\alpha|n_1-n_2|\Psi(n_1,n_2)=E\Psi(n_1,n_2).\end{aligned} \qquad (8)$$

We present its solution in the form

$$\Psi_j(n_1,n_2)=\exp\left[i\frac{Q}{2}(n_1+n_2)\right]\times\sum_k \exp[ik(n_1-n_2)]\Psi_j(k,Q), \tag{9}$$

where $j=1,2$ for the $n_1<n_2$ and $n_1>n_2$ regions, respectively.

Parametrizing the eigenvalues of the problem

$$E=-4T\cos\frac{Q}{2}\cosh p, \tag{10}$$

and substituting Eq. (9) into Eq. (8), with due account of Eq. (10), yields the following equations:

$$4T\cos\frac{Q}{2}(\cos k-\cosh p)\Psi_j(k,Q)=\mp i\alpha\frac{d\Psi_j}{dk}, \tag{11}$$

where the upper sign on the right-hand side corresponds to $j=1$, and the lower one, to $j=2$.

Integration of Eq. (11) yields

$$\Psi_j(k,Q)=c\exp(\pm iz\sin k\mp i\nu k),$$

$$z=\frac{4T}{\alpha}\cos\frac{Q}{2},\quad \nu=z\cosh p, \tag{12}$$

and, by transferring to the muffin-tin representation with the use of Eq. (9), we come finally to the following wave function

$$\Psi(n_1,n_2)=c\exp\left[i\frac{Q}{2}(n_1+n_2)\right]J_{\nu+|n_1-n_2|}(z), \tag{13}$$

where $J_\mu(z)$ is the Bessel function of the first kind.

Wave function (13) satisfies the following asymptotic relation: $\Psi(n_1,n_2)\rightarrow 0$, $|n_1-n_2|\rightarrow\infty$.

4. To find the spectrum of the problem, we first note that

$$c=\Psi(k=0)=\sum_{n=0}^{\infty}\Psi(n). \tag{14}$$

Summing both parts of the equality

$$\Psi(n_1-n_2)=cJ_{\nu+|n_1-n_2|}(z) \tag{14a}$$

in (n_1,n_2), we come to the following equation for determination of the spectrum

$$\sum_{n=1}^{\infty}J_{\nu-n}(z)=J_\nu(z). \tag{15}$$

Introducing the notation

$$\varphi_\nu(z)=\int_0^z J_\nu(z)dz, \tag{16}$$

we recast Eq. (16) in the form[8]

$$\varphi_{\nu+1}(z)-\varphi_\nu(z)=0\,. \tag{17}$$

Introduce translation operator in index ν:

$$\varphi_{\nu+1}(z)=\exp\left(\frac{d}{d\nu}\right)\varphi_\nu(z), \tag{18}$$

which can be done if ν does not depend on z. Then Eq. (18) will take on the form

$$\exp\left(\frac{d}{d\nu}\right)\varphi_\nu(z)=\varphi_\nu(z), \tag{19}$$

or

$$\varphi_\nu(z)-\exp\left(-\frac{d}{dn}\right)\varphi_\nu(z)=0\,, \tag{20}$$

so that

$$\varphi_{\nu-1}(z)-\varphi_{\nu+1}(z)=0\,. \tag{21}$$

Recalling the recurrence relation for the Bessel functions

$$J_{\mu+1}(z)-J_{\mu-1}(z)=2\frac{d}{dz}J_\mu(z), \tag{22}$$

we can recast Eq. (21) to

$$J_\mu(z)=0\,. \tag{23}$$

Thus the eigenvalues of the problem are solutions to Eq. (23).

Consider the region of values $z\ll 1$ corresponding to an infinitely narrow electron band. Then Eq. (23) rewrites as

$$\frac{z^\nu}{\Gamma(\nu+1)}=0\,, \tag{24}$$

whose solutions are

$$\nu=-(m+1),\quad m=0,1,2,\ldots. \tag{25}$$

Taking this into account and recalling Eq. (24), one should analyze the equation

$$J_{-\nu}(z)=0 \tag{26}$$

whose solutions in the limiting case of $z\ll 1$ are

$$\nu=(m+1). \tag{27}$$

To find the boundaries of the spectrum, we shall use the $z\ll 1$ approximation in wave functions (12)

$$\Psi(n_1-n_2)=\frac{\exp\left(-\frac{|n_1-n_2|}{R}\right)}{\Gamma(\nu+|n_1-n_2|+1)}, \tag{28}$$

whence, if we take into account Eqs. (25) and (27), it follows that $m\leqslant|n_1-n_2|$.

Thus the energy spectrum of the system

$$E=\pm\alpha(m+1) \tag{29}$$

is bounded from below (for $m>|n_1-n_2|$ the wave function vanishes identically).

Eq. (28) describes a two-electron bound state in a narrow band, with wave function damping at large distances occurring faster than exponentially, and therefore the quantity R cannot be interpreted as the bound-state radius. The system has a ground state, but no continuum. In accordance with Eq. (19), the lower sign in Eq. (29) corresponds to strongly excited states. It should be pointed out that in this approximation the energy levels depend on the band width $4T$.

It was shown[9,10] that hole confinement sets in in an antiferromagnetically ordered lattice close to half filling, and that this result does not depend on lattice dimension. The effective interaction potential (7) obtained in our work is valid for a one-dimensional lattice only and is repulsive, so that the binding is due to the electron energy band being finite.

[1] J. G. Bednorz and K. A. Müller, Z. Phys. B **64**, 189 (1986).
[2] L. Chen and Ch. Mei, Phys. Rev. B **39**, 9006 (1989).
[3] S.-J. Dong and Ch. N. Yang, Rev. Math. Phys. **28**, 146 (1989).
[4] J.-P. Gallinar and D. C. Mattis, J. Phys. A **18**, 2583 (1985).
[5] B. N. Zakhar'ev, Élem. Chast. At. Yadro **23**, 1387 (1992).
[6] I. M. Lifshits, Zh. Éksp. Teor. Fiz. **17**, 1076 (1947).
[7] A. N. Kocharyan and A. A. Saakyan, in *Proceedings Meeting on Low-Temp. Physics* (Kazan, 1992), Vol. 2, 131 pp.
[8] H. Bateman and A. Erdélyi, *Higher Transcendental Functions, Vol. 2* (McGraw-Hill, New York, 1953) [Russian trans., Nauka, Moscow, 1974].
[9] L. N. Bulaevskiĭ and D. I. Khomskiĭ, Zh. Éksp. Teor. Fiz. **52**, 1603 (1967) [Sov. Phys. JETP **25**, 1067 (1967)].
[10] L. N. Bulaevskiĭ, É. L. Nagaev, and D. I. Khomskiĭ, Zh. Éksp. Teor. Fiz. **54**, 1562 (1968) [Sov. Phys. JETP **27**, 836 (1968)].

Translated by G. Skrebtsov

On the isotope effect in the relaxation model of electron-stimulated desorption

S. Yu. Davydov

A. F. Ioffe Physicotechnical Institute, Russian Academy of Sciences, 194021 St. Petersburg, Russia

(Submitted October 23, 1997)
Fiz. Tverd. Tela (St. Petersburg) **40**, 764–767 (April 1998)

The dependence of the ESD yield of ions on their mass has been studied. The influence of short-range electronic-shell repulsion on the isotope effect is discussed. The isotope effect is shown to be depressed with increasing non-Coulombic initial velocity. © *1998 American Institute of Physics.* [S1063-7834(98)04104-5]

Under the isotope effect in electron-stimulated desorption (ESD) one understands the dependence of the ESD yield of ions on their mass M.[1,2] In the traditional model of Menzel, Gomer, and Redhead the isotope effect is determined by the dependence on mass of the probability F that the ion will not be reneutralized in the course of desorption by electrons of the metallic substrate: $F \propto \exp(-M^{1/2}\text{const})$.[3,4] Within the relaxation model,[1] where desorption is related to the existence on the surface of a local electric field, the isotope effect manifests itself as the dependence on M of a critical time t_c, i.e. the time during which the local substrate field has to accelerate the desorbing ion to eject it to infinity.[5,6] We shall discuss this effect here in more detail.

1. ISOTOPE EFFECT IN COULOMBIC DECAY OF AN ADSORPTION SYSTEM

The relaxation model is essentially as follows.[1,5,6] Incident electrons (or photons) destroy the chemisorption bonding between adatom 2 and surface atom 1 by the mechanism of Knotek–Feibelman[7,8] (atom 1 may be a substrate atom or, for instance, a fragment of an adsorbed diatomic molecule[5,6]). The electrons become redistributed so that Coulombic repulsion sets in between ions 1 and 2. Ion 2 begins to accelerate in the field created by ion 1. At a certain moment the two-hole state at ion 1 breaks down, and the local accelerating field disappears. If by that time ion 2 has built up its kinetic energy to a level high enough to overcome the attraction produced by the image forces of ion 2 in the metallic substrate, then it will desorb. Otherwise ion 2 will return back to the surface. An analytical theory of this process has been developed.[5,6]

If desorption occurs only under the action of Coulomb forces, and the short-range repulsion of electronic shells at the moment of breaking the adsorption bond can be neglected (see the relevant discussion in Ref. 9), then the probability f_E of observing an ESD ion with energy E is given by the following expressions: a) for $E \to E_{\min} = 0$,

$$f_E = \exp\left[-\frac{t_c}{\tau}\sqrt{1+(2E/V)}\right],$$

$$t_c = r\sqrt{M}[2V/W(2W-V)]^{1/2}; \tag{1}$$

b) for $E \to E_{\max} = (W-V)/2$

$$f_E = \exp\left\{-\frac{r}{2\tau}\sqrt{M}[W/E_{\max}(E_{\max}-E)]^{1/2}\right\}. \tag{2}$$

Here r is the initial position of desorbing ion 2 relative to the metal surface, and τ is the lifetime of the two-hole state at ion 1 ($\tau \cong 10^{-14}$ s),

$$W = \frac{4z_1 z_2 e^2 d}{r^2}, \quad V = \frac{z_2^2 e^2}{2r}, \tag{3}$$

$z_{1,2}$ are the charges of ions 1 and 2, respectively, at the instant of bond breaking, d is the position of ion 1 relative to the metallic surface (see Refs. 5 and 6), and e is the positronic charge. Note that W is the doubled energy of dipole-dipole repulsion (at the instant of bond breaking) of ion 2 from the dipole formed by ion 1 and its image in the metal. Parameter V is the doubled energy of interaction of ion 2 with its image in the metal at the initial moment.

The energy distribution of ESD ions, $dN(E)/dE \equiv \rho_E$, can be presented in the form[10]

$$\rho_E = C\sqrt{E-E_{\min}}\, f_E, \tag{4}$$

where C is a normalization constant with dimension $(\text{eV})^{-3/2}$. The ESD ion yield q can be written

$$q = \int_{E_{\min}}^{E_{\max}} \rho_E dE. \tag{5}$$

Substituting Eqs. (1) and (4) into Eq. (5) we come to an approximate result (see Appendix)

$$q = CA\theta^{-3/2}\exp(-\theta)R,$$

$$R = \frac{\sqrt{\pi}}{2}\Phi(\sqrt{\theta u}) - \sqrt{\theta u}\exp(-\theta u),$$

$$\theta = t_c/\tau, \quad u = (W/V)^{1/2} - 1\,. \tag{6}$$

Here A is a coefficient with dimension $(\text{eV})^{3/2}$ (see Appendix), and Φ is the probability integral[11]. Since t_c and, hence, θ are proportional to $\sqrt{M}$ [see Eq. (1)], an increase in isotope mass results in a decrease of the ESD ion yield. (Note that parameter u is always positive. Indeed, as shown in Ref. 5, desorption can occur only if the inequality $z_1 > z_{1c} \equiv z_2 r/8d$, which corresponds to the inequality $W/V > 1$, is met).

Consider now the change in ESD ion yield δq resulting from a change in ion mass, $M \to M+\delta M$. We shall assume that $\eta \equiv \delta M/M \ll 1$. Then we shall obtain, in first order in η,

$$\frac{\delta q}{q} \cong \frac{\eta}{2}\left[-\frac{3}{2}-\theta+(\theta u)^{3/2}\exp(-\theta u)R^{-1}\right]. \tag{7}$$

Consider simple special cases. For $\sqrt{\theta u} \ll 1$

$$q \cong CA\frac{2}{3}u^{3/2}\exp(-\theta), \quad \delta q/q \cong -\frac{1}{2}\eta\theta. \tag{8}$$

For $\sqrt{\theta u} \gg 1$.

$$q \cong CA\frac{\sqrt{\pi}}{2}\theta^{-3/2}, \quad \delta q/q \cong -\frac{1}{2}\eta\left(\theta+\frac{3}{2}\right). \tag{9}$$

Thus, as parameter θu increases, the relative decrease (for $\eta > 0$) of the ESD ion yield increases, and hence, the isotope effect becomes enhanced.

2. INFLUENCE OF SHORT-RANGE ELECTRON-SHELL REPULSION ON THE ISOTOPE EFFECT

Some cases require taking into account within the relaxation model not only the Coulombic collapse of the adsorption system but the contribution of short-range repulsion V_{rep} of the electronic shells of ions 1 and 2 as well.[9,12] For example, the inclusion of V_{rep} is needed when considering the reversible mechanism of desorption by Antoniewicz,[13] which was demonstrated by a theoretical analysis[12,14] of the temperature dependence of ESD yield of alkali-metal ions from tungsten and iridium surface covered by a silicon film[15–17].

It was shown[9,12] that including the contribution $V_{\mathrm{rep}} = B\exp[-b(z-r)]$ (z is the coordinate, and b is a characteristic reciprocal length) to ion desorption can be taken into account by introducing into the equation of motion as the initial condition nonzero initial velocity

$$v=\sqrt{2B/M}. \tag{10}$$

An analysis[9,12] shows that, if the inequality

$$Mv^2 > V \tag{11}$$

is met (i.e., if the kinetic energy acquired by ion 2 in the repulsion of its shell and the shell of ion 1 exceeds the energy of interaction of its charge z_2 with the image charge $-z_2$), ion 2 goes to infinity, and there is no more need to accelerate it by the dipole field generated by ion 1 and its image. Thus the velocity $v^* = \sqrt{V/M}$ separates in a natural way the regions of small ($v < v^*$) and large ($v > v^*$) initial velocities.

Consider the region of small velocities with the additional condition

$$Mv^2 \ll W(2W-V)/2V. \tag{12}$$

One can now show that the probability f_E (here and subsequently the tilde denotes the quantities relating to the $v \neq 0$ case) of observing an ESD ion with energy E is

$$\tilde{f}_E \cong f_E K, \tag{13}$$

where the probability f_E for the $v=0$ case is given by Eqs. (1) or (2), and

$$K=\exp\left[M\frac{2vr}{\tau(2W-V)}\right], \tag{14}$$

or, recalling Eq. (10),

$$K=\exp\left[\sqrt{M}\frac{2r\sqrt{2B}}{\tau(2W-V)}\right]. \tag{15}$$

Expression (13) was obtained in the lowest (linear in the argument of the exponential) approximation in v. It can now readily be shown that the ESD ion yield $\tilde{q}$

$$\tilde{q}=qK, \tag{16}$$

$$\frac{\delta\tilde{q}}{\tilde{q}}=\frac{\delta q}{q}+\frac{\eta}{2}\ln K, \tag{17}$$

where $\delta q/q$ is given by Eq. (7). Since $\delta q/q < 0$ [see Eqs. (8) and (9)], and the second term on the right-hand side of Eq. (17) is positive (for $\eta > 0$), the magnitude of the isotope effect decreases. Moreover, in the case of $\sqrt{\theta u} \ll 1$ [see Eq. (8)] and when the inequality $B > V(1-V/2W)$ is met, the second term in Eq. (17) is larger than the first one, which makes the ratio $\delta\tilde{q}/\tilde{q}$ positive. Note that the energy distribution of ESD ions in the small-velocity domain starts from $E_{\min}=0$ and extends up to $E_{\max}=(Mv^2+W-V)/2$.[9,12] Thus the width of the ESD ion energy distribution increases with initial velocity.

Let us turn now to the region of high velocities, which satisfy the inequality inverse to (11). In this case, the energy distribution of ESD ions is confined between $E_{\min}=(Mv^2-V)/2$ and $E_{\max}=(Mv^2+W-V)/2$.[9,12] As the initial velocity increases, the energy distribution shifts toward high energies, with its width remaining constant and equal to $W/2$. An analysis[12] shows that for $E \to E_{\min}$ the probability $\tilde{f}_E$ has the form

$$\tilde{f}_E=\exp\left(-\frac{r}{v\tau}\frac{2E+V-Mv^2}{2W}\right), \tag{18}$$

which yields $\tilde{f}_E=1$ for $E=E_{\min}$. On the other hand, for $v\to\infty$ and $E \to E_{\max}$ the probability $\tilde{f}_E$ also tends to one [see Eq. (2)]. Using Eqs. (4) and (5), we come now to

$$\tilde{q}=\frac{2}{3}C(W/2)^{3/2}. \tag{19}$$

This expression obtained under the assumption of $v\to\infty$ is valid for any initial velocity provided it satisfies the criterion $Mv^2 > V$, which follows from simple physical considerations, namely, that each ion which has built up a velocity $v > v^* = \sqrt{V/M}$ will go to infinity on overcoming the image potential forces. It is also clear that no isotope effect will be present here.

3. NUMERICAL ESTIMATES

For illustration, consider the increase in yield of Li_6^+ ions compared to Li_7^+ from a submonolayer lithium film, which is adsorbed on a silicon monolayer deposited on a tungsten substrate (Li–Si/W). This system was studied in Refs. 15–17. Theoretical estimates of the model parameters for this system are presented in Ref. 12. Parameter d (half of the arm of the dipole formed by ion 1, which here is silicon, and its image) entering Eq. (3) is assumed to be equal to the Si atomic radius, $d=1.17$ Å. The initial position of the lithium ion relative to tungsten surface is $r=2d+r_i(\mathrm{Li})$, where the last term stands for the lithium ion radius, 0.68 Å. Estimates give for the charge of the Si^+ ion produced by electron bombardment $z_1 \cong 1.13$.[12] Recalling that $z_2=1$, we obtain $W=8.35$ eV and $V=2.38$ eV, which yields $u=0.87$ [see Eq. (6)]. For the Li_7 isotope, the critical time $t_c=1.65\times10^{-14}$ s. Taking the value $\tau=4.84\times10^{-14}$ s from Ref. 12, we obtain $\theta=0.34$. Substituting the parameters thus found into Eq. (7) and taking into account that $\eta=(6-7)/7\cong-0.14$, we obtain $\delta q/q\cong0.11$. Unfortunately, in Refs. 15–17 the isotope effect was not studied. For a similar system of lithium on oxidized tungsten it was found[18], however, that $q(\mathrm{Li}_6^+)/q(\mathrm{Li}_7^+)=1.2\pm0.1$, i.e. $\delta q/q=0.1-0.3$. Thus our estimate appears reasonable.

To estimate the influence of initial velocity on the isotope effect, consider desorption of Na^+ ions from the Na–Si/W system bombarded by 100-eV electrons[16]. It was shown[14,16] that desorption occurs in this case by the reversible mechanism, where short-range repulsion must apparently be included. Estimates based on Ref. 14 give $v=0.14\times10^4$ m/s for the initial velocity, $\tau=0.56\times10^{-14}$ s for the effective lifetime of the two-hole state at the silicon ion, $z_1=1$, $d=1.17$ Å, $r=3.26$ Å, $W=6.34$ eV, and $V=2.21$ eV. This yields $t_c=4.11\times10^{-14}$ s, $\theta=7.35$, and $u=0.69$. We take the longest-lived sodium isotope Na_{22}.[19] Substituting the above values into Eq. (17) gives $\delta q/q=0.19$, $(\eta/2)\ln K=-0.04$, and, hence, $\delta\tilde{q}/\tilde{q}=0.15$. It thus follows that even very small velocities (in our case the initial velocity corresponds to a sodium ion energy of 0.23 eV, which is substantially smaller than the potentials W and V) affect considerably the isotope effect.

APPENDIX

Integral (5) with f_E defined by Eq. (1) reduces to

$$q=\frac{C}{\sqrt{2}}(V)^{3/2}\int_1^a y\sqrt{y^2-1}\,e^{-\theta y}dy, \tag{A1}$$

where $a=(W/V)^{1/2}$ and $\theta=t_c/\tau$. Integral (A1) cannot be calculated exactly. In a general case, however, it is the functions $\exp(-\theta y)$ and $\sqrt{y-1}$ in the integrand that undergo the largest change within the region of integration. The more smoothly varying function $y\sqrt{y+1}$ can be averaged appropriately and taken outside the integral. We thus obtain

$$q=CA\int_0^u \sqrt{\xi}\,e^{-\theta\xi}d\xi, \tag{A2}$$

where $u=(W/V)^{1/2}-1$. Taking a lower estimate of the integral (at the lower limit of integration), we obtain $V^{3/2}$ for coefficient A, whereas an upper estimate (at the upper limit of integration) yields $A=V^{3/2}(W/V)^{1/2}[(W/V)^{1/2}+1]^{1/2}$. The integral in Eq. (A2) is taken by parts yielding Eq. (6). Note that, similar to our preceding papers[9,12,14], we extrapolate the probability function f_E defined by Eq. (1) and valid, strictly speaking, only for $E\to0$ to the whole energy distribution region. This approximation does not entail a large error in integration.

The author is grateful to V. N. Ageev and N. D. Potekhina for stimulating discussions.

Support of the ‘‘Atomic Surface Structures’’ Program is gratefully acknowledged.

[1] V. N. Ageev, O. P. Burmistrova, and Yu. A. Kuznetsov, Usp. Fiz. Nauk **158**, 389 (1989) [Sov. Phys. Usp. **32**, 588 (1989)].
[2] R. D. Ramsier and J. T. Yates, Surf. Sci. Rep. **12**, 244 (1991).
[3] D. Menzel and R. Gomer, J. Chem. Phys. **41**, 3311 (1964).
[4] P. A. Redhead, Can. J. Phys. **42**, 886 (1964).
[5] S. Yu. Davydov, Fiz. Tverd. Tela (St. Petersburg) **35**, 2525 (1993) [Phys. Solid State **35**, 1251 (1993)].
[6] S. Yu. Davydov, Fiz. Tverd. Tela (St. Petersburg) **37**, 1758 (1995) [Phys. Solid State **37**, 957 (1995)].
[7] M. L. Knotek and P. J. Feibelman, Phys. Rev. Lett. **40**, 964 (1978).
[8] P. J. Feibelman and M. L. Knotek, Phys. Rev. B **18**, 6531 (1978).
[9] S. Yu. Davydov, Fiz. Tverd. Tela (St. Petersburg) **39**, 1679 (1997) [Phys. Solid State **39**, 1498 (1997)].
[10] Z. W. Gortel and A. Wierbicki, Phys. Rev. B **43**, 7487 (1991).
[11] E. Jahnke, F. Emde, and F. Lösch, *Tafeln Höherer Funktionen* (Teubner, Stutgart, 1960) [Russ. trans., Nauka, Moscow (1977), 342 pp.].
[12] S. Yu. Davydov, Zh. Tekh. Fiz. **67**, No. 5, 109 (1997) [Tech. Phys. **42**, 555 (1997)].
[13] P. R. Antoniewicz, Phys. Rev. B **21**, 3811 (1980).
[14] S. Yu. Davydov, Zh. Tekh. Fiz. **67**, No. 11, 77 (1997) [Tech. Phys. **42**, 555 (1997)].
[15] V. N. Ageev, O. P. Burmistrova, A. M. Magomedov, and B. V. Yakshinskiĭ, Fiz. Tverd. Tela (Leningrad) **32**, 801 (1990) [Sov. Phys. Solid State **32**, 472 (1990)].
[16] V. N. Ageev, A. M. Magomedov, and B. V. Yakshinskiĭ, Fiz. Tverd. Tela (Leningrad) **33**, 158 (1991) [Sov. Phys. Solid State **33**, 91 (1991)].
[17] V. N. Ageev and B. V. Yakshinskiĭ, Fiz. Tverd. Tela (St. Petersburg) **37**, 483 (1995) [Phys. Solid State **37**, 261 (1995)].
[18] V. N. Ageev, O. P. Burmistrova, and B. V. Yakshinskii, Surf. Sci. **194**, 101 (1988).
[19] Yu. M. Shirokov and N. P. Yudin, *Nuclear Physics* [in Russian], Nauka, Moscow (1980), 728 pp.

Translated by G. Skrebtsov

PHYSICS OF THE SOLID STATE VOLUME 40, NUMBER 4 APRIL 1998

Electron-stimulated desorption of sodium atoms from oxidized molybdenum

V. N. Ageev and Yu. A. Kuznetsov

A. F. Ioffe Physicotechnical Institute, Russian Academy of Sciences, 194021 St. Petersburg, Russia

(Submitted November 11, 1997)
Fiz. Tverd. Tela (St. Petersburg) **40**, 768–772 (April 1998)

The time-of-flight technique combined with a surface-ionization-based detector has been used to investigate the yield and energy distribution of sodium atoms escaping in electron-stimulated desorption (ESD) from adlayers on the surface of molybdenum oxidized to various degrees and maintained at $T=300$ K as functions of incident electron energy and surface coverage by sodium. The sodium-atom ESD threshold is about 25 eV, irrespective of sodium coverage and extent of molybdenum oxidation. Molybdenum covered by an oxygen monolayer exhibits secondary thresholds at ~40 eV and ~70 eV, as well as low-energy tailing of the energy distributions, its extent increasing with surface coverage by sodium Θ. The most probable kinetic energies of sodium atoms are about 0.23 eV, irrespective of the degree of molybdenum oxidation and incident electron energy at $\Theta=0.125$, and decrease to 0.17 eV as the coverage grows to $\Theta=0.75$. The results obtained are interpreted within a model of Auger-stimulated desorption, in which adsorbed sodium ions are neutralized by Auger electrons appearing as the core holes in the $2s$O, $4s$Mo, and $4p$Mo levels are filled. It has been found that the appearance of secondary thresholds in ESD of neutrals, as well as the extent of their energy distributions, depend on surface coverage by the adsorbate. [S1063-7834(98)04204-X]

Although electron-stimulated desorption (ESD) has been a subject of intense study for more than three decades, nevertheless the available information on cross sections and energy distributions of desorbing neutrals is still not reliable enough to construct a detailed model of this phenomenon.[1] We observed ESD of alkali-metal atoms from layers adsorbed on the surface of oxidized tungsten[2] and measured cross sections and energy distributions of desorbing atoms[3,4]. It was found that ESD of alkali-metal atoms is initiated by ionization from oxygen and alkali-metal core levels.[5] These results were interpreted in terms of a model of Auger-stimulated desorption, which takes into account competition between reionization of the alkali-metal atoms and relaxation of the negative charge on oxygen ions.[6]

Subsequent ESD measurements on potassium and cesium atoms from the surface of oxidized molybdenum showed that ESD can arise in molybdenum core-level ionization,[7] with the process having a resonant character associated with core-exciton formation[8].

This work reports measurements of ESD cross sections and energy distributions of sodium atoms escaping from adlayers on oxidized molybdenum, which were performed in order to study the effect of alkali-metal characteristics on ESD of neutrals from this substrate.

1. EXPERIMENTAL TECHNIQUES

The experimental setup used and the measurement techniques are described in detail elsewhere.[3] All measurements of the ESD cross sections and energy distributions for Na atoms escaping from adlayers on oxidized molybdenum were performed with the target maintained at room temperature. The energy distributions of Na atoms were obtained by the time-of-flight technique with the target bombarded by a pulsed electron beam with 1 μs-long pulses at a 1-kHz repetition frequency. The Na atoms were ionized at a surface-ionization-based detector at ionizer iridium-ribbon temperature of 1800 K. To increase the signal/noise ratio at detector output, the output signal was gated by voltage pulses synchronized with the electron beam pulses. The residual pressure in the instrument stainless-steel chamber was not above 5×10^{-10} Torr. The residual-gas composition and the purity of the Na atom beam were monitored by a MS-7302 quadrupole mass spectrometer.

We used as targets $70\times2\times0.01$-mm texturized molybdenum ribbons with a predominantly (100)-oriented surface. Prior to measurements, the ribbons were treated by the standard procedure, namely, annealing in ultrahigh vacuum at $T=2000$ K for 5 h by passing ac current, which favors emergence of the (100) face onto the surface,[9] heating in oxygen ambient $[p(O_2)\cong1\times10^{-6}$ Torr$]$ at $T=1800$ K for 3 h to remove carbon impurities, and finally, after the pumping out of the oxygen, bakeout at $T=2200$ K for 3 min to remove oxygen.

Prior to ESD measurements, oxygen was deposited on the surface of the molybdenum ribbons in two ways. To obtain monolayer oxygen coverage, the ribbons were exposed for 10 s to oxygen at a pressure $p(O_2)\cong1\times10^{-6}$ Torr and temperature $T=1400$ K. To form a thick oxide layer, the ribbons were maintained for 1 h in oxygen at $p(O_2)\cong1\times10^{-6}$ Torr and temperature $T=1000$ K.[10]

Sodium was deposited on oxidized molybdenum at room temperature from a Na beam produced in a directly-heated evaporator by thermal decomposition of sodium chromate.

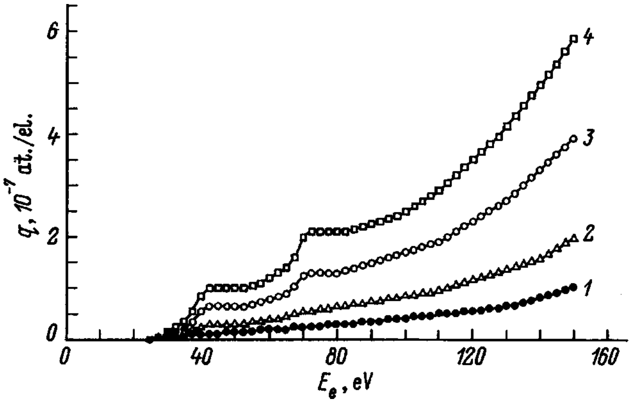

FIG. 1. Sodium-atom ESD yield *q vs* incident electron energy E_e from molybdenum surface covered by an oxygen monolayer at $T=300$ K, measured for different sodium coverages Θ: *1* — 0.125, *2* — 0.25, *3* — 0.5, and *4* — 0.75.

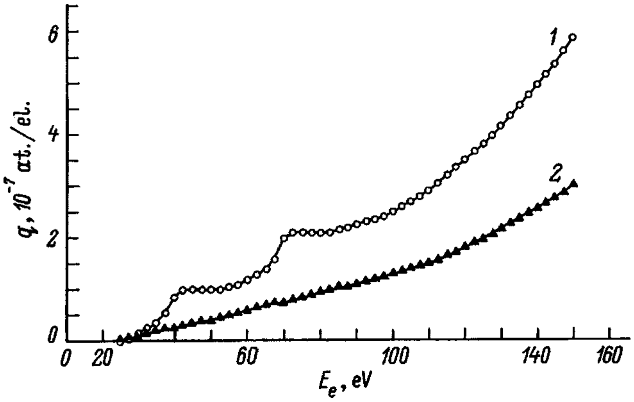

FIG. 2. Sodium-atom ESD yield *q vs* incident electron energy E_e from (*1*) molybdenum surface covered by an oxygen monolayer and (*2*) molybdenum oxide at $T=300$ K. Sodium coverage $\Theta=0.75$.

The surface density of deposited sodium was determined from the deposition time at constant flux, whose intensity was found by measuring the total surface ionization current at the target at the temperature corresponding to current saturation ($T>1750$ K). The sodium surface density corresponding to monolayer coverage was taken equal to $N_0=1\times10^{15}$ at/cm^2. At this level the concentration dependence of Na ESD yield attains saturation.

The electron beam density did not exceed 10^{-6} A/cm^2 at electron energy $E_e=100$ eV, and bombardment by electrons did not result in noticeable target heating.

2. RESULTS

Bombardment by electrons of a sodium film adsorbed on oxidized molybdenum at $T=300$ K was observed to result in desorption of Na atoms. Figure 1 presents the yield *q* of Na atoms from a molybdenum surface covered by an oxygen monolayer, on which sodium was deposited to different coverages Θ, on incident electron energy E_e. Irrespective of the coverage Θ, the ESD appearance threshold for Na atoms is seen to lie at the same electron energy $E_e\approx25$ eV, which, taking into account the contact potential difference between the electron emitter and the target, is close to the ionization energy of the 2*s* O level[11]. As the sodium coverage Θ grows, additional thresholds appear on the $q(E_e)$ curves at electron energies $E_e\approx40$ eV and $E_e\approx70$ eV, with the former being seen already for $\Theta>0.125$, whereas the latter threshold becomes noticeable only for $\Theta>0.25$. These additional thresholds correlate quite well with the ionization energies of the 4*p* Mo and 4*s* Mo core levels, respectively,[11] and do not change with increasing Θ.

The additional Na atom thresholds disappear with increasing molybdenum oxidation, and the neutral yield does not saturate with increasing electron energy up to $E_e=500$ eV. Similar effects were observed earlier in ESD of K and Cs atoms from oxidized molybdenum.[7] An increase in the extent of molybdenum oxidation from a monatomic oxygen layer to an oxide film a few ML thick brings about a decrease of Na yield to about one half irrespective of electron energy E_e and sodium coverage Θ (Fig. 2). Note that the changes in Na atom yield at the additional thresholds resemble rounded-off steps rather than the sharp peaks observed by us earlier for K and Cs atoms escaping by ESD from the corresponding adlayers on molybdenum surface covered by an oxygen monolayer[8].

The sodium yield *q* grows practically linearly with sodium coverage up to $\Theta=0.9$, where *q* reaches saturation, with the slope of the $q(\Theta)$ graphs increasing with E_e (Fig. 3).

Figure 4 plots normalized ESD energy distributions of Na atoms from adlayers on molybdenum coated by an oxygen monolayer for different sodium coverages Θ. For $\Theta<0.125$, the energy distributions are nearly bell-shaped, with the falloff at high energies being somewhat smoother than the low-energy rise. Within $0.125<\Theta<0.75$, the Na energy distributions shift with increasing Θ toward lower energies, accompanied by a simultaneous appearance of a low-energy tail, whose extent grows with increasing Θ, until at $\Theta=0.75$ the energy distributions start at zero kinetic energy, similar to those of K and Cs atoms[7] (Fig. 5). The extent of the low-energy tails decreases as one goes from Cs to Na, irrespective of Θ. As the degree of molybdenum oxidation increases, this tail in the energy distributions of Na atoms disappears, as it does also in the case of K and Cs (Ref. 8).

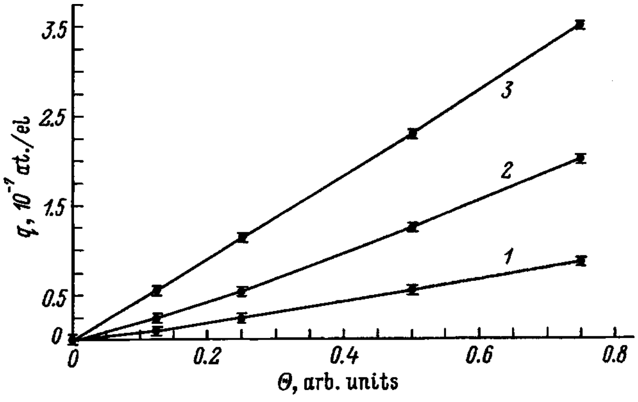

FIG. 3. Sodium-atom ESD yield *q vs* sodium coverage Θ from molybdenum surface covered by an oxygen monolayer at $T=300$ K, measured for different incident electron energies E_e(eV): *1* — 40, *2* — 70, *3* — 120.

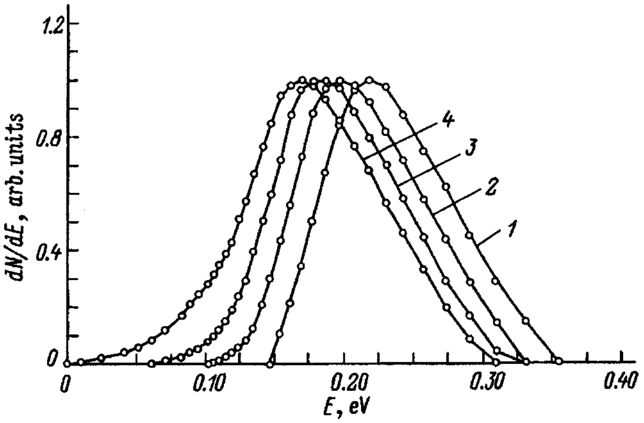

FIG. 4. Normalized energy distributions of sodium atoms in ESD from molybdenum surface covered by an oxygen monolayer at 300 K, measured for different cesium coverages Θ: *1* — 0.125, *2* — 0.25, *3* — 0.5, *4* — 0.75. Incident electron energy $E_e = 80$ eV.

Variation of the primary electron energy does not affect the shape of the normalized Na atom energy distributions.

3. DISCUSSION OF RESULTS

Adsorption of alkali metals on transition-metal oxides is accompanied by a decrease in the work function, which depends on the ionization potential of the alkali metal and its amount on the surface.[12,13] For low coverages, alkali metals adsorb in ionic form, and their adsorption may bring about a partial reduction of the oxide.[14,15] For $\Theta > 0.5$, increasing dipole-dipole repulsion among adsorbed particles weakens their binding to the substrate, and as a result of dipole depolarization a transition to neutral adsorption takes place.[16,17]

Figure 6 shows an electron level diagram for the Mo–O–Na adsorption system. ESD of Na atoms can be qualitatively explained in terms of the model of Auger-stimulated desorption, which was proposed[3,18] to describe ESD of alkali-metal atoms and ions from oxidized tungsten and used[7,8] for interpretation of the K and Cs ESD from oxidized molybdenum. Let a primary electron produce a core hole in the 2*s*O level, which is filled by an electron from the 2*p* level of oxygen, with the corresponding Auger electron neutralizing the adsorbed Na^+ ion. If the positive oxygen ion recovers its negative charge by trapping electrons from the substrate faster than the sodium atom reionizes, then the negative oxygen ion will start to repel the sodium atom through overlap of their valence orbitals, and the sodium atom will be ejected from the surface.

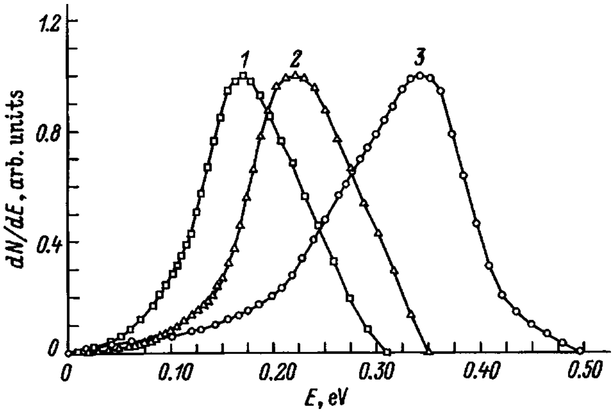

FIG. 5. Normalized energy distributions of (*1*) sodium, (*2*) potassium, and (*3*) cesium atoms in ESD from molybdenum surface covered by an oxygen monolayer at 300 K, measured at an alkali-metal coverage $\Theta = 0.75$. Incident electron energy $E_e = 80$ eV.

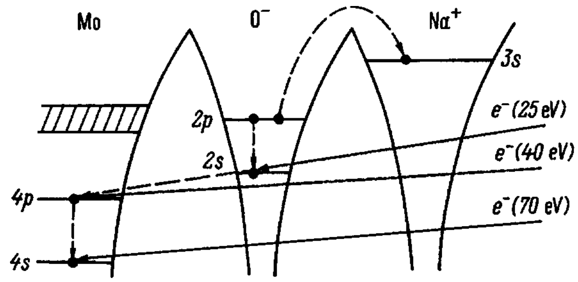

FIG. 6. Electron energy level diagram for the Mo–O–Na adsorption system.

It appears most reasonable to attribute the additional Na appearance thresholds at $E_e \approx 40$ eV and $E_e \approx 70$ eV to ionization of the 4*s*Mo and 4*p*Mo levels. Although the former threshold could be assigned to ionization of the sodium 2*p* level,[11] the fact that both additional thresholds are observed also in ESD of K and Cs atoms[7] argues for the first conjecture. The observation of additional thresholds suggests the existence of Auger processes involving the 4*s* and 4*p* levels of molybdenum, which result in neutralization of adsorbed Na^+ ions. Filling of the core holes in these levels directly by valence-band electrons can hardly produce efficient neutralization of adsorbed Na^+ ions because of the too high energy of the corresponding Auger electrons, an argument corroborated by the absence of ESD of alkali-metal atoms from tungsten covered by a silicon film[19]. It is more probable that even after the molybdenum core levels have been ionized, Na^+ ions continue to be neutralized by Auger electrons from the 2*p* O levels, which are ejected after the filling of core holes in the 2*s* O levels appearing as a result of interatomic core-hole Auger decay in the molybdenum levels. In this case the positive charge on oxygen ions should increase with increasing number of cascade Auger processes leading to core hole filling, and it apparently increases as one moves in ionization from the 2*s* O to 4*p* Mo level, and, finally, to 4*s* Mo. Accordingly, the relaxation time of the negative charge on oxygen[20] and the probability of Na reionization also increase in this direction.[6] The more monotonic variation of Na ESD yield in the region of molybdenum 4*p* and 4*s* ionization (Fig. 2) compared to that of Cs and K atoms is apparently connected with the absence of sharp spectral features in the density distribution of free states in the sodium monolayer and their presence in the cesium and potassium monllayers.[21] The higher is the density of unoccupied states in the conduction band, the higher is the probability of resonant electron transitions from the 4*p* Mo and 4*s* Mo levels, and, accordingly, the larger is the yield of neutrals in the vicinity of the thresholds at $E_e = 40$ and 70 eV. The essential point here is that electrons excited to the conduction band are capable of increasing substantially the relaxation rate of the negative charge on positive oxygen ions.[8]

The average density of unoccupied conduction-band states for a monolayer of sodium is considerably lower than that for cesium and potassium monlayers,[21] and therefore the additional thresholds for Na neutrals, in contrast to those for Cs and K atoms, are observed only after deposition of a certain critical density, which compensates the increase in the charge relaxation time for positive oxygen ions. The probability of Na-atom reionization decreases apparently with increasing density of adsorbed sodium because of increasing equilibrium separation of the sodium adlayer from the surface. This assumption is supported by the larger sodium coverage which is needed to observe the additional threshold at 70 eV ($\Theta=0.5$) compared to that at 40 eV ($\Theta=0.25$), as well as by the absence of additional thresholds for neutral Na ESD from an adlayer on molybdenum oxide, where the charge relaxation time for a positive oxygen ion should be considerably longer than that for molybdenum coated by a monolayer of oxygen.[6]

It should, however, be pointed out that a decrease in the probability of Na-atom reionization with increasing Θ should cause an increase in the Na ESD cross section, which has not been observed within experimental accuracy, as this was not detected either in ESD of alkali-metal atoms from oxidized tungsten[5] nor for K and Cs atoms from oxidized molybdenum[7]. This is possibly related to the insignificant contribution of molybdenum core-level ionization to Na ESD compared to that of the ionization of $2s$ O levels. Estimates show this contribution not to exceed a few per cent. The constancy of the Na reionization probability with increasing Θ is attributed to the independence of the structure and position of the oxygen charge between the alkali-metal and substrate atoms.[6] The increase of the positive charge on the oxygen ion after the molybdenum core-hole Auger decay compared to its charge in the case of $2s$ O core-hole Auger decay can change the situation, however, because a change of the oxygen charge may be accompanied by a change in the shape of the potential barrier for electron tunneling from the Na atom to the oxygen ion. The change in the valence-band spectrum of the substrate induced by adsorption of an alkali metal is also capable of affecting the relaxation time of the electronic excitations responsible for electron-stimulated processes. For example, one observed a strong decrease in the cross section of electron-stimulated oxygen disordering on the Mo(110) face at electron energies corresponding to the $4s$ Mo level ionization energy in the case of lithium adsorption, whereas the dependence of this cross section on the energy of the electrons involved in ionization of the $4p$ Mo level did not exhibit any features.[22] The free-state spectrum of molybdenum covered by an oxygen monolayer is also very sensitive to adsorption of an alkali metal, which is demonstrated by the transition from resonant excitation of K and Cs ESD to nonresonant excitation of Na ESD.

It may be conjectured that the appearance of the low-energy tails in the Na energy distributions is connected with the displacement of Na-atom, after their formation, toward the positive oxygen ion.[7,8] Those Na atoms which do not approach the surface before the negative charge relaxation on oxygen has come to an end will desorb with a high kinetic energy, and those which lag behind, with a low energy. Obviously enough, the extent of the tails should increase with increasing atomic mass, and it is this what is actually observed as one goes from Na to Cs atoms.[7] An increase in Θ means an increase in equilibrium distance of Na atoms from the surface and, accordingly, an increase in the extent of the energy distribution tails, because a progressively smaller number of Na atoms can reach the surface during the oxygen charge-relaxation time. In the case of the oxide, this time is long enough for all atoms to acquire a high energy, and no tails are seen.

Another possibility to account for the low-energy tails in the Na energy distributions and for the dependence of their extent on surface coverage by sodium assumes the existence of two repulsive terms to which Na atoms transfer after electronic excitation of the adsorption system. These terms may be associated with different degrees of charge relaxation on the oxygen ion, and, accordingly, one of these states can be metastable. Since the energy distribution tails appear only at sodium coverages $\Theta>0.125$ on oxygen-monolayer-coated molybdenum, and already at primary electron energies $E_e>25$ eV, they are obviously due to electronic excitations associated with $2s$ O core-level ionization and are in no way connected with the appearance of the additional thresholds. If the two repulsive terms differ in steepness, then an increase in Θ should shift the Na energy distributions originating from excitation to different terms relative to one another because of increasing equilibrium distance of Na adatoms from the surface, and, as a result, the tails should become longer. The radius of the atom produced by neutralization of the positive alkali-metal ion increases as one goes from sodium to cesium, and, accordingly, the extent of the energy distribution tails should increase in the same order. The probability of Na reionization when in the metastable term (with an incompletely relaxed oxygen charge) should be higher than that at the ground term, and therefore the number of Na atoms in the tails does not exceed a few per cent of the total desorbed amount. The lifetime of one-electron excitations is, however, short compared to that of many-electron ones, and therefore the second explanation appears less probable.

Thus we report the first observation of an adsorption system for which the appearance of additional thresholds in neutral ESD depends on surface coverage by the adsorbate, with the energy distributions of neutrals exhibiting low-energy tails whose extent likewise depends on surface coverage.

Support of Russian Fund for Fundamental Research (Grant 95-02-04081a) and of the Russian State Program ‘‘Atomic Surface Structures’’ (Grant 95-1.27) is gratefully acknowledged.

[1] V. N. Ageev, Prog. Surf. Sci. **47**, 55 (1994).
[2] V. N. Ageev, Yu. A. Kuznetsov, and B. V. Yakshinskiĭ, Fiz. Tverd. Tela (Leningrad) **24**, 349 (1982) [Sov. Phys. Solid State **24**, 199 (1982)].
[3] V. N. Ageev, O. P. Burmistrova, and Yu. A. Kuznetsov, Fiz. Tverd. Tela (Leningrad) **29**, 1740 (1987) [Sov. Phys. Solid State **29**, 1000 (1987)].
[4] V. N. Ageev, Yu. A. Kuznetsov, and N. D. Potekhina, Fiz. Tverd. Tela (St. Petersburg) **38**, 609 (1996) [Phys. Solid State **38**, 335 (1996)].
[5] V. N. Ageev, Yu. A. Kuznetsov, and N. D. Potekhina, Surf. Sci. **367**, 113 (1996).
[6] V. N. Ageev, Yu. A. Kuznetsov, and N. D. Potekhina, Fiz. Tverd. Tela

(St. Petersburg) **39**, 1491 (1997) [Phys. Solid State **39**, 1324 (1997)].
[7] V. N. Ageev and Yu. A. Kuznetsov, Fiz. Tverd. Tela (St. Petersburg) **39**, 758 (1997) [Phys. Solid State **39**, 671 (1997)].
[8] V. N. Ageev, Yu. A. Kuznetsov, and T. E. Madey, Surf. Sci. **390**, 146 (1997).
[9] É. F. Chaĭkovskiĭ, G. M. Pyatigorskiĭ, and Yu. F. Derkach, Izv. Akad. Nauk SSSR, Ser. Fiz. **38**, 376 (1974).
[10] N. P. Vas'ko and Yu. G. Ptushinskiĭ, Ukr. Fiz. Zh. **13**, 347 (1968).
[11] *Practical Surface Analysis by Auger and X-Ray Photoelectron Spectroscopy*, edited by D. Briggs and M. P. Seach [Wiley, New York (1983); Mir, Moscow (1987), 567 pp.].
[12] E. V. Klimenko and A. G. Naumovets, Ukr. Fiz. Zh. **27**, 1674 (1982).
[13] C. T. Campbell, Surf. Sci. Rep. **27**, 1 (1997).
[14] K. Prabhakaran, D. Purdie, R. Casanova, S. A. Muryn, P. J. Hardman, P. L. Wincott, and G. Tornton, Phys. Rev. B **45**, 6969 (1992).
[15] R. Souda, W. Hayami, T. Aizawa, and I. Ishizawa, Surf. Sci. **285**, 265 (1993).
[16] A. W. Grant and C. T. Campbell, Phys. Rev. B **55**, 1844 (1997).
[17] V. N. Ageev, N. D. Potekhina, B. V. Yakshinskii, M. Akbulut, and T. E. Madey, Phys. Rev. B **54**, R5271 (1996).
[18] V. N. Ageev, O. P. Burmistrova, and B. V. Yakshinskii, Surf. Sci. **194**, 101 (1988).
[19] V. N. Ageev, O. P. Burmistrova, A. M. Magomedov, and B. V. Yakshinskiĭ, Fiz. Tverd. Tela (Leningrad) **32**, 801 (1990) [Sov. Phys. Solid State **32**, 472 (1990)].
[20] P. J. Feibelman, Surf. Sci. **102**, L51 (1981).
[21] E. Wimmer, J. Phys. F **13**, 2313 (1983).
[22] A. G. Fedorus, V. V. Gonchar, A. V. Konash, E. V. Klimenko, A. G. Naumovets, and I. N. Zasimovich, Surf. Sci. **251/252**, 846 (1991).

Translated by G. Skrebtsov

PHYSICS OF THE SOLID STATE VOLUME 40, NUMBER 4 APRIL 1998

POLYMERS. LIQUID CRYSTALS

Adsorption-resistant properties of copper phthalocyanine dispersed in a polymer matrix

A. E. Pochtennyĭ and A. V. Misevich

Belarusian State Technological University, 220630 Minsk, Belarus

D. I. Sagaĭdak and G. G. Fedoruk

Scientific-Research Institute of Applied Physics Problems, 220064 Minsk, Belarus

(Submitted September 12, 1997; resubmitted October 30, 1997)
Fiz. Tverd. Tela (St. Petersburg) **40**, 773–775 (April 1998)

The conduction mechanism in copper phthalocyanine (Cu*Pc*)-polymer composite thin films and their sensitivity to nitrogen dioxide are investigated. It is established that a hopping conduction mechanism in the regime of single electron hops prevails in these materials at 290–350 K, and the magnitude and rate of the adsorption-resistance sensitivity to NO_2 is higher than in pure Cu*Pc*. © *1998 American Institute of Physics.* [S1063-7834(98)04304-4]

The utilization of metal phthalocyanines as the molecular discriminating core of chemical sensors is based on the adsorption-resistant effect, which describes the variation of the conductivity in connection with the selective absorption of molecules of the surrounding gas medium.[1,2] Not only the properties of the phthalocyanine molecules themselves, but also their intermolecular interactions and supramolecular structure are important in this effect. The adsorption-resistant properties can be optimized by chemically modifying the phthalocyanine molecules or by employing various thin-film production methods to regulate the supramolecular structure. Another possible avenue for controlling the adsorption-resistant properties is to disperse phthalocyanine aggregates in an inert polymer matrix.[3–5] The separation of phthalocyanine associations with the polymer medium in this composite structure alters the electrical characteristics of the film and can enhance the accessibility of adsorption centers by molecules from the gas environment. In the present study we give the results of an investigation of the electrical and gas-sensing properties of composite copper phthalocyanine (Cu*Pc*)-polymer structures.

Composite films having thicknesses from 50 nm to 500 nm were prepared by plasma-activated and laser vacuum deposition. In the first case the composites were formed by the simultaneous deposition of thermally sublimated Cu*Pc* and products of the decomposition of benzene in an rf (13.56 MHz) discharge plasma onto a substrate. In the second case the films were formed by using an LGN-703 laser to spray on a powdered mixture of Cu*Pc* and polystyrene in vacuum.[3] Polikor (polyvinyl chromate resin) substrates of dimensions 11×14 mm with an interdigital array of 25 pairs of nickel electrodes were used.

The dc ohmic dark current was measured at a voltage of 10 V by means of a Belvar V7-49 electrometer in the temperature interval 290–350 K in air and in vacuum for various adsorbed oxygen concentrations. Temperature curves of the conductivity were obtained by the rapid cooling technique.[4] The ac conductivity was measured in air at room temperature in the frequency range from 500 Hz to 0.5 MHz by means of a Tesla BM-507 impedance meter. The adsorption-resistance response of the films to nitrogen dioxide was measured in a flow of dry air containing 2 ppm NO_2 at a constant voltage of 10 V and sample temperature of 350–430 K.

The temperature dependence of the dc dark current of metal phthalocyanines obeys the relation

$$G = G_0 \exp(-\varepsilon/kT), \tag{1}$$

where ε is the conduction activation energy, T is the temperature, and k is the Boltzmann constant. The form of the factor G_0 is determined by the conduction mechanism of the substance. It has been shown[4] that the experimental dependences of the electrical resistance on the dosage of ion-implanted oxygen and of G_0 on ε indicate the prevalence of a hopping conduction mechanism in the temperature interval 290–350 K.

Another source of information about the conduction mechanism lies in the frequency dependence of the ac conductivity σ_{ac}, which obeys the following relation for a random spatial distribution of localization centers[6]

$$\sigma_{\mathrm{ac}} \sim \omega^n, \tag{2}$$

where ω is the frequency of the electric field, and the power exponent $n \leqslant 1$.

The observed frequency dependence of σ_{ac} agrees with Eq. (2) and confirms the hopping conduction mechanism in the synthesized structures. Here the experimental values of n are close to unity (0.96–0.99), reflecting conduction in the regime of single electron hops.[6] Similar frequency dependences of the conductivity have been observed for phthalocyanine films Cu*Pc* deposited in plasma activation[7] and also for Co*Pc* (Ref. 8) and Pb*Pc* (Ref. 9) films.

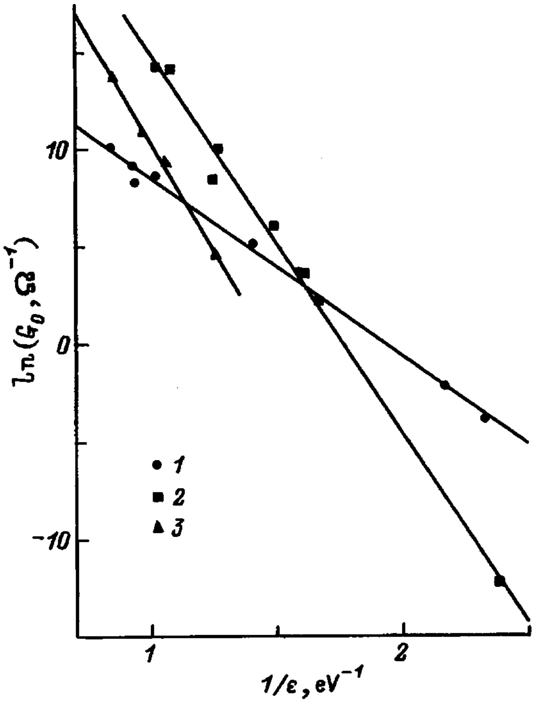

FIG. 1. Preexponential factor G_0 versus the reciprocal of the conduction activation energy for: *1*) pure Cu*Pc*; *2*) plasma-synthesized composite; *3*) laser-deposited composite. The solid lines are calculated from Eq. (3).

The information obtained on the conduction mechanism indicates that the factor G_0 in Eq. (1) characterizes the probability of tunneling between localization centers[10] and is therefore equal to[4]

$$G_0=G_{03}\exp\left[-\left(\frac{4\pi}{3}\right)^{1/3}\frac{\alpha e^2}{\chi a\varepsilon}\right], \tag{3}$$

where $\alpha=1.73$ is the percolation constant, e is the electron charge, χ is the dielectric constant of the substance, a is the electron localization radius, and the factor G_{03} depends on the sample geometry.

Figure 1 shows experimental data in coordinates $(\log G_0, 1/\varepsilon)$ for pure Cu*Pc* and for plasma-synthesized and laser-deposited composites. These data are approximated according to Eq. (3) by a linear relation and can be used to calculate the electron localization radius. Its value for pure Cu*Pc* ($\chi=3.6$, Ref. 11) is 120 ± 12 pm. The slopes of the $\log G_0(1/\varepsilon)$ curves should increase for the composites, because the product χa in Eq. (3) must decrease by virtue of the lower dielectric constant of the composites in comparison with pure Cu*Pc*. And this conjecture is indeed supported experimentally. Moreover, the electron localization radius must also decrease as a result of the weakening of interaction between Cu*Pc* molecules in the composite. Thus, the value of χa determined from the data in Fig. 1 is equal to 430 pm for pure Cu*Pc* and decreases to 180 pm for the Cu *Pc*-polystyrene composite. Since $\chi=2.5$ for pure polystyrene, the value of a cannot be higher than 72 pm in this composite.

Figure 2 shows kinetic curves of the sensitivity S, which represents the ratio of the current I_g in a mixture of air with 2 pmm NO_2 to the current in pure air I_a ($S=I_g/I_a$) for Cu *Pc*-polystyrene composites as a function of the Cu*Pc* content and the temperature. It is evident from a comparison of curves 1–3 that the maximum response for NO_2 is attained at a temperature of 373 K, which is slightly higher than the corresponding temperature for pure Cu*Pc* (353 K). A comparison of the response of 20% and 40% Cu*Pc*-polystyrene composites and pure Cu*Pc* at a temperature of 373 K shows that S increases as the Cu*Pc* content is reduced in the composite.

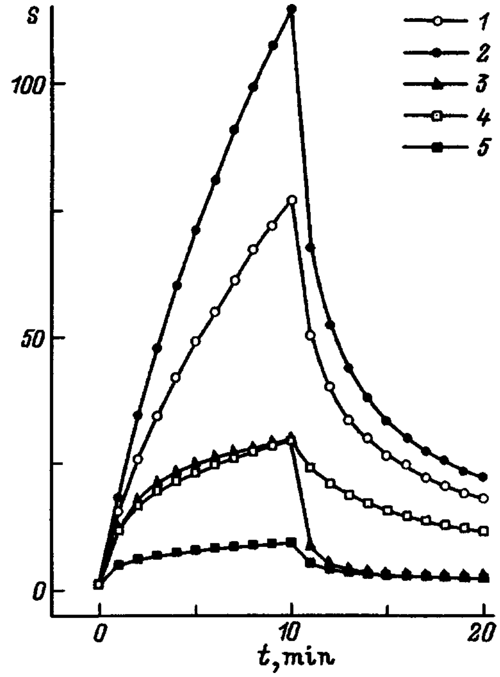

FIG. 2. Kinetic curves of the response of Cu*Pc*-polystyrene composites to nitrogen dioxide. *1*) 20% Cu*Pc* at a temperature of 353 K; *2*) 20% Cu*Pc* at 373 K; *3*) 20% Cu*Pc* at 413 K; *4*) 40% Cu*Pc* at 373 K; *5*) pure Cu*Pc* at 373 K. The exposure to NO_2 begins at time $t=0$ and ends after 10 min.

The sensitivity in metal phthalocyanines is known to obey the Roginskiĭ-Zel'dovich-Elovich equation[2]

$$dS/dt=A\exp(-BS), \tag{4}$$

where A and B are constants. Consequently, the experimental data on the sensitivity kinetics are conveniently represented in coordinates $[\ln(dS/dt),S]$, which linearize Eq. (4). In these coordinates the data for Cu*Pc* and Cu*Pc*-polystyrene composites show that the process runs through two stages, which can be attributed either to a difference in the adsorption-resistance effects on the surface and in the bulk of the sample or to the presence of two types of adsorption centers. The dispersion of Cu*Pc* in polystyrene increases the magnitude and shortens the duration of both the fast and the slow (terminating at the steady-state level) component of the sensitivity kinetics. The two-stage character of the adsorption-resistance effect and an increase in the sensitivity have also been observed for a plasma-synthesized composite.[5]

[1] *Sensors*, Vol. 2, Part 1, edited by W. Göpel, J. Hesse, and J. N. Zemel (VCH, Weinheim, 1991), 706 pp.
[2] J. D. Wright, Prog. Surf. Sci. **31**, 1 (1989).
[3] G. G. Fedoruk, A. V. Misevich, A. E. Pochtenny, and D. I. Sagaidak, in

Physics, Chemistry, and Application of Nanostructures: Reviews and Notes to Nanomeeting-97 (Singapore, 1997), p. 205.

[4] A. E. Pochtennyĭ, D. I. Sagaĭdak, G. G. Fedoruk, and A. V. Misevich, Fiz. Tverd. Tela (St. Petersburg) **38**, 2592 (1996) [Phys. Solid State **38**, 1422 (1996)].

[5] A. E. Pochtennyĭ, D. I. Sagaĭdak, and G. G. Fedoruk, Phys. Rev. **39**, 1199 (1997).

[6] M. Polak and T. H. Geballe, Phys. Rev. **122**, 1743 (1961).

[7] C.-G. Choi, S. Lee, and W.-J. Lee, J. Acoust. Soc. Jpn. **34**, 6178 (1995).

[8] S. I. Shihub, R. G. Gould, and S. Gravon, Physica B **222**, 136 (1996).

[9] M. E. Azim-Araghi, D. Campbell, A. Krier, and R. A. Collins, Semicond. Sci. Technol. **11**, 39 (1996).

[10] B. I. Shklovskiĭ and A. L. Éfros, B. I. Shklovskiĭ and A. L. Éfros, *Electronic Properties of Doped Semiconductors* [Springer-Verlag, Berlin-New York (1984); Nauka, Moscow (1979), 416 pp.].

[11] R. D. Gould, J. Phys. D **9**, 1785 (1986).

Translated by James S. Wood

FULLERENES AND ATOMIC CLUSTERS

Fractal structure of ultradisperse-diamond clusters

M. V. Baĭdakova, A. Ya. Vul', V. I. Siklitskiĭ, and N. N. Faleev

A. F. Ioffe Physicotechnical Institute, Russian Academy of Sciences, 194021 St. Petersburg, Russia

(Submitted October 15, 1997)
Fiz. Tverd. Tela (St. Petersburg) **40**, 776–780 (April 1998)

Ultradisperse-diamond clusters are shown to be fractal objects, and the character of variation of the fractal dimension in the course of the diamond-graphite phase transition under annealing in an inert atmosphere is studied. © *1998 American Institute of Physics.* [S1063-7834(98)04404-9]

The diamond-graphite structural phase transition has recently been studied in clusters of ultradisperse diamond obtained by detonation.[1]

X-ray diffraction measurements showed the coherent-scattering regions to be $L \cong 43$ Å in size, which is in good agreement with data derived from Raman scattering spectra. It was found that ultradisperse-diamond clusters contain, besides a crystalline diamond core, an amorphous diamond (sp^3) and an amorphous graphite (sp^2) phase, and that the diamond-graphite phase transition in the clusters starts from the cluster surface at substantially lower temperatures than it does in bulk single-crystal diamond.

The objective of this work was to clarify the variations in ultradisperse-diamond cluster structure during the phase transition.

The interest in the structural changes stems from several causes. First, ultradisperse-diamond clusters were shown to be fractal objects.[2] Second, it appeared of interest to investigate the changes in cluster surface topology accompanying the phase transition. Third, since ultradisperse-diamond nanoclusters merge to form aggregates,[3] a question arose of the changes in aggregate structure (i.e. changes in fractal dimension) associated with the phase transition.

1. SAMPLES AND MEASUREMENT TECHNIQUES

The studies were made on ultradisperse-diamond samples obtained from the detonation product, which forms in an explosion of carbon-containing materials, viz. a mixture of TNT and hexogen (TNT/hexogen 60/40), similar to the technique used in Refs. 4,5 The pressure and temperature in the detonation wave (P-T parameters) were chosen to lie in the region of thermodynamic stability of diamond [$P \geqslant 10$ GPa, $T \geqslant 3000$ K (Ref. 6)].

We studied samples of two types differing in the kinetics of detonation-product cooling, namely, in samples obtained by the dry technique the coolant was carbon dioxide,[5] whereas the samples prepared by the wet technique were cooled by water[7].

Ultradisperse-diamond samples prepared by the dry method were shown[1] to have much higher contents of the amorphous sp^2 phase, which is due to the longer time the material resides during its preparation in the region of kinetic instability of diamond ($T \geqslant 2000$ K). Indeed, after the passage of the detonation wave the pressure drops rapidly, as a result of which the P-T parameters enter the region where diamond is thermodynamically unstable, but the temperature is still high enough to support a high mobility of carbon atoms, which favors transformation of the diamond thus obtained into graphite. When the product is cooled still more, the temperature lowers to enter the region where diamond is kinetically stable. The lower is the cooling rate, the longer is the time the detonation product stays in the region of kinetic instability of diamond and, accordingly, the higher is the probability of the reverse, diamond-graphite phase transition in the course of the synthesis. Figure 1 shows the phase diagram and cooling kinetics for two idealized limiting cases of cooling, namely, when the rate of cooling is substantially higher and substantially lower than that of pressure decrease. In the first case, synthesis does not pass through the region where diamond is kinetically unstable, and in the second, the synthesized material resides the longest possible time in this region. The wet synthesis is closer to the former, and the dry technique, to the latter limiting case.

Both types of ultradisperse-diamond samples were isolated in the same way from the detonation product, viz. by high-temperature processing with an aqueous nitric acid solution under pressure to remove carbon allotropes other than diamond. The amount of the diamond phase extracted from the material produced by detonation is naturally larger in the case of wet preparation.

The structural phase transition was achieved by annealing ultradisperse-diamond samples in an argon flow at temperatures varied within the 720–1400 K range. The quartz crucibles containing ultradisperse diamond powder were placed into a graphite cassette mounted in a quartz reactor. Following evacuation and reactor purge with argon, the material was heated and maintained at the prescribed anneal temperature for three hours. The temperature was maintained constant to better than 0.5 K. After the annealing, the samples were left to cool with the furnace turned off.

The fractal structure of nanoclusters was studied in the

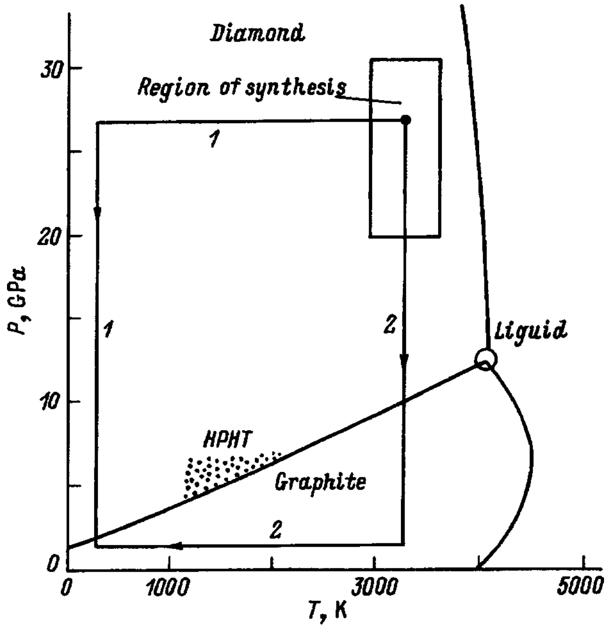

FIG. 1. Phase diagram of carbon and kinetics of detonation product cooling for two idealized cases: rate of cooling substantially higher (*1*) and substantially lower (*2*) than that of pressure decrease.

traditional approach[8] by analyzing the dependence of small-angle x-ray scattering intensity I on wave vector q in the range $0.036<q<0.8$ Å^{-1}, which corresponds to scattering angles $0.5°<4\theta_{\mathrm{Br}}<10°$ (in Ref. 3, the experiment was carried out in the range $5\times10^{-3}<q<3\times10^{-2}$ Å^{-1}). As this will be shown later, the position of the maximum in the $I(q)$ curve permits determination of the characteristic probed size of the scattering cluster L, and the slope of the curve, the fractal dimension D. The scattering intensity was measured in the single-crystal mode in $(\theta, 2\theta)$ geometry on a RIGAKU Dmax-B/RC diffractometer equipped with a special collimation arrangement limiting the divergence of the primary beam. Copper radiation was used ($\lambda=1.54183$ Å). Besides the small-angle scattering, x-ray characterization of the samples was performed within a broad angular range.

2. EXPERIMENTAL RESULTS

Typical x-ray diffraction and scattering curves are displayed in Figs. 2 and 3. The broad symmetrical diffraction maxima (Fig. 2) at $2\theta_{\mathrm{Br}}=43.9°$ correspond to the (111) reflection from diamond lattice. At $2\theta_{\mathrm{Br}}\approx17°$ one observes diffuse scattering (a halo) and a progressive increase in scattered intensity as one approaches the primary beam. By analogy with the origin of the halo observed[9] in glasses, we put forward a suggestion[1] that this halo is due to scattering from structural elements similar to benzene rings.

X-ray diffraction curves obtained on samples after annealing at 1400 K exhibit satellites at the (111) diamond reflection, a halo at $2\theta_{\mathrm{Br}}\approx39°$ (Ref. 1), and features corresponding to the diffraction pattern from onionlike carbon structures[10].

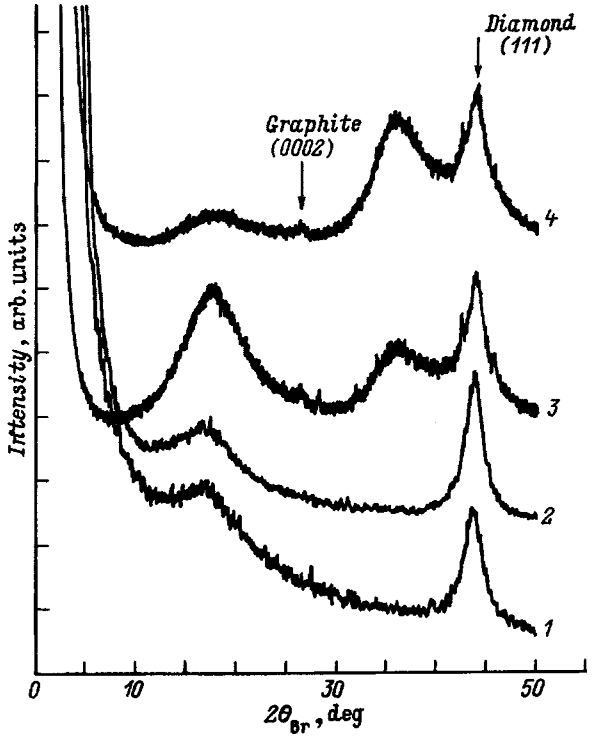

FIG. 2. X-ray diffraction from ultradisperse diamond samples. *1* — dry-prepared sample before anneal; *2* — wet-prepared sample before anneal; *3* — dry-prepared sample after anneal at 1400 K in argon; *4* — wet-prepared sample after anneal at 1400 K.

3. EXPERIMENTAL DATA TREATMENT AND DISCUSSION

By traditional theory[11] assuming the scatterer to have a smooth surface the scattered intensity $I(q)$ is a power-law function of wave vector q with a negative integer exponent

$$I(q)\sim q^{-\alpha}$$

where $q=(4\pi/\lambda)\sin\theta_{\mathrm{Br}}$, and λ is the scattered wavelength. For scatterer with a smooth spherical surface the exponent α is exactly four, and for a scattering sphere it is three.[11,12]

It is known that in the case of a fractal cluster exponent α may serve as a characteristic of the scatterer.[12,13] If α is within 3–4, the scatterer is a cluster with a fractal surface, and for $\alpha=0-3$ it is a bulk fractal. Note that fractal dimension for a fractal surface is given by the relation $D=6-\alpha$, whereas for a bulk fractal $D=\alpha$. At the same time the position of the maximum in the $I(q)$ relation determines the characteristic size of the scatterer, $L\approx2\pi/q_{\mathrm{max}}$.[14]

As seen from Fig. 3 plotting small-angle scattering intensity on a log-log scale, within $0.2<q<0.8$ Å^{-1} these graphs can be well fitted by a power-law function for samples prepared by the dry technique, with a maximum appearing for $q\leqslant0.2$ Å^{-1}. For wet-preparation samples the fit is also good, with the exception of one annealing temperature. It was found that the value of α determined by the above method is not an integer, and that it indicates the scattering cluster to be a fractal, irrespective of the type of preparation and of annealing temperature.[3,12]

Generally speaking, a noninteger value of α may appear for a certain size distribution of ultradisperse-diamond clusters.[13] It has, however, been pointed out more than

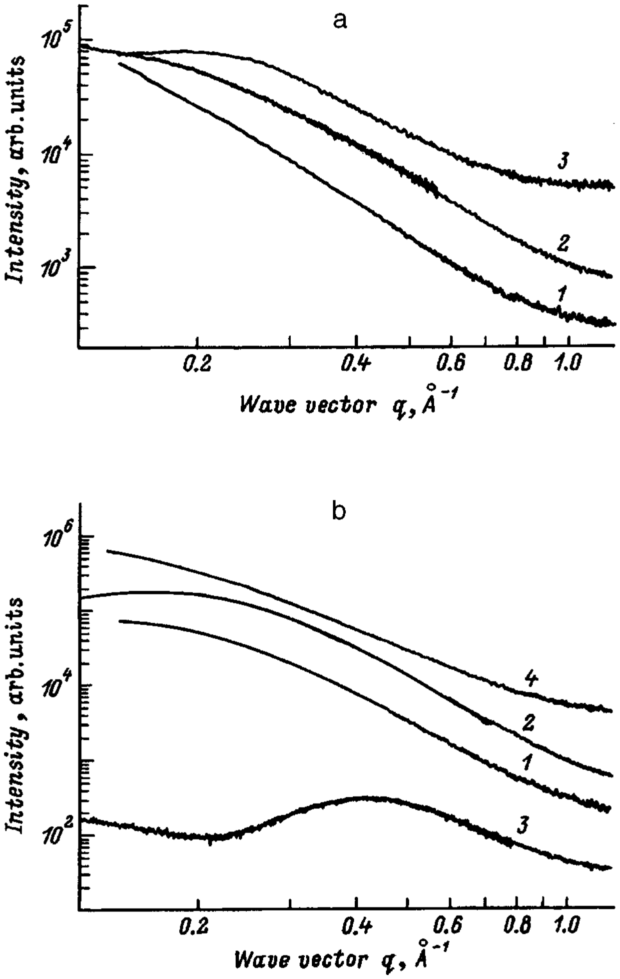

FIG. 3. Small-angle x-ray scattering from ultradisperse-diamond samples subjected to different anneal temperatures. (a) Dry-preparation sample before (*1*) and after annealing at (*2*) 720 K and (*3*) 1400 K. (b) Wet-preparation sample before (*1*) and after annealing at (*2*) 720 K, (*3*) 850 K, and (*4*) 1400 K.

once[3,15] that ultradisperse-diamond clusters have a delta-shaped distribution in size with a peak at about 43 Å, and therefore in our opinion the noninteger α argues unambiguously for the fractal nature of these clusters.

Table I presents the parameters D and L which were derived from the relations shown in Fig. 3.

As seen in Table I, ultradisperse-diamond clusters are fractal objects, with the type and dimension of the fractal depending on the preparation technique employed.

Wet preparation favors formation in the starting material of clusters possessing fractal scattering surface ($D=2.53$) enveloping a core 44 Å in size, which corresponds to the coherent scattering region for ultradisperse diamond. In samples prepared by the wet technique these scatterers approach most closely in shape the ultradisperse-diamond nanoclusters studied in Ref. 3 and representing spherical grains with distinct boundaries. In our case, however, the particles were not exactly spheres, because the fractal dimension D is not an integer and $D\neq 2$. This implies that the clusters prepared by the wet technique have a deeply scratched surface forming a sharp boundary between the diamond core and the amorphous phase.

By contrast, in ultradisperse diamonds prepared by the dry technique scattering occurs from fractal clusters with $D=2.8$ and $L\geqslant 20$ Å. The fact that the fractal object is larger than the coherent-scattering region for ultradisperse diamonds is a consequence of the fractal nature of the scatterers. In this case scattering takes place from fluctuations of electronic density in the volume of the fractal cluster. Observation of such scattering means that in samples prepared by this technique there is no sharp boundary between the diamond core and the amorphous phase.

The appearance of such scatterers in samples produced in different conditions results from different amounts of the amorphous phase formed on diamond cores through the reverse diamond-graphite transition during the cooling of the detonation products. As for the diamond cores themselves, they differ neither in structural parameters nor in size from one another. Hence the radiation is scattered off the shell enveloping the diamond core and consisting of the amorphized phase. A comparison of diameters of the fractal scatterers with the size of the diamond core shows the shell thickness to be different for samples prepared by different techniques. Estimates of the shell thickness yield about 5 Å for a dry-preparation sample and on the order of atomic separation for a sample produced by the wet method.

Annealing affects not only the size of the fractal but its

TABLE I. Cluster parameters D and L.

Item No.	Anneal ambient	Anneal temperature T, K	Type of fractal	Fractal dimension D	Cluster size L, (Å)
1	2	3	4	5	6
		Dry technique			
1	Before anneal		Vol	2.84	52
2	Ar	720	Vol	2.57	52
3	Ar	1400	Vol	2.2	30
		Wet technique			
1	Before anneal		Surf	2.53	44
2	Ar	720	Surf	2.2	35–40
3	Ar	850	Vol-Surf	2.94	15
4	Ar	1400	Vol	2.8	⩾50

type as well; moreover, scattering in samples annealed at certain temperatures is determined not by ultradisperse-diamond clusters.

The fractal in a sample prepared by dry technique becomes more loose (the fractal dimension decreases) while the size of the scatterers does not change. When the (111) planes of the diamond core become involved in graphitization, the scatterer size decreases too ($L=30$ Å at 1400 K).

The pattern observed in ultradisperse diamonds prepared by the wet technique is more complex. Annealing reduces the dimension of the fractal surface, and the type itself of the scattering fractal cluster changes at 850 K. After annealing at this temperature, scattering occurs primarily from another object, namely, spherical grains with clearly defined boundaries (fractals with $D=2.94$), about 15 Å in size. It may be conjectured that these particles are aggregated, because scattering is observed at wave vectors smaller than $q_{\mathrm{max}}=0.4$ (i.e., for $L>15$ Å) as well. This suggests formation of a network of dense carbon spherical particles enclosing isolated ultradisperse-diamond clusters.

Above 1400 K, the fractal sp^2 shell takes active part in graphitization of ultradisperse diamond grains, which results in formation of bulk fractal clusters ($D=2.8, L\geqslant 44$ Å for $T=1400$ K).

Irrespective of the type of the starting material (type of scatterer), after anneal at 1400 K ultradisperse diamond transforms into bulk fractal scatterers with a well developed periphery (i.e. with fractal dimension). This correlates with the observation[1] that the phase transition at this temperature involves already the (111) planes of the diamond core. The structures thus formed do not have a crystallographic lattice with three-dimensional symmetry and strong chemical bonding to the diamond planes of the core (the onionlike form of carbon). This is why these structures are described in terms of fractal geometry as loose bulk fractals. The apparent difference in scatterer size between the samples obtained by the dry and wet techniques at 1400 K, $L=30$ Å and $L\geqslant 50$ Å, can be attributed to different electronic density distributions, i.e., different degrees of looseness of the fractal cluster ($D=2.2$ and $D=2.8$, respectively). Indeed, as follows from the definition of fractal dimension, $D_1/D_2=\ln L_1/\ln L_2$ (where index 1 refers to dry, and index 2, to wet preparation). But then the scatterer in a wet-prepared sample should be, after the annealing, 75 Å in size, which corresponds to a wave vector $q<5\times 10^{-1}$ Å^{-1} and is in accord with the data in Table I.

Note that the plots in Fig. 3 exhibit a slight deviation from a power-law relation for samples with low fractal dimensions. This may be associated with the deviation of the scatterer distribution in size from the δ function setting in in the course of the phase transition.

Support of the Russian Fund for Fundamental Research (Grant 96-02-19445) is gratefully acknowledged. One of the authors (V. I. S.) was supported by Grant No. 97003 within the Russian program ''Physics of Solid-State Nanostructures.''

[1] A. E. Aleksenskiĭ, M. V. Baidakova, A. Ya. Vul', V. Yu. Davydov, and Yu. A. Pevtsova, Fiz. Tverd. Tela (St. Petersburg) **39**, 158 (1997) [Phys. Solid State **39**, 1007 (1997)].

[2] M. V. Baidakova, V. I. Siklitski, and A. Ya. Vul', in *Proceedings of the International Symposium ''Nanostructures: Physics and Technology''* (St. Petersburg, Russia, 1997), p. 227.

[3] A. P. Ershov and A. L. Kupershtokh, Fiz. Goreniya Vzryva **27**, 111 (1991).

[4] A. M. Staver, N. V. Gubareva, A. I. Lyamkin, and E. A. Petrov, Fiz. Goreniya Vzryva **20**, 100 (1984).

[5] A. I. Lyamkin, E. A. Petrov, A. P. Ershov, G. V. Sakovich, A. M. Staver, and V. M. Titov, Dok. Akad. Nauk SSSR **302**, 611 (1988) [Sov. Phys. Dokl. **33**, 705 (1988)].

[6] F. P. Bundy, Physica A **156**, 169 (1989).

[7] V. V. Danilenko, in *Proceedings of the V All-Union Meeting on Detonation* (Krasnoyarsk, 1991), Vol. 1, 145 pp.

[8] O. Glatter, J. Appl. Crystallogr. **12**, 166 (1979).

[9] S. R. Elliott, Phys. Rev. Lett. **67**, 711 (1991).

[10] R. Franklin, Acta Crystallogr. **3**, 107 (1950).

[11] A. Guinier, C. Fournet, C. B. Walker, and K. L. Yudowitch, *Small-Angle Scattering of X-Rays* (Wiley, New York, 1955).

[12] V. I. Siklitsky, V. I. Ivanov-Omskii, and M. V. Baidakova, in *Diamond-Based Composites and Related Materials*, edited by M. Prelas (Kluwer, London, 1997), p. 197–202.

[13] P. Pfeifer and D. Avnir, J. Chem. Phys. **79**, 3558 (1983); D. Avnir, D. Farin, and D. Pfeifer, *ibid.*, 3566 (1983).

[14] C. F. Bohren and D. R. Huffman, *Absorption and Scattering of Light by Small Particles* (Chichester, New York, 1983).

[15] V. L. Kuznetsov, M. N. Aleksandrov, I. V. Zagoruiko, A. L. Chuvilin, E. M. Moroz, V. N. Kolomiichuk, V. A. Likholobov, P. M. Brylyakov, and G. V. Sakovich, Carbon **29**, 665 (1991).

Translated by G. Skrebtsov

Electrical, galvanomagnetic, and thermoelectric properties of PbSe in the void sublattice of opal

L. I. Arutyunyan, V. N. Bogomolov, D. A. Kurdyukov, V. V. Popov, A. V. Prokof'ev, and I. A. Smirnov

A. F. Ioffe Physicotechnical Institute, Russian Academy of Sciences, 194021 St. Petersburg, Russia

(Submitted November 4, 1997)
Fiz. Tverd. Tela (St. Petersburg) **40**, 781–783 (April 1998)

A study of transport phenomena, namely, electrical resistivity, thermopower, Hall coefficient, and magnetoresistance of p PbSe synthesized in opal voids has been carried out in the 4–300 K range. The parameters of the semiconducting material have been determined at different void filling levels. An anomalous behavior of the hole mobility associated with surface scattering from insulating opal-matrix walls has been observed. © *1998 American Institute of Physics.* [S1063-7834(98)04504-3]

Fabrication of three-dimensional regular semiconducting and superconducting nanostructures with a periodically modulated thickness of the conducting material has considerable potential both for development of devices of a new type[1] and for investigation of low-dimensionality cluster crystals. Among promising directions in production of such structures is filling with a conducting material the regularly distributed voids in an insulating opal matrix, which may be considered as a closely packed array of spherical particles of amorphous silica SiO_2.[2] When studying the properties of semiconductors incorporated in the opal matrix it is essential to separate the changes in these properties associated with uncontrollable doping of the material from those due to size quantization effects. Lead chalcogenides are a convenient material for studying the latter, because carrier concentration in them is dominated by intrinsic defects[3], and depends to a much weaker extent on foreign impurities than it does in III-IV compounds and other classical semiconductors.

This work deals with the electrical, thermoelectric, and galvanomagnetic properties of p PbSe synthesized in voids of the opal matrix. The opals were filled by the following technique. First the sample was impregnated with a lead nitrate solution, which was subsequently thermally decomposed in air down to the oxide. This procedure was repeated cyclically to obtain the desired opal filling by PbO. After this, the sample with PbO was treated with hydrogen selenide. The PbSe thus obtained exhibited a distinct crystalline phase, whose lattice constant practically coincided with that of single-crystal bulk material. No impurities were detected in the opal matrix voids.[4]

The parameters of the two samples studied are listed in Table I. Figure 1 plots the temperature behavior of the resistivity ρ of the opal samples with PbSe, and Fig. 2, that of thermopower α. We readily see that despite the difference in magnitude, the $\rho(T)$ relation of both samples follows the same pattern, and the $\alpha(T)$ dependences are linear and close in magnitude. The Hall coefficients R of the two samples differ by an order of magnitude (see Table I). At the same time R has the same value in each sample at $T=77$ and 300 K, which implies that the carrier concentration $p\sim 1/R$ is practically independent of temperature. The expressions for the thermopower and carrier concentration in the case of arbitrary degeneracy can be written[5]

$$\alpha=-\frac{k}{e}\left[\frac{r+2}{r+1}\,\frac{F_{r+1}(\mu^*)}{F_r(\mu^*)}-\mu^*\right], \tag{1}$$

$$p=\frac{4\pi(2m^*kT)^{3/2}}{h^3}F_{1/2}(\mu^*), \tag{2}$$

where

$$F_r(\mu^*)=\int_0^\infty\frac{x^r\,dx}{e^{x-\mu^*}+1}$$

is the Fermi integral, and $\mu^*=\mu/kT$ is the reduced chemical potential. Assuming the scattering parameter r to be known, we can now extract the hole concentration in PbSe from α. The effective mass of the density of states for PbSe was assumed to be $m^*=0.043m_0$ (Ref. 3). Information on the

TABLE I. Calculated and experimental characteristics of opal samples with different lead selenide filling.

		Measured sample parameters		Calculated parameters of incorporated material				
Sample No.	Filling %	R(77 K, 300 K), $cm^3\cdot C^{-1}$	ρ(77 K) $\Omega\cdot$cm	R_p(77 K), $cm^3\cdot C^{-1}$	ρ_p(77 K), $\Omega\cdot$cm	$p=e/R_p$, 10^{18} cm-3	α (77 K), μV$\cdot$K-1	p_α, 10^{18} cm^{-3}
1	82	40	79	3.9	7.8	1.6	57	1.6
2	63	500	1010	38	76.5	0.16	67	1.2

Note: The void filling is the ratio of the volume of incorporated material to the total void volume and is determined gravimetrically.

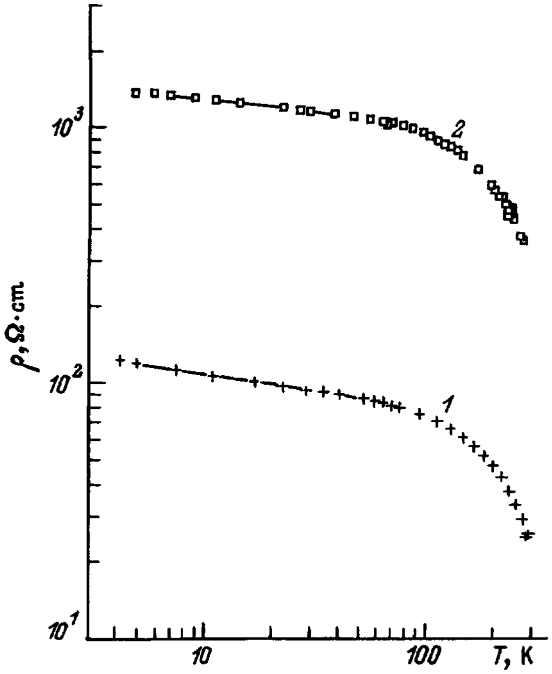

FIG. 1. Temperature dependence of the resistivity of opal samples with PbSe. Opal void filling by lead selenide (%): *1* — 82, *2* — 63.

character of scattering can be derived from the temperature behavior of mobility $u = R/\rho$ (Fig. 3). We see that the mobility is the same in both samples, and that for $T < 80$ K, $u(T) \propto T^{1.3}$. In nondegenerate semiconductors a dependence of this type ($u \propto T^{1.5}$) is characteristic of scattering from impurity ions ($r = 2$). Setting $r = 2$, Eqs. (1) and (2) yield concentrations p_α which are close for the two samples (Table I). The difference between the values of ρ and R for the samples could be explained by different degrees of filling their voids. We shall estimate the intrinsic parameters of the material in the voids. In the simplest case, one can expect the conducting material to cover uniformly the surface of the channels and voids. The 3D lattice of voids in the opal can be presented as an array of alternating spheres of two diameters interconnected by cylindrical tubes.[6] The size of the voids can be expressed through one parameter, namely, the radius of the SiO_2 sphere $r_0 = 1000$ Å (the radii of the spherical voids used to simulate the octahedral and tetrahedral pores are $r_1 = 0.414\, r_0$ and $r_2 = 0.23\, r_0$, respectively; the cylindrical channels alternately connecting the spherical voids have a radius $r_3 = 0.155\, r_0$ and length $L = 0.586\, r_0$). We simulated the void system with a cubic lattice made up of spheres of radius r_1 interconnected by tubes $2L + 2r_2$ long and 1.5 r_3 in radius. After such an increase in tube radius, the total void volume amounts to 26%, which corresponds to the void volume in the case of closely packed silica spheres (and is confirmed experimentally). By comparing the known volume percentage of void filling with the size of the voids proper, one can calculate the thickness of the uniform layer on the void walls and the total cross section S_j of the conducting material determining the current density. The true parameters of the void filler, R_p and ρ_p, will now be expressed through the R and ρ of the sample: $R_p = R(S_j/S)$ and $\rho_p = \rho(S_j/S)$, where S is the measured cross section area of the opal sample. Under these conditions, the mobility $u = R/\rho$ will not depend on S_j/S. The values of R_p and ρ_p calculated in this way, as well as the hole concentrations $p_p = e/R_p$, are presented in Table I. We see that the hole concentration calculated by this model for a sample with 82% filling is close to the value of concentration derived from thermopower measurements. At the same time for a sample with a smaller filling (63%) these values differ by a factor of six. This suggests that, at low fillings, the model of uniform void coverage is inapplicable because of disrupted current paths in some of the conducting tubes. For these conditions, the true area S_j becomes smaller than the calcu-

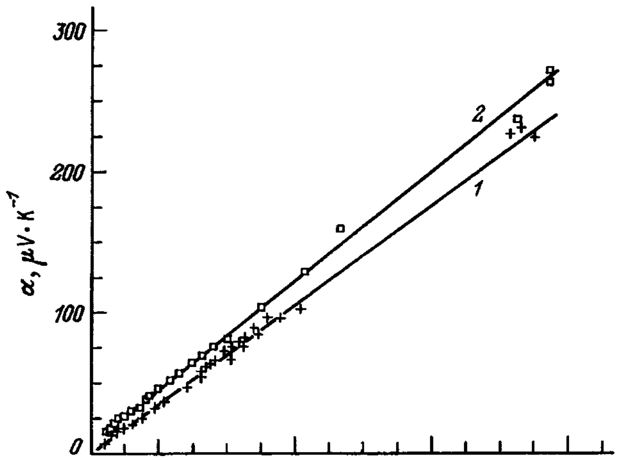

FIG. 2. Temperature dependence of the thermopower of opal samples with PbSe. Same notation as in Fig. 1.

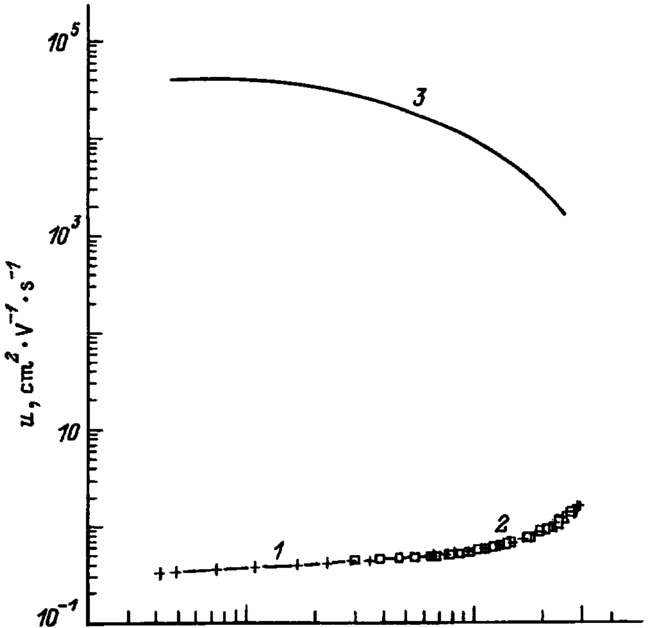

FIG. 3. Temperature dependence of the mobility of opal samples with PbSe. Same notation as in Fig. 1. Curve *3* — mobility for bulk PbSe.[7]

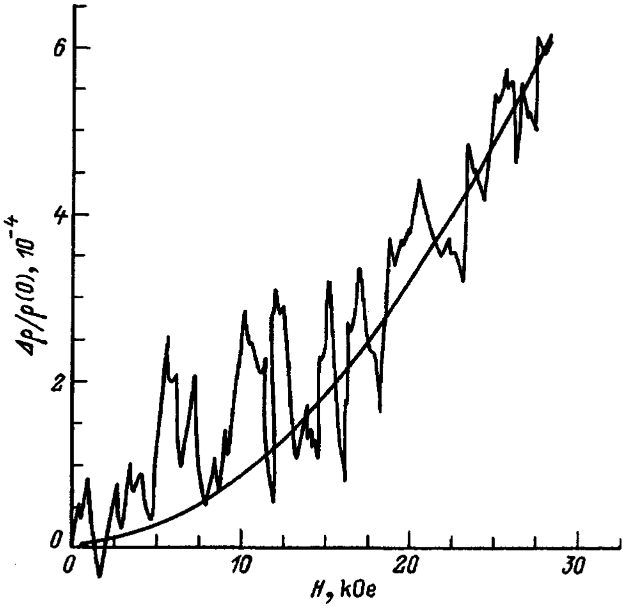

FIG. 4. Magnetoresistance of sample 1 (see Table I) at 77 K.

lated value. The measured R and ρ of the sample increase, whereas α and u remain unaffected by the change in the number of conducting links.

Figure 3 presents also the temperature behavior of the mobility in bulk PbSe (Ref. 7). We readily see that the mobility of PbSe filling the opal voids is several orders of magnitude less than that of the bulk material and that it grows with temperature throughout the temperature range studied. The low mobility leads also to very small values of positive magnetoresistance. As seen from Fig. 4, $\Delta\rho/\rho = [\rho(H) - \rho(0)]/\rho(0) \propto (uH)^2$. A decrease of mobility by a factor three to four compared to the bulk material was observed in lead chalcogenide films and was attributed to the contribution of scattering from point defects and grain boundaries.[8] Relations of the type $u(T) \propto T^{1.5}$, where mobility grows up to room temperature, were demonstrated in very thin (<500 Å) semiconducting films of Te.[9] To explain such an unusual behavior in nanometer-scale objects, one has to invoke, besides scattering from ionized impurities, diffuse scattering from the surface of the insulating matrix as well. Nonuniformities in carrier concentration over the layer thickness due to band warping at a charged surface are capable of contributing to this scattering.[10] This specific mechanism of carrier scattering in opal voids, which results in a sharp drop of mobility, apparently predominates over other mechanisms (including the one involving phonons, which determines mobility decrease with increasing temperature in bulk samples) throughout the temperature range covered here.

The authors are grateful to N. F. Kartenko and N. V. Sharenkova for x-ray diffraction measurements.

Support of the Russian Fund for Fundamental Research (Grants 96-02-16852a and 96-03-32458a) is gratefully acknowledged.

[1] V. N. Bogomolov, V. V. Zhuravlev, Yu. A. Kumzerov, V. P. Petranovskiĭ, S. G. Romanov, and L. V. Samoĭlovich, Fiz. Tverd. Tela (Leningrad) **32**, 365 (1990) [Sov. Phys. Solid State **32**, 186 (1990)].

[2] J. V. Sanders, Nature **204**, 35 (1964).

[3] Yu. I. Ravich, B. A. Efimova, and I. A. Smirnov, *Methods of Semiconductor Investigation as Applied to the Lead Chalcogenides PbTe, PbSe, and PbS* [in Russian] (Nauka, Moscow, 1968), 384 pp.

[4] L. I. Arutyunyan, V. N. Bogomolov, N. F. Kartenko, D. A. Kurdyukov, V. V. Popov, A. V. Prokof'ev, I. A. Smirnov, and N. V. Sharenkova, Fiz. Tverd. Tela (St. Petersburg) **39**, 586 (1997) [Phys. Solid State **39**, 510 (1997)].

[5] B. M. Askerov, *Transport Phenomena in Semiconductors* [in Russian], Nauka, Leningrad (1970), 303 pp.

[6] K. Kh. Babamuratov, V. V. Zhuravlev, Yu. A. Kumzerov, S. G. Romanov, and S. A. Khachaturov, Fiz. Tverd. Tela (St. Petersburg) **35**, 1577 (1993) [Phys. Solid State **35**, 795 (1993)].

[7] R. S. Allgaier and W. W. Scanlon, Phys. Rev. **111**, 1029 (1958).

[8] T. S. Gudkin, I. A. Drabkin, V. I. Kaĭdanov, and O. G. Sterlyadkina, Fiz. Tekh. Poluprovodn. **8**, 2233 (1974) [Sov. Phys. Semicond. **8**, 1453 (1974)].

[9] K. V. Shalimova, V. S. Soldatov, A. A. Smotrakov, V. B. Titov, and O. V. Sapozhnikova, Fiz. Tekh. Poluprovodn. **7**, 1457 (1973) [Sov. Phys. Semicond. **7**, 977 (1973)].

[10] I. R. Schrieffer, Phys. Rev. **97**, 641 (1955).

Translated by G. Skrebtsov